

Walter Lacarbonara
Balakumar Balachandran
Jun Ma · J. A. Tenreiro Machado
Gabor Stepan *Editors*

Nonlinear Dynamics of Structures, Systems and Devices

Proceedings of the First International
Nonlinear Dynamics Conference
(NODYCON 2019), Volume I

Nonlinear Dynamics of Structures, Systems and Devices

@Seismicisolation

Walter Lacarbonara • Balakumar Balachandran
Jun Ma • J. A. Tenreiro Machado • Gabor Stepan
Editors

Nonlinear Dynamics of Structures, Systems and Devices

Proceedings of the First International
Nonlinear Dynamics Conference
(NODYCON 2019), Volume I



Springer

@Seismicisolation

Editors

Walter Lacarbonara 

Department of Structural and Geotechnical
Engineering
Sapienza University of Rome
Rome, Italy

Jun Ma

Department of Physics
Lanzhou University of Technology
Lanzhou, Gansu, China

Gabor Stepan

Department of Applied Mechanics
Budapest University of Technology
and Economics
Budapest, Hungary

Balakumar Balachandran

Department of Mechanical Engineering
University of Maryland
College Park, MD, USA

J. A. Tenreiro Machado

Department of Electrical Engineering
Polytechnic of Porto - School
of Engineering (ISEP)
Porto, Portugal

ISBN 978-3-030-34712-3

ISBN 978-3-030-34713-0 (eBook)

<https://doi.org/10.1007/978-3-030-34713-0>

© Springer Nature Switzerland AG 2020

This work is subject to copyright. All rights are reserved by the Publisher, whether the whole or part of the material is concerned, specifically the rights of translation, reprinting, reuse of illustrations, recitation, broadcasting, reproduction on microfilms or in any other physical way, and transmission or information storage and retrieval, electronic adaptation, computer software, or by similar or dissimilar methodology now known or hereafter developed.

The use of general descriptive names, registered names, trademarks, service marks, etc. in this publication does not imply, even in the absence of a specific statement, that such names are exempt from the relevant protective laws and regulations and therefore free for general use.

The publisher, the authors, and the editors are safe to assume that the advice and information in this book are believed to be true and accurate at the date of publication. Neither the publisher nor the authors or the editors give a warranty, expressed or implied, with respect to the material contained herein or for any errors or omissions that may have been made. The publisher remains neutral with regard to jurisdictional claims in published maps and institutional affiliations.

This Springer imprint is published by the registered company Springer Nature Switzerland AG.

The registered company address is: Gewerbestrasse 11, 6330 Cham, Switzerland

@Seismicisolation

Preface

This volume is part of three volumes collecting the *Proceedings of the First International Nonlinear Dynamics Conference (NODYCON 2019)* held in Rome, February 17–20, 2019. NODYCON was launched to foster the tradition of the conference series originally established by Prof. Ali H. Nayfeh in 1986 at Virginia Polytechnic Institute and State University (Virginia Tech), Blacksburg, VA, USA, as the Nonlinear Vibrations, Stability, and Dynamics of Structures Conference. With the passing in 2017 of Prof. Nayfeh, who was also the founder of the Springer journal *Nonlinear Dynamics* in 1990, NODYCON 2019 was organized as a collective tribute of the community to Prof. Nayfeh for being one of the most influential leaders of nonlinear dynamics. NODYCON 2019 was also established to look to and dream about the future. The call for papers attracted contributions dealing with established nonlinear dynamics research topics as well as with the latest trends and developments. At the same time, to reflect the rich spectrum of topics covered by the journal *Nonlinear Dynamics*, the call included diverse and multidisciplinary topics, to mention a few, multi-scale dynamics, experimental dynamics, dynamics of structures/industrial machines/equipment/facilities, dynamics of adaptive, multifunctional, metamaterial structures, dynamics of composite/nanocomposite structures, reduced-order modeling, nonsmooth dynamics, fractional-order system dynamics, nonlinear interactions and parametric vibrations, computational techniques, nonlinear system identification, dynamics of NEMS/MEMS/nanomaterials, multibody dynamics, fluid/structure interaction, influence of nonlinearities on vibration control systems, human–machine interaction, nonlinear wave propagation in discrete and continuous media, chaotic map-based cryptography, ecosystem dynamics, social media dynamics, complexity in engineering, and network dynamics.

For NODYCON 2019, the organizers received 450 two-page abstracts and based on 467 reviews from the Program Committee, the Steering and Advisory Committees, and external reviewers, 391 papers and 17 posters were accepted, published in the Book of Abstracts (NODYS Publications, Rome, ISBN 978-88-944229-0-0), and presented by nearly 400 participants from 68 countries. The diverse topics covered by the papers were organized along four major themes to organize the technical sessions:

- (a) Concepts and methods in nonlinear dynamics
- (b) Nonlinear dynamics of mechanical and structural systems
- (c) Nonlinear dynamics and control
- (d) Recent trends in nonlinear dynamics

The authors of a selection of approximately 60 papers were invited to publish in the Special Issue of *Nonlinear Dynamics* entitled “NODYCON 2019 First International Nonlinear Dynamics Conference.” Over 200 full papers were submitted to the *Proceedings of the First International Nonlinear Dynamics Conference* (NODYCON 2019) and only 121 of them were accepted. These papers have been collected into three volumes, which are listed below together with a sub-topical organization.

Volume 1: Nonlinear Dynamics of Structures, Systems, and Devices

- (a) Methods for nonlinear dynamics
- (b) Bifurcations and nonsmooth systems
- (c) Nonlinear phenomena in mechanical systems and structures
- (d) Experimental dynamics, system identification and monitoring
- (e) Fluid–structure interaction, multibody system dynamics
- (f) Turning processes, rotating systems, and systems with time delays

Volume 2: Nonlinear Dynamics and Control

- (g) Vibration absorbers and isolators
- (h) Control of nonlinear systems
- (i) Sensors and actuators
- (j) Network synchronization

Volume 3: New Trends in Nonlinear Dynamics

- (k) Smart materials, metamaterials, composite and nanocomposite materials, and structures
- (l) MEMS/NEMS and energy harvesters
- (m) Nonlinear phenomena in bio- and ecosystem dynamics
- (n) Chaos in electronic systems
- (o) Fractional-order systems

I wish to acknowledge the work of the Co-Editors of the NODYCON 2019 Proceedings: Prof. Balakumar Balachandran (University of Maryland, College Park, MD, USA), Prof. Jun Ma (Lanzhou University of Technology, China), Prof. J. A. Tenreiro Machado (Instituto Superior de Engenharia do Porto, Portugal), Prof. Gabor Stepan (Budapest University of Technology and Economics, Hungary).

The success of NODYCON 2019 relied primarily on the efforts, talent, energy, and enthusiasm of researchers in the field of nonlinear dynamics who wrote and submitted these papers. Special praise is also deserved for the reviewers who invested significant time in reading, examining, and assessing multiple papers, thus ensuring a high standard of quality for this conference proceedings.

Rome, Italy
August 2019

Walter Lacarbonara

Preface for Volume 1: Nonlinear Dynamics of Structures, Systems, and Devices

Volume 1 of the NODYCON Proceedings is composed of 55 papers, which are spread across the following groupings: (a) methods for nonlinear dynamics (8 papers), (b) bifurcations and nonsmooth systems (8 papers), (c) nonlinear phenomena in mechanical systems and structures (12 papers), (d) experimental dynamics, system identification, and monitoring (8 papers), (e) fluid–structure interaction and multibody system dynamics (9 papers), and (f) turning processes, rotating systems, and systems with time delays (10 papers). It is acknowledged that a paper placed in one grouping could have easily been placed in another grouping as well. As one reads through these 55 contributions, one will note the use of a wide range of experimental, analytical, and numerical techniques for study of the nonlinear dynamics of a wealth of systems across different length and time scales.

In the work of N. Potosakis, E. Paraskevopoulos, and S. Natsiavas, an augmented Lagrangian formulation is used to construct models of nonlinear mechanical systems such as vehicle systems subjected to bilateral scleronomous motion constraints. A. O. Belyakov and A. P. Seyranian study domains of stability for parametrically excited systems by using high-order approximations of the monodromy matrix. A. Liu and D. Wagg examine normal form analysis for a two-degree-of-freedom system. E. Kremer investigates system vibratory responses to amplitude-modulated and phase-modulated excitations. A. M. Bersani, A. Borri, A. Milanesi, G. Tomassetti, and P. Vellucci summarize some recent results obtained from studies of the asymptotic properties of important enzyme reactions. Z. Wang, Z. Tang, J. H. Park, and Y. Wang study system modeling for the Hammerstein nonlinear model with unknown but bounded noise. For strongly nonlinear systems, H.-E. Du, G.-K. Er, and V. P. Lu consider construction of frequency-response curves and determination of unstable response regions. Soliton solutions of the Korteweg-de Vries equation are investigated by S. Carillo, M. L. Schiavo, and C. Schiebold.

Two types of bifurcations related to limit directions of nonsmooth vector fields are examined by M. Anatali and G. Stepan. S. Natsiavas and E. Paraskevopoulos study dynamics of multibody systems experiencing impacts with friction. H. Xu and J. Ji use state feedback control to create Neimark–Sacker bifurcation in a vibro-impact system. H. Z. Horvath and D. Takacs consider the stability of suitcases

and trailers that are subjected to non-holonomic constraints. I. D. Atanasovska, K. R. Hedrih, and D. B. Momcilovic study the vibro-impact dynamics of spur gears with wear. M. Ramírez, J. Collado, and F. Dohnal provide an efficient means for computing the stability transition curves of coupled Mathieu equations. M. Yadav, S. S. Chaurasia, and S. Sinha study the symmetry in a group of Stuart–Landau oscillators; in particular, with regard to oscillation death states. Dynamics and bifurcations of solutions of the so-called Sprott A system are studied by M. Messias and A. C. Reinol.

J. Awrejcewicz, R. Starosta, and G. Sypniewska-Kamińska examine the dynamics of a three-degree-of-freedom pendulum-spring-damper system in the presence of an external resonance and a two-to-one internal resonance. In the presence of internal resonances, the influence of initial geometric imperfections on the dynamics of a slender cylindrical panel nonlinear response is investigated by F. M. A. Silva, W. A. Vaz, and P. B. Gonçalves. M. Farid and O. V. Gendelman treat sloshing dynamics in partially filled storage tanks. Free oscillations of arbitrarily sagged and inclined cables oscillating around a catenary static profile are studied by A. Mansour, G. Rega, and O. B. Mekki. Nonlinear interactions between flexural and sway oscillations of a laterally braced column are examined by D. Orlando, J. M. P. Raimundo, and P. B. Gonçalves. The influence of temperature on cable dynamics under different excitations is considered by Y. Zhao, H. Lin, L. Chen, and Z. Guo. Behavior of a harmonically forced nonlinear system with a shape memory alloy-based spring is investigated by S. Ramnarace and J. Bridge. Static behavior and free oscillations of shallow circular arches are treated by U. Eroglu and G. Ruta. G. Liu and W. Zhang investigate the response of a composite cantilever plate placed in a subsonic air flow and study the frequency response of this system. A hysteresis damper is examined by D. Li and H. Fang. Nonlinear oscillations of an axially excited beam embedded in a viscoelastic medium are treated by E. Babilio. Energy localization in a chain of coupled, nonlinear oscillators is investigated by A. Kovaleva.

N. Barbieri, M. J. Mannala, R. Barbieri, and G. Barbieri use experimental data based on torsional response to tune nonlinear models of transmission line cables. Nonlinear, stochastic dynamics of a Duffing oscillator are studied by L. G. G. Villani, S. Silva, and A. Cunha, Jr. Hysteretic behavior of wire rope isolators is considered by N. Vaiana, F. Marmo, S. Sessa, and L. Rosati. Nonlinear behavior of rubber shear springs is experimentally examined by S. Gong, S. Oberst, and X. Wang. Experimental studies on the responses of a six-degree-of-freedom parallel manipulator are reported by K. Ringgaard and O. Balling. N. Cavalagli, M. Ciano, G. Fagotti, M. Gioffrè, V. Gusella, and C. Pepi discuss experimental investigations into the dynamic response of a two-storey masonry structure mounted on a shaker table and subjected to a transient excitation with a strong vertical component. Rate dependence of a hysteretic device is experimentally investigated and characterized by M. Antonelli, B. Carboni, W. Lacarbonara, D. Bernardini, and T. Kalmár-Nagy. K. R. Hedrih, S. V. Brčić, and S. Paunović discuss the use of photoelasticity for nonlinear dynamic studies for different applications, including dams.

A combined analytical, experimental, and numerical investigation is used to explore the dynamics of an acoustically levitated sphere by A. Dolev and I. Bucher. Vortex-induced vibrations are studied by V. Kurushina, E. Pavlovskaia, A. Postnikov, G. R. Franzini, and M. Wiercigroch. C. Mannini studies vortex-induced vibrations and galloping dynamics of a cylinder with a rectangular cross section. Dynamics of an aeroelastic system is investigated by C. Demartino, G. Matteoni, and C. T. Georgakis. Computational dynamics of a multibody system in a vertical fluid flow is the subject of the work of Z. Terze, V. Pandža, and D. Zlatar. M. Eugeni, F. Mastroddi, and F. Saltari examine damping models used in flutter analysis of highly flexible aircraft. P. Rosatelli, W. Lacarbonara, A. Arena, and D. J. Inman examine morphing wing dynamics by using computational means. Multibody dynamic studies are carried out by P. Masarati, A. Zanoni, V. Muscarello, R. Paolini, and G. Quaranta to understand how the interactions between the vehicle dynamics and human biomechanics affect helicopter's handling qualities. The use of absolute nodal coordinate formulation for studies of thin plate dynamics is examined by K.-W. Kim, J.-W. Lee, J.-S. Jang, J.-H. Kang, and W.-S. Yoo.

Chatter in turning process is the subject matter of the work presented by B. Beri and G. Stepan. Aperiodic dynamics of spinning shafts with varying rotation speeds are studied by F. Georgiades. M. A. AL-Shudeifat and C. Nataraj study backward whirling of a rotor with fatigue cracks. Inner race defects in rolling element bearings are treated by T. H. Mohamad, S. Ilbeigi, and C. Nataraj. Turning process dynamics are studied by A. Gouskov, G. Panovko, and D. D. Tung. A. Wang, W. Jin, and Q. Lin investigate regenerative effects and friction force effects on chatter during turning operations. Y. Jin and P. Xu study noise-induced transitions in a triple well potential system with a time delay. Dimension reduction for rotor dynamic studies is the topic of the work of K. Lu, H. Zhang, H. Zhou, Y. Jin, Y. Yang, and C. Fu. Drum-type washing machines are studied by C. Baykal, E. Cigeroglu, and Y. Yazicioglu. Wear effects in hydrodynamic bearings used in rotating systems are examined by T. J. Machado and G. C. Stroti.

In conclusion, this volume represents a multifaceted cross section of recent advances in computational methods for nonlinear dynamics, bifurcations, nonlinear phenomena in mechanical systems and structures, experimental dynamics, nonlinear system identification, fluid–structure interaction and multibody system dynamics, turning processes, rotating systems, and nonsmooth system dynamics including systems with time delays. We hope that readers will benefit from the rich work portrayed here on nonlinear dynamics of structures, systems, and devices and that new ideas and future contributions will be inspired.

Rome, Italy
College Park, MD, USA
Lanzhou, China
Porto, Portugal
Budapest, Hungary
August 2019

Walter Lacarbonara
Balakumar Balachandran
Jun Ma
J. A. Tenreiro Machado
Gabor Stepan

Contents

Part I Methods for Nonlinear Dynamics

Nonlinear Dynamics of Multibody Systems Using an Augmented Lagrangian Formulation	3
Nikolaos Potosakis, Elias Paraskevopoulos, and Sotirios Natsiavas	
Stability Boundary Approximation of Periodic Dynamics	13
Anton O. Belyakov and Alexander P. Seyranian	
ϵ^2-Order Normal Form Analysis for a Two-Degree-of-Freedom Nonlinear Coupled Oscillator.....	25
Xuanang Liu and David J. Wagg	
Vibrational Mechanics of Systems with Amplitude and Phase Modulation of Excitation	35
Eugen Kremer	
Singular Perturbation Techniques and Asymptotic Expansions for Some Complex Enzyme Reactions	43
Alberto Maria Bersani, Alessandro Borri, Alessandro Milanesi, Giovanna Tomassetti, and Pierluigi Vellucci	
A Novel Two-Stage Ellipsoid Filtering Based System Modeling Algorithm for a Hammerstein Nonlinear Model with an Unknown Noise Term	55
Ziyun Wang, Ze Tang, Ju H. Park, and Yan Wang	
A New Method for the Frequency Response Curve and Its Unstable Region of a Strongly Nonlinear Oscillator	65
Hai-En Du, Guo-Kang Er, and Vai Pan Iu	
Matrix Soliton Solutions of the Modified Korteweg–de Vries Equation ...	75
Sandra Carillo, Mauro Lo Schiavo, and Cornelia Schiebold	

Part II Bifurcations and Nonsmooth Systems

Bifurcations of Limit Directions at Codimension-2 Discontinuities of Vector Fields	87
Mate Antali and Gabor Stepan	
Boundary Layer Dynamics of Multibody Systems Involving Impact and Friction	97
Sotirios Natsiavas and Elias Paraskevopoulos	
Creation of Neimark-Sacker Bifurcation for a Three-Degree-of-Freedom Vibro-Impact System with Clearances	107
Huidong Xu and Jinchen Ji	
Analogue Models of Rocking Suitcases and Snaking Trailers	117
Zoltan Horvath and Denes Takacs	
A Theoretical Model for Vibro-Impact Dynamics of Spur Gears with Tooth Flanks Wear	127
Ivana D. Atanasovska, Katica R. (Stevanović) Hedrih, and Dejan B. Momcilovic	
Stability of Coupled and Damped Mathieu Equations Utilizing Symplectic Properties	137
Miguel Ramírez Barrios, Joaquín Collado, and Fadi Dohnal	
Asymmetry in the Basin Stability of Oscillation Death States Under Variation of Environment-Oscillator Links	147
Manish Yadav, Sudhanshu Shekhar Chaurasia, and Sudeshna Sinha	
The Occurrence of Zero-Hop Bifurcation in a Generalized Sprott A System	157
Marcelo Messias and Alisson C. Reinol	
Part III Nonlinear Phenomena in Mechanical Systems and Structures	
External and Internal Resonances in a Mass-Spring-Damper System with 3-dof	169
Jan Awrejcewicz, Roman Starosta, and Grażyna Sypniewska-Kamińska	
Internal Resonances in an Imperfect Circular Cylindrical Panel	179
Frederico M. A. Silva, Wanclaine A. Vaz, and Paulo B. Gonçalves	
Weakly Nonlinear Liquid Sloshing: Modelling and Exploration of Response Regimes	187
Maor Farid and Oleg V. Gendelman	
Catenary-Based Nonlinear Multimodal Theory of Cable Free Vibrations	197
Achref Mansour, Giuseppe Rega, and Othman Ben Mekki	

Flexural and Sway Interaction in the Nonlinear Vibrations of a Phenomenological Model of a Laterally Braced Column.....	207
Diego Orlando, Juliana M. P. Raimundo, and Paulo B. Gonçalves	
Influences of Temperature on Dynamic Behaviors of Suspended Cables Under Primary and Sub-Harmonic Excitations Simultaneously ..	217
Yaobing Zhao, Henghui Lin, Lincong Chen, and Zixiong Guo	
Analysis of a Shape Memory Alloy Spring System Under Harmonic Excitation	227
Shivan Ramnarace and Jacqueline Bridge	
Vibration of Pre-Loaded Shallow Circular Arches.....	237
Uğurcan Eroğlu and Giuseppe Ruta	
Nonlinear Vibration Responses of Laminated Composite Cantilever Plate in Subsonic Air Flow	247
Gen Liu and Wei Zhang	
Adaptation of Energy Dissipation in a Laminated Module with Tunable Twin Wells	257
Dejian Li and Hui Fang	
The Duffing–Mathieu Equation Arising from Dynamics of Post-Buckled Beams	267
Enrico Babilio	
Resonance-Induced Energy Localization in Weakly Dissipative Anharmonic Chains	277
Agnessa Kovaleva	
Part IV Experimental Dynamics, System Identification and Monitoring	
Torsional Analysis of Transmission Line Cables	289
Nilson Barbieri, Marcos José Mannala, Renato Barbieri, and Gabriel de Sant'Anna Vitor Barbieri	
Application of a Stochastic Version of the Restoring Force Surface Method to Identify a Duffing Oscillator	299
Luis G. G. Villani, Samuel da Silva, and Americo Cunha Jr.	
Modeling of the Hysteretic Behavior of Wire Rope Isolators Using a Novel Rate-Independent Model	309
Nicolò Vaiana, Francesco Marmo, Salvatore Sessa, and Luciano Rosati	
A Non-linear Model of Rubber Shear Springs Validated by Experiments	319
Sanpeng Gong, Sebastian Oberst, and Xinwen Wang	

Operational Modal Analysis on a Six-Degree-of-Freedom Parallel Manipulator: Reproducibility, Excitation and Pose Dependency	329
Kasper Ringgaard and Ole Balling	
Shaking Table Investigation on the Masonry Structures Behaviour to Earthquakes with Strong Vertical Component	337
Nicola Cavalagli, Matteo Ciano, Gianluca Fagotti, Massimiliano Gioffrè, Vittorio Gusella, and Chiara Pepi	
Quantifying Rate-Dependence of a Nonlinear Hysteretic Device	347
Marco Antonelli, Biagio Carboni, Walter Lacarbonara, Davide Bernardini, and Tamás Kalmár-Nagy	
Application of Photoelasticity to Some Nonlinear Dynamic Problems and Stress State Analysis in Dams: A Brief Overview Inspired by the Results of Prof. Vlatko Brčić	357
Katica R. (Stevanović) Hedrih, Stanko V. Brčić, and Stepa Paunović	
Part V Fluid–Structure Interaction, Multibody System Dynamics	
Levitated and Parametrically Excited Sphere Dynamics in a Single-Axis Ultrasonic Levitator	369
Amit Dolev and Izhak Bucher	
Modelling VIV of Transversally Oscillating Rigid Structures Using Nonlinear Fluid Oscillators	379
Victoria Kurushina, Ekaterina Pavlovskaya, Andrey Postnikov, Guilherme Rosa Franzinzi, and Marian Wiercigroch	
Asymptotic Analysis of a Dynamical System for Vortex-Induced Vibration and Galloping	389
Claudio Mannini	
A Quasi-Steady 3-DoFs Sectional Aerodynamic Model: Preliminary Results	399
Cristoforo Demartino, Giulia Matteoni, and Christos T. Georgakis	
Lie Group Dynamics of Multibody System in Vortical Fluid Flow	409
Zdravko Terze, Viktor Pandža, and Dario Zlatar	
Damping Models in Aircraft Flutter Analyses	419
Marco Eugeni, Franco Mastroddi, and Francesco Saltari	
Dynamic Response of a Morphing Wing	429
Patrizio Rosatelli, Walter Lacarbonara, Andrea Arena, and Daniel J. Inman	
Helicopter Pilot Biomechanics by Multibody Analysis	439
Pierangelo Masarati, Andrea Zanon, Vincenzo Muscarello, Rita Paolini, and Giuseppe Quaranta	

Derivation of Non-dimensional Equation of Motion for Thin Plate in Absolute Nodal Coordinate Formulation.....	449
Kun-Woo Kim, Jae-Wook Lee, Jin-Seok Jang, Ji-Heon Kang, and Wan-Suk Yoo	
Part VI Turning Processes, Rotating Systems, and Systems with Time Delays	
Approximated Dynamics of Chatter in Turning Processes	463
Bence Beri and Gabor Stepan	
Chaotic Dynamics in Spinning Shafts with Non-constant Rotating Speed Described by Variant Lyapunov Exponents	471
Fotios Georgiades	
Post-Resonance Backward Whirl in a Jeffcott Rotor with a Breathing Crack Model	485
Mohammad A. Al Shudeifat and C. Nataraj	
Proper and Smooth Orthogonal Decompositions for Detection of Inner Race Defects in Rolling Element Bearings with Variable Rotational Speeds	493
Turki H. Mohamad, Shahab Ilbeigi, and C. Nataraj	
Effect of the Compliance of the Part on the Double-Turning Process.....	503
Alexander Gouskov, Grigory Panovko, and Dinh Duc Tung	
Effect of the Regenerative and Frictional Force on Chatter in Turning Process	513
An Wang, Wuyin Jin, and Qian Lin	
Noise-Induced Transitions and Resonances in a Delayed Triple-Well Potential System	523
Yanfei Jin and Pengfei Xu	
Application of the Second Dimension Reduction Method in Nonlinear Rotor Dynamic System.....	533
Kuan Lu, Haopeng Zhang, Hao Zhou, Yulin Jin, Yongfeng Yang, and Chao Fu	
Vibration Analysis of Washing Machines in the Drum Plane	549
Cem Baykal, Ender Cigeroglu, and Yiğit Yazıcıoğlu	
Nonlinear Model for Wear Effects in Hydrodynamic Bearings Applied to Rotating Systems	561
Tiago Henrique Machado and Gustavo Chaves Storti	
Author Index.....	569
Subject Index	583

Contributors

Mohammad A. Al Shudeifat Department of Aerospace Engineering, Khalifa University, Abu Dhabi, UAE

Mate Antali Budapest University of Technology and Economics, Budapest, Hungary

Marco Antonelli Department of Structural and Geotechnical Engineering, Sapienza University of Rome, Rome, Italy

Andrea Arena Department of Structural and Geotechnical Engineering, Sapienza University of Rome, Rome, Italy

Ivana D. Atanasovska Mathematical Institute of the Serbian Academy of Sciences and Arts, Belgrade, Serbia

Jan Awrejcewicz Department of Automation Biomechanics and Mechatronics, Lodz University of Technology, Lodz, Poland

Enrico Babilio Department of Structures for Engineering and Architecture (DiSt), University of Naples “Federico II”, Naples, Italy

Balakumar Balachandran Department of Mechanical Engineering, University of Maryland, College Park, MD, USA

Ole Balling Mechanical and Materials Engineering, Department of Engineering, Aarhus University, Aarhus, Denmark

Nilson Barbieri Pontifícia Universidade Católica do Paraná-PUCPR, Curitiba, Paraná, Brazil

Universidade Tecnológica Federal do Paraná-UTFPR, Curitiba, Paraná, Brazil

Renato Barbieri Universidade do Estado de Santa Catarina-UDESC, Joinville, Santa Catarina, Brazil

Cem Baykal Middle East Technical University, Ankara, Turkey

Anton O. Belyakov Moscow School of Economics, Lomonosov Moscow State University, Moscow, Russia

National Research Nuclear University “MEPhI”, Moscow, Russia

Central Economics and Mathematics Institute, Russian Academy of Sciences, Moscow, Russia

Bence Beri Department of Applied Mechanics, Budapest University of Technology and Economics, Budapest, Hungary

Davide Bernardini Department of Structural and Geotechnical Engineering, Sapienza University of Rome, Rome, Italy

Alberto Maria Bersani Department of Mechanical and Aerospace Engineering, Sapienza University, Roma, Italy

Alessandro Borri Institute for System Analysis and Computer Science “Antonio Ruberti”, Roma, Italy

Stanko V. Brčić Faculty of Civil Engineering, University of Belgrade, Belgrade, Serbia

Jacqueline Bridge Department of Mechanical and Manufacturing Engineering, The University of the West Indies, St. Augustine, Trinidad and Tobago

Izhak Bucher Faculty of Mechanical Engineering, Technion—Israel Institute of Technology, Haifa, Israel

Biagio Carboni Department of Structural and Geotechnical Engineering, Sapienza University of Rome, Rome, Italy

Sandra Carillo Università di Roma “La Sapienza”, Dip. S.B.A.I., Rome, Italy
I.N.F.N.—Sezione Roma1, Gr. IV—M.M.N.L.P., Rome, Italy

Nicola Cavalagli Department of Civil and Environmental Engineering, University of Perugia, Perugia, Italy

Sudhanshu Shekhar Chaurasia Indian Institute of Science Education and Research (IISER), Mohali, Punjab, India

Lincong Chen College of Civil Engineering, Huaqiao University, Xiamen, Fujian, China

Matteo Ciano Department of Civil and Environmental Engineering, University of Perugia, Perugia, Italy

Ender Cigeroglu Middle East Technical University, Ankara, Turkey

Joaquín Collado Automatic Control Department, CINVESTAV, México City, México

Americo Cunha Jr. UERJ—Universidade do Estado do Rio de Janeiro, NUMERICO—Nucleus of Modeling and Experimentation with Computers, Rio de Janeiro, Brazil

Samuel da Silva UNESP – Universidade Estadual Paulista, Faculdade de Engenharia, Departamento de Engenharia Mecânica, São Paulo, Brazil

Cristoforo Demartino Department of Energy, Environment, and Infrastructure Sciences, Zhejiang University–University of Illinois (ZJUI), Zhejiang University, Haining, China

Gabriel de Sant'Anna Vitor Barbieri Pontifícia Universidade Católica do Paraná-PUCPR, Curitiba, Paraná, Brazil
Universidade Tecnológica Federal do Paraná-UTFPR, Curitiba, Paraná, Brazil

Fadi Dohnal Division for Mechatronics Lienz, UMIT – Private University for Health Sciences, Medical Informatics and Technology, Lienz, Austria

Amit Dolev Faculty of Mechanical Engineering, Technion—Israel Institute of Technology, Haifa, Israel

Hai-En Du Department of Civil and Environmental Engineering, University of Macau, Macau SAR, China

Guo-Kang Er Department of Civil and Environmental Engineering, University of Macau, Macau SAR, China

Ügurcan Eroğlu Istanbul Technical University, Istanbul, Turkey

Marco Eugeni Department of Mechanical and Aerospace Engineering, Sapienza University of Rome, Rome, Italy

Gianluca Fagotti Ufficio Speciale Ricostruzione Umbria, Foligno, Italy

Hui Fang Institute of Coastal and Ocean Engineering, School of Engineering, Ocean University of China, Qingdao, China

Maor Farid Faculty of Mechanical Engineering, Technion—Israel Institute of Technology, Haifa, Israel

Guilherme Rosa Franzini Offshore Mechanics Laboratory, Escola Politécnica, University of São Paulo, São Paulo, Brazil

Chao Fu Institute of Vibration Engineering, Northwestern Polytechnical University, Xi'an, P. R. China

MIIT Key Laboratory of Dynamics and Control of Complex Systems, Northwestern Polytechnical University, Xi'an, P. R. China

Oleg V. Gendelman Faculty of Mechanical Engineering, Technion—Israel Institute of Technology, Haifa, Israel

Christos T. Georgakis Department of Engineering-Structural Monitoring and Dynamics, Aarhus University, Aarhus, Denmark

Fotios Georgiades School of Engineering, College of Science, University of Lincoln, Lincoln, UK

Massimiliano Gioffrè Department of Civil and Environmental Engineering, University of Perugia, Perugia, Italy

Paulo B. Gonçalves Department of Civil Engineering, Pontifical Catholic University, Rio de Janeiro, Brazil

Sanpeng Gong School of Chemical and Environmental Engineering, China University of Mining and Technology, Beijing, China

Center for Audio, Acoustics and Vibration, University of Technology, Sydney, NSW, Australia

Alexander Gouskov Mechanical Engineering Research Institute of Russian Academy of Sciences, Moscow, Russia

Zixiong Guo College of Civil Engineering, Huaqiao University, Xiamen, Fujian, China

Vittorio Gusella Department of Civil and Environmental Engineering, University of Perugia, Perugia, Italy

Zoltan Horvath Department of Applied Mechanics, Budapest University of Technology and Economics, Budapest, Hungary

Shahab Ilbeigi Villanova Center for Analytics of Dynamic Systems, Villanova University, Villanova, PA, USA

Daniel J. Inman Department of Aerospace Engineering, University of Michigan, Ann Arbor, MI, USA

Vai Pan Iu Department of Civil and Environmental Engineering, University of Macau, Macau SAR, China

Jin-Seok Jang Korea Institute of Industrial Technology, Daegu, South Korea

Jincheng Ji University of Technology Sydney, Broadway, NSW, Australia

Wuyin Jin School of Mechanical and Electronical Engineering, Lanzhou University of Technology, Lanzhou, China

Yanfei Jin Department of Mechanics, Beijing Institute of Technology, Beijing, China

Yulin Jin School of Aeronautics and Astronautics, Sichuan University, Chengdu, P. R. China

Tamás Kalmár-Nagy Department of Fluid Mechanics, Faculty of Mechanical Engineering, University of Technologies and Economics, Budapest, Hungary

Ji-Heon Kang Pusan National University, Busan, South Korea

Kun-Woo Kim Korea Institute of Industrial Technology, Daegu, South Korea

Agnessa Kovaleva Space Research Institute, Moscow, Russia

Eugen Kremer Schaeffler Automotive Buehl GmbH & Co. KG, Buehl, Baden, Germany

Institute for Problems in Mechanical Engineering of Russian Academy of Sciences, St. Petersburg, Russia

Victoria Kurushina Department of Transport of Hydrocarbon Resources, Institute of Transport, Industrial University of Tyumen, Tyumen, Russia

Centre for Applied Dynamics Research, School of Engineering, University of Aberdeen, Kings' College, Aberdeen, Scotland, United Kingdom

Walter Lacarbonara Department of Structural and Geotechnical Engineering, Sapienza University of Rome, Rome, Italy

Jae-Wook Lee Korea Institute of Industrial Technology, Daegu, South Korea

Dejian Li Institute of Coastal and Ocean Engineering, School of Engineering, Ocean University of China, Qingdao, China

Henghui Lin College of Civil Engineering, Huaqiao University, Xiamen, Fujian, China

Qian Lin Editorial Department of Journal of Lanzhou University of Technology, Lanzhou University of Technology, Lanzhou, China

Gen Liu Beijing Key Laboratory of Nonlinear Vibrations and Strength of Mechanical, College of Mechanical Engineering, Beijing University of Technology, Beijing, P. R. China

Xuanang Liu Department of Mechanical Engineering, University of Sheffield, Sheffield, UK

Kuan Lu Institute of Vibration Engineering, Northwestern Polytechnical University, Xi'an, P. R. China

MIIT Key Laboratory of Dynamics and Control of Complex Systems, Northwestern Polytechnical University, Xi'an, P. R. China

Jun Ma Department of Physics, Lanzhou University of Technology, Lanzhou, Gansu, China

Tiago Henrique Machado Department of Integrated Systems, School of Mechanical Engineering, University of Campinas, Campinas, Brazil

J. A. Tenreiro Machado Department of Electrical Engineering, Polytechnic of Porto - School of Engineering (ISEP), Porto, Portugal

Marcos José Mannala Instituto de Tecnologia para o Desenvolvimento-LACTEC, Curitiba, Paraná, Brazil

Claudio Mannini CRIACIV-Department of Civil and Environmental Engineering, University of Florence, Florence, Italy

Achref Mansour Université de Tunis El Manar, Ecole Nationale d'Ingénieurs de Tunis LGC, Tunis, Tunisia

University Grenoble Alpes, Inria, CNRS, Grenoble INP, LJF, Grenoble, France

Francesco Marmo Department of Structures for Engineering and Architecture, University of Naples Federico II, Naples, Italy

Pierangelo Masarati Department of Aerospace Science and Technology, Politecnico di Milano, Milano, Italy

Franco Mastroddi Department of Mechanical and Aerospace Engineering, Sapienza University of Rome, Rome, Italy

Giulia Matteoni Arup, London, UK

Othman Ben Mekki Université de Tunis El Manar, Ecole Nationale d'Ingénieurs de Tunis, LGC, Tunis, Tunisia

Marcelo Messias Universidade Estadual Paulista (UNESP), Faculdade de Ciências e Tecnologia, Departamento de Matemática e Computação, Presidente Prudente, SP, Brazil

Alessandro Milanesi Department of Basic and Applied Sciences for Engineering, Sapienza University, Roma, Italy

Turki H. Mohamad Villanova Center for Analytics of Dynamic Systems, Villanova University, Villanova, PA, USA

Dejan B. Momcilovic Institute for Testing of Materials-IMS Institute, Belgrade, Serbia

Vincenzo Muscarello Department of Aerospace Science and Technology, Politecnico di Milano, Milano, Italy

C. Nataraj Department of Mechanical Engineering, Villanova Center for Analytics of Dynamic Systems, Villanova University, Villanova, PA, USA

Sotirios Natsiavas Department of Mechanical Engineering, Aristotle University, Thessaloniki, Greece

Sebastian Oberst Center for Audio, Acoustics and Vibration, University of Technology, Sydney, NSW, Australia

Diego Orlando State University of Rio de Janeiro, Rio de Janeiro, Brazil

Viktor Pandža Chair of Flight Vehicle Dynamics, Faculty of Mechanical Engineering and Naval Architecture, University of Zagreb, Zagreb, Croatia

Grigory Panovko Mechanical Engineering Research Institute of Russian Academy of Sciences, Moscow, Russia

Rita Paolini Department of Aerospace Science and Technology, Politecnico di Milano, Milano, Italy

Elias Paraskevopoulos Department of Mechanical Engineering, Aristotle University, Thessaloniki, Greece

Ju H. Park Department of Electrical Engineering, Yeungnam University, Kyongsan, Republic of Korea

Stepa Paunović Department of Mechanics, Mathematical Institute of the Serbian Academy of Sciences and Arts, Belgrade, Serbia

Ekaterina Pavlovskaya Centre for Applied Dynamics Research, School of Engineering, University of Aberdeen, Kings' College, Aberdeen, Scotland, United Kingdom

Chiara Pepi Department of Civil and Environmental Engineering, University of Perugia, Perugia, Italy

Andrey Postnikov School of Engineering, University of Lincoln, Lincoln, United Kingdom

Nikolaos Potosakis Department of Mechanical Engineering, Aristotle University, Thessaloniki, Greece

Giuseppe Quaranta Department of Aerospace Science and Technology, Politecnico di Milano, Milano, Italy

Juliana M. P. Raimundo Pontifical Catholic University of Rio de Janeiro, Rio de Janeiro, Brazil

Miguel Ramírez Barrios Professional Interdisciplinary Unit of Biotechnology, National Polytechnic Institute, Mexico City, México

Shivan Ramnarace Department of Mechanical and Manufacturing Engineering, The University of the West Indies, St. Augustine, Trinidad and Tobago

Giuseppe Rega Dipartimento di Ingegneria Strutturale e Geotecnica, Università di Roma La Sapienza, Roma, Italy

Alisson C. Reinol Universidade Tecnológica Federal do Paraná (UTFPR), Departamento Acadêmico de Matemática, Apucarana, PR, Brazil

Kasper Ringgaard Mechanical and Materials Engineering, Department of Engineering, Aarhus University, Aarhus, Denmark

Patrizio Rosatelli Sapienza University of Rome, Rome, Italy

Luciano Rosati Department of Structures for Engineering and Architecture, University of Naples Federico II, Naples, Italy

Giuseppe Ruta University "La Sapienza" and National Group for Mathematical Physics, Roma, Italy

Francesco Saltari Department of Mechanical and Aerospace Engineering, Sapienza University of Rome, Rome, Italy

Mauro Lo Schiavo Università di Roma “La Sapienza”, Dip. D.I.S.G., Rome, Italy

Cornelia Schiebold Department of Mathematics and Science Education, Mid Sweden University, Sundsvall, Sweden

Instytut Matematyki, Uniwersytet Jana Kochanowskiego w Kielcach, Kielce, Poland

Salvatore Sessa Department of Structures for Engineering and Architecture, University of Naples Federico II, Naples, Italy

Alexander P. Seyranian Institute of Mechanics, Lomonosov Moscow State University, Moscow, Russia

Frederico M. A. Silva School of Civil and Environmental Engineering, Federal University of Goiás, Goiânia, Brazil

Sudeshna Sinha Indian Institute of Science Education and Research (IISER), Mohali, Punjab, India

Roman Starosta Institute of Applied Mechanics, Poznań University of Technology, Poznań, Poland

Gabor Stepan Department of Applied Mechanics, Budapest University of Technology and Economics, Budapest, Hungary

Katica R. (Stevanović) Hedrih Department of Mechanics, Mathematical Institute of the Serbian Academy of Sciences and Arts, Belgrade, Serbia

Gustavo Chaves Storti Department of Integrated Systems, School of Mechanical Engineering, University of Campinas, Campinas, Brazil

Grażyna Sypniewska-Kamińska Institute of Applied Mechanics, Poznań University of Technology, Poznań, Poland

Dénes Takács MTA-BME Research Group on Dynamics of Machines and Vehicles, Budapest, Hungary

Ze Tang Key Laboratory of Advanced Process Control for Light Industry (Ministry of Education), Jiangnan University, Wuxi, Jiangsu, PR China

Zdravko Terze Chair of Flight Vehicle Dynamics, Faculty of Mechanical Engineering and Naval Architecture, University of Zagreb, Zagreb, Croatia

Giovanna Tomassetti Department of Basic and Applied Sciences for Engineering, Sapienza University, Roma, Italy

Dinh Duc Tung Bauman Moscow State Technical University, Moscow, Russia

Nicolò Vaiana Department of Structures for Engineering and Architecture, University of Naples Federico II, Naples, Italy

Wanclaine A. Vaz School of Civil and Environmental Engineering, Federal University of Goiás, Goiânia, Brazil

Pierluigi Vellucci Department of Economics, Roma Tre University, Rome, Italy

Luis G. G. Villani UERJ – Universidade do Estado do Rio de Janeiro, NUMERICO – Nucleus of Modeling and Experimentation with Computers, Rio de Janeiro, Brasil

David J. Wagg Department of Mechanical Engineering, University of Sheffield, Sheffield, UK

An Wang School of Mechanical and Electronical Engineering, Lanzhou University of Technology, Lanzhou, China

Xinwen Wang School of Chemical and Environmental Engineering, China University of Mining and Technology, Beijing, China

Yan Wang Key Laboratory of Advanced Process Control for Light Industry (Ministry of Education), Jiangnan University, Wuxi, Jiangsu, PR China

Ziyun Wang Key Laboratory of Advanced Process Control for Light Industry (Ministry of Education), Jiangnan University, Wuxi, Jiangsu, PR China

Marian Wiercigroch Centre for Applied Dynamics Research, School of Engineering, University of Aberdeen, Kings' College, Aberdeen, Scotland, United Kingdom

Huidong Xu Taiyuan University of Technology, Taiyuan, P. R. China

Pengfei Xu Department of Mechanics, Beijing Institute of Technology, Beijing, China

Department of Mathematics, Changzhi University, Changzhi, China

Manish Yadav Indian Institute of Science Education and Research (IISER), Mohali, Punjab, India

Yongfeng Yang Institute of Vibration Engineering, Northwestern Polytechnical University, Xi'an, P. R. China

MIIT Key Laboratory of Dynamics and Control of Complex Systems, Northwestern Polytechnical University, Xi'an, P. R. China

Yiğit Yazıcıoglu Middle East Technical University, Ankara, Turkey

Wan-Suk Yoo Pusan National University, Busan, South Korea

Andrea Zanoni Department of Aerospace Science and Technology, Politecnico di Milano, Milano, Italy

Haopeng Zhang Institute of Vibration Engineering, Northwestern Polytechnical University, Xi'an, P. R. China

MIIT Key Laboratory of Dynamics and Control of Complex Systems, Northwestern Polytechnical University, Xi'an, P. R. China

Wei Zhang Beijing Key Laboratory of Nonlinear Vibrations and Strength of Mechanical, College of Mechanical Engineering, Beijing University of Technology, Beijing, P. R. China

Yaobing Zhao College of Civil Engineering, Huaqiao University, Xiamen, Fujian, China

Hunan Provincial Key Laboratory of Structures for Wind Resistance and Vibration Control, Hunan University of Science and Technology, Xiangtan, Hunan, China

Hao Zhou Institute of Vibration Engineering, Northwestern Polytechnical University, Xi'an, P. R. China

MIIT Key Laboratory of Dynamics and Control of Complex Systems, Northwestern Polytechnical University, Xi'an, P. R. China

Dario Zlatar Chair of Flight Vehicle Dynamics, Faculty of Mechanical Engineering and Naval Architecture, University of Zagreb, Zagreb, Croatia

Part I

Methods for Nonlinear Dynamics

Nonlinear Dynamics of Multibody Systems Using an Augmented Lagrangian Formulation



Nikolaos Potosakis, Elias Paraskevopoulos, and Sotirios Natsiavas

Abstract A class of multibody systems subject to bilateral scleronomous motion constraints is investigated. The formulation is based on a new set of equations of motion, expressed as a coupled system of strongly nonlinear second-order ordinary differential equations. After putting these equations in a weak form, the position, velocity, and momentum type quantities are assumed to be independent, leading to a three-field set of equations of motion. Next, an equivalent augmented Lagrangian formulation is set up by introducing a set of penalty terms. This final set of equations is then used as a basis for developing a new time integration scheme, which is applied to several example systems. In those examples, special emphasis is put on illustrating the advantages of the new method when applied to mechanical systems, involving redundant constraints or singular configurations.

Keywords Analytical mechanics · Multibody dynamics · Bilateral motion constraints · Weak form of equations of motion · Augmented Lagrangian

1 Introduction

Research on multibody dynamics helps in developing more efficient and robust numerical techniques for solving challenging engineering problems. This in turn yields useful design gains in many areas, including mechanisms, robotics, biomechanics, automotive, railway, and aerospace structures [1–4]. Typically, the equations of motion for this class of systems are derived and cast in the form of a set of differential-algebraic equations (DAEs) of high index. Earlier attempts to solve these equations are based on index reduction or coordinate partitioning techniques [3, 4]. In contrast, the main objective of this chapter is to first create and employ

N. Potosakis · E. Paraskevopoulos · S. Natsiavas (✉)
Department of Mechanical Engineering, Aristotle University, Thessaloniki, Greece
e-mail: natsiava@auth.gr

a better theoretical foundation and then proceed to development of more advanced numerical schemes.

In the new approach, the equations of motion employed are second-order ordinary differential equations (ODEs). This is achieved by combining concepts of Analytical Dynamics and differential geometry and leads to a natural elimination of singularities associated with DAE formulations from the onset [5]. Since the ulterior motive is the development of an efficient numerical integration scheme, these equations are first put in a convenient weak form. Moreover, the position, velocity, and momentum type quantities are assumed to be independent, forming a three-field set of equations [6]. Finally, the set of equations obtained is solved by application of an augmented Lagrangian formulation, which is set up after introducing appropriate penalty terms [7]. Next, the validity and efficiency of this scheme is tested and illustrated by applying it to a number of characteristic example mechanical systems.

The set of equations of motion employed is included in Sect. 2. Originally, they appear in a strong form and are subsequently put in a three-field weak form. After introducing penalty terms, they are cast eventually in an augmented Lagrangian form. Then, a temporal discretization scheme is developed and numerical results are presented for two mechanical examples in Sect. 3.

2 Equations of Motion: Augmented Lagrangian Formulation

This chapter employs a new set of equations of motion, obtained for a class of multibody mechanical systems subject to equality constraints. The motion is described by a finite number of generalized coordinates $q = (q^1 \dots q^n)$, at any time t [1, 2]. In this way, it can be represented by the motion of a fictitious point, say p , along a curve on the n -dimensional configuration manifold M of the system. Moreover, the tangent vector \underline{v} to this curve belongs to an n -dimensional vector space $T_p M$, the tangent space of manifold M at p [2]. The systems examined are subject to a set of k motion constraints. For simplicity, these constraints are assumed to be scleronomic, with form

$$\dot{\psi}^R \equiv a_i^R(q)\dot{q}^i = 0. \quad (1)$$

When a constraint is holonomic, its equation can be integrated in the algebraic form

$$\phi^R(q) = 0. \quad (2)$$

The equations of motion of the class of systems examined can be cast in the form

$$\tilde{h}^* \equiv \tilde{h}_M^* - \tilde{h}_C^* = 0 \quad (3)$$

on manifold M , where

$$\underline{h}_M^* = h_i \underline{e}^i \quad \text{with} \quad h_i = \left(g_{ij} v^j \right) \dot{\cdot} - \Lambda_{\ell i}^m g_{mj} v^j v^\ell - f_i \quad (4)$$

and

$$\underline{h}_C^* = \sum_{R=1}^k h_R a_i^R \underline{e}^i \quad \text{with} \quad h_R = \left(\bar{m}_{RR} \dot{\lambda}^R \right) \dot{\cdot} + \bar{c}_{RR} \dot{\lambda}^R + \bar{k}_{RR} \lambda^R - \bar{f}_R. \quad (5)$$

In Eq. (5), the summation convention on repeated indices does not apply to index R . Moreover, the coefficients \bar{m}_{RR} , \bar{c}_{RR} , \bar{k}_{RR} , and \bar{f}_R are determined by the constraints [5]. Equation (3) represents a set of n second-order coupled strongly nonlinear ODEs in the $n + k$ unknowns q^i and λ^R . A complete mathematical formulation is obtained by incorporating the k equations of the constraints, which are expressed originally by Eqs. (1) and (2). In particular, these equations are replaced eventually by

$$g_R = \left(\bar{m}_{RR} \dot{\phi}^R \right) \dot{\cdot} + \bar{c}_{RR} \dot{\phi}^R + \bar{k}_{RR} \phi^R = 0 \quad \text{and} \quad g_R = \left(\bar{m}_{RR} \dot{\psi}^R \right) \dot{\cdot} + \bar{c}_{RR} \dot{\psi}^R = 0, \quad (6)$$

respectively, for $R = 1, \dots, k$ [5].

Taking into account Eq. (3) leads first to

$$\int_{t_1}^{t_2} \left(\underline{h}_M^* - \underline{h}_C^* \right) (\underline{w}) dt = 0, \quad \forall \underline{w} \in T_p M, \quad (7)$$

along a natural trajectory on the manifold and within any time interval $[t_1, t_2]$. Moreover, as variation of a function f is defined the derivative of f along vector \underline{w} , by

$$\delta f \equiv \underline{w}(f) = f_i w^i. \quad (8)$$

Then, $w^i = \delta q^i$ for each holonomic coordinate, while a little more involved relation is obtained in case of nonholonomic coordinates [6]. In addition, the position, velocity, and momentum variables are considered as independent quantities in the sequel. For this, a new velocity field \underline{v} is introduced on manifold M , which should eventually be forced to become identical to the true velocity field \underline{v} . This means that

$$v^i = v^i \Rightarrow \delta v^i = \delta v^i, \quad (9)$$

with variations defined through Eq. (8) by $\delta v^i = \underline{w}(v^i)$ and $\delta v^i = \underline{w}(v^i)$. In analogy to the action leading to Eq. (7), conditions (9) are imposed by

$$\int_{t_1}^{t_2} \left[\delta\pi_i \left(v^i - v^i \right) + \pi_i \left(\delta v^i - \delta v^i \right) \right] dt = 0, \quad (10)$$

where the quantities $\delta\pi_i$ and π_i are components of co-vectors belonging to the cotangent space T_p^*M . In the same spirit, by considering the motion constraints expressed by Eq. (6), the following relation must also be satisfied

$$\int_{t_1}^{t_2} g_R \delta\lambda^R dt = 0, \quad (11)$$

for an arbitrary multiplier $\delta\lambda^R$ and each $R = 1, \dots, k$. Then, integrating by parts the first term in the integrand for a holonomic constraint yields

$$\left(\bar{m}_{RR} \dot{\phi}^R \delta\lambda^R \right) \Big|_{t_1}^{t_2} - \int_{t_1}^{t_2} \left[\bar{m}_{RR} \dot{\phi}^R \left(\delta\lambda^R \right) \dot{\phi}^R - \left(\bar{c}_{RR} \dot{\phi}^R + \bar{k}_{RR} \phi^R \right) \delta\lambda^R \right] dt = 0, \quad (12)$$

while a similar result is also obtained for a nonholonomic constraint.

Next, a similar action is also taken for the velocity components $\dot{\lambda}^R$, by introducing a new vector field on $T_{pR}M_R$ for each constraint manifold M_R , with components μ^R , together with a new set of Lagrange multipliers σ_R , belonging to the cotangent space $T_{pR}^*M_R$. As a consequence, the weak formulation is augmented by the terms

$$\int_{t_1}^{t_2} \left[\delta\sigma_R \left(\mu^R - \dot{\lambda}^R \right) + \sigma_R \left(\delta\mu^R - \delta\dot{\lambda}^R \right) \right] dt = 0, \quad (R = 1, \dots, k), \quad (13)$$

where $\delta\sigma_R$ represents the component of a co-vector on $T_{pR}^*M_R$. Then, one can relate the strong time derivatives v^i (of q^i or ϑ^i , for a true or a pseudo-coordinate, respectively) and $\dot{\lambda}^R$ of the position type variables to weak velocities, denoted by v^i and μ^R , through two new sets of Lagrange multipliers, denoted by $\delta\pi_i$ and $\delta\sigma_R$, respectively.

Finally, appending the terms in Eqs. (10)–(13) to Eq. (7) and performing lengthy manipulations leads eventually to an involved three-field set of equations [6]. Then, since the variations w^i , $\delta\lambda^R$, δv^i , $\delta\mu^R$, $\delta\pi_i$, and $\delta\sigma_R$ are independent, collecting the terms in these equations multiplied by these quantities leads to a coupled set of nonlinear algebraic equations. In fact, by adding suitable penalty terms due to the constraints, it is found that the form of these equations remains unaffected, making the substitution

$$\bar{\mu}^R = \mu^R - \xi_R \dot{\phi}^R \quad \text{and} \quad \bar{\lambda}^R = \lambda^R - \xi_R \phi^R, \quad (14)$$

when μ^R and λ^R is multiplied by \bar{m}_{RR} or \bar{c}_{RR} and \bar{k}_{RR} , respectively. This provides a convenient and strong basis for developing an appropriate temporal discretization of the equations of motion. For the purposes of the present chapter, this task was

performed within the framework of the augmented Lagrangian formulation, leading to a convenient block-type iterative technique within each time step.

3 Numerical Results

Some characteristic results are presented next for two selected examples. The first example is of academic interest, while the second corresponds to an industrial application.

3.1 Planar Slider-Crank Mechanism

First, in Fig. 1 are compared results obtained by applying the new method with similar results reported for a typical benchmark problem [8]. The planar slider-crank mechanism shown in the inset of Fig. 1b is examined. This represents multibody systems passing through a singular configuration. The two rods have an equal length of 1 m and a uniformly distributed mass of 1 kg, while the slider has a negligible mass and is constrained to move along the ground axis Ox. Consequently, the number of degrees of freedom increases instantaneously from one to two when

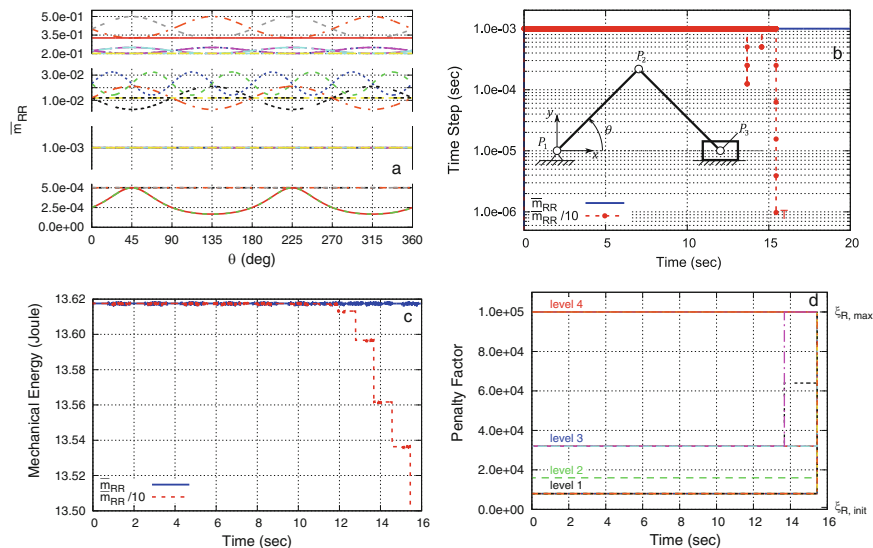


Fig. 1 Results for a slider-crank mechanism: (a) values of \bar{m}_{RR} as a function of θ , (b) time step variation for \bar{m}_{RR} and $\bar{m}_{RR}/10$, (c) mechanical energy for \bar{m}_{RR} and $\bar{m}_{RR}/10$, and (d) changes in the values of the penalty factors leading to convergence up to about 16 s for $\bar{m}_{RR}/10$

$\theta = n\pi/2$, with $n = 0, 1, \dots$. The mechanism starts from the position with $\theta = \pi/4$, so that the initial velocity of point P_3 is 4 m/s along the $-x$ direction and executes oscillations due to the action of gravity, acting along the $-y$ direction, with gravity acceleration equal to 9.81 m/s².

Based on standard modeling requirements, the model employed consists of four rigid bodies, corresponding to 24 dof. In addition, it is subject to a total of $k = 26$ bilateral constraints. This means that three of these constraints are redundant. First, in Fig. 1a are presented the values of all the \bar{m}_{RR} parameters, obtained over a full rotation of the two members. A significant variation is observed to occur in the value of \bar{m}_{RR} for some of the constraints over the complete rotation. In addition, a much bigger difference is observed in the values from one constraint to another. Next, in Fig. 1b is shown the time step history. When the correct values were selected for \bar{m}_{RR} the step was found to remain constant and equal to the initial selection. Also, some of the penalty factors kept their initial value ($\xi_R = 1000$), while some other were increased up to 2000. However, when a wrong value of $\bar{m}_{RR}/10$ was selected, instead, the time step decreased occasionally and eventually fell below the minimum allowable value. In Fig. 1c is shown the corresponding mechanical energy of the system, showing an observable drop in its value at times where a decrease in the time step is performed. Also, the penalty values had to be increased by two orders of magnitude when $\bar{m}_{RR}/10$ was selected, as depicted in Fig. 3d. Moreover, even that increase was not sufficient to guarantee continuation of the simulation beyond the first 16 s of the motion.

Next, in Fig. 2a, b are shown the time step and the mechanical energy of the mechanism, by using the correct values of \bar{m}_{RR} but keeping the same constant penalty values for all the constraints. The results indicate that a convergence is possible to occur in the numerical solution, within the time interval examined, provided that the penalty values lie within a specific interval (here 10^3 – 10^4). The explanation for this behavior is that for an excessive value of the penalty value, the part associated with the corresponding constraint term dominates the Jacobian matrix of the resulting set of linear algebraic equations at each iteration step, leading to ill-conditioning. On the other hand, relatively small values of the penalty factors make a small contribution to the Jacobian matrix and this implies that a larger number of iteration is required for convergence at each step.

Likewise, in Fig. 2c, d are shown the same quantities, obtained as a function of time for the correct values of \bar{m}_{RR} , by keeping constant all the penalty factors to their initial values, again. Moreover, the results of the new method, represented by the dashed line, are compared to those obtained by applying the same method after setting $\bar{m}_{RR} = 0$, $\bar{c}_{RR} = 0$, $\bar{k}_{RR} = 1$ and $\bar{f}_R = 0$ in Eq. (5), so that $h_R = \lambda^R$. In addition, it was also set $\bar{m}_{RR} = 1$ in Eq. (6). In this way, the set of equations employed is reduced to the set of equations of motion employed by current multibody dynamics formulations [9, 10]. This case is referred to as a modified augmented Lagrangian formulation (M-ALF). Comparison of the results shows that the numerical performance gets worse, demonstrating the advantages associated with the new set of equations of motion.

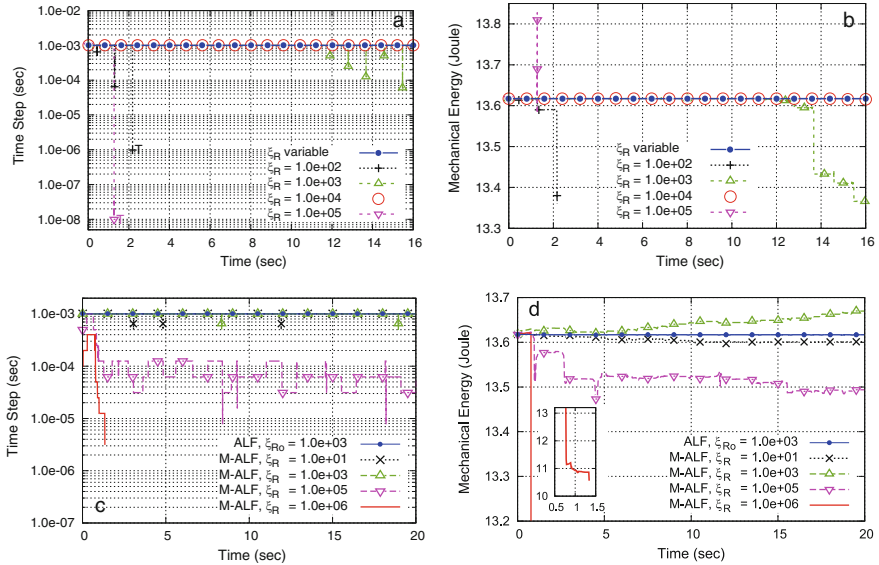


Fig. 2 Numerical results for a slider-crank mechanism: (a) time step variation, (b) mechanical energy for different constant values of the penalty factors, (c) time step variation, and (d) mechanical energy obtained by the modified augmented Lagrangian formulation (M-ALF)

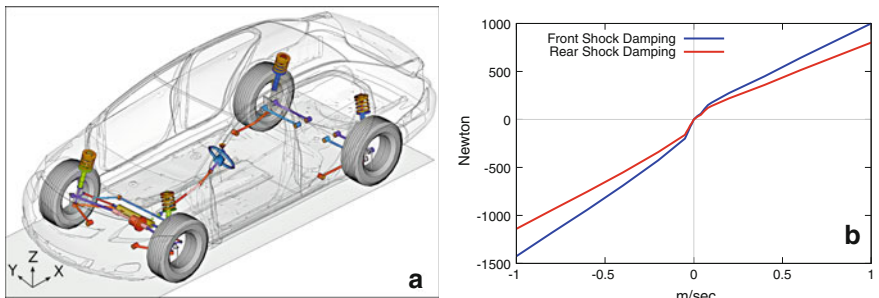


Fig. 3 (a) Complete vehicle model and (b) forces in the front and rear shock dampers as a function of relative velocity

3.2 Complex Model of a Ground Vehicle

In the second example, a model of a real ground vehicle was examined, shown in Fig. 3a. Many of its components exhibit strongly nonlinear behavior. For instance, in Fig. 3b are shown the forces developed in the front and rear shock dampers as a function of the relative velocity. Finally, the tires were modeled using the Pacejka tire model. In total, the model consists of 53 rigid bodies, interconnected with 49 kinematical constraints, 29 bushings, 9 spring-damper systems, and 9 action-reaction force elements. As a consequence, the total number of degrees of freedom of the final model is 134.

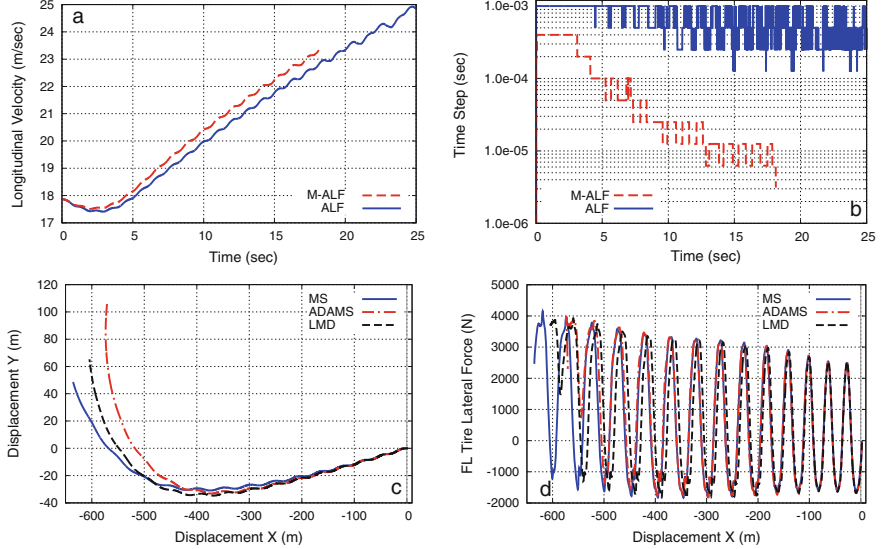


Fig. 4 Results for a repeated swept steering maneuver: (a) history of the longitudinal velocity of the car, (b) size of the time step, (c) comparison of trajectories, and (d) comparison of tire lateral forces obtained with two BDF solvers

The vehicle was subjected to a repeated swept steering maneuver, by applying a torque at the car's differential and imposing the steering angle imposed on the steering wheel during the motion. First, in Fig. 4a is shown the history of the longitudinal velocity of the car. The results of the new method are represented by the continuous curve. These results are first compared with those obtained by applying the modified augmented Lagrangian formulation (M-ALF), as was defined in Sect. 3.1. In the latter case, a sudden interruption of the time integration occurred after about 17 s of motion, as indicated by the broken curve. The reason for this interruption is explained by the results of Fig. 4b, where the size of the time step employed by the two methods is shown. Besides this, the results illustrate that the new method, using variable penalty factors and correct values for the parameters \bar{m}_{RR} , \bar{c}_{RR} , \bar{k}_{RR} , and \bar{f}_R , leads to substantially smaller time steps, especially as the duration of the event increases. Next, in Fig. 4c is shown a comparison of the resulting car trajectories on the horizontal plane, obtained by two state of the art commercial codes [11, 12]. These codes set up the equations of motion and solves them numerically as a system of index-3 DAEs by employing a classical integration scheme, based on backward differentiation formulas (BDF). Likewise, Fig. 4d presents a comparison of the corresponding lateral force developed in the front left tire. Here, the deviations observed between the results of the new method and the codes grow gradually and become large at the final stages of the maneuver.

References

1. Greenwood, D.T.: Principles of Dynamics. Prentice-Hall Inc., Englewood Cliffs (1988)
2. Bloch, A.M.: Nonholonomic Mechanics and Control. Springer, New York (2003)
3. Geradin, M., Cardona, A.: Flexible Multibody Dynamics. Wiley, New York (2001)
4. Bauchau, O.A.: Flexible Multibody Dynamics. Springer, London (2011)
5. Natsiavas, S., Paraskevopoulos, E.: A set of ordinary differential equations of motion for constrained mechanical systems. *Nonlinear Dyn.* **79**, 1911–1938 (2015)
6. Paraskevopoulos, E., Natsiavas, S.: Weak formulation and first order form of the equations of motion for a class of constrained mechanical systems. *Int. J. Non linear Mech.* **77**, 208–222 (2015)
7. Bertsekas, D.P.: Constraint Optimization and Lagrange Multiplier Methods. Academic Press, New York (1982)
8. IFToMM TC for Multibody Dynamics, Library of Computational Benchmark Problems. <http://www.ifomm-multibody.org/benchmark>
9. Bayo, E., Ledesma, R.: Augmented Lagrangian and mass-orthogonal projection methods for constrained multibody dynamics. *Nonlinear Dyn.* **9**, 113–130 (1996)
10. Dopico, D., Gonzalez, F., Cuadrado, J., Kovacs, J.: Determination of holonomic and nonholonomic constraint reactions in an index-3 augmented Lagrangian formulation with velocity and acceleration projections. *ASME J. Comput. Nonlinear Dyn.* **9**, 041006 (2014)
11. MSC Adams, User Guide. MSC Software Corporation, Newport Beach (2016)
12. MotionSolve v14.0, User Guide. Altair Engineering Inc., Irvine

Stability Boundary Approximation of Periodic Dynamics



Anton O. Belyakov and Alexander P. Seyranian

Abstract We develop here the method for obtaining approximate stability boundaries in the space of parameters for systems with parametric excitation. The monodromy (Floquet) matrix of linearized system is found by averaging method. For system with two degrees of freedom (DOF) we derive general approximate stability conditions. We study domains of stability with the use of fourth order approximations of monodromy matrix on example of inverted position of a pendulum with vertically oscillating pivot. Addition of small damping shifts the stability boundaries upwards, thus resulting in both stabilization and destabilization effects.

Keywords Floquet multipliers · Monodromy matrix · Parametric pendulum · Averaging method

1 Introduction

Let us study the stability of the equilibrium $y \equiv 0$ of a nonlinear system governed by ordinary differential equations $\dot{y} = \mathbf{J}(t)y + f(t, y)$, where for nonlinear vector-function f exist constants c and $\nu > 1$, such that $|f(t, y)| \leq c|y|^\nu$ for all $t \geq 0$ and $y \in \mathbb{R}^n$. Vector-function $f(t, y)$ and matrix $\mathbf{J}(t)$ are piecewise continuous in t . Moreover $\mathbf{J}(t)$ is bounded and T -periodic.

According to Lyapunov's theorem the trivial solution of such a nonlinear system is *asymptotically stable* if all *Lyapunov exponents* of the linear system $\dot{x}(t) =$

A. O. Belyakov (✉)

Moscow School of Economics, Lomonosov Moscow State University, Moscow, Russia

National Research Nuclear University “MEPhI”, Moscow, Russia

Central Economics and Mathematics Institute, Russian Academy of Sciences, Moscow, Russia
e-mail: belyakov@mse-msu.ru

A. P. Seyranian

Institute of Mechanics, Lomonosov Moscow State University, Moscow, Russia
e-mail: seyran@imec.msu.ru

$\mathbf{J}(t) x(t)$ are strictly negative and the solution is unstable if at least one Lyapunov exponent is strictly positive.¹ Asymptotic stability of the periodic linear system determines the asymptotic stability of the nonlinear system equilibrium and *vice versa*.² Stability of linear systems with time-periodic coefficients was also studied by Gaston Floquet [1]. Lyapunov exponent λ of the linear periodic system can be expressed via its corresponding *Floquet multiplier* ρ as $\lambda = \ln |\rho|$. The theorem can also be reformulated to compare absolute values of Floquet multipliers with 1. Floquet multipliers are the eigenvalues of the *monodromy matrix* which is the fundamental matrix of the linear system taken at time T .

Monodromy matrix and Floquet multipliers can always be numerically calculated. Stability can also be checked by studying solutions of the system, see, e.g. [2–4] and references therein. But in practice it is often useful to have analytical approximations of stability regions in parameter space. To obtain a straightforward technique for deriving such analytical stability boundary approximations of any order we combine Floquet theory with asymptotic method of *averaging*, [4].

This technique yields same results as expansion of monodromy matrix in series in [5] up to the terms of higher order than the order of approximation. These terms are automatically eliminated in the averaging scheme making the technique more convenient in practice.

We demonstrate the proposed technique on the example of inverted pendulum, where destabilizing effect of damping (shift of the lower stability boundary) is manifested in the fourth approximation, see [6], though it would be natural to expect stabilization by damping, see, e.g. [2, 7]. But there is also stabilizing effect (shift of the upper boundary) demonstrated numerically in [8]. Here we obtain approximations of both stability boundaries and study analytically both effects of stabilization and destabilization by damping. Moreover, the fourth approximation yields in addition boundaries of another stability domain.

2 Statement of the Problem

Consider linearization, $\dot{x}(t) = \mathbf{J}(t) x(t)$, of a nonlinear system about its equilibrium, where $x(t)$ is the vector of state variable perturbations and $\mathbf{J}(t)$ is piecewise continuous, T -periodic and thus integrable *Jacobian matrix* of the original nonlinear system. Solution of the matrix differential equation with the initial value being the identity matrix \mathbf{I}

$$\dot{\mathbf{X}}(t) = \mathbf{J}(t) \cdot \mathbf{X}(t), \quad \mathbf{X}(0) = \mathbf{I}, \quad (1)$$

¹Lyapunov regularity condition of the linear system holds when its matrix is periodic.

²Periodic linear system is asymptotically stable if, and only if, it is exponentially stable. Exponential stability of $\dot{x}(t) = \mathbf{J}(t) x(t)$ results in exponential stability, and hence asymptotic stability, of the nonlinear system solution $y \equiv 0$.

yields fundamental matrix and the monodromy matrix $\mathbf{F} = \mathbf{X}(T)$. If all eigenvalues of the monodromy matrix, *Floquet multipliers*, have absolute values smaller than one, then the equilibrium of the nonlinear system is asymptotically stable, and if at least one eigenvalue has absolute value greater than one, then the equilibrium is unstable, see, e.g. [5]. To have analytical approximations of stability regions in parameter space we apply the following.

3 Averaging Scheme

Let the Jacobian matrix $\mathbf{J}(t)$ be expended into the series

$$\mathbf{J}(t) = \mathbf{J}_0(t) + \mathbf{J}_1(t) + \mathbf{J}_2(t) + \mathbf{J}_3(t) + \dots, \quad (2)$$

where the lower index denotes the order of smallness. Suppose we know solution $\mathbf{X}_0(t)$ of the matrix initial value problem $\dot{\mathbf{X}}_0(t) = \mathbf{J}_0(t) \cdot \mathbf{X}_0(t)$, where $\mathbf{X}_0(0) = \mathbf{I}$. Then the change of variable $\mathbf{X}(t) = \mathbf{X}_0(t) \cdot \mathbf{Y}(t)$ converts (1) to the standard form:

$$\dot{\mathbf{Y}}(t) = \mathbf{H}(t) \cdot \mathbf{Y}(t), \quad \mathbf{Y}(0) = \mathbf{I}, \quad (3)$$

where matrix $\mathbf{H}(t) := \mathbf{X}_0^{-1}(t) \cdot (\mathbf{J}(t) - \mathbf{J}_0(t)) \cdot \mathbf{X}_0(t)$ is small for $t \in [0, T]$. Approximate solution of (3) can be found with *averaging method* as follows. Let

$$\mathbf{H}(t) = \mathbf{H}_1(t) + \mathbf{H}_2(t) + \mathbf{H}_3(t) + \dots, \quad (4)$$

where $\mathbf{H}_j(t) := \mathbf{X}_0^{-1}(t) \cdot \mathbf{J}_j(t) \cdot \mathbf{X}_0(t)$ for all $j \geq 1$. We will find solution as

$$\mathbf{Y}(t) = (\mathbf{I} + \mathbf{U}_1(t) + \mathbf{U}_2(t) + \dots) \cdot \mathbf{Z}(t), \quad (5)$$

where $\mathbf{U}_j(t)$ are matrix-functions, such that $\mathbf{U}_j(0) = \mathbf{U}_j(T) = 0$ and $\mathbf{Z}(t)$ is the solution of the autonomous *averaged differential equation*:

$$\dot{\mathbf{Z}}(t) = \mathbf{A} \cdot \mathbf{Z}(t), \quad \mathbf{Z}(0) = \mathbf{I}, \quad (6)$$

where $\mathbf{A} = \mathbf{A}_1 + \mathbf{A}_2 + \mathbf{A}_3 + \dots$, which can be written via the matrix exponential:

$$\mathbf{Z}(t) = \exp([\mathbf{A}_1 + \mathbf{A}_2 + \mathbf{A}_3 + \dots] t). \quad (7)$$

The matrices \mathbf{A}_j and matrix-functions $\mathbf{U}_j(t)$ can be found one by one using the following expressions.³

³The expressions are derived by differentiating (5) w.r.t. time

$$\dot{\mathbf{Y}}(t) = (\dot{\mathbf{U}}_1(t) + \dot{\mathbf{U}}_2(t) + \dots) \cdot \mathbf{Z}(t) + (\mathbf{I} + \mathbf{U}_1(t) + \mathbf{U}_2(t) + \dots) \cdot \dot{\mathbf{Z}}(t),$$

For the first order approximation we calculate \mathbf{A}_1 as the average of $\mathbf{H}_1(t)$

$$\mathbf{A}_1 = \frac{1}{T} \int_0^T \mathbf{H}_1(t) dt, \quad (8)$$

under assumption that \mathbf{A}_1 and $\mathbf{H}_1(t)$ are of the same order of smallness. In particular we assume that $\mathbf{H}_1(t)$ does not contain periodic functions with small frequencies, which would appear in the denominator during integration and could cause high value of \mathbf{A}_1 , thus violating the assumption of its smallness.

For the second order approximation we have to calculate

$$\mathbf{U}_1(t) = \int_0^t (\mathbf{H}_1(\tau) - \mathbf{A}_1) d\tau, \quad (9)$$

$$\mathbf{A}_2 = \frac{1}{T} \int_0^T (\mathbf{H}_2(t) + \mathbf{H}_1(t) \cdot \mathbf{U}_1(t) - \mathbf{U}_1(t) \cdot \mathbf{A}_1) dt, \quad (10)$$

using matrix \mathbf{A}_1 already obtained in (8).

For the third order approximation we have

$$\mathbf{U}_2(t) = \int_0^t (\mathbf{H}_2(\tau) - \mathbf{A}_2 + \mathbf{H}_1(\tau) \cdot \mathbf{U}_1(\tau) - \mathbf{U}_1(\tau) \cdot \mathbf{A}_1) d\tau, \quad (11)$$

$$\begin{aligned} \mathbf{A}_3 = & \frac{1}{T} \int_0^T (\mathbf{H}_3(t) + \mathbf{H}_2(t) \cdot \mathbf{U}_1(t) - \mathbf{U}_1(t) \cdot \mathbf{A}_2 \\ & + \mathbf{H}_1(t) \cdot \mathbf{U}_2(t) - \mathbf{U}_2(t) \cdot \mathbf{A}_1) dt. \end{aligned} \quad (12)$$

and so on for the $n + 1$ -th order approximation we calculate

substituting there expressions for time derivatives from (3) and (6)

$$\begin{aligned} & (\mathbf{H}_1(t) + \mathbf{H}_2(t) + \dots) \cdot (\mathbf{I} + \mathbf{U}_1(t) + \mathbf{U}_2(t) + \dots) \cdot \mathbf{Z} \\ & = (\dot{\mathbf{U}}_1(t) + \dot{\mathbf{U}}_2(t) + \dots) \cdot \mathbf{Z} + (\mathbf{I} + \mathbf{U}_1(t) + \mathbf{U}_2(t) + \dots) \cdot (\mathbf{A}_1 + \mathbf{A}_2 + \dots) \cdot \mathbf{Z}, \end{aligned}$$

collecting there terms of the same order, and canceling non-degenerate matrix \mathbf{Z} , which yield the following equalities:

First order: $\mathbf{H}_1(t) = \dot{\mathbf{U}}_1(t) + \mathbf{A}_1$.

Second order: $\mathbf{H}_2(t) + \mathbf{H}_1(t) \cdot \mathbf{U}_1(t) = \dot{\mathbf{U}}_2(t) + \mathbf{U}_1(t) \cdot \mathbf{A}_1 + \mathbf{A}_2$,

Third order: $\mathbf{H}_3(t) + \mathbf{H}_1(t) \cdot \mathbf{U}_2(t) + \mathbf{H}_2(t) \cdot \mathbf{U}_1(t) = \dot{\mathbf{U}}_3(t) + \mathbf{U}_2(t) \cdot \mathbf{A}_1 + \mathbf{U}_1(t) \cdot \mathbf{A}_2 + \mathbf{A}_3$,

Fourth order: $\mathbf{H}_4(t) + \mathbf{H}_1(t) \cdot \mathbf{U}_3(t) + \mathbf{H}_2(t) \cdot \mathbf{U}_2(t) + \mathbf{H}_3(t) \cdot \mathbf{U}_1(t) = \dot{\mathbf{U}}_4(t) + \mathbf{U}_3(t) \cdot \mathbf{A}_1 + \mathbf{U}_2(t) \cdot \mathbf{A}_2 + \mathbf{U}_1(t) \cdot \mathbf{A}_3 + \mathbf{A}_4$, and so on.

$$\begin{aligned} \mathbf{U}_n(t) &= \int_0^t (\mathbf{H}_n(\tau) - \mathbf{A}_n + \mathbf{H}_{n-1}(\tau) \cdot \mathbf{U}_1(\tau) - \mathbf{U}_1(\tau) \cdot \mathbf{A}_{n-1} \\ &\quad \dots \\ &\quad + \mathbf{H}_1(\tau) \cdot \mathbf{U}_{n-1}(\tau) - \mathbf{U}_{n-1}(\tau) \cdot \mathbf{A}_1) d\tau, \end{aligned} \quad (13)$$

$$\begin{aligned} \mathbf{A}_{n+1} &= \frac{1}{T} \int_0^T (\mathbf{H}_{n+1}(t) + \mathbf{H}_n(t) \cdot \mathbf{U}_1(t) - \mathbf{U}_1(t) \cdot \mathbf{A}_n \\ &\quad \dots \\ &\quad + \mathbf{H}_1(t) \cdot \mathbf{U}_n(t) - \mathbf{U}_n(t) \cdot \mathbf{A}_1) dt. \end{aligned} \quad (14)$$

4 Monodromy Matrix Approximation

Due to $\mathbf{Y}(T) = \mathbf{Z}(T)$ we have

$$\mathbf{F} = \mathbf{X}(T) = \mathbf{F}_0 \cdot \mathbf{Y}(T) = \mathbf{F}_0 \cdot \mathbf{Z}(T) = \mathbf{F}_0 \cdot (\mathbf{I} + \mathbf{Z}_1(T) + \mathbf{Z}_2(T) + \dots), \quad (15)$$

where we denote $\mathbf{F}_0 := \mathbf{X}_0(T)$ as the zero order approximation of monodromy matrix, $\mathbf{F} \approx \mathbf{F}_0$. Hence, we can write expressions to find terms of the expansion $\mathbf{F} = \mathbf{F}_0 + \mathbf{F}_1 + \mathbf{F}_2 + \mathbf{F}_3 + \mathbf{F}_4 + \dots$, where $\mathbf{F}_j = \mathbf{F}_0 \cdot \mathbf{Z}_j(T)$ with $\mathbf{Z}_0(T) = \mathbf{I}$. Expansion of the matrix exponential in (7) yields expressions for \mathbf{F}_j via \mathbf{A}_k , where $k \leq j$.

For the first order approximation we have $\mathbf{Z}_1(T) = \mathbf{A}_1 T$, so that

$$\mathbf{F}_1 = \mathbf{F}_0 \cdot \mathbf{Z}_1(T) = \mathbf{F}_0 \cdot \mathbf{A}_1 T. \quad (16)$$

For the second order approximation the expansion of the matrix exponential in (7) up to the second order terms yields $\mathbf{Z}_2(T) = \mathbf{A}_2 T + \frac{1}{2} \mathbf{A}_1^2 T^2$ and

$$\mathbf{F}_2 = \mathbf{F}_0 \cdot \left(\mathbf{A}_2 T + \frac{1}{2} \mathbf{A}_1^2 T^2 \right). \quad (17)$$

For the third order approximation we have

$$\mathbf{F}_3 = \mathbf{F}_0 \cdot \left(\mathbf{A}_3 T + \frac{1}{2} (\mathbf{A}_1 \cdot \mathbf{A}_2 + \mathbf{A}_2 \cdot \mathbf{A}_1) T^2 + \frac{1}{6} \mathbf{A}_1^3 T^3 \right). \quad (18)$$

For the fourth order approximation we calculate

$$\begin{aligned}\mathbf{F}_4 = \mathbf{F}_0 \cdot & \left(\mathbf{A}_4 T + \frac{1}{2} (\mathbf{A}_1 \mathbf{A}_3 + \mathbf{A}_2^2 + \mathbf{A}_3 \mathbf{A}_1) T^2 \right. \\ & \left. + \frac{1}{6} (\mathbf{A}_1^2 \mathbf{A}_2 + \mathbf{A}_1 \mathbf{A}_2 \mathbf{A}_1 + \mathbf{A}_2 \mathbf{A}_1^2) T^3 + \frac{1}{24} \mathbf{A}_1^4 T^4 \right),\end{aligned}\quad (19)$$

and so on.

5 Stability Conditions in 2-Dimensional Case

The eigenvalues of the monodromy matrix, *Floquet multipliers*, determine the stability of the solution $x = (0, 0)'$ of the linearized system. Since \mathbf{F} is the 2×2 matrix its eigenvalues can be found analytically as roots ρ_1 and ρ_2 of the characteristic polynomial:

$$\rho^2 - \text{tr}(\mathbf{F}) \rho + \det(\mathbf{F}) = 0. \quad (20)$$

Stability conditions ($|\rho_1| \leq 1$ and $|\rho_2| \leq 1$) written in the case of real roots as $\rho \in [-1, 1]$ and in the case of complex conjugate roots as $\rho_1 \rho_2 \leq 1$, with the use of (20) and Vieta's formula $\rho_1 \rho_2 = \det(\mathbf{F})$ correspondingly, take the form

$$|\text{tr}(\mathbf{F})| - 1 \leq \det(\mathbf{F}) \quad \text{and} \quad \det(\mathbf{F}) \leq 1, \quad (21)$$

where for asymptotic stability all inequalities should be strict, see, e.g. [9, p. 213]. For instability, it is sufficient that at least one of the conditions in (21) is violated.

Let us find approximations of stability conditions. Trace can be written as

$$\text{tr}(\mathbf{F}) = \text{tr}(\mathbf{F}_0) + \text{tr}(\mathbf{F}_1) + \text{tr}(\mathbf{F}_2) + \text{tr}(\mathbf{F}_3) + \text{tr}(\mathbf{F}_4) + \dots, \quad (22)$$

with $\mathbf{F}_1, \mathbf{F}_2, \mathbf{F}_3$, and \mathbf{F}_4 calculated by (16), (17), (18), and (19).

Notice that due to Liouville's formula, see, e.g. [10], we have

$$\det(\mathbf{F}) = e^{\int_0^T \text{tr}(\mathbf{J}(\tau)) d\tau} = e^{\int_0^T \text{tr}(\mathbf{J}_0(\tau)) d\tau} e^{\int_0^T (\text{tr}(\mathbf{J}_1(\tau)) + \text{tr}(\mathbf{J}_2(\tau)) + \text{tr}(\mathbf{J}_3(\tau)) + \dots) d\tau}$$

and since $\mathbf{F} = \mathbf{F}_0 \cdot \mathbf{Z}(T)$ and (7) determinant can be written as

$$\det(\mathbf{F}) = \det(\mathbf{F}_0) \det(\mathbf{Z}(T)) = e^{\int_0^T \text{tr}(\mathbf{J}_0(\tau)) d\tau} e^{\text{tr}(\mathbf{A}_1) T + \text{tr}(\mathbf{A}_2) T + \text{tr}(\mathbf{A}_3) T + \dots},$$

so that for any dimension for all $j \geq 1$ we have

$$\text{tr}(\mathbf{A}_j) = \frac{1}{T} \int_0^T \text{tr}(\mathbf{J}_j(\tau)) d\tau. \quad (23)$$

Then expansion of the matrix exponential yields

$$\det(\mathbf{F}) = e^{\int_0^T \text{tr}(\mathbf{J}_0(\tau)) d\tau} \left(1 + \text{tr}(\mathbf{A}_1)T + \text{tr}(\mathbf{A}_2)T + \frac{1}{2}(\text{tr}(\mathbf{A}_1)T)^2 + \dots \right). \quad (24)$$

The first order approximation of stability conditions $|\text{tr}(\mathbf{F})| - 1 \leq \det(\mathbf{F}) \leq 1$ can be written with the use of (22) and (24) as

$$|\text{tr}(\mathbf{F}_0) + \text{tr}(\mathbf{F}_1)| - 1 \leq e^{\int_0^T \text{tr}(\mathbf{J}_0(\tau)) d\tau} (1 + \text{tr}(\mathbf{A}_1)T) \leq 1$$

and so on.

6 Two DOF System with Impulse Parametric Excitation

6.1 High Frequency Stabilization of Inverted Pendulum

Let us show that motion of an inverted pendulum can be stable if we supply to the suspension point rather high frequency vibrations in vertical direction $l\ddot{\phi} + b\dot{\phi} + (g \pm c) \sin(\varphi) = 0$, where l is the length of the pendulum, $a \ll l$ is the amplitude of the vibrations of the pivot. The period of the pivot vibrations is normalized to $T = 2\pi$. Moreover, in any semi-period the acceleration of the pivot is constant and is equal $\pm c$, whose sign changes after each semi-period. We assume linear viscous friction with coefficient b . It turns out that for rather low relative eigenfrequency $\omega \ll 1$ the inverted position becomes stable. The equation of motion can be written in the form

$$\dot{\varphi} = s, \quad (25)$$

$$\dot{s} = -\beta\omega s - (\omega^2 \pm \varepsilon) \sin(\varphi), \quad (26)$$

where $\omega^2 = g/l$ is the relative eigenfrequency, $\varepsilon = c/l$ is the relative excitation acceleration, and $\beta = b/g$ is the new damping coefficient. Stability condition for this problem without damping can be found in [11]. The linearized case without damping coincides with the Meissner equation, [12].

This system, linearized about inverted vertical position $(\phi, s) = (\pi, 0)$, has the form $\dot{x}(t) = \mathbf{J}(t)x(t)$, with vector $x(t)$ corresponding to the perturbation of vector $(\varphi(t), s(t))'$ and $\mathbf{J}(t)$ being the piecewise constant Jacobian matrix of the original system: $\mathbf{J}(t) = \mathbf{J}^+$ if $t \in [0, \pi]$ and $\mathbf{J}(t) = \mathbf{J}^-$ if $t \in [\pi, 2\pi]$, where

$$\mathbf{J}^+ = \begin{pmatrix} 0 & 1 \\ \omega^2 + \varepsilon & -\beta\omega \end{pmatrix}, \quad \mathbf{J}^- = \begin{pmatrix} 0 & 1 \\ \omega^2 - \varepsilon & -\beta\omega \end{pmatrix}. \quad (27)$$

It is easy to find exact stability conditions to which approximate conditions converge as we shall demonstrate.

6.2 Exact Stability Conditions

We have the following explicit expression of the monodromy matrix via matrix exponentials

$$\mathbf{F} = \exp(\pi \mathbf{J}^-) \cdot \exp(\pi \mathbf{J}^+). \quad (28)$$

Since the determinant of a matrix product equals the product of the determinants, we have from (28)

$$\det(\mathbf{F}) = e^{\pi \operatorname{tr}(\mathbf{J}^-)} e^{\pi \operatorname{tr}(\mathbf{J}^+)} = e^{-2\pi\beta\omega}, \quad (29)$$

where we take into account that $\det(\exp(\pi \mathbf{J}^\pm)) = e^{2\pi \operatorname{tr}(\mathbf{J}^\pm)}$. The same expression as (29), $\det(\mathbf{F}) = e^{-2\pi\beta\omega}$, can be obtained by Liouville's formula for any piecewise continuous integrable 2π -periodic modulation function, see [10]. So with positive damping coefficient, $\beta > 0$, asymptotic stability can only be lost when the first condition in (21) is violated, i.e., when

$$|\operatorname{tr}(\mathbf{F})| - 1 > e^{-2\pi\beta\omega}. \quad (30)$$

We compare exact stability borders, determined by (27), (28), and (30) as

$$\left| \operatorname{tr} \left(\exp \left[\pi \begin{pmatrix} 0 & 1 \\ \omega^2 - \varepsilon & -\beta\omega \end{pmatrix} \right] \cdot \exp \left[\pi \begin{pmatrix} 0 & 1 \\ \omega^2 + \varepsilon & -\beta\omega \end{pmatrix} \right] \right) \right| - 1 = e^{-2\pi\beta\omega}, \quad (31)$$

with approximate stability boundaries obtained for this example.

6.3 Approximate Stability Conditions

We expand this matrix in the series $\mathbf{J}^\pm = \mathbf{J}_0 + \mathbf{J}_1^\pm + \mathbf{J}_2$, where

$$\mathbf{J}_0 = \begin{pmatrix} 0 & 1 \\ 0 & 0 \end{pmatrix}, \quad \mathbf{J}_1^\pm = \begin{pmatrix} 0 & 0 \\ \pm\varepsilon & 0 \end{pmatrix}, \quad \mathbf{J}_2 = \begin{pmatrix} 0 & 0 \\ \omega^2 & -\beta\omega \end{pmatrix}, \quad (32)$$

assuming that ε , ω , and β have the same order of smallness.

$$\mathbf{X}_0(t) = \exp(\mathbf{J}_0 t) = \begin{pmatrix} 1 & t \\ 0 & 1 \end{pmatrix}, \quad \mathbf{X}_0^{-1}(t) = \exp(-\mathbf{J}_0 t) = \begin{pmatrix} 1 & -t \\ 0 & 1 \end{pmatrix}. \quad (33)$$

According the formula $\mathbf{H}_j(t) := \mathbf{X}_0^{-1}(t) \cdot \mathbf{J}_j(t) \cdot \mathbf{X}_0(t)$ we have

$$\mathbf{H}_1^\pm(t) = \pm \varepsilon \begin{pmatrix} -t & -t^2 \\ 1 & t \end{pmatrix}. \quad (34)$$

Formula (8) reads as

$$\mathbf{A}_1 = \frac{1}{2\pi} \int_0^\pi \mathbf{H}_1^+(t) dt + \frac{1}{2\pi} \int_\pi^{2\pi} \mathbf{H}_1^-(t) dt = \frac{\varepsilon}{2\pi} \begin{pmatrix} \pi^2 & 2\pi^3 \\ 0 & -\pi^2 \end{pmatrix}. \quad (35)$$

The zero order approximation of monodromy matrix is the following:

$$\mathbf{F}_0 = \mathbf{X}_0(2\pi) = \exp(\mathbf{J}_0 2\pi) = \begin{pmatrix} 1 & 2\pi \\ 0 & 1 \end{pmatrix}. \quad (36)$$

With (16) we find the first order adjustment of monodromy matrix

$$\mathbf{F}_1 = \mathbf{F}_0 \cdot \mathbf{A}_1 2\pi = \pi^2 \varepsilon \begin{pmatrix} 1 & 0 \\ 0 & -1 \end{pmatrix}. \quad (37)$$

Thus $\text{tr}(\mathbf{F}_0) = 2$, $\text{tr}(\mathbf{F}_1) = 0$, and $\text{tr}(\mathbf{A}_1) = 0$.

For the second order approximation we take $\mathbf{H}_2(t) = \begin{pmatrix} -t\omega^2 & -t(\omega^2 t - \beta\omega) \\ \omega^2 & \omega^2 t - \beta\omega \end{pmatrix}$ and obtain with (9) and (10) the matrix

$$\mathbf{A}_2 = \frac{1}{2\pi} \begin{bmatrix} \frac{2}{3}\varepsilon^2\pi^4 - 2\pi^2\omega^2 & \frac{4\varepsilon^2\pi^5}{15} - \frac{8}{3}\pi^3\omega^2 + 2\pi^2\beta\omega \\ -\frac{2}{3}\varepsilon^2\pi^3 + 2\pi\omega^2 & -\frac{2}{3}\varepsilon^2\pi^4 + 2\pi^2\omega^2 - 2\pi\beta\omega \end{bmatrix}.$$

We calculate according (17) the second order adjustment of monodromy matrix

$$\mathbf{F}_2 = \begin{bmatrix} -\frac{1}{6}\pi^4\varepsilon^2 + 2\pi^2\omega^2 & -\frac{1}{15}\pi^5\varepsilon^2 + \frac{4}{3}\pi^3\omega^2 - 2\pi^2\beta\omega \\ -\frac{2}{3}\pi^3\varepsilon^2 + 2\pi\omega^2 & -\frac{1}{6}\pi^4\varepsilon^2 + 2\pi^2\omega^2 - 2\pi\beta\omega \end{bmatrix}, \quad (38)$$

Thus $\text{tr}(\mathbf{F}_2) = -\frac{1}{3}\pi^4\varepsilon^2 + 4\pi^2\omega^2 - 2\pi\beta\omega$ and $\text{tr}(\mathbf{A}_2) = -2\pi\beta\omega$.

Second order approximation of stability border written from (30) as

$$|\text{tr}(\mathbf{F}_0) + \text{tr}(\mathbf{F}_1) + \text{tr}(\mathbf{F}_2)| - 1 = 1 - 2\pi\beta\omega$$

yields $4\pi^2\omega^2 - \varepsilon_p^2\pi^4/3 = 0$ and $4 - 4\pi\beta w + 4\pi^2\omega^2 - \varepsilon_n^2\pi^4/3 = 0$ in cases of positive and negative value of the sum $\text{tr}(\mathbf{F}_0) + \text{tr}(\mathbf{F}_1) + \text{tr}(\mathbf{F}_2)$ correspondingly. Hence, we have the corresponding stability borders denoted by indexes p and n

$$\varepsilon_p = \frac{2\sqrt{3}}{\pi}\omega, \quad \varepsilon_n = \frac{2\sqrt{3}}{\pi}\sqrt{\omega^2 - \frac{\beta\omega}{\pi} + \frac{1}{\pi^2}},$$

same as in the third approximation, see dashed lines in Fig. 1 on the left, because (11)–(18) yield $\text{tr}(\mathbf{F}_3) = 0$ and $\text{tr}(\mathbf{A}_3) = 0$.

Fourth order approximation, where stability boundary equation reads as

$$|\text{tr}(\mathbf{F}_0) + \text{tr}(\mathbf{F}_1) + \text{tr}(\mathbf{F}_2) + \text{tr}(\mathbf{F}_3) + \text{tr}(\mathbf{F}_4)| - 1 = 1 - 2\pi\beta\omega + \frac{1}{2}(2\pi\beta\omega)^2,$$

yields in cases of positive and negative sums of traces the following two equations:

$$\begin{aligned} \frac{\pi^8\varepsilon_p^4}{1260} - \frac{\pi^4}{3}\left(1 + \frac{4\pi^2\omega^2}{15} - \pi\beta\omega\right)\varepsilon_p^2 + 4\pi^2\omega^2\left(1 + \frac{\pi^2\omega^2}{3} - \beta\omega\pi\right) &= 0, \\ \frac{\pi^8\varepsilon_n^4}{1260} - \frac{\pi^4}{3}\left(1 + \frac{4\pi^2\omega^2}{15} - \pi\beta\omega\right)\varepsilon_n^2 + 4\left(1 - \beta\pi\omega + \pi^2\omega^2 \right. \\ \times \left. \left(1 + \frac{\pi^2\omega^2}{3} - \beta\omega\pi + \beta^2\right)\right) &= 0. \end{aligned}$$

Solutions of these two equations with respect to ε^2 give us four borders, drawn in Fig. 1 with solid lines, while the two exact stability domains determined by (31) are marked in gray.

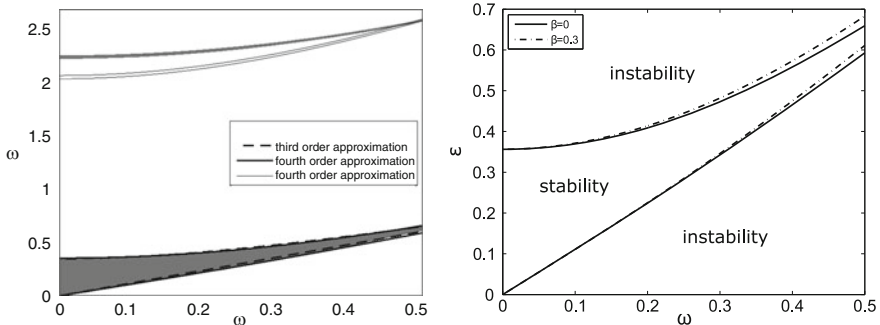


Fig. 1 Comparison of approximate stability boundaries of the third (dashed lines) and fourth (solid lines) orders with exact stability domains (gray areas) on the left. Damping stabilization and destabilization of the inverted vertical pendulum position on the right

7 Conclusion

We develop a convenient algorithm for obtaining approximate stability boundaries of parametrically excited systems. We demonstrate how this algorithm can be applied to the particular case of parametric pendulum for obtaining approximate stability domains even in the case of damping and impulse parametric excitation. Stabilizing and destabilizing effects of damping on inverted equilibrium of the parametric pendulum are revealed with the use of the fourth order approximation of stability boundaries.

In Fig. 1 on the right we showed approximate stability boundaries of inverted vertical pendulum position. Addition of small linear viscous friction β shifts both stability boundaries upward. Thus, at the lower boundary additional friction destabilizes the inverted pendulum while at the upper boundary friction stabilizes the pendulum position.

Acknowledgement A.O. Belyakov received funding from the Russian Science Foundation grant 19-11-00223.

References

1. Floquet, G.: Sur les équations différentielles linéaires à coefficients périodiques. *Ann. Sci. Ecol. Norm. Super.* **12**, 47–88 (1883)
2. Xu, X., Wiercigroch, M.: Approximate analytical solutions for oscillatory and rotational motion of a parametric pendulum. *Nonlinear Dyn.* **47**(1–3), 311–320 (2007)
3. Butikov, E.I.: A physically meaningful new approach to parametric excitation and attenuation of oscillations in nonlinear systems. *Nonlinear Dyn.* **88**(4), 2609–2627 (2017)
4. Bogoliubov, N.N., Mitropolsky, Y.A.: Asymptotic Methods in the Theory of Non-Linear Oscillations. Gordon and Breach, New York (1961)
5. Seyranian, A.P., Mailybaev, A.A.: Multiparameter Stability Theory with Mechanical Applications. World Scientific, New Jersey (2003)
6. Seyranian, A.A., Seyranian, A.P.: The stability of an inverted pendulum with a vibrating suspension point. *J. Appl. Math. Mech.* **70**, 754–761 (2006)
7. Arkhipova, I.M., Luongo, A.: On the effect of damping on the stabilization of mechanical systems via parametric excitation. *Zeitschrift für angewandte Mathematik und Physik* **67**(3), 69 (2016). <https://doi.org/10.1007/s00033-016-0659-6>
8. Belyakov, A.O.: Another mechanical model of parametrically excited pendulum and stabilization of its inverted equilibrium position. In: Proceedings of 8th European Nonlinear Dynamics Conference, ENOC 2014
9. Kuznetsov, S.P.: Dynamical Chaos. Phymatlit, Moscow (2006) (in Russian)
10. Yakubovich, V.A., Starzhinskii, V.M.: Parametric Resonance in Linear Systems. Nauka, Moscow (1987)
11. Arnold, V.I.: Ordinary Differential Equations. Springer, New York (1992)
12. Meissner, E.: Ueber Schüttelerscheinungen in Systemen mit periodisch veränderlicher Elastizität. *Schweizerische Bauzeitung* **72**(11), 95–98 (1918)

ε^2 -Order Normal Form Analysis for a Two-Degree-of-Freedom Nonlinear Coupled Oscillator



Xuanang Liu and David J. Wagg

Abstract In this paper, we describe an ε^2 -order normal form decomposition for a two-degree-of-freedom oscillator system that has a mass supported with horizontal and vertical support springs. This system has nonlinear terms that are not necessarily ε^1 -order small when compared to the linear terms. As a result, analytical approximate methods based on an ε expansion would typically need to include higher-order components in order to capture the nonlinear dynamic behaviour. In this paper we show how this can be achieved using a direct normal form transformation up to order ε^2 . However, we will show that the requirement for including ε^2 components is primarily due to the way the direct normal form method deals with quadratic coupling terms rather than the relative size of the coefficients.

Keywords Nonlinear oscillator · Normal form · ε^2 -order

1 Introduction

Normal form transformations are a classical method for studying dynamical systems first introduced by Poincaré [1]. The historical background of normal form transformations can be found in a number of texts including [2–4]. This work is motivated by vibration problems involving coupled nonlinear oscillators, where the objective of a normal form transformation is to both simplify the system, but also to identify potential nonlinear resonances that might occur. For vibration problems, Jezequel and Lamarque [5] proposed a normal form decomposition for a system of two coupled oscillators with cubic nonlinearities and both forcing and damping. The relationship between the normal form transformation and nonlinear normal modes was established by Touzé and co-workers [6, 7], based on examples of coupled oscillator systems that included both quadratic and cubic nonlinear terms.

X. Liu and D. J. Wagg (✉)

Department of Mechanical Engineering, University of Sheffield, Sheffield, UK
e-mail: david.wagg@sheffield.ac.uk

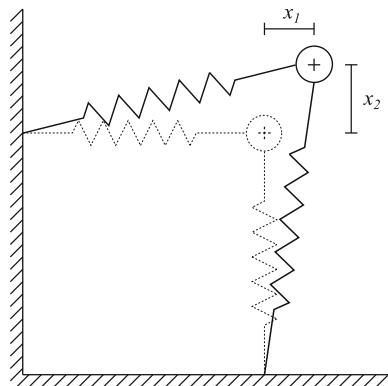
In this paper, we will consider an oscillator system consisting of a mass supported by vertical and horizontal springs that are attached to solid supports. This system is shown schematically in Fig. 1. The equations of motions of this example system, as derived by Touzé et al. [6], are taken to be

$$\begin{aligned}\ddot{x}_1 + 2\xi_1\omega_1\dot{x}_1 + \omega_1^2x_1 + a_1x_1^2 + a_2x_1x_2 + a_3x_2^2 + a_4x_1^3 + a_5x_1x_2^2 &= f_1 \cos(\Omega t), \\ \ddot{x}_2 + 2\xi_2\omega_2\dot{x}_2 + \omega_2^2x_2 + b_1x_1^2 + b_2x_1x_2 + b_3x_2^2 + b_4x_1^2x_2 + b_5x_2^3 &= f_2 \cos(\Omega t),\end{aligned}\quad (1)$$

where the coefficients of the nonlinear terms a_i, b_i for $i, j = 1, 2, \dots, 5$ are of the same size order as the natural frequencies ω_1 and ω_2 , respectively. The other coefficients are damping ratios ξ_i , and forcing amplitudes f_i , for each degree of freedom $i = 1, 2$ and the external forcing frequency is Ω .

This system has been studied in depth by several previous authors [6–8]. In particular, Touzé and Amabili [7] showed how a single-linear-mode approximation to the system dynamics would predict hardening instead of softening behaviour for a specific set of parameter values, whereas a nonlinear normal mode type analysis predicts the correct softening resonance, behaviour. Furthermore, in Touzé and Amabili [7] backbone curves for the system were computed, and these curves were compared with forced-damped simulations of the system. In [8] a detailed study of methods for computing backbone curves was carried out. As part of their study Breunung and Haller, [8], used the current example to make a comparison between a spectral sub-manifold method and the methods of Touzé and Amabili [7] and Neild and Wagg [9]. This comparison showed that the ε^1 direct normal form proposed by Neild and Wagg [9] gave the incorrect approximations for this example. In fact, using the ε^1 version gave a result similar to the linear-mode approximation first discussed by Touzé and Amabili [7]—predicting hardening instead of softening behaviour. In this paper, we will show that the ε^2 terms are required in the direct

Fig. 1 The example system considered in this paper



normal form method of Neild and Wagg [9] to give the correct solutions. Typically the direct normal form method, [9], is applied to systems where the nonlinear, damping and forcing terms are assumed to be of order ε^1 small (or higher orders of ε) when compared to the linear terms [10–14]. The linear terms are the natural frequencies, taken to be of order ε^0 , meaning that the ε^1 nonlinear terms are typically an order smaller than the natural frequencies. In Eq. (1) this is not the case, and it is possible for the nonlinear coefficients to be of the same size order as the natural frequencies. As a result, the normal form approximation would typically need to be extended to include higher-order terms. Here, we show that an ε^2 -order analysis is sufficient to capture the required behaviour, although in fact the need for the ε^2 -order terms is actually because of the quadratic coupling terms, as will be explained below.

2 ε^2 -Order Normal Form Analysis

We follow the method set out in Chapter 4 of [15] for a ε^2 direct normal form method. The coefficients of the nonlinear terms in Eq. (1) are taken to be

$$\begin{aligned} a_1 &= \frac{3}{2}\omega_1^2 & a_2 &= \omega_2^2 & a_3 &= \frac{1}{2}\omega_1^2 & a_4 &= \frac{1}{2}(\omega_1^2 + \omega_2^2) & a_5 &= \frac{1}{2}(\omega_1^2 + \omega_2^2) \\ b_1 &= \frac{1}{2}\omega_2^2 & b_2 &= \omega_1^2 & b_3 &= \frac{3}{2}\omega_2^2 & b_4 &= \frac{1}{2}(\omega_1^2 + \omega_2^2) & b_5 &= \frac{1}{2}(\omega_1^2 + \omega_2^2). \end{aligned} \quad (2)$$

As the conservative form of Eq. (1) is naturally linearly decoupled, it can be described in the matrix form as $\ddot{\mathbf{q}} + \boldsymbol{\Lambda}\mathbf{q} + \mathbf{N}_q(\mathbf{q}) = \mathbf{0}$ by setting $\mathbf{q} = [q_1, q_2]^\top = [x_1, x_2]^\top$, where

$$\boldsymbol{\Lambda} = \begin{bmatrix} \omega_1^2 & 0 \\ 0 & \omega_2^2 \end{bmatrix}, \quad \text{and} \quad \mathbf{N}_q(\mathbf{q}) = \begin{pmatrix} a_1q_1^2 + a_2q_1q_2 + a_3q_2^2 + a_4q_1^3 + a_5q_1q_2^2 \\ b_1q_1^2 + b_2q_1q_2 + b_3q_2^2 + b_4q_1^2q_2 + b_5q_2^3 \end{pmatrix}, \quad (3)$$

although as noted above $\mathbf{N}_q(\mathbf{q})$ is not ε^1 small in this example. Here the non-internal-resonant case is considered, such that the detuned response frequencies $\omega_{ri} \neq n\omega_{rj}$ for $i, j = 1, 2$ with $i \neq j$ and $n = 1, 2, \dots$. Note that other rational resonances, such as $n = 3/5$ are not considered here. The exact detuning mechanism is explained in detail in [15].

Next we carry out a ε^2 near identity transformation $\mathbf{q} = \mathbf{u} + \varepsilon\mathbf{h}_{(1)}(\mathbf{u}) + \varepsilon^2\mathbf{h}_{(2)}(\mathbf{u})$. The first step in this process is to substitute $\mathbf{q} = [q_1, q_2]^\top = [u_{1p} + u_{1m}, u_{2p} + u_{2m}]^\top$ into Eq. (3). This then leads to a $[30 \times 1]$ dimension \mathbf{u}^* vector, which is used to redefine $\mathbf{N}_q(\mathbf{u}) = \mathbf{n}_1\mathbf{u}^*$ and $\mathbf{h}_{(1)}(\mathbf{u}) = \mathbf{h}_1\mathbf{u}^*$, such that \mathbf{n}_1 and \mathbf{h}_1 are coefficient

matrices for the ε^1 terms. The objective is to obtain a normal form of $\ddot{\mathbf{u}} + \boldsymbol{\Lambda}\mathbf{u} + \mathbf{N}_u(\mathbf{u}) = \mathbf{0}$, with $\mathbf{N}_u = \varepsilon\mathbf{n}_{u(1)} + \varepsilon^2\mathbf{n}_{u(2)}$. To find the transformed vectors $\mathbf{n}_{u(1)}$ and $\mathbf{n}_{u(2)}$, solutions to the following equations are required

$$\varepsilon^1 : \quad \ddot{\mathbf{h}}_{(1)}(\mathbf{u}) + \boldsymbol{\Upsilon}\mathbf{h}_{(1)}(\mathbf{u}) + \mathbf{n}_{(1)}(\mathbf{u}) = \mathbf{n}_{u(1)}(\mathbf{u}), \quad (4a)$$

$$\varepsilon^2 : \quad \ddot{\mathbf{h}}_{(2)}(\mathbf{u}) + \boldsymbol{\Upsilon}\mathbf{h}_{(2)}(\mathbf{u}) + \mathbf{n}_{(2)}(\mathbf{u}) = \mathbf{n}_{u(2)}(\mathbf{u}), \quad (4b)$$

where $\boldsymbol{\Upsilon}$ is a $\{N \times N\}$ diagonal matrix of the square of the response frequencies, ω_{ri}^2 such that $\boldsymbol{\Lambda} = \boldsymbol{\Upsilon} + \varepsilon\boldsymbol{\Delta}$, and

$$\mathbf{n}_{(1)}(\mathbf{u}) = \mathbf{N}_q(\mathbf{q} = \mathbf{u}), \quad (5a)$$

$$\mathbf{n}_{(2)}(\mathbf{u}) = \left(\boldsymbol{\Delta} + \frac{\partial \mathbf{N}_q(\mathbf{q})}{\partial \mathbf{q}} \Big|_{\mathbf{q}=\mathbf{u}} \right) \mathbf{h}_{(1)}(\mathbf{u}). \quad (5b)$$

Solving Eq. (4a) we can first obtain the ε^1 terms as

$$\mathbf{n}_{u(1)} = \begin{pmatrix} 3a_4(u_{1p}^2 u_{1m} + u_{1p} u_{1m}^2) + 2a_5(u_{1p} u_{2p} u_{2m} + u_{1m} u_{2p} u_{2m}) \\ 2b_4(u_{1p} u_{1m} u_{2p} + u_{1p} u_{1m} u_{2m}) + 3b_5(u_{2p}^2 u_{2m} + u_{2p} u_{2m}^2) \end{pmatrix}. \quad (6)$$

For the ε^2 terms, we must determine Eq. (5b) up to cubic order which should provide an accurate solution for this example, and thus the nonlinear terms vector $\mathbf{n}_{(2)}$ is truncated at $\mathcal{O}(\mathbf{u}^4)$. As a result we can simplify \mathbf{N}_q because we only need terms up to order $\mathcal{O}(\mathbf{u}^2)$ in the partial derivative, and so we write $\mathbf{N}_q(\mathbf{u}) = \tilde{\mathbf{N}}_q(\mathbf{u}) + \mathcal{O}(\mathbf{u}^3)$. Then we have

$$\boldsymbol{\Delta} = \begin{bmatrix} \omega_{n1}^2 - \omega_{r1}^2 & 0 \\ 0 & \omega_{n2}^2 - \omega_{r2}^2 \end{bmatrix} = \begin{bmatrix} \delta_1 & 0 \\ 0 & \delta_2 \end{bmatrix}, \quad \text{and} \quad (7a)$$

$$\frac{\partial \tilde{\mathbf{N}}_q(\mathbf{u})}{\partial \mathbf{u}} = \begin{bmatrix} 2a_1(u_{1p} + u_{1m}) + a_2(u_{2p} + u_{2m}) & a_2(u_{1p} + u_{1m}) + 2a_3(u_{2p} + u_{2m}) \\ 2b_1(u_{1p} + u_{1m}) + b_2(u_{2p} + u_{2m}) & b_2(u_{1p} + u_{1m}) + 2b_3(u_{2p} + u_{2m}) \end{bmatrix}. \quad (7b)$$

Therefore we can compute $\mathbf{n}_{(2)}$ using

$$\mathbf{n}_{(2)} = \begin{bmatrix} \delta_1 & 0 \\ 0 & \delta_2 \end{bmatrix} \mathbf{h}_1 \mathbf{u}^* + \frac{\partial \tilde{\mathbf{N}}_q(\mathbf{u})}{\partial \mathbf{u}} \tilde{\mathbf{h}}_1 \tilde{\mathbf{u}}^* + \mathcal{O}(\mathbf{u}^4), \quad (8)$$

where $\tilde{\mathbf{h}}_1$ and $\tilde{\mathbf{u}}^*$ are the respective projections of \mathbf{h}_1 and \mathbf{u}^* to $\mathcal{O}(\mathbf{u}^2)$. This allows the vector of nonlinear terms up to order ε^2 to be obtained as

$$\begin{aligned}
\mathbf{n}_{u(2)} = & \left(-\frac{10}{3\omega_{r1}^2}a_1^2 + \frac{3\omega_{r2}^2 - 8\omega_{r1}^2}{(4\omega_{r1}^2 - \omega_{r2}^2)\omega_{r2}^2}a_2b_1 \right) (u_{1p}^2 u_{1m} + u_{1p} u_{1m}^2) \\
& \left(-\frac{10}{3\omega_{r2}^2}b_3^2 + \frac{3\omega_{r1}^2 - 8\omega_{r2}^2}{(4\omega_{r2}^2 - \omega_{r1}^2)\omega_{r1}^2}a_3b_2 \right) (u_{2p}^2 u_{2m} + u_{2p} u_{2m}^2) \\
& + \left(\frac{2}{\omega_{r2}^3 - 4\omega_{r1}^2}a_2^2 - \frac{4}{\omega_{r1}^2}a_1a_3 + \frac{4}{\omega_{r1}^2 - 4\omega_{r2}^2}a_3b_2 - \frac{2}{\omega_{r2}^2}a_2b_3 \right) \\
& \times (u_{1p}u_{2p}u_{2m} + u_{1m}u_{2p}u_{2m}) \\
& + \left(\frac{2}{\omega_{r1}^3 - 4\omega_{r2}^2}b_2^2 - \frac{4}{\omega_{r2}^2}b_1b_3 + \frac{4}{\omega_{r2}^2 - 4\omega_{r1}^2}a_2b_1 - \frac{2}{\omega_{r1}^2}a_1b_2 \right) \\
& \times (u_{1p}u_{1m}u_{2p} + u_{1p}u_{1m}u_{2m})
\end{aligned} \tag{9}$$

Now using $\mathbf{N}_u = \mathbf{n}_{u(1)} + \mathbf{n}_{u(2)}$, the direct normal form for the system (for the non-internally resonant case) is given by

$$\begin{aligned}
\ddot{u}_1 + \omega_1^2 u_1 + A(u_{1p}^2 u_{1m} + u_{1p} u_{1m}^2) + B(u_{1p}u_{2p}u_{2m} + u_{1m}u_{2p}u_{2m}) &= 0, \\
\ddot{u}_2 + \omega_2^2 u_2 + C(u_{2p}^2 u_{2m} + u_{2p} u_{2m}^2) + D(u_{1p}u_{1m}u_{2p} + u_{1p}u_{1m}u_{2m}) &= 0,
\end{aligned} \tag{10}$$

where

$$A = 3a_4 - \frac{10}{3\omega_{r1}^2}a_1^2 + \frac{3\omega_{r2}^2 - 8\omega_{r1}^2}{(4\omega_{r1}^2 - \omega_{r2}^2)\omega_{r2}^2}a_2b_1, \tag{11a}$$

$$B = 2a_5 + \frac{2}{\omega_{r2}^3 - 4\omega_{r1}^2}a_2^2 - \frac{4}{\omega_{r1}^2}a_1a_3 + \frac{4}{\omega_{r1}^2 - 4\omega_{r2}^2}a_3b_2 - \frac{2}{\omega_{r2}^2}a_2b_3, \tag{11b}$$

$$C = 3b_5 - \frac{10}{3\omega_{r2}^2}b_3^2 + \frac{3\omega_{r1}^2 - 8\omega_{r2}^2}{(4\omega_{r2}^2 - \omega_{r1}^2)\omega_{r1}^2}a_3b_2, \tag{11c}$$

$$D = 2b_4 + \frac{2}{\omega_{r1}^3 - 4\omega_{r2}^2}b_2^2 - \frac{4}{\omega_{r2}^2}b_1b_3 + \frac{4}{\omega_{r2}^2 - 4\omega_{r1}^2}a_2b_1 - \frac{2}{\omega_{r1}^2}a_1b_2. \tag{11d}$$

Substituting $u_{1p} = (\frac{U_1}{2}e^{-i\phi_1})e^{i\omega_{r1}t}$ and $u_{1m} = (\frac{U_1}{2}e^{i\phi_1})e^{-i\omega_{r1}t}$ into Eq. (10) enables expressions for the backbone curves to be obtained as

$$\left[-\omega_{r1}^2 + \omega_1^2 + \frac{1}{4}AU_1^2 + \frac{1}{4}BU_2^2 \right] \frac{U_1^2}{2} = 0, \tag{12a}$$

$$\left[-\omega_{r2}^2 + \omega_2^2 + \frac{1}{4}CU_1^2 + \frac{1}{4}DU_2^2 \right] \frac{U_2^2}{2} = 0, \quad (12b)$$

where U_i is the displacement amplitude of u_i , for $i = 1, 2$. Successively setting U_2 and U_1 to zero will give the S_1 and S_2 backbone curves

$$S1 : \quad \omega_{r1}^2 = \omega_1^2 + \frac{1}{4}AU_1^2, \quad (13a)$$

$$S2 : \quad \omega_{r2}^2 = \omega_2^2 + \frac{1}{4}CU_2^2. \quad (13b)$$

Note that these are now implicit expressions for ω_{r1}^2 and ω_{r2}^2 , respectively, which can be solved numerically to find the backbone curves.

Finally, the physical displacement responses may be computed using the corresponding reverse transform $u_1 \rightarrow q_1 = x_1$, and $u_2 \rightarrow q_2 = x_2$ such that

$$\begin{aligned} x_1 &= q_1 = u_1 + h_{1,1}\mathbf{u}^* + h_{2,1}^+\mathbf{u}^+, \\ x_2 &= q_2 = u_2 + h_{1,2}\mathbf{u}^* + h_{2,2}^+\mathbf{u}^+, \end{aligned} \quad (14)$$

where $h_{i,j}$ are row vectors taken from the \mathbf{h}_1 and \mathbf{h}_2^+ coefficient matrices based on the fact that $\mathbf{h}_{(2)}$ has been redefined as $\mathbf{h}_{(2)} = \mathbf{h}_2^+\mathbf{u}^+$ —see Chapter 4 of [15] for full details of this procedure.

3 Numerical Results

The simulation uses the parameters $\omega_1 = 2$, $\omega_2 = 4.5$, $\zeta_1 = 0.001$, $\zeta_2 = 0.001$, $f_k = 0.0015$ and $f_\ell = 0$ for the two different forcing cases $k = 1, \ell = 2$ and $k = 2, \ell = 1$. The results for the $S1$ and $S2$ backbone curves computed using Eqs. (13) are shown as the red lines in Figs. 2 and 3. For comparison, the order ε^1 backbone curves are shown as blue lines in the figures. In order to verify the analytically approximated ε^2 backbone results, resonance response curves for the corresponding forced, damped case are computed using the continuation Matlab toolbox—COCO [16]. These are shown as black lines in Figs. 2 and 3.

The plots in Fig. 2 are presented in the projection of the response amplitude of the physical coordinates, X_i , against the forcing frequency, Ω (or ω_r for the undamped backbone curves). In each figure X_1 against Ω is shown in plot (a) and X_2 against Ω is shown in plot (b). Consequently, in Fig. 2 where the forcing is applied to the x_1 equation, the dominant response is in the X_1 amplitude (plot Fig. 2a), and the response in plot (b) of X_2 vs Ω is primarily due to the harmonic terms via Eq. (14).

Values of ω_i are chosen as they are exactly the same as those used by previous studies [6, 8] to demonstrate the non-internally resonant dynamics of the system.

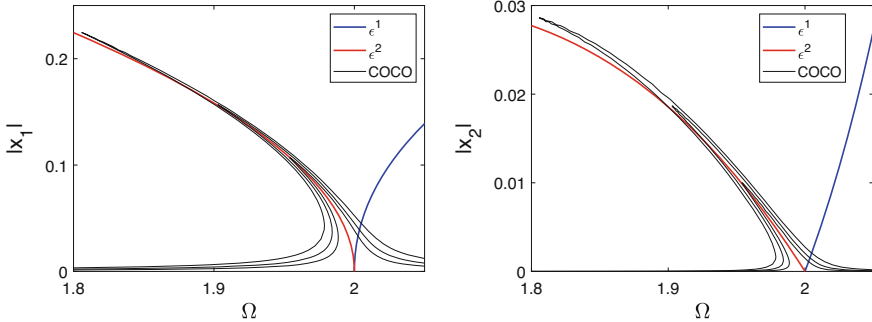


Fig. 2 The backbone curves S_1 , and resonance response curves of the two-degree-of-freedom example system described in Eq.(1) for the case where its horizontal mode is dominant. The red and black lines denote the backbone curves and numerically computed forced response curves using COCO, respectively. Parameters: $\omega_1 = 2$, $\omega_2 = 4.5$, $\zeta_1 = 0.001$, $\zeta_2 = 0.001$. There are three different forcing amplitude curves $f_1 = 0.001, 0.0016, 0.0025$ and $f_2 = 0$. Note that the stability of the solution curves is not indicated on this figure

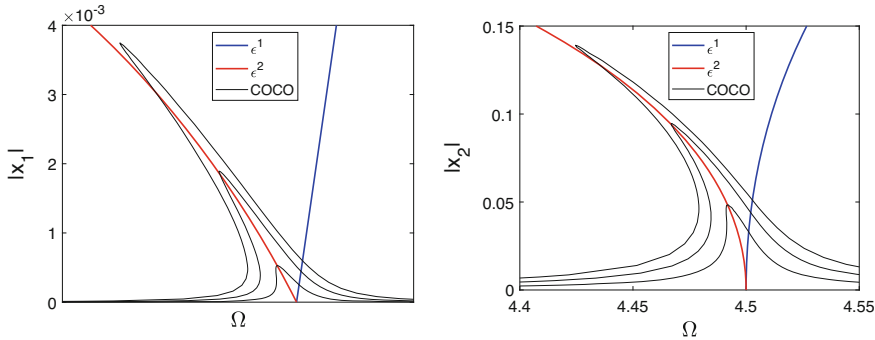


Fig. 3 The backbone curves S_2 , and resonance response curves of the two-degree-of-freedom example system described in Eq. 1 for the case where its horizontal mode is dominant. The red and black lines denote the backbone curves and numerically computed forced response curves using COCO, respectively. Parameters: $\omega_1 = 2$, $\omega_2 = 4.5$, $\zeta_1 = 0.001$, $\zeta_2 = 0.001$. Here there are three different forcing amplitude curves shown $f_2 = 0.002, 0.004, 0.006$, and $f_1 = 0$. Note that the stability of the solution curves is not indicated on this figure

For the damping values, $\zeta_1 = 0.001$ was used previously by Touzé et al. [6], but here we have used $\zeta_2 = 0.001$ as well so that the COCO continuation curves are very close to the undamped case. It can be seen that the analytical backbone curves correctly predict the softening dynamics of the example system which is consistent with the findings in [6]. However, it is important to note that the backbone curve expression computed with just the ε^1 terms gives a hardening response, which does not match the system behaviour correctly, as shown by the blue lines in Figs. 2 and 3 (and also the comparison presented by Breunung and Haller [8]).

The specific reason for this can be seen in Eq. (11) which gives the coefficients for the S_1 and S_2 backbone curves in Eqs. (13). Specifically for the S_1 backbone

the coefficient producing curvature is A . In the ε^1 case, $A = 3a_4$, which will give a hardening S_1 curve. However in the ε^2 case, A is given by Eq. (11a) and there are two additional terms that reverse the curvature of S_1 , for the given parameters, to produce a softening backbone curve. In fact reducing the ω_2 value to a value of 3.8rad/s (whilst keeping all other parameters the same) results in the backbone curve switching to hardening.

This is consistent with the finding of [7] that the quadratic terms of the type found in this example will generate cubic terms in the nonlinear coordinate transformation. As we have shown, in the direct normal form method of Neild and Wagg [9], these generated terms from the quadratics are only captured in the ε^2 expansion not the ε^1 version. This explains why the ε^1 version of the direct normal form will not show the correct softening nonlinear behaviour—as also shown in the comparison by Breunung and Haller [8]. It is also clear from the results presented above that this can be rectified by the inclusion of the ε^2 terms.

Although not the specific cause (and therefore less important) we note that the direct normal form method does rely on the nonlinear terms being small in the sense that they should be significantly smaller than the ω_{ni}^2 values. However, in this example the nonlinear coefficients are of the same order as the ω_{ni}^2 values, and yet despite this, by adding ε^2 terms, the direct normal form method gives a very good approximation to the solution. Specifically, the maximum response position of the COCO curves is very close to the backbone curves for both S_1 and S_2 .

4 Conclusions

In this paper, ε^2 -order approximate analytical expressions for the backbone curves of a coupled two-degree-of-freedom system have been obtained using the direct normal form method proposed by Neild and Wagg. The motivation for this study was the observation that the ε^1 version of the direct normal form method did not predict the correct softening type of behaviour for this example. In fact, we have shown in this paper that the primary cause of this discrepancy is due to how the direct normal form treats the quadratic coupling terms of the type found in this example.

This is because during the backbone curve approximation process quadratic terms actually generate terms up to cubic order. These terms are significant in obtaining a representative model for the backbone curve. In the method proposed by Neild and Wagg, these additional cubic terms are captured only in the ε^2 part of the approximation. As a result, if using this method for a system with quadratic nonlinearities, then the ε^2 version is needed to fully capture the relevant dynamic behaviour.

In addition to this, and despite the fact that the direct normal form assumes small nonlinear terms, which are not the case in this example, the results obtained from the ε^2 version and the numerical method agree well.

Acknowledgements The authors would like to acknowledge the support of the Engineering and Physical Science Research Council. This work was started while D.J.W was supported by EPSRC grant EP/K003836/2, and finished under the grant EP/R006768/1. X. L. was supported by a Department of Mechanical Engineering studentship and also EPSRC grant EP/J016942/1. The authors would also like to thank Ayman Nasir for useful discussions regarding this work.

References

1. Poincaré, H. (translated by Goroff, D.): New methods of celestial mechanics (English translation of: *Les méthodes nouvelles de la mécanique céleste*, 1892). American Institute of Physics, United States, College Park (1993)
2. Arnold, V.I.: Geometrical Methods in the Theory of Ordinary Differential Equations. Springer, Berlin (1988)
3. Nayfeh, A.H.: Method of Normal Forms. Wiley, London (1993)
4. Kahn, P.B., Zarmi, Y.: Nonlinear dynamics: a tutorial on the method of normal forms. *Am. J. Phys.* **68**, 907–919 (2000)
5. Jezequel, L., Lamarque, C.H.: Analysis of nonlinear dynamic systems by the normal form theory. *J. Sound Vib.* **149**, 429–459 (1991)
6. Touzé, C., Thomas, O., Chaigne, A.: Hardening/softening behaviour in non-linear oscillations of structural systems using non-linear normal modes. *J. Sound Vib.* **273**, 77–101 (2004)
7. Touzé, C., Amabili, M.: Nonlinear normal modes for damped geometrically nonlinear systems: application to reduced-order modelling of harmonically forced structures. *J. Sound Vib.* **298**, 958–981 (2006)
8. Breunung, T., Haller, G.: Explicit backbone curves from spectral submanifolds of forced-damped nonlinear mechanical systems. *Proc. R. Soc. A* **474**, 20180083 (2018)
9. Neild, S.A., Wagg, D.J.: Applying the method of normal forms to second-order nonlinear vibration problems. In: Proceedings of the Royal Society of London A: Mathematical, Physical and Engineering Sciences, vol. 467, pp. 1141–1163. The Royal Society, London (2011)
10. Xin, Z., Neild, S., Wagg, D.J., Zuo, Z.: Resonant response functions for nonlinear oscillators with polynomial type nonlinearities. *J. Sound Vib.* **332**, 1777–1788 (2013)
11. Hill, T., Cammarano, A., Neild, S., Wagg, D.: Interpreting the forced responses of a two-degree-of-freedom nonlinear oscillator using backbone curves. *J. Sound Vib.* **349**, 276–288 (2015)
12. Neild, S.A., Champneys, A.R., Wagg, D.J., Hill, T.L., Cammarano, A.: The use of normal forms for analysing nonlinear mechanical vibrations. *Philos. Trans. R. Soc. A* **373**, 20140404 (2015)
13. Liu, X., Cammarano, A., Wagg, D.J., Neild, S.A., Barthorpe, R.: $N - 1$ modal interactions of a three-degree-of-freedom system with cubic elastic nonlinearities. *Nonlinear Dyn.* **83**, 497–511 (2016)
14. Hill, T.L., Cammarano, A., Neild, S.A., Barton, D.A.W.: Identifying the significance of nonlinear normal modes. *Proc. R. Soc. A* **473**(2199), 20160789 (2017)
15. Wagg, D.J., Neild, S.A.: Nonlinear Vibration with Control: For Flexible and Adaptive Structures, vol. 218. Springer, Berlin (2014)
16. Dankowicz, H., Schilder, F.: Recipes for Continuation, vol. 11. SIAM (2013)

Vibrational Mechanics of Systems with Amplitude and Phase Modulation of Excitation



Eugen Kremer 

Abstract An oscillator under the influence of high-frequency harmonic excitation with the amplitude and phase depending on the coordinate, velocity, and slow time is considered. Within the framework of the concept of vibrational mechanics, an equation is derived for the averaged motion of this system, containing an additional so-called vibrational force. In this case, a modification of the method of direct separation of motions is used that involves the introduction of a small parameter and considers the idea of two-scale decomposition. The resulting general formula for the vibrational force makes it possible to reveal some regularities connecting the original and averaged systems. Numerical verification of the method is performed for the example of a mechanical vibrator under the action of a high-frequency kinematic excitation with phase modulation.

Keywords Vibrational mechanics · Amplitude modulation · Phase modulation · Method of direct separation of motion · Averaged motion

1 Introduction

The concept of vibrational mechanics was proposed by Blekhman [1] and developed in a number of studies, a survey of which can be found, for example, in [1–5]. Vibrational mechanics, including the method of direct separation of motions, represents a compact and efficient calculation tool, which has been used in the development of many new vibrating machines and technologies [3].

E. Kremer (✉)

Schaeffler Automotive Buehl GmbH & Co. KG, Buehl, Baden, Germany

Institute for Problems in Mechanical Engineering of Russian Academy of Sciences,
St. Petersburg, Russia

e-mail: Eugen.Kremer@Schaeffler.com

It is known that for many processes and systems, such as, for example, the vibrational transportation of bulk material [1], the most interesting is averaged motion, and the details of high-frequency oscillations are not essential. Meanwhile, the high-frequency component in the excitation cannot generally be neglected, although it has a zero mean. How should such systems be analyzed? Of course, there is always the possibility of calculating the total motion, followed by averaging the result. However, such an approach is obviously uneconomic, since most of the information obtained in this way is unnecessary and discarded in the process of averaging.

Vibrational mechanics offers another way: replacing the original system with some system equivalent to the original one with respect to slow motions, the so-called averaged system. This results in a system that does not contain fast oscillating forces and simultaneously its motion coincides with the averaged motions of the original system. To obtain the averaged system, Blekhman proposed a method of direct separation of motion [1] and showed that, instead of the rapid excitation, the averaged system involves a certain additional slow force known as the vibrational force. This force is the price for hiding the fast motions. The appearance of a vibrational force leads to interesting and unexpected physical effects in averaged systems. Among them are Chelomei's pendulum, the Stephenson–Kapitza pendulum, the Indian rope, vibrational transportation, and many other phenomena, a large collection of which are described in [1]. Thomsen [2] selected three groups of effects, stiffening, biasing, and smoothing, which appear in different systems with fast excitation, independent of their physical nature. Another direction of vibrational mechanics, along with the analysis of specific physical systems, is the analysis of the causes and the structure of vibrational forces for different classes of systems [4, 5]. Thus, in [4], a system with amplitude modulation of excitation is analyzed. The term “amplitude modulation” is used here, as in signal processing, for a variation of the amplitude: a sinusoidal high-frequency excitation has amplitude that depends on the coordinate, velocity, and slow time. As shown in this chapter, the nature of the dependence of the excitation amplitude on these quantities determines five different scenarios for the generation of a vibrational force:

- the nonlinearity of the initial slow force with respect to velocity;
- the dependence of the modulation amplitude on the coordinate;
- the dependence of the modulation amplitude on the velocity;
- the dependence of the modulation amplitude on the velocity and on the coordinate; and
- the explicit dependence of the modulation amplitude on the slow time and on the velocity

These results were extended in [5] to the case of modulated stochastic excitation and applied to the problem of stochastic resonance.

The purpose of the present chapter is to further generalize these results and to extend them to the case of amplitude phase and in particular phase modulation, i.e., to the case of a high-frequency sinusoidal excitation with a variation of its phase in dependence on the coordinate, velocity, and slow time. This problem is of

interest in connection with the search for new effective controlled vibro-excitors for vibrational technologies.

2 Vibrational Forces for a System with Amplitude and Phase Modulation

2.1 Formulation of Problem

A system with a modulated fast single-frequency excitation with equation

$$\frac{d^2x}{dt^2} = \Theta \left(x, \frac{dx}{dt}, t, \omega t \right) \quad (1)$$

is considered. The force Θ has the following form

$$\Theta \left(x, \frac{dx}{dt}, t, \omega t \right) = F \left(x, \frac{dx}{dt}, t \right) + B \left(x, \frac{dx}{dt}, t \right) \sin \left(\theta + \alpha \left(x, \frac{dx}{dt}, t \right) \right), \quad (2)$$

with $\theta = \omega t$, and $\omega \gg 1$. The continuous functions F , B and α of the coordinate x , velocity dx/dt , and slow time t are the “slow” force, the amplitude and the phase of the fast excitation, respectively. The variables are assumed to be normalized, so that the mass (or more generally the inertia matrix) is unity. The problem consists in finding the averaged system for the variable $X = \frac{1}{2\pi} \int_0^{2\pi} x \, d\theta$ in the form

$$\frac{d^2X}{dt^2} = F \left(X, \frac{dX}{dt}, t \right) + V \left(X, \frac{dX}{dt}, t \right) \quad (3)$$

In other words, the task is to find the vibrational force V .

2.2 The Formula for Vibrational Force

To determine the vibrational force, a method similar to that applied in [4] is used. This is a modification of the method of the direct separation of movements that involves the introduction of a small parameter $1/\omega$ and some elements of a two-scale technique [6]. The solution to Eq. (1) can be presented as a superposition of the time-dependent mean value X and the fast oscillation ψ :

$$x = X(t) + \psi(t, \theta), \langle \psi \rangle = \frac{1}{2\pi} \int_0^{2\pi} x \, d\theta = 0 \quad (4)$$

Following the method of direct separation of motions [1], we replace Eq. (1) by two integral-differential equations for X and ψ as follows:

$$\begin{aligned}\frac{d^2X}{dt^2} &= \left\langle \Theta \left(X + \psi, \frac{dX}{dt} + \frac{d\psi}{dt}, t, \theta \right) \right\rangle \\ \frac{d^2\psi}{dt^2} &= \Theta \left(X + \psi, \frac{dX}{dt} + \frac{d\psi}{dt}, t, \theta \right) - \left\langle \Theta \left(X + \psi, \frac{dX}{dt} + \frac{d\psi}{dt}, t, \theta \right) \right\rangle\end{aligned}\quad (5)$$

with $\frac{d\psi}{dt} = \dot{\psi} + \omega\psi'$, $\frac{d^2\psi}{dt^2} = \ddot{\psi} + 2\omega\dot{\psi}' + \omega^2\psi''$, $\dot{f} = \frac{\partial f}{\partial t}$ and $f' = \frac{\partial f}{\partial \theta}$

We search ψ as $\psi(t, \theta) = \xi(t, \theta)/\omega^2$ and introduce $\Phi = B_s \sin(\theta) + B_c \cos(\theta)$ with $B_s = \cos(\alpha)$ and $B_c = \sin(\alpha)$. Then, Eq. (5) takes the form

$$\begin{aligned}\ddot{X} &= F + \frac{\xi'^2}{2\omega^2} \frac{\partial^2 F}{\partial \dot{X}^2} + \frac{1}{\omega^2} \xi \frac{\partial \Phi}{\partial \dot{X}} + \frac{1}{\omega^2} \dot{\xi} \frac{\partial \Phi}{\partial \dot{X}} + \frac{1}{\omega} \xi' \frac{\partial \Phi}{\partial \dot{X}} + \frac{1}{2\omega^2} \xi'^2 \frac{\partial^2 \Phi}{\partial \dot{X}^2} \xi'' \\ &+ \frac{2}{\omega} \dot{\xi}' + \frac{1}{\omega^2} \ddot{\xi} = \Phi + \frac{\xi}{\omega^2} \frac{\partial F}{\partial \dot{X}} + \left(\frac{\xi'}{\omega} + \frac{\dot{\xi}}{\omega^2} \right) \frac{\partial F}{\partial \dot{X}} + \frac{1}{2\omega^2} (\xi'^2 - \dot{\xi}'^2) \frac{\partial^2 F}{\partial \dot{X}^2} \\ &+ \frac{1}{\omega^2} \left(\xi \frac{\partial \Phi}{\partial \dot{X}} - \dot{\xi} \frac{\partial \Phi}{\partial \dot{X}} + \dot{\xi} \frac{\partial \Phi}{\partial \dot{X}} - \dot{\xi} \frac{\partial \Phi}{\partial \dot{X}} + \frac{1}{2} \xi'^2 \frac{\partial^2 \Phi}{\partial \dot{X}^2} - \frac{1}{2} \xi'^2 \frac{\partial^2 \Phi}{\partial \dot{X}^2} \right) + \frac{1}{\omega} \left(\xi' \frac{\partial \Phi}{\partial \dot{X}} - \dot{\xi}' \frac{\partial \Phi}{\partial \dot{X}} \right)\end{aligned}\quad (6)$$

In accordance with the method of the direct separation of motions, the averaged motion X and its derivatives are considered initially as given and the second equation (6) is solved with respect to ξ . This solution is obtained asymptotically as $\xi = \xi_0 + \xi_1/\omega$ with balancing the terms of the same order and integrating the corresponding equations related to θ . The integration constants are chosen such that ξ_0 and ξ_1 are periodical with respect to θ . In this case, the appropriate particular solution has the form

$$\xi = \xi_s + \xi_c \quad (7)$$

with

$$\begin{aligned}\xi_s &= -B_s \sin(\theta) + \frac{1}{\omega} \left(-2\dot{B}_s \cos(\theta) + \frac{\partial F}{\partial \dot{X}} B_s \cos(\theta) - \frac{1}{8} \frac{\partial B_s}{\partial X} B_s \sin(2\theta) \right) \\ \xi_c &= -B_c \cos(\theta) + \frac{1}{\omega} \left(2\dot{B}_c \sin(\theta) + \frac{\partial F}{\partial \dot{X}} B_c \sin(\theta) - \frac{\partial B_c}{\partial X} B_c \sin(2\theta) \right)\end{aligned}$$

where

$$\dot{B}_s = \dot{X} \frac{\partial B_s}{\partial X} + \ddot{X} \frac{\partial B_s}{\partial \dot{X}} + \frac{\partial B_s}{\partial t}, \quad \dot{B}_c = \dot{X} \frac{\partial B_c}{\partial X} + \ddot{X} \frac{\partial B_c}{\partial \dot{X}} + \frac{\partial B_c}{\partial t}$$

The obtained function ξ is substituted in the first equation (6). Calculation of the integrals in this equation and solving it with respect to \ddot{X} leads to the following final expression for the vibrational force

$$V = (H_B + H_\alpha + H_N) B^2 / (2\omega_0^2) \quad (8)$$

where the values H_B , H_α and H_N are calculated with $\sigma = \ln B$ as follows

$$H_B = F \left(\frac{\partial \sigma}{\partial \dot{X}} \right)^2 - \frac{\partial \sigma}{\partial \dot{X}} \frac{\partial F}{\partial \dot{X}} - \frac{\partial \sigma}{\partial X} + \dot{X} \frac{\partial \sigma}{\partial \dot{X}} \frac{\partial \sigma}{\partial X} + \frac{\partial \sigma}{\partial \dot{X}} \frac{\partial \sigma}{\partial t}, \quad (9)$$

$$H_\alpha = F \left(\frac{\partial \alpha}{\partial \dot{X}} \right)^2 + \dot{X} \frac{\partial \alpha}{\partial \dot{X}} \frac{\partial \alpha}{\partial X} + \frac{\partial \alpha}{\partial \dot{X}} \frac{\partial \alpha}{\partial t}, \quad (10)$$

$$H_N = \frac{1}{2} \partial^2 F / \partial \dot{X}^2 \quad (11)$$

2.3 Analysis and Main Regularities

Analysis of Eqs. (3) and (4) allows us to identify the following regularities.

The vibrational force is proportional to the square of the excitation amplitude with the coefficient consisting of three terms H_B , H_α and H_N which respond, respectively, to the amplitude modulation, to the phase modulation, and to a nonlinearity of the slow force F as a function of the velocity. In this case, the occurrence of a vibrational force is possible only if at least one of the following conditions is fulfilled:

- The slow force F is a nonlinear function of velocity. This causes additional dissipative effects.
- The amplitude modulation depends on the coordinate. In this case, the vibrational force is potential.
- The amplitude modulation depends on speed. Only under this condition, the explicit dependence of the amplitude on the slow time can influence the vibrational force.
- The phase modulation depends on velocity. Only under this condition, the explicit dependences of the phase on the slow time and coordinate can influence the vibrational force.

2.4 Example

Let us consider, as an example, a mechanical vibrator under the action of a high-frequency kinematic excitation with phase modulation described by Eq. (1) with

$$F = -\lambda^2 x - 2D \frac{dx}{dt}, \alpha = \gamma \sin t + \kappa \frac{dx}{dt}, B = 1 \quad (12)$$

where the dimensionless parameters λ , D , γ and κ are obtained from the physical parameters by some scaling.

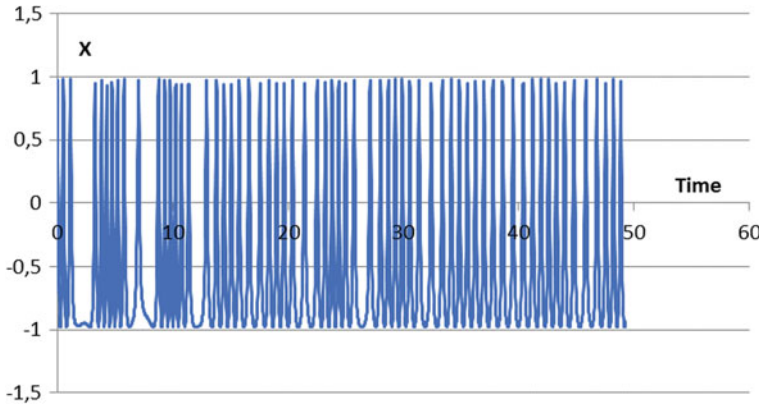


Fig. 1 Phase excitation

According to Eqs. (3), (8)–(11), the averaged system is a usual linear oscillator with a low-frequency harmonic excitation and a reduced mass

$$\frac{1}{\chi} \frac{d^2 x}{dt^2} = F + A \sin t \quad (13)$$

The amplitude of the low-frequency excitation A is equal to $A = \lambda^4 \kappa \gamma / (2\omega_0^2 \chi)$. The reduced mass $1/\chi$ is calculated with the parameter $\chi = 1 + \lambda^4 \kappa^2 / (2\omega_0^2)$.

The test simulations for the original (12) and for the averaged system (13) were fulfilled with the following values of the parameters: $\lambda^2 = 0.98$, $D = 0.03$, $\kappa = 10$, $\gamma = 10$ and $\omega = 8$.

The high-frequency phase modulated excitation is presented in Fig. 1.

The motion $x(t)$ of the original (blue) and of the averaged (red) vibrator is shown in Fig. 2.

The coincidence of the results for the original and for the averaged system is good, even though the “small parameter” $1/\omega = 0.125$ is not very small.

The given example is of interest not only for verification of the proposed method but also in connection with the search for new effective controlled excitors for vibratory technologies.

3 Conclusions

For the first time, the formula for the vibrational force in the general case of the amplitude and phase modulation of excitation was obtained (Eq. 8). This formula shows that the vibration force consists of three components connected with the effect of the amplitude modulation, the effect of the nonlinearity of the slow forces, and

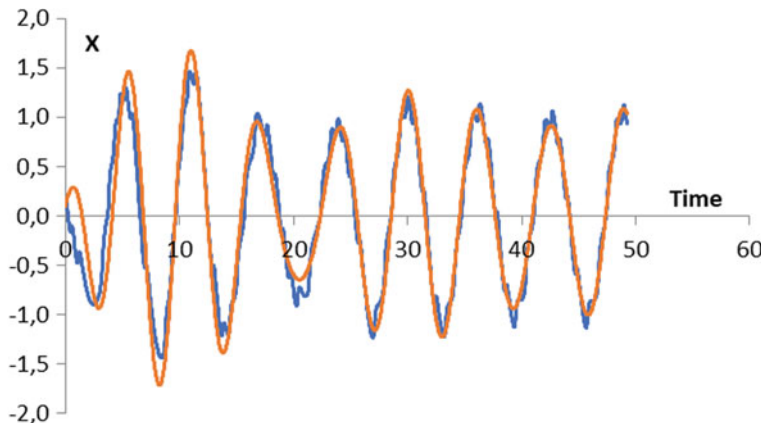


Fig. 2 Coordinate run of the original (blue) and the averaged (red) vibrator

the effect of the phase modulation. Unlike the first two effects, the effect of the phase modulation is considered for the first time. It was found that its occurrence is possible only if the excitation phase depends on the velocity. Only under this condition can the explicit dependences of the phase on the slow time and coordinate be detected in the vibrational force.

The verification of the results is performed using the example of a mechanical vibrator under the action of a high-frequency kinematic excitation with phase modulation. This example is of practical interest in connection with the vibratory technologies.

Acknowledgments The chapter's study was carried out at the expense of the grant of the Russian Science Foundation No. 17-79-30056 (the project of the NPK "Mekhanobr-tehnika").

References

1. Blekhman, I.: Vibrational Mechanics: Nonlinear Dynamic Effects, General Approach, Applications. World Scientific, Singapore (2000)
2. Thomsen, J.: Slow high-frequency effects in mechanics: problems, solutions, potentials. Int. J. Bifurcation Chaos. **15**, 2799–2818 (2005)
3. Blekhman, I., Vaisberg, L., Indeitsev, D.: Theoretical and experimental basis of advanced vibrational technologies. In: Vibration Problems ICOVP, pp. 133–138. Springer, Heidelberg (2011)
4. Kremer, E.: Slow motions in systems with fast modulated excitation. J. Sound Vib. **383**, 295–308 (2016)
5. Kremer, E.: Low-frequency dynamics of systems with modulated high-frequency stochastic excitation. J. Sound Vib. **437**, 422–436 (2018)
6. Nayfeh, A.H.: Perturbation Methods. Wiley, New York (2008)

Singular Perturbation Techniques and Asymptotic Expansions for Some Complex Enzyme Reactions



Alberto Maria Bersani, Alessandro Borri, Alessandro Milanesi,
Giovanna Tomassetti, and Pierluigi Vellucci

Abstract We summarize some recent results concerning the study of the asymptotic properties of four important enzyme reactions, which are ubiquitous in every intracellular enzyme reaction network. Mainly following the fundamental ideas by Nayfeh, after ad hoc adimensionalizations, we apply classical singular perturbation techniques in order to determine the matched expansions of the solutions, in terms of a suitable parameter, up to the first order. We show some numerical results, for the different mechanisms and different parameter values.

Keywords Singular perturbation techniques · Michaelis–Menten kinetics · Asymptotic expansions

1 Introduction

The information processing within the cell involves an intricate network of interacting “modules,” each with a well-defined role and molecular interactions. The long-term aim of our past and current studies is the integration of the “modules” in a “virtual cell,” in order to reproduce the global behavior of a specific cell type and to use it for basic, pharmacological, and medical research. This approach is within the systems biology program [16], which takes into account the implementation of mathematical models for the study of the emerging network properties of the cell. In

A. M. Bersani (✉)

Department of Mechanical and Aerospace Engineering, Sapienza University, Roma, Italy
e-mail: alberto.bersani@sba1.uniroma1.it

A. Borri

Institute for System Analysis and Computer Science “Antonio Ruberti”, Roma, Italy

A. Milanesi · G. Tomassetti

Department of Basic and Applied Sciences for Engineering, Sapienza University, Roma, Italy

P. Vellucci

Department of Economics, Roma Tre University, Rome, Italy

this sense, a reliable mathematical modeling can be a valid tool for pharmacological pre-clinical research [4, 8, 31].

The mathematical models of enzymatic processes have been proposed at the beginning of the last century [6, 14, 15, 17] and have been used for the quantitative study of several metabolic processes. The *Michaelis–Menten (MM) kinetics* represents a fundamental milestone in biochemistry, as it gives a very good description of the dynamics of the different enzymes involved. Since then, several researches have been involved in the mathematical study of MM kinetics (see, for example, [2, 9], for a review).

A key step in the MM kinetics is represented by the *standard quasi-steady state approximation* (sQSSA) [18], which consists in the assumption that the complex concentration is approximately constant after a short transient phase. However, the approximation may lead to many misinterpretations of the model and, in order to overcome them (see, for example, the review [2]), other researchers [5, 32, 33] have introduced and explored a new approximation, called total quasi-steady state approximation (tQSSA), which has been shown to be always roughly valid for a broader range of parameter values covering both high and low enzyme concentrations, in the case of an isolated reaction (as revisited in [2]).

The tQSSA has been recently applied to more complex mechanisms, like the completely reversible enzyme kinetics [32], the antagonist toggle switch [28], the completely competitive inhibition [3, 25], the double phosphorylation [25], the Goldbeter–Koshland switch, which models the single phosphorylation–dephosphorylation cycle [7, 24, 26], the double phosphorylation–dephosphorylation cycle and the ubiquitous MAPK cascade, which is one of the most important mechanisms present in the great majority of the reaction networks in eukaryotic cells [1, 10, 23].

In the context of mathematical modeling of chemical reactions our contribution falls under the area of ODEs system. The ODEs system describing the behavior of a (sub)network depends on a set of parameters, i.e., the initial concentration of dynamical molecular species and the kinetic constants which quantitatively describe the velocity of every single reaction. The fundamental step is modeling all of the intermediate reactions, including binding, dissociation, and release of the product, using mass action and conservation laws. This leads to an ODE for each involved complex and substrate, where the concentration variation for each reactant is proportional to the reactant concentrations. We refer to this as the full system.

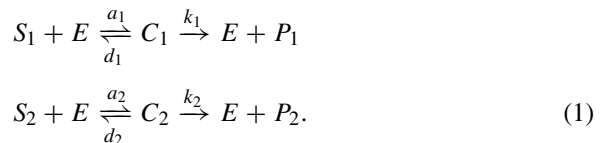
The application of these models to the study in silico of the complex intracellular mechanisms, in view of the so-called *virtual cell*, implicates approximations which must be as much precise as possible. In this framework, the tQSSA is much more efficient than the sQSSA. This is the most important reason for our studies, where the application of even standard perturbation techniques can bring to important improvements of the models.

In the fully competitive inhibition [27, 29] two substrates S_1 and S_2 compete for the same enzyme E . For example, competitive inhibitors are used to make drugs such as methotrexate that is a chemotherapy drug acting as a competitive inhibitor which prevents the cancer cells to grow and divide. In the linear double

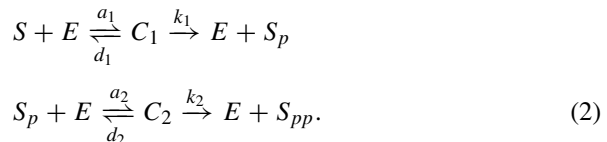
phosphorylation reaction [22] the substrate S is phosphorylated by the enzyme E (usually a kinase) to form the phosphorylated substrate S^* ; then S^* is activated by the same enzyme E to form S^{**} , so that S is actually activated twice by E , i.e., S is double-phosphorylated. In the Goldbeter–Koshland switch [13] a substrate S is modified by an enzyme to the form P and, vice versa, P is transformed back to S by another enzyme. An example of this process is given by the phosphorylation-dephosphorylation cycle, where the substrate S is activated by phosphorylation to the form S^* and S^* is transformed back (i.e., inactivated by dephosphorylation) to S by a phosphatase. In the auxiliary reactions [12] a primary substrate S_1 binds with an enzyme E_1 , releasing an auxiliary substrate S_2 , which then binds with a second enzyme E_2 , synthesizing a product P .

Here below we give the schemes of the four mechanisms, which are the topics of our recent research results.

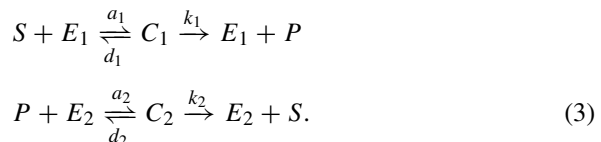
Completely competitive inhibition (where two substrates S_1 and S_2 compete for the same enzyme E):



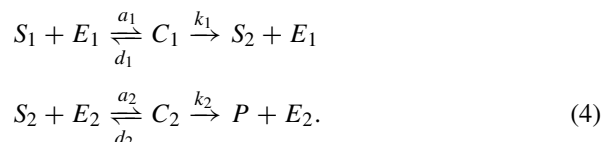
Double phosphorylation (where the same enzyme E binds with the substrate S and its activated form S_p):



Goldbeter–Koshland switch (where the substrate S is activated by the enzyme E , while its activated product P is inactivated by another enzyme F):



Auxiliary reaction (which is very similar to the double phosphorylation reaction, but in this case the activated substrate S_2 binds with a second enzyme E_2):



2 Auxiliary Enzyme Reactions—Theoretical Framework

Just as an example, here we recall the main passages of the mechanism described by (4). Using the mass action law (which states that the rate of any chemical reaction is proportional to the product of the masses or concentrations of the reacting substances), we arrive at the following system:

$$\begin{aligned}\frac{dS_1}{dt} &= -a_1 E_1 S_1 + d_1 C_1 \\ \frac{dC_i}{dt} &= a_i S_i E_i - (d_i + k_i) C_i = a_i (S_i E_i - K_{iM} C_i) \\ \frac{dS_2}{dt} &= k_1 C_1 - a_2 E_2 S_2 + d_2 C_2 \\ \frac{dE_i}{dt} &= -[a_i S_i E_i - (d_i + k_i) C_i] = -a_i (S_i E_i - K_{iM} C_i) \\ \frac{dP}{dt} &= k_2 C_2\end{aligned}\tag{5}$$

(where $K_{iM} = \frac{d_i + k_i}{a_i}$ are the so-called Michaelis constants), with initial conditions $S_1(0) = S_T$, $E_1(0) = E_{1T}$, $E_2(0) = E_{2T}$, $C_i(0) = 0$, $(i = 1, 2)$, $S_2(0) = 0$, $P(0) = 0$. Introducing the total substrates $\bar{S}_1 = S_1 + C_1$, $\bar{S}_2 = S_2 + C_2$, by conservation laws we have

$$\bar{S}_1 + \bar{S}_2 + P = S_T, \quad E_i + C_i = E_{iT} \quad (i = 1, 2).\tag{6}$$

Replacing (6) in the system (5) leads to a system of four ODEs:

$$\begin{aligned}\frac{d\bar{S}_1}{dt} &= -k_1 C_1 \\ \frac{d\bar{S}_2}{dt} &= k_1 C_1 - k_2 C_2 \\ \frac{dC_1}{dt} &= a_1 [(\bar{S}_1 - C_1)(E_{1T} - C_1) - K_{1M} C_1] \\ \frac{dC_2}{dt} &= a_2 [(\bar{S}_2 - C_2)(E_{2T} - C_2) - K_{2M} C_2].\end{aligned}\tag{7}$$

In order to expand the solutions of the system in asymptotic series [19], we have to choose a suitable perturbation parameter. According to Palsson's theory [21, 22],

we have a sufficient condition for the separation of the reaction time scales and then we can choose

$$\epsilon = \max \left\{ \epsilon_i := \frac{K_i E_{iT}}{(E_{iT} + K_{iM} + S_T)^2}, i = 1, 2 \right\}$$

(where $K_i = \frac{k_i}{a_i}$) as perturbation parameter. Let us observe that, differently from the parameters used in the application of the sQSSA, this parameter is not immediately related to biological properties of the system. It is a limit for the parameter, which is present in every application of the tQSSA [5, 11, 20, 30, 33]. Nevertheless, its usefulness is mainly related to the fact that, differently from the other parameters used in literature, it is easy to show that $\epsilon_i < \frac{1}{4}$ for every choice of data. As in this case the situation between the substrates is not symmetric, we should have to focus our attention on two cases, $\epsilon = \epsilon_1$ and $\epsilon = \epsilon_2$. However, for the sake of simplicity, in this paper we will consider only the case $\epsilon = \epsilon_1$. With this choice the following change of variables

$$\begin{aligned} \overline{S}_i &= S_T s_i \quad (i = 1, 2), \quad C_i = \beta_i c_i = \left(\frac{E_{iT} S_T}{E_{iT} + K_{iM} + S_T} \right) c_i, \\ t &= \gamma \tau = \frac{1}{a_1 (E_{1T} + K_{1M} + S_T)^2}, \end{aligned}$$

provides the following *adimensionalization* of the model equations for the inner solution, related to the initial, transient phase [19]:

$$\begin{aligned} \dot{s}_1 &= -\epsilon c_1 \\ \dot{s}_2 &= \epsilon \left[c_1 - c_2 \frac{k_2 \eta_2}{k_1 \eta_1} \right] \\ \dot{c}_1 &= \sigma_1 \eta_1 c_1^2 - (\eta_1 + \kappa_{1M} + \sigma_1 s_1) c_1 + s_1 \\ \dot{c}_2 &= \frac{a_2}{a_1} \left[\sigma_1 \eta_2 c_2^2 - \frac{\sigma_1}{\sigma_2} (\eta_2 + \kappa_{2M} + \sigma_2 s_2) c_2 + \frac{\sigma_1}{\sigma_2} s_2 \right] \end{aligned} \tag{8}$$

with initial conditions $s_1(0) = 1$, $c_i(0) = s_2(0) = 0$ ($i = 1, 2$) and where $(\cdot)^\cdot = \frac{d(\cdot)}{d\tau}$ and

$$\begin{aligned} \sigma_i &= \frac{S_T}{E_{iT} + K_{iM} + S_T}, \quad \eta_i = \frac{E_{iT}}{E_{iT} + K_{iM} + S_T}, \\ \kappa_{iM} &= \frac{K_{iM}}{E_{iT} + K_{iM} + S_T} \quad (i = 1, 2), \end{aligned}$$

(note that $\sigma_i + \eta_i + \kappa_{iM} = 1$). We now write the system of equations that gives the *outer solutions*, related to the quasi-steady phase [19]. To this aim we set $\bar{\gamma} := \frac{1}{k_1 \eta_1}$ and, putting $T = \frac{t}{\bar{\gamma}} = \epsilon \tau$ and denoting $(\cdot)' = \frac{d(\cdot)}{dT}$, we see that

$$\begin{aligned} s'_1 &= -c_1 \\ s'_2 &= c_1 - c_2 \frac{k_2}{k_1} \frac{\eta_2}{\eta_1} \\ \epsilon c'_1 &= \sigma_1 \eta_1 c_1^2 - (\eta_1 + \kappa_{1M} + \sigma_1 s_1) c_1 + s_1 \\ \epsilon c'_2 &= \frac{a_2}{a_1} \left[\sigma_1 \eta_2 c_2^2 - \frac{\sigma_1}{\sigma_2} (\eta_2 + \kappa_{2M} + \sigma_2 s_2) c_2 + \frac{\sigma_1}{\sigma_2} s_2 \right]. \end{aligned} \quad (9)$$

Let us now expand asymptotically the solutions of the inner and outer systems (8) and (9) with respect to the perturbation parameter ϵ . Taking a value $\epsilon \cong 0.0008 \ll 1$, it will be sufficient to stop our expansion at the 0-th order. Introducing $\Delta = 1 - 4\eta_1\sigma_1$; $c_{10}^\pm = \frac{1 \pm \sqrt{\Delta}}{2\eta_1\sigma_1}$, we obtain

$$s_{10}(\tau) = 1; \quad s_{20}(\tau) = 0; \quad c_{10}(\tau) = \frac{1}{\eta_1\sigma_1} \left[\frac{e^{\sqrt{\Delta}\tau} - 1}{c_{10}^+ e^{\sqrt{\Delta}\tau} - c_{10}^-} \right]; \quad c_{20}(\tau) = 0 \quad (10)$$

for the inner solution, and

$$\begin{aligned} \frac{d\Sigma_{10}}{dT} &= -\Gamma_{10} \\ \eta_1\sigma_1\Gamma_{10}^2 - (\sigma_1\Sigma_{10} + \kappa_{1M} + \eta_1)\Gamma_{10} + \Sigma_{10} &= 0 \\ \frac{d\Sigma_{20}}{dT} &= \Gamma_{10} - \frac{k_2\eta_2}{k_1\eta_1}\Gamma_{20} \\ \eta_2\sigma_2\Gamma_{20}^2 - (\sigma_2\Sigma_{20} + \kappa_{2M} + \eta_2)\Gamma_{20} + \Sigma_{20} &= 0 \end{aligned} \quad (11)$$

for the outer system, with initial conditions

$$\Sigma_{10}(0) = \lim_{\tau \rightarrow \infty} s_{10}(\tau) =: s_{10}^{as} = 1; \quad \Sigma_{20}(0) = \lim_{\tau \rightarrow \infty} s_{20}(\tau) =: s_{20}^{as} = 0;$$

$$\Gamma_{10}(0) = \lim_{\tau \rightarrow \infty} c_{10}(\tau) =: c_{10}^{as} = c_{10}^-; \quad \Gamma_{20}(0) = \lim_{\tau \rightarrow \infty} c_{20}(\tau) =: c_{20}^{as} = 0.$$

The matching between the inner and the outer solutions gives us the **matched** expansion at order 0:

$$s_{10}^{un}(\tau) = s_{10}(\tau) + \Sigma_{10}(\epsilon\tau) - s_{10}^{as}(\tau) = \Sigma_{10}(\epsilon\tau)$$

$$s_{20}^{un}(\tau) = s_{20}(\tau) + \Sigma_{20}(\epsilon\tau) - s_{20}^{as}(\tau) = \Sigma_{20}(\epsilon\tau)$$

$$c_{10}^{un}(\tau) = c_{10}(\tau) + \Gamma_{10}(\epsilon\tau) - c_{10}^{as}(\tau) = \frac{1}{\eta_1\sigma_1} \left[\frac{e^{\sqrt{\Delta}\tau} - 1}{c_{10}^+ e^{\sqrt{\Delta}\tau} - c_{10}^-} \right] + \Gamma_{10}(\epsilon\tau) - c_{10}^-$$

$$c_{20}^{un}(\tau) = c_{20}(\tau) + \Gamma_{20}(\epsilon\tau) - c_{20}^{as}(\tau) = \Gamma_{20}(\epsilon\tau). \quad (12)$$

3 Numerical Results and Conclusion

In the following we show some numerical examples of the matched expansions obtained for the four mechanisms taken into consideration. In Fig. 1 we show only the 0-th order expansion for the auxiliary reactions, because $\epsilon = 0.0008 \ll 1$. In Figs. 2, 3, and 4 we consider the expansions up to 1-st order for the inhibition ($\epsilon = 0.045$), the Goldbeter–Koshland switch ($\epsilon = 0.12$), and the double phosphorylation

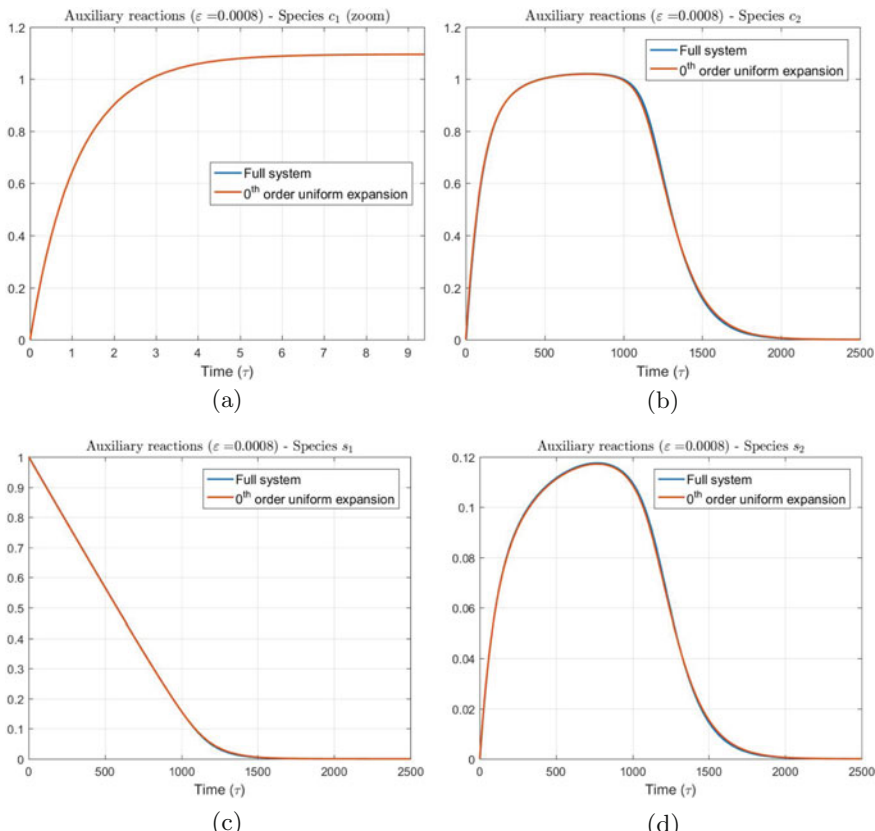


Fig. 1 Auxiliary reactions. Comparison between the solutions of the full system and their matched 0-th order asymptotic expansion beyond the tQSSA. Parameters: $a_1 = k_1 = 1$, $d_1 = 1$, $K_1 = 1$, $K_{1M} = 2$, $a_2 = k_2 = 1$, $d_2 = 0.01$, $K_2 = 1$, $K_{2M} = 1.01$, $E_0 = 2$, $S_0 = 0.01$, $\epsilon = 0.0008$. (a) c_1 zoom. (b) c_2 . (c) s_1 . (d) s_2

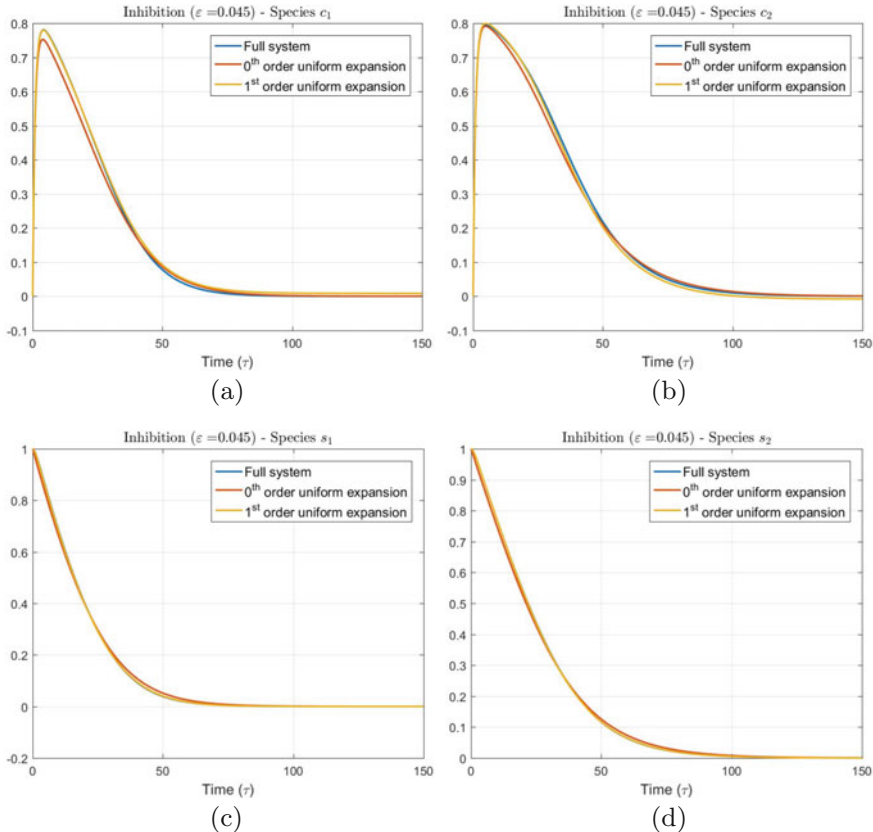


Fig. 2 Fully competitive inhibition. Comparison between the solutions of the full system and their matched 1-st order asymptotic expansion beyond the tQSSA. Parameters: $a_1 = 3$, $k_1 = 1$, $d_1 = 0.7$, $K_1 = 0.33$, $K_{1M} = 0.57$, $a_2 = 3$, $k_2 = 0.7$, $d_2 = 1$, $K_2 = 0.23$, $K_{2M} = 0.57$, $E_T = 0.7$, $S_{1T} = S_{2T} = 1$, $\epsilon = 0.045$. **(a)** c_1 . **(b)** c_2 . **(c)** s_1 . **(d)** s_2

($\epsilon = 0.22$), respectively. In every case considered in this paper, the approximation is absolutely satisfactory, even in the last case, where we have stressed the parameter values, but where we can appreciate the improvement of the approximation, passing from the 0-th order to the 1-st order approximation.

These preliminary results allow us to continue our research in this direction, in order to give, for every module composing any reaction network, approximate formulas which can be very useful to analytically predict the cell functioning in several physiological situations.

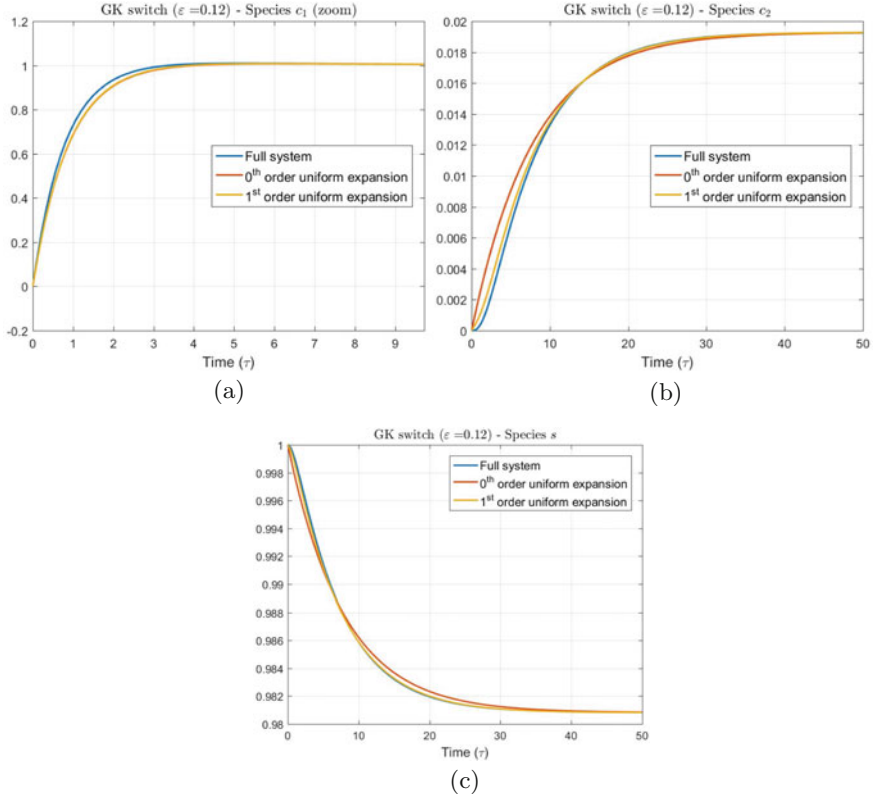


Fig. 3 Goldbeter–Koshland switch. Comparison between the solutions of the full system and their matched 1-st order asymptotic expansion beyond the tQSSA. Parameters: $a_1 = 1$, $k_1 = 0.1$, $d_1 = 0.01$, $K_1 = 0.1$, $K_{1M} = 0.11$, $a_2 = 0.2$, $k_2 = d_2 = 1$, $K_2 = 5$, $K_{2M} = 10$, $E_T = 5$, $F_T = 10$, $S_T = 0.1$, $\epsilon = 0.12$. **(a)** c_1 zoom. **(b)** c_2 . **(c)** s

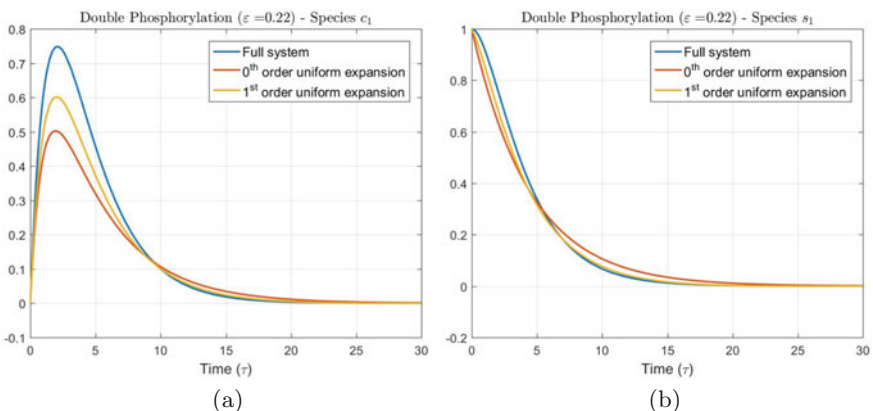


Fig. 4 Double phosphorylation. Comparison between the solutions of the full system and their matched 1-st order asymptotic expansion beyond the tQSSA. Parameters: $a_1 = k_1 = d_1 = 1$, $K_1 = 1$, $K_{1M} = 2$, $a_2 = k_2 = 1$, $d_2 = 0.1$, $K_2 = 1$, $K_{2M} = 1.1$, $E_T = 1$, $S_T = 0.01$, $\epsilon = 0.22$. **(a)** c_1 . **(b)** s_1

References

1. Bersani, A.M., Dell'Acqua, G., Tomassetti, G.: On stationary states in the double phosphorylation-dephosphorylation cycle. In: AIP Conference Proceedings, vol. 1389(1), pp. 1208–1211 (2011)
2. Bersani, A.M., Bersani, E., Dell'Acqua, G., Pedersen, M.G.: New trends and perspectives in nonlinear intracellular dynamics: one century from Michaelis–Menten paper. *Contin. Mech. Thermodyn.* **27**(4), 659–684 (2015)
3. Bersani, A., Borri, A., Milanesi, A., Vellucci, P.: Tihonov theory and center manifolds for inhibitory mechanisms in enzyme kinetics. *Commun. Appl. Ind. Math.* **8**(1), 81–102 (2017)
4. Bisswanger, H.: Enzyme Kinetics: Principles and Methods. Wiley, London (2017)
5. Borghans, J., de Boer, R., Segel, L.: Extending the quasi-steady state approximation by changing variables. *Bull. Math. Biol.* **58**, 43–63 (1996)
6. Briggs, G.E., Haldane, J.B.S.: A note on the kinetics of enzyme action. *Biochem. J.* **19**(2), 338 (1925)
7. Ciliberto, A., Capuani, F., Tyson, J.J.: Modeling networks of coupled enzymatic reactions using the total quasi-steady state approximation. *PLoS Comput. Biol.* **3**(3), e45 (2007)
8. Cornish-Bowden, A.: Fundamentals of Enzyme Kinetics, vol. 510. Wiley-Blackwell Weinheim, Germany (2012)
9. Cornish-Bowden, A.: One hundred years of Michaelis–Menten kinetics. *Perspect. Sci.* **4**, 3–9 (2015)
10. Dell'Acqua, G., Bersani, A.M.: Bistability and the complex depletion paradox in the double phosphorylation-dephosphorylation cycle. In: BIOINFORMATICS, pp. 55–65 (2011)
11. Dell'Acqua, G., Bersani, A.M.: A perturbation solution of Michaelis–Menten kinetics in a “total” framework. *J. Math. Chem.* **50**(5), 1136–1148 (2012)
12. Eilertsen, J., Schnell, S.: A kinetic analysis of coupled (or auxiliary) enzyme reactions. *Bull. Math. Biol.* **80**(12), 3154–3183 (2018)
13. Goldbeter, A., Koshland, D.E.: An amplified sensitivity arising from covalent modification in biological systems. *Proc. Natl. Acad. Sci.* **78**(11), 6840–6844 (1981)
14. Henri, V.: Recherches sur la loi de l'action de la sucrase. *CR Hebd. Acad. Sci.* **133**, 891–899 (1901)
15. Henri, V.: Über das gesetz der wirkung des invertins. *Z. Phys. Chem.* **39**(1), 194–216 (1902)
16. Kitano, H.: Systems biology: a brief overview. *Science* **295**(5560), 1662–1664 (2002)
17. Michaelis, L., Menten, M.L.: The kinetics of the inversion effect. *Biochem. Z* **49**, 333–369 (1913)
18. Murray, J.: Mathematical Biology: An Introduction. Springer, New York (2002)
19. Nayfeh, A.H.: Perturbation Methods. Wiley, New York (2000)
20. Palsson, B.O.: On the dynamics of the irreversible Michaelis–Menten reaction mechanism. *Chem. Eng. Sci.* **42**(3), 447–458 (1987)
21. Palsson, B.O., Lightfoot, E.N.: Mathematical modelling of dynamics and control in metabolic networks. I. On Michaelis–Menten kinetics. *J. Theor. Biol.* **111**(2), 273–302 (1984)
22. Palsson, B.O., Palsson, H., Lightfoot, E.N.: Mathematical modelling of dynamics and control in metabolic networks. iii. linear reaction sequences. *J. Theor. Biol.* **113**(2), 231–259 (1985)
23. Pedersen, M.G., Bersani, A.M., Bersani, E.: Quasi steady-state approximations in complex intracellular signal transduction networks—a word of caution. *J. Math. Chem.* **43**(4), 1318–1344 (2008)
24. Pedersen, M.G., Bersani, A.M.: Introducing total substrates simplifies theoretical analysis at non-negligible enzyme concentrations: pseudo first-order kinetics and the loss of zero-order ultrasensitivity. *J. Math. Biol.* **60**(2), 267–283 (2010)
25. Pedersen, M.G., Bersani, A.M., Bersani, E.: The total quasi-steady-state approximation for fully competitive enzyme reactions. *Bull. Math. Biol.* **69**(1), 433–457 (2006)
26. Pedersen, M.G., Bersani, A.M., Bersani, E., Cortese, G.: The total quasi-steady-state approximation for complex enzyme reactions. *Math. Comput. Simul.* **79**(4), 1010–1019 (2008)

27. Rubinow, S., Lebowitz, J.L.: Time-dependent Michaelis–Menten kinetics for an enzyme-substrate-inhibitor system. *J. Am. Chem. Soc.* **92**(13), 3888–3893 (1970)
28. Sabouri-Ghomie, M., Ciliberto, A., Kar, S., Novak, B., Tyson, J.J.: Antagonism and bistability in protein interaction networks. *J. Theor. Biol.* **250**(1), 209–218 (2008)
29. Schnell, S., Mendoza, C.: Time-dependent closed form solutions for fully competitive enzyme reactions. *Bull. Math. Biol.* **62**(2), 321–336 (2000)
30. Schnell, S., Maini, P.: Enzyme kinetics far from the standard quasi-steady-state and equilibrium approximations. *Math. Comput. Model.* **35**(1–2), 137–144 (2002)
31. Steuer, R., Gross, T., Selbig, J., Blasius, B.: Structural kinetic modeling of metabolic networks. *Proc. Natl. Acad. Sci.* **103**(32), 11868–11873 (2006)
32. Tzafirri, A., Edelman, E.: The total quasi-steady-state approximation is valid for reversible enzyme kinetics. *J. Theor. Biol.* **226**(3), 303–313 (2004)
33. Tzafirri, A.R., Edelman, E.R.: Quasi-steady-state kinetics at enzyme and substrate concentrations in excess of the Michaelis–Menten constant. *J. Theor. Biol.* **245**(4), 737–748 (2007)

A Novel Two-Stage Ellipsoid Filtering Based System Modeling Algorithm for a Hammerstein Nonlinear Model with an Unknown Noise Term



Ziyun Wang, Ze Tang, Ju H. Park, and Yan Wang

Abstract This paper considers the system modeling problem for the Hammerstein nonlinear model with unknown but bounded noise. A two-stage ellipsoid filtering based modeling algorithm is proposed and the unknown noise term is wrapped in an ellipsoid during each recursive step. The normalized ellipsoid is varying and its center, as well as its volume, is updated by using the volume minimization criteria of the ellipsoid. Finally, the given simulations visually illustrate the feasible parameter set variation process and the motion trail of the ellipsoids, which shows the effectiveness and the accuracy of the proposed algorithm.

Keywords Ellipsoidal space · Filtering method · Hammerstein system · Nonlinear model · Unknown noise term

1 Introduction

System modeling [1, 2] is one of the most common methods to find the true value of the complex models and analyze the relation between the input and output signals. In the recent years, the set membership modeling algorithm is studied for estimating the parameters of the systems with unknown but bounded noise term [3–5]. Some geometric spaces with regular structures are commonly used for describing the bounded noise terms, i.e., the ellipsoidal space is usually adopted for the simplicity of its formulation [6, 7]. However, the space sets listed in the previous works are

Z. Wang (✉) · Z. Tang · Y. Wang

Key Laboratory of Advanced Process Control for Light Industry (Ministry of Education),
Jiangnan University, Wuxi, Jiangsu, PR China
e-mail: wangzy0601@163.com

J. H. Park

Department of Electrical Engineering, Yeungnam University, Kyongsan, Republic of Korea

commonly fitted for the linear system identification field, rather than in the system modeling for the nonlinear ones, i.e., the Hammerstein system. Considering the computational complexity and the estimation accuracy, in this paper, the ellipsoidal space is employed for constructing the known boundary of the noise term.

Differing from the works in [6, 7], in order to diminish the impact of unknown but bounded colored noise term, this paper considers the modeling problem of Hammerstein models and a two-stage ellipsoid filtering modeling algorithm is studied. The main contributions of this paper are listed as follows: (1) a two-stage filtering method is proposed for the Hammerstein system modeling by filtering the nonlinear model with unknown noises into two different subsystems, one contains the noise term and the other includes the system parameters; (2) the minimization criteria is adopted to determine the recursive step and find the minimum value of the ellipsoid volume; (3) the simulation results show the motion trail of the ellipsoidal sets via the sample time, which can directly illustrate the parameter estimation process.

Briefly, the rest of this paper is organized as follows. Section 2 gives the Hammerstein system with an unknown but bounded noise term and its identification model. Section 3 presents a two-stage ellipsoid volume minimization based filtering algorithm by adopting different ellipsoids to wrap the boundary of the feasible parameter sets. Section 4 provides an example to illustrate the accuracy and the effectiveness of the proposed algorithm. Finally, the conclusions and some future works are offered in Sect. 5.

2 Problem Statement

The following single input/single output nonlinear system is further considered:

$$y(t) = B(z) \sum_{i=1}^{n_c} c_i f_i(u(t)) + D(z)v(t), \quad \|v(t)\| \leq \delta, \quad \delta > 0, \quad (1)$$

where $\{u(t), y(t)\}$ is the pair of the signal sequences at time t , $v(t)$ is the unknown but bounded noise term with a priori bound δ . $B(z)$ and $D(z)$ are combinations of negative powers that are defined by $B(z) := 1 + \sum_{i=1}^{n_b} b_i z^{-i}$ and $D(z) := 1 + \sum_{j=1}^{n_d} d_j z^{-j}$

in the unit delay operator z^{-1} [$z^{-1}y(t) = y(t-1)$].

The aim of identifying this nonlinear Hammerstein system is to propose a geometrical recursive algorithm to consistently estimate the unknown parameter vectors $\mathbf{b} := [b_1, b_2, \dots, b_{n_b}]^T \in \mathbb{R}^{n_b}$, $\mathbf{c} := [c_1, c_2, \dots, c_{n_c}]^T \in \mathbb{R}^{n_c}$ and $\mathbf{d} := [d_1, d_2, \dots, d_{n_d}]^T \in \mathbb{R}^{n_d}$, from the measured data $\{u(t), y(t)\}_{t=1}^L$. From Eq. (1), the identification model can be rewritten as

$$\begin{aligned}
y(t) &= B(z)\bar{u}(t) + D(z)v(t) \\
&= \sum_{i=1}^{n_b} b_i \bar{u}(t-i) + \sum_{i=1}^{n_c} c_i f_i(u(t)) + \sum_{i=1}^{n_d} d_i v(t-i) + v(t) \\
&= \boldsymbol{\varphi}^T(t)\boldsymbol{\theta} + v(t),
\end{aligned} \tag{2}$$

where

$$\begin{aligned}
\boldsymbol{\varphi}(t) &:= [\bar{u}(t-1), \bar{u}(t-2), \dots, \bar{u}(t-n_b), f_1(u(t)), f_2(u(t)), \dots, f_{n_c}(u(t)), \\
&\quad v(t-1), v(t-2), \dots, v(t-n_d)]^T \in \mathbb{R}^{n_b+n_c+n_d}, \\
\boldsymbol{\theta} &:= [\mathbf{b}^T, \mathbf{c}^T, \mathbf{d}^T]^T \in \mathbb{R}^{n_b+n_c+n_d}.
\end{aligned}$$

From Eq. (2), since the error bound of the model is known, the parameters belong to the membership set $S(L) := \{\boldsymbol{\theta} | y(t) - \delta \leq \boldsymbol{\varphi}^T(t)\boldsymbol{\theta} \leq y(t) + \delta, t \in [1, L]\}$. In the geometry, the set $S(L)$ is delimited by L pairs of parallel hyperplanes, i.e., $H_1(t) := \{\boldsymbol{\theta} | \boldsymbol{\varphi}^T(t)\boldsymbol{\theta} = y(t) - \delta\}$ and $H_2(t) := \{\boldsymbol{\theta} | \boldsymbol{\varphi}^T(t)\boldsymbol{\theta} = y(t) + \delta\}$. In the whole parametric space, the hyperplanes are the boundaries of different subspaces.

3 The Ellipsoid Volume Minimization Based Filtering Algorithm

Based on the input and output signals, the identification model in Eq. (2) can be changed into a controlled autoregressive model by adopting the unknown filter $D^{-1}(z)$. The filtered model can be written as

$$y_f(t) = B(z)\bar{u}_f(t) + v(t), \tag{3}$$

where $\bar{u}_f(t) := \sum_{i=1}^{n_c} c_i U_i(t)$ and $y_f(t) := \frac{1}{D(z)}y(t)$. The intermediate variable $U_j(t)$ is defined by $U_j(t) := \frac{1}{D(z)}f_j(u(t)), j = 1, 2, \dots, n_c$. Then, Eq. (3) can be written as

$$y_f(t) = \sum_{i=1}^{n_c} c_i U_i(t) + \sum_{i=1}^{n_b} b_i \bar{u}_f(t-i) + v(t), \|v(t)\| \leq \delta, \delta > 0. \tag{4}$$

Define the filtered information vector and two parameter vectors:

$$\begin{aligned}
\boldsymbol{\varphi}_f(t) &:= [\bar{u}_f(t-1), \bar{u}_f(t-2), \dots, \bar{u}_f(t-n_b), \\
&\quad U_1(t), U_2(t), \dots, U_{n_c}(t)]^T \in \mathbb{R}^{n_b+n_c},
\end{aligned} \tag{5}$$

$$\boldsymbol{\theta}_s := [\mathbf{b}^T, \mathbf{c}^T]^T = [b_1, b_2, \dots, b_{n_b}, c_1, c_2, \dots, c_{n_c}]^T \in \mathbb{R}^{n_b+n_c}, \tag{6}$$

$$\boldsymbol{\theta}_n := \mathbf{d} = [d_1, d_2, \dots, d_{n_d}]^T \in \mathbb{R}^{n_d}. \tag{7}$$

From Eq. (4), the parameters c_i and b_j are determined by a feasible set and the two parallel hyperplanes $H_{1,f}(t)$, $H_{2,f}(t)$ that divide the n-dimensional space, are listed as follows:

$$H_{1,f}(t) = \left\{ \boldsymbol{\theta}_s \mid \sum_{i=1}^{n_c} c_i U_i(t) + \sum_{i=1}^{n_b} b_i \bar{u}_f(t-i) = y_f(t) + \delta \right\},$$

$$H_{2,f}(t) = \left\{ \boldsymbol{\theta}_s \mid \sum_{i=1}^{n_c} c_i U_i(t) + \sum_{i=1}^{n_b} b_i \bar{u}_f(t-i) = y_f(t) - \delta \right\}.$$

However, the true values of the parameters are all in a part of the space instead of the whole space, i.e.,

$$H_f^+(t) = H_{1,f}^+(t) \cap H_{2,f}^+(t), \quad (8)$$

$$H_{1,f}^+(t) = \left\{ \boldsymbol{\theta}_s \mid \sum_{i=1}^{n_c} c_i U_i(t) + \sum_{i=1}^{n_b} b_i \bar{u}_f(t-i) \leq y_f(t) + \delta \right\}, \quad (9)$$

$$H_{2,f}^+(t) = \left\{ \boldsymbol{\theta}_s \mid \sum_{i=1}^{n_c} c_i U_i(t) + \sum_{i=1}^{n_b} b_i \bar{u}_f(t-i) \geq y_f(t) - \delta \right\}. \quad (10)$$

Since the unknown but bounded noise term $v(t) = y_f(t) - \boldsymbol{\varphi}_f^T(t)\boldsymbol{\theta}_s$ determines the spatial distance between the two parallel hyperplanes $H_{1,f}(t)$, $H_{2,f}(t)$, the ellipsoidal set membership idea [8, 9] can be adopted in estimating $\hat{\boldsymbol{\theta}}(t)$ as the first stage in solving all the parameter estimates. The filtered model in Eq. (4) can be rewritten in a vector form:

$$y_f(t) = \boldsymbol{\varphi}_f^T(t)\boldsymbol{\theta}_s + v(t), \quad (11)$$

or

$$v(t) = y_f(t) - \boldsymbol{\varphi}_f^T(t)\boldsymbol{\theta}_s, \quad (12)$$

where $y_f(t) = y(t) - \sum_{i=1}^{n_d} d_i y_f(t-i)$. Because of the unknown parameters d_i , it is impossible to use $\bar{u}_f(t)$ to construct the known parameter vector $\boldsymbol{\varphi}_f(t)$ in Eq. (5). The solution here is to use their estimates to derive the following filtering based ellipsoid recursive algorithm for the Hammerstein models. For the filtered model in Eq. (11), the normalized ellipsoidal set is [7]

$$E(P_s^{-1}, \hat{\boldsymbol{\theta}}_s) = \{\boldsymbol{\theta}_s \in \mathbb{R}^{n_s} : (\boldsymbol{\theta}_s - \hat{\boldsymbol{\theta}}_s)^T P_s^{-1}(\boldsymbol{\theta}_s - \hat{\boldsymbol{\theta}}_s) \leq \sigma_s^2\}. \quad (13)$$

The a priori assumed noise bound σ_s also represents the radius of the ellipsoid $E(P_n^{-1}, \hat{\theta}_n)$ and the error bound of feasible parameter θ_s is lower than θ , that is, $\sigma_s \leq \sigma$. The estimates $\hat{B}(t, z)$ and $\hat{D}(t, z)$ are constructed by $\hat{B}(t, z) := 1 + \sum_{i=1}^{n_b} \hat{b}_i(t)z^{-i}$ and $\hat{D}(t, z) := 1 + \sum_{j=1}^{n_d} \hat{d}_j(t)z^{-j}$, respectively.

In the first stage, the intermediate variable estimates are $\hat{w}(t) := \hat{\phi}_n^T(t)\hat{\theta}_n(t-1) + \hat{v}(t)$, where the $\hat{\phi}_n(t)$ is determined by the estimates $\hat{v}(t-i)$, $i = 1, 2, \dots, n_d$. Similarly to the procedure of forming the normalized ellipsoid in Eq. (13), the set of feasible parameter vectors θ_n is defined as follows:

$$E(P_n^{-1}, \hat{\theta}_n) = \{\theta_n \in \mathbb{R}^{n_n} : (\theta_n - \hat{\theta}_n)^T P_n^{-1}(\theta_n - \hat{\theta}_n) \leq \sigma_n^2\}. \quad (14)$$

Using the ellipsoid volume minimization principle, we list the ellipsoid volume minimization based filtering (EVMF for short) algorithm in the first stage to compute $\hat{\theta}_n(t)$:

$$\begin{aligned} \hat{\theta}_n(t) &= \hat{\theta}_n(t-1) + \beta_n(t)P_n(t)\hat{\phi}_n(t)r_n(t), \\ r_n(t) &= \hat{w}(t) - \hat{\phi}_n^T(t)\hat{\theta}_n(t-1), \\ P_n(t) &= \frac{1}{\alpha_n(t)} \left[P_n(t-1) - \frac{\beta_n(t)P_n(t-1)\hat{\phi}_n(t)\hat{\phi}_n^T(t)P_n(t-1)}{\alpha_n(t) + \beta_n(t)g_n(t)} \right], \\ \sigma_n^2(t) &= 1 + q_n(t) - \frac{\alpha_n(t)\beta_n(t)r_n^2(t)}{\alpha_n(t) + \beta_n(t)g_n(t)}, \\ g_n(t) &= \hat{\phi}_n^T(t)P_n(t-1)\hat{\phi}_n(t), \\ \alpha_n(t) &= \frac{1}{\sigma_n^2(t-1)}, \\ \beta_n(t) &= \frac{q_n(t)}{\delta^2(t)}. \end{aligned}$$

The intermediate variable $q_n(t)$ is the positive real root of the equation

$$\lambda_{n,2}(t)q_n^2(t) + \lambda_{n,1}(t)q_n(t) + \lambda_{n,0}(t) = 0, \quad (15)$$

where $\lambda_{n,2}(t) := (n_d - 1)\sigma_n^4(t-1)g_n^2(t)$, $\lambda_{n,1}(t) := [(2n_d - 1)\delta^2(t) - \sigma_n^2(t-1)g_n(t) + r_n^2(t)]\sigma_n^2(t-1)g_n(t)$, $\lambda_{n,0}(t) := [n_d(\delta^2(t) - r_n^2(t)) - \sigma_n^2(t-1)g_n(t)]\delta^2(t)$. If Equation (15) does not have any positive real root, i.e., the sampling data at time t does not update the ellipsoid $E(P_n^{-1}, \hat{\theta}_n)$, let $q_n(t) = 0$ at time t .

In the second stage, the other ellipsoidal set in Eq. (13) is to be formed. The filter $\hat{D}^{-1}(t, z)$ is obtained after running the first stage of the EVMF algorithm and it is easy to compute the estimates, such as $\hat{u}_f(t) = \sum_{i=1}^{n_c} \hat{c}_i(t)\hat{U}_i(t)$, $\hat{y}_f(t) =$

$-\sum_{j=1}^{n_d} \hat{d}_j(t) \hat{y}_f(t-j) + y(t)$. The intermediate term $\hat{U}_k(t)$ can be computed by

$\hat{U}_k(t) := \frac{1}{D(z)} f_k(u(t)) = -\sum_{l=1}^{n_d} \hat{d}_l(t) \hat{U}_k(t-l) + f_k(u(t))$. Construct the estimate of $\varphi_f(t)$ with $\hat{u}_f(t)$ and $\hat{U}_j(t)$:

$$\hat{\varphi}_f(t) = [\hat{u}_f(t-1), \hat{u}_f(t-2), \dots, \hat{u}_f(t-n_b), \hat{U}_1(t), \hat{U}_2(t), \dots, \hat{U}_{n_c}(t)]^T.$$

Similar to the first stage of EVMF algorithm, by using the ellipsoid volume minimization principle, the estimation of $\hat{\theta}_s(t)$ can be obtained in the second stage. By replacing $v(t)$, $y_f(t)$, $\varphi_f(t)$, and θ_s in Eq.(12) with their estimates $\hat{v}(t)$, $\hat{y}_f(t)$, $\hat{\varphi}_f(t)$, and $\hat{\theta}_s(t)$ at time t , the filtered noise vector can be computed as

$$\hat{v}(t) = \hat{y}_f(t) - \hat{\varphi}_f^T(t) \hat{\theta}_s(t).$$

4 Example

Consider the simplified wind turbine model in Fig. 1. The hydraulic pitch system can be modeled as in [10].

$$\begin{bmatrix} \dot{\beta} \\ \dot{\beta}_a \end{bmatrix} = \begin{bmatrix} 0 & 1 \\ -\omega_n^2 & -2\zeta\omega_n \end{bmatrix} \begin{bmatrix} \beta \\ \beta_a \end{bmatrix} + \begin{bmatrix} 0 \\ \omega_n^2 \end{bmatrix} \beta_r, \quad (16)$$

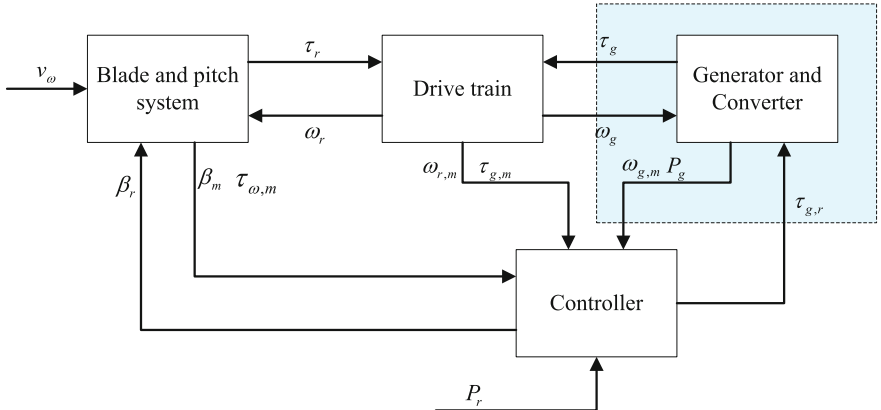


Fig. 1 The wind turbine system structure

where β and β_a are the pitch angle and angular velocity, respectively. β_r is the pitch angle reference value, ω_n and ζ are the nominal system's bandwidth and the nominal system's damping, respectively. In this paper, we set $\omega_n = 11.11\text{rad/s}$ and $\zeta = 0.6$ be the system natural frequency and the damping factor, respectively [11]. The hydraulic pitch system of the wind turbine model can be approximated to a second-order transfer function [11, 12]:

$$\frac{y}{\bar{u}} = \frac{\omega_n^2}{s^2 + 2\xi\omega_n s + \omega_n^2}, \quad (17)$$

where $y = \beta$ and $\bar{u} = \beta_r$. Set the discrete time $T_s = 0.01\text{s}$ [10]. Define $s = \frac{2}{T_s} \frac{z-1}{z+1}$ and we use the bilinear transformation method and discretize the given model in Eq. (17), the given model in Eq. (17) can be transformed to

$$\begin{aligned} \frac{y(t)}{\bar{u}(t)} &= \frac{\omega_n^2}{(\frac{2}{T_s} \frac{z-1}{z+1})^2 + 2\xi\omega_n \frac{2}{T_s} \frac{z-1}{z+1} + \omega_n^2} \\ &= \frac{\omega_n^2 T_s^2 z^2 + 2\omega_n^2 T_s^2 z + \omega_n^2 T_s^2}{\alpha z^2 + \beta z + \gamma}, \end{aligned} \quad (18)$$

where $\alpha = 4 + 4\xi\omega_n T_s + \omega_n^2 T_s^2$, $\beta = 2\omega_n^2 T_s^2 - 8$, $\gamma = 4 - 4\xi\omega_n T_s + \omega_n^2 T_s^2$.

Thus, Eq. (17) can be rewritten as

$$\frac{y(t)}{\bar{u}(t)} = \frac{0.0029z^2 + 0.0058z + 0.0029}{z^2 - 1.8638z + 0.8754}. \quad (19)$$

The above function can be changed to the model $y(t) = B(z)\bar{u}(t)$ via the long division method. After the regularization step that set $b_0 = 1$, and consider the disturbance from the noise term $v(t)$, the hydraulic pitch system can be described by the finite impulse response model as follows:

$$y(t) = B(z)\bar{u}(t) + D(z)v(t), \quad (20)$$

where $B(z) = 1 + 0.0112z^{-1} + 0.0213z^{-2}$, $\bar{u}(t) = -0.4802u(t)$, $D(z) = 1 - 0.2678z^{-1} + 0.0505z^{-2}$. In the simulation, the input and noise signals are uniform random numbers that are randomly distributed in the interval $[-1, 1]$. When adopting the proposed EVMF algorithm, the ellipsoidal set of the noise terms via sampling time are shown in Fig. 2.

From Fig. 2, it can be seen that the parameters of the hydraulic pitch system are quickly estimated, which shows the given EVMF algorithm also has a good performance on estimating the wind turbine system structure under the available benchmark data.

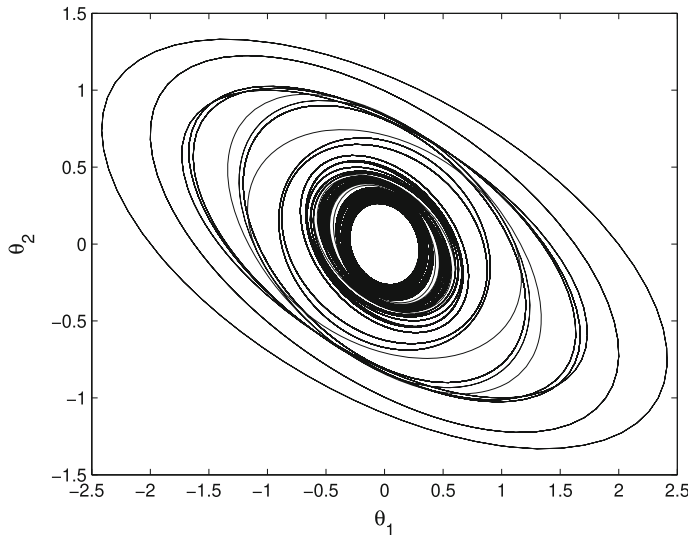


Fig. 2 Variation of the feasible noise term parameter ellipsoidal sets of the hydraulic pitch system

5 Conclusions

This paper presents a two-stage ellipsoid estimation algorithm for the Hammerstein nonlinear system with unknown noises. The probability distribution of the noise term is unknown and ellipsoidal sets are formed to contain the feasible noise parameters. This work can be also extended to deal with other types of nonlinear system modeling problems, such as the Wiener nonlinear system modeling and parameter estimation for the error-in-variables systems.

Acknowledgements This work is supported in part by Basic Science Research Programs through the National Research Foundation of Korea (NRF) funded by the Ministry of Education (Grant number NRF-2017R1A2B2004671), the National Natural Science Foundation of China (61802150, 61803180), Natural Science Foundation of Jiangsu Province (BK20170196, BK20180599), the China Postdoctoral Science Foundation Funded Project (2018M642161), the Fundamental Research Funds for the Central Universities with Grant (JUSRP11860), the Fundamental Research Funds for the Central Universities(JUSRP51912B), and Jiangsu Key Laboratory of Advanced Food Manufacturing Equipment & Technology (FM-2019-07).

References

1. Sersour, L., Djamah, T., Bettayeb, M.: Nonlinear system identification of fractional Wiener models. *Nonlinear Dyn.* **92**(4), 1493–1505 (2018). <https://doi.org/10.1007/s11071-018-4142-0>
2. Voros, J.: Iterative identification of nonlinear dynamic systems with output backlash using three-block cascade models. *Nonlinear Dyn.* **79**(3), 2187–2195 (2015). <https://doi.org/10.1007/s11071-014-1804-4>

3. Wang, Z., Tian, Q., Hu, H.Y.: Dynamics of spatial rigid-flexible multibody systems with uncertain interval parameters. *Nonlinear Dyn.* **84**(2), 527–548 (2016). <https://doi.org/10.1007/s11071-015-2504-4>
4. Zheng, Z.S., Liu, Z.G., Zhao, H.Q., Yu, Y., Lu, L.: Robust set-membership normalized subband adaptive filtering algorithms and their application to acoustic echo cancellation. *IEEE Trans. Circuits Syst. Regul. Pap.* **64**(8), 2098–2111 (2017). <https://doi.org/10.1109/TCSI.2017.2685679>
5. Wang, Y., Wang, Z.H., Puig, V., Cembrano, G.: Zonotopic set-membership state estimation for discrete-time descriptor LPV systems. *IEEE Trans. Autom. Control* **64**(5), 2092–2099 (2019). <https://doi.org/10.1109/TAC.2018.2863659>
6. Goudjil, A., Pouliquen, M., Pigeon, E., Gehan, O.: Identification algorithm for MIMO switched output error model in presence of bounded noise. In: *IEEE Conference on Decision and Control*, pp. 5286–5291 (2017). <https://doi.org/10.1109/CDC.2017.8264441>
7. Liu, Y.S., Zhao, Y., Wu, F.L.: Ellipsoidal state-bounding-based set-membership estimation for linear system with unknown-but-bounded disturbances. *IET Control Theory Appl.* **10**(4), 431–442 (2016). <https://doi.org/10.1049/iet-cta.2015.0654>
8. Polyak, B.T., Nazin, S.A., Durieu C., Walter, E.: Ellipsoidal parameter or state estimation under model uncertainty. *Automatica* **40**(7), 1171–1179 (2004). <https://doi.org/10.1016/j.automatica.2004.02.014>
9. Chai, W., Qiao, J.: Non-linear system identification and fault detection method using RBF neural networks with set membership estimation. *Int. J. Model. Identif. Control.* **20**(2), 114–120 (2013). <https://doi.org/10.1504/IJMIC.2013.056183>
10. Casau, P., Rosa, P., Tabatabaeipour, S.M., Silvestre, C., Stoustrup, J.: A set-valued approach to FDI and FTC of wind turbines. *IEEE Trans. Control Syst. Technol.* **23**(1), 245–263 (2015). <https://doi.org/10.1109/tcst.2014.2322777>
11. Wu, D.H., Li, Y.: Fault diagnosis of variable pitch for wind turbines based on the multi-innovation forgetting gradient identification algorithm. *Nonlinear Dyn.* **79**(3), 2069–2077 (2015). <https://doi.org/10.1007/s11071-014-1795-1>
12. Tabatabaeipour, S.M.: Active fault detection and isolation of discrete-time linear time-varying systems: a set-membership approach. *Int. J. Syst. Sci.* **46**(11), 1917–1933 (2015). <https://doi.org/10.1080/00207721.2013.843213>

A New Method for the Frequency Response Curve and Its Unstable Region of a Strongly Nonlinear Oscillator



Hai-En Du, Guo-Kang Er, and Vai Pan Iu

Abstract In order to determine the frequency response curve and its unstable region of a strongly nonlinear oscillator, a new method is proposed. This method is based on splitting the system parameters and introducing some unknown parameters into the system. The evaluation of the introduced parameters is done by optimizing the cumulative equation error induced by multiple-scales solution. The Duffing oscillator, the Helmholtz–Duffing oscillator, and an oscillator with both nonlinear restoring and nonlinear inertial forces are analyzed as examples to reveal the validity of the proposed method. The frequency response curves obtained by numerical continuation method are adopted to compare with those obtained by the proposed method and the conventional multiple-scales method. The unstable regions obtained by the harmonic balance method are adopted to examine those obtained by the conventional multiple-scales method and the proposed method. The efficiency of the proposed method is tested by comparing the computational time of each method.

Keywords Strong nonlinearity · Multiple-scales method · Frequency response · Unstable region

1 Introduction

The identification of the frequency response curve (FRC) and its unstable region to nonlinear oscillators is important as the FRC is not only able to reflect the nonlinear characteristics of the system but also the steady-state response of the system at each excitation frequency. However, many methods are not able to obtain an accurate FRC and an unstable region if the nonlinearity of the oscillator is strong. In recent years, some analytical methods were developed for the solutions to strongly nonlinear oscillators. They are harmonic balance method (HBM),

H.-E. Du (✉) · G.-K. Er · V. P. Iu

Department of Civil and Environmental Engineering, University of Macau, Macau SAR, China
e-mail: haiendu@outlook.com

homotopy analysis method (HAM), and various modified versions of perturbation methods. However, some shortcomings can be found in each method. They are reviewed and discussed in the following prior to presenting the proposed method.

Harmonic Balance Method The HBM assumes the solution can be represented by a linear combination of sinusoids, then balances each sinusoid to construct nonlinear algebraic equations. Baily and Lindenlaub firstly conducted the HBM in 1968 and 1969 to analyze the nonlinear circuits, respectively [1, 2]. Generally speaking, there are no explicit solutions to the nonlinear algebraic equations. In such a case, numerical methods are adopted to search for a numerical solution to these nonlinear algebraic equations. In other words, if the systems are too complicated, the HBM suffers from the efficiency problem as the numerical methods are inefficient in such a case. Moreover, only the steady-state response can be obtained by HBM method as an original assumption of the method.

Homotopy Analysis Method The HAM was first devised in 1992 by Liao for obtaining the approximate solutions to strongly nonlinear problems [3] based on homotopy theory. Further modifications of the HAM can be found in [4]. However, the selection of the “auxiliary parameter” \hbar has a significant influence on the convergence of the solution given by the HAM [5]. To overcome this problem, an updated version of HAM was proposed by Liao in 2010 [6] by introducing $k + 1$ unknown “convergence-control parameter” (c_0, \dots, c_k) to control the convergence of the HAM. However, it is computationally inefficient to obtain the $k + 1$ convergence-control parameter by solving $k + 1$ nonlinear algebraic equations.

Modified Perturbation Methods As the secularities can be eliminated by using the multiple-scales (MS) method or the Lindstedt–Poincaré (LP) method to solve nonlinear problems, there are many versions of perturbation methods formulated by modifying these two improved perturbation methods. However, the above-mentioned methods are not valid for strongly nonlinear systems. To overcome the weakness of the MS method, a modified MS method is devised and applied to solve the forced vibration of an oscillator with cubic nonlinear term or an oscillator with quintic nonlinear term by Burton and Rahman [7]. To overcome the weakness of LP method, a three-dimensional nonlinear autonomous dynamic system is studied and a modified LP method is proposed for obtaining its analytical solution by Chen et al. [8]. However, the above-mentioned methods are only feasible for the oscillators with odd nonlinearity. A new expanding parameter was introduced to the LP method by Cheung et al. in [9]. In Cheung’s method, the large perturbation parameter in the strongly nonlinear oscillator is transformed into a small one. With this method, the transformation form is assumed in a different way for different oscillators [10].

Motivation In this paper, a new method is proposed for improving the solutions obtained by the perturbation methods that can also be regarded as a modified version of the MS method. The strategy of this method is that the coefficients of the parameters are split by introducing some unknown parameters. Based on the solution obtained by the MS method, the evaluation of the introduced parameters is done by minimizing the cumulative residual error of the original equation of motion.

Therefore, the whole solution procedure is named parameter-splitting multiple-scales (PSMS) method in the following discussions. Three examples including the Duffing oscillator, the Helmholtz–Duffing oscillator, and an oscillator with both nonlinear restoring force and nonlinear inertial force are analyzed to show the validity of the PSMS method. For brevity, an oscillator with both nonlinear restoring force and nonlinear inertial force is named “an oscillator with complex nonlinearity” in the following. The FRCs obtained by the numerical continuation method (NCM) are adopted to compare to those obtained by the MS method and the PSMS method. The solutions by the NCM were obtained with the software “MATCONT.” Also, the unstable regions of the FRCs obtained by the HBM are adopted to compare to those obtained by the MS method and the PSMS method. The efficiency of the PSMS method is examined by comparing the computational time of each mentioned method.

2 Parameter-Splitting-Multiple-Scales Method

In the following, a damped and harmonically forced Duffing oscillator is adopted to show detailed procedures of the PSMS method. The procedures of applying the PSMS method to the Helmholtz–Duffing oscillator or to an oscillator with complex nonlinearity are similar to those described in the following when considering some other types of nonlinearity. Considering a non-dimensional, damped, and harmonically forced Duffing oscillator as follows:

$$\ddot{q} + u\epsilon^2 \dot{q} + \omega_0^2 q + \eta\epsilon q^3 = F\epsilon^2 \cos(\Omega t), \quad (1)$$

where q is the response, Ω is the excitation frequency, ω_0 is the natural frequency of oscillator, u is the damping coefficient, ϵ is the perturbation parameter, η is the coefficient of cubic term, F is the excitation amplitude, and t is the time.

2.1 Parameter Splitting

The natural frequency ω_0 and the nonlinear parameter η are split and represented as

$$\omega_0^2 = \omega_{00}^2 + \omega_{01}^2\epsilon + \omega_{02}^2\epsilon^2 + O(\epsilon^3) \quad \text{and} \quad \eta = \eta_1 + \eta_2\epsilon + O(\epsilon^2). \quad (2)$$

Then the equation of motion can be rewritten as

$$\ddot{q} + u\epsilon^2 \dot{q} + \omega_{00}^2 q + \omega_{01}^2 \epsilon q + \omega_{02}^2 \epsilon^2 q + \eta_1 \epsilon q^3 + \eta_2 \epsilon^2 q^3 = F\epsilon^2 \cos(\Omega t) \quad (3)$$

up to corrections of order $O(\epsilon^2)$.

2.2 The Solution to the Split System by the MS Method

With the MS method, the response of the oscillator is assumed to be

$$q = q_0(T_0, T_1, T_2) + \epsilon q_1(T_0, T_1, T_2) + \epsilon^2 q_2(T_0, T_1, T_2) + O(\epsilon^3), \quad (4)$$

where T_0 , T_1 , and T_2 are the fast and slow time scales expressed by

$$T_0 = t, \quad T_1 = \epsilon t \quad \text{and} \quad T_2 = \epsilon^2 t. \quad (5)$$

By chain rule, the operators of time derivatives are

$$\frac{d}{dt} = D_0 + \epsilon D_1 + \epsilon^2 D_2 + \dots, \quad (6)$$

$$\frac{d^2}{dt^2} = D_0^2 + 2\epsilon D_0 D_1 + \epsilon^2 (D_1^2 + 2D_0 D_2) + \dots, \quad (7)$$

where $D_n = \partial/\partial T_n$ and $D_n^2 = \partial^2/\partial T_n^2$. Substituting Eqs. (4), (6), and (7) into Eq. (3) and equating the coefficients of ϵ^m ($m = 0, 1, 2$) to zero lead to the following equations:

$$O(\epsilon^0) : \quad D_0^2(q_0) + \omega_{00}^2 q_0 = 0, \quad (8)$$

$$O(\epsilon^1) : \quad D_0^2(q_1) + \omega_{00}^2 q_1 = -\omega_{01}^2 q_0 - 2D_0 D_1(q_0) - \eta_1 q_0^3 \quad (9)$$

$$O(\epsilon^2) : \quad D_0^2(q_2) + \omega_{00}^2 q_2 = F \cos(\Omega t) - \omega_{01}^2 q_1 - \omega_{02}^2 q_0 - 2D_0 D_1(q_1) \\ - D_1^2(q_0) - 2D_0 D_2(q_0) - u D_0(q_0) - 3\eta_1 q_0^2 q_1 - \eta_2 q_0^3. \quad (10)$$

The solution to the $O(\epsilon^0)$ equation is expressed as

$$q_0 = C(T_1, T_2) e^{i\omega_{00} T_0} + \bar{C}(T_1, T_2) e^{-i\omega_{00} T_0}, \quad (11)$$

where C is a function of time scales T_1 and T_2 which can be determined by omitting the secular terms in the $O(\epsilon^1)$ equation. Substituting Eq. (11) into the right-hand side of the $O(\epsilon^1)$ equation and eliminating the secular terms yield

$$3C^2 \eta_1 \bar{C} e^{i\omega_{00} T_0} + 2i D_1(C) \omega_{00} e^{i\omega_{00} T_0} + C \omega_{01}^2 e^{i\omega_{00} T_0} = 0 \quad (12)$$

and

$$q_1 = \Lambda e^{3i\omega_{00} T_0} + \bar{\Lambda} e^{-3i\omega_{00} T_0} \quad \text{in which} \quad \Lambda = \frac{\eta_1 C^3}{8\omega_{00}^2}. \quad (13)$$

Substituting the expressions of q_0 and q_1 into the $O(\epsilon^2)$ equation, eliminating the secular terms, and using the expression $\Omega = \omega_{00} + \epsilon^2\sigma$ where σ is a detuning parameter that can be determined if Ω is given, yield

$$\begin{aligned} D_2(C) = & \frac{Fe^{i\sigma T_2}}{4i\omega_{00}} - \frac{uC}{2} - \frac{C\omega_{02}^2}{2i\omega_{00}} + \frac{C\omega_{01}^4}{8i\omega_{00}^3} - \frac{15i\eta_1^2 C^3 \bar{C}^2}{16\omega_{00}^3} \\ & - \frac{3\eta_2 C^2 \bar{C}}{2i\omega_{00}} + \frac{3\eta_1 C^2 \bar{C} \omega_{01}^2}{4i\omega_{00}^3} \end{aligned} \quad (14)$$

and

$$q_2 = \Gamma_1 e^{3i\omega_{00}T_0} + \Gamma_2 e^{5i\omega_{00}T_0} + \bar{\Gamma}_1 e^{-3i\omega_{00}T_0} + \bar{\Gamma}_2 e^{-5i\omega_{00}T_0}, \quad (15)$$

in which

$$\Gamma_1 = \frac{\eta_2 C^3}{8\omega_{00}^2} - \frac{\eta_1 C^3 \omega_{01}^2}{8\omega_{00}^4} - \frac{21\eta_1^2 C^4 \bar{C}}{64\omega_{00}^4} \quad \text{and} \quad \Gamma_2 = \frac{\eta_1^2 C^5}{64\omega_{00}^4}. \quad (16)$$

It is noted that the expression of the nearness of the excitation frequency to the resonance frequency is specially selected due to different kinds of nonlinearity [7, 9]. For example, in Cheung's method, if the oscillator studied is of cubic nonlinearity, the nearness of the excitation frequency to the resonance frequency is assumed to be $\omega^2 = \omega_0^2 + \sum_{n=1}^{\infty} \epsilon^n \omega_n$; if the oscillator studied is of quadratic nonlinearity, the nearness of the excitation frequency to the resonance frequency is assumed to be $\omega^4 = \omega_0^4 + \sum_{n=2}^{\infty} \epsilon^n \omega_n$. If the problem to be investigated is a mixture of different nonlinearities, a valid expression of the nearness of the excitation frequency to the resonance frequency is still unknown. In conclusion, the general form of the expression of the nearness of the excitation frequency to the resonance frequency is missing.

2.2.1 Frequency Response Curve

The derivative of C with respect to time can be expressed as

$$\frac{dC}{dt} = \epsilon D_1(C) + \epsilon^2 D_2(C) + O(\epsilon^3). \quad (17)$$

The expression of C is assumed to be in the polar form as

$$C = \frac{1}{2} A e^{ib}, \quad (18)$$

where A is the response amplitude and b is the phase of oscillator response. Substituting Eqs. (12), (13), and (18) into Eq.(17) and separating the real and imaginary parts yield

$$\begin{aligned}\dot{A} = \frac{F\epsilon^2}{2\omega_{00}} \sin \gamma - \frac{uA\epsilon^2}{2} \quad \text{and} \quad \dot{\gamma} = \Omega - \omega_{00} - \frac{\epsilon\omega_{01}^2}{2\omega_{00}} - \frac{\epsilon^2\omega_{02}^2}{2\omega_{00}} + \frac{\epsilon^2\omega_{01}^4}{8\omega_{00}^3} \\ - \frac{3A^2\eta_2\epsilon^2}{8\omega_{00}} + \frac{15A^4\eta_1^2\epsilon^2}{256\omega_{00}^3} - \frac{3A^2\eta_1\epsilon}{8\omega_{00}} + \frac{\epsilon^2 F \cos(\gamma)}{2A\omega_{00}} + \frac{3A^2\eta_1\epsilon^2\omega_{01}^2}{16\omega_{00}^3},\end{aligned}\quad (19)$$

where $\gamma = \sigma T_2 - b$. In steady state, the time derivatives of A and γ are equal to zero. Eliminating γ and σ in Eq. (19) yields the FRC. The relation between the excitation frequency and the response amplitude at steady state is then obtained to be

$$\begin{aligned}\Omega = \omega_{00} + \frac{\epsilon\omega_{01}^2}{2\omega_{00}} + \frac{\epsilon^2\omega_{02}^2}{2\omega_{00}} - \frac{\epsilon^2\omega_{01}^4}{8\omega_{00}^3} - \frac{15A^4\eta_1^2\epsilon^2}{256\omega_{00}^3} + \frac{3A^2\eta_1\epsilon}{8\omega_{00}} - \frac{\epsilon^2 F \cos(\gamma)}{2A\omega_{00}} \\ - \frac{3A^2\eta_1\epsilon^2\omega_{01}^2}{16\omega_{00}^3}.\end{aligned}\quad (20)$$

2.2.2 Unstable Region

By the definition, the unstable region can be derived by setting equal to zero the denominator of $\frac{dA}{ds^2}$ and its expression is given as

$$\begin{aligned}\left[4\Omega\omega_{00}A - 4\omega_{00}A\left(\omega_{00} + \frac{\epsilon\omega_{01}^2}{2\omega_{00}} + \frac{\epsilon^2\omega_{02}^2}{2\omega_{00}} - \frac{\epsilon^2\omega_{01}^4}{8\omega_{00}^3} - \frac{15\epsilon^2\eta_1^2A^4}{256\omega_{00}^3} + \frac{3\epsilon\eta A^2}{8\omega_{00}}\right.\right. \\ \left.\left. - \frac{3\epsilon^2\eta_1\omega_{01}^2A^2}{16\omega_{00}^3}\right)\right]\left[2\Omega\omega_{00} - 2\omega_{00}\left(\omega_{00} + \frac{\epsilon\omega_{01}^2}{2\omega_{00}} + \frac{\epsilon^2\omega_{02}^2}{2\omega_{00}} - \frac{\epsilon^2\omega_{01}^4}{8\omega_{00}^3} - \frac{15\epsilon^2\eta_1^2A^4}{256\omega_{00}^3}\right.\right. \\ \left.\left. + \frac{3\epsilon\eta A^2}{8\omega_{00}} - \frac{3\epsilon^2\eta_1\omega_{01}^2A^2}{16\omega_{00}^3}\right) + 2\omega_{00}A\left(-\frac{3\epsilon\eta A}{4\omega_{00}} + \frac{15\epsilon^2\eta_1^2A^3}{64\omega_{00}^3} + \frac{3\epsilon^2\eta_1\omega_{01}^2A}{8\omega_{00}^3}\right)\right] \\ + 2\epsilon^4 u^2 \omega_{00}^2 A = 0.\end{aligned}\quad (21)$$

2.2.3 Approximate Response

Approximated response of the oscillator is obtained to be

$$q_a = \mathbb{A}_1 \cos(\Omega t - \gamma) + 2\mathbb{A}_3 \cos(3\Omega t - 3\gamma) + 2\mathbb{A}_5 \cos(5\Omega t - 5\gamma), \quad (22)$$

in which $\mathbb{A}_1 = A$, $\mathbb{A}_3 = \frac{\eta\epsilon A^3}{64\omega_{00}^2} - \frac{21\eta_1^2\epsilon^2 A^5}{2048\omega_{00}^4} - \frac{A^3\epsilon^2\eta_1\omega_{01}^2}{64\omega_{00}^4}$ and $\mathbb{A}_5 = \frac{\eta_1^2\epsilon^2 A^5}{2048\omega_{00}^4}$.

2.2.4 Determination of Split Parameters

The split parameters $(\omega_{00}, \omega_{01}, \omega_{02}, \eta_1, \eta_2)$ in Eqs. (20)–(22) are determined by optimizing the error given in Eq. (23) with constraints given by Eq. (2).

$$R_e = \int_0^T [\ddot{q}_a + u\epsilon^2 \dot{q}_a + \omega_0^2 q_a + \eta\epsilon q_a^3 - F\epsilon^2 \cos(\Omega t)]^2 dt, \quad (23)$$

where $T = \frac{2\pi}{\Omega}$. From Eq. (23) it is seen that the expression of q_a can be considered as a function of $f(\omega_{01}, \omega_{02}, \eta_1)$ once the system parameters $\omega_0, u, \eta, \Omega$, and F are given. The determination of ω_{01}, ω_{02} , and η_1 is done by minimizing the value of R_e expressed by Eq. (23) via interior point method for a given value of excitation frequency.

3 Illustrative Examples

Three oscillators with different kinds of nonlinearity are analyzed to examine the validity of the PSMS method in determining the FRC and the unstable region if the system nonlinearity is strong. Firstly, a strongly nonlinear, damped, and harmonically forced Duffing oscillator is analyzed. It is commonly used for testing the feasibility of methods for analyzing strongly nonlinear systems and can be found in many applications. Moreover, a strongly nonlinear, damped, and harmonically forced Helmholtz–Duffing oscillator is analyzed. Due to the co-existence of quadratic nonlinearity and cubic nonlinearity, many interesting phenomena of it were reported in [11]. Also, a damped and harmonically forced Helmholtz–Duffing oscillator can be found in the planar motion of a suspended cable or a Duffing oscillator with a harmonic force as well as a constant force [12], etc. Last but not least, an oscillator with both strongly nonlinear restoring force and strongly nonlinear inertial force is analyzed. It can be used to model the planar motion of a cantilever beam by using inextensible assumption. The FRCs of these three oscillators obtained with the conventional MS method and the PSMS method are compared with those obtained by the NCM to reveal the capability of the PSMS method in determining the FRC of the oscillator. Moreover, the unstable regions of these three oscillators obtained by the conventional MS method and the PSMS method are compared with that obtained by the three-term harmonic balance method to examine the capability of the PSMS method in determining the unstable region. They are shown in Figs. 1, 2, and 3, respectively. Besides for the comparisons of frequency response curves and unstable regions, the efficiency of the PSMS method is examined. The computational time of each method is listed in the figure captions.

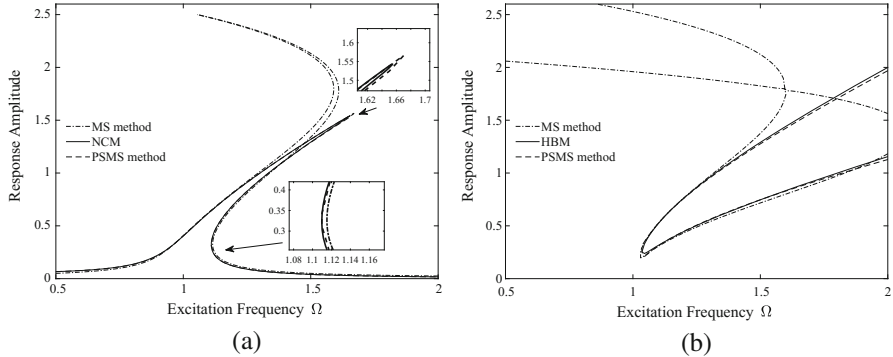


Fig. 1 FRCs and their unstable regions of a Duffing oscillator given as $\ddot{q} + 0.02\dot{q} + q + q^3 = 0.05 \cos(\Omega t)$. (The computational time needed by NCM and the PSMS method for obtaining the shown FRCs is 181.39 s and 20.32 s, respectively. The computational time needed by TTHBM and the PSMS method for obtaining the shown unstable regions is 72.48 s and 27.36 s). **(a)** Frequency response curves. **(b)** Unstable regions

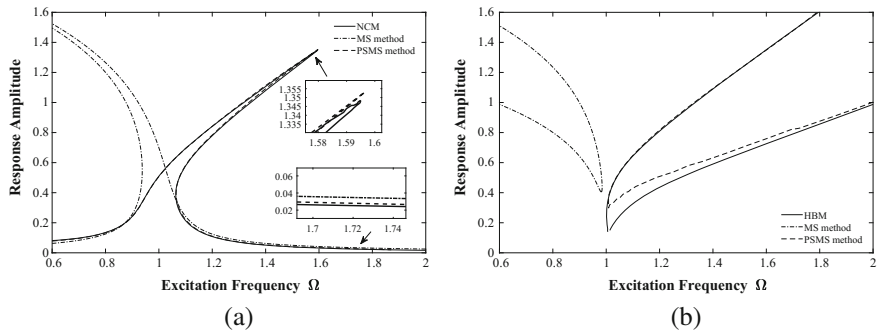


Fig. 2 FRCs and their unstable regions of a Helmholtz–Duffing oscillator given as $\ddot{q} + 0.02\dot{q} + q + q^2 + q^3 = 0.05 \cos(\Omega t)$. (The computational time needed by NCM and the PSMS method for obtaining the shown FRCs is 156.67 s and 141.92 s, respectively. The computational time needed by TTHBM and the PSMS method for obtaining the shown unstable regions is 593.94 s and 178.39 s). **(a)** Frequency response curve. **(b)** Unstable region

4 Conclusions

A new method named PSMS method is proposed for determining the FRCs and its unstable regions of some strongly nonlinear oscillators. A strongly nonlinear Duffing oscillator, a strongly nonlinear Helmholtz–Duffing oscillator, and an oscillator with complex nonlinearity are analyzed as examples to examine the capability of the PSMS method in determining the FRCs and its unstable regions of the strongly nonlinear oscillators. Through analyzing these three oscillators, it can be concluded that the PSMS method can give a valid and accurate solution to these strongly nonlinear oscillators. Unlike the modified version of MS method or LP method

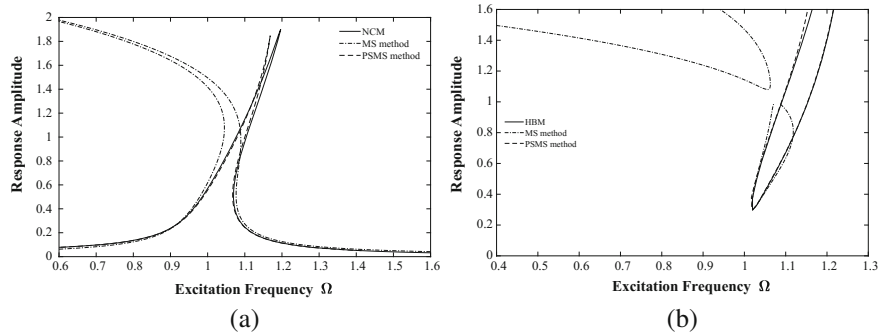


Fig. 3 FRCs and their unstable regions of an oscillator with complex nonlinearity given as $(1 + q^2)\ddot{q} + 0.02\dot{q} + q + q\dot{q}^2 + q^3 = 0.05 \cos(\Omega t)$. (The computational time of NCM and the PSMS method for obtaining the shown FRCs is 172.08 s and 186.98 s, respectively. The computational time of TTHBM and the PSMS method for obtaining the shown unstable regions is 139.97 s and 154.63 s). **(a)** Frequency response curve. **(b)** Unstable region

proposed by Burton, Chen, and Cheung in [7–9], PSMS method imposes less restrictions on system nonlinearity type. Moreover, the description of the nearness of the excitation frequency to the resonance frequency is not limited as in [7, 9]. The nearness of the excitation frequency to the resonance frequency can be chosen in general to be $\Omega = \omega_{00} + \epsilon^2\sigma$ where ω_{00} is one of the split parameters. As seen via the solution procedure, it is easy to implement the PSMS method. As seen from the efficiency examination of the PSMS method, the PSMS method is faster than the NCM and the three-term harmonic balance method in the first oscillator when the number of split parameters is five. With a larger number of split parameters, such as seven or nine, in the second and third oscillators, respectively, the computational time of the PSMS method is still acceptable and slightly faster than the NCM and much faster than the HBM in the second oscillator. However, the PSMS method is slightly slower than the NCM and the HBM in the third oscillator.

Acknowledgements The results presented in this paper were obtained under the supports of the Science and Technology Development Fund of Macau (Grant No. 042/2017/A1) and the Research Committee of University of Macau (Grant No. MYRG2018-00116-FST).

References

1. Baily, E.: Steady-state harmonic analysis of nonlinear networks, Ph.D. thesis, Stanford University (1968). <https://books.google.com/books?id=INZYnQEACAAJ>
2. Lindenlaub, J.C.: An approach for finding the sinusoidal steady state response of nonlinear systems. In: Proceedings of the 7th Annual Allerton Conference on Circuit and System Theory, University of Illinois (1969)
3. Liao, S.J.: The proposed homotopy analysis technique for the solution of nonlinear problems, Ph.D. thesis, Shanghai Jiao Tong University (1992)

4. Liao, S.J.: Notes on the homotopy analysis method: some definitions and theorems. *Commun. Nonlinear Sci. Numer. Simul.* **14**(4), 983–997 (2009)
5. Odibat, Z.M.: A study on the convergence of homotopy analysis method. *Appl. Math. Comput.* **217**, 782–789 (2010)
6. Liao, S.J.: An optimal homotopy-analysis approach for strongly nonlinear differential equations. *Commun. Nonlinear Sci. Numer. Simul.* **15**, 2003–2016 (2010)
7. Burton, T.D., Rahman, Z.: On the multiple-scale analysis of strongly non-linear forced oscillators. *Int. J. Non-Lin. Mech.* **21**(2), 135–146 (1986)
8. Chen, S., Shen, J., Sze, K.: A new perturbation procedure for limit cycle analysis in three-dimensional nonlinear autonomous dynamical systems. *Nonlinear Dyn.* **56**(3), 255–268 (2009)
9. Cheung, Y., Chen, S., Lau, S.: A modified Lindstedt–Poincaré method for certain strongly non-linear oscillators. *Int. J. Non-Lin. Mech.* **26**(3–4), 367–378 (1991)
10. Wu, B., Zhou, Y., Lim, C. W., Sun, W.: Analytical approximations to resonance response of harmonically forced strongly odd nonlinear oscillators. *Arch. Appl. Mech.* **88**(12), 2123–2134 (2018)
11. Hayashi, C.: *Nonlinear Oscillations in Physical Systems*. Princeton University Press, New York (2014)
12. Benedettini, F., Rega, G.: Non-linear dynamics of an elastic cable under planar excitation. *Int. J. Non-Lin. Mech.* **22**(6), 497–509 (1987)

Matrix Soliton Solutions of the Modified Korteweg–de Vries Equation



Sandra Carillo, Mauro Lo Schiavo, and Cornelia Schiebold

Abstract Nonlinear non-abelian Korteweg–de Vries (KdV) and modified Korteweg–de Vries (mKdV) equations and their links via Bäcklund transformations are considered. The focus is on the construction of *soliton solutions* admitted by matrix modified Korteweg–de Vries equation. Matrix equations can be viewed as a specialisation of operator equations in the finite dimensional case when operators admit a matrix representation. Bäcklund transformations allow to reveal structural properties (Carillo and Schiebold, J Math Phys 50:073510, 2009) enjoyed by non-commutative KdV-type equations, such as the existence of a recursion operator. *Operator methods* combined with Bäcklund transformations allow to construct explicit solution formulae (Carillo and Schiebold, J Math Phys 52:053507, 2011). The latter are adapted to obtain solutions admitted by the 2×2 and 3×3 matrix mKdV equation. Some of these matrix solutions are visualised to show the *solitonic* behaviour they exhibit. A further key tool used to obtain the presented results is an *ad hoc* construction of computer algebra routines to implement non-commutative computations.

Keywords Nonlinear non-commutative (termed also non-Abelian) equations · Korteweg–de Vries and modified Korteweg–de Vries non-commutative equations · Matrix soliton solutions · Bäcklund transformations · Computer algebra manipulation

S. Carillo (✉)

Università di Roma “La Sapienza”, Dip. S.B.A.I., Rome, Italy

I.N.F.N. – Sezione Roma 1, Gr. IV – M.M.N.L.P., Rome, Italy

e-mail: sandra.carillo@uniroma1.it;

<https://www.sbai.uniroma1.it/~sandra.carillo/index.html>

M. L. Schiavo

Università di Roma “La Sapienza”, Dip. D.I.S.G., Rome, Italy

C. Schiebold

Department of Mathematics and Science Education, Mid Sweden University, Sundsvall, Sweden

Instytut Matematyki, Uniwersytet Jana Kochanowskiego w Kielcach, Kielce, Poland

1 Introduction

The so-called *soliton equations* are widely investigated since the late 1960s when the first exact solution of the Korteweg–de Vries equation was obtained, as reported, for instance, in the well-known book by Calogero and Degasperis [2]. The name *soliton equations* is generally used to indicate nonlinear evolution equations which admit exact solutions in the Schwartz space of smooth *rapidly decreasing functions*.¹ The relevance of Bäcklund transformations in studying nonlinear evolution equations is well known both under the viewpoint of finding solutions to given initial boundary value problems, see [25–27] as well as in giving insight in the study of their structural properties, such as symmetry properties, admitted conserved quantities and Hamiltonian structure, see, e.g., [6] and the references therein. The important role played by Bäcklund transformations to investigate properties enjoyed by nonlinear evolution equations is based on the fact that most of the properties of interest are preserved under Bäcklund transformations [16, 17]. Thus, the construction of a net of Bäcklund transformation to connect nonlinear evolution equations allowed to prove new results both in the case of *scalar* equations [3–5], [18, 19], as well as in the generalised case of operator equations [7–12]². A comparison between the scalar (Abelian) and the operator (non-Abelian) cases referring to third-order KdV-type equations, Bäcklund transformations connecting them and related properties is comprised in [9]. Notably, Bäcklund transformations indicate a way to construct solutions to nonlinear evolution equations [20] and also to nonlinear ordinary differential equations [13] and [14]. Then, the operator approach [1, 15, 24, 28, 29], allows to construct solutions admitted by the whole hierarchies of nonlinear operator equations which are connected via Bäcklund transformations, see [3–11] and the references therein. The special case under investigation concerns solutions of the 2×2 and 3×3 mKdV matrix equation. Matrix equations are studied in [23] and in [21], where, respectively, solutions admitted by Burgers and KdV equations are obtained. A motivation for investigations on matrix equations is connected to quantum mechanics.

The material is organised as follows. Section 2 briefly reminds the needed notions on Bäcklund transformation, recalling also the links among KdV-type equations. In the subsequent Sect. 3, a short overview is provided on the method to obtain matrix solutions in the finite dimensional case. Then, some solutions of the matrix mKdV equation are graphically represented and, finally, relevant remarks and research perspectives are in the closing Sect. 4.

¹It is generally assumed that M is space of functions $u(x, t)$ which, \forall fixed t , belong to the Schwartz space S of *rapidly decreasing functions* on \mathbb{R}^n , in the, i.e., $S(\mathbb{R}^n) := \{f \in C^\infty(\mathbb{R}^n) : \|f\|_{\alpha, \beta} < \infty, \forall \alpha, \beta\}$, where $\|f\|_{\alpha, \beta} := \sup_{x \in \mathbb{R}^n} |x^\alpha D^\beta f(x)|$, $D^\beta := \partial^\beta / \partial x^\beta$.

²An overview on non-commutative equations is given in [22].

2 Non-commutative Potential KdV, KdV and Modified KdV Hierarchies

The well-known potential Korteweg–de Vries (pKdV), Korteweg–de Vries (KdV) and modified Korteweg–de Vries (mKdV) equations, in turn

$$w_t = w_{xxx} + 3w_x^2, \quad u_t = u_{xxx} + 6uu_x \quad \text{and} \quad v_t = v_{xxx} + 6v^2v_x \quad (1)$$

are nonlinear evolution equations in the unknown real functions, respectively w , u and v . All the equations (1) admit *soliton solutions*, see, among a wide literature, e.g., [2], namely solutions which represent nonlinear waves which propagate preserving energy and shape. The aim of the present investigation is to consider a generalisation of equations (1), on introduction of operator-valued equations according to the approach in [1, 15]. Thus, the non-commutative equations, counterpart, respectively, of (1), are given by

$$W_t = W_{xxx} + 3W_x^2, \quad U_t = U_{xxx} + 3\{U, U_x\}, \quad \text{and} \quad V_t = V_{xxx} + 3\{V^2, V_x\}, \quad (2)$$

where the square and curly brackets denote, in turn, the commutator and the anti-commutator, that is $\forall T, S, [T, S] := TS - ST$ and $\{T, S\} := TS + ST$.

According to the definition, [16, 17], two different evolution equations, e.g., (1)₁ and (1)₂, are termed *connected via the Bäcklund transformation* $B(u, v) = 0$ whenever given two solutions they admit, say, $u(x, t)$ and $v(x, t)$, if

$$B(u(x, t), v(x, t))|_{t=0} = 0 \quad \text{implies} \quad B(u(x, t), v(x, t))|_{t=\tau} = 0, \quad \forall \tau > 0. \quad (3)$$

Well-known examples of Bäcklund transformations are the introduction of a *bona fide* potential and the Miura transformation which, respectively, relate the pKdV to the KdV and the latter to the mKdV equation. The non-commutative extensions are

$$B_1 : U - W_x = 0 \quad M : \quad U - iV_x - V^2 = 0. \quad (4)$$

Notably, [10, 31], the links via Bäcklund transformations, combined with the knowledge of the hereditary recursion operator of the KdV equation, allow to construct the recursion operator admitted by the pKdV as well as by mKdV equation and, hence, to extend the same links to the whole corresponding hierarchies (see [7] and the references therein for details).

That is, given the KdV recursion operator $\Phi(U)$ then, the mKdV recursion operator and the pKdV recursion operator are obtained [10]. All the corresponding members in the three *hierarchies* of pKdV, KdV and mKdV equations follow to be linked via the transformations (4). Remarkably, these connections [10] allow, given a solution of the non-commutative pKdV equation, to construct the corresponding solutions of the non-commutative KdV and mKdV equations.

3 Matrix Soliton Solutions

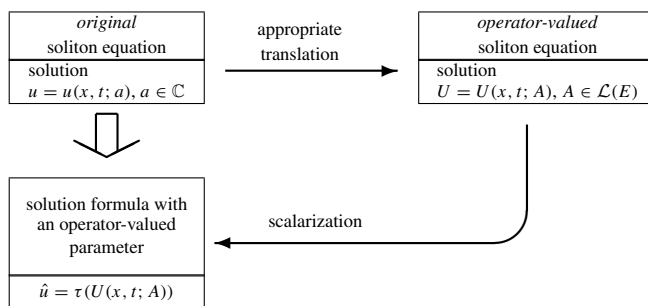
This section aims to summarise the essential steps in the construction of solutions on application of the operator method devised in [1, 15], further developed in [29, 30] and extended to hierarchies in [11]. A very short outline on how this method can be adopted to construct solutions of the matrix mKdV equation is provided. Indeed, the study in [7, 8, 10] is devoted to study nonlinear evolution equations in which the unknown is an operator on a Banach space. The idea of the method can be sketched as follows:

- Consider the operator method to obtain pKdV solutions.
- Use the links, via Bäcklund transformations, between the pKdV, KdV and mKdV equations to construct solutions of the KdV and mKdV equations.
- Implementation and visualisation of the explicit solutions via computer algebra routines.

The quite involved technical details can be found in [11]. The following first two subsections provide the schematic idea of the adopted method. In the third subsection some explicit soliton solutions of the 2×2 and 3×3 -matrix mKdV equation are presented.

3.1 Operator Method

The solution method, [1, 29], can be sketched via the following diagram



where a and A are parameters which, in turn, represent a generally complex number and an operator.

3.2 Soliton Solutions of mKdV Matrix Equation

The following theorem (cf. Theorem 11 b) in [11] where the matrix mKdV hierarchy is treated allows to construct non-commutative soliton solutions of the mKdV equation

$$V_t = V_{xxx} + 3\{V^2, V_x\}. \quad (5)$$

More precisely, (5) is to be read as an equation in which the dependent variable $V = V(x, t)$ takes values in the $d \times d$ -matrices. For the proof and the notation related to Banach spaces we refer to [11].

Theorem 1 *Let E be a Banach space and \mathcal{A} a quasi-Banach ideal equipped with a continuous determinant δ . Let $A \in \mathcal{L}(E)$ with $\text{spec}(A) \subseteq \{\lambda \in \mathbb{C} | \text{Re}(\lambda) > 0\}$. Moreover, assume that $B \in \mathcal{A}(E)$ satisfies the d -dimensionality condition*

$$AB + BA = \sum_{j=1}^d d^{(j)} \otimes c^{(j)} \quad (6)$$

with linearly independent $d^{(j)} \in E'$ and $c^{(j)} \in E$, $j = 1, \dots, d$. Then the matrix-function

$$V = \frac{i}{2} \left(\frac{\delta(I + i(L + L^{(i,j)}))}{\delta(I + iL)} - \frac{\delta(I - i(L + L^{(i,j)}))}{\delta(I - iL)} \right)_{i,j=1}^d,$$

where

$$L^{(i,j)} = d^{(i)} \otimes \left(\exp(Ax + A^3t) c^{(j)} \right), \quad L = \exp(Ax + A^3t)B, \quad (7)$$

and $I = I_E$ denotes the identity operator on E , solves the matrix mKdV (5) with values in the $d \times d$ -matrices on every product domain $(-\infty, c) \times G$ ($c \in \mathbb{R}$, G a domain in \mathbb{R}^{n-1}) on which $\delta(I \pm iL) \neq 0$.

3.3 Some Explicit Solutions of the Matrix Modified KdV Equation

The final step consists in the implementation, via computer algebra, of suitable routines amenable to visualise the matrix solutions of the mKdV equation. Indeed, multisoliton solutions admitted by the matrix KdV equation are given by Goncharenko in [21]: these solutions are obtained via a generalisation of the inverse scattering method. As shown in [11], the solution class of the matrix KdV equation that corresponds to the class constructed in Theorem 1 comprises Goncharenko's multisoliton solutions. In the present subsection, soliton solutions of the matrix

modified KdV are visualised using Mathematica. Some of such explicit 2-soliton solutions of the matrix mKdV, in the present subsection, are visualised using *Mathematica*.

Without going into details, we briefly explain the choices in Theorem 1 to realise 2-soliton solutions of the $d \times d$ -matrix mKdV. To reflectionless spectral data with discrete eigenvalues k_1, k_2 and spectral matrices B_1, B_2 of size $d \times d$, we associate $A = \begin{pmatrix} k_1 I_d & 0 \\ 0 & k_2 I_d \end{pmatrix}$, $B = \left(\frac{i}{k_i + k_j} B_j \right)_{i,j=1}^2$, in particular, $E = \mathbb{C}^{2d}$. In the plots below the case $B_1 = B_2$ is considered (Fig. 1).

The examples of solutions of the mKdV equation, graphically represented in the Figs. 2, 3, and 4, represent different 3×3 matrix solutions: the elements of the spectral matrices are indicated in the caption. The pictures show the behaviour of *two-soliton solutions* admitted by the matrix mKdV equation.

Note that the crucial features of interaction between two different solitons well known on the scalar case seem to characterise also matrix solutions. These

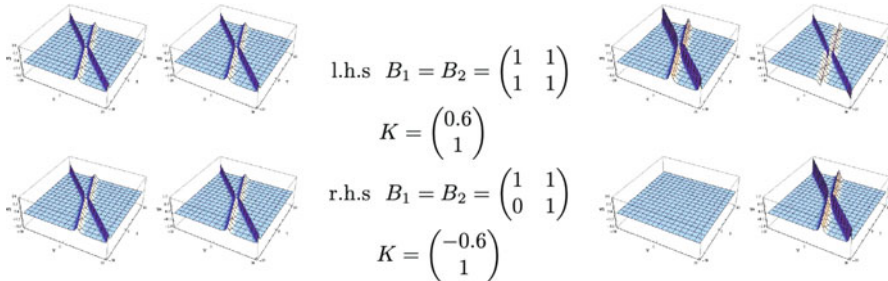


Fig. 1 Two examples of two-soliton solutions of 2×2 matrix mKdV equation; the elements of the spectral matrices $B := B_1 = B_2$ are specified as follows: $B_{h,k} = 1, \forall h, k$, on the l.h.s. and $B_{1,1} = B_{1,2} = B_{2,2} = 1, B_{2,1} = 0$, on the l.h.s.

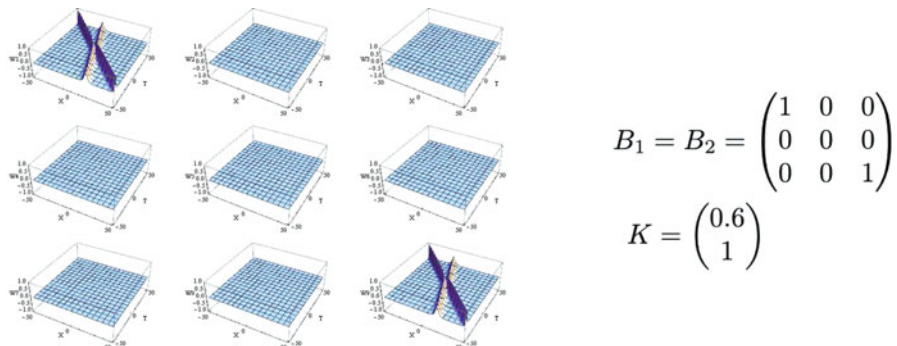


Fig. 2 Two-soliton solutions of 3×3 matrix mKdV equation; all the matrix elements in $B := B_1 = B_2$ are equal to zero expect the two diagonal elements $B_{1,1} = B_{3,3} = 1$

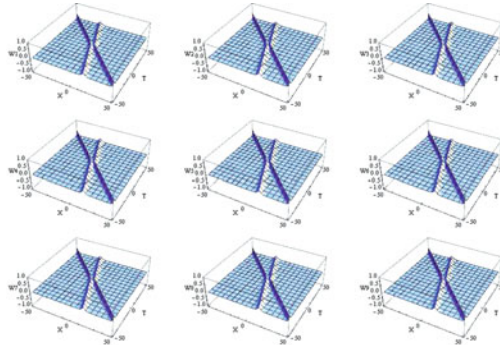


Fig. 3 Two-soliton solution of 3×3 matrix mKdV equation; all the matrix elements in $B := B_1 = B_2$ are equal to one, i.e. $B_{h,k} = 1$, $1 \leq h, k \leq 3$

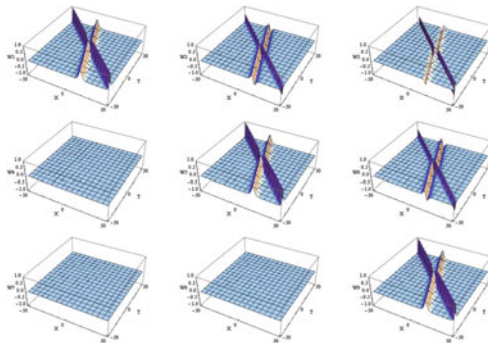


Fig. 4 Two-soliton solution of 3×3 matrix mKdV equation; $B_{h,h} = 1$, $1 \leq h \leq 3$ and $B_{h,h+1} = 1$, $1 \leq h \leq 2$ all the other matrix elements in $B := B_1 = B_2$ are equal to zero

$$B_1 = B_2 = \begin{pmatrix} 1 & 1 & 1 \\ 1 & 1 & 1 \\ 1 & 1 & 1 \end{pmatrix}$$

$$K = \begin{pmatrix} 0.6 \\ 1 \end{pmatrix}$$

$$B_1 = B_2 = \begin{pmatrix} 1 & 1 & 0 \\ 0 & 1 & 1 \\ 0 & 0 & 1 \end{pmatrix}$$

$$K = \begin{pmatrix} 0.6 \\ 1 \end{pmatrix}$$

pictures represent only an example of a study, currently in progress, aiming to construct additional solutions as well as their interpretation. In particular, if the spectral matrices are diagonal, then also the solution enjoys the same property, see Fig. 2. Conversely, Fig. 4, shows that, when *off diagonal* elements in the spectral matrix are different from zero, the situation changes. For example, given the initial datum $B_{1,3} = 0$, in the spectral matrices, the corresponding element of the two-soliton solution, depicted in Fig. 4, is not zero. A detailed study on these solutions is currently under investigation. One of the main issues concerns the energy conservation and its partition among the matrix elements. The appropriate functional which represents the energy of the interacting solitons is expected to play a crucial role to understand the phenomenology under investigation.

4 Concluding Remarks

The aim of the present study is to emphasise some of the properties of solutions admitted by matrix mKdV equation. Notably, depending on the spectral data, a variety of soliton solutions may be observed. The crucial feature seems to be the appearance, also in the matrix case, of localised solutions which can be termed *solitons* on the basis of their interaction properties. A much richer interaction phenomenology, with respect to the scalar case, can be observed when matrix solutions are investigated. Indeed, as soon as the spectral matrices have non-zero off-diagonal terms, the solution exhibits non-zero solutions in further matrix elements. In addition, a variety of different solutions can be observed. However, in all cases, a form of energy distribution seems to be observed: the most appropriate way to define a functional suitable to represent the *energy* related to a matrix soliton solution is, in the authors opinion, one of the interesting questions this work arises. The obtained results motivate further investigations to provide a better understanding of the interesting phenomenology already observed.

Acknowledgements Under the financial support of G.N.F.M.-I.N.d.A.M., I.N.F.N. and Università di Roma LA SAPIENZA, Rome, Italy. C. Schiebold acknowledges Dip. S.B.A.I., Università di Roma LA SAPIENZA, for the kind hospitality.

References

1. Aden, H., Carl, B.: On realizations of solutions of the KdV equation by determinants on operator ideals. *J. Math. Phys.* **37**, 1833–1857 (1996)
2. Calogero, F., Degasperis, A.: Spectral Transform and Solitons I, Studies in Mathematics and Its Application vol. 13, North Holland, Amsterdam (1980)
3. Carillo, S.: Nonlinear evolution equations: Bäcklund transformations and Bäcklund charts. *Acta Appl. Math.* **122**(1), 93–106 (2012)
4. Carillo, S.: KdV-type equations linked via Bäcklund transformations: remarks and perspectives. *Appl. Numer. Math.* **141**, 81–90 (2019). <https://doi.org/10.1016/j.apnum.2018.10.002>
5. Carillo, S., Fuchssteiner, B.: The abundant symmetry structure of hierarchies of nonlinear equations obtained by reciprocal links. *J. Math. Phys.* **30**, 1606–1613 (1989)
6. Carillo, S., Lo Schiavo, M., Porten, E., Schiebold, C.: A novel noncommutative KdV-type equation, its recursion operator and solitons. *J. Math. Phys.* **59**, 043501 (2018)
7. Carillo, S., Lo Schiavo, M., Schiebold, C.: Bäcklund transformations and non-abelian nonlinear evolution equations: a novel Bäcklund chart. *SIGMA* **12**, 087 (2016)
8. Carillo, S., Lo Schiavo, M., Schiebold, C.: Recursion operators admitted by non-Abelian Burgers equations: some remarks. *Math. Comput. Simul.* **147C**, 40–51 (2018)
9. Carillo, S., Lo Schiavo, M., Schiebold, C.: Abelian versus non-Abelian Bäcklund charts: some remarks. *E.E.C.T.* **8**(1), 43–55 (2019). <https://doi.org/10.3934/eect.2019003>
10. Carillo, S., Schiebold, C.: Non-commutative KdV and mKdV hierarchies via recursion methods. *J. Math. Phys.* **50**, 073510 (2009)
11. Carillo, S., Schiebold, C.: Matrix Korteweg-de Vries and modified Korteweg-de Vries hierarchies: non-commutative soliton solutions. *J. Math. Phys.* **52**, 053507 (2011)
12. Carillo, S., Schiebold, C.: On the recursion operator for the noncommutative Burgers hierarchy. *J. Nonlinear Math. Phys.* **19**(1), 27–37 (2012)

13. Carillo, S., Zullo, F.: Ermakov–Pinney and Emden–Fowler equations: new solutions from novel Bäcklund transformations. *Theor. Math. Phys.* **196**(3), 1268–1281 (2018)
14. Carillo, S., Zullo, F.: The Gross-Pitaevskii equation: Bäcklund transformations and admitted solutions. *Ricerche Mat.* (2019). arXiv:1803.09228
15. Carl, B., Schiebold, C.: Nonlinear equations in soliton physics and operator ideals. *Nonlinearity* **12**, 333–364 (1999)
16. Fokas, A.S., Fuchssteiner, B.: Bäcklund transformation for hereditary symmetries. *Nonlin. Anal. Theory Methods Appl.* **5**(4), 423–432 (1981)
17. Fuchssteiner, B.: Application of hereditary symmetries to nonlinear evolution equations. *Nonlinear Anal. Theory Methods Appl.* **3**(6), 849–862 (1979)
18. Fuchssteiner, B., Carillo, S.: Soliton structure versus singularity analysis: third-order completely integrable nonlinear differential equations in $1 + 1$ -dimensions. *Phys. A* **154**, 467–510 (1989)
19. Fuchssteiner, B., Carillo, S.: The action-angle transformation for soliton equations. *Phys. A* **166**, 651–676 (1990)
20. Fuchssteiner, B., Schulze, T., Carillo, S.: Explicit solutions for the Harry Dym equation. *J. Phys. A: Math. Gen.* **25**, 223–230 (1992)
21. Goncharenko, V.M.: Multisoliton solutions of the matrix KdV equation. *Theor. Math. Phys.* **126**, 81–91 (2001)
22. Kupershmidt, B.A.: KP or mKP. Noncommutative Mathematics of Lagrangian, Hamiltonian, and Integrable Systems. American Mathematical Society, Providence (2000)
23. Levi, D., Ragnisco, O., Bruschi, M.: Continuous and discrete matrix Burgers' hierarchies. *Nuovo Cimento B* **74**(1), 33–51 (1983)
24. Marchenko, V.A.: Nonlinear Equations and Operator Algebras. Reidel, Kufstein (1988)
25. Rogers, C., Ames, W.F.: Nonlinear Boundary Value Problems in Science and Engineering. Academic Press, Boston (1989)
26. Rogers, C., Schief, W.K.: Bäcklund and Darboux Transformations: Geometry and Modern Applications in Soliton Theory. Cambridge University Press, Cambridge (2002)
27. Rogers, C., Shadwick, W.F.: Bäcklund Transformations and Their Applications. Mathematics in Science and Engineering, vol. 161. Academic Press, New York (1982)
28. Schiebold, C.: An operator-theoretic approach to the Toda lattice equation. *Phys. D* **122**, 37–61 (1998)
29. Schiebold, C.: Explicit solution formulas for the matrix-KP. *Glasgow Math. J.* **51**, 147–155 (2009)
30. Schiebold, C.: Noncommutative AKNS systems and multisolitons solutions to the matrix sine-Gordon equation. *Discrete Contin. Dyn. Syst. Suppl.* **2009**, 678–690 (2009)
31. Schiebold, C.: Structural properties of the noncommutative KdV recursion operator. *J. Math. Phys.* **52**, 113504 (2011)

Part II

Bifurcations and Nonsmooth Systems

Bifurcations of Limit Directions at Codimension-2 Discontinuities of Vector Fields



Mate Antali and Gabor Stepan

Abstract In this paper, nonsmooth vector fields are considered, where the discontinuity is located in a codimension-2 subset of the phase space (called extended Filippov systems). Although there are continuously many directions which are orthogonal to the discontinuity set, the trajectories of the system typically tend to the discontinuity along a few specific directions (called limit directions). During the current research, we present two types of bifurcations related to these limit directions: the tangency bifurcation and the fold of two limit directions. The analysis of this type of discontinuity is motivated by three-dimensional contact of rigid bodies in the presence of Coulomb friction.

Keywords Bifurcations · Limit direction · Codimension-2 discontinuity · Extended Filippov systems

1 Introduction

Filippov systems are nonsmooth dynamical systems which possess codimension-1 discontinuities in the phase space (see [1] or [2] for an overview). One of the physical sources of these systems is dry friction with the assumption of the Coulomb friction model. But when spatial (three-dimensional) contact of rigid bodies is modelled by dry friction, the resulting dynamical system contains more complicated discontinuities in their phase space.

In the limit case where the contacting bodies are completely rigid and the contact area is infinitesimally small, the simple three-dimensional Coulomb friction leads to codimension-2 discontinuities (see [3]). This type of vector field can be called an *extended Filippov system*, whose basic definitions and properties have been published recently (see [4]). Note that the assumption of finite contact area with

M. Antali (✉) · G. Stepan
Budapest University of Technology and Economics, Budapest, Hungary
e-mail: antali@mm.bme.hu

drilling friction and rolling resistance (see [5, 6]) would lead to higher codimensional discontinuities, which systems are not covered by the present analysis.

In the present work, we focus on the bifurcations of the so-called *limit directions* of extended Filippov systems. These objects are the possible directions where the trajectories of the system are connected to the discontinuity set.

2 Extended Filippov Systems

2.1 Definition of Extended Filippov Systems

Consider the vector field $F(x)$ where $x = (x_1, x_2, \dots, x_n)$ and $n \geq 3$. Assume that $F(x)$ is defined everywhere in \mathbb{R}^n except for the set

$$\Sigma = \{x : x_1 = x_2 = 0\} = \{(0, 0, x_3, \dots, x_n)\}. \quad (1)$$

As the vector field $F(x)$ is not defined in Σ , the $n - 2$ dimensional space Σ is called a **codimension-2 discontinuity set of F** .

There are continuously many unit vectors orthogonal to Σ , denoted by

$$n(\phi) := (\cos \phi, \sin \phi, 0, \dots, 0), \quad (2)$$

where $\phi \in [0, 2\pi)$ shows the angle around the discontinuity set. Let us formally calculate the directional limit depending on the angle ϕ at a point $x^0 \in \Sigma$:

$$F^*(x^0)(\phi) = \lim_{\varepsilon \rightarrow 0^+} F(x^0 + \varepsilon n(\phi)). \quad (3)$$

At a chosen x^0 , we denote the **limit vector field** shorty by $F^*(\phi)$.

Definition 1 (Extended Filippov System) A system

$$\dot{x} = \frac{dx}{dt} = F(x), \quad F : \mathbb{R}^n \setminus \Sigma \rightarrow \mathbb{R}^n \quad (4)$$

is called an **extended Filippov system**, if the following three properties are satisfied:

- (a) The vector field $F(x)$ is smooth on $\mathbb{R}^n \setminus \Sigma$.
- (b) The limit (3) exists for all $x^0 \in \Sigma$ and $\phi \in [0, 2\pi)$.
- (c) For all $x^0 \in \Sigma$, there exist $\phi_1, \phi_2 \in [0, 2\pi)$ such that $F^*(x^0)(\phi_1) \neq F^*(x^0)(\phi_2)$.

In other words: the discontinuity is restricted to Σ (see (a)), there is indeed a discontinuity in all points of Σ (see (c)), and the discontinuity is regular in some sense (see (b)).

In the definition of extended Filippov systems, the state space could be an open set in \mathbb{R}^n and Σ could be a smooth $n - 2$ dimensional manifold (see [4]), but the restricted definitions above can be used without loss of generality. Note that $F(x)$ is *not defined* on Σ . By using a convex combination (see [4]), the vector field can be extended to some parts of Σ , but this is not covered by the current paper.

2.2 Limit Directions

Consider a point $x^0 \in \Sigma$ of the discontinuity set. The orthogonal complement of Σ at x^0 is a plane defined by

$$O_\Sigma(x^0) := \left\{ x^0 + (x_1, x_2, 0, \dots, 0) \right\}, \quad (5)$$

which is referred simply as *orthogonal space*. Let us write the limit vector field $F^*(\phi)$ into the form

$$F^*(\phi) = F_O^*(\phi) + F_T^*(\phi) = \underbrace{R(\phi) \cdot n(\phi)}_{\text{orthogonal to } \Sigma} + \underbrace{V(\phi) \cdot n(\phi + \pi/2)}_{\text{tangent to } \Sigma} + \underbrace{F_T^*(\phi)}_{}, \quad (6)$$

where $F_O^*(\phi)$ lays in the orthogonal space and $F_T^*(\phi)$ is tangent to Σ . The scalar-valued, 2π -periodic functions $R(\phi)$ and $V(\phi)$ are defined by

$$\begin{aligned} R(\phi) &:= F_1^*(\phi) \cos \phi + F_2^*(\phi) \sin \phi, \\ V(\phi) &:= F_2^*(\phi) \cos \phi - F_1^*(\phi) \sin \phi, \end{aligned} \quad (7)$$

where F_1^* and F_2^* are the first two components of F^* . The component $R(\phi)$ describes the *radial* part of the limit vector around the discontinuity set Σ . The component $V(\phi)$ describes the *circumferential* dynamics around Σ . This structure gives the idea to transform the system into polar coordinates (see the next section).

To describe the structure of the dynamics in the vicinity of the discontinuity set Σ , we look for the trajectories which are connected to Σ . Although the vector field $F(x)$ is not defined in Σ , the trajectories of $F(x)$ can tend to Σ in forward or in backward time. Assume that a trajectory of F tends to a point $x^0 \in \Sigma$ and the trajectory has a well-defined asymptote at x^0 with a direction of ϕ_0 measured around the discontinuity set. Along the line of the asymptote, the orthogonal part $F_O^*(\phi)$ must be parallel to $n(\phi)$. Then, we can see from (6) that the circumferential dynamics $V(\phi_0)$ vanishes. This motivates the following definition:

Definition 2 (Limit Direction) Consider a point $x^0 \in \Sigma$ with the functions defined in (7). If $V(\phi_0) = 0$ for $\phi_0 \in [0, 2\pi)$, then the angle ϕ_0 is called a *limit direction* of x^0 .

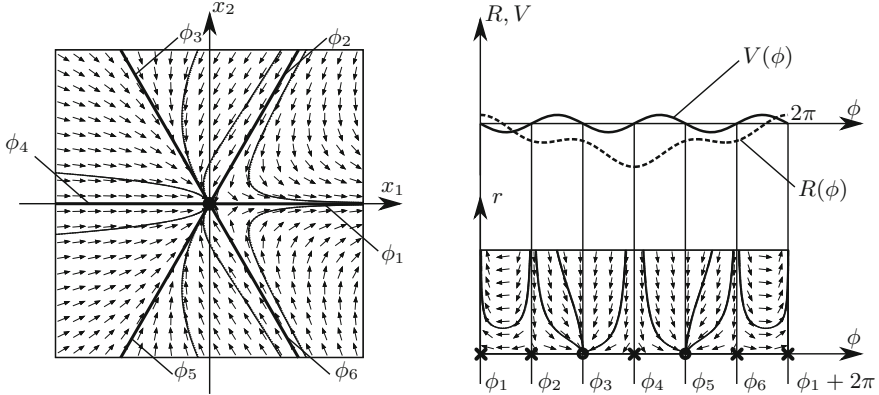


Fig. 1 Example of different types of limit directions. Left panel: the phase portrait of the system $F(x) = (-x_1/(x_1^2 + x_2^2)^{1/2} + 2x_1^2/(x_1^2 + x_2^2) - 1/2, -x_2/(x_1^2 + x_2^2)^{1/2}, -x_3)$ projected into the orthogonal plane of $x^0 = 0$. Right panel: the radial $R(\phi)$ and the circumferential $V(\phi)$ components of the dynamics and the phase portrait of the associated system (11). Attracting directions: $\phi_2, \phi_3, \phi_4, \phi_5, \phi_6$, repelling direction: ϕ_1 . Dominant directions: ϕ_3, ϕ_5 , isolated directions: $\phi_1, \phi_2, \phi_4, \phi_6$

The limit directions have important role in organizing the dynamics in the vicinity of Σ (see Fig. 1). If x^0 possesses limit directions then all trajectories of $F(x)$ connected to x^0 must tend to x^0 along one of these limit directions. In some sense, the limit directions are similar to the eigenvectors of nodes and saddles of smooth systems, but there are some fundamental differences: The limit directions are uni-directional, and it can be shown that the trajectories reach the discontinuity in *finite time* along a limit direction. It is possible that x^0 does not have any limit directions, that is, $V(\phi) \neq 0$ for all $\phi \in [0, 2\pi]$.

2.3 Types of Limit Directions

Let us categorize the limit directions according to the structure of the surrounding trajectories. According to the *radial* component, the trajectories either tend towards the discontinuity set Σ (attracting) or they move outwards from Σ (repelling). These two cases can be separated according to the sign of the radial component $R(\phi)$ of the dynamics:

Definition 3 (Attracting and Repelling Limit Directions) Consider a point $x^0 \in \Sigma$ and a corresponding limit direction ϕ_0 satisfying $V(\phi_0) = 0$. The limit direction is called **attracting** if $R(\phi_0) < 0$ and it is called **repelling** if $R(\phi_0) > 0$.

The sign of the derivative $V' := dV/d\phi(\phi_0)$ decides whether the nearby trajectories are getting closer or further to each other in the *circumferential* direction

as the time is evolving. If the sign of $R(\phi_0)$ is considered, as well, we can decide whether the trajectories are contracting *in the direction towards the discontinuity set*:

Definition 4 (Dominant and Isolated Limit Directions) Consider a point $x^0 \in \Sigma$ and a corresponding limit direction ϕ_0 satisfying $V(\phi_0) = 0$. The limit direction is called **dominant** if $R(\phi_0) \cdot V'(\phi_0) > 0$ and it is called **isolated** if $R(\phi_0) \cdot V'(\phi_0) < 0$.

The change of the type of a limit direction causes structural change in the dynamics in the vicinity of the discontinuity set. In the next section, we create a 2D system by projecting $F(x)$ into the orthogonal space $O_\Sigma(x^0)$. The analysis of that system helps to explore the bifurcations of limit directions.

3 Analysis of the Associated Smooth System

3.1 The Associated Smooth System in Polar Coordinates

For each point x^0 of the discontinuity set Σ , we create an associated smooth system, whose equilibrium point corresponds to the limit direction of the original system. Let us express the variables x_1 and x_2 in polar coordinates in the form

$$x_1 = r \cos \phi, \quad x_2 = r \sin \phi, \quad (8)$$

where $r > 0$ is the *distance* from the discontinuity set Σ and $\phi \in [0, 2\pi)$ is the angle around Σ which we have already used. The dynamics of these variables is given by

$$\dot{r} = F_1(x) \cos \phi + F_2(x) \sin \phi, \quad \dot{\phi} = \frac{1}{r} \cdot (F_2(x) \cos \phi - F_1(x) \sin \phi), \quad (9)$$

where F_1 and F_2 are the first two components of F .

Let us restrict (9) to the orthogonal space $O_\Sigma(x^0)$ (see (5)) and take the projection of $F(x)$ into this orthogonal space. Then (9) leads to a planar dynamical system of the variables r and ϕ in the form

$$\dot{r} = F_r(r, \phi), \quad \dot{\phi} = \frac{1}{r} F_\phi(r, \phi), \quad (10)$$

where F_r and F_ϕ are *smooth* functions on $(r, \phi) \in [0, \infty) \times [0, 2\pi)$.

Note that (10) is singular at $r = 0$, which corresponds to $x = x^0 \in \Sigma$. Let us introduce a new time variable τ defined by $dr/d\tau = \dot{r} \cdot r$, where the dash denotes the differentiation with respect to the new time variable. Then, it can be shown that (10) becomes

$$\begin{aligned} \frac{dr}{d\tau} &= R(\phi) \cdot r + S(\phi) \cdot r^2 + \mathcal{O}(r^3), \\ \frac{d\phi}{d\tau} &= V(\phi) + W(\phi) \cdot r + \mathcal{O}(r^2), \end{aligned} \quad (11)$$

where $R(\phi)$ and $V(\phi)$ are the same functions we defined in (7), $S(\phi)$ and $W(\phi)$ are 2π -periodic functions, and \mathcal{O} denotes the higher order terms in r . Note that the terms $R(\phi)$ and $V(\phi)$ originate from the *discontinuous* part of $F(x)$, while the terms $S(\phi)$ and $W(\phi)$ originate from the *linear* part of $F(x)$.

The equilibrium points of the system (11) are strongly related to those of the limit directions of the original system. As (11) is a *smooth* 2D system, a usual bifurcation analysis can be applied to its equilibrium points.

3.2 Equilibrium Points and Bifurcations

The trivial equilibrium points of (11) are $(r, \phi) = (0, \phi_0)$ where $V(\phi_0) = 0$. The Taylor expansion around an equilibrium $(0, \phi_0)$ is given by

$$\begin{pmatrix} \frac{dr}{d\tau} \\ \frac{d\phi}{d\tau} \end{pmatrix} = \begin{pmatrix} R(\phi_0) & 0 \\ W(\phi_0) & V'(\phi_0) \end{pmatrix} \cdot \begin{pmatrix} r \\ \phi - \phi_0 \end{pmatrix} + \mathcal{O}(r^2, (\phi - \phi_0)^2). \quad (12)$$

It can be seen from the Jacobian matrix that the eigenvalues of the equilibrium are $\lambda_1 = R(\phi_0)$ and $\lambda_2 = V'(\phi_0)$.

Bifurcations of the equilibrium points can occur when one of these eigenvalues becomes zero. These are expressed in the following two theorems. The theorems can be proved by careful but straightforward application of the general conditions of the basic bifurcations (see, e.g., [7, p. 338]).

Theorem 1 (Transcritical Bifurcation) *Consider a family of the systems in the form (11) depending smoothly on a scalar parameter p . At $p = 0$, consider an equilibrium point $(r, \phi) = (0, \phi_0)$ satisfying $V(\phi_0) = 0$, and assume that the following statements are true:*

$$R(\phi_0) = 0, \quad V'(\phi_0) \neq 0, \quad S(\phi_0) \cdot V'(\phi_0) - W(\phi_0) \cdot R'(\phi_0) \neq 0. \quad (13)$$

*Moreover, assume that by considering the dependence of the parameter p , the derivative $\partial R / \partial p$ is non-zero. Then, a **transcritical bifurcation** occurs at $(r, \phi) = (0, \phi_0)$ and $p = 0$.*

In the case of this transcritical bifurcation, the examined trivial equilibrium passes over a *non-trivial* equilibrium with $r \neq 0$ for $p \neq 0$. The coordinate r of this non-trivial equilibrium would change sign at the critical parameter value $p = 0$. However, the region $r < 0$ is not part of the phase space of the system, that is, the non-trivial equilibrium exists either below or above of the critical parameter value $p = 0$.

Theorem 2 (Saddle-Node Bifurcation) Consider a family of the systems in the form (11) depending smoothly on a scalar parameter p . At $p = 0$, consider an equilibrium point $(r, \phi) = (0, \phi_0)$ satisfying $V(\phi_0) = 0$, and assume that the following statements are true:

$$V'(\phi_0) = 0, \quad R(\phi_0) \neq 0, \quad V''(\phi_0) \neq 0. \quad (14)$$

Moreover, assume that by considering the dependence of the parameter p , the derivative $\partial V/\partial p$ is non-zero. Then, a **saddle-node bifurcation** occurs at $(r, \phi) = (0, \phi_0)$ and $p = 0$.

In this saddle-node bifurcation, two trivial equilibria are involved on the line $r = 0$. Due to this bifurcation, the number of the trivial equilibria changes by two, which is simply the number of roots of the function $V(\phi)$ on $[0, 2\pi]$.

4 Bifurcations of the Limit Directions

4.1 Relation Between the Associated System and the Original System

Based on the results of the associated smooth planar system presented above, we can analyse the bifurcations of the limit directions in extended Filippov systems.

The line $r = 0$ in the system (11) corresponds to the selected point x^0 of the discontinuity set in the original system (4). Moreover, the location of the trivial equilibria of (11) is determined by $V(\phi_0) = 0$, which coincides with the condition of Definition 2. That leads to the following statement:

Proposition 1 Each limit direction ϕ_0 of $x^0 \in \Sigma$, corresponds to an equilibrium point of the associated system (11) at $(r, \phi) = (0, \phi_0)$.

When we want to transfer the results about the bifurcations to the original system (4), we should not forget about the effect of the *projection* performed at the creation of the associated system (11). It is possible to repeat the calculations of the previous section in the whole space \mathbb{R}^n , where the polar coordinates r and ϕ are complemented by coordinates x_3, \dots, x_n of $x^0 \in \Sigma$ (see (1)). Then, it can be showed that the bifurcations presented in the previous section *do not suffer a qualitative change by the projection*.

Consequently, we can transfer the bifurcations declared in Theorems 1–2 to the limit directions of the extended Filippov system (4). Note that the parametric dependence of the system (4) is not considered. However, the choice of x^0 modifies the associate system (11) as a dependence of $n - 2$ parameters. Therefore, the simple codimension-1 bifurcations of (11) become $n - 3$ dimensional bifurcation surfaces in the discontinuity set Σ . These surfaces divide Σ into parts according to the structurally different kinds of behaviour of the trajectories in the vicinity of the discontinuity.

In case of both bifurcations, we first define the new type of bifurcation and then state a theorem about the structural properties of the bifurcation. The proof of these theorems are the direct consequences of Theorems 1–2 and Definitions 2–4.

4.2 Tangency Bifurcation

Definition 5 (Tangency Bifurcation) Consider a point $x^0 \in \Sigma$ with the functions defined in (7). Assume that there exists $\phi_0 \in [0, 2\pi]$ such that $V(\phi_0) = 0$, $R(\phi_0) = 0$, $V'(\phi_0) \neq 0$ and $(S \cdot V' - W \cdot R')(\phi_0) \neq 0$. Then, we say that a **tangency bifurcation** occurs at x^0 .

Theorem 3 (Structural Changes at the Tangency Bifurcation) *In the tangency bifurcation, one limit direction of x^0 is changing from attracting to repelling or vice versa. In the meantime, the limit direction is changing from dominant to isolated or vice versa. The corresponding limit vector $F^*(\phi_0)$ is tangent to the discontinuity set Σ .*

Note that the non-trivial equilibrium involved to the transcritical bifurcation of (11) corresponds to the intersection of the nullclines of $F_1(x)$ and $F_2(x)$, which causes the tangency of $F^*(\phi_0)$ field to Σ at x_0 . The phrase *tangency bifurcation* is based on the strong analogy to the tangency bifurcation of classical Filippov systems (see [1]). Note that for the evaluation of the conditions of Definition (5), the *linear part* of the vector field $F(x)$ is required (contained in $S(\phi)$ and $W(\phi)$).

4.3 Fold of Limit Directions

Definition 6 (Fold of Limit Directions) Consider a point $x^0 \in \Sigma$ with the functions defined in (7). Assume that there exists $\phi_0 \in [0, 2\pi]$ such that $V(\phi_0) = V'(\phi_0) = 0$, $R(\phi_0) = 0$ and $V''(\phi_0) \neq 0$. Then, we say that a **fold of limit directions** occurs at x^0 .

Theorem 4 (Structural Changes at the Fold of Limit Directions) *In the fold of limit directions, two limit directions are joined and destroyed. Both limit directions are either attracting or repelling. One of the involved limit directions is dominant and the other one is isolated.*

The term *fold* (or saddle-node) bifurcation is a natural choice based on the corresponding bifurcation in Theorem 2. Independently on the linear and higher order terms of $F(x)$, this type of bifurcation depends on the limit vector field $F^*(\phi)$ only.

5 Conclusion

Limit directions have an important role in understanding the structure of trajectories tending to the codimension-2 discontinuities in extended Filippov systems. At each point of the discontinuity set, an associated planar smooth system was created in polar coordinates. The results of the bifurcation analysis of this smooth system were transferred to the original nonsmooth system. A bifurcation of the limit directions can occur either when the limit direction turns around (tangency bifurcation) or when two limit directions merge (fold bifurcation). Both types of these bifurcations have been identified in mechanical systems containing dry friction between rigid bodies (see [3]). Further research will explore the detailed mechanical consequences of these bifurcations.

Acknowledgements The research work of the first author is supported by the Hungarian Academy of Sciences in the Premium Postdoctoral Fellowship Programme under the grant number PPD2018-014/2018.

References

1. di Bernardo, M., et al.: Piecewise-smooth Dynamical Systems. Springer, London (2008)
2. Leine, R., Nijmeijer, H.: Dynamics and Bifurcations of Non-Smooth Mechanical Systems. Springer, Berlin (2004)
3. Antali, M., Stepan, G.: Nonsmooth analysis of three-dimensional slipping and rolling in the presence of dry friction. *Nonlinear Dyn.* **97**(3), 1799–1817 (2019)
4. Antali, M., Stepan, G.: Sliding and crossing dynamics in extended Filippov systems. *J. Appl. Dyn. Syst.* **17**(1), 823–858 (2019)
5. Kudra, G., Awrejcewicz, J.: Tangens hyperbolicus approximations of the spatial model of friction coupled with rolling resistance. *Int. J. Bifurcation and Chaos* **21**(10), 2905–2917 (2011)
6. Kudra, G., Awrejcewicz, J.: Approximate modelling of resulting dry friction forces and rolling resistance for elliptic contact shape. *Eur. J. Mech. A Solids* **42**, 358–375 (2013)
7. Perko, L.: Differential Equations and Dynamical Systems. Springer, Berlin (2001)

Boundary Layer Dynamics of Multibody Systems Involving Impact and Friction



Sotirios Natsiavas and Elias Paraskevopoulos

Abstract A new method is presented on the dynamics of multibody systems subject to a combination of bilateral constraints and a unilateral constraint, related to a frictional impact. The analysis is performed by using concepts of Analytical Dynamics and differential geometry. This sets a strong foundation for applying Newton's law of motion and leads to an illuminating description of the dynamics. Using the unilateral constraint, a boundary is first defined on the original configuration manifold, surrounding a subspace of possible motions. Then, the emphasis is shifted on the dynamic action within the boundary layer. A set of numerical results is also presented, which is obtained for two characteristic examples.

Keywords Analytical dynamics · Unilateral constraint · Manifold with boundary · Frictional contact

1 Introduction

Studies on the dynamics of constrained mechanical systems span over a large research domain and are part of a long tradition in mechanics [1–3]. Specifically, systems with impact and friction appear in many applications and are associated to a lot of theoretical challenges [3–7]. Two main approaches are employed in this area. The first is based on the principles of linear and angular momentum, together with a definition of restitution coefficients and development of impact laws in order to predict post-impact velocities and impulsive reactions. This includes a considerable body of literature where contact events are studied by using tools from Non-smooth Mechanics [5–7]. The second approach is known as a Darboux–Keller method and leads to a set of ordinary differential equations (ODEs), describing dynamics of

S. Natsiavas (✉) · E. Paraskevopoulos
Department of Mechanical Engineering, Aristotle University, Thessaloniki, Greece
e-mail: natsiava@auth.gr

particles or rigid bodies during the impact time interval, by employing the normal impulse as an independent variable [3, 4, 8].

This chapter is based on previous studies of the authors on constrained systems [9, 10]. An Analytical Dynamics framework is adopted, together with some basic results from the theory on manifolds with boundary [11]. The manifold boundary is first determined by using the unilateral constraint. This defines a subspace of the original configuration manifold where the figurative particle, representing the motion of the system, is allowed to move. Then, each bilateral constraint causes a correction in the direction of the main impulse in the configuration manifold. When friction effects are negligible, the dominant action occurs along this direction and is described by a nonlinear ODE. The presence of friction converts this to a system of three ODEs, capturing the essential dynamics in a subspace, arising by bringing the image of the friction cone from the physical to the configuration space.

The present chapter is organized as follows. First, the basic geometric properties (i.e., metric and connection) of a manifold with boundary are summarized in Sect. 2. The effect of bilateral constraints is considered in Sect. 3. Next, the analytical part is completed by including friction. Finally, a set of numerical results is presented in Sect. 4.

2 Mechanical Systems with a Single Frictionless Impact

The motion of the systems examined is described by a set of generalized coordinates, $q = (q^1, \dots, q^n)$ [1, 2]. These entities determine the position of a point p , moving as a function of time t , on an n -dimensional configuration manifold M . When a contact occurs, the allowable motions on M are restricted by an inequality

$$\rho(p) \geq 0. \quad (1)$$

Function ρ defines a constrained manifold

$$X = \{p \in M : \rho(p) \geq 0\}, \quad (2)$$

with boundary ∂X and interior $X^o = X \setminus \partial X$, so that $X = X^o \sqcup \partial X$. Then, the motion is represented by a curve on X . The tangent vector to such a curve at a point p belongs to the n -dimensional tangent space $T_p X$ at p . Then, if $\mathcal{B}_e = \{\underline{e}_1 \dots \underline{e}_n\}$ is a basis of $T_p X$ and using the summation conventions

$$u^I \underline{e}_I = \sum_{I=1}^n u^I \underline{e}_I \text{ and } u^i \underline{e}_i = \sum_{i=2}^n u^i \underline{e}_i,$$

the elements of $T_p X$ appear in the form

$$u = u^I \underline{e}_I = u^1 \underline{e}_1 + u^i \underline{e}_i. \quad (3)$$

Each element \underline{u}^* of the corresponding cotangent space T_p^*X , known as a covector, is related to a vector \underline{u} by using the duality pairing

$$\underline{u}^*(\underline{w}) = \langle \underline{u}, \underline{w} \rangle, \quad \forall \underline{w} \in T_p X, \quad (4)$$

where $\langle \cdot, \cdot \rangle$ is the inner product of $T_p X$. Also, a dual basis $\mathfrak{B}_{e'}^* = \{\underline{e}^1 \dots \underline{e}^n\}$ to \mathfrak{B}_e is obtained for T_p^*X , by applying the conditions $\underline{e}^I(\underline{e}_J) = \delta_J^I$ [2]. Vector spaces $T_p X$ and T_p^*X are needed in obtaining the tangent and cotangent vector bundles over X , by $TX = \bigsqcup_{p \in X} T_p X$ and $T^*X = \bigsqcup_{p \in X} T_p^*X$.

Next, if $V(X)$ represents the space of all smooth vector fields on X , their subset $V_b(X)$ includes only those which are tangent to the boundary. Also, there exists a new vector bundle over X , denoted by ${}^b TX$, where the component vector space ${}^b T_p X$ is n -dimensional even at points of the boundary. A companion b-cotangent bundle ${}^b T^*X$ can also be defined. The b-bundles ${}^b TX$ and ${}^b T^*X$ coincide with the ordinary bundles TX and T^*X , respectively, away from the boundary [11].

The geometric properties of manifold X can be determined by employing two special coordinate bases in ${}^b T_p X$. The first one is related to a set of coordinates $x = (x^1, \dots, x^n)$ introduced at a boundary point p with $x^1 = \rho \geq 0$, while the second is related to the original q -coordinate system. Then, any vector in ${}^b T_p X$ is expressed as

$${}^b \underline{v} = \dot{x}^I \underline{e}_I = \dot{q}^{I'} \underline{e}_{I'}, \quad (5)$$

where $\mathfrak{B}_{e'} = \{\underline{e}_{1'} \dots \underline{e}_{n'}\}$ is the basis of the q -coordinate system, with

$$\underline{e}_{I'} = A_{I'}^I \underline{e}_I \text{ or } \underline{e}_I = B_I^{I'} \underline{e}_{I'}, \quad (6)$$

for $I, I' = 1, \dots, n$, where $B = [B_I^{I'}] = A^{-1}$. Then, the components of the b-metric tensor in the x -coordinate system can be put in matrix \bar{G} , with elements

$$\bar{g}_{IJ} = g_{IJ} + \hat{g}_{IJ}, \quad (7)$$

so that $\bar{g}_{IJ} = g_{IJ}$ over X^o , where $G = [g_{IJ}]$ is the metric matrix away from the boundary. Inside the boundary, term \bar{g}_{11} is replaced by

$$\hat{g}_{11} = \left(\frac{b}{x^1} \right)^2 g_{11}, \quad (8)$$

where b is the width of the boundary layer [10], while $\hat{g}_{i1} = \hat{g}_{1j} = \hat{g}_{ij} = 0$. Next, in analogy to Eq. (7), the b-affinities are also decomposed in the form

$$\bar{\Lambda}_{IJ}^K = \Lambda_{IJ}^K + \mathbf{A}_{IJ}^K, \quad (9)$$

in a basis of the x -coordinate system, so that $\overline{\Lambda}_{IJ}^K = \Lambda_{IJ}^K$ over X^o . The terms Λ_{IJ}^K are negligible away from ∂X [11], but component A_{11}^1 has the form

$$A_{11}^1 = \overline{\Lambda}_{11}^1 = -1/x^1. \quad (10)$$

The true path on the configuration manifold is determined by Newton's second law [9]. On manifold X , this law appears in the form

$${}^b \underline{\tilde{h}}^* \equiv {}^b \nabla_{\underline{\tilde{p}}} \overline{p}^* - \overline{f}^* = \underline{\tilde{0}}, \quad (11)$$

where the components of the generalized momentum are given by

$$\overline{p}_I = \overline{g}_{IJ} \overline{v}^J, \quad (12)$$

the covariant differential appears in the form

$${}^b \nabla_{\underline{\tilde{p}}} \overline{p}^* = \left(\dot{\overline{p}}_I - \overline{\Lambda}_{JI}^L \overline{p}_L \overline{v}^J \right) \underline{\tilde{e}}^I, \quad (13)$$

while \overline{f}^* represents the generalized applied forces on the system examined.

Obviously, the metric components and the affinities are affected in a significant way only within a layer starting at ∂X . This layer has a relatively small width b , while the law of motion expressed by Eq. (11) within the interior X^o of X is identical to that in the original configuration manifold M . These are illustrated in Fig. 1. First, Fig. 1a shows the constrained configuration manifold X , defined by condition (1), as a subset of manifold M . Then, while Fig. 1b presents a magnified picture around a point p on the boundary ∂X .

Next, keeping only the dominant terms, Eq. (11) is replaced by

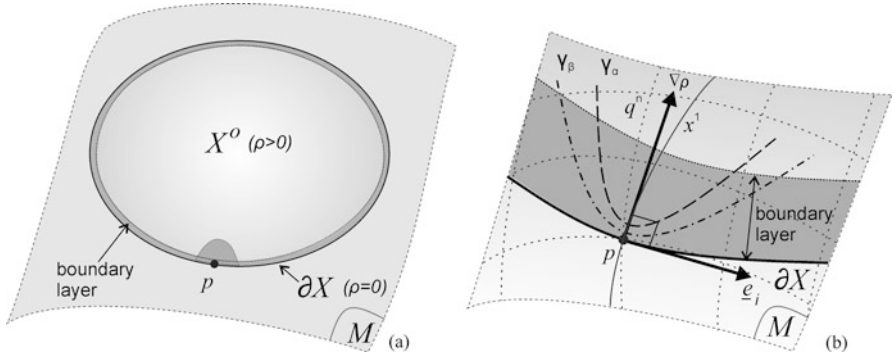


Fig. 1 (a) Constrained configuration manifold X as a subset of the original manifold M for a system with a single inequality constraint. (b) Magnified picture around a boundary point p

$${}^b h_1 \approx \dot{\hat{p}}_1 - \overline{\Lambda}_{11}^1 \hat{p}_1 v^1 - \hat{f}_1 = 0 \quad (14)$$

in a local x -coordinate system and points at the boundary, together with

$${}^b h_i \approx \dot{p}_i - \Lambda_{ji}^\ell p_\ell v^j - \overline{f}_i = 0, \quad \text{for } i = 2, \dots, n, \quad (15)$$

where $\hat{p}_1 = \hat{g}_{11} v^1$, $p_i = g_{ij} v^j$ and $\overline{f}_I \equiv f_I + \hat{f}_I$. For a contact without friction, all the terms \hat{f}_i in the last equation are equal to zero, while

$$\hat{f}_1(x^1, \dot{x}^1) = \left[\frac{k_1}{x^1} - \frac{c_1 \dot{x}^1}{(x^1)^2} \right] \hat{s}(x^1; a, b) \quad (16)$$

The first term in the right side represents a force pushing the figurative point away from the boundary. The second term is associated with the dissipation of energy during the motion within the boundary layer [10]. Function $\hat{s}(x^1; a, b)$ was introduced to guarantee a smooth transition of the boundary force from the inner to the outer region of the layer.

3 Addition of Bilateral Constraints and Friction Effects

Next, introduce a new set of motion constraints in the q -coordinate system with form

$$\dot{\psi}^R(q, \dot{q}) \equiv a_{I'}^R(q) \dot{q}^{I'} = 0, \quad (I' = 1, \dots, n \quad \text{and} \quad R = 1, \dots, k). \quad (17)$$

In some cases, these equations can be integrated and put in the algebraic (holonomic) form $\phi^R(q) = 0$. Then, the equations of motion can be written as

$$h_{I'} = \sum_{R=1}^k a_{I'}^R h_R, \quad (18)$$

for $I' = 1, \dots, n$, with components in the q -coordinate system of M determined by

$$h_{I'} = \dot{p}_{I'} - \Lambda_{J'I'}^L p_{L'} v^{J'} - f_{I'} \quad \text{and} \quad h_R = \left(\overline{m}_{RR} \dot{\lambda}^R \right)' + \overline{c}_{RR} \dot{\lambda}^R + \overline{k}_{RR} \lambda^R - \overline{f}_R, \quad (19)$$

where the terms \overline{m}_{RR} , \overline{c}_{RR} , \overline{k}_{RR} and \overline{f}_R can be determined explicitly for each constraint [9]. This is a set of n second order ODEs in the $n + k$ unknowns $q^{I'}$ and λ^R . The additional information is obtained by the k equations of constraints, put in the form

$$\left(\bar{m}_{RR}\dot{\psi}^R\right) + \bar{c}_{RR}\dot{\psi}^R = 0 \quad \text{or} \quad \left(\bar{m}_{RR}\dot{\phi}^R\right) + \bar{c}_{RR}\dot{\phi}^R + \bar{k}_{RR}\phi^R = 0. \quad (20)$$

First, the normal vector to the new boundary ∂X_C , induced within manifold M by the action of all the constraints, is selected to be the representative of the co-vector

$$\underbrace{e^1}_\sim = d\rho - \sum_{R=1}^k \gamma_R \underbrace{a^R}_\sim. \quad (21)$$

Co-vector $\underbrace{a^R}_\sim$ has components a^R_I , while $d\rho$ is the differential of ρ in T_p^*M , with

$$\underbrace{\eta^1}_\sim \equiv d\rho = \partial\rho/\partial q^I \underbrace{e^I}_\sim. \quad (22)$$

Then, $\mathfrak{B}_e^* = \{\underbrace{e^I}_\sim\} \equiv \{\underbrace{e^1}_\sim \underbrace{g^2}_\sim \dots \underbrace{g^m}_\sim \underbrace{a^1}_\sim \dots \underbrace{a^k}_\sim\}$ is chosen as a dual basis of an x -coordinate system, where $\underbrace{g^\gamma}_\sim$ are chosen as linearly independent and orthogonal to $\underbrace{e^1}_\sim$ and all $\underbrace{a^R}_\sim$. Also, $\underbrace{e^1}_\sim$ is orthogonal to all $\underbrace{a^R}_\sim$, providing γ_R in Eq. (21). Finally, the equations of motion inside the boundary layer appear in the component form

$$\left(\hat{g}_{11}v^1\right)^\cdot - \overline{A}_{11}^1 \hat{g}_{11}v^1 v^1 - \hat{f}_1 = 0, \quad \text{for } I = 1, \quad (23)$$

$$(g_{\gamma\delta}v^\delta)^\cdot - A_{j\gamma}^\ell g_{\ell k}v^k v^j - f_\gamma = 0, \quad \text{for } \gamma = 2, \dots, m, \quad (24)$$

$$\left(\sum_{S=1}^k g_{\hat{R}\hat{S}}v^{\hat{S}}\right)^\cdot - A_{j\hat{R}}^\ell g_{\ell k}v^k v^j - \overline{f}_{\hat{R}} = h_R, \quad \text{for } R = 1, \dots, k, \quad (25)$$

where $\hat{R} = m + R$ and $\hat{S} = m + S$ [10], while the constraints expressed by Eq. (17) yield

$$v^{\hat{R}} \equiv a_I^{\hat{R}} v^I = 0, \quad \text{for } R = 1, \dots, k. \quad (26)$$

This eliminates the first term in Eq. (25). Then, Eq. (23) can be solved independently for v^1 , while Eq. (24) yields the components v^γ , with $\gamma = 2, \dots, m$. Finally, solution of Eq. (25) furnishes the corresponding multipliers λ^R , for each $R = 1, \dots, k$.

The terms in Eq. (23) are $O(1/x^1)$, while the terms of Eq. (24) are $O(1)$. This means that the essential dynamics takes place along a single direction, as in the case with no equality constraints [10]. Here, the impulse occurs along the direction $\underbrace{e^1}_\sim$ of ${}^bT_p^*X$ and is affected by the bilateral constraints. Also, the impulse is transferred to the directions $\underbrace{a^R}_\sim$. Finally, the impulse is diffused to all the directions of the q -coordinates.

When friction is present, the relative velocity \underline{V} at the contact point is written in terms of the generalized velocities in the configuration space through a mapping

$$\underline{V} = D\dot{\underline{q}}. \quad (27)$$

Then, the dual mapping between the contact force $\underline{F} = F_\alpha \underline{n}^\alpha$ ($\alpha = 1, 2, 3$), in the physical space and the generalized forces is expressed by

$$\overline{\underline{f}}^* = \underline{F}D = \left(F_\alpha \underline{n}^\alpha \right) D = F_\alpha \underline{\eta}^\alpha. \quad (28)$$

This shows that $\overline{\underline{f}}^*$ belongs to a subspace of ${}^bT_p^*X$, at each point of the configuration manifold, spanned by three special co-vectors only. These convectors are defined by

$$\underline{\eta}^1 = \underline{n}^1 D = d\rho, \quad \underline{\eta}^2 = \underline{n}^2 D \quad \text{and} \quad \underline{\eta}^3 = \underline{n}^3 D. \quad (29)$$

Since terms \hat{f}_2^* and \hat{f}_3^* are $O(1/x^1)$, while the terms $\Lambda_{j\ell}^\ell p_\ell v^j$ of Eq. (24) are $O(1)$, the only way to balance them inside the boundary layer is to assume that the terms \dot{p}_2 and \dot{p}_3 vary rapidly there. This means that they are $O(1/x^1)$ within the layer. Then, the first two equations in Eq. (24) separate from the rest and become

$$\dot{p}_2 - \hat{f}_2^* = 0 \quad \text{and} \quad \dot{p}_3 - \hat{f}_3^* = 0. \quad (30)$$

Then, Eqs. (23) and (30) form a set of three ODEs, describing the dynamics in the three dimensional cotangent distribution of the configuration space where the contact action is important.

4 Numerical Results

Next, a set of numerical results is presented for two example systems, shown in Fig. 2.

First, the example shown in Fig. 2a includes a massless bar of length ℓ , having one end pinned at point O through a spherical joint. At the other end, a mass m is attached, which can hit a rigid wall, at a distance s below O. The position of the free body is located by the Cartesian coordinates $q^{1'}$, $q^{2'}$ and $q^{3'}$. Then, $M = \mathbb{R}^3$, with

$$G_q = [g_{I'J'}] = m I_3 \quad \text{and} \quad \Lambda_{I'J'}^{K'} = 0, \quad (I', J', K' = 1, 2, 3). \quad (31)$$

Moreover, the system is subject to a holonomic equality constraint

$$\phi^1(q) = (q^{1'})^2 + (q^{2'})^2 + (q^{3'})^2 - \ell^2 = 0 \quad (32)$$

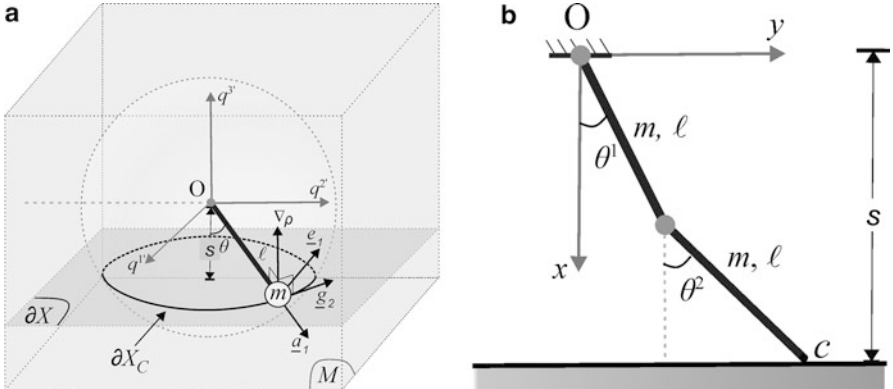


Fig. 2 Collision of: (a) a pendulum and (b) a double planar pendulum, with a rigid wall

and an inequality constraint

$$\rho(q) = q^{3'} + s \geq 0. \quad (33)$$

Using Eqs. (32) and (33) with Eqs. (17) and (22) yields

$$\underbrace{\dot{a}^1}_{\sim} = [a_{I'}^1] = (2q^{1'} \ 2q^{2'} \ 2q^{3'}) \quad \text{and} \quad \underbrace{\eta^1}_{\sim} = d\rho = (0 \ 0 \ 1).$$

Here, the boundary ∂X induced by the inequality constraint is the plane $q^{3'} = -s$. Also, the boundary ∂X_C , arising by the combined action of all the constraints, is a circle on this plane [10]. It can be shown that the equations of motion obtained for large values of the force parameter k are identical to those arising after application of the Darboux–Keller approach [4]. Consequently, for Coulomb friction with a coefficient of friction μ , there exist two special values, μ_c and $\bar{\mu}$. The first leads to straight trajectories of the contact point on the contact plane, while the second value gives a lower limit of μ for a stick to insist [4].

In Fig. 3 are shown results corresponding to $\theta = \pi/4$, which lead to $\mu_c = \sqrt{2}$ and $\bar{\mu} = 1$. First, in Fig. 3a are presented hodographs of the contact point on plane (V^1, V^2) , resulting for $k = 1$ and $c = 0$. All these hodographs originate from the same point, with $V^1(0) = -V^2(0) = -V^3(0)$ and evolve for a selected set of values of μ . In all cases, it is apparent that the slip direction changes continuously (swerves) when friction is present. Then, in Fig. 3b are depicted similar results for $k = 10$. The results of the last case are almost coincident with those derived by applying the Darboux–Keller (D-K) approach [4]. No permanent stick occurs within the interval $0 \leq \mu < \bar{\mu}$. However, when the trajectory reaches point $(0, 0)$ and $\mu > \bar{\mu}$, the stick insists until the end of the impact. Also, for the case with $\mu = \mu_c$, the hodograph tends to become an isocline as the value of k increases.

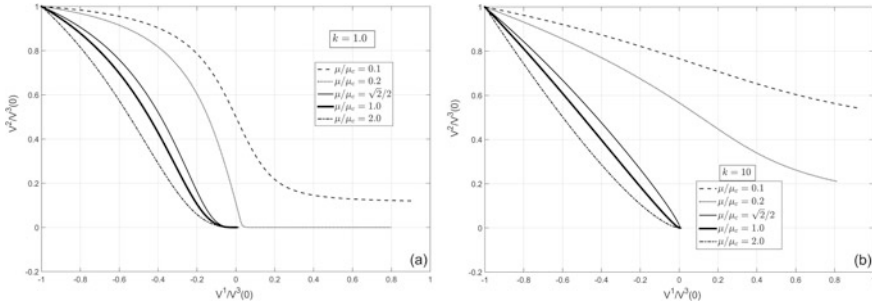


Fig. 3 Slip trajectories of a spherical pendulum for $\theta = \pi/4$ and (a) $k = 1$, (b) $k = 10$

The second example includes two rigid bars, with mass m and length ℓ , as shown in Fig. 2b. Here, the motion takes place in the O_{xy} plane, while all the joints are cylindrical. In particular, the free end of the second bar can hit a rigid wall at a distance s from O . The position of the first bar is located by two Cartesian coordinates, $q^{1'} = x^1$ and $q^{2'} = y^1$ plus a rotational coordinate $q^{3'} = \theta^1$, while the second bar is located by coordinates $q^{4'} = x^2$, $q^{5'} = y^2$ and $q^{6'} = \theta^2$. This implies that the configuration manifold M has a dimension of six, with

$$G_q = \text{diag} (m \ m \ m \ell^2 / 12 \ m \ m \ m \ell^2 / 12) \quad \text{and} \quad \Lambda_{I'J'}^{K'} = 0. \quad (34)$$

Also, the system is subjected to the following motion constraints

$$\begin{aligned} \phi^1(q) &= q^{1'} - \frac{\ell}{2} \cos q^{3'} = 0, & \phi^2(q) &= q^{2'} - \frac{\ell}{2} \sin q^{3'} = 0, \\ \phi^3(q) &= q^{1'} + \frac{\ell}{2} \cos q^{3'} - \left(q^{4'} - \frac{\ell}{2} \cos q^{6'} \right) = 0, \\ \phi^4(q) &= q^{2'} + \frac{\ell}{2} \sin q^{3'} - \left(q^{5'} - \frac{\ell}{2} \sin q^{6'} \right) = 0, \\ \rho(q) &= - \left(q^{4'} + \frac{\ell}{2} \cos q^{6'} \right) + s \geq 0. \end{aligned}$$

Again, it can be shown that for large values of the force parameter k , the equations of motion are identical to Eqs. (23) or (30) in [4], obtained by the Darboux–Keller method.

Finally, the set of results shown in Fig. 4 refer to loss in mechanical energy during impact. The ratio $(T_o - T_f)/T_o$, with T_o and T_f representing kinetic energy of the system just before and after impact, respectively, is depicted versus μ . First, in Fig. 4a are shown results for $c = 0$, with $k = 1$ and $k = 10$. Then, a similar set of results is included in Fig. 4b, obtained for no dissipation in the contact force ($c > 0$).

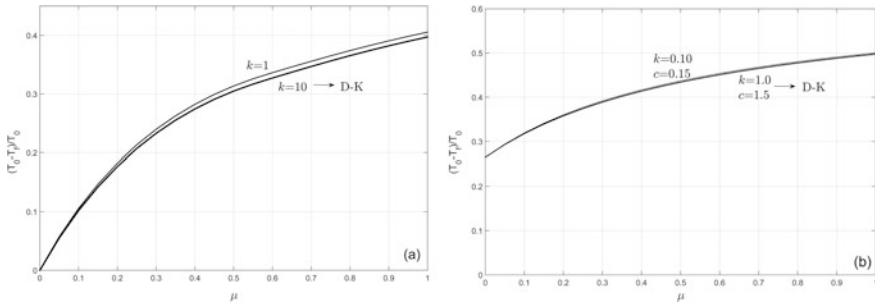


Fig. 4 Energy loss during impact of a double pendulum with a rough wall for: (a) $c = 0$ and (b) $c > 0$

References

1. Greenwood, D.T.: Principles of Dynamics. Prentice-Hall Inc, Englewood Cliffs (1988)
2. Bloch, A.M.: Nonholonomic Mechanics and Control. Springer, New York (2003)
3. Routh, E.J.: Dynamics of a System of Rigid Bodies, 6th edn. Macmillan and Co., London (1897)
4. Stronge, W.J.: Impact Mechanics. Cambridge University Press, Cambridge (2000)
5. Pfeiffer, F., Glocker, C.: Multibody Dynamics with Unilateral Contacts. Wiley, New York (1996)
6. Brogliato, B.: Nonsmooth Mechanics: Models, Dynamics and Control, 3rd edn. Springer, London (2016)
7. Leine, R.I., Nijmeijer, H.: Dynamics and Bifurcations of Non-smooth Mechanical Systems. Springer, Berlin (2013)
8. Keller, J.B.: Impact with friction. ASME J. Appl. Mech. **53**, 1–4 (1986)
9. Natsiavas, S., Paraskevopoulos, E.: A set of ordinary differential equations of motion for constrained mechanical systems. Nonlinear Dyn. **79**, 1911–1938 (2015)
10. Natsiavas, S., Paraskevopoulos, E.: A boundary layer approach to multibody systems involving single frictional impacts. ASME J. Comput. Nonlinear Dyn. **14**, 011002 (2019)
11. Melrose, R.B.: The Atiyah-Patodi-Singer Index Theorem, Research Notes in Mathematics, vol. 4. A. K. Peters Ltd., Wellesley (1993)

Creation of Neimark-Sacker Bifurcation for a Three-Degree-of-Freedom Vibro-Impact System with Clearances



Huidong Xu and Jinchen Ji

Abstract The impulsive state feedback control is used to create Neimark-Sacker bifurcation for a three-degree-of-freedom vibro-impact system with clearances. The linear control gains are determined to guarantee the existence of Neimark-Sacker bifurcation by using the explicit criteria of Neimark-Sacker bifurcation without directly using eigenvalues. Differently, the nonlinear control gains are selected to determine the direction and stability of Neimark-Sacker bifurcation by using center manifold reduction theory and normal form approach. The amplitude of the created invariant cycle from Neimark-Sacker bifurcation is analytically obtained to achieve the control of the amplitude by selecting appropriate nonlinear control gains. Numerical experiments are provided to show the effectiveness of the proposed control method.

Keywords Bifurcation control · Neimark-Sacker bifurcation · Vibro-impact system · Impulsive state feedback control

1 Introduction

The motions with impacts widely exist in engineering applications such as rattling gears, vibration absorbers, and pile driving machines. The complex and rich dynamical behaviors caused by the strong nonlinearity of impacts have been investigated by many researchers. The bifurcations of vibro-impact systems can be modified using an appropriate control, which was referred to as bifurcation control [1]. Impulsive control is a discrete-in-time feedback control method, which has been used for the control of chaos and chaos synchronization [2, 3] due to its simplicity.

H. Xu (✉)

Taiyuan University of Technology, Taiyuan, P. R. China

J. Ji

University of Technology Sydney, Broadway, NSW, Australia

e-mail: Jin.Ji@uts.edu.au

The impulsive control with variable time is a state-dependent feedback control method, i.e., the pulse time varies depending on the state variables. This method has been successfully applied to the control of the stability and existence of periodic solution of smooth systems. It would be more suitable to implement the strategy for the bifurcation control of the vibro-impact system based on the fact that the impact causes the discontinuity of the system state variables. To the authors' best knowledge, little literature has been focused on studying impulsive control problems of bifurcation in the vibro-impact system.

The main objective of this chapter is to create Neimark-Sacker bifurcation with certain desired characteristics in the vibro-impact system by developing an impulsive state feedback control method. The linear control gains are selected to guarantee the existence of Neimark-Sacker bifurcation, and the nonlinear control gains to ensure the direction and stability of Neimark-Sacker bifurcation created. The novelty of this chapter lies in the design of the impulsive state feedback control for the vibro-impact systems, the analytical construction of the amplitude of the created invariant cycle, and the use of the nonlinear control gains to adjust the amplitude of the cycle.

2 Vibro-Impact System Under Impulsive State Feedback Control

The vibro-impact system under the impulsive state feedback control in Fig. 1 can be expressed as:

$$\begin{aligned} M\ddot{x} + C\dot{x} + Kx &= F_0 \sin(\omega t + \tau), \quad x_1 - x_2 < \delta \\ \dot{x}_+ &= R(\dot{x}_-), \\ \Delta X |_{t=\pi_i(X)} &= I_i(X), \quad i = 1, 2, \dots, x_1 - x_2 = \delta \end{aligned} \quad (1)$$

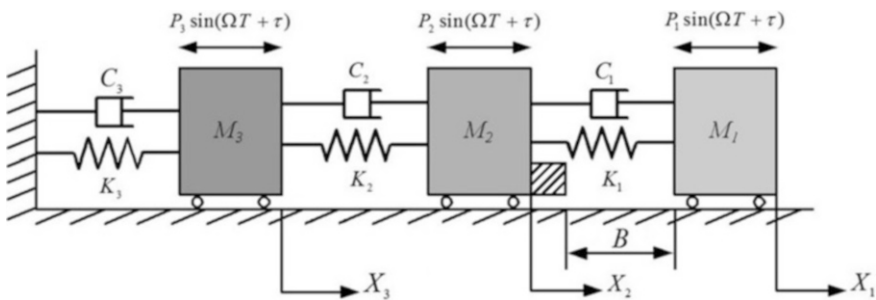


Fig. 1 A three-degree-of-freedom vibro-impact system with clearances

where M , C , and K represent the mass, damping, and stiffness matrixes, respectively. F_0 is the amplitude vector of external excitations. $x = (x_1, x_2, x_3)^T$ is the displacement of the masses. \dot{x}_- and \dot{x}_+ denote the instant velocities of the masses just before and immediately after the impact. R is the function of restitution of impact. $X = (x_1, \dot{x}_1, x_2, \dot{x}_2, x_3, \dot{x}_3)^T$ is the impulsive variables. Define $\Delta X|_{t=\pi_i(X)} = X(\pi_i^+) - X(\pi_i^-)$ as the jump operator for a function $X(t)$. $X(\pi_i^+) = \lim_{h \rightarrow 0+} X(\pi_i + h)$ is the right limit position of the trajectory and $X(\pi_i^-) = \lim_{h \rightarrow 0-} X(\pi_i - h)$ is the left limit of the position of the trajectory at the moment π_i . The impulse function has the explicit expression $I_i(X) = A(K_L)(X - X^*) + \sum_{j=2}^n B_j \left(K_{NL}, \underbrace{X - X^* \dots X - X^*}_j \right)$ with the linear control gain K_L and nonlinear control gain K_{NL} . B_j is the higher order terms. X^* is a fixed point that is different from the following fixed point \tilde{X}^* .

In order to generate the Neimark-Sacker bifurcation by impulsive control, it is convenient to establish a Poincaré map as

$$\tilde{X} \mapsto \tilde{F}(\tilde{X}, \mu; K) \quad (2)$$

where the variable $\tilde{X} = (\dot{x}_1, x_2, \dot{x}_2, x_3, \dot{x}_3, \tau)^T$ and the parameter K includes the linear control gain K_L and nonlinear control gain K_{NL} .

3 Creation of a Stable Neimark-Sacker Bifurcation

3.1 Design of Linear Control Gains for the Existence of Neimark-Sacker Bifurcation

The primary task of creating Neimark-Sacker bifurcation in the impact system is to determine the linear control gain K_L to guarantee the existence of bifurcation at a specified system parameter location. Here, the explicit criteria without directly using eigenvalues are employed to induce a Neimark-Sacker bifurcation in the vibro-impact system.

The characteristic polynomial of the linearization matrix $D_{\tilde{X}} \tilde{F}(\tilde{X}^*, \mu; K_L)$ of map (2) at fixed point \tilde{X}^* is assumed to have the following form:

$$p_{\mu, K_L}(\lambda) = \lambda^6 + a_1 \lambda^5 + a_2 \lambda^4 + a_3 \lambda^3 + a_4 \lambda^2 + a_5 \lambda + a_6 \quad (3)$$

where the linearization matrix $D_{\tilde{X}} \tilde{F}(\tilde{X}^*, \mu; K_L)$ is a combination of the part of linearization of smooth map, switch map of impact, and impulse control map.

Lemma 1 The Neimark–Sacker bifurcation [4] of map (2) occurs at the bifurcation point $\mu = \mu_0$ if and only if the following conditions (H1)–(H3) are satisfied,

(H1) Eigenvalue assignment:

$$g_1(\mu_0, K_L) = \Delta_5^-(\mu_0, K_L) = 0 \quad (4a)$$

$$g_2(\mu_0, K_L) = 1 + a_6 > 0 \quad (4b)$$

$$g_3(\mu_0, K_L) = 1 - a_6 > 0 \quad (4c)$$

$$\begin{aligned} g_4(\mu_0, K_L) = & 1 + a_6 + a_4 + a_4 a_6 - a_1 a_5 - a_6 a_2 - a_5^2 - a_6^2 \\ & + a_6 a_1^2 - a_6^2 a_2 - a_6^3 + a_6 a_1 a_5 > 0 \end{aligned} \quad (4d)$$

$$\begin{aligned} g_5(\mu_0, K_L) = & 1 - a_6 - a_4 + a_4 a_6 + a_1 a_5 + a_6 a_2 - a_5^2 - a_6^2 \\ & - a_6 a_1^2 - a_6^2 a_2 + a_6^3 + a_6 a_1 a_5 > 0 \end{aligned} \quad (4e)$$

$$g_6(\mu_0, K_L) = 1 + a_1 + a_2 + a_3 + a_4 + a_5 + a_6 > 0 \quad (4f)$$

$$g_7(\mu_0, K_L) = 1 - a_1 + a_2 - a_3 + a_4 - a_5 + a_6 > 0 \quad (4g)$$

$$g_8(\mu_0, K_L) = \Delta_5^+(\mu_0, K_L) > 0 \quad (4h)$$

(H2) Transversality condition:

$$G(\mu_0, K_L) = \left. \frac{dg_1(\mu, K_L)}{d\mu} \right|_{\mu=\mu_0} \neq 0 \quad (5)$$

(H3) Non-resonance condition:

$$\eta_m(\mu_0, K_L) = \cos(2\pi/m) - \rho \neq 0, \quad \rho = 1 - \frac{p_{\mu_0, K_L}(1)\Delta_3^-(\mu_0, K_L)}{2\Delta_4^+(\mu_0, K_L)}, \quad (6)$$

$$m = 3, 4, 5, \dots$$

From Lemma 1, the explicit criteria formulated by the coefficients of the characteristic polynomial (3) are not involved with the direct calculation of eigenvalues. Thus the control gains can be explicitly formulated. This is more convenient to create Neimark–Sacker bifurcation than the classical criteria, especially for high dimensional maps with uncertain control parameters.

3.2 Design of Nonlinear Control Gains for Stabilizing Neimark-Sacker Bifurcation

The direction and stability of Neimark-Sacker bifurcation of map (2) can be determined by $\sigma(K_{NL})$ as [5]

$$\sigma(K_{NL}) = -\frac{\operatorname{Re} \left[\langle p, C(q, q, \bar{q}) \rangle - 2 \left\langle p, B(q, A^{-1}B(q, \bar{q})) \right\rangle + \left\langle p, B(\bar{q}, (2iw_0I - A)^{-1}B(q, q)) \right\rangle \right]}{2\omega_0} \quad (7)$$

Based on the stability criterion [5], a stable invariant cycle can appear in the vibro-impact system through a supercritical Neimark-Sacker bifurcation if $\sigma(K_{NL}) < 0$, and an unstable invariant cycle arises in the system if $\sigma(K_{NL}) > 0$. Therefore, the stability control of Neimark-Sacker bifurcation can be achieved by adjusting the nonlinear control gains K_{NL} to change the sign of $\sigma(K_{NL})$.

3.3 Nonlinear Control Gains Chosen for Adjusting the Amplitude of the Creating Invariant Cycle

The resultant bifurcating solution from Neimark-Sacker bifurcation presents an invariant cycle on the Poincaré section. The amplitude of the cycle can be controlled by selecting the nonlinear gain K_{NL} after a stable invariant cycle is created by impulsive control in Sects. 3.1 and 3.2. The amplitude of the invariant cycle will be obtained by studying the normal form under the complex coordinate system and polar coordinate system.

Through using center manifold reduction theory and normal form approach, the map (2) can be simplified into the normal form as [5]

$$z \mapsto \tilde{F}(z, \varepsilon; K_L, K_{NL}) = \lambda(\varepsilon; K_L)z + \eta(\varepsilon; K_L, K_{NL})z^2\bar{z} + O(|z|^4) \quad (8)$$

$$\text{where } \eta(\varepsilon; K_L, K_{NL}) = \frac{g_{21}}{2} + \frac{|g_{11}|^2}{1-\lambda} + \frac{|g_{02}|^2}{2(\lambda^2-\lambda)} + \frac{2\lambda-1}{2\lambda[1-\lambda]}g_{11}g_{20}.$$

By introducing the polar transformation

$$z = r e^{2\pi i \phi}, \quad \tilde{F}(z, \varepsilon; K_L, K_{NL}) = R e^{2\pi i \Phi}, \quad (9)$$

map (8) can be transformed into the form as

$$\begin{aligned} r &\mapsto R(r, \phi, \varepsilon; K_L, K_{NL}) = (1 + b\varepsilon)r + ar^3 + O(|\varepsilon|^2r + |\varepsilon|r^3 + r^4) \\ \phi &\mapsto \Phi(r, \phi, \varepsilon; K_L, K_{NL}) = \phi + \theta_0 + \theta_1\varepsilon + \omega_1r^2 + O(|\varepsilon|^2 + |\varepsilon|r^2 + r^3) \\ &\pmod{1} \end{aligned} \quad (10)$$

where $a = \operatorname{Re}(\eta(0; K_L, K_{NL})\bar{\lambda}(0; K_L))$, $b = \frac{d|\lambda(\varepsilon; K_L)|}{d\varepsilon}\Big|_{\varepsilon=0} = \frac{\frac{dg_1(\varepsilon+\mu_0, K_L)}{d\varepsilon}}{-2 \prod_{l=1}^6 (1-\lambda_l\lambda_q)}\Big|_{\varepsilon=0}$.

Based on the truncated form of map (10) at a small scale of $\varepsilon = 0$, the amplitude is obtained as

$$r(K_{NL}) = \sqrt{\frac{dg_1(\mu_0, K_L)/d\mu}{2 \operatorname{Re}(\eta(0; K_L, K_{NL})\bar{\lambda}(0; K_L)) \prod_{l=1}^6 (1-\lambda_l\lambda_q)}} (\mu - \mu_0) \quad (11)$$

It can be seen from Eq. (11) that the amplitude of the invariant cycle is not involved in the calculation of the derivatives of eigenvalues. This is convenient for controlling the amplitude by selecting the nonlinear gains. In addition, the nonlinear control gains should also be chosen in the stability region determined by $\sigma(K_{NL}) < 0$ given in Sect. 3.2 when the amplitude of invariant cycle is adjusted.

4 Numerical Experiments

The non-dimensional parameters $m_2 = 1.47$, $m_3 = 1.5$, $k_2 = 1.21$, $k_3 = 2.5$, $\delta = 0.01$, $R = 0.8$, $\gamma = 0.06$, $f_{10} = 0.2$, $f_{20} = 0.6$, $f_{30} = 0$ are taken as an example, and the parameter $\mu = \omega$ is chosen as the bifurcation parameter. $\omega = 3.3$ ($\mu_0 = 3.3$) is chosen as a specified system parameter location.

By implementing conditions (H1) and (H3) in Lemma 1, the bifurcation diagram with the linear control parameters $K_L = \begin{pmatrix} k_{11} & 0 \\ 0 & k_{12} \end{pmatrix}$ is shown in Fig. 2a.

The inequalities $g_i(\mu_0, k_{11}, k_{12})$ ($i = 2, \dots, 8$) are all satisfied in the blank area surrounded by the yellow curve AE , blue curve ED , cyan curve DC , and blue curve CA in Fig. 2a, whereas at least one inequality of $g_i(\mu_0, k_{11}, k_{12})$ fails in other gray regions. This means that the blank area is the parameter region for selecting potential control gains. The red curve l_1 and l_2 are obtained by equation $g_1(\mu_0, k_{11}, k_{12}) = 0$.

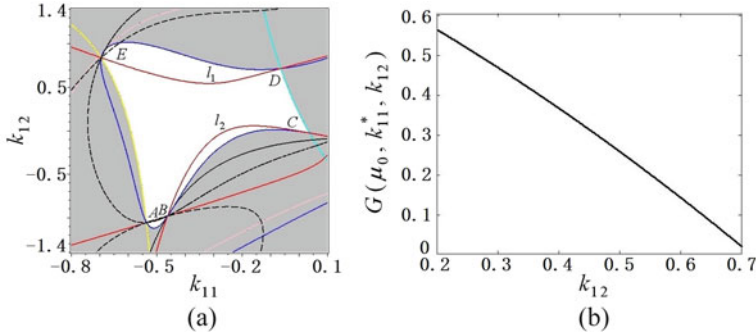
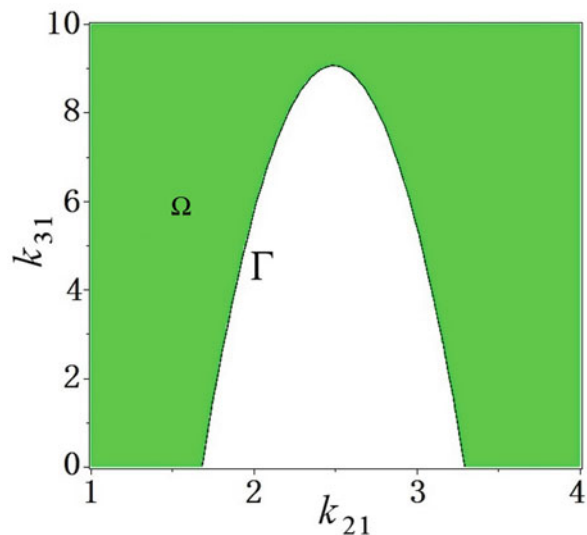


Fig. 2 Linear control for the existence of Neimark-Sacker bifurcation; **(a)** The bifurcation diagram in the plane of linear control gains, **(b)** The curve of the transversality condition

Fig. 3 The control region of stability of the Neimark-Sacker bifurcation



The points on the red curves in gray regions cannot ensure that the other eigenvalues $\lambda_j(\mu)$ ($j = 3, \dots, 6$) are within the unit circle. Therefore the points on red curves in blank region are reasonable control parameter points. The black dashed lines are obtained by the resonance condition $\eta_3(\mu_0, k_{11}, k_{12}) = 0$ ($m = 3$). The intersection points B and E of the red curves and black dashed lines are third-order resonance points. The control gains should be chosen to avoid these resonance points.

The gain k_{11} on the red curve l_1 is fixed as $k_{11}^* = -0.5$. The curve of the transversality condition determined by equation $G(\mu_0, k_{11}^*, k_{12}) = 0$ in the condition (H2) is shown in Fig. 2b. The value of the curve in the vertical axis is not equal to zero when k_{12} is in a region $e = (0.2, 0.7)$ from Fig. 3, which indicates that the transversality condition is satisfied. Thus the other gain k_{12} can be determined as $k_{12}^* = 0.63725823$ in the region $e = (0.2, 0.7)$.

Based on the expression (7) in Sect. 3.2, the equation determining stability of the Neimark-Sacker bifurcation with the quadratic terms $K_{NL,2} = \begin{pmatrix} k_{21} & 0 \\ 0 & k_{22} \end{pmatrix}$ and cubic terms $K_{NL,3} = \begin{pmatrix} k_{31} & 0 \\ 0 & k_{32} \end{pmatrix}$ is obtained as

$$\begin{aligned} \sigma(k_{21}, k_{22}, k_{31}, k_{32}) = & -0.36598214k_{21}^2 - 0.01187005k_{22}^2 \\ & - 0.24911456k_{21}k_{22} - 0.66998610k_{21} \\ & - 0.09899298k_{22} - 0.02630618k_{31} \\ & + 0.00038485k_{32} - 1.83409593 \end{aligned} \quad (12)$$

The nonlinear gains $k_{22} = -10$ and $k_{32} = 10$ are fixed and the other two nonlinear gains k_{21} and k_{31} are chosen as control parameters. By using Eq. (12), the control region of stability of the Neimark-Sacker bifurcation is shown in Fig. 3.

The black curve Γ in Fig. 3 is obtained by the equation $\sigma(k_{21}, k_{22}, k_{31}, k_{32}) = 0$ with $k_{22} = -10$ and $k_{32} = 10$. The green field Ω represents the stability region of the Neimark-Sacker bifurcation.

The amplitude of the created stable invariant cycle can be modified by adjusting the nonlinear gains. From the expression (11) in Sect. 3.3, the amplitude of the invariant cycle at $k_{22} = -10$ and $k_{32} = 10$ is obtained as

$$r(k_{21}, k_{31}) = \sqrt{\frac{0.00132315(\mu - \mu_0)}{0.36598214k_{21}^2 - 1.82115953k_{21} + 0.02630618k_{31} + 2.02732285}} \quad (13)$$

On the basis of Eq. (13), when the gain $k_{31} = 0.3$ is fixed, the variation of the amplitude of the invariant cycle with the nonlinear control gain is shown in Fig. 4a.

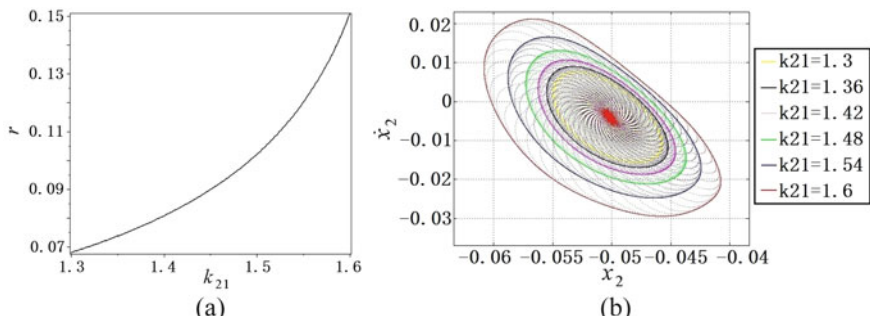


Fig. 4 The effect of the nonlinear gains on the amplitude of the created invariant cycle; (a) The variation of the amplitude with the control gain k_{21} , (b) The invariant cycles created by adjusting the gain k_{21}

The amplitude of the invariant cycle increases with the increase of the gain k_{21} from Fig. 4a when the gain k_{31} is fixed. This indicates that the effect of the control gain k_{21} on the amplitude has a positive relationship. Thus different gains can be chosen to achieve the control of amplitude according to control requirements. The effect of the nonlinear gains on the amplitude of the invariant cycle is further shown in Fig. 4b on the phase diagrams of Poincaré section.

5 Conclusion

In this chapter, an impulsive state feedback control method for creating Neimark-Sacker bifurcation has been proposed for a three-degree-of-freedom vibro-impact system with clearances. The linear control gains for guaranteeing the existence of Neimark-Sacker bifurcation were determined by using the explicit criteria of bifurcation without directly using eigenvalues. The nonlinear control gains for adjusting the stability of Neimark-Sacker bifurcation and the amplitude of the creating invariant cycle were determined by using center manifold reduction theory and normal form approach. Numerical experiments have been carried out to validate the feasibility of the proposed control method.

Acknowledgements This chapter's work was supported by the Applied Basic Research Program of Shanxi Province of China (No. 201801D121021).

References

1. Abed, E.H., Fu, J.H.: Local feedback stabilization and bifurcation control, part I. Hopf bifurcation. *Syst. Control Lett.* **7**, 11–17 (1986)
2. Matias, M.A., Güémez, J.: Stabilization of chaos by proportional pulses in the system variables. *Phys. Rev. Lett.* **72**, 1455–1458 (1994)
3. Luo, M., Liu, X., Zhong, S., et al.: Synchronization of stochastic complex networks with discrete-time and distributed coupling delayed via hybrid nonlinear and impulsive control. *Chaos, Solitons Fractals.* **114**, 381–393 (2018)
4. Wen, G.: Criterion to identify Hopf bifurcations in maps of arbitrary dimension. *Phys. Rev. E.* **72**(2), 026201 (2005)
5. Kuznetsov, Y.A.: Elements of Applied Bifurcation Theory, 2nd edn. Springer-Verlag, New York (1998)

Analogue Models of Rocking Suitcases and Snaking Trailers



Zoltan Horvath and Denes Takacs

Abstract A mechanical model is constructed for the stability analysis of two-wheeled suitcases and trailers. The main assumptions of the model are summarized and the linearized equations of motion are presented. The linear stability of the rectilinear motion is investigated, critical parameter values are determined for the different level of complexity of the model. Numerical simulations are used to verify the applicability of the model for the nonlinear analysis of the rocking motion of trailers.

Keywords Two-wheeled suitcase · Trailer · Non-smooth system · Non-holonomic system

1 Introduction

The instability of towed vehicles (e.g. trailers, semi-trailers) is a relevant safety risk in road transport. Namely, under certain conditions (badly chosen load conditions and speed), a snaking motion may appear (see [1, 2]), which can even lead to the rocking motion of the trailer when it jumps from one of its wheels to the other. As a final result, the linear instability of the rectilinear motion of the trailer may cause the roll-over of the vehicle. This phenomenon can also be observed in case of a towed two-wheeled suitcase (see [3–6]), moreover similar mechanical models can be composed for the investigations of the stability behaviour. The analogies of the problems and the mechanical models are illustrated in Fig. 1.

Z. Horvath (✉)

Department of Applied Mechanics, Budapest University of Technology and Economics,
Budapest, Hungary

e-mail: horvath.hanna.zsofia@gmail.com

D. Takacs

MTA-BME Research Group on Dynamics of Machines and Vehicles, Budapest, Hungary
e-mail: takacs@mm.bme.hu

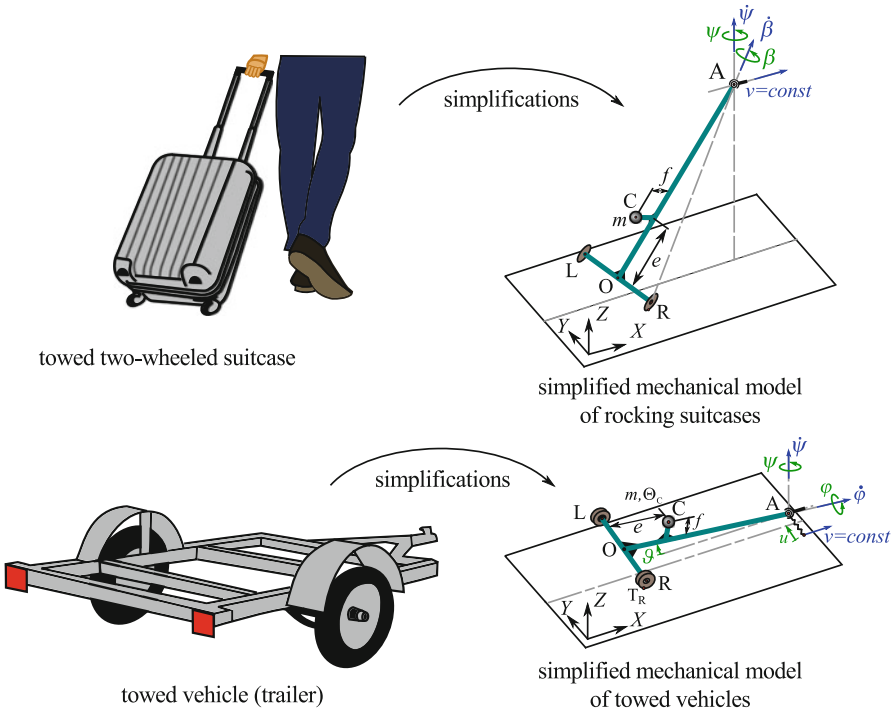


Fig. 1 Illustration of the analogy between rocking suitcases and snaking trailers with respect to their mechanical models

In our former study, we used the mechanical model of the rocking suitcase shown in the right top panel of Fig. 1 to analyse the linear stability and the basis of attraction of the rectilinear motion by means of numerical simulations and experiments (see [7]). The most exciting problem in the analysis of the mechanical model arises in the fact that governing equations of the mechanical model are non-smooth since different equations of motion describe the motion states of the suitcase (namely, when both wheels are on the ground, left or right wheel is on the ground, none of the wheels is on the ground). In addition, a kinematic constraint can be defined for the rolling wheels having point-like contact with the ground. The switching between the motion states is a complex task since switching appears when one of the wheels has an impact with the ground or when one of the wheels leaves the ground. Nevertheless, by implementing the mechanical model with its intricate non-smooth properties in a simulation code, one can investigate the effects of the initial conditions (e.g. initial tilting angle) and the different parameters (e.g. towing speed v , geometrical parameters e and f).

Of course, similar investigation can be done experimentally. A model-based experimental setup was also built and placed on a conveyor belt in [7]. The towed suitcase was perturbed at its left wheel by placing a cylindrical obstacle (with

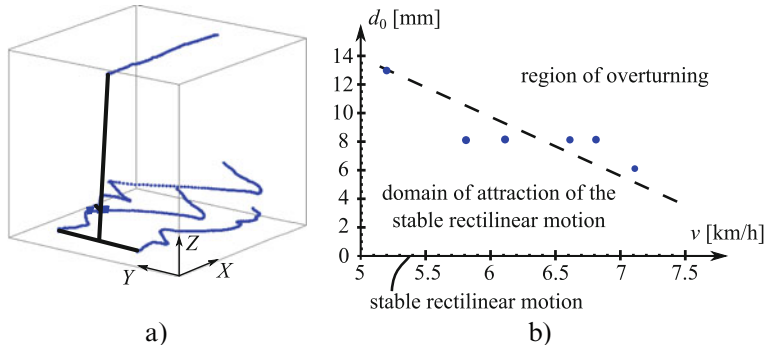


Fig. 2 (a) The trajectories of the retro-reflective markers attached to the suitcase at left and the right wheels, the centre of mass and the towing point, (b) basis of attraction of the rectilinear motion identified by experiments.

diameter d_0) onto to conveyor belt, and the motion of the suitcase was recorded by a motion capturing system using retro-reflective markers (see the left panel of Fig. 2). The detected basis of attraction of the rectilinear motion and its dependence on the towing speed can be seen in the right panel Fig. 2, where blue dots refer to the measurement points and dashed line illustrates the boundary of the basis of attraction. Both the numerical and experimental results confirmed that the attractive domain is smaller for larger speeds. In this study, we modify the mechanical model of the rocking suitcase to make it suitable for the analysis of the stability problem of trailers. In order to do this, the elasticities of the tyres and the wheel suspension system are taken into account. Although these modifications increase the degrees of freedom and the number of the parameters of the model, the mechanical model turns to be holonomic and the motion can be described uniquely with the same generalized coordinates independently from the actual motion state. After the short summary of the derivation of the equations of motion, the linear stability of the rectilinear motion is shown in the paper and numerical simulations are carried out to verify the applicability of the constructed mechanical model for the investigation of the nonlinear dynamics of rocking trailers.

2 Mechanical Model of Snaking Trailers

The mechanical model of snaking trailers can be seen on the left panel of Fig. 3. The motion of the trailer can be described with the yaw angle ψ , the pitch angle ϑ , the roll angle φ and the lateral displacement u of the joint at point A. Thus, the system has $n = 4$ degrees of freedom (DoF), the vector of the generalized coordinates is

$$\mathbf{q} = [\psi \ \vartheta \ \varphi \ u]^T. \quad (1)$$

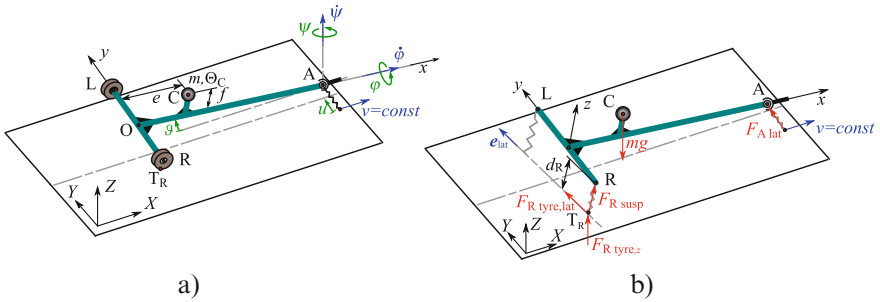


Fig. 3 (a) The mechanical model, (b) active forces acting on trailer

The towing length and the track width of the trailer are denoted by l and $2b$, respectively. The position of the centre of mass C can be described with parameters e and f . The overall stiffness and damping of the wheel suspension and tyres are denoted by k and c , while the lateral stiffness and damping at point A are k_l and c_l . The equations of motion can be derived with the Lagrange equation of the second kind:

$$\frac{d}{dt} \frac{\partial T}{\partial \dot{q}_k} - \frac{\partial T}{\partial q_k} = Q_k, \quad k = 1, \dots, n, \quad (2)$$

where T is the kinetic energy, q_k is the k th generalized coordinate and Q_k is the k th component of the generalized force. The kinetic energy is calculated as

$$T = \frac{1}{2} m v_C^2 + \frac{1}{2} \boldsymbol{\omega}^T \boldsymbol{\Theta}_C \boldsymbol{\omega}, \quad (3)$$

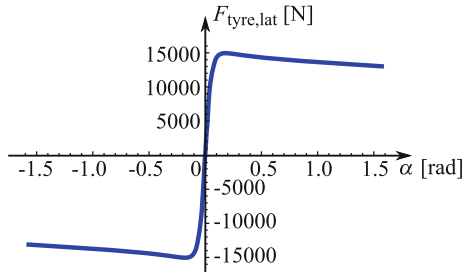
where the velocity of point C is $v_C = |\mathbf{v}_C| = |\mathbf{v}_A + \boldsymbol{\omega} \times \mathbf{r}_{AC}|$. The velocity of the towing point is $\mathbf{v}_A = [v \; \dot{u} \; 0]^T$ given in the ground fixed (X, Y, Z) coordinate system. The angular velocity of the trailer given in the trailer fixed (x, y, z) coordinate system is

$$\boldsymbol{\omega} = \begin{bmatrix} \dot{\phi} - \dot{\psi} \sin \vartheta \\ \dot{\vartheta} \cos \varphi + \dot{\psi} \cos \vartheta \sin \varphi \\ \dot{\psi} \cos \vartheta \cos \varphi - \dot{\vartheta} \sin \varphi \end{bmatrix}_{(x,y,z)}. \quad (4)$$

Let us consider the mass moment of inertia matrix as

$$\boldsymbol{\Theta}_C = \begin{bmatrix} \Theta_{C,x} & 0 & 0 \\ 0 & \Theta_{C,y} & 0 \\ 0 & 0 & \Theta_{C,z} \end{bmatrix}_{(x,y,z)}. \quad (5)$$

Fig. 4 The characteristics of the tyre forces in case of $F_z = 15,000$ N. The factors: $B = 10$ (stiffness factor), $C = 1.9$ (shape factor), $D = 1$ (peak factor), $E = 0.97$ (curvature factor)



The generalized force can be obtained from the virtual power:

$$\delta P = \mathbf{G} \cdot \delta \mathbf{v}_C + \mathbf{F}_{R_{\text{tyre}}} \cdot \delta \mathbf{v}_{T_R} + \mathbf{F}_{R_{\text{susp}}} \cdot \delta \mathbf{v}_R + \mathbf{F}_{L_{\text{tyre}}} \cdot \delta \mathbf{v}_{T_L} \\ + \mathbf{F}_{L_{\text{susp}}} \cdot \delta \mathbf{v}_L + \mathbf{F}_{A_{\text{lat}}} \cdot \delta \mathbf{v}_A , \quad (6)$$

where \mathbf{G} is the gravitational force, $\mathbf{F}_{R_{\text{tyre}}}$ and $\mathbf{F}_{L_{\text{tyre}}}$ represent the forces acting on the tyres at points T_R and T_L . $\mathbf{F}_{R_{\text{susp}}}$ and $\mathbf{F}_{L_{\text{susp}}}$ are the forces acting on the chassis of the trailer at points R and L due to the elastic deformation of the suspensions. $\mathbf{F}_{A_{\text{lat}}}$ is the lateral force acting at point A. These forces are shown in the right panel of Fig. 3.

The tyre forces can be calculated with the help of the Magic Formula of Pacejka (see [8]):

$$F_{\text{tyre},\text{lat}}(\alpha, F_z) = F_z D \sin(C \arctan(B\alpha - E(B\alpha - \arctan(B\alpha)))) , \quad (7)$$

where B, C, D, E are the tyre parameters and F_z is the vertical load on the tyre. The tyre force characteristics can be seen in Fig. 4. The side slip angle of the right wheel can be calculated as

$$\alpha_R = -\arctan\left(\frac{\mathbf{v}_{T_R} \cdot \mathbf{e}_{\text{lat}}}{\mathbf{v}_{T_R} - (\mathbf{v}_{T_R} \cdot \mathbf{e}_{\text{lat}})\mathbf{e}_{\text{lat}}}\right) , \quad (8)$$

where unit vector \mathbf{e}_{lat} refers to the lateral direction of the trailer projected to the ground. The side slip angle of the left wheel can be calculated similarly.

The force originated in the wheel suspension acts on the trailer in the z direction, its magnitude is

$$F_{R_{\text{susp}}} = ((L_{R,0} - d_R)k + (v_{T_R,z} - v_{R,z})c) \cdot H(L_{R,0} - d_R) \\ \cdot H((L_{R,0} - d_R)k + (v_{T_R,z} - v_{R,z})c) \quad (9)$$

for the right wheel, where the Heaviside-function $H(x) = (1 + \tanh(x/\varepsilon))/2$ with the smoothing parameter ε is used to make the system to be smooth. The parameter

$L_{R,0}$ is the free length of the spring while d_R is the actual length of the spring (see panel (b) in Fig. 3). The force originated in the left wheel suspension can be calculated similarly.

3 Linear Stability Analysis

The rectilinear motion of the trailer corresponds to: $\psi(t) \equiv \psi_0 = 0$, $\vartheta(t) \equiv \vartheta_0 = 0$, $\varphi(t) \equiv \varphi_0 = 0$, $u(t) \equiv u_0 = 0$ in case of the spring free length $L_{R,0} \equiv L_{L,0} = h + mg(l - e)/(2kl)$. The linearized equation of motion can be written as

$$\mathbf{M}\ddot{\mathbf{q}} + \mathbf{C}\dot{\mathbf{q}} + \mathbf{K}\mathbf{q} = \mathbf{0}, \quad (10)$$

where the mass matrix is

$$\mathbf{M} = \begin{bmatrix} m(e-l)^2 + \Theta_{C,z} & 0 & mf(l-e) & m(e-l) \\ 0 & mf^2 + m(e-l)^2 + \Theta_{C,y} & 0 & 0 \\ mf(l-e) & 0 & mf^2 + \Theta_{C,x} & -mf \\ m(e-l) & 0 & -mf & m \end{bmatrix}, \quad (11)$$

the damping matrix is

$$\mathbf{C} = \begin{bmatrix} \frac{BCDmg(l-e)}{v} & 0 & \frac{BCDmgh(e-l)}{v} & \frac{BCDmg(e-l)}{v} \\ 0 & 2cl^2 & 0 & 0 \\ \frac{BCDmgh(e-l)}{v} & 0 & \frac{2b^2clv+BCDmgh^2(l-e)}{lv} & \frac{BCDmgh(e-l)}{lv} \\ \frac{BCDmg(e-l)}{v} & 0 & \frac{BCDmgh(e-l)}{lv} & \frac{c_l lv+BCDmgh^2(l-e)}{lv} \end{bmatrix} \quad (12)$$

and the stiffness matrix is

$$\mathbf{K} = \begin{bmatrix} BCDmg(l-e) & 0 & mg(e-l) & 0 \\ 0 & 2l^2k - mgf & 0 & 0 \\ \frac{BCDmgh(e-l)}{l} & 0 & 2b^2k - mgf & 0 \\ \frac{BCDmgh(e-l)}{l} & 0 & \frac{mg(l-e)}{l} & k_l \end{bmatrix}. \quad (13)$$

It is worth to notice that the stiffness matrix is asymmetric. As it can be seen, the system can be separated into two subsystems: the second component of (10) corresponding to the pitch motion can be separated, the other equations are coupled ($n = 3$ DoF subsystem).

3.1 The Pitch Motion of the Trailer

The equation of motion of the separable subsystem is a second-order ordinary differential equation, from which the critical value of the stiffness k can be expressed:

$$k_{\text{cr}} = \frac{mgf}{2l^2}. \quad (14)$$

This critical value corresponds to static loss of stability, namely the trailer overturns about the lateral axis for $k < k_{\text{cr}}$.

3.2 The Yaw and Roll Motion of the Trailer

The equations of motion of the coupled subsystem consist of three second-order ordinary differential equations. By using the trial solution

$$\mathbf{q} = \mathbf{A}e^{\lambda t} \quad (15)$$

with the characteristic root λ , the characteristic equation becomes

$$\det(\lambda^2 \mathbf{M} + \lambda \mathbf{C} + \mathbf{K}) = 0. \quad (16)$$

The stability of the rectilinear motion can be investigated by Routh–Hurwitz criteria. Unfortunately, no closed form expression can be given for the critical parameter values in general case. But for $k_l \rightarrow \infty$ (i.e. when the joint at A is laterally rigid), the system simplifies to a $n = 3$ DoF system and critical stiffness values can be determined for the undamped ($c = 0$) case:

$$k_{\text{cr},1} = \frac{mg(l(f+h) - eh)}{2b^2l}, \quad (17)$$

and

$$k_{\text{cr},2} = \frac{mg l^2 (l(e-l)\Theta_{C,x} + fh\Theta_{C,z})}{2b^2l^2 (me^2h - mel(f+2h) + mfl^2 + h(\Theta_{C,z} + ml^2))} - \frac{mgBCDh(e-l)(me^2h^2 - 2mehl(f+h) + h^2\Theta_{C,z} + ml^2(f+h)^2 + \Theta_{C,x}l^2)}{2b^2l^2 (me^2h - mel(f+2h) + mfl^2 + h(\Theta_{C,z} + l^2m))}. \quad (18)$$

Static stability loss occurs if $k < k_{\text{cr},1}$, namely the trailer falls over. Dynamic loss of stability happens if $k_{\text{cr},1} < k < k_{\text{cr},2}$, and the rectilinear motion is stable for $k_{\text{cr},2} < k$. These critical values can be also identified by the numerical calculation

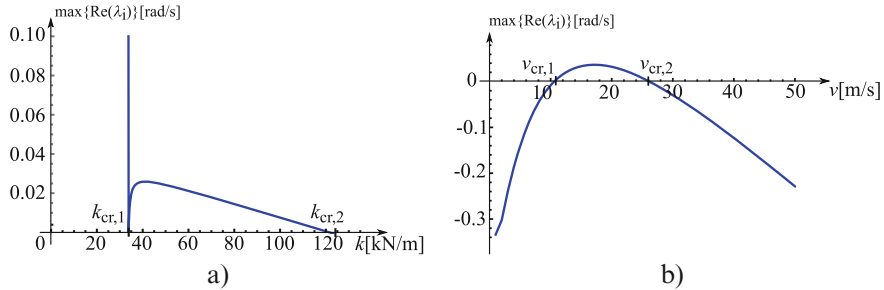


Fig. 5 The real part of the rightmost characteristic root of the linearized system. (a) Critical spring stiffness values for the 3 DoF model, (b) unstable speed range in case of the 4 DoF model. Parameter values: $l = 3$ m, $b = 0.8$ m, $e = 1$ m, $f = 1$ m, $h = 0.5$ m, $m = 3000$ kg, $k = 60,000$ N/m, $c = 6000$ Ns/m, $B = 10$, $C = 1.9$, $D = 1$, $E = 0.97$, (a) $k_l \rightarrow \infty$, (b) $k_l = 10,000$ N/m, $c_l = 100$ Ns/m

of the characteristic roots, see panel (a) of Fig. 5, where the real part of the rightmost characteristic root is plotted versus the stiffness.

Of course, the linear stability of original four degree-of-freedom mechanical model can also be investigated numerically. Panel (b) of Fig. 5 shows the real part of the rightmost characteristic root versus the towing speed v . For a certain velocity range (approx. between 10 and 26 m/s), the rectilinear motion is unstable.

4 Simulation

Numerical simulations were run in order to verify the critical parameter values given by the linear stability analysis and to check the nonlinear dynamics of the trailer. Fourth order Runge–Kutta method was used with fix time step. The simulations were run for different initial conditions and for different spring stiffness values (3 DoF model) or for different towing velocity values (4 DoF model). Here we present only a simulation result for $k_l \rightarrow \infty$ and for $k = 75,000$ N/m. As it can be seen, the motion tends to a large amplitude rocking motion, see Fig. 6.

Based on the numerical simulations, one can also draw the bifurcation diagram of the four degree-of-freedom system. The top left panel of Fig. 7 depicts the amplitude of the roll angle with respect to the bifurcation parameter v . Subcritical Hopf bifurcation is suspected, which could be validated by using a bifurcation software. Panel (b) of Fig. 7 shows the effects of parameters f and e on the linear stability of the rectilinear motion. The red areas correspond to linearly unstable rectilinear motion (snaking, rocking, roll-over of the trailer may appear), while the green areas correspond to linearly stable rectilinear motion.

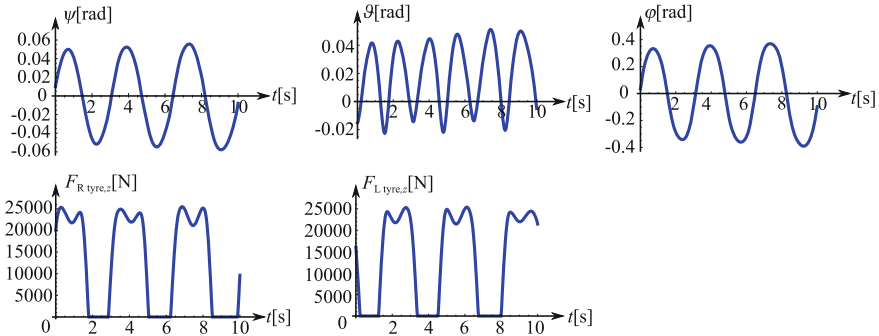


Fig. 6 The time histories of the generalized coordinates and the vertical forces acting on the left or the right wheel in case of $k = 75,000 \text{ N/m}$

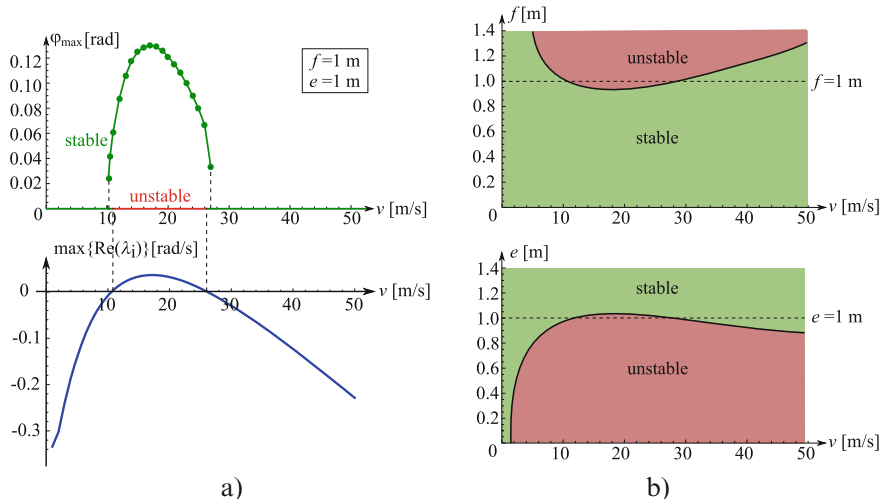


Fig. 7 (a) The bifurcation diagram of the four degree-of-freedom system, in case of $k = 75,000 \text{ N/m}$ (top panel) and the real part of the rightmost characteristic root of the linearized system (bottom panel). (b) The effects of parameters f and e on the linear stability of the rectilinear motion. The green areas correspond to linearly stable, the red areas to linearly unstable motion

5 Conclusions

A mechanical model was introduced by which both the stability of two-wheeled suitcases and trailers can be investigated. It was shown that the linear stability of the rectilinear motion depends on the speed if the lateral displacement of the towing joint is considered. Critical stiffness values were also determined for the wheel suspensions. Simulation results also confirmed that the model can exhibit the

large amplitude rocking motion and the nonlinear analysis of the model may lead to relevant information about the instability of the trailer.

Acknowledgements This research has been supported by the UNKP-18-2-I-BME-173 New National Excellence Program of the Ministry of Human Capacities Hungary. This research was funded by the National Research, Development and Innovation Office under grant no. NKFI-128422. The publication of the work reported herein has been supported by ETDB at BME.

References

1. Troger, H., Zeman, K.: A nonlinear-analysis of the generic types of loss of stability of the steady-state motion of a tractor-semitrailer. *Veh. Syst. Dyn.* **13**(4), 161–172 (1984)
2. Darling, J., Tilley, D., Gao, B.: An experimental investigation of cartrailer high-speed stability. *Proc. Inst. Mech. Eng. D: J. Autom. Eng.* **223**(4), 471–484 (2009)
3. Suherman, S., Plaut, R.H., Watson, L.T., Thompson, S.: Effect of human response time on rocking instability of a two-wheeled suitcase. *J. Sound Vib.* **207**(5), 617–625 (1997)
4. Plaut, R.H.: Rocking instability of a pulled suitcase with two wheels. *Acta Mech.* **117**, 165–179 (1996)
5. O'Reilly, O.M., Varadi, P.C.: A travelers woes: some perspectives from dynamical systems. In: Moon, F.C. (ed.) IUTAM Symposium on New Applications of Nonlinear and Chaotic Dynamics in Mechanics Kluwer, Dordrecht, pp. 397–406 (1999)
6. Facchini, G., Sekimoto, K., Courrech du Pont, S.: The rolling suitcase instability: a coupling between translation and rotation. *Proc. R. Soc. A: Math. Phys. Eng. Sci.* **473**(2202), 20170076 (2017)
7. Horvath, H.Zs., Takacs, D.: Modelling and Simulation of Rocking Suitcases. *Acta Polytech. CTU Proc.* **18**, 61–65 (2018). <https://doi.org/10.14311/APP.2018.18.0061>
8. Pacejka, H.B.: Tyre and Vehicle Dynamics, Elsevier Butterworth-Heinemann, Oxford (2002)

A Theoretical Model for Vibro-Impact Dynamics of Spur Gears with Tooth Flanks Wear



Ivana D. Atanasovska, Katica R. (Stevanović) Hedrih,
and Dejan B. Momcilovic

Abstract The main performance of involute gears operation leads to the appearance of nonlinear dynamic behavior and impact. In this chapter the influence of mild wear of the tooth flanks of gears without machine finishing and surface hardening on the vibro-impact behavior is considered. For this purpose, a new theoretical model for vibro-impact dynamics of spur gears with mild wear on tooth flanks is developed and described. The developed theoretical model is based on the main postulates of a model of the central centric collision of two fictive rolling disks with radii equal to the radii of kinematic diameters of the pinion and the wheel, as well as on a combined analytical/numerical approach used finite element analysis for the calculation of contact deformations, contact pressure, and wear on tooth flanks surfaces. A particular gear pair for earth moving machine is used for presenting the developed model. The conclusions about the influence of mild wear on the vibro-impact oscillations during running-in period are described.

Keywords Vibro-impact oscillations · Spur gears · Wear

1 Introduction

The wear is one of the most frequent types of gear tooth damages, which appears in different forms [1, 2]. In some specific cases of gear pairs with high value of transmission ratio and large diameter of the wheel, mainly designed for low angular velocities, a quality of the surface manufacturing of tooth flanks of a pinion and a wheel are not the same. In such cases, the wheel tooth flanks are manufactured without final surface machining and surface hardening and therefore it is expected

I. D. Atanasovska (✉) · K. R. (Stevanović) Hedrih

Mathematical Institute of the Serbian Academy of Sciences and Arts, Belgrade, Serbia
e-mail: iatanasovska@mi.sanu.ac.rs; khedrih@sbb.rs

D. B. Momcilovic

Institute for Testing of Materials-IMS Institute, Belgrade, Serbia

that these surfaces are more susceptible to the mild wear process resulting in a vibro-impact excitation parameter. This is a general case for geared transmissions on earth excavators and some other machines with large gear pairs not placed in gear boxes. These gears work mainly in the un-lubricated conditions and are specially subjected to different kinds of wear process.

The spur involute gears during operation are characterized with total deformations variation, which is in first place a result of the variable number of teeth pairs in contact. These variations in combination with other sources of the tooth profile pitch deviations during operation (profile deviations, wear, damages, etc.) is the main source of backlash, generation of internal dynamic forces and impacts [3]. In special cases of tooth profile shape and dimensions, a vibro-impact phenomenon could appear during spur gear operation. The vibro-impact dynamics of spur gear pair is characterized with successive collisions of series of teeth pairs in forward-backward collision contacts, which can cause a serious noise in the geared transmission system.

In this chapter, occurrence of mild wear on the wheel teeth of spur gear pairs is analyzed. The new theoretical model of a vibro-impact dynamics of spur gears with tooth flanks wear is developed as an extension of the model of vibro-impact dynamics of spur gears [3], which used the main postulates of the model of the central centric collision of two fictive rolling disks with radii equal to the radii of the kinematic diameters of pinion and wheel, and with the current rolling axes in collision coincided with the rotation axis of the pinion and the wheel [4].

2 A Mechanism of Mild Wear at Gears Tooth Flanks

The mild wear in gears is a slow process in general, which could be a part of the running-in period and can initially lead to the smoother contact surfaces on the tooth flanks. From the point of vibro-impact appearance, only the initial part of wear process is important, because the vibro-impact phenomenon is impossible in the case of deeply worn out teeth.

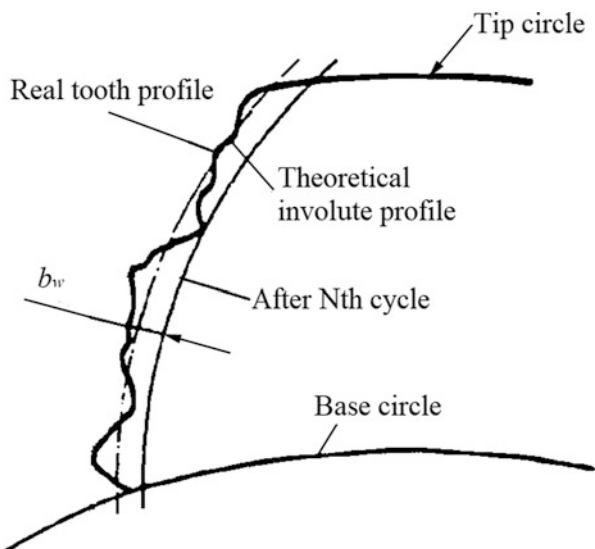
The theoretical model of a mild wear in spur gear teeth can be described by the generalized Archard's wear law [2]. The generalized Archard's wear equation [5] determines the wear depth by integrating the product of sliding distance and contact pressure during the time of contact. It can be expressed with the following relation:

$$\frac{dh}{dt} = kp v \quad (1)$$

where k is a wear coefficient, p is a local contact pressure, and v is a sliding velocity in contact point.

The wear coefficient k is a characteristic of the contact and depends primarily on the materials in contact, but also depends on the operating conditions, the tooth flank manufacturing process, and on the lubricant in case of lubricated contacts [6]. The research presented in this chapter is devoted to the gear pairs which operate

Fig. 1 Schematic presentation of real tooth profile with mild wear



in special conditions without lubrication. Therefore, the gears material can be considered as a main influential characteristic for selection of the wear coefficient. The wear coefficient has a value of $5 \cdot 10^{-16} \text{ m}^2/\text{N}$ for the contact surfaces made from steel [5]. In Fig. 1, the schematic presentation of the tooth flank with mild wear is presented.

The real tooth profile deviates from the theoretical involute profile in accordance with the standard defined deviations values. These deviations can be removed during the running-in period as a result of the mild wear phenomenon. In the presented research this period is modeled with N cycles of wear in order to analyze the variations in vibro-impact oscillations as a result of wearing process.

3 A Vibro-Impact Model of Spur Gears with Tooth Flanks Wear

3.1 The Analytical Procedure Description

The approximately constant transmission ratio is the main characteristic of the involute cylindrical gears, which leads to their wide application. The transmission ration is in the general case defined as $i = \omega_1/\omega_2$. But, as a result of the deviation previously mentioned, a disturbance of angular velocities ration can appear and leads to a vibro-impact dynamics. The disturbance angular velocity of a pinion can be defined as [3]:

$$\Delta\omega_1 = \omega_1 - i\omega_2 > 0 \quad (2)$$

and could be studied as a source for vibro-impact vibrations in the gear pairs with characteristics which lead to possible vibro-impact appearance. The mechanism of vibro-impact of spur gears is described in detail in the previous chapter [3].

The developing of formulae for calculation the disturbance pinion angular velocity is the main task within the analytical procedure for vibro-impact oscillations of spur gears. The disturbance pinion angular velocity depends from the tooth profile pitch deviation, which is a result of deformations, manufacturing deviations and wear:

$$b = K_b m_n + b_w \quad (3)$$

where: m_n is a standard normal tooth profile module, K_b is an error coefficient due to contact deformations and other sources of profile pitch deviations and b_w is a profile pitch deviation due to wear.

The coefficient K_b can be very precisely determined by finite element analysis (FEA) [3] by modeling the real contact geometry and operation loads or by Hertz contact theory, and b_w can be determined by integrating the product of sliding distance and contact pressure during the time of contact on the base of the generalized Archard's wear equation (1):

$$\frac{db_w}{dt} = k^w \sigma_y v \quad (4)$$

where k^w is a wear coefficient, σ_y is a local contact pressure obtained by FEA calculation and v is a sliding velocity which depends of the angular velocity and the gears geometry.

The time which is required by a pinion tooth to pass the total tooth pitch deviation can be expressed as:

$$T(b) = \frac{K_b m_n + b_w}{r_1} \frac{1}{\omega_1} \quad (5)$$

The pinion disturbance angular velocity can be calculated in accordance with the postulate that the rotation time of a pinion gear will be the same in the cases with and without deviation b [3]:

$$\frac{2\pi}{\omega_1} = \frac{2\pi + \frac{K_b m_n + b_w}{r_1}}{\omega_1 + \Delta\omega_1} \quad \text{i.e.} \quad \Delta\omega_1 = \frac{K_b m_n + b_w}{2\pi r_1} \omega_1 \quad (6)$$

3.2 The Angular Velocities Variation During Vibro-Impact

The vibro-impact dynamics of gears with mild wear can be solved in accordance with the relations (7) and (8) which define the new model of the central centric

collision of two fictive rolling disks [4]. The solution take into consideration that the radii of these disks are equal to the radii of pitch diameters of the pinion and the wheel, as well as that the instantaneous rolling axes of these disks in collision are coincided with the rotation axis of the pinion and the wheel [3].

$$\omega_{P1}(t_0 + \tau) = \omega_{P1}(t_0) - \frac{1 + \varepsilon}{1 + a} (\omega_{P1}(t_0) - \omega_{P2}(t_0)) \quad (7)$$

$$\omega_{P2}(t_0 + \tau) = \omega_{P2}(t_0) + \frac{1 + \varepsilon}{1 + b} (\omega_{P1}(t_0) - \omega_{P2}(t_0)) \quad (8)$$

where: $a = \frac{J_{p1}}{J_{p2}}$ and $b = \frac{J_{p2}}{J_{p1}}$ are the ratios of axial mass inertia moments for the pinion J_{p1} and the wheel J_{p2} ; ε is a coefficient of restitution for the case of collision of two rolling disks, which is calculated as a ratio of the differences of angular velocities of rolling disks before collision and after collision (this coefficient depends on the material characteristics and for steel has a value of 5/9). The Mathcad code is developed for the calculation of the angular velocities during vibro-impact phenomenon at involute gears.

4 Results and Discussion: A Case Study

4.1 Determination of Input Parameters

The presented theoretical method has been used for calculation of the angular velocities of the pinion and the wheel before and after every collision, and before and after every successive collision impact [3, 4] for a particular spur gear pair. The chosen gear pair has such characteristics of the tooth profile which can lead to vibro-impact vibration behavior. The main characteristics of the case study gear pair are: number of pinion teeth: 20; number of wheel teeth: 96, 80 and 60; transmission ratio: 4.8, 4 and 3; the coefficient of profile modification: 0.7 and -0.2; facewidth: 350 mm; profile module: 24 mm; rpm for the wheel: 4.1596 min^{-1} , wheel torque: 2526.8 KN·m; material: steel.

The tooth profile pitch deviations as a result of mild wear are calculated in accordance with the equation (4). The local contact pressure values are calculated with finite element analysis (FEA) developed for the chosen gear pair [7] for the characteristic contact points during tooth pair contact. The obtained results are shown at Fig. 2 for two external load cases. It can be concluded that the wear at the zone with two tooth pairs in contact is lower than that at the zone with single tooth pair in contact. This difference is greater for the cases with lower loads, which is a reason to avoid the low-loaded gear pairs.

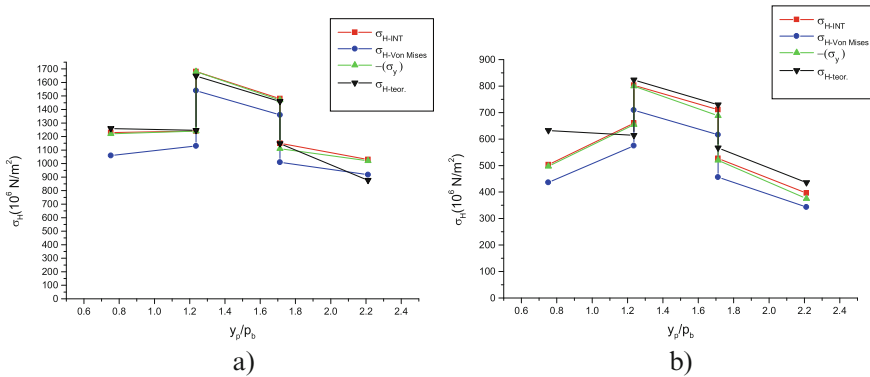


Fig. 2 Results for contact stresses along line of action obtained by finite element analysis and Hertz theory for particular gear pair: (a) for full external load; (b) for quarter of full external load

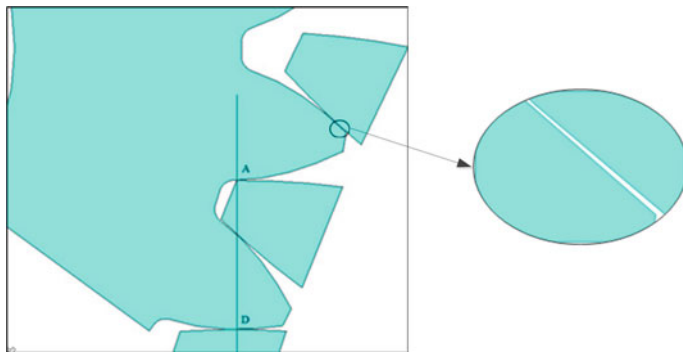


Fig. 3 The CAD contact model for a tooth pair—point A at the Line of action

In accordance with the calculated pressures and acceptable manufacturing deviations, the contact CAD models are created with nonuniform pitch deviation. The CAD models developed for the critical contact positions of meshed tooth pair with incorporated tooth profile pitch deviations as a result of deformations, manufacturing process, and mild wear are shown at Figs. 3 and 4.

The first contact point along the Line of action—point A (Fig. 3) and the first point of double contact period at the Line of action—point B (Fig. 4) are identified as the critical contact points during every teeth pair contact period.

4.2 Results for Vibro-Impact Oscillations

In accordance with the obtained results for total pitch deviations, the disturbance angular velocity defined with relation (6) is calculated. Then, the time periods

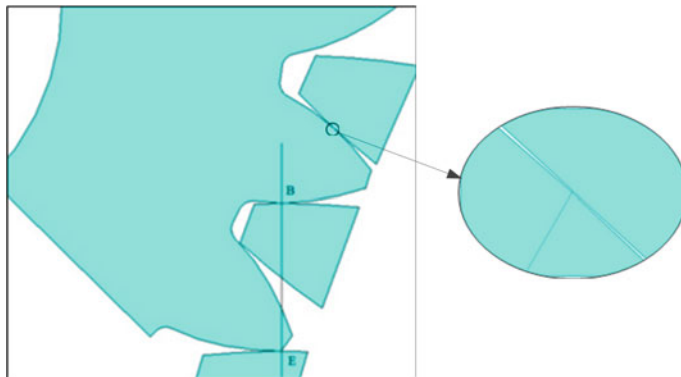


Fig. 4 The CAD contact model for a tooth pair—point B at the Line of action

$a \leftarrow 0.0018838$ $b \leftarrow 530.8416$ $\omega_1 \leftarrow 2.09088$ $\omega_2 \leftarrow 0.4356$ $k \leftarrow \frac{5}{9}$ for $j \in 1..20$ $\Delta\omega_1 \leftarrow 0.0003165$ $\Delta\omega_2 \leftarrow 0$ $z \leftarrow \Delta\omega_1 - \Delta\omega_2$ for $i \in 1..30$	$\Delta\omega_1 \leftarrow \Delta\omega_1 - \frac{1+k}{1+a} \cdot z$ $\text{trace}(\Delta\omega_1)$ $\Delta\omega_2 \leftarrow \Delta\omega_2 + \frac{1+k}{1+b} \cdot z$ $\text{trace}(\Delta\omega_2)$ $z \leftarrow \Delta\omega_1 - \Delta\omega_2$ $\begin{pmatrix} \Delta\omega_1 \\ \Delta\omega_2 \end{pmatrix}$ $\begin{pmatrix} \omega_1 \\ \omega_2 \end{pmatrix}$
--	--

Fig. 5 The Mathcad code for a gear pair

between teeth collisions, as well as between teeth successive collision impacts after each collision, have been calculated in accordance with the relations derived and explained in [3]. The developed Mathcad code is then used for the calculation of the angular velocities of the pinion and the wheel before and after every collision, and before and after every successive collision impact, Fig. 5. Obtained results for the variations of the pinion and the wheel angular velocities are presented with diagrams at Figs. 6 and 7.

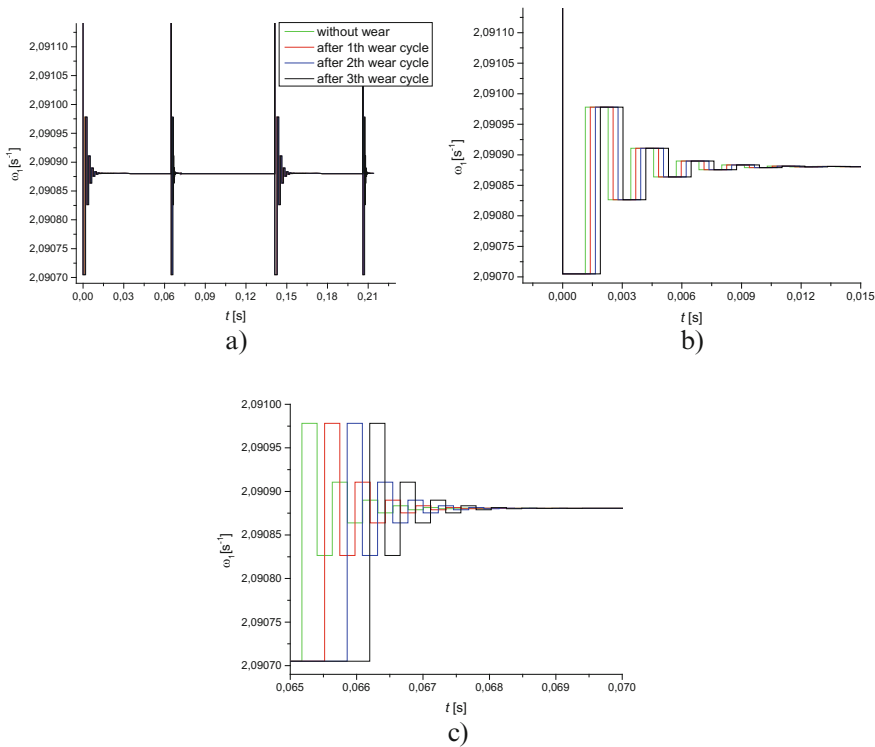


Fig. 6 The results for the pinion angular velocity variation during two contact periods for transmission ration of $i = 4.8$ (a) with zoom in points A (b) and B (c)

5 Conclusions

The new model for analyzing the vibro-impact of spur gears has potential to include different sources of vibro-impact excitation (elastic deformations, profile deviations and roughness, wear, damages, etc.). Presented model gives the possibility to consider the vibro-impact phenomenon apart from overall gear dynamics. The future research can be focused on the incorporating of this model to the approach for stability analysis of whole system.

For the analyzed gear pair it is shown that the wear at the zone with two tooth pairs in contact is lower than that at the zone with single tooth pair in contact, which is consequence of the lower values of the contact pressure. Also, this difference is larger in the case of low-loaded operation conditions, which can lead to the extremely nonuniform wear on tooth flanks. The selection of optimal tooth profile for defined real load conditions can overcome the nonuniform wear and shorten the running-in time.

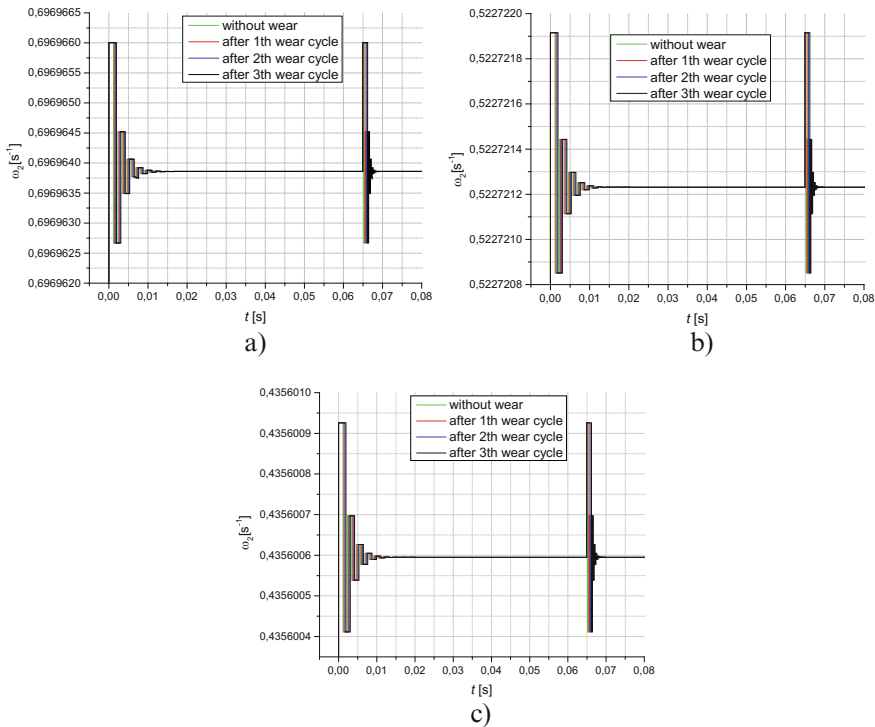


Fig. 7 The results for the wheel angular velocity variation during a contact period for different transmission ration: (a) $i = 3$; (b) $i = 4$ and (c) $i = 4.8$

The obtained results for the variations of the pinion and the wheel angular velocities are presented with diagrams where the characteristic points on the Line of action are easily recognized. The comparative analysis of the influence of the different wear level during gears operation could result in the real benefits in selection the optimal working conditions for gear pairs which are the part of machines and other facilities within the power plants, in accordance with the results of the periodical inspections. The presented research shows that for a particular gear pair the wear level affects only the time periods between variations of angular velocities within the vibro-impact phenomenon. After a few cycles of the mild wearing, the conditions no longer lead to the vibro-impact occurrence, and this emphasizes the importance of a uniform wear process.

Acknowledgement Parts of this research were supported by the Ministry of Sciences of Republic Serbia through Mathematical Institute of SASA Belgrade. Grant OI 174001: Dynamics of hybrid systems with complex structures. Mechanics of materials.

References

1. Atanasovska, I., Momcilovic, D.: The effect of teeth failures on machine safety—testing and analysis. *Struct. Integr. Life.* **7**(1), 37–46 (2007)
2. Flodin, A., Andersson, S.: Simulation of mild wear in spur gears. *Wear.* **207**, 16–23 (1997)
3. Atanasovska, I., Hedrih (Stevanovic), K.: The new collision model for analyzing of spur gears vibro-impact. *Trans. FAMENA.* **42**(2), 1–13 (2018)
4. Hedrih (Stevanovic), K.: Nonlinear phenomena in vibro-impact dynamics: central collisions and energy jumps between two rolling bodies. *Nonlinear Dyn.* **91**(3), 1885–1907 (2018)
5. Brauer, J., Andersson, S.: Simulation of wear with flank interference—a mixed FE and analytical approach. *Wear.* **254**, 1216–1232 (2003)
6. Brandão, J.A., PedroCerqueira, P., Seabra, J.H.O., Castro, M.J.D.: Measurement of mean wear coefficient during gear tests under various operating conditions. *Tribol. Int.* **102**, 61–69 (2016)
7. Atanasovska, I., Mitrovic, R., Momcilovic, D., Subic, A.: Analysis of the nominal load effects on gear load capacity using the finite element method. *Proc. Inst. Mech. Eng. C.* **224**(11), 2539–2548 (2010)

Stability of Coupled and Damped Mathieu Equations Utilizing Symplectic Properties



Miguel Ramírez Barrios, Joaquín Collado, and Fadi Dohnal

Abstract Several theoretical studies deal with the stability transition curves of the Mathieu equation. A few others present numerical and asymptotic methods to describe the stability of coupled Mathieu equations. However, sometimes the averaging and perturbation techniques deal with cumbersome computations, and the numerical methods spend considerable resources and computation time. This contribution extends the definition of linear Hamiltonian systems to periodic Hamiltonian systems with a particular dissipation. This leads naturally to a generalization of symplectic matrices, to μ -symplectic matrices. This definition enables an efficient way for calculating the stability transition curves of coupled Mathieu equations.

Keywords Hamiltonian systems · Parametric excitation · Symplectic matrices

1 Introduction

Dynamical systems represented by ordinary differential equations with periodic coefficients are presented in many engineering problems. Therefore, using numerical and asymptotic methods several theoretical studies deal with the stability transition curves of the periodic systems, in particular with the Mathieu equation [1, 2]. Sometimes the asymptotic perturbation techniques lead to cumbersome

M. Ramírez Barrios

Professional Interdisciplinary Unit of Biotechnology, National Polytechnic Institute, México City, México

e-mail: mramirez@ctrl.cinvestav.mx

J. Collado

Automatic Control Department, CINVESTAV, México City, México
e-mail: jcollado@ctrl.cinvestav.mx

F. Dohnal (✉)

Division for Mechatronics Lienz, UMIT - Private University for Health Sciences, Medical Informatics and Technology, Lienz, Austria
e-mail: fadi.dohnal@umit.at

computations [3] and the numerical methods have a considerable computation time. The present contribution extends the result presented in [4] where coupled Mathieu equations are analyzed as a Hamiltonian system. The power of symplectic and Hamiltonian matrices lies in the fact that the dynamics of Hamiltonian systems are described by symplectic maps. In this contribution we attempt to define a new type of linear periodic Hamiltonian systems with a particular dissipation. For this purpose, the properties of the γ -Hamiltonian and μ -symplectic matrices are introduced and developed. This enables a proof that the state transition matrix of any γ -Hamiltonian system is μ -symplectic. μ -symplectic matrices possess a symmetry property in its eigenvalues which is exploited to describe the stability of time-periodic systems. Using this theory and the Floquet theory, two coupled Mathieu equations are fully described which leads to an efficient calculation procedure of the stability and instability regions.

2 Floquet Theory Review

In the following, the main results on linear *periodic* systems are summarized. More details can be found in [1, 5].

Consider the linear periodic system

$$\dot{x} = B(t)x \quad (1)$$

with $B(t) = B(t + \Omega)$ where $x \in \mathbb{R}^n$, $B \in \mathbb{R}^{n \times n}$ and Ω the fundamental period.

Theorem 1 (Floquet) *The state transition matrix $\Phi(t, t_0)$ of the system in Eq. (1) may be factorized as $\Phi(t, t_0) = P^{-1}(t)e^{Rt}$ where $P^{-1}(t) = \Phi(t, 0)e^{-Rt}$, $P^{-1}(t) = P^{-1}(t + \Omega)$ is a periodic matrix of the same period Ω and R is in general a complex constant matrix [6].*

Definition 1 The monodromy matrix M associated with the system in Eq. (1) is defined as $M = e^{R\Omega} = \Phi(\Omega, 0)$

The eigenvalues λ_i of M are called *characteristic multipliers*. If we define a coordinates change as $z(t) = P(t)x(t)$ then the system Eq. (1) can be transformed into a linear time invariant system $\dot{z}(t) = Rz(t)$ where R is the constant matrix defined in the Floquet theorem. Therefore, any periodic system Eq. (1) is reducible to a system $\dot{z}(t) = Rz(t)$ with constant coefficients [1, 5].

3 μ -Symplectic and γ -Hamiltonian Matrices

Let $J = \begin{bmatrix} 0 & I_n \\ -I_n & 0 \end{bmatrix}$ be a real square matrix where I_n is the $n \times n$ identity matrix. It is clear that $J^T = -J = J^{-1}$, $J^2 = -I_{2n}$, $\det(J) = 1$. The forthcoming definition

and lemmas are a generalization of the symplectic matrices introduced in [7, 8]. From definition 2 the determinant of S reads $\det(S) = \mu^n$. Certainly, if $\mu = 1$, Eq. (2) defines a symplectic matrix [7, 8].

Definition 2 The matrix $S \in \mathbb{R}^{2n \times 2n}$ is said a μ -symplectic matrix if the equation

$$S^T JS = \mu J \quad (2)$$

is fulfilled for $\mu \in (0, 1]$.

Lemma 1 *The characteristic polynomial of S satisfies: $P_S\left(\frac{\mu}{\lambda}\right) = \frac{\mu^n}{\lambda^{2n}} P_S(\lambda)$.*

Proof From Eq. (2) $J^T = \mu JS^{-1}J^{-1}$ then $P_S(\lambda) = \det[\lambda I_{2n} - \mu JS^{-1}J^{-1}] = \mu^n \det\left[-\frac{\lambda}{\mu}\left(\frac{\mu}{\lambda}I_{2n} - S\right)\right] = \frac{\lambda^{2n}}{\mu^n} P_S\left(\frac{\mu}{\lambda}\right)$. ■

From the last lemma, the eigenvalues of a μ -symplectic matrix S satisfy the relation: $\lambda \in \sigma(S) \mapsto \left(\frac{\mu}{\lambda}\right) \in \sigma(S)$. Furthermore, if all eigenvalues have the same magnitude, i.e., $\lambda_i = r \exp(\theta_i) \implies \prod_{i=1}^{2n} |\lambda| = \prod_{i=1}^{2n} |re^{\theta_i}| = r^{2n} = \det(S) = \mu^n$, from which we find that $r = \sqrt{\mu}$, independent of n . This fact may be interpreted as a “symmetry” with respect to the circle of radius $r = \sqrt{\mu}$, that we will name as “ μ -circle.” Additionally, since S is a real matrix, if λ is an eigenvalue then its conjugate $\bar{\lambda}$, $\mu\lambda^{-1}$, and $\mu\bar{\lambda}^{-1}$ are also eigenvalues. On the other hand, the characteristic polynomial of S , $P_S(\lambda) = a_{2n}\lambda^{2n} + \dots + a_1\lambda + a_0$ satisfies $a_0 = a_{2n}\mu^n$, $a_1 = a_{2n-1}\mu^{n-1}, \dots, a_{2n} = 1 = a_0\mu^{-n}$, i.e., $P_S(\lambda)$ is reciprocal and depends on n coefficients only. Thus, performing the transformation

$$\delta = \lambda + \frac{\mu}{\lambda}, \quad (3)$$

the characteristic polynomial $P_S(\lambda)$ of degree $2n$, associated to a μ -symplectic matrix, is reduced to an auxiliary polynomial $Q_S(\delta)$ of degree n . For instance, when $n = 2$ these polynomials read

$$P_S(\lambda) = \lambda^4 + a\lambda^3 + b\lambda^2 + a\mu\lambda + \mu^2, \quad Q_S(\delta) = \delta^2 + a\delta + b - 2\mu. \quad (4)$$

The last computations can be generalized for any n , but in this contribution, we focus on $n = 2$ only. In the following, the definition of γ -Hamiltonian matrices is given briefly.

Definition 3 A matrix $A \in \mathbb{R}^{2n \times 2n}$ ($A \in \mathbb{C}^{2n \times 2n}$) is called γ -Hamiltonian matrix if the equation: $A^T J + JA = -2\gamma J$ is satisfied, for some $\gamma \geq 0$.

4 Linear γ -Hamiltonian Systems

Definition 4 Any linear system that can be written as

$$\dot{x} = J [H(t) + \gamma J] x, \quad (5)$$

with $x \in \mathbb{R}^{2n}$, $H^T(t) = H(t)$, and $\gamma \geq 0$, is named as **linear γ -Hamiltonian system**.

Lemma 2 The state transition matrix of a linear γ -Hamiltonian system of the form in Eq. (5) is μ -symplectic with $\mu = e^{-2\gamma t}$.

Proof Let be $N(t) = \Phi(t, 0)$ the state transition matrix of Eq. (5) then $\frac{d}{dt}[N(t)] = (J[H(t) + \gamma J])N(t)$. Additionally, the following holds¹:

$$\frac{d}{dt}N^T J N = \dot{N}^T J N + N^T J \dot{N} = -2\gamma N^T J N. \quad (6)$$

Since $N^T(0) J N(0) = J$ and from Eq. (6) we obtain $N^T(t) J N(t) = e^{-2\gamma t} J = \mu J$. Therefore, N is μ -symplectic. ■

4.1 Periodic γ -Hamiltonian Systems

Definition 5 Any linear periodic system that can be written as follows:

$$\dot{x} = J [H(t) + \gamma J] x \quad \text{with } H(t) = H(t + \Omega). \quad (7)$$

We will name **linear periodic γ -Hamiltonian system**, where $x \in \mathbb{R}^{2n}$, $H^T(t) = H(t)$ is a $2n \times 2n$ matrix and $\gamma \geq 0$.

Then, according to the Lemma 2, the state transition matrix $\Phi(t, t_0)$ of Eq. (7) is μ -symplectic, in particular, the state transition matrix evaluated over one period Ω , namely the monodromy matrix. Furthermore, based on the Floquet–Lyapunov transformation, we conclude that any linear periodic γ -Hamiltonian system is reducible into a linear time-invariant γ -Hamiltonian system $\dot{z}(t) = Rz(t)$.

Corollary 1 The monodromy matrix $M = \Phi(\Omega, 0) = e^{R\Omega}$ and the R matrix of the periodic system (7) are μ -symplectic and γ -Hamiltonian matrices, respectively, with $\mu = e^{-2\gamma\Omega}$.

¹The matrix product $(\frac{d}{dt}N^T J N) N^T J N = N^T J N (\frac{d}{dt}N^T J N)$ is commutative.

Proof Based on the definition of the μ -symplectic matrix $M^TJM = \mu J$ we obtain $e^{R^T\Omega} = \mu J \left\{ I_{2n} - R\Omega + \frac{RR\Omega^2}{2} - \frac{RRR\Omega^3}{3!} + \dots \right\} J^{-1} = \mu e^{-JRJ^{-1}\Omega}$ and consequently, $R^T J + JR = -2\gamma J$. ■

Theorem 2 The system in Eq. (7) for $n = 2$ is asymptotically stable if and only if the following inequalities are fulfilled:

$$b \geq -a(1 + \mu) - (1 + \mu^2) \quad (8)$$

$$b \geq a(1 + \mu) - (1 + \mu^2) \quad (9)$$

$$(1 + \mu)^2 b \leq \mu^4 + 2\mu^3 + 2\mu^2 + a^2\mu + 2\mu + 1, \quad (10)$$

where a and b are the coefficients of the characteristic polynomial of the monodromy matrix associated with Eq. (7), namely $P_M(\lambda) = \lambda^4 + a\lambda^3 + b\lambda^2 + a\mu\lambda + \mu^2$.

Proof Based on Corollary 1, the monodromy matrix of Eq. (7) is a μ -symplectic matrix. Thus, for $n = 2$ its characteristic and the auxiliary polynomial are given in Eq. (4) which finally results in

$$a = -\text{tr}(M) = \lambda_1 + \frac{\mu}{\lambda_1} + \lambda_3 + \frac{\mu}{\lambda_3} = \delta_1 + \delta_2, \quad 2b = (\text{tr}(M))^2 - \text{tr}(M^2). \quad (11)$$

According to the Floquet–Lyapunov theorem [1, 5, 6], the stability of periodic systems is determined by the position of the multipliers related to the unit circle, e.g., the system is unstable if at least one multiplier lies outside the unit circle. The stability transition boundaries are characterized by having at least one eigenvalue $|\lambda| = 1$. The simplest cases are if $\lambda = 1$ (or $\delta = 1 + \mu$) and $\lambda = -1$ (or $\delta = -1 - \mu$). Substituting these two values into $P_M(\lambda)$ in Eq. (4) we have: $\lambda = 1 : b = -a(1 + \mu) - (1 + \mu^2)$ and $\lambda = -1 : b = a(1 + \mu) - (1 + \mu^2)$.

For the general case $\lambda \in \mathbb{C}$, the stability transition boundary can be obtained by considering the symmetry of the multipliers with respect to the real axis and with respect to the μ -circle (with radius $r = \sqrt{\mu}$). Then, for the four eigenvalues $|\lambda| = \sqrt{x^2 + y^2} = 1$ and read $\lambda_{1,3} = x \pm iy$, $\lambda_{2,4} = \frac{\mu}{\lambda_{1,3}} = \mu(x \mp iy)$. Considering the transformation in Eq. (3), results: $\delta_1 = \lambda_1 + \frac{\mu}{\lambda_1} = x(1 + \mu) + iy(1 - \mu)$ and $\delta_2 = \lambda_3 + \frac{\mu}{\lambda_3} = x(1 + \mu) - iy(1 - \mu)$, then adding δ_1 and δ_2 we obtain $\delta_1 + \delta_2 = 2x(1 + \mu)$. On the other hand, solving the quadratic equation in Eq. (4) for δ , $\delta_{1,2} = \frac{-a}{2} \pm \frac{\sqrt{a^2 + 8\mu - 4b}}{2}$ then $\delta_1 + \delta_2 = -a$ therefore $\delta_1 + \delta_2 = 2x(1 + \mu) = -a$. Thus, we must find the real part x , solving for λ in Eq. (3) with $\delta_{1,2}$ it is obtained $4x = 4\Re\{\lambda_1\} = -a + \sqrt{w - 4\mu - 2b + a^2}$ where $w = 2\sqrt{-4a^2\mu + (b + 2\mu)^2}$, then the inequality (10) holds. ■

Two intersection points exist between the boundary lines Eqs. (8), (9), and (10) and can be given explicitly

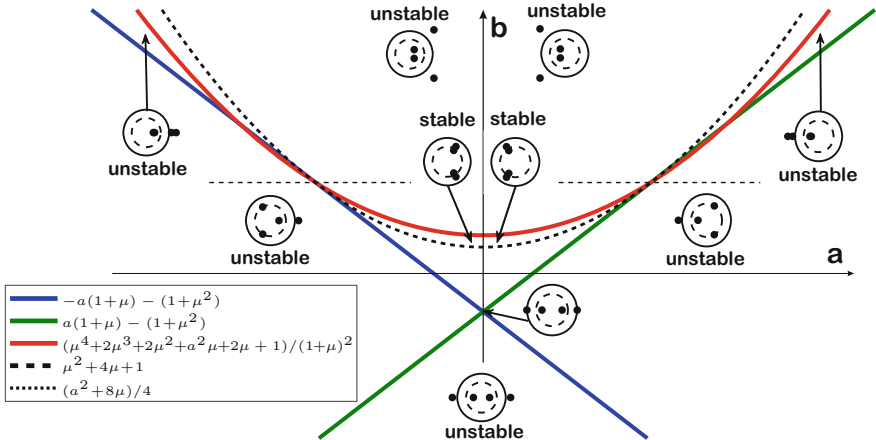


Fig. 1 Multiplier map in case of $n = 2$: Horizontal and vertical axes are the coefficients a and b of the characteristic polynomial of the monodromy matrix M in Eq. (4). The solid lines represent the borders of the inequalities in Theorem 2, Eqs. (8), (9), and (10). The dots indicate the position of multipliers associated to the system in Eq. (7) in case of $n = 2$. The dashed circle depicts the μ -circle

$$b = \frac{1}{\mu} \left(\mu^4 + \mu^3 + 2\mu^2 + \mu + 1 \right), \quad b = \mu^2 + 4\mu + 1. \quad (12)$$

The lines in Eq. (12) are visualized by dashed lines in Fig. 1

Following the procedure of the last proof, the multiplier positions in relation to the unit circle and the μ -circle are determined by the inequalities in Theorem 2. Thus, the parameter (a, b) -plane is split into six regions as it is highlighted in Fig. 1. All possible positions of the multipliers with respect to the μ -circle and the unit circle are visualized. The diagram is “symmetric” in terms of the multipliers according that if λ is an multiplier $\bar{\lambda}$, $\mu\bar{\lambda}^{-1}$ and $\bar{\lambda}\bar{\lambda}^{-1}$ are also.

5 Coupled Mathieu Equations with Damping

Consider two coupled and damped Mathieu equations of the following form:

$$\begin{bmatrix} \ddot{z}_1 \\ \ddot{z}_2 \end{bmatrix} + \begin{bmatrix} \Theta_{11} & \Theta_{12} \\ \Theta_{21} & \Theta_{22} \end{bmatrix} \begin{bmatrix} \dot{z}_1 \\ \dot{z}_2 \end{bmatrix} + \left(\begin{bmatrix} \omega_1^2 & 0 \\ 0 & \omega_2^2 \end{bmatrix} + \beta \begin{bmatrix} Q_{11} & Q_{12} \\ Q_{21} & Q_{22} \end{bmatrix} \begin{bmatrix} z_1 \\ z_2 \end{bmatrix} \cos(\nu t) \right) \begin{bmatrix} z_1 \\ z_2 \end{bmatrix} = 0. \quad (13)$$

The system in Eq. (2) can be cast into the form in Eq. (7) iff $\Theta_{12} = \Theta_{21}$ and $Q_{12} = Q_{21}$, i.e., the coefficient matrices Θ and Q are symmetric. The following numerical values are chosen for the analysis of a specific system $\omega_1^2 = 8$, $\omega_2^2 = 26$, $Q_{11} = Q_{22} = 2$, $Q_{12} = Q_{21} = -2$. Figure 2a depicts the multiplier chart

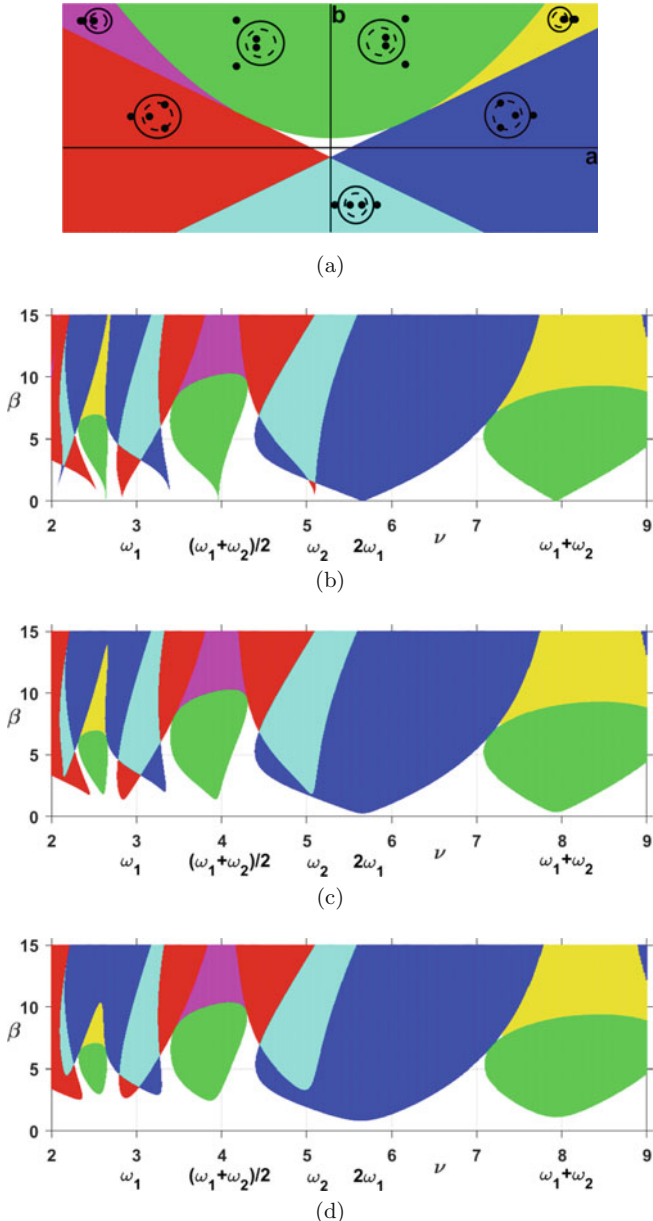


Fig. 2 Multiplier map and stability charts for example system in Eqs. (2). Multiplier map corresponds to Fig. 1 but now with colored regions for the different unstable multiplier configurations. Stability charts are given for different values of damping. (a) Multiplier map: a and b are the coefficients of the corresponding characteristic polynomial of the monodromy matrix. (b) Stability chart of coupled Mathieu equations without damping: $\Theta_{12} = \Theta_{21} = 0$ and $\Theta_{11} = \Theta_{22} = 0$. Color code is according to (a). (c) Stability chart of coupled Mathieu equations with small damping: $\Theta_{12} = \Theta_{21} = 0$ and $\Theta_{11} = \Theta_{22} = 0.1$. (d) Stability chart of coupled Mathieu equations with high damping $\Theta_{12} = \Theta_{21} = 0$ and $\Theta_{11} = \Theta_{22} = 0.3$

similar to Fig. 1. The unstable regions in the parameter space are colored, the stable regions are kept white. Each color depicts a specific configuration of the multiplier positions within the unit circle and the μ -circle according to the inequalities stated in Theorem 2 and visualized in Figs. 1 and 2a. Yellow, magenta, and cyan colors refer to the configuration of four real-valued multipliers, two of them inside and two outside of the unit circle. These multipliers are either all negative (magenta region), all positive (yellow region), or two positive and two negative (cyan region). The blue and red regions indicate two complex conjugate multipliers on the μ -circle while the other two are real with $|\lambda| > 1$. The two real multipliers are either positive (blue) or negative (red). Then, all four multipliers are complex conjugate within the green region. In this case, two multipliers lie inside and two outside of the unit circle. On the other hand, parametric primary resonances occur at parametric excitation frequencies $v = 2\omega_i/k$ ($k \in \mathbb{N}^+$) and parametric combination resonances of summation type occur at $v = (\omega_1 + \omega_2)/k$ [3, 5]. These frequencies are also observed for the example system in Fig. 2b. The green regions mark parametric combination resonances. The blue and red regions correspond to parametric primary resonances.

The presented calculation technique can be categorized as a semi-analytical method. After rewriting the original system into the form in Eq. (7), the monodromy matrix is constructed by integrating the equations of motion using numerical methods. Subsequently, the coefficients of the characteristic polynomial of the monodromy matrix can be computed as: $a = -\text{tr}(M)$ and $2b = (\text{tr}(M))^2 - \text{tr}(M^2)$. This technique **avoids the computation of the eigenvalues**. The main advantage is that numerical problems of computing the eigenvalues are avoided, e.g., numerically sensitive multipliers. Additionally, the computation time is decreased. For instance, the stability charts in Fig. 2 were calculated within a few seconds. An efficient numerical implementation utilizing a GPU can be found in [9]. For comparison, the stability chart corresponding to Eq. (2) is 64% faster by utilizing Theorem 2 compared to computing the stability chart based on eigenvalues computation. The performance improvement by avoiding the computation of eigenvalues was checked for a stability chart with a resolution of 800×800 points in the parameter space (v, β) .

6 Conclusions

In this work, definitions of μ -symplectic and γ -Hamiltonian matrices are introduced. These definitions allow the analysis of a linear periodic Hamiltonian system with a particular dissipation. The main result of the proposed theory lies in Lemma 2 which states that the state transition matrix of any γ -Hamiltonian system is μ -symplectic. The symmetry properties of the eigenvalues of μ -symplectic matrices lead to an efficient calculation of the stability boundaries of this type of system. The general framework is applied for the example analysis of two damped and coupled Mathieu equations confirming the faster and robust computation of the stability

chart. The procedure can be extended to a higher number of coupled Mathieu equations which is subject of ongoing research.

Acknowledgement The first and third author are thankful for the financial support within the Austrian IWB project LaZu-CLLD_IWB_TIROL_OSTT_005 (Campus Technik Lienz).

References

1. Sinha, S.C. Butcher, E., Dávid, A.: Construction of dynamically equivalent time-invariant forms for time-periodic systems. *Nonlinear Dyn.* **16**(3), 203–221 (1998)
2. Biswas, S., Bhattacharjee, J.: On the properties of a class of higher-order Mathieu equations originating from a parametric quantum oscillator. *Nonlinear Dyn.* **96**(1), 737–750 (2009)
3. Dohnal, F., Verhulst, F.: Averaging in vibration suppression by parametric stiffness excitation. *Nonlinear Dyn.* **54**(3), 231–248 (2008)
4. Collado, J.: Hill Equation: From 1 to 2 Degrees of Freedom. New Perspectives and Applications of Modern Control Theory, pp. 43–71. Springer, Berlin (2018)
5. Yakubovich, V., Starzhinskii, V.: Linear Differential Equations With Periodic Coefficients. Wiley, London (1975)
6. Butcher, E., Sinha, S.C.: Normal forms and the structure of resonance sets in nonlinear time-periodic systems. *Nonlinear Dyn.* **23**(1), 35–55 (2000)
7. Meyer, K., Hall, G., Offin, D.: Introduction to Hamiltonian Dynamical Systems and the N -body Problem, vol. 90. Springer, Berlin (2008)
8. Howard, J., MacKay, R.: Linear stability of symplectic maps. *J. Math. Phy.* **28**(5), 1036–1051 (1987)
9. Ramírez, M., Collado, J.: Calculation of the stability zones of Hill's equation with a GPU on Matlab. In: International Conference on Supercomputing, pp. 225–239. Springer, Berlin (2015)

Asymmetry in the Basin Stability of Oscillation Death States Under Variation of Environment-Oscillator Links



Manish Yadav, Sudhanshu Shekhar Chaurasia, and Sudeshna Sinha

Abstract We explore the effect of a common external system, which may be considered as a common environment, on the oscillation death(OD) states of a group of Stuart–Landau(SL) oscillators. It was found in Chaurasia et al. (Phys Rev E 98:032223, 2018), that the group of oscillators, when uncoupled to the common environment, yield a completely symmetric oscillation death state, i.e. there is an equal probability of occurrence of positive and negative oscillation death states. However, remarkably, this symmetry is significantly broken, when coupled to a common external system. For exponentially decaying common environment, the symmetry breaking of the OD states was found to be very pronounced for low environmental damping and strong oscillator-environment coupling. Here we consider the effect of disconnections of the oscillator-environment links on this asymmetry in the basin stability of the OD states. Interestingly, we find that the asymmetry induced by environmental coupling decreases with increase in fraction of such disconnections, and at some intermediate fraction close to half the symmetry is restored. However, further increase in disconnections induces asymmetry in the OD state again, until all oscillator-environment links are switched off. This suggests that a balance of on-off oscillator-environment links restores the symmetry of the OD state, and when half of the environmental connections are switched off one obtains the positive and negative OD states with almost equal probability.

Keywords Symmetry breaking · Oscillation death · Basin stability · Steady states

M. Yadav · S. S. Chaurasia (✉) · S. Sinha

Indian Institute of Science Education and Research (IISER) Mohali, Punjab, India
e-mail: sudhanshushekhar@iisermohali.ac.in; sudeshna@iisermohali.ac.in

1 Introduction

In the context of many real world systems, interactions can occur through a common medium. For instance, chemical oscillations of catalyst-loaded reactants have been found in a medium of catalyst-free solution, where the coupling is through exchange of chemicals with the surrounding medium [1]. Similarly, in the context of genetic oscillators coupling occurs by diffusion of chemicals between cells and extracellular medium [2]. Further, in a collection of circadian oscillators, the concentration of neurotransmitter released by each cell can induce collective behaviour [3]. In general, such cases occur due to the common medium, referred to as a common environment, interacting with the dynamical systems. In this work we will investigate a generic model that unifies many specific models of particular systems such as biochemical oscillators coupled through an environment, and allows us to obtain some basic general results which potentially apply to all of them.

It was found in [4] that coupling a group of oscillators to a common external medium [5] destroyed the symmetry in occurrence of the oscillation death (OD) states [6–8], also known as inhomogeneous steady states (IHSS), in the system. That is, the oscillator death states in the presence of environmental coupling are no longer symmetrically distributed. Rather the distribution of the emergent OD states is significantly skewed. This implies that the basin stability of the OD states is no longer the same. Instead there is coupling induced *asymmetry in the basin stability* [9] which leads to the system evolving preferentially towards one of the OD states. This manifests as a remarkable asymmetric distribution of the OD states, though both states are linearly stable. So one observes that the average fraction of oscillators going to a particular OD state is not the same.

Specifically, here we will study a group of globally coupled oscillators. The oscillators will be considered in the oscillation death regime, by setting appropriate values of the control parameters of the individual oscillators [10]. Each oscillator is also connected with the common external medium. This environmental coupling effectively pushes all the oscillators towards negative OD-state. We then go on to investigate the dynamics as the environment-oscillator links are disconnected one by one. We will show how cutting off the environment-oscillator links leads to a restoration of symmetry in the distribution of OD states. We will further demonstrate that one can use the external medium coupling strength and the environmental damping constant to control the distribution of oscillators in the different OD-states for a given fraction of environment-oscillator links.

2 Coupling via Common Environment

Our representative model is described by the generalized equation given below in Eq. (1) and schematically elucidated with Fig. 1:

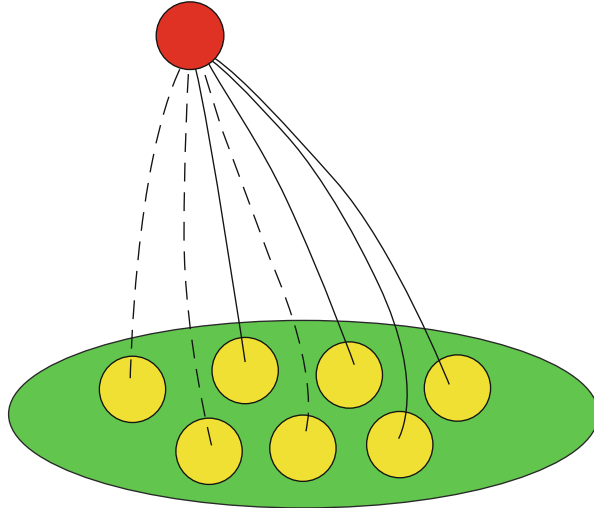


Fig. 1 Schematic diagram of group of oscillators connected to a common external environment

$$\begin{aligned}\dot{X}_i &= F(X_i) + \varepsilon_{intra} \alpha(q\bar{X} - X_i) + \varepsilon_{ext} \beta u, \\ \dot{u} &= -ku + \frac{\varepsilon_{ext}}{N} \beta^T \sum_{i=1}^N X_i\end{aligned}\quad (1)$$

X_i is the column vector representing an m -dimensional nonlinear oscillator, each of the oscillators are connected within the group with mean-field diffusive coupling and with an external common environment (u). All the oscillators are connected with each other with the given global mean-field diffusive coupling with coupling parameter ε_{intra} and the mean diffusion is controlled by the diffusion coefficient q within this group. α is the $(m \times m)$ matrix with elements 0 and 1 to represent the components of m -dimensional oscillator taking part in the intra-group coupling. Here, we are taking α to be a diagonal matrix; $\alpha = \text{diag}(\alpha_1, \alpha_2, \dots, \alpha_m)$. For external coupling of each of the oscillators with common environment we use ε_{ext} as coupling parameter and again to decide the component of oscillator to receive the external coupling we use β as the m -dimensional column matrix.

In this paper, we use Stuart–Landau oscillators ($m = 2$; x and y variables) as the unit component of the group and a damped environment as the external common medium (with damping constant k). We are taking α to be $\alpha = \text{diag}(1, 0)$ such that only x -variable will take part in within the group coupling. We take $\beta = (0, 1)$, i.e. the y -variable of each Stuart–Landau oscillator gives and receives signals from the damped common medium. So the dynamics of the full system comprised of the group of Stuart–Landau oscillators and the common external medium is:

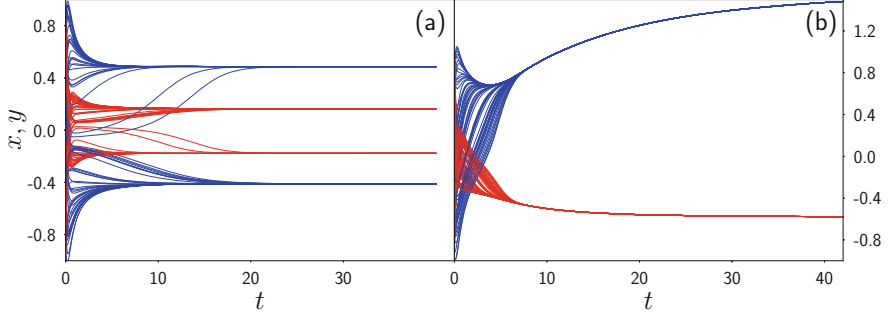


Fig. 2 Time series of x variable (red) and y variable (blue) with $\varepsilon_{intra} = 6$, $q = 0.4$ (a) without external coupling and (b) with externally coupled with $\varepsilon_{ext} = 0.5$, $k = 0.1$ for $N = 64$ oscillators in the group

$$\begin{aligned}\dot{x}_i &= (1 - x_i^2 - y_i^2)x_i - \omega y_i + \varepsilon_{intra}(q\bar{x} - x_i) \\ \dot{y}_i &= (1 - x_i^2 - y_i^2)y_i + \omega x_i + \varepsilon_{ext}u \\ \dot{u} &= -ku + \varepsilon_{ext}\bar{y}\end{aligned}\quad (2)$$

The mean-field diffusive coupling has been observed to show oscillation death (OD) states in limit cycle oscillators in the parameter space of coupling parameter ε and control parameter q . Here we consider the group in the OD-state, with $\varepsilon = 6$ and $q = 0.4$ (cf. time series shown in Fig. 2a). Our aim here is to analyse the effects of the common external environment on the stable OD-states. So we connect each oscillator of the group to the common external medium according to Eq. (1). The time series of the group in the presence of the common environment is shown in Fig. 2b, with $\varepsilon_{ext} = 0.5$ and the intrinsic environment damping constant $k = 0.1$. It is clearly evident that the presence of such a damped common medium results in all the oscillators of the group evolving to one of the OD states. This gives rise to a very asymmetric distribution of the oscillators among the two OD states as most oscillators now preferentially go to one particular state. Now, in the subsequent sections we will analyse mechanisms that restore this broken symmetry in the probability of obtaining an OD state in the oscillator group induced by the common medium.

3 Fractionally Disconnected Links

Previously, in Fig. 2 we saw that coupling to an external damped environment lead all the oscillators to one particular OD state, thereby breaking the symmetry of the distribution of the OD states. Now, we will disconnect the oscillator-environment links one at a time till all of the oscillators in the group are uncoupled to the external

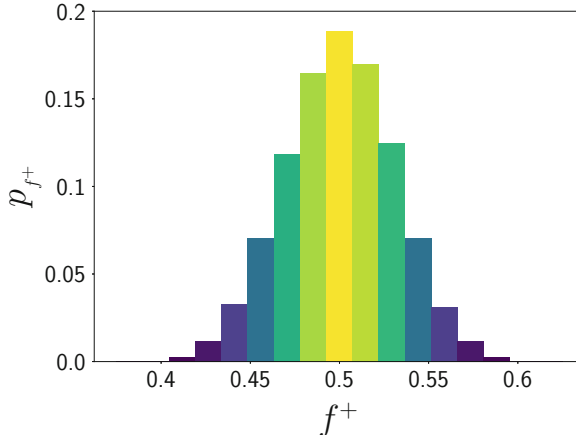


Fig. 3 Histogram showing the probability of the fraction of oscillators in positive state when the coupling of the oscillator group to the environment $\varepsilon_{ext} = 0$

medium and look for the changes in distribution of oscillators in the oscillation death states. In our case, we have two OD states on either side of the origin i.e. positive x which we will call x^+ and another on the negative side which we name x^- from now on. Without any external environment the oscillators occur almost equally (statistically speaking) in the positive and negative OD states. To quantify this observation we show in Fig. 3 the probability distribution of the oscillators in the positive x^+ steady state, obtained by sampling over 50,000 initial conditions, uniformly distributed over phase space volume $[-1, 1]$, of globally coupled SL oscillators without external environment.

In Fig. 4 we plot the fraction of oscillators that go to the positive OD state (x^+) with respect to varying number of oscillator-environment links. In particular, we disconnect one environment-oscillator link at a time, and we denote the fraction of disconnected links by f_{disc} . So $f_{disc} = 0$ corresponds to the case where all oscillators in the group are connected to the external environment, while $f_{disc} = 1$ corresponds to the limit of a group of SL oscillators having no interactions with the common environment. We observe changes in the fraction of oscillators in the positive OD-state, averaged over different initial conditions, denoted by $\langle f^+ \rangle$, as a function of f_{disc} . That is, we investigate how the distribution of the oscillators between the two available OD states changes as the number of environment-oscillator links changes. The results of the dependence of $\langle f^+ \rangle$ on f_{disc} for different values of external environment coupling ($\varepsilon_{ext} = 0.2$ and 0.5) are displayed. It is clear that this dependence is *non-monotonic* and has several non-trivial features. For instance, if we consider the case of $\varepsilon = 0.5$ in Fig. 4, we find that at $f_{disc} \simeq 0.2$ the oscillators are predominately in the negative OD state and $\langle f^+ \rangle \simeq 0.2$, i.e. around 20% of the oscillators in the group go to the positive OD state, while the rest are attracted to the negative OD state. As we change f_{disc} the probability of being in the

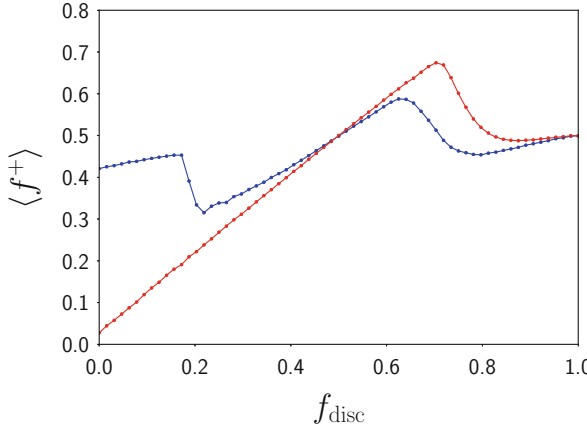


Fig. 4 Average fraction of oscillators in positive OD-state ($\langle f^+ \rangle$), obtained by sampling over 10,000 initial conditions, with respect to the fraction of oscillators-environment links for $\varepsilon_{ext} = 0.2$ (blue) and 0.5 (red). Here $N = 64$ and $k = 0.1$

positive OD state increases to a maximum of $\langle f^+ \rangle \simeq 0.7$ at $f_{disc} \simeq 0.7$. After that, $\langle f^+ \rangle$ decreases again and reaches 0.5, namely the completely symmetric situation, in the limit of $f_{disc} = 1$ where we have completely disconnected the oscillator group from the environment. One remarkable observation is that at $f_{disc} \simeq 0.5$ the value of $\langle f^+ \rangle$ is 0.5. This implies that when half of the oscillators are connected with the external common medium the statistical symmetry of the OD states returns i.e. both the positive and negative OD states are equally occupied by the oscillators. So when half of the oscillators in the group are connected to the environment ($f_{disc} = 0.5$) we obtain a dynamical outcome that is equivalent to the case of the oscillator group being completely unconnected to the external environment ($f_{disc} = 1$).

Further, we examine the effect of the damping constant k of the external environment on the distribution of the oscillators between the positive and negative OD-states, i.e. the dependence of $\langle f^+ \rangle$ and $\langle f^- \rangle$ on k for different values of f_{disc} . To illustrate this, we show results for three values of external coupling ($\varepsilon_{ext} = 0.25, 0.5$, and 0.7) in Fig. 5. For $f_{disc} = 0.25$ (blue), the fraction of positive OD-state ($\langle f^+ \rangle$) always remains less than 50% for the entire range of k sampled, and it slowly increases to $\sim 50\%$ for $k \geq 0.85$. The oscillator distribution tends to maintain its symmetry (i.e. $\langle f^+ \rangle \sim 0.5$) for all values of k when only half of the oscillators are connected/disconnected with the external environment (i.e. $f_{disc} = 0.5$). For $f_{disc} = 0.7$ (green) the oscillator distribution reaches its most skewed position when $\langle f^+ \rangle$ becomes maximum at ~ 0.7 (cf. Fig. 4). On increasing k , this again approaches $\langle f^+ \rangle \sim 0.5$ as k approaches 1. This suggests that the environmental damping constant can be utilized as a parameter to control the distribution of oscillators in the positive and negative OD-states.

The coupling strength between the external medium and the oscillators in the group (ε_{ext}) is vital in controlling the flow of information between the group of

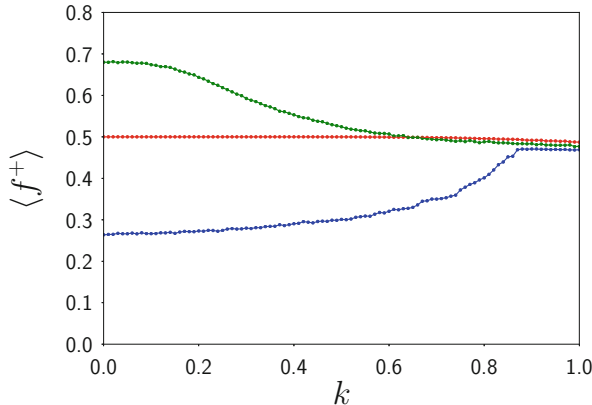


Fig. 5 Average fraction of oscillators in positive OD-state ($\langle f^+ \rangle$), obtained by sampling over 10,000 initial conditions, with respect the damping constant of the common external environment k , for $f_{disc} = 0.25$ (blue), 0.5 (red), and 0.7 (green). Here $\varepsilon_{ext} = 0.5$ and $N = 64$

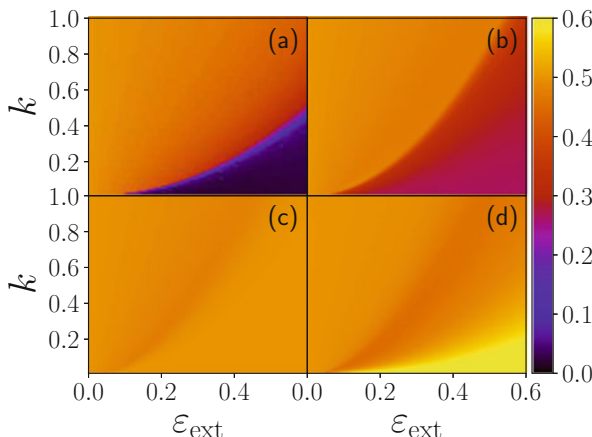


Fig. 6 Average fraction of oscillators in positive OD-state ($\langle f^+ \rangle$), estimated by sampling over 10,000 initial conditions, in the parameter space of $\varepsilon_{ext} - k$ for f_{disc} **(a)** 0.0, **(b)** 0.25, **(c)** 0.5 and **(d)** 0.75, with $N = 64$

oscillators. So we look for changes in $\langle f^+ \rangle$ in the parameter space of $\varepsilon_{ext} - k$. Figure 6a shows $\langle f^+ \rangle$ when all oscillators are connected to the environment (i.e. $f_{disc} = 0.0$). This will act as a reference for comparison with the case where some fraction of environment-oscillator links are disconnected. For higher ε_{ext} values and lower damping constant (k) the fraction $\langle f^+ \rangle$ is almost 0 (or $\langle f^- \rangle \simeq 1$). Interestingly, at this particular region of the $\varepsilon_{ext} - k$ parameter space, $\langle f^+ \rangle$ increases for increasing f_{disc} . This demonstrates that as increasing number of disconnections of the environment-oscillator links, the number of oscillators going to the positive

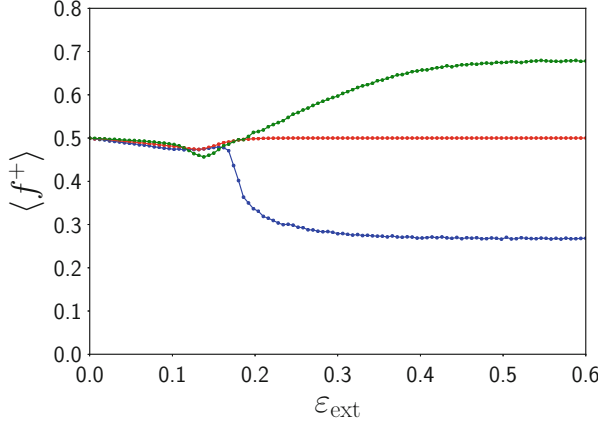


Fig. 7 Average fraction of oscillators in positive OD-state ($\langle f^+ \rangle$), estimated by sampling over 10,000 initial conditions, with respect to ε_{ext} , for $f_{disc} = 0.25$ (blue), 0.5 (red), and 0.7 (green), with $k = 0.1$ and $N = 64$

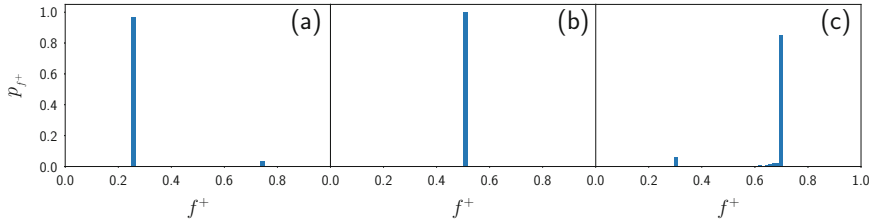


Fig. 8 Histogram showing the probability of the fraction of oscillators in positive state when the coupling of the oscillator group to the environment $\varepsilon_{ext} = 0.5$ and damping constant of the environment $k = 0.1$, with fraction of disconnected links (a) $f_{disc} = 0.25$, (b) $f_{disc} = 0.5$, (c) $f_{disc} = 0.7$

OD state increases, leading to a more symmetric distribution of oscillators among the two OD states. Further we consider the variation of $\langle f^+ \rangle$ with respect to ε_{ext} at fixed k in Fig. 7, for $k = 0.1$. Three scenarios become clearly evident from the figure, corresponding to three different fractions of disconnected links. So we can conclude that along with environmental damping constant (k), oscillator-environment coupling strength (ε_{ext}) is also an important parameter controlling the distribution of oscillators between the positive and negative OD-states.

We had shown the histogram of the probability of obtaining fraction f^+ in the positive OD state, in Fig. 3, for globally coupled SL oscillators in OD-state without environmental coupling, and seen a symmetric distribution of the oscillators around 0.5. Similarly, we now estimate the distribution of oscillators in the positive OD-state in the presence of a common environment. We explore cases with different fractions of disconnected environment-oscillator links. In Fig. 8a we show the distribution for $f_{disc} = 0.25$, with $\varepsilon_{ext} = 0.5$ and $k = 0.1$. Interestingly, there

is no spread in the distribution of oscillators, as is clearly seen from the single pronounced peak in the distribution at 0.5 for Fig. 8b and around 0.7 in Fig. 8c. This sharp localization of oscillators in one of the two available stable states is in contradistinction to the usual statistical spread observed in Fig. 3. This is especially remarkable for the case of the symmetric distribution that arises in Fig. 8b, vis-a-vis the statistically symmetric case seen in Fig. 3. So we can infer that one can tailor the distribution of oscillators in positive and negative OD-states by disconnecting a suitable number of environment-oscillator links (f_{disc}) and adjusting the control parameters ε_{ext} and k .

4 Discussion

We investigated the impact of a common environment, which acts as a common external system, on a group of Stuart–Landau oscillators. First, we considered the group of oscillators completely disconnected from the external environment. When there is no coupling to an external system, and the group of Stuart–Landau oscillators are only coupled to each other via mean-field interaction, one obtains a completely symmetric distribution of oscillation death states, i.e. half of the oscillators attain positive OD states and other half attain negative OD states. This symmetry is significantly broken, when the same group of oscillators are connected to an external common environment. The symmetry breaking depends on damping constant of the external system k , environment-oscillator coupling strength ε_{ext} and the fraction of oscillators connected to the external system. When very few oscillators are connected to the environment, the OD states are almost symmetrically distributed. On the other hand when a large fraction of oscillators are coupled to the environment, the symmetry is broken to a very high extent, for high environment-oscillator coupling strengths and low environmental damping constants. Interestingly, when half the environment-oscillator links are disconnected, the symmetry is restored, independent of the damping constant of the environment and the environment-oscillator coupling strength. In fact in this case, exactly half of the oscillators attain positive OD states and the other half attain negative OD states. So our work here suggests a potent method to control the basin stability of the oscillation death states.

References

1. Wolf, J., Heinrich, R.: Dynamics of two-component biochemical systems in interacting cells; synchronization and desynchronization of oscillations and multiple steady states. *BioSystems* **43**, 1–24 (1997)
2. Wolf, J., Heinrich, R.: Effect of cellular interaction on glycolytic oscillations in yeast: a theoretical investigation. *Biochem J.* **345**, 321–334 (2000)

3. Geier, F., Becker-Weimann, S., Kramer, A., Herzel, H.: Entrainment in a model of the mammalian circadian oscillator. *J. Biol. Rhythms* **20**, 83–93 (2005)
4. Chaurasia, S.S., Yadav, M., Sinha, S.: Environment-induced symmetry breaking of the oscillation-death state. *Phys. Rev. E* **98**, 032223 (2018)
5. Yadav, M., Sharma, A., Shrimali, M.D., Sinha, S.: Revival of oscillations via common environment. *Nonlinear Dyn.* **91**, 2219 (2018)
6. Koseska, A., Volkov, E., Kurths, J.: Oscillation quenching mechanisms, amplitude vs. oscillation death. *Phys. Rep.* **531**, 173–199 (2013)
7. Hens, C.R., Olusola, O.I., Pal, P., Dana, S.K.: Oscillation death in diffusively coupled oscillators by local repulsive link. *Phys. Rev. E* **88**, 034902 (2013)
8. Koseska, A., Volkov, E., Kurths, J.: Parameter mismatches and oscillation death in coupled oscillators. *Chaos* **20**, 023132 (2010)
9. Menck, P.J., Heitzig, J., Marwan, N., Kurths, J.: How basin stability complements the linear-stability paradigm. *Nat. Phys.* **9**, 89–92 (2013)
10. Sharma, A., Shrimali, M.D.: Amplitude death with mean-field diffusion. *Phys. Rev. E* **85**, 057204 (2012)

The Occurrence of Zero-Hopf Bifurcation in a Generalized Sprott A System



Marcelo Messias and Alisson C. Reinol

Abstract From the normal form of polynomial differential systems in \mathbb{R}^3 having a sphere as invariant algebraic surface, we obtain a class of quadratic systems depending on ten real parameters, which encompasses the well-known Sprott A system. For this reason, we call them *generalized Sprott A systems*. In this paper, we study the dynamics and bifurcations of these systems as the parameters are varied. We prove that, for certain parameter values, the z -axis is a line of equilibria, the origin is a non-isolated zero-Hopf equilibrium point, and the phase space is foliated by concentric invariant spheres. By using the averaging theory we prove that a small linearly stable periodic orbit bifurcates from the zero-Hopf equilibrium point at the origin. Finally, we numerically show the existence of nested invariant tori around the bifurcating periodic orbit.

Keywords Sprott A system · Invariant sphere · Zero-Hopf bifurcation · Linearly stable periodic orbit · Invariant torus

1 Introduction

Consider the polynomial differential system in \mathbb{R}^3 defined by

$$\dot{x} = P(x, y, z), \quad \dot{y} = Q(x, y, z), \quad \dot{z} = R(x, y, z), \quad (1)$$

where P , Q , and R are relatively prime real polynomials in the variables x , y , z and the dot denotes derivative with respect to the independent variable t . We say that

M. Messias (✉)

Universidade Estadual Paulista (UNESP), Faculdade de Ciências e Tecnologia, Departamento de

Matemática e Computação, Presidente Prudente, SP, Brazil

e-mail: marcelo.messias1@unesp.br

A. C. Reinol

Universidade Tecnológica Federal do Paraná (UTFPR), Departamento Acadêmico de
Matemática, Apucarana, PR, Brazil

$m = \max\{\deg(P), \deg(Q), \deg(R)\}$ is the *degree* of system (1). If $m = 2$, it is a quadratic polynomial differential system.

For $m \geq 2$, the dynamical behavior of system (1) is in general very difficult to be studied, especially when it exhibits chaos. In the last decades, chaotic differential systems have been intensively studied, as the Lorenz system, Chen system, Lü system, and many others [1]. Recently, there is an increasing interest in finding and studying three categories of chaotic systems: without equilibrium points, with an infinity of equilibria, and with only stable equilibrium points. In these systems are frequently found attractors whose basin of attraction does not intercept with points in small neighborhoods of equilibrium points. These kinds of attractors are called *hidden attractors* and have theoretical and applied interests. They allow, for instance, unexpected and potentially disastrous responses to perturbations in structures like bridges and airplane wings, for details see [2, 3] and references therein.

The oldest and best-known chaotic differential system having no equilibrium points is the *Sprott A system* [4], given by

$$\dot{x} = y, \quad \dot{y} = -x - yz, \quad \dot{z} = y^2 - a, \quad (2)$$

where $a \in \mathbb{R}$. This system was shown to be chaotic for $a = 1$, even without having equilibrium points for this parameter value. From the physical point of view, the Sprott A system is a special case of the well-known and widely studied Nosé–Hoover oscillator [5, 6] as pointed out in [7]. Moreover, it plays an important role in nonlinear dynamics studies, since its structure became source of inspiration for the study of many new quadratic chaotic differential systems in \mathbb{R}^3 . Chaotic systems without equilibrium points, as the Sprott A system, appear naturally in the mathematical modeling of some electromechanical problems with rotation and in electrical circuits with cylindrical phase space, as presented for instance in [8]. In this way, the bifurcation analysis of these kind of systems helps to better understand the phenomena described by them.

In this context and motivated by the studies developed in [9, 10], we propose and study a more general class of quadratic polynomial differential systems which contains the Sprott A system and have similar, and even richer, dynamical behavior. Here we call these systems *generalized Sprott A systems*, which are given by

$$\dot{x} = -y P_1 + z P_2, \quad \dot{y} = x P_1 - z P_3, \quad \dot{z} = -x P_2 + y P_3 - \alpha, \quad (3)$$

where $P_i = P_i(x, y, z) = a_i x + b_i y + c_i z + d_i$ with $\alpha, a_i, b_i, c_i, d_i \in \mathbb{R}$, for $i = 1, 2, 3$. Taking $d_1 = -1, b_3 = 1, \alpha = a$, and the other parameters equal to zero into system (3), we obtain the Sprott A system (2).

In this paper, we study the dynamical behavior of system (3) as the parameter value α varies and under certain conditions on the other parameters. The paper is organized as follows. In Sect. 2 we prove that system (3) is the most general quadratic differential system in \mathbb{R}^3 having a family of concentric invariant spheres and give some additional properties of its phase space. In Sect. 3, for the sake of

completeness and to fix the notation we present a result of the averaging theory of first order, then we use it to prove the existence of a small linearly stable periodic orbit bifurcating from the origin of system (3). In Sect. 4 we present some numerical simulations from which we show the existence of nested invariant tori around the bifurcating periodic orbit. Finally, in Sect. 5 some concluding remarks are given.

2 Invariant Spheres of Generalized Sprott A System

In [11], the authors determined the normal form of all polynomial differential systems in \mathbb{R}^3 having a sphere as an invariant algebraic surface. More precisely, they proved the following result.

Theorem 1 *Assume that a sphere $S = 0$ is an invariant algebraic surface of the polynomial differential system (1). Then, after an affine change of coordinates, system (1) can be written as*

$$\dot{x} = S Q_1 - y P_1 + z P_2, \quad \dot{y} = S Q_2 + x P_1 - z P_3, \quad \dot{z} = S Q_3 - x P_2 + y P_3, \quad (4)$$

where $Q_i = Q_i(x, y, z)$ and $P_i = P_i(x, y, z)$, for $i = 1, 2, 3$, are arbitrary real polynomials and $S = x^2 + y^2 + z^2 - 1 = 0$ is the invariant sphere of system (4).

The following result holds.

Theorem 2 *For $\alpha = 0$, system (3) is the most general class of quadratic polynomial differential systems whose phase space is foliated by concentric invariant spheres. In this case, if $d_1 \neq 0$ and $c_i = d_i = 0$, for $i = 2, 3$, then the z -axis is a line of equilibrium points, the origin is a non-isolated zero-Hopf equilibrium point and it is the center of the invariant spheres.*

Proof Suppose that system (1) has degree $m = 2$ and $S = 0$ is an invariant sphere of this system. By Theorem 1, after an affine change of coordinates, system (1) can be written as (4), with $Q_i = q_i$ and $P_i = a_i x + b_i y + c_i z + d_i$, where $a_i, b_i, c_i, d_i, q_i \in \mathbb{R}$, for $i = 1, 2, 3$, and the equation of the invariant sphere is $S = x^2 + y^2 + z^2 - 1 = 0$, with cofactor $K = 2q_1 x + 2q_2 y + 2q_3 z$. If $K \equiv 0$ then the phase space of system (4) is foliated by concentric invariant spheres. Observe that it is equivalent to take $q_1 = q_2 = q_3 = 0$, from which we obtain system (3) with $\alpha = 0$.

Now considering the flow of system (3), with $\alpha = 0$, restricted to the z -axis, we obtain

$$\dot{x} = z(c_2 z + d_2), \quad \dot{y} = -z(c_3 z + d_3), \quad \dot{z} = 0.$$

Then taking $c_i = d_i = 0$, for $i = 2, 3$, the z -axis is a line of equilibrium points of system (3). The eigenvalues of the linear part of system (3) at the origin are

$\lambda_1 = 0$ and $\lambda_{2,3} = \pm i d_1$. Hence, for $d_1 \neq 0$, the origin is a non-isolated zero-Hopf equilibrium point. This proves Theorem 2. \square

Remark 1 The eigenvalues of the linear part of system (3) at the equilibrium points in the z -axis are $\lambda_1 = 0$ and $\lambda_{2,3} = \beta z \pm \sqrt{\gamma}$, where

$$\begin{aligned}\beta &= \frac{1}{2} (a_2 - b_3) \quad \text{and} \\ \gamma &= \frac{1}{4} z^2 (a_2 + b_3)^2 - (c_1 z + d_1)^2 + z [(a_3 + b_2)(z c_1 + d_1) - a_3 z b_2].\end{aligned}$$

Hence, if $\gamma \neq 0$ and $\beta^2 z^2 > |\gamma|$, then the equilibrium points $(0, 0, z)$ with $z < 0$ and $z > 0$ have opposite stability, as it occurs in the Sprott A system, as shown in [9, 10].

3 Zero-Hopf Bifurcation via Averaging Theory

Recall that an equilibrium point of a differential system in \mathbb{R}^3 is a *zero-Hopf equilibrium* if the Jacobian matrix at this point has one zero and a pair of purely imaginary eigenvalues. It is known that, generically, a zero-Hopf bifurcation takes place in this kind of equilibrium point and, in some cases, this type of bifurcation can imply a local birth of chaos [12]. For $\alpha = 0$, $d_i \neq 0$ and $c_i = d_i = 0$, $i = 2, 3$, the origin is a zero-Hopf equilibrium point of system (3), as stated in Theorem 2. In this section we will use the averaging theory to prove the existence of a periodic orbit bifurcating from the origin of system (3). For the sake of completeness and to fix the notation which will be used ahead, in the next subsection we present the main result from averaging theory, whose proof can be found in [13].

3.1 Averaging Theory of First Order

Consider the initial value problems

$$\dot{\mathbf{x}} = \varepsilon F_1(t, \mathbf{x}) + \varepsilon^2 F_2(t, \mathbf{x}, \varepsilon), \quad \mathbf{x}(0) = \mathbf{x}_0, \quad (5)$$

and

$$\dot{\mathbf{y}} = \varepsilon g(\mathbf{y}), \quad \mathbf{y}(0) = \mathbf{x}_0, \quad (6)$$

with \mathbf{x} , \mathbf{y} , and \mathbf{x}_0 in some open subset Ω of \mathbb{R}^n , $t \in [0, \infty)$, and $\varepsilon \in (0, \varepsilon_0]$, for some fixed $\varepsilon_0 > 0$ small enough. Suppose that F_1 and F_2 are periodic functions of period T in the variable t , and set

$$g(\mathbf{y}) = \frac{1}{T} \int_0^T F_1(t, \mathbf{y}) dt.$$

Denote by $D_{\mathbf{x}}g$ and $D_{\mathbf{x}\mathbf{x}}g$ all the first and second derivatives of g , respectively. Under these assumptions, the following result is proved in [13].

Theorem 3 *Let F_1 , $D_{\mathbf{x}}F_1$, $D_{\mathbf{x}\mathbf{x}}F_1$, and $D_{\mathbf{x}}F_2$ be continuous and bounded by a constant, which does not depend on ε , in $[0, \infty) \times \Omega \times (0, \varepsilon_0]$ and assume that $\mathbf{y}(t) \in \Omega$ for $t \in [0, 1/\varepsilon]$. Then, the following statements hold.*

1. *For $t \in [0, 1/\varepsilon]$, we have $\mathbf{x}(t) - \mathbf{y}(t) = \mathcal{O}(\varepsilon)$ as $\varepsilon \rightarrow 0$.*
2. *If $p \neq 0$ is an equilibrium point of system (6) such that $\det[D_{\mathbf{y}}g(p)] \neq 0$, then system (5) has a periodic solution $\phi(t, \varepsilon)$ of period T , which is close to p and such that $\phi(0, \varepsilon) - p = \mathcal{O}(\varepsilon)$ as $\varepsilon \rightarrow 0$.*
3. *The stability of the periodic solution $\phi(t, \varepsilon)$ is given by the stability of the equilibrium point p .*

Based on Theorem 3, in the next subsection we provide necessary conditions under the parameters of system (3) for the existence of a periodic orbit bifurcating from the origin.

3.2 Existence of a Periodic Orbit

Theorem 4 *Consider system (3) with $d_1 \neq 0$ and $c_i = d_i = 0$, for $i = 2, 3$. If $b_2 = a_3$ and $b_3 - a_2 \neq 0$, then, for $\alpha > 0$ sufficiently small, there exists a periodic orbit γ_α in the phase space of system (3), which tends to the non-isolated zero-Hopf equilibrium point at the origin as $\alpha \rightarrow 0$. Moreover, γ_α is linearly stable if $a_2 < b_3$ and it is unstable (of saddle type) if $a_2 > b_3$.*

Proof Consider system (3) with $c_i = d_i = 0$, for $i = 2, 3$, $b_2 = a_3$, and $d_1 \neq 0$. Without loss of generality, take $d_1 = 1$. In order to apply Theorem 3, we write the obtained system in cylindrical coordinates (r, θ, z) , where $x = r \cos \theta$ and $y = r \sin \theta$. Then it becomes

$$\begin{aligned} \dot{r} &= [-b_3 + (a_2 + b_3) \cos^2 \theta] r z, \\ \dot{\theta} &= 1 - (a_3 - c_1) z + b_1 r \sin \theta + [a_1 r - z (a_2 + b_3) \sin \theta] \cos \theta, \\ \dot{z} &= b_3 r^2 - (a_2 + b_3) r^2 \cos^2 \theta - \alpha. \end{aligned} \quad (7)$$

Introduce the variable $\varepsilon > 0$ into system (7) considering $\alpha = \varepsilon^2$ and doing the change of coordinates $(r, \theta, z) \rightarrow (R, \theta, Z)$, where $r = \varepsilon R$ and $z = \varepsilon Z$. Then, taking θ as the independent variable and doing the Taylor expansion of order 2 of the obtained equations at $\varepsilon = 0$, we get

$$\begin{aligned}\frac{dR}{d\theta} &= -R Z [b_3 - (a_2 + b_3) \cos^2 \theta] \varepsilon + \mathcal{O}(\varepsilon^2), \\ \frac{dZ}{d\theta} &= -[1 - b_3 R^2 + (a_2 + b_3) R^2 \cos^2 \theta] \varepsilon + \mathcal{O}(\varepsilon^2).\end{aligned}\tag{8}$$

Using the notation of Theorem 3, consider

$$\begin{aligned}\mathbf{x} &= \begin{pmatrix} R \\ Z \end{pmatrix}, \quad t = \theta, \quad T = 2\pi, \\ F_1(\theta, \mathbf{x}) &= \begin{pmatrix} -[b_3 - (a_2 + b_3) \cos^2 \theta] R Z \\ -[1 - b_3 R^2 + (a_2 + b_3) R^2 \cos^2 \theta] \end{pmatrix}.\end{aligned}$$

In this way we have

$$g(\mathbf{y}) = \frac{1}{2\pi} \int_0^{2\pi} F_1(\theta, \mathbf{x}) d\theta = \frac{1}{2} \begin{pmatrix} -(b_3 - a_2) R Z \\ -2 + (b_3 - a_2) R^2 \end{pmatrix}.$$

Hence, $g(\mathbf{y}) = 0$ has the unique real solution

$$p = (R, Z) = \left(\sqrt{\frac{2}{b_3 - a_2}}, 0 \right),$$

which satisfies $\det[D_{\mathbf{y}}g(p)] = b_3 - a_2 \neq 0$. Then, by Theorem 3, for $\varepsilon > 0$ sufficiently small, system (8) has a periodic solution $\phi(\theta, \varepsilon) = (R(\theta, \varepsilon), Z(\theta, \varepsilon))$ such that $\phi(0, \varepsilon) \rightarrow p$ as $\varepsilon \rightarrow 0$. Moreover the eigenvalues of the matrix $[D_{\mathbf{y}}g(p)]$ are $\pm\sqrt{a_2 - b_3}$. Thus, the obtained periodic orbit is linearly stable if $a_2 - b_3 < 0$ and unstable (of saddle type) if $a_2 - b_3 > 0$.

Changing back the coordinates to system (3), we have that, for $\alpha > 0$ sufficiently small, such system has a periodic solution γ_α of period approximately 2π given by

$$x_\alpha(t) = \sqrt{\frac{2\alpha}{b_3 - a_2}} \cos t + \mathcal{O}(\alpha), \quad y_\alpha(t) = \sqrt{\frac{2\alpha}{b_3 - a_2}} \sin t + \mathcal{O}(\alpha), \quad z_\alpha(t) = \mathcal{O}(\alpha).$$

Note that γ_α tends to the origin, which is a non-isolated zero-Hopf equilibrium point, as $\alpha \rightarrow 0$. \square

4 Existence of Nested Invariant Tori

Under generic assumptions, the presence of a linearly stable periodic orbit implies the occurrence of rich dynamics: it forces, for example, the existence of a subset of positive measure in the phase space filled by invariant tori, as stated for instance in

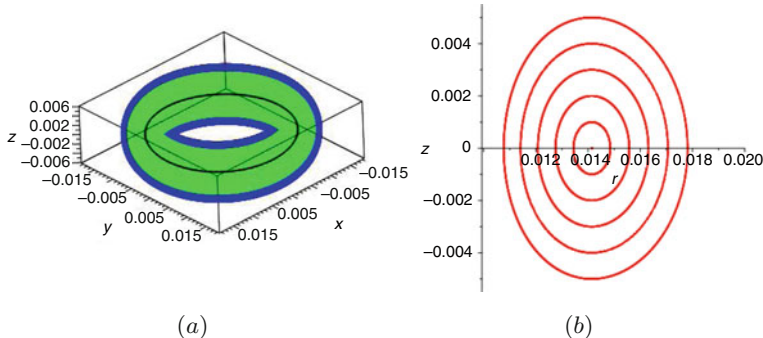


Fig. 1 (a) Periodic orbit and nested invariant tori of system (3) with $c_2 = c_3 = d_2 = d_3 = 0$, $a_1 = a_2 = a_3 = b_1 = b_2 = c_1 = d_1 = 1$ and $b_3 = 2$. (b) Respective 2π -Poincaré map of system (3). In both cases $\alpha = 10^{-4}$

[12]. In this context, in [9, 10] the authors showed the existence of nested invariant tori surrounding a bifurcating linearly stable periodic orbit in the phase space of the Sprott A system. Performing a detailed numerical study, we obtained the following similar result for the more general differential system (3).

Numerical Result Around the linearly stable periodic orbit γ_α of differential system (3) with $\alpha > 0$ small, described in Theorem 4, there exist nested invariant tori, as shown in Fig. 1.

In Fig. 1a is shown the nested invariant tori around the periodic orbit γ_α of system (3) for $\alpha > 0$ small and, in Fig. 1b, its respective 2π -Poincaré map, which was obtained as follows. We consider system (3) in cylindrical coordinates (r, θ, z) and take θ as the independent variable, obtaining a system in the variables $(r(\theta), z(\theta))$, 2π -periodic in θ . We compute the solutions of the obtained system, taking initial conditions near of the periodic orbit γ_α , for discrete values $\theta = 2k\pi$, where $k = 0, 1, \dots, N$, with N sufficiently large, obtaining Fig. 1b. The fixed point representing the periodic orbit γ_α , given in Theorem 4, is surrounded by concentric circles, suggesting the existence of nested invariant tori around it.

It is also possible to explain the existence of invariant tori as a deformation of invariant spheres. Indeed, for $\alpha = 0$, $d_i \neq 0$ and $c_i = d_i = 0$, $i = 2, 3$, we proved in Theorem 2 that the phase space of system (3) is foliated by invariant spheres and the z -axis is a line of equilibria. For suitable choices of the parameter values (see Remark 1) and for z small, the equilibrium points in the z -axis are foci with opposite stability for $z < 0$ and $z > 0$. In this case, there exist heteroclinic orbits on each invariant sphere, connecting the (unstable) south pole to the (stable) north pole, see Fig. 2a. For $\alpha > 0$ sufficiently small, a linearly stable periodic orbit γ_α bifurcates from the origin of system (3), as stated in Theorem 4 and shown in black color in Fig. 2b. Based on the numerical simulations performed, it is possible to observe that the concentric invariant spheres evolve to nested invariant tori around the periodic

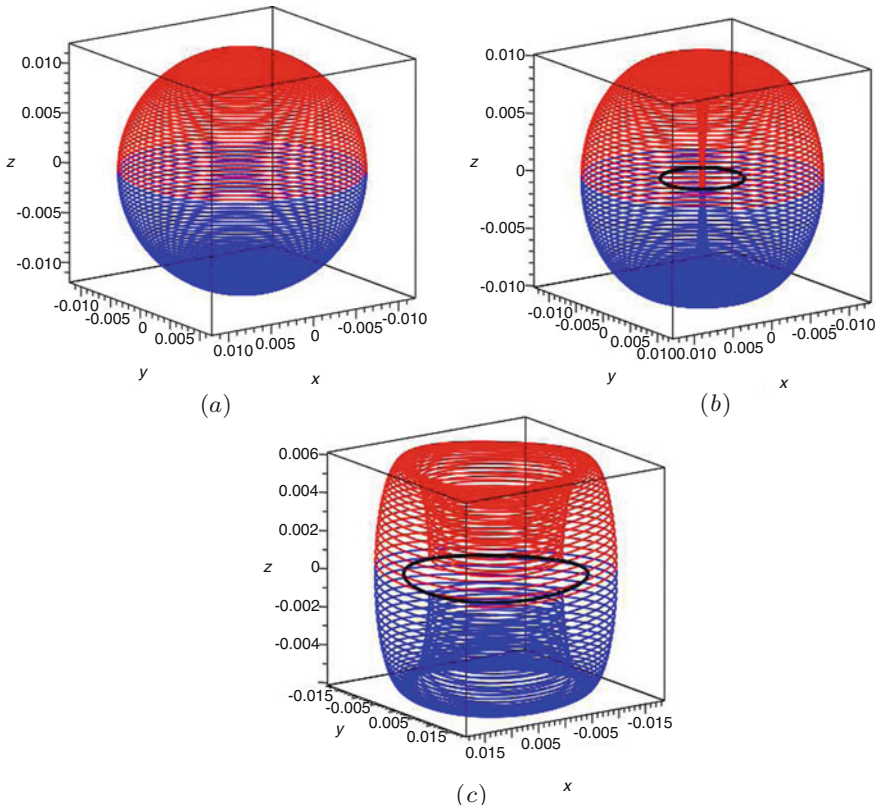


Fig. 2 Periodic orbit γ_α of system (3) (black) and orbit with initial condition $(\sqrt{2\alpha/(b_3 - a_2)}, 1.2 \cdot 10^{-2}, 0)$ for $t < 0$ (blue) and $t > 0$ (red), with $c_2 = c_3 = d_2 = d_3 = 0$, $a_1 = a_2 = a_3 = b_1 = b_2 = c_1 = d_1 = 1$ and $b_3 = 2$. For the parameter α we consider: **(a)** $\alpha = 0$, **(b)** $\alpha = 10^{-5}$, and **(c)** $\alpha = 10^{-4}$

orbit γ_α , as the parameter α increases, as shown in Fig. 2a–c, considering one of the concentric invariant spheres.

5 Concluding Remarks

Whereas the Sprott A system is claimed to be the simplest conservative differential system presenting chaotic behavior, in this paper we consider system (3), which is a more general and comprehensive class of differential systems containing and presenting similar dynamical behavior to the Sprott A system, for small values of the parameter α . In this way, system (3) can contain other nonlinear oscillators besides the Nosé–Hoover oscillator (or the Sprott A system). For appropriate choices of parameters values in system (3), we proved that for $\alpha > 0$ small enough a linearly

stable periodic orbit bifurcates from a zero-Hopf equilibrium point located at the origin and we numerically show the existence of nested invariant tori around the periodic orbit. These elements can generate complex and interesting dynamical behavior, as shown in [4, 6, 9, 10] for Sprott A system, where the existence of a linearly stable periodic orbit and nested invariant tori around it play an important role in the formation of chaotic behavior in that system. We believe that the same is true for the more general system (3). It will be studied in future works.

Acknowledgements The first author was supported by State of São Paulo Foundation (FAPESP) grant number 2019/10269-3 and by CNPq-Brazil grant number 311355/2018-8.

References

1. Lassoued, A., Boubaker, O.: On new chaotic and hyperchaotic systems: a literature survey. *Nonlinear Anal. Model. Control* **21**, 770–789 (2016)
2. Dudkowski, D., Jafari, S., Kapitaniak, T., Kuznetsov, N., Leonov, G.A., Prasad, A.: Hidden attractors in dynamical systems. *Phys. Rep.* **637**, 1–50 (2016)
3. Leonov, G.A., Kuznetsov, N.V.: Hidden attractors in dynamical systems: from hidden oscillations in Hilbert–Kolmogorov, Aizerman and Kalman problems to hidden chaotic attractor in Chua circuits. *Int. J. Bifurcation Chaos Appl. Sci. Eng.* **23**, 1330002 (2013)
4. Sprott, J.C.: Some simple chaotic flows. *Phys. Rev. E* **50**, R647–R650 (1994)
5. Nosé, S.: A unified formulation of the constant temperature molecular-dynamics methods. *J. Chem. Phys.* **81**, 511–519 (1984)
6. Posch, H.A., Hoover, W.G., Vesely, F.J.: Canonical dynamics of the Nosé oscillator: stability, order, and chaos. *Phys. Rev. A* **33**, 4253–4265 (1986)
7. Hoover, W.G.: Remark on ‘some simple chaotic flows’. *Phys. Rev. E* **51**, 759–760 (1995)
8. Kiseleva, M.A., Kuznetsov, N.V., Leonov, G.A.: Hidden attractors in electromechanical systems with and without equilibria. *IFAC-PapersOnLine* **49**, 51–55 (2016)
9. Messias, M., Reinol, A.C.: On the formation of hidden chaotic attractors and nested invariant tori in the Sprott A system. *Nonlinear Dyn.* **88**, 807–821 (2017)
10. Messias, M., Reinol, A.C.: On the existence of periodic orbits and KAM tori in the Sprott A system—a special case of the Nosé–Hoover oscillator. *Nonlinear Dyn.* **92**, 1287–1297 (2018)
11. Llibre, J., Messias, M., Reinol, A.C.: Normal forms for polynomial differential systems in \mathbb{R}^3 having an invariant quadric and a Darboux invariant. *Int. J. Bifurcation Chaos Appl. Sci. Eng.* **25**, 1550015 (2015)
12. Scheurle, J., Marsden, J.: Bifurcation to quasi-periodic tori in the interaction of steady state and Hopf bifurcations. *SIAM J. Math. Anal.* **15**, 1055–1074 (1984)
13. Sanders, J.A., Verhulst, F., Murdock, J.: *Averaging Methods in Nonlinear Dynamical Systems*. Springer, New York (2007)

Part III

**Nonlinear Phenomena in Mechanical
Systems and Structures**

External and Internal Resonances in a Mass-Spring-Damper System with 3-dof



Jan Awrejcewicz, Roman Starosta, and Grażyna Sypniewska-Kamińska

Abstract The chapter deals with the analytical investigation of the physical pendulum mounted on the spring-damper suspension. The pendulum exhibits three degrees of freedom in plane motion. Three types of external loading and viscous damping are considered. The method of multiple scales is used to solve the initial value problem defined through Lagrange formalism. The proposed analytical method allows for the prediction of resonance conditions. The amplitude-frequency response curves have been determined for the external resonance, and their stability has been assessed using the Routh–Hurwitz criterion. The modulation equations of the amplitudes and phases are the basis for studying the impact of the chosen parameters on the internal resonance 1:2.

Keywords Plane pendulum · Asymptotic analysis · Resonance

1 Introduction

The pendulum-like systems may serve as a reliable model for many machine and measurement devices, manipulators, and the human body parts [1–3]. Moreover, they can be used to develop, test, and validate the new approaches employed to study the dynamics of multi-body systems. The pendulums could exhibit very complicated behavior due to the strong nonlinearity of a geometrical nature and coupling between their components [4].

Many pendulum-like systems are analytically studied in reference [5]. The asymptotic approach aimed at analyzing the kinematically excited spring pendulum near parametric resonances is presented in [6, 7].

J. Awrejcewicz

Department of Automation Biomechanics and Mechatronics, Lodz University of Technology,
Lodz, Poland

R. Starosta (✉) · G. Sypniewska-Kamińska

Institute of Applied Mechanics, Poznań University of Technology, Poznań, Poland
e-mail: roman.starosta@put.poznan.pl

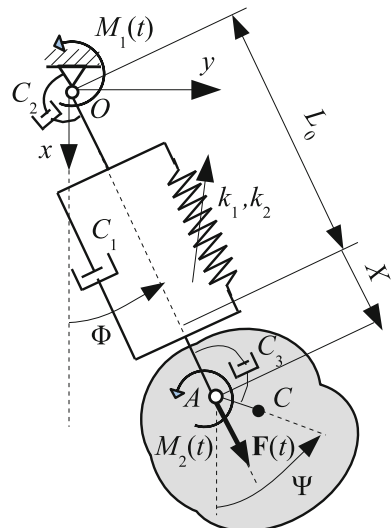
The application of the multiple-scale method (MSM) allows one to perform a qualitative analysis of the behavior of the system, for instance, to recognize all possible resonance conditions which can appear in the system. Here, we analyze the external and internal resonances of the spring physical pendulum. The present work extends the investigations presented in [6] by introducing a more reliable model of damping at the joints, considering the internal resonance and using three time scales in the MSM solution, which is not an easy task.

2 Description of the Problem

The physical model of the system is presented in Fig. 1. We assume that the spring is massless and nonlinear. The nonlinearity of the spring is of a cubic type, where k_1 and k_2 are constant elastic coefficients. L_0 denotes the nominal length of the spring. The viscous damper and the spring are set up in parallel to one another. The distance between the point A and the body mass center C is denoted by S and called the eccentricity. The body moment of inertia relative to the axis passing through the center of mass C and perpendicular to the plane of motion is denoted by I_c . The relative rotation around joints O and A is attenuated by viscous dampers. The coefficients C_1 , C_2 , and C_3 correspond to the damping forces. The motion is excited by the harmonic force \mathbf{F} acting along the direction OA , where $F(t) = F_0 \cos \Omega_1 t$, and by two torques $M_1(t) = M_{01} \cos (\Omega_2 t)$ and $M_2(t) = M_{02} \cos (\Omega_3 t)$.

Since the motion is considered in the vertical plane, the body has three degrees of freedom. The total elongation of the spring $X(t)$ and two angles $\Phi(t)$ and $\Psi(t)$ stand for the generalized coordinates. The spring elongation at the static equilibrium denoted by X_r satisfies the following equation

Fig. 1 Spring physical pendulum with 3-dof



$$k_2 X_r^3 + k_1 X_r = mg. \quad (1)$$

The kinetic and potential energies of the system are as follows:

$$\begin{aligned} T &= mS\dot{\Psi}(\dot{X}\sin(\phi - \Psi) + \dot{\Phi}(L_0 + X)\cos(\Phi - \Psi)) \\ &\quad + \frac{m}{2} \left(R_A^2 \dot{\Psi}^2 + (L_0 + X)^2 \dot{\Phi}^2 + \dot{X}^2 \right), \end{aligned} \quad (2)$$

$$V = \frac{1}{2}k_1 X^2 + \frac{1}{4}k_2 X^4 - mg((L_0 + X)\cos\Phi + S\cos\Psi), \quad (3)$$

where R_A is the radius of gyration of the body with respect to the axis passing through the joint A and perpendicular to the plane of motion.

3 Mathematical Model

The governing equations have been derived using Lagrange's formalism. All external and damping forces are treated as the generalized forces. The dimensionless form of the equations of motion is as follows:

$$\ddot{\xi} + c_1 \dot{\xi} + \xi + \alpha \xi^3 + 3\xi_r \alpha \xi^2 + 3\xi_r^2 \alpha \xi - w_2^2 (\cos\varphi - 1) - s \cos(\varphi - \gamma) \dot{\gamma}^2 + s \sin(\varphi - \gamma) \ddot{\gamma} = f_1 \cos(p_1 \tau), \quad (4)$$

$$\begin{aligned} \ddot{\varphi}(1 + \xi)^2 + w_2^2 \sin\varphi(1 + \xi) + c_2 \dot{\varphi} + 2\dot{\xi}\dot{\varphi} + 2\xi\dot{\xi}\dot{\varphi} \\ + s(1 + \xi) \dot{\gamma}^2 \sin(\varphi - \gamma) + s(1 + \xi) \ddot{\gamma} \cos(\varphi - \gamma) = f_2 \cos(p_2 \tau), \end{aligned} \quad (5)$$

$$\begin{aligned} \ddot{\gamma} + w_3^2 \sin\gamma + c_3 \dot{\gamma} + 2\frac{w_3^2}{w_2^2} \dot{\xi} \dot{\varphi} \cos(\varphi - \gamma) - \frac{w_3^2}{w_2^2} (1 + \xi) \dot{\varphi}^2 \sin(\varphi - \gamma) \\ + \frac{w_3^2}{w_2^2} \ddot{\xi} \sin(\varphi - \gamma) + \frac{w_3^2}{w_2^2} \ddot{\varphi} \cos(\varphi - \gamma) = f_3 \cos(p_3 \tau), \end{aligned} \quad (6)$$

where $\tau = \omega_1 t$ is the dimensionless time and $\omega_1 = \sqrt{k_1/m}$.

The functions $\xi(\tau)$, $\varphi(\tau)$, and $\gamma(\tau)$ correspond to the generalized coordinates $X(t)$, $\Phi(t)$, and $\Psi(t)$, respectively. The dimensionless static elongation of the spring $\xi_r = \frac{X_r}{L}$ and it satisfies the equilibrium equation

$$\alpha \xi_r^3 + \xi_r = w_2^2. \quad (7)$$

Taking ω_1 as a reference quantity, the other dimensionless parameters are defined in the following manner.

$$c_1 = \frac{C_1}{m\omega_1}, c_2 = \frac{C_2}{mL^2\omega_1}, c_3 = \frac{C_3}{mL^2\omega_1 r_A^2}, f_1 = \frac{F_0}{mL\omega_1^2}, f_2 = \frac{M_{01}}{mL^2\omega_1^2}, f_3 = \frac{M_{01}}{mL^2\omega_1^2 r_A^2}, \\ \alpha = \frac{k_2 L^2}{\omega_1^2 m}, w_2 = \frac{\omega_2}{\omega_1}, w_3 = \frac{\omega_3}{\omega_1}, p_1 = \frac{\Omega_1}{\omega_1}, p_2 = \frac{\Omega_2}{\omega_1}, p_3 = \frac{\Omega_3}{\omega_1}, \omega_2^2 = \frac{g}{L}, \omega_3^2 = \frac{Sg}{R_A^2}, \\ s = \frac{S}{L}, \xi = \frac{X}{L} \text{ and } L = L_0 + X_r.$$

Equations (4–6) are supplemented by the following initial conditions

$$\xi(0)=u_{01}, \quad \dot{\xi}(0)=u_{02}, \quad \varphi(0)=u_{03}, \quad \dot{\varphi}(0)=u_{04}, \quad \gamma(0)=u_{05}, \quad \dot{\gamma}(0)=u_{06}, \quad (8)$$

where the dimensionless quantities u_{01}, \dots, u_{06} are known a priori.

4 Approximate Analytical Solution

The initial value problem (4–8) is solved using the method of multiple scales (MMS) in the time domain. The trigonometric functions of the generalized coordinates in Eqs. (4–6) are replaced by their power series, whereas the expansion is truncated up to the third order (small oscillations around an equilibrium position are considered).

The functions ξ , φ , and γ are approximated by the power series with respect to the small perturbation parameter ε in the following way

$$\begin{aligned} \xi &= \sum_{k=1}^3 x_k(\tau_0, \tau_1, \tau_2) + O(\varepsilon^4), \\ \varphi &= \sum_{k=1}^3 \phi_k(\tau_0, \tau_1, \tau_2) + O(\varepsilon^4), \\ \gamma &= \sum_{k=1}^3 \chi_k(\tau_0, \tau_1, \tau_2) + O(\varepsilon^4), \end{aligned} \quad (9)$$

where $\tau_0 = \tau$, $\tau_1 = \varepsilon\tau$, $\tau_2 = \varepsilon^2\tau$ are time scales.

The amplitudes of the generalized forces, the damping coefficients, the eccentricity, and the nonlinearity parameter are assumed to be small, and hence we take.

$$f_k = \varepsilon^3 \tilde{f}_k, \quad c_k = \varepsilon^3 \tilde{c}_k, \quad e = \varepsilon^2 \tilde{e}, \quad \alpha = \varepsilon^2 \tilde{\alpha}, \quad k = 1, 2, 3. \quad (10)$$

The above assumptions and the series (9) are introduced into governing Eqs. (4–6), and the ordinary derivatives are replaced by the differential operators for complex functions (9). In this way, we obtain three equations containing small parameter ε of various powers. These equations should be satisfied for any value

of ε , so after sorting them with respect to powers of the small parameter, we get three sets of equations of the first-, second-, and third-order approximation, and solve them recurrently. The solving procedure has been described in detail in [6, 7]. The solutions to the first-order approximation equations are as follows:

$$x_1 = \frac{a_1}{2\varepsilon} e^{i(\tau_0+\psi_1)} + \text{CC}, \quad \phi_1 = \frac{a_2}{2\varepsilon} e^{i(\tau_0+\psi_2)} + \text{CC}, \quad \chi_1 = \frac{a_3}{2\varepsilon} e^{i(\tau_0+\psi_3)} + \text{CC}, \quad (11)$$

where real-valued functions $a_i(\tau_1, \tau_2)$ and $\psi_i(\tau_1, \tau_2)$ for $i = 1, 2, 3$ correspond to amplitudes and phases, and CC denotes complex conjugates.

Apart from the approximate analytical solution to the problem (3–8), MSM allows to indicate the conditions for:

1. main resonances: $p_1 \approx 1, p_2 \approx w_2, p_3 \approx w_3$
2. internal and combined resonances: $w_2 \approx \frac{1}{2}, w_2 \approx w_3, w_3 \approx \frac{1}{2}, p_2 \approx w_3, w_3 \approx 1, w_2 \approx 3w_3, w_3 \approx 3w_2, w_2 + w_3 \approx 1, w_2 - w_3 \approx 1, w_2 + w_3 \approx 2, w_2 - w_3 \approx 2$

The satisfaction of a resonance condition means that the behavior of the system becomes very complex due to a high level of energy exchange between several modes or/and with the surrounding. A significant increase in the amplitude is usually observed as a result of the interaction of various resonances.

5 External Resonance

Let us consider the case when three main resonances occur simultaneously, i.e., $p_1 \approx 1, p_2 \approx w_2, p_3 \approx w_3$. For this purpose, we introduce the so-called detuning (small) parameters $\sigma_1, \sigma_2, \sigma_3$. Then, we introduce the following relations

$$p_1 = 1 + \sigma_1, \quad p_2 = w_2 + \sigma_2, \quad p_3 = w_3 + \sigma_3 \quad (12)$$

into Eqs. (4–6). All secular terms should be eliminated because the bounded solutions are expected. This demand leads to the solvability conditions, which allow one to obtain the modulation equations for amplitudes and phases of the following form

$$\dot{a}_1 = \frac{1}{2} (-c_1 a_1 + f_1 \sin(\sigma_1 \tau - \psi_1)), \quad (13)$$

$$\dot{a}_2 = -\frac{c_3 w_2^4 + c_2 (w_2^2 - w_3^2)^2}{2(w_2^2 - w_3^2)^2} a_2 + \frac{f_2}{2w_2} \sin(\sigma_2 \tau - \psi_2), \quad (14)$$

$$\dot{a}_3 = -\frac{c_3 w_3^2 (w_2^6 - 2(s+1)w_2^4 w_3^2 + w_2^2 w_3^4 + s w_3^6)}{2s w_2^4 (w_2^2 - w_3^2)^2} a_3 + \frac{f_3 \sin(\sigma_3 \tau - \psi_3)}{2w_3}, \quad (15)$$

$$\dot{\psi}_1 = \frac{3w_2^2 (w_2^2 - 1)}{4(4w_2^2 - 1)} a_2^2 + \frac{3\xi_e^2 \alpha}{2} - \frac{f_1}{2a_1} \cos(\sigma_1 \tau - \psi_1), \quad (16)$$

$$\begin{aligned} \dot{\psi}_2 = & \frac{w_2 (w_2^2 - 1) (12a_1^2 - (1 + 8w_2^2) a_2^2)}{16(4w_2^2 - 1)} \\ & + \frac{sw_2 w_3^2 (4w_2^4 + (3s - 8)w_2^2 w_3^3 + (4 - 7s)w_3^4)}{8(w_2^2 - w_3^2)^3} - \frac{f_2}{2w_2 a_2} \cos(\sigma_2 \tau - \psi_2), \end{aligned} \quad (17)$$

$$\begin{aligned} \dot{\psi}_3 = & -\frac{c_3^2 w_3^3}{8s^2 w_2^4} - \frac{sw_3^5 (4w_2^6 - 8w_2^4 w_3^2 + (4 - 7s)w_2^2 w_3^4 + 3s w_3^6)}{8w_2^4 (w_2^2 - w_3^2)^3} \\ & - \frac{w_3^3 a_1^2}{4w_2^4 (4w_3^2 - 1)} + \frac{w_3^3 (w_3^2 - 2w_2^2) a_2^2}{8(w_2^2 - w_3^2)^2} - \frac{w_3 a_3^2}{16} - \frac{f_3 \cos(\sigma_3 \tau - \psi_3)}{2w_3 a_3}. \end{aligned} \quad (18)$$

The modulation Eqs. (13–18) are crucial in the qualitative analysis of the steady and unsteady motion near resonance. Some examples of the resonance curves for the parameters: $\alpha = 0.01$, $f_1 = f_2 = f_3 = 0.0001$, $c_1 = c_2 = 0.001$, $c_3 = 0.0001$, $w_2 = 0.3676$, $w_3 = 0.244$, $s = 0.02$, $\sigma_1 = -0.01$, $\sigma_3 = -0.01$, are presented in Fig. 2. The main resonant effect concerns the angle φ . Observe that the resonance response curve is of the soft-type, and the maximal increase in the amplitude a_2 is more than four times. The values of other amplitudes decrease, while the change is much smaller for the amplitude a_3 . Red and blue parts of the resonance curves denote stable and unstable branches, respectively. The stability estimation is carried out using the Routh–Hurwitz criterion for the perturbed linearized modulation equations.

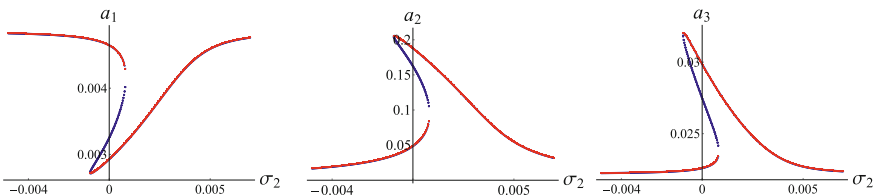


Fig. 2 Resonance curves for the external resonance

6 Internal Resonance

Let us consider the internal resonance $w_3 \approx 1 : 2$ which occurs due to the coupling between two generalized coordinates ξ and γ . For this purpose, we introduce the detuning parameter σ in the following manner

$$w_3 = \frac{1}{2} + \sigma. \quad (19)$$

The modulation equations which describe the internal resonance have the form

$$\dot{a}_1 = \frac{1}{8} \left(-4c_1 a_1 + s a_3^2 \sin(\psi_1 - 2\psi_3) \right), \quad (20)$$

$$\dot{a}_2 = -\frac{c_2 - 8c_2 w_2^2 + 16(c_2 + c_3) w_2^4}{2(4w_2^2 - 1)^2} a_2, \quad (21)$$

$$\begin{aligned} \dot{a}_3 = & \frac{c_3 (-s - 4w_2^2 + 32(1+s)w_2^4 - 64w_2^6) a_3}{32s w_2^4 (4w_2^2 - 1)^2} \\ & + \frac{(-s + 4(s-1)w_2^2 + 4(8+s)w_2^4 - 64w_2^6) a_1 a_3 \sin(\psi_1 - 2\psi_3)}{32w_2^4 (1 - 4w_2^2)^2}, \end{aligned} \quad (22)$$

$$\dot{\psi}_1 = \frac{3w_2^2 (w_2^2 - 1)}{4(4w_2^2 - 1)} a_2^2 + \frac{3\xi_e^2 \alpha}{2} + \frac{s a_3^2 \cos(\psi_1 - 2\psi_3)}{8a_1}, \quad (23)$$

$$\begin{aligned} \dot{\psi}_2 = & \frac{s w_2 (4 - 7s + 4(-8 + 3s)w_2^2 + 64w_2^4)}{8(4w_2^2 - 1)^3} \\ & - \frac{w_2 (w_2^2 - 1) (-12a_1^2 + (1 + 8w_2^2) a_2^2)}{16 (4w_2^2 - 1)}, \end{aligned} \quad (24)$$

$$\begin{aligned} \dot{\psi}_3 = & \frac{3a_1^2}{128w_2^4} + \frac{(s - 4(-1 + s)w_2^2 - 4(8 + s)w_2^4 + 64w_2^6)a_1 \cos(\psi_1 - 2\psi_3)}{32w_2^4 (1 - 4w_2^2)^2} \\ & + \frac{-3s^4 - 4c_3^2 (4w_2^2 - 1)^3 + 4s^2 w_2^2 (7s^2 - 4s(4w_2^2 - 1)^2 + 64w_2^2 (4w_2^2 - 1)^3 \sigma)}{256s^2 w_2^4 (4w_2^2 - 1)^3} \\ & + \frac{1}{32} \left(\frac{2(1 - 8w_2^2) a_2^2}{(1 - 4w_2^2)^2} - a_3^2 \right). \end{aligned} \quad (25)$$

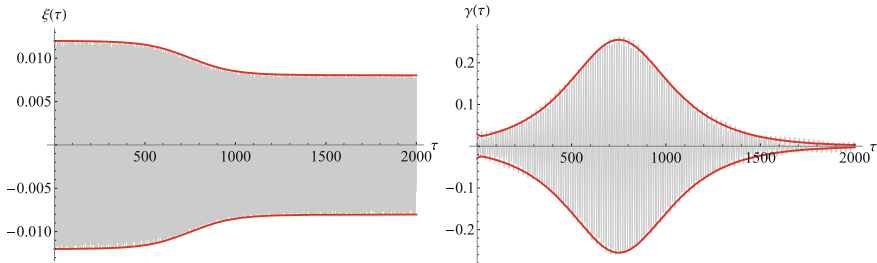


Fig. 3 Time histories of the general coordinates ξ and γ in the case of the internal resonance

The solution to Eqs. (20–25), obtained numerically, allows one to complement the approximate solution obtained using MMS. Moreover, the modulation equations can be used to study the internal resonance.

The time histories of the generalized coordinates ξ and γ , which interact with each other in the case of the internal resonance, are presented in Fig. 3. The calculations were carried out for the following values of the parameters: $\alpha = 0.03$, $w_2 = 0.243$, $s = 0.001$, $c_1 = c_2 = c_3 = 0.00001$, $f_1 = f_2 = f_3 = 0.0001$, $p_1 = 0.287$, $p_2 = 0.105$, $p_3 = 0.00893$, $\sigma = -0.001$, $a_{10} = 0.012$, $a_{20} = 0.008$, $a_{30} = 0.03$, $\psi_{10} = \psi_{20} = \psi_{30} = 0$.

The red solid curves (envelopes) of the fast-changing oscillations represent the amplitudes $a_1(\tau)$ and $a_3(\tau)$, respectively.

The graphs reported in Fig. 4 show the influence of some parameters on the shape of the modulation curves. It turns out that damping at the joint A has the crucial impact on the form of the amplitude modulation. From Fig. 4, one can note that there is a critical value of the damping c_3 , for which the internal resonance is revealed by just one peak of the amplitude a_3 . This peak is accompanied by a decrease in the amplitude a_1 occurring at the same time interval. However, for $c_3 = 5.2 \cdot 10^{-6}$ (red line), the second local maximum of the amplitude a_3 appears.

When the value of c_3 decreases more, the modulation process becomes oscillating, and the subsequent maxima start disappearing. The exclusion of the damping coefficient c_3 from the model yields periodic amplitude changes as shown in Fig. 5.

Any small damping in the joint A significantly weakens the resonance effects between the generalized coordinates ξ and γ related to the longitudinal vibration and the rotation of the body.

7 Concluding Remarks

The mathematical model governing the motion of the three-degree-of-freedom physical spring pendulum has been derived. The solution to the initial value problem has been solved using the method of multiple scales in the time domain. The solutions have been achieved up to the third-order approximation. Their analytical

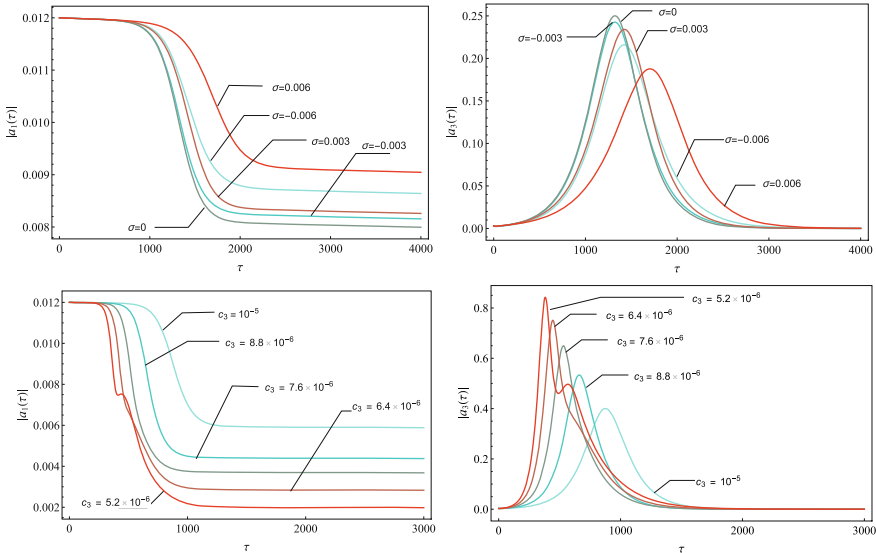


Fig. 4 Influence of the detuning parameter σ and the damping coefficient c_3 on the modulation curves associated with the general coordinates ξ and γ in the internal resonance

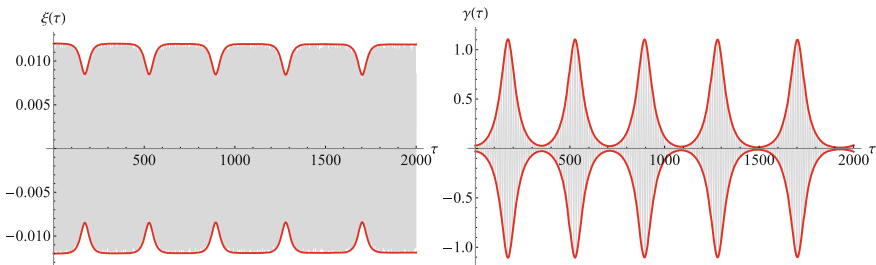


Fig. 5 The resonant modulation curves related to the general coordinates ξ and γ for $c_3 = 0$

form allows for a comprehensive analysis of the motion of the system for a wide spectrum of parameters.

The pendulum exhibits complex behavior, especially near resonance. Two resonant cases have been studied: three main simultaneous resonances and an internal resonance coupling generalized coordinates ξ and γ . The modulation equations allow for a qualitative and quantitative analysis of motion. In the steady state, which is possible for the main resonance, the amplitude curves and their stability have been presented. The correctness of the analytical results has been validated by the numerical simulation.

The equations allow one to analyze the system behavior in the space of amplitudes and phases (or modified phases) using the idea of the so-called limiting phase trajectory, which has been discussed in [8].

References

1. Parks, H.V., Faller, J.E.: A simple pendulum laser interferometer for determining the gravitational constant. *Philos Trans A Math Phys Eng Sci.* **372**(2026), 20140024 (2014)
2. Lefrancois, S., Gosselin, C.: Point-to-point motion control of a pendulum-like 3-dof underactuated cable-driven robot. In: Proceedings of the 2010 IEEE International Conference on Robotics and Automation, ICRA 2010, 3–7, pp. 5187–5193 (2010)
3. Loram, I.D., Lakie, M.: Human balancing of an inverted pendulum: position control by small, ballistic-like, throw and catch movements. *J. Physiol.* **540**(Pt 3), 1111–1124 (2002)
4. Starosvetsky, Y., Gendelman, O.V.: Dynamics of a strongly nonlinear vibration absorber coupled to a harmonically excited two-degree-of-freedom system. *J. Sound Vib.* **312**, 234–256 (2008)
5. Sado, D.: Regular and Chaotic Vibration of Some Systems with Pendula. WNT, Warsaw (2010). (in Polish)
6. Starosta, R., Sypniewska-Kamińska, G., Awrejcewicz, J.: Plane motion of a rigid body suspended on nonlinear spring-damper. In: Problems of Nonlinear Mechanics and Physics of Materials, pp. 157–170. Springer, Switzerland (2018)
7. Awrejcewicz, J., Starosta, R., Sypniewska-Kamińska, G.: Asymptotic analysis of resonances in nonlinear vibrations of the 3-dof pendulum. *Differ. Equ. Dyn. Syst.* **21**(1&2), 123–140 (2013)
8. Manevitch, L.I., Musienko, A.I.: Limiting phase trajectories and energy exchange between anharmonic oscillator and external force. *Nonlinear Dynam.* **58**, 633–642 (2009)

Internal Resonances in an Imperfect Circular Cylindrical Panel



Frederico M. A. Silva Wanclaine A. Vaz and Paulo B. Gonçalves

Abstract The aim of the present work is to investigate the influence of initial geometric imperfections on a slender cylindrical panel nonlinear response, considering the presence of internal resonances. Nonlinear Donnell shallow shell theory is used to obtain the nonlinear equations of motion. To obtain a consistent modal solution, the transversal displacement field is obtained from a perturbation technique which takes into account the phenomena of modal coupling and interaction in simply supported cylindrical panels. Then, the standard Galerkin method is applied to reduce the problem to a system of differential equations in time domain to obtain the backbone curves, which is solved by using the shooting method. The resonance curves are obtained by continuation methods displaying a complex bifurcation scenario. The influence of the shape and amplitude of the geometrical imperfection on the resonance curves is investigated.

Keywords Cylindrical panel · Modal coupling · Modal interaction · Geometrical imperfections · Nonlinear dynamics

1 Theoretical Formulation

Slender cylindrical panels are circular sectors of the cylindrical shells and can be described by the theory of the slender shallow shells. Despite a simple geometry, the slenderness of this element makes it susceptible to loss of stability and excessive vibrations when subjected to static and dynamic loads, which can lead the structure to damage or even collapse. Among the many important nonlinear phenomena exhibited by cylindrical panels, modal coupling due to the geometric nonlinearities

F. M. A. Silva () · W. A. Vaz

School of Civil and Environmental Engineering, Federal University of Goiás, Goiânia, Brazil
e-mail: silvafma@ufg.br

P. B. Gonçalves

Department of Civil Engineering, Pontifical Catholic University, Rio de Janeiro, Brazil
e-mail: paulo@puc-rio.br

and modal interaction that occurs when different buckling modes have the same critical load or different vibration modes have proportional natural frequency [1, 2]. Therefore, this study aims to contribute to the understanding of the phenomena of modal coupling and modal interaction in simply supported cylindrical panels with a geometrical imperfection [1, 6].

For the mathematical formulation, Donnell's nonlinear shallow shell theory is used, considering that the cylindrical panel is simply supported and subjected to a time-dependent transversal load. The material is assumed as linear, homogeneous, and isotropic. The transversal equation of motion and the compatibility equation are given in terms of the transversal displacement w and Airy stress function f respectively by:

$$\begin{aligned} \rho h \ddot{w} + 2\eta_1 \rho h \Omega_0 \dot{w} + D \left(w_{,xxxx} + \frac{2}{R^2} w_{,\theta\theta xx} + \frac{1}{R^4} w_{x\theta\theta\theta} \right) - f_{,\theta\theta} (w_{,x} + w_{0,x})_{,x} \\ + R f_{,xx} - f_{,xx} (w_{,\theta} + w_{0,\theta})_{,\theta} - 2f_{x\theta} (w_{,\theta x} + w_{0,\theta x}) - p(t) = 0 \end{aligned} \quad (1)$$

$$\frac{\nabla^4 f}{Eh} = \frac{1}{R^4} \left(w_{,x\theta}^2 - w_{,xx} w_{,\theta\theta} + R w_{,xx} + 2w_{,x\theta} w_{0,x\theta} - w_{,xx} w_{0,\theta\theta} - w_{,\theta\theta} w_{0,xx} \right) \quad (2)$$

where $D(=Eh^3/12(1 - \nu^2))$ is the flexural stiffness, η_1 is the viscous damping coefficient, E is the Young's modulus, ν is the Poisson coefficient, ρ is the mass density, Ω_0 is the natural frequency of perfect cylindrical panel, R is the radius of curvature, h is the cylindrical panel thickness. The initial geometrical imperfection is described by a pre-defined function w_0 .

The transversal harmonic pressure load is given by:

$$p(t) = pl \sin(nr) \sin(mq) \cos(\Omega t) \quad (3)$$

where $r = \pi\theta/\Theta$, $q = \pi x/L$, pl is load magnitude, Ω is the excitation frequency, Θ is the opening angle of cylindrical panel, and m and n are the number of axial and circumferential half-wave, respectively.

The following imperfection shapes are considered:

$$w_{01} = C_1 \sin(q) \sin(r); \quad w_{02} = C_2 \sin(q) \sin(2r); \quad w_{03} = C_3 \sin(2q) \sin(r) \quad (4)$$

where C_i ($i = 1, 3$) is the imperfection magnitude.

2 Numerical Results

In order to determine the geometries that may exhibit modal interaction, linear free vibration results are obtained for a simply supported panel, using the classical vibration modes of a simply supported cylindrical panel:

$$w(r, q, t) = w_{mn} \sin(nr) \sin(mq) \cos(\Omega t) \quad (5)$$

The adopted geometrical and material parameters are: $R = 1$ m, $h = 0.001$ m, $E = 2.06 \times 10^{11}$ N/m², $\rho = 7800$ kg/m³, and $\nu = 0.3$. Table 1 presents the data of a cylindrical panel that exhibits 1:1 internal resonance, while Table 2 shows the data of a cylindrical panel that exhibits 1:1:2 internal resonance.

The transversal displacement field is obtained by applying the perturbation technique described in [1–8]. To start the perturbation procedure, it is necessary to consider a seed solution, which in this work is the sum of the linear vibration modes involved in the internal resonance (Tables 1 and 2) [3, 4]. The perturbation procedure leads to a modal solution that considers naturally all modal coupling and interaction concerning these modes. However, the obtained general modal solution is enormous and for easy understanding purpose we show only the considered modes in this work to analyze the influence of initial geometrical imperfections on the nonlinear behavior of cylindrical panels with 1:1, or 1:1:2, internal resonances.

The modal solution for the cylindrical panel with 1:1 internal resonance is given by:

$$\begin{aligned} w = & [A1_{11}(t) \sin(r) + A1_{13}(t) \sin(3r) + A2_{11}(t) \sin(2r) + A2_{13}(t) \sin(6r)] \sin(q) \\ & + \{A3_{22}(t) [3/4 - \cos(2r) + 1/4 \cos(4r)] \\ & + A4_{22}(t) [3/4 - \cos(4r) + 1/4 \cos(8r)]\} [3/4 - \cos(2q) + 1/4 \cos(4q)] \end{aligned} \quad (6)$$

Table 1 Cylindrical panel with 1:1 internal resonance: geometry, imperfection magnitudes, and natural frequencies ($L = 0.1$ m)

Axial half-wave	Θ (rad)	Internal resonance	Circumferential half-wave	C_1/h	C_2/h	Natural frequency (Hz)
$m = 1$	0.1658	1:1	$n = 1$	0.0	0.0	686.29
$m = 1$			$n = 2$			686.29
				0.10	0.0	697.89
						699.64
				-0.10	0.0	673.46
						676.77
				0.0	0.10	664.66
						709.63
				0.0	-0.10	664.66
						709.63

Table 2 Geometry with modal interaction between three modes. ($\Theta = 0.169$ rad)

Axial half-wave	L (m)	Internal resonance	Circumferential half-wave	C_1/h	C_3/h	Natural frequency (Hz)
$m = 1$	0.091	1:1:2	$n = 1$	0.0	0.0	741.88
						741.88
						1483.75
			$n = 2$	0.10	0.0	755.06
						755.34
						1493.18
			$n = 1$	-0.10	0.0	729.82
						732.05
						1474.97
			$n = 3$	0.0	0.10	742.22
						745.37
						1490.33
			$n = 4$	0.0	-0.10	742.22
						745.37
						1490.33

while the modal solution for the cylindrical panel with 1:1:2 internal resonance is

$$\begin{aligned} w = & [A_{111}(t) \sin(r) + A_{211}(t) \sin(2r) + A_{213}(t) \sin(6r) + A_{313}(t) \sin(3r)] \sin(q) \\ & + [A_{311}(t) \sin(r) + A_{313}(t) \sin(3r)] \sin(2q) + \{A_{422}(t) [3/4 - \cos(2r) + 1/4 \cos(4r)] \\ & + A_{522}(t) [3/4 - \cos(4r) + 1/4 \cos(8r)]\} [3/4 - \cos(2q) + 1/4 \cos(4q)] \\ & + A_{622}(t) [3/4 - \cos(2r) + 1/4 \cos(4r)] [3/4 - \cos(4q) + 1/4 \cos(8q)] \end{aligned} \quad (7)$$

These modal solutions, Eqs. (6 and 7), ensure the convergence of the backbone and resonance curves up to vibration amplitudes of the same order as the shell thickness. These expressions satisfy the following transversal boundary conditions:

$$\begin{aligned} w(0, \theta) &= w(L, \theta) = w(x, 0) = w(x, \Theta) = 0 \\ M_x(0, \theta) &= M_x(L, \theta) = M_\theta(x, 0) = M_\theta(x, \Theta) = 0 \end{aligned} \quad (8)$$

To obtain the Airy stress function f , the modal expansion in Eq. (6), or Eq. (7), is substituted into Eq. (2), together with the chosen geometrical imperfection function, Eq. (4), and the compatibility equation is solved analytically. The obtained stress function and the chosen modal expansion are then substituted into equation of motion, Eq. (1), and discretized by using the standard Galerkin method. The nonlinear frequency-amplitude relations are determined by applying the shooting method to the reduced order discrete model [8].

Figure 1 shows the variation of the maximum normalized amplitude of the vibration mode as a function of the frequency normalized with respect to the natural frequency of perfect cylindrical panel (backbone curves). The black curve illustrates

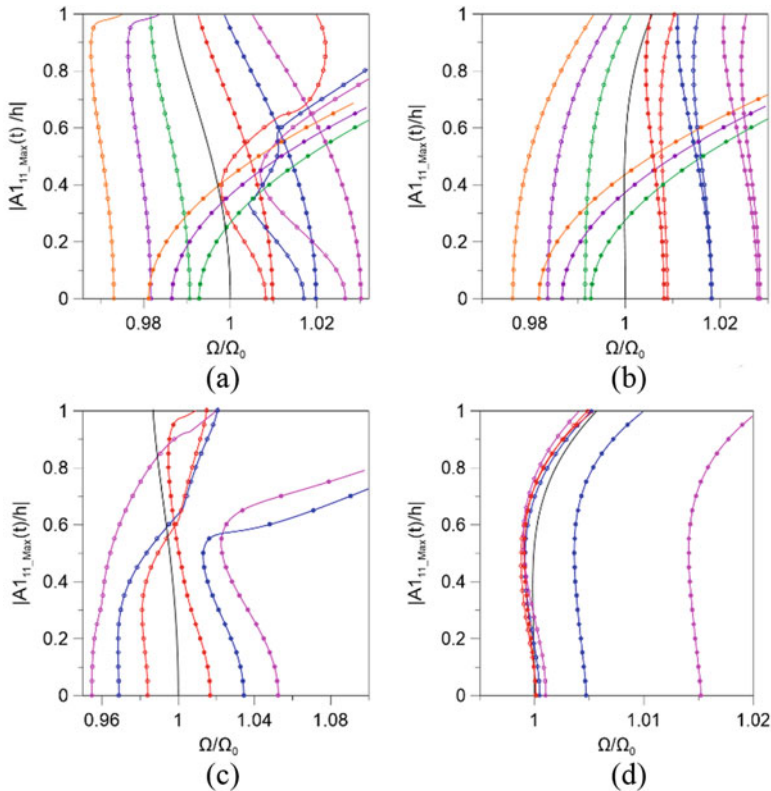


Fig. 1 Frequency-amplitude relation for (a, c) 1:1 and (b, d) 1:1:2 internal resonance cases, considering different geometrical imperfection's amplitude. (— $C_i/h = 0.0$; -·— $C_i/h = 0.05$; —·— $C_i/h = 0.10$; -·— $C_i/h = 0.15$; —·— $C_i/h = -0.05$, —·— $C_i/h = -0.10$, —·— $C_i/h = -0.15$, to $i = 1, 3$). (a) 1:1 internal resonance and imperfection in C_1 ($C_2 = 0$). (b) 1:1:2 internal resonance and imperfection in C_1 ($C_3 = 0$). (c) 1:1 internal resonance and imperfection in C_2 ($C_1 = 0$). (d) 1:1:2 internal resonance and imperfection in C_3 ($C_1 = 0$)

the response of the perfect system with equal frequencies. For the imperfect shell, the imperfection amplitude acts as a detuning parameter and the two frequencies associated with the interacting modes split apart. The backbone curve for the lowest frequency is identified by (-o-) while the backbones curves for the second value of frequency is represented by (presented symbol -·-). Positive values of C_1 increase both natural frequencies while negative values of C_1 decrease the natural frequencies. In the perfect case, the shell displays a softening behavior. For negative values of C_1 , a sudden change is observed with the first mode exhibiting a softening nonlinearity and the second mode a hardening behavior. In this case, the effect of modal interaction disappears. Positive imperfections also have a palpable influence on the backbone curves and the influence of both modes on the nonlinear response remains. Figure 1b shows the influence of the imperfection magnitude C_1

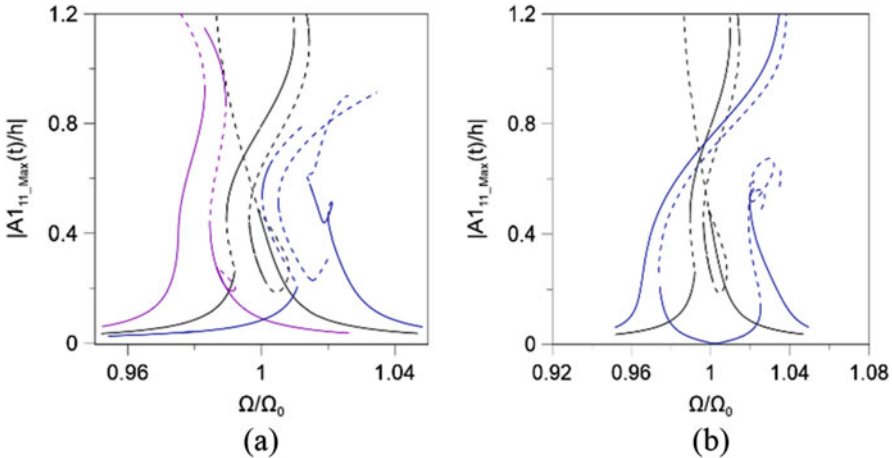


Fig. 2 Resonance curve for 1:1 internal resonance case, $pl = 1 \text{ kN/m}^2$, $\eta_1 = 0.001$, considering different geometrical amplitude of imperfection. (— $C_{1(\text{or } 2)}/h = 0.0$; — $C_{1(\text{or } 2)}/h = 0.10$; — $C_{1(\text{or } 2)}/h = -0.10$). (a) Imperfections in C_1 . (b) imperfections in C_2

on the natural frequencies and backbone curves for the panel with the 1:1:2 internal resonance. For all analyzed imperfection amplitudes, the ratio between the natural frequency of vibration modes remains close to the ideal case influencing the 1:1:2 internal resonances (see Table 2 for $C_1/h = \pm 0.10$).

Figure 1c shows the influence of the positive and negative values of C_2 on the results. The imperfection decreases the frequency to the first mode and increases the natural frequency of the second vibration mode, and the 1:1 internal resonance is destroyed (see Table 1 for $C_2/h = \pm 0.10$). On the other hand, as shown in Fig. 1d, positive and negative values of C_3 increase the natural frequency of both modes of vibration and the 1:1:2 internal resonance case is maintained (see Table 2 for $C_3/h = \pm 0.10$).

To evaluate the nonlinear forced vibrations of the simply supported cylindrical panels, a lateral distributed harmonic load is applied in the form of the first vibration mode, $m = n = 1$ in Eq. (3) is considered. The obtained resonance curves are shown in Figs. 2 and 3 for each case of internal resonance studied here. These curves were obtained by the continuation method, which allows the determination of the stable and unstable branches of solutions. In these figures, the maximum amplitude of vibration is plotted as a function of the forcing frequency. The stable paths of the resonance curve are represented by the continuous line (—) and the unstable paths are represented by the dashed line (---).

In Fig. 2a the resonance curves were obtained considering the imperfections with $C_1/h = \pm 0.10$ while in Fig. 2b the resonance curves were obtained considering the imperfections with $C_2/h = \pm 0.10$. It is observed in Fig. 2a that the geometric imperfection changes the dynamic stability scenario, creating new stable and unstable paths depending on the value of amplitude of imperfection ($C_1/h = \pm 0.10$).

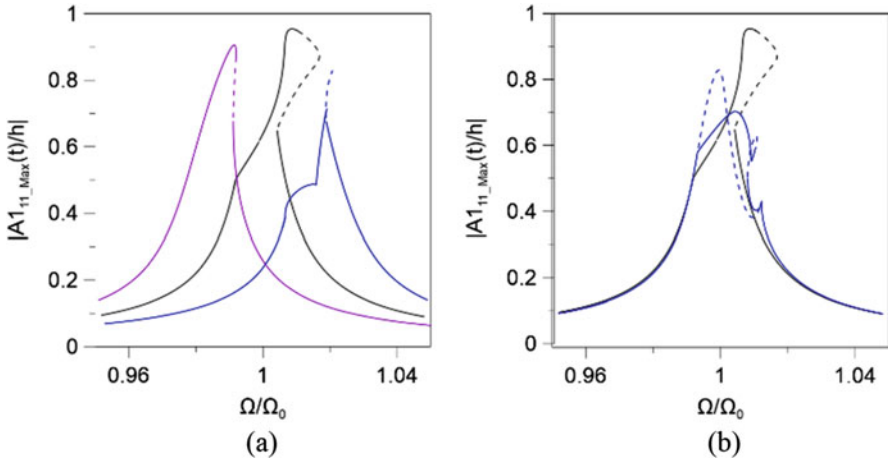


Fig. 3 Resonance curve for 1:1:2 internal resonance case. $pl = 1.5 \text{ kN/m}^2$, $\eta_1 = 0.001$, considering different geometric imperfection amplitudes. (— $C_{1(\text{or } 3)}/h = 0.0$; — $C_{1(\text{or } 3)}/h = 0.10$; — $C_{1(\text{or } 3)}/h = -0.10$). (a) Imperfections in C_1 . (b) imperfections in C_3

It is also observed in Fig. 2a that in the case of positive values of C_1 the resonance curves move to the right due to the increase in the natural frequency of cylindrical panel while for negative values the resonance curves move to the left due to the decrease in the natural frequency of cylindrical panel. In Fig. 2b, the negative and positive amplitudes of C_2 lead to coincident resonance curves but with two new resonant peaks in the vicinity of the resonant peak of perfect cylindrical panel. These changes are due to the competition of the backbones curves of both linear vibration modes.

Figure 3 shows the resonance curves for a cylindrical panel with 1:1:2 internal resonance, considering different values of imperfection magnitudes C_1 and C_3 . In Fig. 3a, the amplitude of the geometric imperfection C_1/h changes the dynamic stability of the system, the shape of the resonance curve, and the amplitude of vibration for positive values and to negative values of C_1 . In Fig. 3b, it is verified that the values of C_3 also change the dynamic stability of the system, the shape of the resonance curve, and the vibration amplitude, in addition to the coincident resonance curves for positive and negative amplitudes of C_3 .

3 Concluding Remarks

This work investigates the influence of modal coupling and modal interaction on the nonlinear free vibrations of an imperfect cylindrical panel. A new consistent modal solution is developed, which takes into account the modal interaction between two or three different modes of vibration. Significant changes in nonlinear free vibration

can be observed. The geometric imperfection magnitude and sign may increase or decrease the stiffness of the cylindrical panel, thus changing the natural frequencies. Imperfection in the second mode always decreases the stiffness of the cylindrical panel with 1:1 internal resonance case. However, the cylindrical panel displays a hardening effect when the imperfection in the form of the third vibration mode in the case of 1:1:2 internal resonances is considered. The modal interaction can be destroyed with increasing imperfections. The forced response of the cylindrical panel is also affected by the imperfection shape, size, and magnitude.

Acknowledgements This work was made possible by the support of the Brazilian Ministry of Education, CAPES, CNPq, and FAPEG.

References

1. Gonçalves, P.B., Batista, R.C.: Non-linear vibration analysis of fluid-filled cylindrical shells. *J. Sound Vib.* **127**, 133–143 (1988)
2. Gonçalves, P.B., Del Prado, Z.J.G.N.: Effect of non-linear modal interaction on the dynamic instability of axially excited cylindrical shells. *Comput. Struct.* **82**, 2621–2634 (2004)
3. Rodrigues, L., Silva, F.M.A., Gonçalves, P.B., Del Prado, Z.J.G.N.: Effects of modal coupling on the dynamics of parametrically and directly excited cylindrical shells. *Thin-Walled Struct.* **81**, 210–224 (2013)
4. Rodrigues, L., Gonçalves, P.B., Silva, F.M.A.: Internal resonances in a transversally excited imperfect circular cylindrical shell. *Procedia Eng.* **199**, 838–843 (2017)
5. Silva, F.M.A., Gonçalves, P.B., Del Prado, Z.J.G.N.: An alternative procedure for the non-linear vibration analysis of fluid-filled cylindrical shells. *Nonlinear Dynam.* **66**, 303–333 (2011)
6. Silva, F.M.A., Sattler, H.A.R., Gonçalves, P.B., Del Prado, Z.J.G.N.: Influence of modal coupling on the nonlinear vibration of simply supported cylindrical panels. *Appl. Mech. Mater.* **849**, 106–118 (2016)
7. Vaz, W.A.S., Silva, F.M.A.: Considerations about modal coupling and modal interaction for nonlinear vibrations analysis of cylindrical panels. In: 15th International Symposium on Dynamic Problems of Mechanics, pp. 1–9. ABCM, Buzios-RJ (2019).
8. Mattos, H.S.C.: Shooting method solving unidimensional strucutres (in Portuguese). *Disser-tação de Mestrado–DEM*, Pontifícia Universidade Católica do Rio de Janeiro (1984)

Weakly Nonlinear Liquid Sloshing: Modelling and Exploration of Response Regimes



Maor Farid and Oleg V. Gendelman

Abstract This chapter describes both steady-state and quasi-periodic response regimes in equivalent mechanical model of partially filled liquid storage tank which is subjected to external ground excitation. Nonlinear and moderate amplitude sloshing is considered. The sloshing mass is essentially smaller than the overall mass of the tank, so the reduced-order model (ROM) is actually equivalent to the thoroughly studied cubic nonlinear energy sink (NES). The dynamical responses captured by the ROM are qualitatively in good agreement with previous experimental, computational, and theoretical results.

Keywords Liquid sloshing · Reduced-order model · Nonlinear energy sink

1 Introduction

Partially filled liquid tanks are commonly used in various engineering fields, such as aircrafts and vehicles [1, 2]. During external excitation, sloshing takes place which can lead to significant increase in mechanical stresses in the foundations of the tank. Those resulting stresses may have significant effect of the robustness of the tank. The most hazardous sloshing regime is associated with hydraulic impacts, also referred to as vibro-impact sloshing, which usually occurs in vicinity of resonance. High amplitude sloshing is the source of significant nonlinearities which lead to richness in terms of dynamical regimes, for example, multiple periodic solutions [3], quasi-periodic [4], and strongly modulated response (SMR) [5]. Previous experimental results [6] point out that the aforementioned nonlinear regimes can be described well by a cubic nonlinearity.

In the current study, we adopt an equivalent phenomenological model with cubic nonlinearity in order to capture and describe the moderately nonlinear sloshing regimes [7–9] taking place in a seismically excited liquid storage tank. This

M. Farid (✉) · O. V. Gendelman

Faculty of Mechanical Engineering, Technion—Israel Institute of Technology, Haifa, Israel
e-mail: maorfarid@gmail.com

analysis gives one a better understanding about the occurrence of those regimes. However, some regimes cannot be described using the current model, such as three-dimensional regimes, i.e., rotary sloshing, or more violent sloshing behaviors, such as vibro-impact sloshing.

Since the sloshing mass is much smaller than the overall mass of the overall tank-liquid system, it is conceptually identical to the well-studied cubic NES [10, 11], in both mathematical description and dynamical behavior. The NES is a passive device for vibration mitigation and includes a relatively small mass which is coupled to the system via an essentially nonlinear attachment. The slow-flow dynamics of several NES designs in vicinity of 1:1 resonance can be naturally described by the slow invariant manifold (SIM). The different dynamical regimes emerging in the current system are thoroughly described using analytical tools. Theoretical results are verified numerically and compared to previous experimental and computational studies.

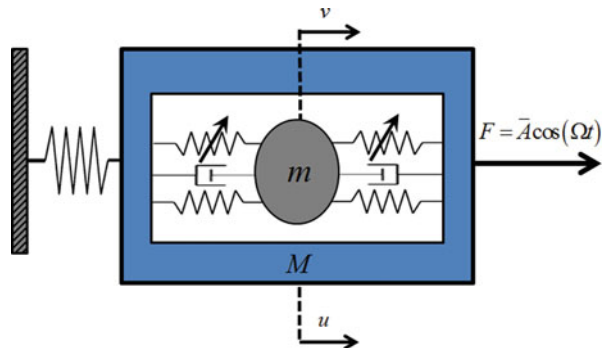
2 Model Description

As one can see in Fig. 1, the overall system of the tank and the static liquid portion is modelled by a primary structure (PS) with mass M , and the sloshing portion is modelled by an internal particle (IP) with mass m , and their absolute displacements are denoted by $u(t)$ and $v(t)$, respectively. Both masses are attached by linear and cubic springs, and a linear dashpot. The PS is subjected to harmonic excitation, with frequency Ω and amplitude \bar{A} .

As a continuous system, the internal fluid of the partially filled liquid tank can be modelled with help of an infinite series of pendula of mass-spring systems, associated with the modal masses of the infinite sloshing modes. However, it was shown [6] that those modal masses decrease drastically for higher modes. Hence, it is reasonable to consider only the lowest sloshing modes as a first approximation.

The equations of motion are obtained using Lagrangian formalism, and the following coordinate transformation is adopted: $X(\tau) = u(\tau) + \varepsilon v(\tau)$, $w(\tau) = u(\tau) - v(\tau)$:

Fig. 1 Mechanical scheme of the system



$$\begin{aligned}\ddot{X} + \frac{1+\varepsilon\sigma}{1+\varepsilon} X + \frac{\varepsilon(1+\varepsilon\sigma)}{1+\varepsilon} w &= \varepsilon A \cos(\tau) \\ \ddot{w} + \frac{1+\varepsilon\sigma}{1+\varepsilon} X + \varepsilon\eta w + (1+\varepsilon)\lambda\dot{w} + k(1+\varepsilon)w^3 &= \varepsilon A \cos(\tau)\end{aligned}\quad (1)$$

The relations between the dimensional and non-dimensional parameters are as follows:

$$\begin{aligned}\omega_1^2 &= \frac{k_1}{M}, \quad \omega_2^2 = \frac{k_2}{m}, \quad \Omega = \frac{\omega_1}{\sqrt{1+\varepsilon\sigma}}, \quad \varepsilon A = \frac{\bar{A}}{M\Omega^2} \\ \varepsilon\beta &= \left(\frac{\omega_2}{\omega_1}\right)^2 (1+\varepsilon\sigma), \quad k = \frac{\bar{k}}{m\Omega^2}, \quad \lambda = \frac{c}{m\Omega}, \quad \eta = \frac{1+\varepsilon\sigma}{1+\varepsilon} + \beta(1+\varepsilon)\end{aligned}\quad (2)$$

Differentiation with respect to dimensionless time scale $\tau = \Omega t$ is denoted by dot. The amplitude and frequency of the external excitation are denoted by εA and Ω , respectively. The natural frequencies of the PS and the IP are ω_1 and ω_2 . Non-dimensional damping and nonlinear coupling are denoted by λ and k , respectively.

3 Dynamical Regimes

In the current section, the dynamical regimes which arise in the aforementioned system will be analyzed analytically.

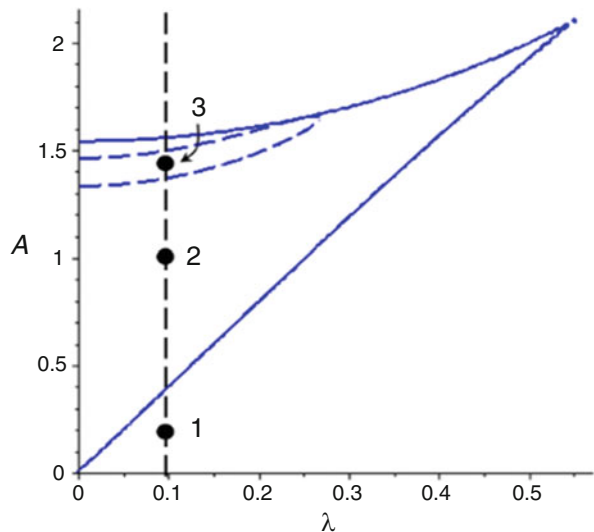
3.1 Periodic Responses

The following complex variable transformation, shown by Manevitch [12], is applied on Eq. (1): $\dot{X} + iX = \varphi_1 e^{i\tau}$, $\dot{w} + iw = \varphi_2 e^{i\tau}$. Since we are interested in dynamical regimes associated with internal resonance of 1:1, we collect merely the slow-varying terms as follows:

$$\begin{aligned}\varphi'_1 + \frac{i\varepsilon(1-\sigma)}{2(1+\varepsilon)}\varphi_1 - \frac{i\varepsilon(1+\varepsilon\sigma)}{2(1+\varepsilon)}\varphi_2 &= \frac{\varepsilon A}{2} \\ \varphi'_2 + \frac{i}{2}(1-\varepsilon\eta)\varphi_2 + \frac{\lambda(1+\varepsilon)}{2}\varphi_2 - \frac{i(1+\varepsilon\sigma)}{2(1+\varepsilon)}\varphi_1 - \frac{3ki(1+\varepsilon)}{8}|\varphi_2|^2\varphi_2 &= \frac{\varepsilon A}{2}\end{aligned}\quad (3)$$

Bar and apostrophe represent complex conjugate and differentiation with respect to time, respectively. Periodic responses correspond to stationary solutions of Eq. (3). The complex modulation functions, associated with stationary responses, are denoted by φ_{10} and φ_{20} . After neglecting the derivatives, and substituting the second equation into the first equation in Eq. (3), the following double-cubic polynomial is obtained: $\alpha_3 Z_0^3 + \alpha_2 Z_0^2 + \alpha_1 Z_0 + \alpha_4 = 0$, when $\varphi_{20} = N_0 e^{i\theta_0}$, $Z_0 = N_0^2$, and its coefficients are given by the following expressions:

Fig. 2 Boundaries of SN (solid line) and Hopf (dashed line) bifurcations on the (A, λ) plane, for $\varepsilon = 0.05$, $k = 4/3$, $\beta = 5$, $\sigma = 5$; Point 1: $A = 0.1$ a unique periodic solution; point 2: $A = 1$ coexistence of two periodic solutions; point 3: $A = 1.4$ coexistence of both multiple periodic solutions and weakly quasi-periodic responses



$$\begin{aligned} \alpha_1 &= \lambda^2 + \frac{\sigma^2}{(1-\sigma)^2} + \frac{2\beta\varepsilon\sigma}{1-\sigma} + \beta^2\varepsilon^2, & \alpha_2 &= \frac{3k}{2(1-\sigma)} (\sigma + \varepsilon\beta(1-\sigma)) \\ \alpha_3 &= \frac{9k^2}{16}, & \alpha_4 &= -\frac{A^2}{(1-\sigma)^2} \end{aligned} \quad (4)$$

Existence of multiple solutions is associated with saddle-node (SN) bifurcation, taking place when the discriminant of the aforementioned polynomial equals to zero. The SN boundary (Fig. 2, solid line) is described by the following expression:

$$3\alpha_3(\alpha_1\alpha_2 - 9\alpha_3\alpha_4)^2 + 2\alpha_2(\alpha_1\alpha_2 - 9\alpha_3\alpha_4)(6\alpha_1\alpha_3 - 2\alpha_2^2) + \alpha_1(6\alpha_1\alpha_3 - 2\alpha_2^2)^2 = 0 \quad (5)$$

In Fig. 2, the area that surrounds the solid-line curve corresponds to a unique periodic solution, while the inner corresponds to the multiple solutions. The bifurcation values of λ and A are as follows:

$$\lambda_{\text{SN,cr}} = \frac{1}{\sqrt{3}} \left| \frac{\sigma}{1-\sigma} + \varepsilon\beta \right|, \quad A_{\text{SN,cr}} = \frac{4}{9} \sqrt{\frac{2}{|k(\sigma-1)|}} (\sigma - \varepsilon\beta(\sigma-1))^{3/2} \quad (6)$$

3.2 Weak Quasi-Periodic Responses

Weak quasi-periodic solution is associated with loss of stability of the periodic solution described above and formation of limit cycles via Hopf bifurcation.

We add a small perturbation around φ_{10} and φ_{20} as follows: $\varphi_1 = \varphi_{10} + \delta_1$, $\varphi_2 = \varphi_{20} + \delta_2$, and substitute these perturbed expressions to Eq. (3). Then, we nullify the derivatives, obtaining the characteristic polynomial of the resulting system, and express its roots. Hopf bifurcation takes place when those roots cross the imaginary axis:

$$\Omega_H = \pm \frac{1}{2} \sqrt{\frac{\varepsilon(1+\varepsilon\sigma)}{1+\varepsilon}} \quad (7)$$

The boundary of Hopf bifurcation is marked by a dashed line in Fig. 2.

Critical λ value for occurrence of Hopf bifurcation $\lambda_{H,cr}$ is as follows:

$$\lambda_{H,cr} = \frac{1}{\sqrt{3}} \left| \bar{\beta} + \frac{\varepsilon\sigma - 1}{(1+\varepsilon)} \right| \quad (8)$$

3.3 Strongly Modulated Responses (SMRs)

When SMR takes place [11, 13], the modulation of the dynamical response changes in both fast and slow time scales in vicinity of 1:1 resonance. Hence, in contradiction to weakly modulated responses introduced above, SMR cannot be analyzed with the help of perturbation methods.

We apply multiple-scales method on the second equation of Eq. (3): $\varphi_2 = \varphi_2(T_0, T_1)$, $T_n = \varepsilon^n \tau$, $n = 0, 1, \dots$, $d/d\tau = D_0 + \varepsilon D_1$. Then, we nullify the derivatives, and integrate the resulting equation with respect to T_0 , to yield the following expression:

$$Z \left(\lambda^2 + \left(1 - \frac{3k}{4} Z \right)^2 \right) = 4|C(T_1)|^2 \quad (9)$$

Here $\Phi(T_1) = N(T_1) e^{i\theta(T_1)}$, $Z(T_1) = N(T_1)^2$, and $C(T_1)$ is an arbitrary function which is constant with respect to T_0 . This cubic polynomial can have either one or three real solutions. The threshold value of damping between those two regions is $\lambda = 1/\sqrt{3}$, which corresponds to a SN bifurcation. Equation (9) represents the slow invariant manifold (SIM) of the system, which is presented in Fig. 3. As shown in [14], fast transition between both stable branches of the SIM corresponds to relaxation oscillations.

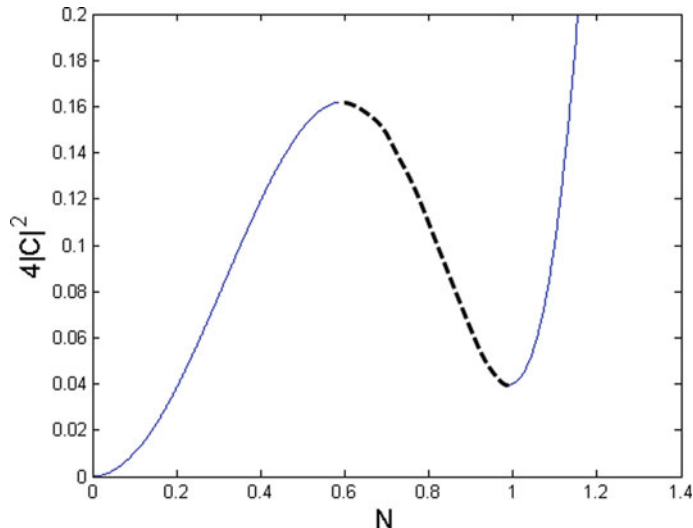


Fig. 3 Projection of the SIM on $(N, 4|C(T_1)|^2)$ plane, for: $k = 4/3$, $\lambda = 0.2$

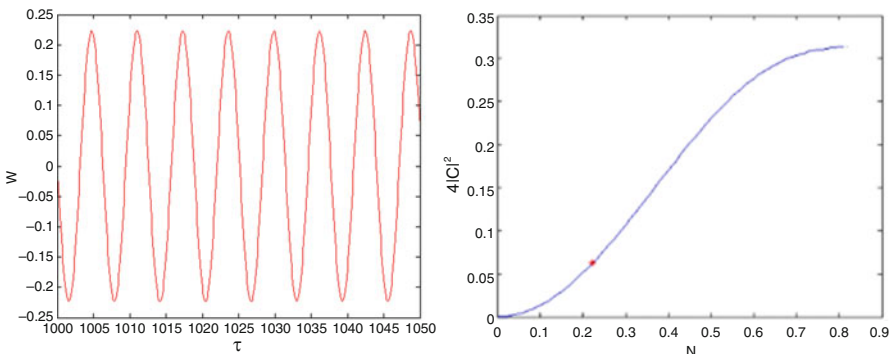


Fig. 4 Unique periodic solution, left: time history, right: the slow-flow of the system (red asterisk) on the SIM (blue line), for: $k = 4/3$, $\sigma = 5$, $\varepsilon = 0.05$, $\beta = 5$ and zero initial conditions

4 Numerical Results

In the current section, the analytical prediction obtained in previous sections is verified numerically. All numerical simulations are obtained by integrating the equations of motion of system (1).

In Fig. 4, one can see that since the SIM is monotonous, existence of multiple solution is impossible. One can see that a stationary periodic signal corresponds to a single point on the SIM.

In Fig. 5, the SIM is not monotonous, and a multiple-solutions area emerges. Hence, two stable solutions take place for different sets of initial condition.

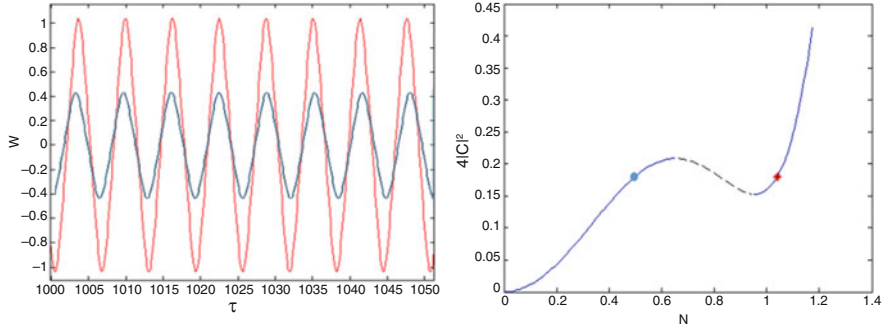


Fig. 5 Multiple periodic solutions, left: time histories, right: the slow-flow responses (blue dot and red asterisk) on the SIM (blue line). The time histories colored in blue and red correspond to the blue and red dots on the SIM. The former correspond to zero initial conditions, and the latter to $\dot{u}_0 = 0.5$; $k = 4/3$, $\sigma = 5$, $\varepsilon = 0.05$, $\beta = 5$, $A = 1.62$

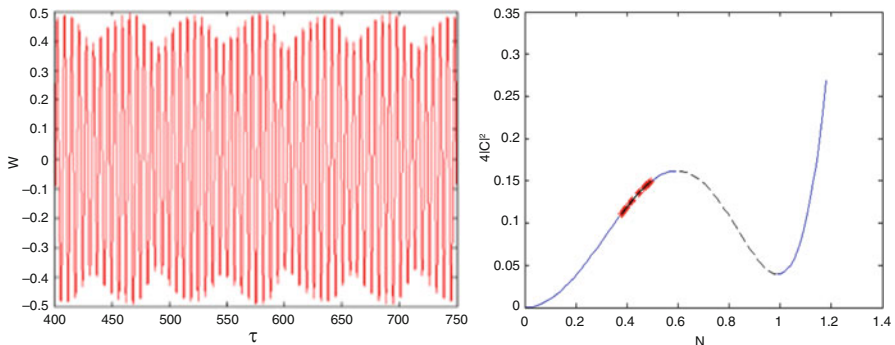


Fig. 6 Weakly quasi-periodic solution, left: time history, right: the slow-flow of the system (red asterisks linked by black solid lines) on the SIM (blue line), for: $k = 4/3$, $\sigma = 5$, $\varepsilon = 0.05$, $\beta = 5$, $A = 1.4$ and initial conditions: $u_0 = 0$, $v_0 = 0$, $\dot{u}_0 = 0.5$, $\dot{v}_0 = 0$

In Fig. 6, one can see that modulations in the time history correspond to an alternating motion of the slow-flow dynamics on one of the stable branches of the SIM.

In Fig. 7, one can see that the strong modulations correspond to transitions, or “jumps,” of the slow-flow from one branch to the other. Rapid increase corresponds to jump from the left branch to the right branch, while rapid decrease corresponds to jump from the right branch to the left branch.

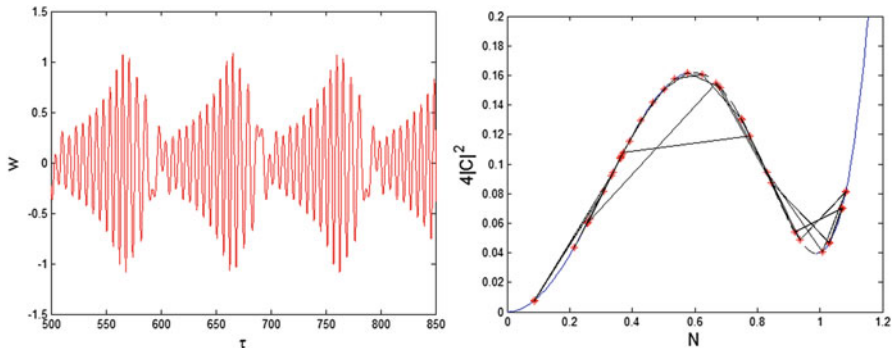


Fig. 7 SMR regime, left: time history, right: the slow-flow of the system (red asterisks linked by black solid lines) on the SIM (blue line), for: $k = 4/3$, $\sigma = 5$, $\varepsilon = 0.05$, $\beta = 5$, $A = 0.3$ and initial conditions: $u_0 = 0.29$, $v_0 = -0.5$, $\dot{u}_0 = 0.9$, $\dot{v}_0 = -0.15$

5 Concluding Remarks

Simple and novel phenomenological model was suggested, aiming to capture and describe the most dominant two-dimensional sloshing regimes taking place in forced partially filled liquid storage tank, i.e., single and multiple periodic responses, weakly quasi-periodic responses, and SMR. All response types were explained with analytical tools, and theoretical results were verified numerically. However, the current model is limited to two-dimensional regimes with moderate amplitude, involving mainly a single sloshing mode. Further exploration will deal with three-dimensional models with multiple sloshing modes.

References

1. Yu, D., Li, X., Liu, H., Dong, J.: Research on liquid sloshing model of partially-filled tank by nonlinear external excitation. *J. Vibroeng.* **17**(6), 3224–3236 (2015)
2. Cooper, R.M.: Dynamics of liquids in moving containers. *ARSJ*. **30**(8), 725–729 (1960)
3. Abramson, H.N.: The dynamic behavior of liquids in moving containers. NASA SP-106, vol. 106, 1966
4. Ikeda, T., Ibrahim, R.A., Harata, Y., Kuriyama, T.: Nonlinear liquid sloshing in a square tank subjected to obliquely horizontal excitation. *J. Fluid Mech.* **700**, 304–328 (2012)
5. Zhang, C., Li, Y., Meng, Q.: Fully nonlinear analysis of second-order sloshing resonance in a three-dimensional tank. *Comput. Fluids.* **116**, 88–104 (2015)
6. Bauer, H.F.: Nonlinear mechanical model for the description of propellant sloshing. *AIAA J.* **4**(9), 1662–1668 (1966)
7. El-Sayad, M.A., Hanna, S.N., Ibrahim, R.A.: Parametric excitation of nonlinear elastic systems involving hydrodynamic sloshing impact. *Nonlinear Dynam.* **18**(1), 25–50 (1999)
8. Ibrahim, R.A., Pilipchuk, V.N., Ikeda, T.: Recent advances in liquid sloshing dynamics. *Appl. Mech. Rev.* **54**(2), 133 (2001)

9. Farid, M., Gendelman, O.V.: Internal resonances and dynamic responses in equivalent mechanical model of partially liquid-filled vessel. *J. Sound Vib.* **379**, 191–212 (2016)
10. Gendelman, O.V., Starosvetsky, Y.: Quasi-periodic response regimes of linear oscillator coupled to nonlinear energy sink under periodic forcing. *J. Appl. Mech.* **74**(2), 325 (2007)
11. Gendelman, O.V., Starosvetsky, Y., Feldman, M.: Attractors of harmonically forced linear oscillator with attached nonlinear energy sink I: description of response regimes. *Nonlinear Dynam.* **51**(1–2), 31–46 (2007)
12. Manevitch, L.I.: Complex representation of dynamics of coupled nonlinear oscillators. In: Mathematical Models of Non-Linear Excitations, Transfer, Dynamics, and Control in Condensed Systems and Other Media, pp. 269–300. Springer, Boston, MA (1999)
13. Starosvetsky, Y., Gendelman, O.V.: Response regimes of linear oscillator coupled to nonlinear energy sink with harmonic forcing and frequency detuning. *J. Sound Vib.* **315**(3), 746–765 (2008)
14. Guckenheimer, J., Hoffman, K., Weckesser, W.: Bifurcations of relaxation oscillations near folded saddles. *Int. J. Bifurcation Chaos*. **15**(11), 3411–3421 (2005)

Catenary-Based Nonlinear Multimodal Theory of Cable Free Vibrations



Achref Mansour, Giuseppe Rega, and Othman Ben Mekki

Abstract A new multimodal theory is developed analytically using the method of multiple scales to investigate the dynamic behavior of arbitrarily sagged and inclined cables oscillating around a catenary static profile. Fully non-condensed kinematics are adopted to solve the eigenvalue problem and the enhanced modal properties obtained at this stage are used as first inputs to the resolution of the nonlinear time dependent problem leading to original results where the contribution of longitudinal vibration is better captured and the modal coupling is accurately described in both space and frequency domains.

Keywords Cable · Nonlinear vibrations · Multimodal · Catenary · Method of multiple scales · Condensation

1 Introduction

Modeling and solution assumptions in the analysis of nonlinear cable vibrations have been widely discussed in about the last decade. This is not surprising in the case of such structures exhibiting rich and complex dynamic phenomena. It may be cited the work of Arena [1] concerning the importance of flexural stiffness of the modal properties of flexural torsional-extensible cables, as well as the studies of Srinil et al. on the use of non-condensed models for the analysis of free oscillations

A. Mansour (✉)

Université de Tunis El Manar, Ecole Nationale d'Ingénieurs de Tunis, LGC, Tunis, Tunisia

University Grenoble Alpes, Inria, CNRS, Grenoble INP, LJK, Grenoble, France

e-mail: achref.elmansour@inria.fr

G. Rega

Dipartimento di Ingegneria Strutturale e Geotecnica, Università di Roma La Sapienza, Roma, Italy

O. B. Mekki

Université de Tunis El Manar, Ecole Nationale d'Ingénieurs de Tunis, LGC, Tunis, Tunisia

of both arbitrarily sagged cables via numerical (finite difference) techniques [11, 12] and of shallow cables via analytical (multiple scale) techniques [13]. On the other hand, analytical frameworks were developed by Lacarbonara et al. to investigate the role as well as the activation conditions of internal resonances and coupled nonlinear normal modes [3, 4]. However, a detailed review of the literature found in [10] has highlighted how the majority of existing models are based on several assumptions related to cable geometrical and mechanical aspects, reducing consequently their accuracy as well as their range of validity. In fact, most researches account for the so-called “kinematic condensation” where longitudinal inertia and dynamic deformation are neglected, leading to the reduction of the in-plane dynamics to its transverse component. This is mainly due to the definition of the dynamic equilibrium configuration with respect to the parabolic approximation of the real cable static profile given by a catenary geometry: such assumption is justified only in the case of small-sag cables, and may be considered as one of the most critical factors leading to neglect important nonlinear features in cable dynamics. Few efforts have been devoted to the oscillations of non-shallow cables where the catenary geometry has been adopted to define the static reference configuration [5, 6]. Recently, the linear modal properties of arbitrarily sagged and inclined cables have been investigated in the light of a catenary-based model developed analytically by Mansour et al. [8]. Taking into account the induced geometric nonlinearity effect, a new modal spectrum characterized by ratios of internal resonances higher than the ones classically reported in the literature (1:1, 2:1 and 3:1) has been highlighted, where non-normal modes are continuously detected. The present work is pursued in sequence with these recently obtained results. As a matter of fact, a catenary-based theory of nonlinear free vibrations is developed analytically using the method of multiple scales (MMS) [9] in order to solve the dynamic problem in its original nonlinear form. The proposed solution refers to a fully non-condensed model and takes into consideration the geometric nonlinearities induced by the multimodal quadratic and cubic couplings between the dynamic displacement components. Within the limited available space, a comparison with the results obtained by existing models is also accomplished, in order to highlight some main differences caused by the approximation of the initial catenary profile, and by the condensed or classical non-condensed kinematics considered in the literature.

2 Equations of Motion and Discretization

In the present analysis, the attention is held on the free vibrations of a homogeneous linearly elastic cable hanged between two fixed supports at different levels, characterized by a non-deformable cross section denoted by A_c and Young elastic modulus E_c . Accounting for the sole axial extensibility, the cable dynamic motion is governed by the nonlinear differential system:

$$\frac{\partial}{\partial s} \left[\left(T + T^D \right) \frac{\partial u_i}{\partial s} + \frac{dX_i}{ds} T^D \right] = m \frac{\partial^2 u_i}{\partial t^2} \quad (1)$$

where $i \in \{1, 2, 3\}$ refers to the first (longitudinal), second (transversal), and third (out-of-plane) dynamic displacement component, respectively, with: T the equivalent along-the-chord thrust, m the cable mass per unit length, X_i the i th component of the static displacement ($X_3 = 0$), u_i the i th component of the dynamic displacement, and T^D the additional dynamic tension defined as follows:

$$T^D = E_c A_c \left[\frac{\partial u_i}{\partial s} \frac{dX_i}{ds} + \frac{1}{2} \left(\frac{\partial u_i}{\partial s} \right)^2 \right] \quad (2)$$

where summation is made over index i . It should be noted that the following analytical developments aiming to solve system (1) are given in compact form due to the conciseness of the paper. However, details related to mathematical aspects may be found in [7]. In order to highlight geometric nonlinearities due to the coupling between different dynamic displacements, the previous system may be reformulated as:

$$\begin{aligned} \ddot{u}_i + L_i u_i + L_i u_{i^*} &= G_{2,i}(u_i, u_i) + G_{2,i}(u_i, u_{i^*}) + G_{2,i}(u_{i^*}, u_{i^*}) \\ &\quad + G_{3,i}(u_i, u_i, u_i) + G_{3,i}(u_i, u_{i^*}, u_{i^*}) \end{aligned} \quad (3)$$

where summation is performed over index $i^* \neq i$ varying between 1 and 3, and

- L_i is a linear, homogeneous, self-adjoint, positive-definite integral-differential operator, with $L_i u_{i^*} = 0$ for $i = 3$ or $i^* = 3$;
- $G_{2,i}$, $G_{3,i}$ are respectively quadratic and cubic geometric operators defined explicitly in [7], with $G_{2,i}(u_i, u_3) = 0$ for $i \in \{1, 2, 3\}$ and $G_{2,i}(u_{i^*}, u_{i^*}) = 0$ for $i = 3$.

According to the MMS formulation, the dynamic displacement components $u_i(s, t)$ may be written as:

$$u_i(s, t, \epsilon) = \sum_{k=1}^3 \epsilon^k u_{ik}(s, T_0, T_1, T_2) \quad (4)$$

where ϵ is a dimensionless small bookkeeping parameter and T_k are the time scales defined as $T_k = \epsilon^k t$; $k \in \mathbb{N}$. Thus, the first derivative with respect to time is expressed as $\partial/\partial t = D_0 + \epsilon D_1 + \epsilon^2 D_2 + \dots$ where $D_n = \partial/\partial T_n$. By adopting Galerkin method, the additional dynamic displacements may be written in terms of modal shapes and time coordinates, denoted respectively by $\varphi_{k,i}(s)$ and $q_{k,i}(t)$, as below:

$$u_i(s, t) = \sum_{k=1}^N \varphi_{k,i}(s) q_{k,i}(t) \quad (5)$$

leading to the following expression of the time contribution related to the k th mode in the i th direction:

$$q_{k,i}(t, \epsilon) = \sum_{j=1}^3 \epsilon^j q_{k,ij}(T_0, T_1, T_2) \quad (6)$$

The construction of an analytical solution to the nonlinear dynamic system appears then to be deeply dependent on the accuracy of both modal shapes and vibration frequencies obtained for the linear problem and determined according to the adopted kinematics. For the sake of generality and different from the existing models which are based on either condensed or solely spatially non-condensed dynamics, as mentioned in the introduction, the modal functions adopted in the following sections are derived as solutions of the fully non-condensed problem formulated for small dynamic deformations and large static displacements in [7]. The obtained frequencies and modal functions are used as enhanced inputs to the nonlinear dynamic problem defined by system (3): such strategy is characterized by higher efficiency to detect the condensation effect in both space and frequency domains since the longitudinal dynamic motion is treated as completely independent of the transversal one, which is more appropriate especially in the case of large-sagged cables.

3 Multiple Scale Solution

The attention is initially held on the determination of analytical expressions related to the first order expansion of the 3D components of dynamic displacement. For the sake of brevity, a compact form of governing equations as well as obtained solutions is adopted. Accordingly, replacing the modal contributions given by (6) in the differential system (3) leads to:

$$\ddot{q}_{k,i1} \varphi_{k,i} + L_i(\varphi_{k,i}) q_{k,i1} + L_i(\varphi_{k,i*}) q_{k,i*1} = 0 \quad (7)$$

with $L_i(\varphi_{k,i*}) = 0$ for $i^* = 3$ or for $i = 3$. In order to solve the previous system, the integral-differential operators have to be expressed in function of the natural frequencies and associated mode shapes. In fact, the relevant eigenvalue problem reads:

$$\omega_{k,i}^2 \varphi_{k,i} = L_i(\varphi_{k,i}) + L_i(\varphi_{k,i*}) \Rightarrow L_i(\varphi_{k,i}) = \omega_{k,i}^2 \varphi_{k,i} - L_i(\varphi_{k,i*}) \quad (8)$$

where $\omega_{k,i}$ denotes the linear circular frequency of the k th mode. The modal contributions of the dynamic displacement components are then obtained as solutions of the following differential problem, for $i^* \in \{1, 2\}$ with $i^* \neq i$:

$$\ddot{q}_{k,i1} + q_{k,i1} \left[\omega_{k,i}^2 - r_{kj,i1} q_{k,i^*1} \right] + r_{kj,i1} q_{k,i^*1} = 0; \quad r_{kj,i1} = I_{kj,ii^*} \cdot I_{kj,ii}^{-1}$$

$$I_{kj,ii^*} = \int_0^{L_c} L_i(\varphi_{k,i^*}(s)) \varphi_{j,i}(s) ds; \quad I_{kj,ii} = \int_0^{L_c} \varphi_{k,i}(s) \varphi_{j,i}(s) ds \quad (9)$$

where $r_{kj,i1}$ represent the ratio between coefficients I_{kj,ii^*} and $I_{kj,ii}$ related, respectively, to the spatial coupling between modes in different and same directions. Such quantities may be then viewed as dimensionless parametrization of the intra ($I_{kj,ii}$) and extra (I_{kj,ii^*}) modal spatial coupling. It is thus worth noting that new in-plane spatial coupling terms ensue from the non-orthogonal modal shapes also occurring in the relevant eigenvalue problem, in addition to the normal ones, because of the catenary-induced effect on in-plane linear vibrations. In contrast, since the out-of-plane linear vibrations are not affected by the catenary-induced nonlinearities, then only normal modes exist and the term $r_{kj,31}$ does not occur in the out-of-plane equation (9). Furthermore, the time coordinate related to the projection of the k th mode on the j th component of the enhanced basis used in the present development is assumed to be expressed as follows:

$$q_{k,i1}(t) = \exp(i\Omega_{kj,i}t) \quad (10)$$

where $\Omega_{kj,i}$ are the k th nonlinear circular frequencies.

Thus, the circular frequencies in different in-plane directions are found to be governed by the following relationship:

$$\prod_{i=1}^2 \left[\Omega_{kj,i}^2 + (r_{kj,i1} - \omega_{k,i}^2) \right] = \prod_{i=1}^2 r_{kj,i1} \quad (11)$$

and the out-of-plane frequencies are expressed as:

$$\Omega_{kj,3} = \omega_{k,3} \quad (12)$$

Note that, while circular frequencies $\Omega_{kj,3}$ are directly derived from the out-of-plane modal properties, the in-plane oscillations are found to be highly dependent on the degree of condensation considered in the formulation of the eigenvalue problem. Furthermore, it appears that the linear circular frequencies constitute a particular solution of Eq. (11) for initially small sagged cables: use is made in such case of orthogonal modal functions, due to the condensation assumption, entailing the cancellation of intra/extramodal coupling coefficients and consequently the reduction of nonlinear frequencies to the linear ones. In opposition to the existing

models where time coordinates depend on the linear frequencies ω , the harmonics obtained according to the present development are expressed in terms of nonlinear frequencies Ω characterized by their capacity to capture the effect of spatial coupling between the different modes. In order to take into consideration such dependency on the totality of modal spectrum components, spatial projection of the k th mode is performed with respect to the time contribution of the rest of modes, leading to:

$$q_{k,i}(t) = \exp(i\Omega_{k,i}t); \quad \Omega_{k,i} = \frac{1}{N_0} \sum_{j=1}^{N_0} \Omega_{kj,i} \quad \forall i \in \{1, 2, 3\} \quad (13)$$

where N_0 denotes the number of non-orthogonal j th modes.

Accordingly, to the first order of expansion, the dynamic displacement is given as below:

$$u_{i1}(s, t) = \sum_{k=1}^N \delta_{kM} A_{k,i}(T_1, T_2) \exp(i\Omega_{k,i}t) \varphi_{k,i}(s) + \text{cc} \quad (14)$$

where $A_{k,i}$ denotes the complex-valued amplitude of the k th mode related to the i th component of the dynamic displacement, M are the set of internally resonant modes, and cc is the complex conjugate of the preceding terms.

Replacing $u_{i1}(s, t)$ by its expression (14) in the higher order expansions of system (3) and adopting the same previous strategy of resolution while paying attention to secular terms present in the MMS-based formulation, a compact form related to both second and third order expansions ($m = 2, 3$) of the dynamic displacements may be written as follows:

$$u_{im}(s, t) = \sum_{j=1}^3 \sum_{k=1}^N C_{k,i}(\Lambda_{m-1}, \Gamma_{m-1}, A) \varphi_{k,j}(s) \exp \left[\sum_{j=1}^3 \sum_{k=1}^N i\Omega_{k,j} t \right] \quad (15)$$

where $C_{k,i}$ are correction functions depending on complex amplitudes A and:

- Λ_1 (resp. Λ_2) denoting coefficients specific to quadratic nonlinearity due to spatial coupling between modes obtained at the first (resp. second) order of perturbation.
- $\Gamma_1 = 0$ and Γ_2 denoting coefficients specific to cubic nonlinearity due to spatial coupling between modes obtained at the second order of perturbation.

Letting the complex-valued amplitudes $A_{k,i} = a_{k,i}/2 \exp(i\psi_{k,i})$, and using the method of reconstitution according to which the dynamic displacement $u_i = \sum_{j=1}^3 \epsilon^j u_{ij}$ with $\epsilon = 1$, the following expression of the 3D components of dynamic displacement is obtained:

$$u_i(s, t) = \sum_{j=1}^3 \sum_{k=1}^N C_{k,i}(\Lambda, \Gamma, a) \varphi_{k,j}(s) \cos \left[\sum_{j=1}^3 \sum_{k=1}^N \Omega_{k,j} t + \psi_{k,j} \right] \quad (16)$$

4 Numerical Results

Owing to lack of space, it is not possible to dwell here on the effects of the general modeling framework considered in the present theory (catenary formulation in the strained arclength coordinates, fully non-condensed model) on the extent and features of nonlinear modal coupling in cable oscillations.

So, the numerical analysis is restricted to the comparison of some results provided by the previously formulated theory with those obtained by Srinil et al. in [11, 12], concerning the estimation of the cable final tension defined by $T_f = T + T^D$. The considered cable is characterized according to [11, 12] by a horizontal cable length $l = 850$ m, a non-deformable cross section $A_c = 0.1159$ m², a cable density $\gamma_c = 83.379$ kN/m³, and a Young modulus of elasticity $E_c = 1.794 \times 10^7$ kN/m². By altering both cable inclination and static tension, different configurations may be defined as reported in Table 1. It is worth noting that the non-condensed kinematics adopted in the formulation of the models in [11, 12] is limited to the sole spatial domain, by assuming that the longitudinal component oscillates with the same frequency as the transversal one. The extreme values of cable total tension T_f computed according to the previously mentioned models are presented in Table 2.

In all considered cases, the model developed by Srinil et al. is found to underestimate both extrema of cable final tension when compared to the fully non-condensed model of the previously developed catenary-based theory. This does not

Table 1 Geometrical and mechanical characteristics corresponding to three different cable configurations (α : angle between cable chord and its horizontal projection; λ : Irvine's parameter [2], T : cable static tension)

	Cable 1	Cable 2	Cable 3
α (rad)	0	0	$\pi/4$
λ	0.72π	2π	2π
T (kN)	30,000	15,642	28,790

Table 2 Maximum ($T_{f\max}/T$) and minimum ($T_{f\min}/T$) of tension dimensionless ratio

	Model	Cable 1	Cable 2	Cable 3
$T_{f\max}/T$	Srinil et al.	1.1	1.4	1.35
	Present	1.32	1.6	1.55
$T_{f\min}/T$	Srinil et al.	0.92	0.6	0.7
	Present	0.935	0.935	1

appear surprising: in fact, the condensation assumption entails an underestimation of the cable tension since it reduces the spatial coupling between modal components, and does not provide an accurate framework to detect the real cable dynamic behavior, especially in the case of weakly tensioned cables. When moving to non-condensed models of different generality, such trend is seen to persist, with a difference between the cable tension provided by the space/frequency domain condensation of the present theory and the corresponding one of the solely spatially non-condensed model of about 20–25%. It should be noted that the focus is held on the extreme values of cable tension because of their great importance from the engineering design viewpoint, with the maximum tension governing the cable material resistance and the minimum one affecting the needed non-compression condition.

5 Conclusion

In the framework of a catenary-based formulation, a nonlinear multimodal theory of cable nonlinear free vibrations has been developed via the multiple scale method. Features of modal interaction and cable total tension of the present fully non-condensed model, formulated in the strained arclength coordinate, have been numerically investigated against the results exhibited by a spatially non-condensed finite difference model. With respect to non-condensed models, frequency condensation entails an underestimation of the cable maximum tension which is as larger as the non-condensed model is formulated in the arclength coordinate and accounts for both spatial and frequency modal independence of longitudinal and transversal displacements. The new multimodal asymptotic theory may be considered as a powerful tool to accurately describe the features of nonlinear modal coupling and to determine the cable dynamic responses in terms of additional displacements and tension. In further papers, work will focus also on the use of the present theory to determine the activation conditions of internal resonances of M:1 order, different from those discussed in classical literature, along with the associated stability regions.

References

1. Arena, A.: Free vibration of flexible cables. In: ASME 2015 International Design Engineering Technical Conferences and Computers and Information in Engineering Conference, Boston, vol. 8, pp. V008T13A082. American Society of Mechanical Engineers, New York (2015)
2. Irvine H.M.: Cable Structures. MIT Press, Cambridge (1981)
3. Lacarbonara, W., Rega, G.: Resonant non-linear normal modes. Part II: activation/orthogonality conditions for shallow structural systems. Int. J. Non Linear Mech. **38**(6), 873–887 (2003)

4. Lacarbonara, W., Rega, G., Nayfeh, A.H.: Resonant non-linear normal modes. Part I: analytical treatment for structural one-dimensional systems. *Int. J. Non Linear Mech.* **38**(6), 851–872 (2003)
5. Lacarbonara, W., Paolone, A., Vestroni, F.: Elastodynamics of nonshallow suspended cables: linear modal properties. *J. Vib. Acoust.* **129**(4), 425–433 (2007)
6. Lacarbonara, W., Paolone, A., Vestroni, F.: Non-linear modal properties of non-shallow cables. *Int. J. Non Linear Mech.* **42**(3), 542–554 (2007)
7. Mansour, A.: Nonlinear cable dynamics: a catenary approach. In: Ph.D. Dissertation, Université de Tunis El Manar, Ecole Nationale d'Ingénieurs de Tunis, Tunis, Tunisia (2018)
8. Mansour, A., Ben Mekki, O., Montassar, S., Rega, G.: Catenary-induced geometric nonlinearity effects on cable linear vibrations. *J. Sound Vib.* **413**, 332–353 (2018)
9. Nayfeh A.H.: Perturbation Methods, vol. 1973, 1st edn. Wiley, Hoboken (2008)
10. Rega, G.: Theoretical and experimental nonlinear vibrations of sagged elastic cables. In: Warminski, J., et al. (eds.) *Nonlinear Dynamic Phenomena in Mechanics*, pp. 157–207. Springer, Berlin (2011)
11. Srinil, N., Rega, G., Chucheepsakul, S.: Large amplitude three-dimensional free vibrations of inclined sagged elastic cables. *Nonlinear Dyn.* **33**, 129–154 (2003)
12. Srinil, N., Rega, G., Chucheepsakul, S.: Three-dimensional non-linear coupling and dynamic tension in the large-amplitude free vibrations of arbitrarily sagged cables. *J. Sound Vib.* **26**(3), 823–852 (2004)
13. Srinil, N., Rega, G., Chucheepsakul, S.: Two-to-one resonant multi-modal dynamics of horizontal/inclined cables. Part I: theoretical formulation and model validation. *Nonlinear Dyn.* **48**, 231–252 (2007)

Flexural and Sway Interaction in the Nonlinear Vibrations of a Phenomenological Model of a Laterally Braced Column



Diego Orlando , Juliana M. P. Raimundo, and Paulo B. Gonçalves

Abstract In this work, an archetypal 2D of structural model exhibiting flexural-sway interaction is considered. Although simple, the model exhibits the main nonlinear features found in more complex structures. Depending on the relative values of the flexural stiffness and lateral restraint, interactive buckling may occur. In such case several coupled post-buckling paths appear, leading to multiplicity of solutions for load levels lower than the static critical load and a complex energy landscape. This leads to an intricate nonlinear dynamic behavior of the structure under static and dynamic loads, a topic not investigated in previous literature on the subject. Here, a detailed parametric analysis of the structural system is conducted to study how the lateral stiffness influences the dynamic nonlinear behavior and stability of the structure. The bifurcation analysis shows that the structure may display several coexisting stable and unstable responses, leading to intertwining basins of attraction, whose topology controls the dynamic integrity of the structure in a dynamic environment.

Keywords Interactive buckling · Sway buckling · Nonlinear dynamics · Parametric instability

1 Introduction

As a consequence of recent technological advances, both in the area of new materials and in numerical methods, structural elements with increasing slenderness are observed, leading to lighter and more economic structures. Due to their increasing slenderness, structural elements such as columns and portal frames may lose stability before reaching the load capacity of the cross section. Also large

D. Orlando ()
State University of Rio de Janeiro, FAT, Resende, Brazil
e-mail: dgorlando@gmail.com

J. M. P. Raimundo · P. B. Gonçalves
Pontifical Catholic University of Rio de Janeiro, Rio de Janeiro, Brazil

amplitude vibrations may occur. Depending on the nonlinearities, they may also display sensitivity to geometric and material imperfections, further reducing the load carrying capacity of the structure. Therefore, when analyzing slender structural systems, it is advisable to conduct a detailed nonlinear analysis of its post-critical behavior and obtain the nonlinear equilibrium paths of the imperfect structures. The stability analysis of reticulated structures has been investigated by [1, 2], among others.

The instability of frames is affected by the adjacent members and involves the determination of the critical load and the critical mode. In addition, the post-critical behavior and sensitivity to initial imperfections must be investigated. Structural systems liable to unstable symmetric or asymmetric bifurcation may be rather sensitive to initial geometric imperfections [3–5], loading eccentricities and/or dynamic perturbations and may buckle at load levels much lower than the theoretical critical load.

Another important aspect when studying the stability of framed structures is the phenomenon of modal coupling or modal interaction that may occur when different buckling modes have equal or nearly equal critical loads, generating several post-buckling coupled and uncoupled solutions, generally unstable. Several examples can be found in [3–8], among others. The influence of modal coupling on the nonlinear dynamics of structural systems liable to buckling was highlighted by [9], who studied the static and dynamic instability of the Augusti model [10] and a guyed tower model proposed by [11]. A detailed analysis of these systems can be found in [12–14].

Different conceptual models explaining the phenomenon of modal coupling can be found in [6]. Among the models presented by [6], the discrete column model with two degrees proposed by Raithel and Clemente [15] illustrates the interaction between flexural and lateral stiffness. Depending on the relation between the flexural and lateral stiffness, modal coupling may occur, leading to several unstable coupled and uncoupled post-buckling solutions. The present work studies the interaction between flexural and lateral buckling of slender framed structures, using the phenomenological model proposed by [15]. With the help of the analytical and numerical tools of the static stability theory and nonlinear dynamics, a parametric nonlinear analysis of the model under static axial load and dynamic excitations (axial and base excitations) is conducted. The results show the complexity of the model response and provide a new contribution to the understanding of the static and dynamic instability of structural systems subject to modal coupling, an important topic in the field of nonlinear dynamics [13].

2 Formulation, Static Analysis, and Natural Frequencies

Figure 1a illustrates the discrete model proposed by Raithel and Clemente [15]. It is composed of two rigid bars of length $l/2$, with a mass per-unit length m , and connected by a rotational spring with stiffness k_r . It is pinned at the base and

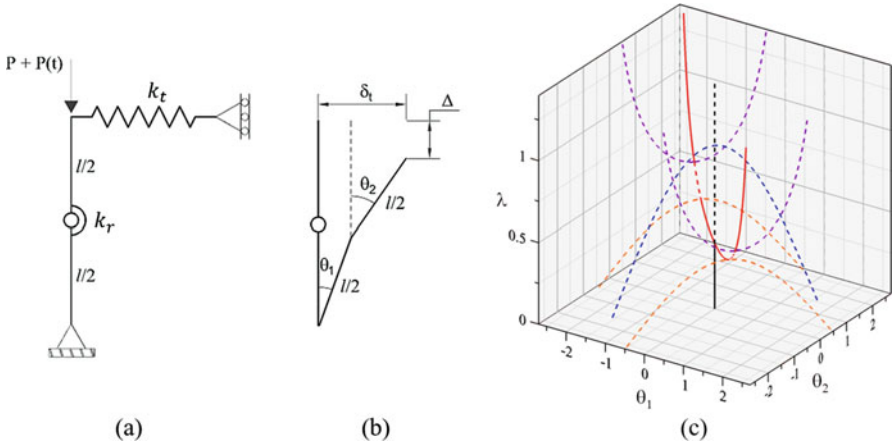


Fig. 1 (a) Undeformed column; (b) deformed column; (c) nonlinear equilibrium paths for $\alpha = 0.10$

supported at the top by a lateral spring with stiffness k_t . P is the static axial load and $P(t) = f \sin(\Omega t)$ is a harmonic axial force. The angles θ_1 and θ_2 (Fig. 1b) are chosen as the two degrees of freedom. The nondimensional kinetic energy, \bar{T} , Rayleigh dissipation function, \bar{F}_r , and potential energy, $\bar{\Pi}$, are given in terms of the generalized coordinates θ_1 and θ_2 as [16, 17]:

$$\bar{T} = \frac{T}{k_t l^2} = \frac{1}{48} \left(3\dot{\theta}_1 \dot{\theta}_2 \cos \theta_1 \cos \theta_2 + 3\dot{\theta}_1 \dot{\theta}_2 \sin \theta_1 \sin \theta_2 + (\dot{\theta}_2)^2 + 4(\dot{\theta}_1)^2 \right), \quad (1)$$

$$\bar{F}_r = F_r / k_t l^2 = \xi_1 (\dot{\theta}_2 - \dot{\theta}_1)^2 + \xi_2 (\dot{\theta}_1 \cos \theta_1 + \dot{\theta}_2 \cos \theta_2)^2, \quad (2)$$

$$\begin{aligned} \bar{\Pi} = \frac{U}{k_t l^2} + \frac{V}{k_t l^2} &= \frac{1}{2} \alpha (\theta_2 - \theta_1)^2 + \frac{1}{8} (\sin \theta_1 + \sin \theta_2)^2 \\ &+ \frac{1}{2} (\lambda + F \sin(\beta \tau)) (2 - (\cos \theta_1 + \cos \theta_2)), \end{aligned} \quad (3)$$

Here, $\tau = \omega t$, $\alpha = k_r / k_t l^2$, $\lambda = P / k_t l$, $\omega^2 = k_t l^2 / A \rho l^3$, $2\omega \xi_1 = C_1 / A \rho l^3$, $2\omega \xi_2 = C_2 l^2 / 4A \rho l^3$, $F = f / k_t l$, and $\beta = \Omega / \omega$ is the relation between excitation (Ω) and frequency parameter (ω).

The nonlinear equilibrium equations are

$$\partial (\bar{\Pi}) / \partial \theta_i = 0; \quad i = 1, 2, \quad (4)$$

and the equations of motion of the system are given by

$$\frac{d}{d\tau} \frac{\partial(\bar{T})}{\partial\dot{\theta}_i} - \frac{\partial(\bar{T})}{\partial\theta_i} + \frac{\partial(\bar{\Pi})}{\partial\theta_i} + \frac{\partial(\bar{F}_r)}{\partial\theta_i} = 0; \quad i = 1, 2. \quad (5)$$

From the linearized equilibrium equations ($\sin\theta_i = \theta_i$ and $\cos\theta_i = 1$) and solving the resulting eigenvalue problem, the two bifurcation loads are obtained: $\lambda_{cr1} = 1.0$ and $\lambda_{cr2} = 4\alpha$. For $\alpha = 1/4 (\alpha_{cr})$, the two critical loads coincide and, therefore, modal interaction may occur ($\lambda_{cr} = 1.0$). Figure 1c shows the fundamental solution ($\theta_1 = \theta_2 = 0.0$) and the post-critical paths for $\alpha = 0.10$. The fundamental equilibrium path is stable up to the critical load (λ_{cr}). There are two post-critical paths: a stable ascending path at -45° associated with $\lambda_{cr1} = 1.0$ (in red) and an unstable descending path at $+45^\circ$ associated with $\lambda_{cr2} = 4\alpha$ (in blue). Another four coupled unstable secondary paths emerge along the ascending post-critical path. Considering the relative spring stiffnesses ($\alpha = k_r/k_t l^2$) [17]: when $k_r < k_t l^2$ ($\alpha < \alpha_{cr}$, $\lambda_{cr} = 4\alpha$, $P_{cr} = 4k_r/l$) the stability of the fundamental solution is controlled by the flexural stiffness. When $k_r > k_t l^2$ ($\alpha > \alpha_{cr}$, $\lambda_{cr} = 1.0$, $P_{cr} = k_t l$), the stability of the fundamental solution is controlled by the lateral stiffness and the system behaves as a system of one degree of freedom with unstable symmetric bifurcation [3–5]. If $\alpha \ll \alpha_{cr}$ (strong lateral bracing system), the secondary bifurcations occur far away from the fundamental equilibrium position and the system behaves as a one degree of freedom system with stable symmetric bifurcation [3–5].

Linearizing the equations of motion and solving the resulting eigenvalue problem, the natural frequencies ω_i and the corresponding vibration modes Θ_i are obtained. Figure 2a shows for the unloaded structure ($\lambda = 0.0$) the variation of the two natural frequencies as a function of the stiffness parameter α . The lowest natural frequency increases from zero and tends asymptotically to a constant value as α increases, while the second frequency increases in almost a linear manner. The variation of the two natural frequencies with the load parameter λ for $\alpha = 0.10$ and $\alpha = 0.25$ are shown in Fig. 2b, c, respectively. As λ increases, the fundamental frequencies decrease and become null at the critical load. The second natural frequency follows the same pattern, being zero at the second bifurcation load. For $\alpha = 0.25$, the two frequencies become zero simultaneously.

3 Nonlinear Dynamics Analysis

Figure 3 shows the bifurcation diagrams of the Poincaré map as a function of the force parameter F for selected values of the excitation frequency β , and considering $\alpha = 0.10$ and $\lambda = 0.0$. These bifurcation diagrams highlight the different bifurcation sequences that lead to parametric instability and escape from the potential pre-buckling well. Continuous lines represent stable solutions and dashed lines represent unstable solutions. These bifurcation diagrams were obtained through the simultaneous use of brute force and continuation methods.

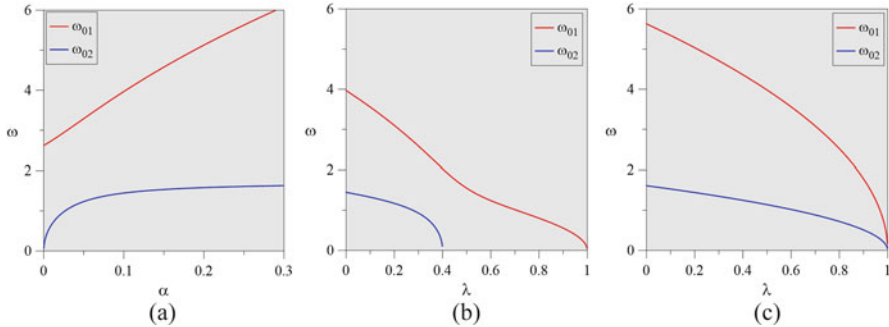


Fig. 2 Variation of the two natural frequencies. **(a)** With the stiffness parameter α , $\lambda = 0.0$. **(b)** With the load parameter λ , $\alpha = 0.10$. **(c)** With the load parameter λ , $\alpha = 0.25$

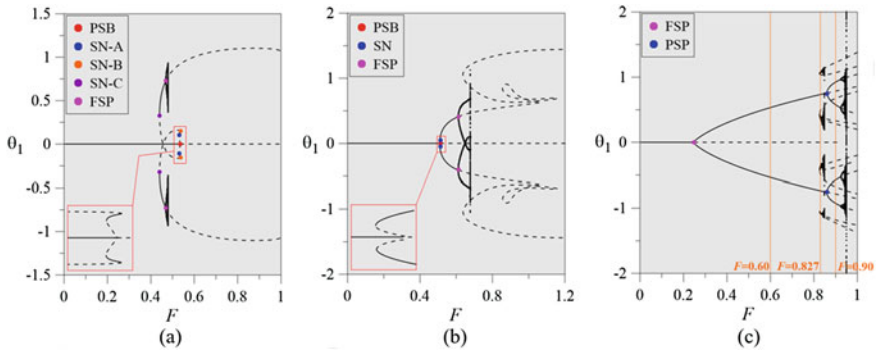


Fig. 3 Bifurcation diagrams for $\alpha = 0.10$ and $\lambda = 0.0$. **(a)** $\beta = 1.00$, **(b)** $\beta = 1.25$, **(c)** $\beta = 2.90$

The initial solution corresponds to the stable trivial solution. This solution becomes unstable, for a given value of the excitation frequency β , at a critical excitation force, F_{cr} , which corresponds to the parametric instability. For $\beta = 1.00$ (Fig. 3a) and $\beta = 1.25$ (Fig. 3b), the trivial solution loses stability through a subcritical pitchfork bifurcation (PSB), where two unstable solutions are born. For $\beta = 1.00$, the unstable solutions becomes stable after a node-saddle bifurcations (SN-A) (see detail in the inset Fig. 3a). After this a new saddle-node bifurcation occurs at SN-B. The ensuing unstable paths become stable due to a third saddle-node bifurcation (SN-C). The resulting stable two mirror solutions undergo a supercritical flip (period-doubling) bifurcation (FSP) leading to escape from the pre-buckling well. For $\beta = 1.25$, the unstable solutions become stable again through a node-saddle bifurcation (SN-A) and followed by the supercritical flip bifurcation (FSP). For $\beta = 2.90$ (Fig. 3c), the trivial solution loses stability through a supercritical flip bifurcation (FSP), where a stable period two solution is born. The stable period two solution is observed for a broad region of the forcing magnitude F and is followed by a supercritical pitchfork bifurcation (PSP). Between $F = 0.82$ and $F = 0.95$

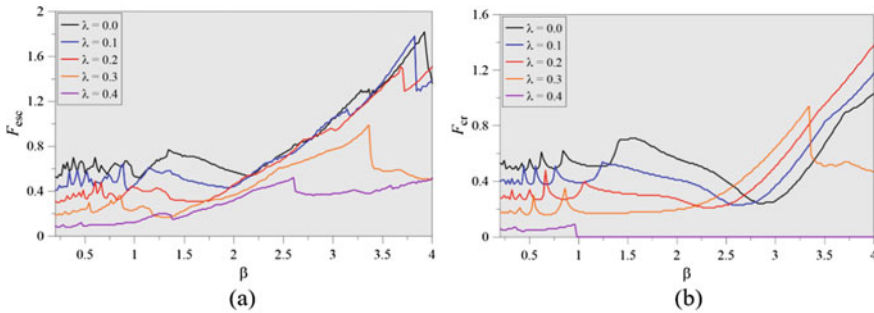


Fig. 4 Stability boundaries for $\alpha = 0.10$. (a) Escape, (b) parametric instability

several bifurcations leading to several coexisting solutions are observed, resulting in a complex dynamic behavior and high sensitivity to initial conditions.

Figure 4 shows the escape and parametric instability boundaries in force control space (forcing frequency vs. forcing magnitude), considering $\alpha = 0.10$ and increasing values of λ . The escape load, F_{esc} , corresponds to escape from the pre-buckling potential well in a slowly evolving system (dynamic buckling) and the parametric instability load, F_{cr} , corresponds to the load where the trivial solution becomes unstable. These boundaries are obtained, as exemplified in Fig. 3, by mapping all the bifurcations prior to escape for a large number of forcing frequencies by increasing slowly the forcing amplitude while holding the frequency constant. The procedure used to determine the escape load does not guarantee that the load obtained corresponds to the load where the full erosion of the basin of attraction occurs. As shown by Soliman and Thompson [18, 19], if at the first point of catastrophic bifurcation (saddle-node or subcritical) there are other solutions within the potential well, the escape becomes indeterminate. Therefore, in the present numerical procedure, depending on the value of load increment and the disturbance in the initial conditions, one may or may not escape in certain regions. The escape and parametric instability boundaries present a similar behavior, decreasing as the compressive static preload parameter λ increases. For the escape boundary a critical region, where F_{esc} reaches a local minimum point, is found between the first natural frequency (ω_1) and twice the first natural frequency ($2\omega_1$), see Fig. 5. The parametric instability boundary shows that F_{cr} reaches a local minimum at twice the first natural frequency ($2\omega_1$), see Fig. 5. The behavior of the model in these critical regions is due to the interaction between the two vibration modes, which show a typical softening behavior [16, 17]. Other resonance regions associated with ω_1 and sub-multiples of ω_1 (sub-harmonics) are also observed. Figure 5 compares the escape and parametric instability boundaries for $\alpha = 0.10$ and two values of λ . For some values of the excitation frequency, β , the parametric and escape loads coincide. This occurs in regions where the bifurcation of the trivial solution is subcritical and there are no other stable solutions for $F > F_{\text{cr}}$ (Fig. 3a).

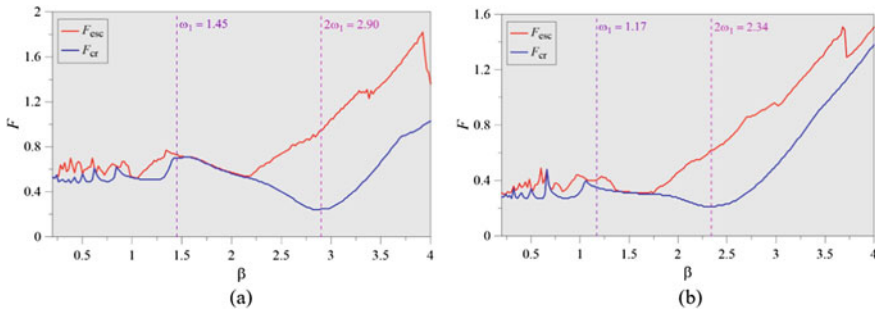


Fig. 5 Stability boundaries, escape versus parametric instability, for $\alpha = 0.10$. (a) $\lambda = 0.0$, (b) $\lambda = 0.2$

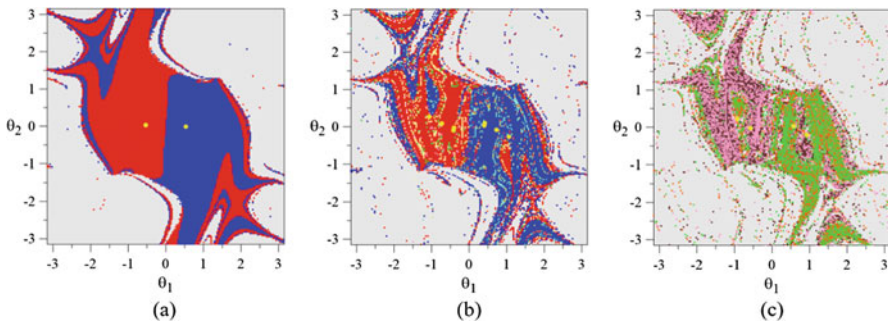


Fig. 6 Basins of attraction for $\alpha = 0.10$, $\lambda = 0.0$, and $\beta = 2.90$. (a) $F = 0.60$, (b) $F = 0.827$, (c) $F = 0.90$

In order to evaluate the safety of a given structure, it is necessary to evaluate the erosion of the basins of attraction as a function of a control parameter [20]. Figure 6 shows the basins of attraction for $\alpha = 0.10$, $\lambda = 0.0$ and $\beta = 2.90$, and increasing values of F , indicated in Fig. 3c. The grey region corresponds to solutions that diverge to infinity or converge to attractors outside the bounds of the initial conditions window. As F increases, the erosion and stratification of the basins of attraction increase. For $F = 0.60$, Fig. 6a, the basin of attraction corresponds to the stable period two solution originating from the supercritical flip bifurcation (FSP), see Fig. 3c, showing the beginning of the erosion of the compact region of the basin of attraction. In Fig. 6b, it is observed for $F = 0.827$, in addition to the period two solution, there is coexisting stable period three solution which contributes to the increasing erosion and stratification process of the compact region. For $F = 0.90$, Fig. 6c, after the supercritical pitchfork bifurcation (PSP), Fig. 3c, there are two stable period two solutions that begin to form a diffuse set of points, that is, a situation that precedes a chaotic region by a cascade of doubling period bifurcations.

4 Conclusion

In this chapter, the static and dynamic behavior of a 2D phenomenological model of a structural system liable to flexural and sway buckling is studied through a detailed parametric analysis. It is shown that, depending on the relative values of the flexural and lateral stiffness, strong modal coupling may occur, leading to various unstable post-buckling solutions that control the geometry of the safe pre-buckling potential well and, consequently, the global behavior of the system under dynamic loads. For a typical case in this region, the nonlinear vibration of the model under harmonic axial force is analyzed. The parametric and escape instability boundaries are obtained and the bifurcations preceding these phenomena are identified. Different types of bifurcations are observed, leading to coexisting attractors and complex basins of attraction, which illustrates the deleterious influence of modal coupling on the dynamic integrity of the structure.

Acknowledgments The authors acknowledge the financial support of the Brazilian research agencies CAPES [finance code 001 and grant number 88881.196767/2018-01], CNPq [grant number 164925/2017-1], and FAPERJ-CNE [grant number E-26/203.020/2015].

References

1. Trahair, N.S.: Steel structures—elastic in-plane buckling of pitched roof portal frames. Limit states data sheet AS 4100 DS04, pp. 1–2. Australian Institute of Steel Construction and Standards Australia (1993)
2. Au, F.T.K., Yan, Z.H.: Dynamic analysis of frames with material and geometric nonlinearities based on the semi-rigid technique. *Int. J. Struct. Stab. Dyn.* **8**(3), 415–438 (2008)
3. Koiter, W.T.: On the stability of elastic equilibrium. Nasa report no TT-F-10833 (translation of: over Stabiliteit van het Elastische Evenwicht, Ph.D. thesis, Delft, ND, 1945) (1967)
4. Croll, J.G., Walker, A.C.: Elements of Structural Stability. Macmillan, London (1972)
5. Thompson, J.M.T., Hunt, G.W.: A General Theory of Elastic Stability. John Wiley and Sons, London (1973)
6. Gioncu, V.: General theory of coupled instabilities. *Thin-Walled Struct.* **19**(2–4), 81–127 (1994)
7. Dubina, D., Ungureanu, V.: Instability mode interaction: from Van Der Neut model to ECBL approach. *Thin-Walled Struct.* **81**, 39–49 (2014)
8. Hancock, G.J.: Coupled instabilities in metal structures (CIMS)—what have we learned and where are we going? *Thin-Walled Struct.* **128**, 2–11 (2018)
9. Orlando, D.: Nonlinear dynamics, instability and control of structural systems with modal interaction. Ph.D. thesis, Pontifícia Universidade Católica do Rio de Janeiro (2010) (in Portuguese)
10. Augosti, G.: Stabilità di Strutture Elastiche Elementari in Presenza di Grandi Spostamenti. Atti Accad. Sci. Fis. Napoli, **4**(5). Serie 3. 1-47 (1964). (in Italian)
11. Thompson, J.M.T., Gaspar, Z.: A buckling model for the set of umbilic catastrophes. *Math. Proc. Camb. Phil. Soc.* **82**, 497 (1977)
12. Orlando, D., Gonçalves, P.B., Rega, G., Lenci, S.: Influence of modal coupling on the nonlinear dynamics of Augosti's model. *J. Comput. Nonlinear Dyn.* **6**(4), 41014 (2011)

13. Orlando, D., Gonçalves, P.B., Rega, G., Lenci, S.: Influence of symmetries and imperfections on the non-linear vibration modes of archetypal structural systems. *Int. J. Non Linear Mech.* **49**, 175–195 (2013)
14. Orlando, D., Gonçalves, P.B., Rega, G., Lenci S.: Nonlinear dynamics and instability as important design concerns for a guyed mast. In: IUTAM Symposium on Nonlinear Dynamics for Advanced Technologies and Engineering Design, Aberdeen (27-30/07), pp. 223–234 (2013)
15. Raithel, A., Clemente, P.: On the stability of pin-joined stiffened frames. *Thin-Walled Struct.* **19**(2–4), 211–220 (1994)
16. Raimundo, J.M.P.: Influência da interação não linear entre flexão e deslocamento lateral na instabilidade estática e dinâmica de um modelo conceitual de coluna. Master Dissertation, Pontifícia Universidade Católica do Rio de Janeiro (2018) (in Portuguese)
17. Raimundo, J.M.P., Gonçalves, P.B., Orlando, D.: Influence of nonlinear interaction between flexural and sway-buckling on the static and parametric instability of column and frame structures. In: Eighth International Conference on Thin-Walled Structures, Lisbon (2018)
18. Soliman, M.S., Thompson, J.M.T.: Integrity measures quantifying the erosion of smooth and fractal basins of attraction. *J. Sound Vib.* **135**, 453–475 (1989)
19. Soliman, M.S., Thompson, J.M.T.: Global dynamics underlying sharp basin erosion in driven oscillators. *Phys. Rev. A.* **45**(6), 3425–3431 (1992)
20. Rega, G., Lenci, S.: Dynamical integrity and control of nonlinear mechanical oscillators. *J. Vib. Control.* **14**, 159–179 (2008)

Influences of Temperature on Dynamic Behaviors of Suspended Cables Under Primary and Sub-Harmonic Excitations Simultaneously



Yaobing Zhao, Henghui Lin, Lincong Chen, and Zixiong Guo

Abstract A better understanding of thermal effects on the nonlinear dynamic system would bring valuable benefits to engineering. Here, the primary and sub-harmonic resonances for a typical nonlinear system, a suspended cable in thermal environments, have been studied. Specifically, by using the perturbation method and direct numerical integrations, one of the simultaneous resonances has been studied. Numerical results demonstrate that the hardening, softening, or mixed hardening–softening spring behaviors are switched owing to temperature variations. The response amplitudes, velocities, and displacements are susceptible to temperature changes, but their periodic motions seem to be independent of thermal effects.

Keywords Suspended cable · Thermal environment · Simultaneous resonance · Perturbation analysis · Vibration characteristic

1 Introduction

As to many engineering applications, structures are always not only subjected to complex external dynamical loadings but also exposed to time changing environmental conditions. In the last decades, environment conditions on vibration characteristics of structures have gained increasing interest. One of the most critical and significant environmental disturbances is the temperature [1]. Many researchers addressed their efforts in investigating dynamic properties of some basic structural elements with thermal effects, such as plates and beams [2–6].

Y. Zhao (✉)

College of Civil Engineering, Huaqiao University, Xiamen, Fujian, China

Hunan Provincial Key Laboratory of Structures for Wind Resistance and Vibration Control,
Hunan University of Science and Technology, Xiangtan, Hunan, China
e-mail: Ybzhaoh@hqu.edu.cn

H. Lin · L. Chen · Z. Guo

College of Civil Engineering, Huaqiao University, Xiamen, Fujian, China

© Springer Nature Switzerland AG 2020

W. Lacarbonara et al. (eds.), *Nonlinear Dynamics of Structures, Systems and Devices*, https://doi.org/10.1007/978-3-030-34713-0_22

217

Due to its inherent flexibility, lightweight, and high-tension resistance, the suspended cable has also aroused general concerns in the last few years [7]. In fact, the suspended cable is susceptible to the ambient environment. The pre-stressed situation is changed, and a new thermally stressed configuration is generated in thermal environments [8]. The most common cause is the tension reduction/increment owing to temperature variations. Specifically, the natural frequencies and mode shapes derived from the eigenvalue analysis of the model in different warming and cool conditions are illustrated in [9–12], while extensions of nonlinear vibration behaviors with thermal effects are presented in [13–16]. In view of these facts, there is a growing interest in studying temperature effects on the nonlinear dynamics of cables.

Actually, both in the engineering applications and the laboratory experiments, the external excitation always contains many different types of resources. Under multi-frequency excitations, the nonlinear systems exhibit abundant and complex nonlinear vibration characteristics by using the analytical, numerical, and experimental techniques [17–24].

The main goal of the work is to investigate how the vibration characteristics of the nonlinear planar oscillations are influenced by temperature changes. Following what has been done in [15, 16], some more in-depth analyses on temperature effects on simultaneous resonance have been given by using the perturbation and numerical methods.

This paper is structured as follows: in Sect. 2, taking into account temperature effects, the partial and ordinary differential equations of motion of the suspended cable are given. Then, the multiple time scales method is applied to obtain the non-trivial solutions in Sect. 3. By plotting the perturbation and numerical solutions, vibration behaviors in different temperature conditions are discussed in Sect. 4. Finally, a set of conclusions round up the paper in Sect. 5.

2 Mathematical Modeling

As shown in Fig. 1, a vibrating suspended cable with span L and initial sag b is considered, and there are three different configurations to the thermal and mechanical loads. $\Delta T = T - T_0$, where T_0 is the initial temperature, and ΔT denotes the temperature variation before loadings. $b_{\Delta T}$ denotes the sag in the thermally stressed configuration. The reference coordinate system ($O - xy$) is presented in Fig. 1, and the displacements are denoted by $v(x, t)$ ($\bar{v}(x, t)$) and $u(x, t)$ ($\bar{u}(x, t)$) along the transverse and longitudinal directions, respectively.

Generally, a suspended cable in thermal environments is affected by temperature changes in many resources, e.g., tension forces (sag-to-span ratios) and material properties. By using the direct force method, a cubic equation is obtained [8, 9]

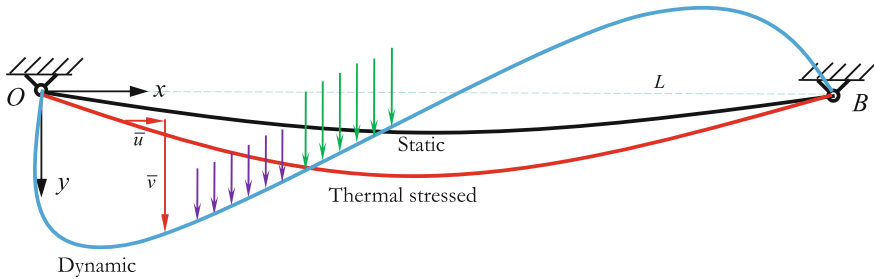


Fig. 1 A schematic figure of a suspended cable in thermal environments

$$\Delta h^3 + \left(2 + \theta_{\Delta T} + \frac{\lambda^2}{24}\right) \Delta h^2 + \left(1 + 2\theta_{\Delta T} + \frac{\lambda^2}{12}\right) \Delta h + \theta_{\Delta T} = 0, \quad (1)$$

where

$$\begin{aligned} \Delta h &= \frac{h}{H}, \quad \theta_{\Delta T} = \frac{\alpha \Delta T L_t}{H L_e} E_{\Delta T} A_{\Delta T}, \quad \lambda_{\Delta T}^2 = \left(\frac{mgL}{H}\right)^2 \frac{E_{\Delta T} A_{\Delta T}}{H L_e}, \\ L_t &= L \left(1 + \frac{m^2 g^2 L^2}{8H^2}\right), \quad L_e = L \left(1 + \frac{m^2 g^2 L^2}{12H^2}\right), \end{aligned} \quad (2)$$

where h is an increment/reduction of the tension force induced by temperature changes; H is the initial horizontal tension force; α is the thermal expansion coefficient; m is the mass per unit length; $A_{\Delta T}$, $E_{\Delta T}$, and $\lambda_{\Delta T}^2$ are the cross-section area, Young's modulus, and Irvine parameter considering thermal effects, respectively. $\Delta T = T - T_0$, where T_0 is the initial temperature, and ΔT denotes the temperature variation before loadings.

Hence, the variation of the tension force and sag could be described by the following non-dimensional parameter [10]

$$\chi_{\Delta T}^2 = 1 + \Delta h = \frac{h + H}{H} = \frac{H_{\Delta T}}{H} = \frac{b}{b_{\Delta T}}, \quad (3)$$

where $b_{\Delta T}$ (b) and $H_{\Delta T}$ (H) are the cable sag and tension force with (without) thermal effects, respectively.

Neglecting temperature effects, by using a kinematic condensation procedure, the partial differential equation of the planar motion of the suspended cable could be obtained [7]. Moreover, an analytical model, including the horizontal suspended and inclined cables, incorporating the temperature effects, has been built by Lepidi and Gattulli [10]. Here, some parameters are closely related to temperature changes, e.g., H , c , E , A , and y (y' , y''). Hence, the partial differential equation of motion is expressed as follows:

$$\begin{aligned}
& m \ddot{\bar{v}} + \underline{c_{\Delta T} \dot{\bar{v}}} - \underline{\chi_{\Delta T}^2 H \bar{v}''} - \frac{E_{\Delta T} A_{\Delta T}}{L} \left(\frac{y''}{\underline{\chi_{\Delta T}^2}} + \bar{v}'' \right) \int_0^L \left(\frac{y' \bar{v}'}{\underline{\chi_{\Delta T}^2}} + \frac{1}{2} \bar{v}'^2 \right) dx \\
& = \sum_{m=1}^2 K_m \cos(\Omega_m t + \theta_m),
\end{aligned} \tag{4}$$

where the prime and overdot denote the partial differential with respect to x and t ; $c_{\Delta T}$ is the viscous damping coefficient; $y(x)$ is the cable initial profile. Two external distributed loads are denoted by $K_m \cos(\Omega_m t + \theta_m)$, ($m = 1, 2$), where K_m , Ω_m and θ_m are the excitation amplitudes, frequencies, and phases, respectively.

The following dimensionless parameters and variables are adopted:

$$\begin{aligned}
\bar{v}^* &= \frac{\bar{v}}{L}, \quad x^* = \frac{x}{L}, \quad y^* = \frac{y}{L}, \quad f^* = \frac{b}{L}, \quad t^* = \sqrt{\frac{g}{8b}} t, \\
c_{\Delta T}^* &= \sqrt{\frac{8b}{g}} \frac{c_{\Delta T}}{m}, \quad \Theta_{\Delta T} = \frac{E_{\Delta T} A_{\Delta T}}{H}, \quad K_m^* = \frac{K_m L}{H}, \quad \Omega_m^* = \sqrt{\frac{8b}{g}} \Omega_m.
\end{aligned} \tag{5}$$

Here, considering the temperature effect, substituting Eqs. (5) into (4) and neglecting asterisk notations, one obtains [10, 16]

$$\begin{aligned}
& \ddot{\bar{v}} + \underline{c_{\Delta T} \dot{\bar{v}}} - \underline{\chi_{\Delta T}^2 \bar{v}''} - \underline{\Theta_{\Delta T}} \left(\frac{y''}{\underline{\chi_{\Delta T}^2}} + \bar{v}'' \right) \int_0^1 \left(\frac{y' \bar{v}'}{\underline{\chi_{\Delta T}^2}} + \frac{1}{2} \bar{v}'^2 \right) dx \\
& = \sum_{m=1}^2 K_m \cos(\Omega_m t + \theta_m).
\end{aligned} \tag{6}$$

The in-plane displacement is decomposed by a sum of the generalized coordinate $q_n(t)$ and mode shapes $\varphi_n(x)$

$$\bar{v}(x, t) = \sum_{n=1}^{\infty} q_n(t) \varphi_n(x). \tag{7}$$

Substituting Eqs. (7) into (6), multiplying the results with $\varphi_n(x)$ and integrating the outcomes from 0 to 1, the following discretized equation is obtained:

$$\begin{aligned}
& \ddot{q}_n + \omega_n^2 q_n + 2\mu_n \dot{q}_n + \sum_{j=1}^{\infty} \sum_{k=1}^{\infty} \Lambda_{jkn} q_j q_k + \sum_{j=1}^{\infty} \sum_{k=1}^{\infty} \sum_{l=1}^{\infty} \Gamma_{jkl n} q_j q_k q_l \\
& = 2 \sum_{m=1}^2 K_m n \cos(\Omega_m t + \theta_m),
\end{aligned} \tag{8}$$

in which coefficients depending on the cable properties with thermal effects are given in [16]. An eigenanalysis on the linear parts of the Eq. (8) is performed [15].

3 Perturbation Analysis

Considering the single-mode discretization, the analytic solutions of Eq. (8) are obtained by using the multiple time scales method in the case of simultaneous resonance (e.g., $\Omega_1 \approx \omega_1$ and $\Omega_2 \approx 2\omega_1$). Firstly, different time scales and derivatives are defined, and the solution is represented from the zeroth order to the second one. After that, the nonlinear and excitation terms are re-ordered, and three ordinary differential equations are obtained and solved. Finally, following the same procedure in [17], the equations governing the steady-state solutions are obtained

$$\begin{aligned} \omega_1 a [\mu_1 + I_{21} \sin(2\gamma + \theta_2)] - K_{11} \sin(\gamma + \theta_1) &= 0, \\ \omega_1 a [\sigma + \alpha_{11} a^2 - I_{21} \cos(2\gamma + \theta_2)] + K_{11} \cos(\gamma + \theta_1) &= 0, \end{aligned} \quad (9)$$

where ω_1 , σ , a , and γ are the natural frequency, detuning parameter, response amplitude, and phase, respectively, and α_{11} , I_{21} and K_{11} are defined in [23].

4 Numerical Examples and Discussions

The following geometrical and material properties are used: $\rho = 7800 \text{ kg/m}^3$, $\mu_1 = 0.005$, $E = 2.0 \times 10^{11} \text{ Pa}$, $A = 7.069 \times 10^{-2} \text{ m}^2$, $\alpha = 1.2 \times 10^{-5}/^\circ\text{C}$, $L = 200 \text{ m}$, and $f = 0.01$. In this simultaneous resonance case, two amplitudes of excitations are 0.001 and 0.005, respectively, and both excitation phases are neglected ($\theta_1 = \theta_2 = 0$).

The stable and unstable non-trivial responses are represented by solid and dotted lines. Numerical analyses considering the direct integration of the original ODEs are given by using the fourth-order Runge–Kutta method. Specifically, both forward and backward variations in excitation frequencies which described by circles and crosses are adopted.

Figure 2 shows the relationships between the excitation frequency and the response amplitude in three different temperature conditions. As shown in Fig. 2, one branch resembles these curves for the sub-harmonic resonance, and the other two branches resemble those for the primary one. Two unstable and three stable steady-state solutions are exhibited in a specific frequency domain.

As to the initial state ($\Delta T = 0^\circ\text{C}$), the resonant frequency-amplitude diagrams of the nonlinear system bend towards the left typical of a softening nonlinear behavior. As shown in Fig. 2b, some good quantitative and qualitative agreements are found in wide response amplitudes except the very large ones. Numerical integration

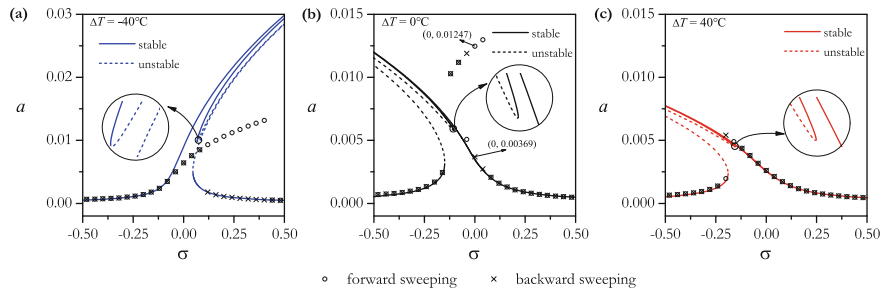


Fig. 2 Vibration behaviors with thermal effects: (a) -40°C ; (b) 0°C ; (c) 40°C

solutions demonstrate that the nonlinear system shows a mixed softening-hardening type behavior in this case. There are two jump-up points and two jump-down ones. Jumping phenomenon occurring from one stable branch to another stable one would be observed at the saddle-node bifurcation.

Provided that the temperature increases ($\Delta T = 40^{\circ}\text{C}$), the nonlinear frequency-amplitude diagrams still bend towards the left side, but the peak value of the response amplitude decreases, just as shown in Fig. 2c. It is noted that the softening behavior becomes stronger with an increase in temperature. In this case, perturbation solutions are found to be in a good agreement with those of direct numerical integration.

However, in the case of -40°C , the curves now bend towards the right side, and the nonlinear system displays a definite hardening type nonlinearity. As shown in Fig. 2a, comparisons between two types of solutions show a good agreement, but some quantitative differences are observed for the large value of response amplitudes. The peak value of the response amplitude obtained with the numerical integration decreases, so the nonlinear system displays a stronger hardening behavior compared with the perturbation solutions. However, the accuracy of the multiple timescales method could be improved if a higher-order solution is adopted.

Furthermore, more nonlinear dynamics with thermal effects are exhibited by investigating time domain response curves (Fig. 3a), phase-plane curves (Fig. 3b), and Poincaré sections (Fig. 3c). For the sake of simplicity, only the case of $\sigma = 0$ is illustrated for an example. Especially, in the case of 0°C , there is a mixed softening-hardening type behavior. There are two stable steady-state solutions $(0, 0.00369)$ and $(0, 0.01247)$ in this case, but which one is finally determined depends on the initial condition.

As shown in Fig. 3, effects of temperature variations produce some apparent quantitative changes in time history curves and phase diagrams. Additionally, as a useful and standard tool, Poincaré sections indeed preserve various characteristics of periodic motions of the nonlinear systems. It is noted that the Poincaré sections include the data between the displacements and the velocities of the suspended cable in a compact form, and these two parameters seem to be sensitive to temperature. As described in Fig. 3b,c, the stable periodic motion is illustrated by just one circle in

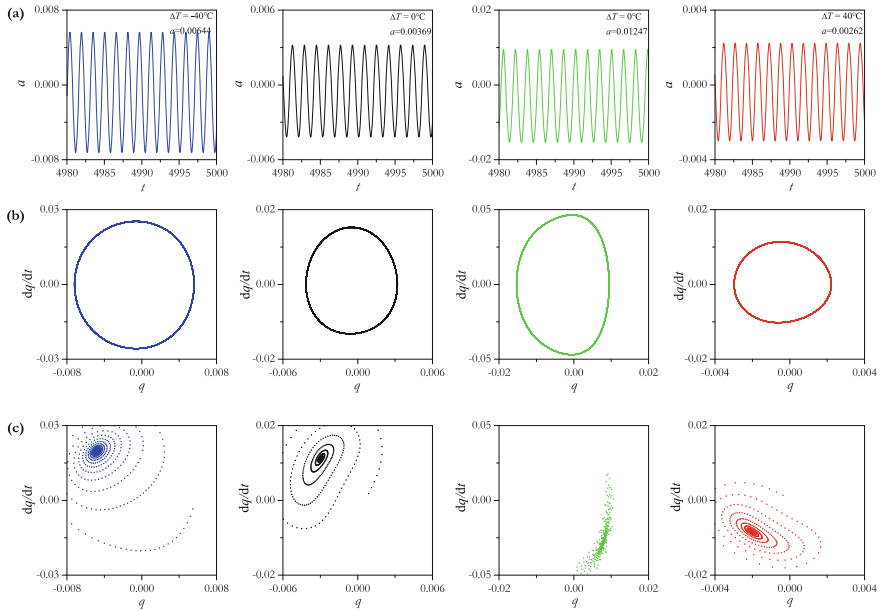


Fig. 3 Vibration behaviors with thermal effects when $\sigma = 0$: (a) time domain response curves; (b) phase-plane diagrams; (c) Poincaré sections

phase-plane curves and by just one clustered point in Poincaré sections. Although the considering temperature variation does slightly change the type of the phase-plane curves and Poincaré sections, it does not change the number of the circle and the clustered point formed by dots. It is noted that the periodic motion is independent of temperature changes in this case.

5 Conclusions

Vibration characteristics are subjected to various changes in thermal environments. These hardening, softening, or mixed softening-hardening type behaviors are switched induced by temperature variations. The velocities and displacements are susceptible to temperature effects. However, the number of the circle in phase-plane diagrams and the cluster points in Poincaré sections seem to be independent of temperature variations.

Acknowledgements The research was financially supported by Natural Science Foundation of China (11602089) and Promotion Program for Young and Middle-aged Teacher in Science and Technology Research of Huaqiao University (ZQN-YX505).

References

1. Xia, Y., Chen, B., Weng, S., Ni, Y.Q., Xu, Y.L.: Temperature effect on the vibration properties of civil structures: a literature review and case studies. *J. Civ. Struct. Heal. Monit.* **2**, 29–46 (2012)
2. Shen, H.S., Wang, Z.X.: Nonlinear vibration of hybrid laminated plates resting on elastic foundations in thermal environments. *Appl. Math. Model.* **36**(12), 6275–6290 (2012)
3. Amabili, M., Carra, S.: Thermal effects on geometrically nonlinear vibrations of rectangular plates with fixed edges. *J. Sound Vib.* **321**(3), 936–954 (2009)
4. Farokhi, H., Ghayesh, M.H.: Thermo-mechanical dynamics of perfect and imperfect Timoshenko microbeams. *Int. J. Eng. Sci.* **91**, 12–33 (2015)
5. Ghayesh, M.H., Amabili, M.: Nonlinear stability and bifurcations of an axially moving beam in thermal environment. *J. Vib. Control* **21**, 2981–2994 (2015)
6. Warminska, A., Manoach, E., Warminski, J.: Nonlinear dynamics of a reduced multimodal Timoshenko beam subjected to thermal and mechanical loadings. *Meccanica* **49**, 1775–1793 (2014)
7. Rega, G.: Nonlinear vibrations of suspended cables, Part I: modeling and analysis. *Appl. Mech. Rev.* **57**, 443–478 (2004)
8. Irvine, H.M.: *Cable Structures*. The MIT Press, Cambridge (1981)
9. Treyyssède, F.: Free linear vibrations of cables under thermal stress. *J. Sound Vib.* **327**, 1–8 (2009)
10. Lepidi, M., Gattulli, V.: Static and dynamic response of elastic suspended cables with thermal effects. *Int. J. Solids Struct.* **49**(9), 1103–1116 (2012)
11. Ashwear, N., Eriksson, A.: Influence of temperature on the vibration properties of tensegrity structures. *Int. J. Mech. Sci.* **99**, 237–250 (2015)
12. Treyyssède, F.: Finite element modeling of temperature load effects on the vibration of local modes in multi-cable structures. *J. Sound Vib.* **413**, 191–204 (2018)
13. Bouaanani, N., Marcuzzi, P.: Finite difference thermoelastic analysis of suspended cables including extensibility and large sag effects. *J. Therm. Stresses* **34**, 18–50 (2011)
14. Montassar, S., Mekki, O.B., Vairo, G.: On the effects of uniform temperature variations on stay cables. *J. Civ. Struct. Heal. Monit.* **5**, 735–742 (2015)
15. Zhao, Y., Peng, J., Zhao, Y., Chen, L.: Effects of temperature variations on nonlinear planar free and forced oscillations at primary resonances of suspended cables. *Nonlinear Dyn.* **89**, 2815–2827 (2017)
16. Zhao, Y., Huang, C., Chen, L., Peng, J.: Nonlinear vibration behaviors of suspended cables under two-frequency excitation with temperature effects. *J. Sound Vib.* **416**, 279–294 (2018)
17. Plaut, R.H., Haquang, N., Mook, D.T.: Simultaneous resonances in non-linear structural vibrations under two-frequency excitation. *J. Sound Vib.* **106**, 361–376 (1986)
18. Hegazy, U.H.: Nonlinear vibrations of a thin plate under simultaneous internal and external resonances. *ASME J. Vib. Acoust.* **132**, 051004 (2010)
19. Sahoo, B., Panda, L.N., Pohit, G.: Two-frequency parametric excitation and internal resonance of a moving viscoelastic beam. *Nonlinear Dyn.* **82**, 1721–1742 (2015)
20. Mao, X.Y., Ding, H., Lim, C.W., Chen, L.Q.: Super-harmonic resonance and multi-frequency responses of a super-critical translating beam. *J. Sound Vib.* **385**, 267–283 (2016)
21. Zulli, D., Luongo, A.: Control of primary and subharmonic resonances of a Duffing oscillator via nonlinear energy sink. *Int. J. Non-Lin. Mech* **80**, 170–182 (2016)
22. Bitar, D., Kacem, N., Bouhaddi, N., Collet, M.: Collective dynamics of periodic nonlinear oscillators under simultaneous parametric and external excitations. *Nonlinear Dyn.* **87**, 2463–2481 (2017)

23. Zhao, Y., Guo, Z., Huang, C., Chen, L., Li, S.: Analytical solutions for planar simultaneous resonances of suspended cables involving two external periodic excitations. *Acta Mech.* **229**(11), 4393–4411 (2018)
24. Bauomy, H.S., El-Sayed, A.T.: Vibration performance of a vertical conveyor system under two simultaneous resonances. *Arch. Appl. Mech.* **88**, 1349–1368 (2018)

Analysis of a Shape Memory Alloy Spring System Under Harmonic Excitation



Shivan Ramnarace and Jacqueline Bridge

Abstract A shape memory alloy (SMA) spring system is analysed to determine its response to harmonic forcing. In particular, the superelasticity effect of the system is investigated. The shape memory alloy is modelled using a piecewise linear force–displacement curve. The SMA spring is arranged so as to introduce a geometric nonlinearity. The system of equations are numerically integrated and frequency response curves are determined. Periodic, quasiperiodic and chaotic motions are observed for different combinations of parameter values.

Keywords Shape memory alloy · Bifurcation · Superelasticity

1 Introduction

Attenuation of vibrations is essential in most engineering equipment. The reduction of high-amplitude oscillations is of particular importance in aerospace structures, civil engineering structures and mechanical machinery [1]. One classical means of vibration control is by attaching a linear vibration absorber to the system. However, this method is limited in that it is only effective over a very narrow frequency bandwidth. The study of nonlinear vibration absorbers has become a field of growing interest as they have been shown to have potential in overcoming this shortcoming. One such case in particular is a nonlinear energy sink (NES). Under certain conditions, an NES can reduce vibrations at multiple resonant (or broadband) frequencies thus becoming far more effective than linear absorbers. Nonlinearity may be imposed on such systems through different means. Some possible sources of nonlinearity include the use of nonlinear springs (such as conical springs), the use of nonlinear materials [2, 3] or the geometrical arrangement of the springs. One simple means of obtaining a nonlinear force–displacement relationship for an

S. Ramnarace · J. Bridge (✉)

Department of Mechanical and Manufacturing Engineering, The University of the West Indies, St. Augustine, Trinidad and Tobago

e-mail: Jacqueline.Bridge@sta.uwi.edu

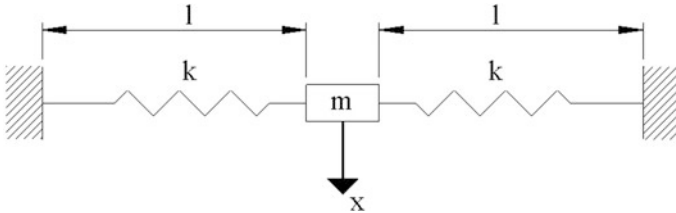


Fig. 1 Orientation of springs to obtain nonlinear stiffness relationship

NES is through the nonlinear geometric relationship obtained by the use of two identical linear springs of stiffness, k and length, l attached to a mass, m oriented perpendicular to the direction of vibration being considered as shown in Fig. 1. As a precursor to examining the absorbing effects of such a nonlinear system, this paper explores the responses that arise from arranging springs made out of shape memory alloy (SMA) as shown in Fig. 1. In particular we explore the effect of superelasticity of the SMA's i.e. the response to the loads which cause the SMA spring to transform between the austenitic and martensitic phases.

2 Mathematical Model

In this paper, the superelasticity relationship is approximated by a piecewise linear force deflection relationship as depicted in Fig. 2, consistent with the works of Madill and Wang [4] and Hu and Noh [5]. The governing equation for the system under harmonic loading is given by:

$$m\ddot{x} + c\dot{x} + 2F_{SMA} \sin\theta = f_0 \sin(\Omega t) \quad (1)$$

where F_{SMA} is the restoring force due to the springs and θ is the deviation in angle between the extended spring and its original orientation. If the initial extension of the spring is δ_0 , then the new length of the spring when the mass is displaced by x from its initial condition is

$$L(x) = \sqrt{((L_0 + \delta_0)^2 + x^2)}$$

resulting in a spring extension, δ of

$$\delta = \sqrt{((L_0 + \delta_0)^2 + x^2)} - L_0$$

and yielding

$$\sin(\theta) = \frac{x}{\sqrt{((L_0 + \delta_0)^2 + x^2)}}$$

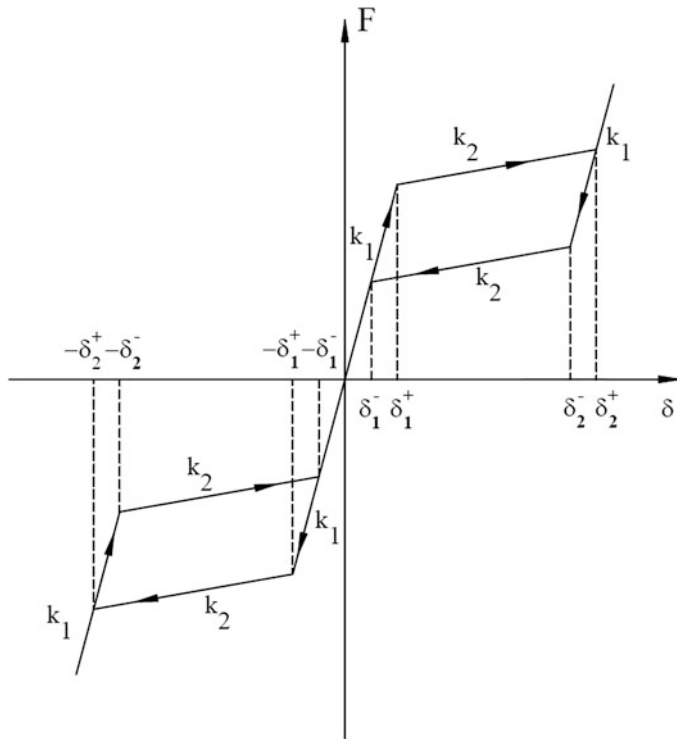


Fig. 2 Force deflection graph of SMA spring above A_f

The force in the SMA spring is dependent on the displacement and velocity of the SMA spring as shown in Fig. 2. The direction of the arrows indicates whether the velocity is positive or negative.

The equations for the system are nondimensionalised using the following relationships:

$$\omega_n^2 = \frac{k_1}{m}, \quad \zeta = \frac{c}{2m\omega_n}, \quad \kappa = \frac{k_2}{k_1}, \quad \tau = \omega_n t, \quad \omega = \frac{\Omega}{\omega_n}$$

$$\gamma = \frac{f_0}{f_{trans}}, \quad \hat{x} = \frac{x}{\delta_2^+}, \quad \hat{\delta}_i^j = \frac{\delta_i^j}{\delta_2^+}$$

Here f_{trans} is the force at which the transformation from austenite to martensite begins. The resulting equation is

$$\hat{x}'' + 2\zeta \hat{x}' + 2F(\hat{\delta}; \hat{\delta}_0) \sin \theta = \gamma \sin(\omega \tau) \quad (2)$$

Table 1 Relationships between the system parameters and the intercept and slope in different segments of the force–displacement curve

Segment	F_i	k_i
1	0	1
2	$(1 - \kappa)\delta_1^+$	κ
3	$(1 - \kappa)(\delta_1^+ - \delta_2^+)$	1
4	$(1 - \kappa)\delta_1^-$	κ
5	0	1
6	$-(1 - \kappa)\delta_1^+$	κ
7	$-(1 - \kappa)(\delta_1^+ - \delta_2^+)$	1
8	$-(1 - \kappa)\delta_1^-$	κ

where $F(\hat{\delta}; \hat{\delta}_0)$ represents the force–displacement curve and can be represented by

$$F(\hat{\delta}; \hat{\delta}_0) = F_i + k_i \hat{\delta}$$

where the values for F_i, k_i within each segment are assigned as per Table 1, and the ' represents differentiation with respect to dimensionless time, τ . For convenience, the ^ has been dropped in the description that follows.

3 Numerical Simulation Method and Results

MATLAB 2018a was used to simulate the system; first the differential equation was rewritten in differential-algebraic form to facilitate the abrupt changes in the slope of the force vs deformation curve. The equation was then solved using an implicit variable step, variable order solver, ode15s, along with a set of event locators. The events correspond to (a) the beginning of the transition from austenite to martensite while the deformation is increasing, (b) the beginning of the transition from martensite to austenite while the deformation is decreasing, (c) the completion of these transformations and (d) the state at which the velocity is zero i.e. the deformation is at a local extremum.

The maximum displacement was plotted as a function of forcing frequency with the initial extension of the spring, the initial displacement and the initial velocity of the mass being held constant at $\delta_0 = 0.1$ and $(x_0, \dot{x}_0) = (1e^{-6}, 0)$, respectively. The amplitude of the force was also constant at half the force required to initiate the transformation from austenite to martensite. The system was undamped, i.e. $\zeta = 0$ in Eq. (2) while the stiffness ratio $\kappa = 0.06$. The system was numerically integrated for 250 periods of the forcing. In determining the maximum displacement, the response during the first 150 periods was ignored to remove the transient effects. The maximum displacement in the latter 100 periods was then recorded.

Figure 3 shows the corresponding frequency response of the system. A variety of steady state solutions exist. These include *regular symmetric period-1* motions as seen in Fig. 4a for $\omega = 0.17$, *asymmetric regular period-1* limit cycles as per

Fig. 3 Frequency response curve for $\delta_0 = 0.1$, $(x_0, \dot{x}_0) = (1e^{-6}, 0)$

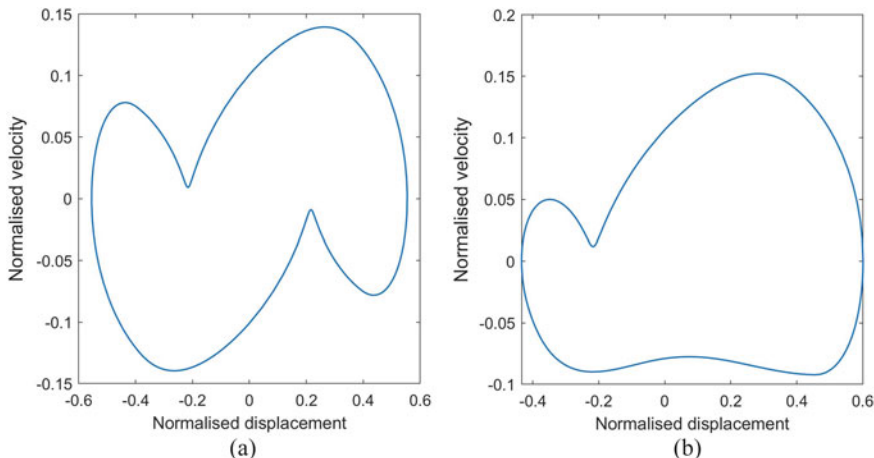
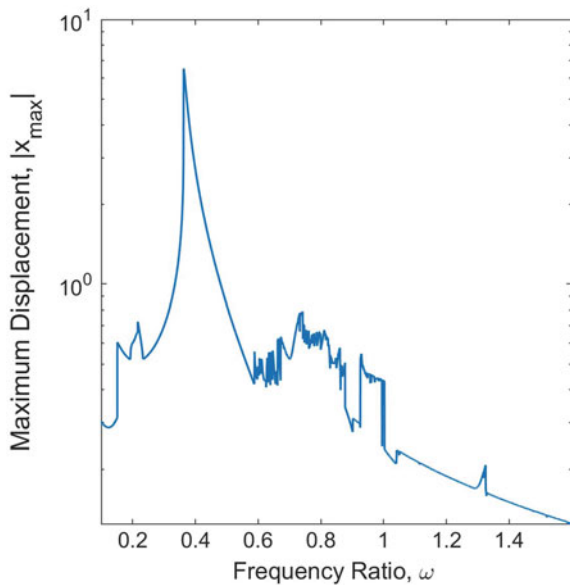


Fig. 4 Phase plots of (a) symmetric period-1 limit cycle at $\omega = 0.17$. (b) Asymmetric period-1 limit cycle at $\omega = 0.2$

Fig. 4b for $\omega = 0.2$, *symmetric regular period-2 limit cycles* as shown in Fig. 5a, b with $\omega = 0.869$ as well as *quasiperiodic* responses (see Fig. 6 corresponding to $\omega = 0.596$) and *chaotic motion* at $\omega = 0.869$ highlighted in Fig. 7.

The step discontinuities in the maximum displacement response (as illustrated at $\omega \approx 0.143$) and the jagged nature of the curve in some regions (such as $0.57 < \omega < 0.97$) suggest that there are coexisting steady state solutions for specific parameters of the system. To test this hypothesis, the system of equations was integrated for the

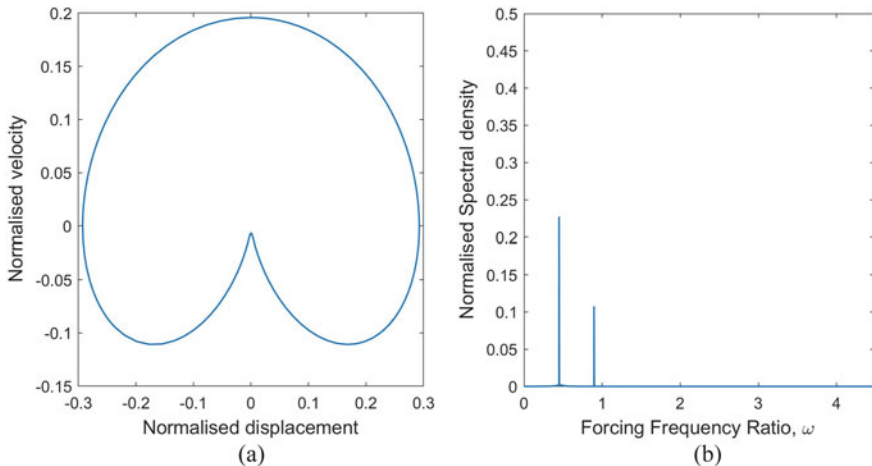


Fig. 5 (a) Phase plots showing a symmetric period-2 limit cycle at $\omega = 0.896$ and (b) Poincaré map for limit cycle at $\omega = 0.896$

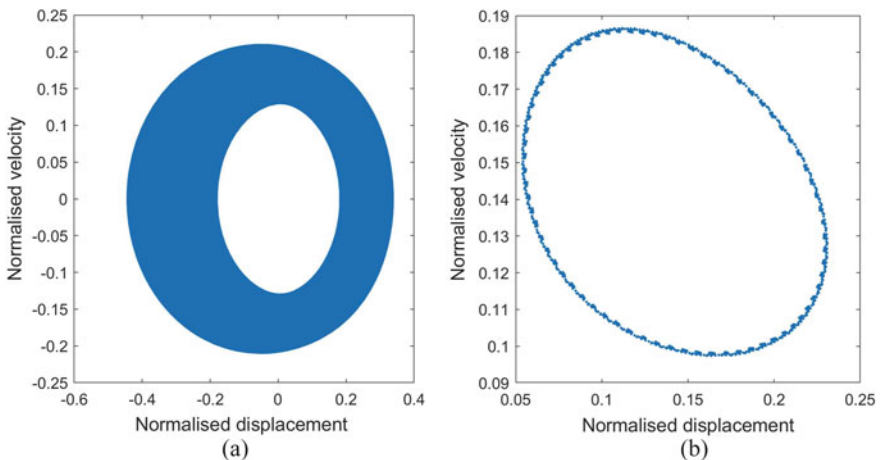


Fig. 6 (a) Phase plots showing a quasiperiodic attractor at $\omega = 0.596$ (b) and its Poincaré map

same initial extension of the springs and the same forcing frequency, but the initial conditions were varied using $(x_0, \dot{x}_0) = (p, 0)$ for $0 < p \leq 0.5$.

Figure 8 shows the frequency response curve for low frequencies. For $\omega = 0.1$, two stable period-1 orbits coexist. The limit cycle with the smaller amplitude, σ_1 , is symmetric while the orbit with the larger amplitude, denoted by σ_2 , is asymmetric. The form of σ_1 remains unchanged while the format of σ_2 varies; it is hypothesised that this is the result of a sequence of period-adding bifurcations following $P_1 \rightarrow P_5 \rightarrow P_3 \rightarrow P_7 \rightarrow P_9 \rightarrow P_5 \rightarrow P_{11}$ at $\omega \approx 0.1034, 0.1042$,

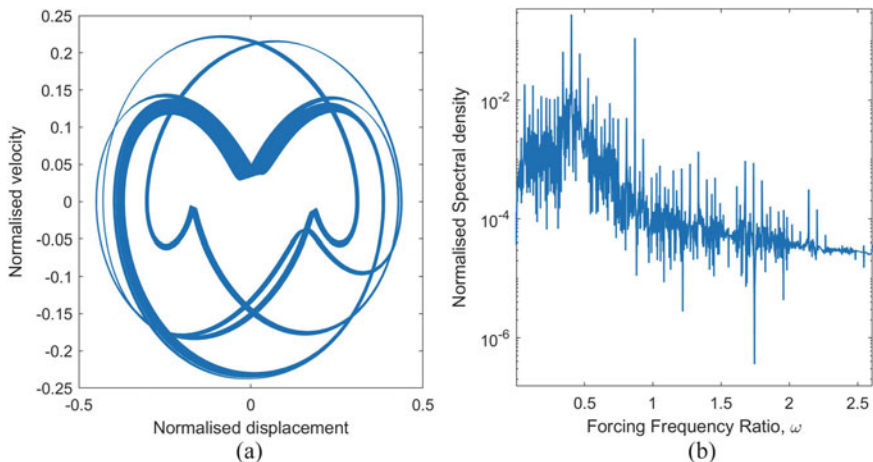
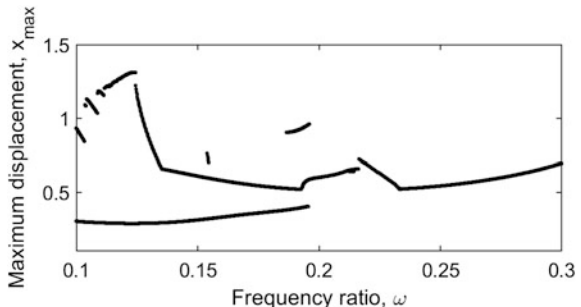


Fig. 7 (a) Phase plots showing a chaotic attractor at $\omega = 0.869$ (b) and its Fourier transform

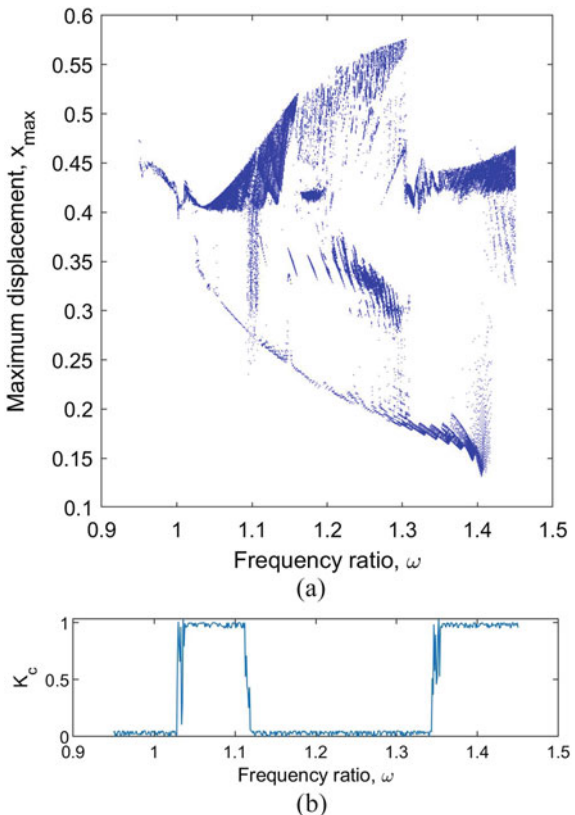
Fig. 8 Bifurcation diagram
for $\delta_0 = 0$, $\gamma = 0.5$ for
 $0.1 < \omega < 0.3$



0.1088, 0.1115, 0.1122, 0.1139, respectively. Here P_k indicates that the period of the response is k times the period of the forcing. This type of bifurcation sequence occurs because of the piecewise nature of the dynamical system and is similar to the period-adding phenomenon described in [6]. Other phenomena of interest include coexistence of two period-1 symmetric orbits and one period-2 asymmetric orbit at $\omega = 0.1925$, with one of the period-1 orbits transitioning to an asymmetric limit cycle by $\omega = 0.1955$; the loss of stability of limit cycles at $\omega \approx 0.2162$ and the change from an asymmetric period-1 cycle to a symmetric period-1 cycle at $\omega \approx 0.2333$.

In the region $0.234 < \omega < 0.54$, only one stable solution exists. Over the interval $1 < \omega < 1.4$, the frequency response function reveals that there is coexistence of quasiperiodic and chaotic responses (Fig. 9a). This is confirmed by the asymptotic growth rate K_{0-1} from the 0–1 test [7], shown in Fig. 9b.

Fig. 9 (a) Bifurcation diagram for $\delta_0 = 0$, $\gamma = 0.5$ for $0.1 < \omega < 0.3$ (a) bifurcation diagram for $\delta_0 = 0$, $\gamma = 0.5$ for $0.95 < \omega < 1.45$ (b) 0–1 test for chaos results



4 Conclusions

In this paper, a system of shape memory alloy springs geometrically arranged to ensure nonlinearity was examined. Various steady state responses were observed including periodic, quasiperiodic and chaotic behaviour. Future work will examine the bifurcation properties of the system as well as experimentally verify the features observed.

References

1. Cuvalci, O., Ertas, A., Ekwaro-Osire, S., Cicek, I.: Non-linear vibration absorber for a system under sinusoidal and random excitation: experiments. *J. Sound Vib.* **249**(4), 701–718 (2002)
2. Lacarbonara, W., Bernardini, D., Vestroni, F.: Nonlinear thermomechanical oscillations of shape-memory devices. *Int. J. Solids Struct.* **41**, 1209–1234 (2004)
3. Oliveira, H., De Paula, A., Savi, M.: Dynamical behavior of a pseudoelastic vibration absorber using shape memory alloys. *Shock. Vib.* (2017). <https://doi.org/10.1155/2017/7609528>

4. Madill, D., Wang, D.: Modeling and L_2 -stability of a shape memory alloy position control system. *IEEE Trans. Control Syst. Technol.* **6**(4), 473–481 (1998)
5. Hu, J., Noh, M.: Seismic response and evaluation of SDOF self-centering friction damping braces subjected to several earthquake ground motions. *Adv. Mater. Sci. Eng.* (2015). <https://doi.org/10.1155/2015/397273>
6. Budd, C.J.: Non-smooth dynamical systems and the grazing bifurcation. In: *Nonlinear Mathematics and Its Applications*, pp. 219–235. Cambridge University Press, Cambridge (1996)
7. Gottwald, G., Melbourne, I.: A new test for chaos in deterministic systems. *Proc. R. Soc. A* **460**, 603–611 (2004)

Vibration of Pre-Loaded Shallow Circular Arches



Uğurcan Eroğlu and Giuseppe Ruta

Abstract We study dynamics of pre-stressed pinned shallow slender circular arches by one-dimensional field equations, simplified and solved by perturbation. The static response to a uniform load and small imperfections is found: the transverse displacement depends in closed form on the load. The first two frequencies of small vibration about the deformed shape, plus possible bifurcations in terms of the initial geometry and the pre-load are found.

Keywords Shallow arch · Perturbation · Vibration · Stability

1 Introduction

Circular arches find many applications. For some values of their geometrical characteristics (e.g., the height-to-span ratio) linear models do not suffice to describe their static and dynamic behavior at different scales [1, 2]; therefore, accurate models are introduced, see e.g. [3–5]. More in detail, we may quote: [6] for studies on boundary conditions; [7] for the effects of shear deformation and of different loading conditions; [8, 9] for transient behavior and dynamic stability; [10] for considerations on thermal effects; and [11] for effects of initial geometric imperfections. A good source on statics of shallow arches is [12], focusing on the effect of mathematical simplifications in the analysis.

Structural identification and health monitoring based on dynamic response has led to studies on pre-loaded structures, since this models their actual operating conditions [13–17]. Furthermore, slender curved structural members offer optimum design solutions in many aspects [18]; hence, their vibration and stability character-

U. Eroğlu

Istanbul Technical University, Istanbul, Turkey

e-mail: ueroglu@itu.edu.tr

G. Ruta (✉)

University “La Sapienza” and National Group for Mathematical Physics, Roma, Italy

e-mail: giuseppe.ruta@uniroma1.it

istics deserve attention [9, 19]. Thence, we study dynamics of pre-loaded shallow slender circular arches, for which the finite 1-D governing equations are simplified. We find the nonlinear static response to a uniform line load; then, by a perturbation approach we study linear elastic small vibration about the deformed shape. We present closed-form results for the natural frequencies, nonlinearily depending on initial deformation, and highlight possible pre- and post-buckling regimes.

2 Statics of Uniformly Loaded Shallow Arches

Let a segment of a circle represent the axis of an arch, seen as a curved beam. Its reference shape is filled by the transverse cross-sections, copies of a prototype compact plane figure attached to the axis and everywhere normal to it.

Let x, y be Cartesian coordinates in the plane of the arch, with relevant unit orthogonal basis $\mathbf{e}_1, \mathbf{e}_2$, and origin at the mid-span of the arch. If f, R are the height and the radius of the arch, the position vector of the axis is

$$\mathbf{r}_0(x) = x\mathbf{e}_1 + y(x)\mathbf{e}_2, \quad (y + R - f)^2 = R^2 - x^2 \quad (1)$$

The (uniform) curvature is $k = 1/R$. If the span has length $2l$ and we consider shallow arches, i.e., $f/l < 0.1$, it is easy to prove that

$$kl \approx 2\frac{f}{l}, \quad ds = |d\mathbf{r}_0(x)| = \frac{1}{\sqrt{1-k^2x^2}}dx \approx dx \quad (2)$$

By Eq. (2)₂ the Cartesian coordinate x very well approximates the curvilinear abscissa s ; all fields on the arch may be thus expressed in terms of s . Let a prime denote derivation with respect to $s \approx x$; unit tangents to the arch axis, $\mathbf{l}(s)$, and their derivative, with magnitude k and directed along the axis normal, are

$$\mathbf{l}(s) = \mathbf{r}'_0(s), \quad k\mathbf{m}(s) = \mathbf{l}'(s) \quad (3)$$

A new shape of the arch is described by the fields $\mathbf{d}(s)$, the vector of the axis displacement, and $\mathbf{R}(s)$, the orthogonal tensor of the cross-sections rotation. Finite strain measures pulled back to the reference configuration are [20–22]

$$\mathbf{u}(s) = \mathbf{R}^T(s)[\mathbf{r}_0(s) + \mathbf{d}(s)]' - \mathbf{l}(s), \quad \mathbf{U}(s) = \mathbf{R}^T(s)\mathbf{R}'(s) \quad (4)$$

The vector \mathbf{u} lists the axis elongation ε and the shearing γ between axis and cross-sections; the component of the skew-symmetric tensor \mathbf{U} is the variation of curvature χ of the axis. If we skip the dependence of all fields on the place along the arch axis for simplicity of notation, the finite strain components are

$$\begin{aligned}\gamma &= -\sin \varphi (u' - kv + 1) + \cos \varphi (v' + ku), \\ \varepsilon &= \cos \varphi (u' - kv + 1) + \sin \varphi (v' + ku) - 1, \quad \chi = \varphi'\end{aligned}\quad (5)$$

where u, v, φ are the displacement components along \mathbf{l}, \mathbf{m} , respectively, and the rotation of the cross-section along the normal to the plane of the arch.

The external actions, defined along the axis and at its ends, are: a force vector field, spending power on the displacement of the arch axis; a couple skew-symmetric tensor field, spending power on the rotation of the cross-sections. They will be denoted $\mathbf{b}, \mathbf{B}, \mathbf{f}, \mathbf{F}$, respectively. Actions by contact among parts of the arch consist of a vector and a skew-symmetric tensor field, spending power on the incremental strains; they will be denoted \mathbf{t}, \mathbf{T} , respectively. The dependence on s will be omitted, as above. All actions are related to those defined in the referential configuration (similar to Piola stress in Cauchy's continua) by

$$\mathbf{b} = \mathbf{R}\mathbf{a}, \quad \mathbf{B} = \mathbf{R}\mathbf{A}\mathbf{R}^T, \quad \mathbf{f} = \mathbf{R}\mathbf{g}, \quad \mathbf{F} = \mathbf{R}\mathbf{G}\mathbf{R}^T, \quad \mathbf{t} = \mathbf{R}\mathbf{s}, \quad \mathbf{T} = \mathbf{R}\mathbf{S}\mathbf{R}^T \quad (6)$$

By usual means and the virtual work principle, the referential balance [20–22]

$$\begin{aligned}s' + \mathbf{U}\mathbf{s} + \mathbf{a} &= \mathbf{0}, \quad \mathbf{S}' + \mathbf{U}\mathbf{S} - \mathbf{S}\mathbf{U} + \mathbf{u} \wedge \mathbf{s} + \mathbf{A} = \mathbf{0} \quad \forall x \in (-l, l) \\ \mathbf{s} &= \mathbf{g}, \quad \mathbf{S} = \mathbf{G} \quad x = \pm l\end{aligned}\quad (7)$$

holds; \wedge is the external product of vectors, providing skew-symmetric tensors.

If the arch is flexible and extensible (i.e., $\gamma = 0$), its linear elastic response is

$$\varepsilon = N/(EA), \quad \chi = M/(EI) \quad (8)$$

with E Young's modulus of the material, A , I the cross-section area and second moment of area with respect to the bi-normal.

To abstract from particular values of the geometrical and physical quantities of the problem, let us introduce the non-dimensional quantities

$$\begin{aligned}\kappa &= kl, \quad \alpha = \frac{f}{l}, \quad v = \frac{u}{l}, \quad \zeta = \frac{v}{l}, \quad \theta = \varphi, \quad \xi = \frac{x}{l} \approx \frac{s}{l}, \\ v &= \frac{Nl^2}{EI}, \quad \tau = \frac{Tl^2}{EI}, \quad \mu = \frac{Ml}{EI}, \quad \lambda = \frac{l}{\sqrt{I/A}}, \quad \Theta_{m,l} = \frac{a_{m,l}l^3}{EI}\end{aligned}\quad (9)$$

Inserting Eq. (9) into Eqs. (5)–(8) and henceforth posing, with abuse of notation, that a prime stands for a ξ -derivative, we obtain the governing equations

$$\begin{aligned}-\sin \theta (v' - \kappa \zeta + 1) + \cos \theta (\zeta' + \kappa v) &= 0, \quad v' - (\kappa + \mu) \tau + \Theta_l = 0, \\ \cos \theta (v' - \kappa \zeta + 1) + \sin \theta (\zeta' + \kappa v) - 1 &= \frac{v}{\lambda^2}, \quad \tau' + (\kappa + \mu) v + \Theta_m = 0, \\ \mu - \theta' &= 0, \quad \mu' + (1 + \varepsilon) \tau = 0\end{aligned}\quad (10)$$

Let us now consider a shallow arch ($\alpha < 0.1$) uniformly loaded by a “vertical” uniformly distributed load. Following numerical and experimental evidence, the transverse displacement v is of the same order of magnitude of f . Furthermore, the tangential and normal components of the line load a_l, a_m are practically zero and equal to the assigned load, respectively. Since the arch ends are pinned, the tangential displacement $u \propto \alpha f$, i.e., it is at least an order smaller than f ; since the arch is slender, the characteristic length of the section is at least an order smaller than l . Under these reasonable and usual assumptions we estimate that

$$\kappa = O(\alpha), \quad v = O\left(\alpha^2\right), \quad \zeta = O(\alpha), \quad \theta = O(\alpha), \quad \lambda^{-1} = O(\alpha) \quad (11)$$

We thus replace the trigonometric functions in strain measures by their series expansions up to $O(\alpha^2)$. Following Mettler’s assumptions [4], the normal force v is uniform along $x \approx s$ and shall be found by imposing pinned ends; moreover, $\varepsilon \ll 1$. Then, if \mathcal{L} is a symbolic differential operator, the system (10) becomes

$$\mathcal{L}[\zeta] = \zeta^{IV} - \zeta''v - 2\alpha v - \Theta_m = 0, \quad v = \frac{\lambda^2}{2} \int_{-1}^1 \left(\frac{1}{2}\zeta^2 - 2\alpha\zeta \right) d\xi \quad (12)$$

Galérkin’s technique requires to replace the actual solution $\zeta(\xi)$ with a sum of admissible functions that verify only boundary conditions, weighted by unspecified amplification factors c_i , then evaluate the residuals obtained by inserting such expression into the governing Eq. (12)

$$R_n(\xi) = \mathcal{L} \left[\sum_{i=1}^{i=n} c_i \zeta_i(\xi) \right] \quad (13)$$

The R_n in Eq. (13) are then projected onto the ζ_i , integrating the product of the residual and each admissible function over $[-1, 1]$. These projections form a set of linear algebraic expressions that are required to vanish.

The boundary conditions for pinned ends and admissible functions are

$$\zeta(-1) = \zeta(1) = \zeta''(-1) = \zeta''(1) = 0, \quad \zeta_1 = \cos[(\pi\xi)/2], \quad \zeta_2 = \sin(\pi\xi) \quad (14)$$

Let the transverse load be the sum of a uniform and a very small skew-symmetric quantity, so to introduce possible initial imperfections:

$$\Theta_l \approx 0, \quad \Theta_m := \Theta = \bar{\Theta}(1 + \epsilon \sin(\pi\xi)) \quad (15)$$

Performing Galérkin’s technique and using Eqs. (12), (14)_{5,6}, (13), (15), in the limit $\epsilon \rightarrow 0$ we find the closed-form expressions

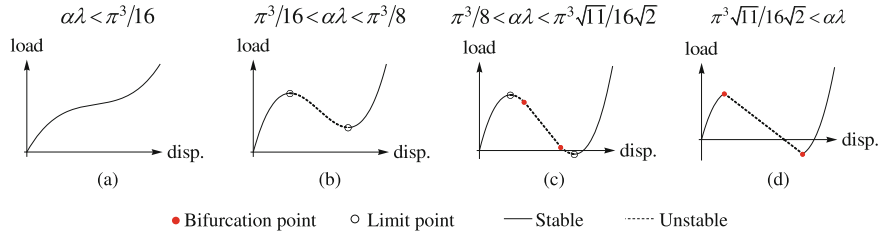


Fig. 1 Load–displacement curves for different geometries. **(a)** stable. **(b)** limit load. **(c)** snapping after the limit load. **(d)** snapping before the limit load

$$\begin{aligned} \bar{\Theta} &= \frac{\pi^6 c_1^3 \lambda^2 - 96\pi^3 \alpha c_1^2 \lambda^2 + 4c_1 [512\alpha^2 \lambda^2 + \pi^6 (2c_2^2 \lambda^2 + 1)] - 128\pi^3 \alpha c_2^2 \lambda^2}{256\pi} \\ c_2 &= \frac{\sqrt{64c_1\alpha\lambda^2 - \pi^3(16 + c_1^2\lambda^2)}}{2\pi^{3/2}\lambda}, \quad 16\pi^3 + c_1(c_1\pi^3 - 64\alpha)\lambda^2 < 0 \\ &\quad 0, \quad 16\pi^3 + c_1(c_1\pi^3 - 64\alpha)\lambda^2 > 0 \end{aligned} \quad (16)$$

Eq. (16)₁ provides a load-displacement relation; to have a non-vanishing c_2 (i.e., a non-trivial approximation of the transverse displacement), we investigated various ranges of the arch parameters product $\alpha\lambda$, which equals the ratio of the height of the arch and the meaningful radius of gyration of the cross-sections. We thus highlighted different qualitative behavior for the arch, see Fig. 1.

Figure 1a shows that for the indicated range of $\alpha\lambda$ the load–displacement curve is monotonic, suggesting stable behavior. As $\alpha\lambda$ increases, the equilibrium path has a point with zero slope and a *limit load* exists, Fig. 1b. Further increment of $\alpha\lambda$ results in a snapping after the limit point (Fig. 1c), which is unlikely to be experienced in real systems, or before the same limit point (Fig. 1d); see also [7]. Labels are attached to the points highlighted in Fig. 1 after investigating small perturbations of the equilibrium path, as described below.

3 Small Vibration About Nonlinear Equilibria

A series expansion of Eq. (10) up to the first order in a small evolution parameter ϵ provides two sets of equations (see also [16]), of which one is identical to Eq. (12), thus giving the equilibrium path presented in the previous section. The other describes small perturbation about these equilibria, known as *fundamental paths*. Considerations similar to those leading to Eq. (11), plus assuming the incremental transverse displacement is now of order α^2 , provide

$$\begin{aligned} \bar{\gamma} &= \bar{\xi}' - \bar{\theta} & \bar{\nu}' - (\kappa + \zeta'') \bar{\tau} - \bar{\chi}\tau + \bar{\Theta}_l &= 0 \\ \bar{\varepsilon} &= \bar{\upsilon}' - (\kappa + \zeta'') \bar{\xi} & \bar{\tau}' + (\kappa + \zeta'') \bar{\nu} + \bar{\chi}\nu + \bar{\Theta}_m &= 0 \\ \bar{\chi} &= \bar{\theta}' & \bar{\mu}' + \bar{\tau} + \bar{\varepsilon}\tau &= 0 \end{aligned} \quad (17)$$

a bar denoting first increments with respect to ϵ . The normal force may still be considered constant, since in the deformed configuration the arch is still shallow, and shearing strain is still negligible. If ρ is the material density, let the only non-vanishing distributed load be transverse inertia due to a harmonic motion,

$$\bar{\zeta} = \hat{\zeta} \cos(\omega t) \Rightarrow \bar{\Theta}_m = -\Omega^2 \bar{\zeta}, \quad \Omega^2 = (\omega^2 \rho A l^4)/(EI) \quad (18)$$

with ω , Ω the angular frequency and its non-dimensional counterpart, and $\hat{\zeta}$ the amplitude of the transverse displacement. By Eqs. (18), (17) becomes

$$\hat{\zeta}^{IV} - \hat{\zeta}'' v - (2\alpha + \zeta'') \hat{v} + \frac{\hat{v}}{\lambda^2} \zeta^{IV} - \Omega^2 \hat{\zeta} = 0, \quad \hat{v} = \frac{\lambda^2}{2} \int_{-1}^1 \left[-(2\alpha + \zeta'') \hat{\zeta} \right] d\xi \quad (19)$$

Boundary conditions are as in Eq. (14)_{1–4}, thus for Galérkin's technique we use the same comparison functions. We obtain a homogeneous linear algebraic system that must be singular to have non-trivial approximated $\zeta(\xi)$, giving

$$\begin{aligned} \Omega^4 + \beta_1 \Omega^2 + \beta_2 &= 0, \\ \beta_1 &= \left\{ 32\pi^3 \alpha c_1 (28\lambda^2 + \pi^2) - c_1^2 (14\pi^6 \lambda^2 + \pi^8) \right. \\ &\quad \left. - 8 \left[512\alpha^2 \lambda^2 + c_2^2 (13\pi^6 \lambda^2 + 8\pi^8) + 17\pi^6 \right] \right\} / (128\pi^2), \\ \beta_2 &= \left\{ 4\pi^3 c_1^2 \left[7168\alpha^2 \lambda^4 + 512\pi^2 \alpha^2 \lambda^2 + c_2^2 (12\pi^6 \lambda^4 + 5\pi^8 \lambda^2) + 26\pi^6 \lambda^2 + 4\pi^8 \right] \right. \\ &\quad - 128\alpha c_1 \left[4(512\alpha^2 \lambda^4 + 13\pi^6 \lambda^2 + \pi^8) + 3c_2^2 (8\pi^6 \lambda^4 + 3\pi^8 \lambda^2) \right] + 32\pi^3 \\ &\quad \times \left[4(512\alpha^2 \lambda^2 + \pi^6) + c_2^2 (512\alpha^2 \lambda^4 + 7\pi^6 \lambda^2 + 2\pi^8) + c_2^4 (3\pi^6 \lambda^4 + 2\pi^8 \lambda^2) \right] \\ &\quad \left. - 96\pi^6 \alpha c_1^3 \lambda^2 (8\lambda^2 + \pi^2) + \pi^9 c_1^4 \lambda^2 (6\lambda^2 + \pi^2) \right\} / (2048\pi) \end{aligned} \quad (20)$$

The solutions of Eq. (20)₁ are the first two natural angular frequencies

$$(\Omega_{1,2})^2 = \frac{-\beta_1 \mp \sqrt{\beta_1^2 - 4\beta_2}}{2} \quad (21)$$

Since Eqs. (20)_{2,3}, (21) are expressed in closed form, it is then possible to provide, as in Fig. 2, plots of the values of $\Omega_{1,2}$ at each point of the equilibrium paths. Figure 2 presents the result for a very shallow arch, for which $\alpha = 0.05$, and is organized as follows: the first and the second column present the plots of the initial load parameter, i.e., a measure of the pre-stress and of the initial response, versus the square of the first and the second natural angular frequency, respectively; the third column shows the corresponding load–displacement curve, thus inserting

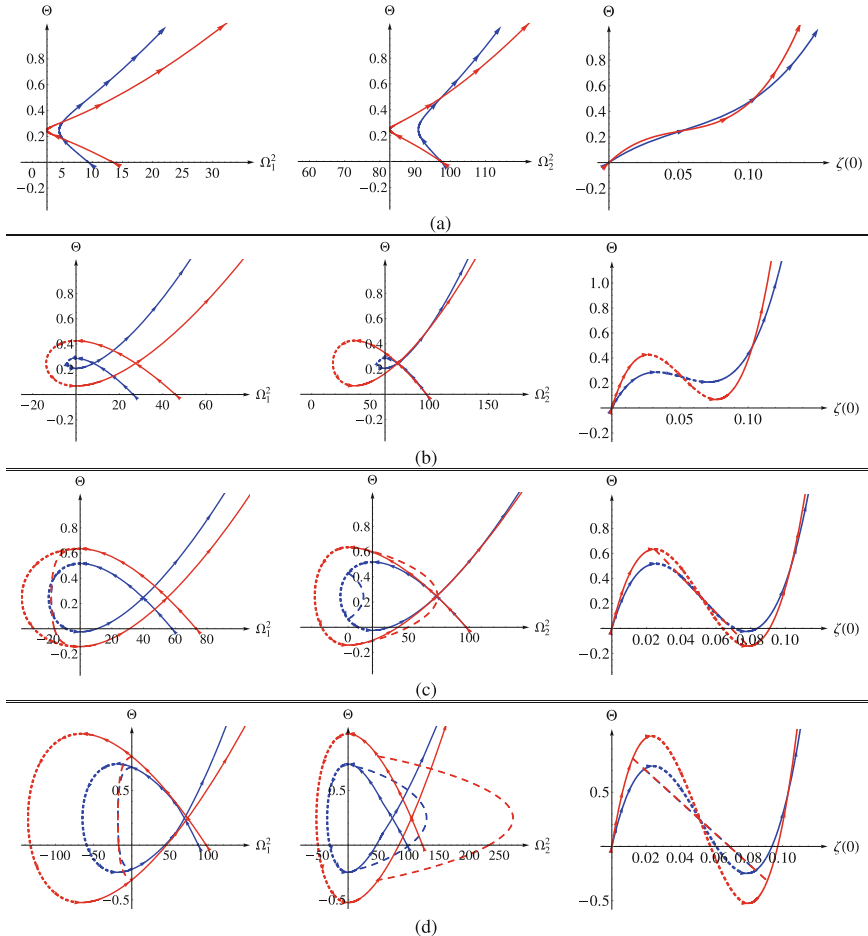


Fig. 2 Natural frequencies and equilibria; solid (dashed): fundamental (bifurcated). **(a)** $\lambda = 20$ (blue), 30 (red). **(b)** $\lambda = 50$ (blue), 70 (red). **(c)** $\lambda = 80$ (blue), 90 (red). **(d)** $\lambda = 100$ (blue), 120 (red)

the description made for Fig. 1 into a general frame; each row presents the results for various values of λ so to sweep the ranges indicated in Eq. (16). In particular, Fig. 2a presents the results for $\lambda = 20, 30$ (blue and red lines, respectively); Fig. 2b does the same for $\lambda = 50, 70$; Fig. 2c is about $\lambda = 80, 90$; Fig. 2d presents the results for $\lambda = 100, 120$. Solid and dashed lines correspond to stable and unstable behavior, respectively, while thin dashed lines represent the bifurcated path. Roughly speaking, once the arch shallowness ratio α is fixed, increasing the value of λ implies a progressive increase of the contribution of the axial stiffness with respect to the bending one.

When the load is zero, i.e., when the circular reference shape remains unaltered, the values of $\Omega_{1,2}$ are the natural angular frequencies of the arch. As physically

motivated, these values increase with λ , since the axial contribution to the arch stiffness increases. As the load grows and the initial geometry is altered, we see from the first row of Fig. 2 that both frequencies exhibit a first branch with a decreasing trend, which is also physically motivated, since the geometrical arch effect is reduced with the deformation of the initial configuration. Correspondingly, the equilibrium path exhibits a positive, yet decreasing, slope, implying a decreasing global stiffness. The frequency curves tend to a cusp, then start increasing again with the load, since now the deformed shape is such that the tangential force has turned into traction and implies a stiffening effect, witnessed also by the load–displacement curve that exhibits a monotonic growth with increasing slope; the paths, however, are always stable. Starting from the second row, i.e., for increasing λ , the frequency curves do not tend to a cusp but form a knot; for the first frequency, part of these knots are in the negative half-space: the null of Ω_1^2 corresponds exactly to the limit load in the equilibrium path, followed by an unstable branch with negative slope. In the third row, we see that still increasing λ the knots remain and also the second frequency crosses the threshold of stability; in addition, unstable paths (jumps, or snaps) occur after the limit point. In the fourth row, such a behavior is somehow exalted, but the jump occurs before the limit point of the equilibrium path. We remind that at the limit point of the fundamental path the real part of first frequency vanish, and remains so until the arch has positive rigidity. Possible bifurcation only alters the imaginary part of the first frequency, while it increases the second frequency considerably, which is due to the change in the geometry.

4 Final Remarks

We examined small-amplitude vibration of shallow arches about a deformed state by a perturbation approach and presented the nonlinear dependence of angular frequencies on initial loading in closed form. The results presented herein may well be used as benchmark solutions for the investigations of the structural characteristics of pre-stressed elements, as well as for their design and optimization based on vibration and stability behavior. The methodology and the results may be used as a means for monitoring and identification of structural arch elements that find applications in many fields of engineering, from actuators of microelectromechanical systems to macro-scale civil realizations.

References

1. Carpinteri, A., Bazzucchi, F., Manuello, A.: Nonlinear instability analysis of long-span roofing structures: the case study of Porta Susa railway station. *Eng. Struct.* **110**, 48–58 (2016)
2. Das, K., Batra, R.C.: Pull-in and snap-through instabilities in transient deformations of microelectromechanical systems. *J. Micromech. Microeng.* **19**, 035008 (2009)

3. Timoshenko, S., Gere, J.M.: Theory of Elastic Stability. McGraw Hill, New York (1961)
4. Mettler, E.: Dynamic buckling. In: Flugge (ed.) Handbook of Engineering Mechanics. McGraw-Hill, New York (1962)
5. Lacarbonara, W.: Nonlinear Structural Mechanics. Springer, Berlin (2013)
6. Pi, Y.L., Bradford, M.A.: Nonlinear elastic analysis and buckling of pinned-fixed arches. *Int. J. Mech. Sci.* **68**, 212–223 (2013)
7. Zhu, J., Attard, A.M., Kellermann, D.C.: In-plane nonlinear buckling of circular arches including shear deformations. *Arch. Appl. Mech.* **84**, 1841–1860 (2014)
8. Chandra, Y., Stanciulessu, I., Virgin, L.N., Eason, T.G., Spottsworth, S.M.: A numerical investigation of snap-through in a shallow arch-like model. *J. Sound Vib.* **332**, 2532–2548 (2013)
9. Chandra, Y., Wiebe, R., Stanciulessu, I., Virgin, L.N., Spottsworth, S.M., Eason, T.G.: Characterizing dynamic transitions associated with snap-through of clamped shallow arches. *J. Sound Vib.* **332**, 5837–5855 (2013)
10. Moghaddasie, B., Stanciulessu, I.: Equilibria and stability boundaries of shallow arches under static loading in a thermal environment. *Int. J. Nonlin. Mech.* **51**, 132–144 (2013)
11. Zhou, Y., Chang, W., Stanciulessu, I.: Non-linear stability and remote unconnected equilibria of shallow arches with asymmetric geometric imperfections. *Int. J. Nonlin. Mech.* **77**, 1–11 (2015)
12. Bradford, M.A., Pi, Y.L., Yang, G., Fan, X.C.: Effects of approximations on non-linear in-plane elastic buckling and postbuckling analyses of shallow parabolic arches. *Eng. Struct.* **101**, 58–67 (2015)
13. Cornil, M.B., Capolungo, L., Qu, V.A., Jairazbhoy, V.A.: Free vibration of a beam subjected to static deflection. *J. Sound Vib.* **303**, 723–740 (2007)
14. Vlajic, N., Fitzgerald, T., Nguyen, V., Balachadaran, B.: Geometrically exact planar beams with initial pre-stress and large curvature: static configurations, natural frequencies, and mode shapes. *Int. J. Solids Struct.* **51**, 3361–3371 (2014)
15. Eroglu, U., Tufekci, E.: Small-amplitude free vibrations of straight beams subjected to large displacements and rotation. *Appl. Math. Model.* **53**, 223–241 (2018)
16. Eroglu, U., Ruta, G.: Fundamental frequencies and buckling in pre-stressed parabolic arches. *J. Sound Vib.* **435**, 104–118 (2018)
17. Addessi, D., Lacarbonara, W., Paolone, A.: Linear vibrations of planar pre-stressed arches undergoing static bifurcations. In: Proceedings of the EURODYN 2005, Paris
18. Cox, B.S., Groh, R.M.J., Avitabile, D., Pirrera, A.: Exploring the design space of nonlinear shallow arches with generalised path-following. *Finite Elem. Anal. Des.* **143**, 1–10 (2018)
19. Zuchowski, B.: Predictive capability for Hypersonic Structural Response and Life Prediction, Phase 1 – Identification of Knowledge Gaps, Air Vehicles Integration and Technology Research (AVIATR) Task Order 0015AFRL-RB-WP-TR-2010-3069, Lockheed Martin Aeronautics Company, Fort Worth (2010)
20. Antman, S.S.: The theory of rods. In: Truesdell, C. (ed.) *Linear Theories of Elasticity and Thermoelasticity*, pp. 641–703. Springer, Berlin (1973)
21. Antman, S.S.: Nonlinear Problems of Elasticity. Springer, New York (1995)
22. Pignataro, M., Rizzi, N., Ruta, G.: A beam model for the flexural-torsional buckling of thin-walled members. *Thin-Walled Struct.* **46**, 816–822 (2008)

Nonlinear Vibration Responses of Laminated Composite Cantilever Plate in Subsonic Air Flow



Gen Liu and Wei Zhang

Abstract The nonlinear vibrations of a laminated composite cantilever plate under subsonic air flow are investigated in this chapter. According to the ideal incompressible fluid condition and the Kutta–Joukowski lift theorem, the subsonic aerodynamic lift on the lifting surface is calculated by using the Vortex Lattice (VL) method. Then, the finite length plate is modeled as a laminated composite cantilever plate based on the Reddy’s third-order shear deformation plate theory. Moreover, the von Karman geometry nonlinearity is introduced. The nonlinear partial differential governing equations of motion for the laminated composite cantilever plate subjected to the subsonic aerodynamic force are established via Hamilton’s principle. The Galerkin method is used to separate the partial differential equations into two nonlinear ordinary differential equations, and the four-dimensional nonlinear averaged equations are obtained by multiple scales method. Through comparing the natural frequencies of the linear system with different material and geometry parameters, the 1:2 internal resonance is considered here. Corresponding to several selected parameters, the frequency-response curves are obtained. The hardening-spring-type behaviors and jump phenomena are exhibited.

Keywords Subsonic air flow · Vortex Lattice method · High-order shear deformation theory · Nonlinear dynamics

1 Introduction

The topic of the vibration of plate and shell structures owing to airflow is a matter of interest because of its significant application in vehicle design and aircraft [1]. Laminated composite plates and shells have been widely used in aerospace field due to high strength-to-weight ratio, light weight, and long fatigue life. The

G. Liu (✉) · W. Zhang

Beijing Key Laboratory of Nonlinear Vibrations and Strength of Mechanical, College of Mechanical Engineering, Beijing University of Technology, Beijing, P. R. China
e-mail: liugen1991@hotmail.com

dynamic behavior of the laminated composite plates in airflow has been paid attention by many researchers. However, there are few research works dealing with the complex nonlinear dynamics of the lifting surface which is simplified as a laminated composite cantilever plate under subsonic air flow. Therefore, the nonlinear dynamics of laminated composite plate in subsonic flow will be worth analyzing.

In the 1990s, the research on plate and shell structure has reached a high level, and the vibration of plate has been studied comprehensively. Some literature review works on the nonlinear vibrations of plates were given by Chia [2, 3] and Sathyamoorthy [4]. The nonlinear vibrations of laminated plates were also entirely investigated by Noor et al. [5–7], Abe et al. [8–10] and Nayfeh et.al. [11–13].

In this chapter, the nonlinear dynamics of the laminated composite cantilever plate under subsonic air flow are investigated. Unlike a two-dimensional airfoil or an infinite length wing, the aerodynamic force of a three-dimensional flat wing is calculated. The subsonic aerodynamic lift on the three-dimensional finite length flat wing is calculated using the Vortex Lattice method. Then, the finite length flat wing is modeled as a laminated composite cantilever plate based on the Reddy's third-order shear deformation plate theory, and the von Karman geometry nonlinearity is introduced. The nonlinear partial differential governing equations of motion for the laminated composite cantilever plate subjected to the subsonic aerodynamic force are established via Hamilton's principle. Through comparing the natural frequencies of the linear system with different material and geometry parameters, the 1:2 internal resonance is considered here. Corresponding to several selected parameters, the frequency-response curves are obtained. The hardening-spring-type behaviors and jump phenomena are exhibited.

2 Derivation of the Subsonic Aerodynamic Force on the Flat Plate

Unlike the two-dimensional flow around the airfoil, the main characteristic of the three-dimensional flow around the wing is the variation of the lift along the wingspan. In order to calculate the lift on the wing surface by using the Vortex Lattice method, the Biot–Savart law is used to calculate the induced velocity on the control point, the vortex strength of the vortex system is obtained, and the pressure difference on the upper and lower surface of the wing surface is deduced.

The velocity induced by a vortex line with a strength of Γ_n and a length of dl is calculated by the Biot–Savart law as

$$d\vec{V} = \frac{\Gamma_n (\vec{dl} \times \vec{r})}{4\pi r^3} \quad (1)$$

As shown in the Fig. 1, this induced velocity is

Fig. 1 Lifting surface discretized by a Vortex Lattice of horseshoe vortices

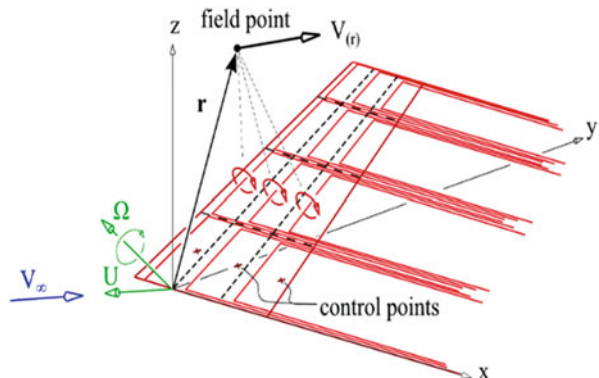
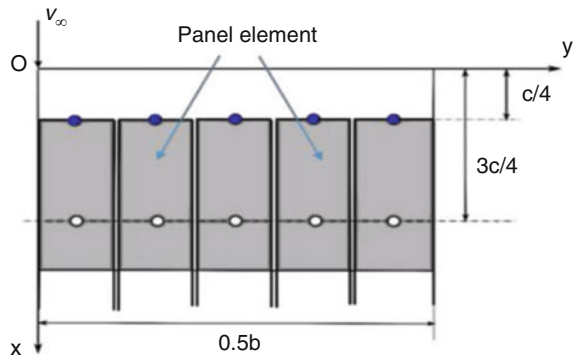


Fig. 2 Layout of the Vortex Lattice on the flat wing surface



$$dV = \frac{\Gamma_n \sin \theta dl}{4\pi r^2} \quad (2)$$

The lift of the wing can be calculated by satisfying the boundary conditions where the air flow is tangent to the object surface at each control point to determine the strength of each vortex (Fig. 2). For any wing that does not have an upper counter angle, the lift is produced by the free flow that crosses the vortex line, because there is no side-washing speed or post-wash speed. According to a finite number of elements, we can get

$$L_0 = \rho_\infty V_\infty \sum_{n=1}^5 \Gamma_n \Delta y_n \quad (3)$$

Because the geometric relationship of each facet is $\Delta y_n = 0.1b$, the lift on the flat plate is

$$L_0 = \rho_\infty V_\infty^2 \pi b^2 \alpha (0.238184) \quad (4)$$

where ρ_∞ is the flow density, V_∞ is the flow velocity, b is half length of the wingspan, α is attack angle. Here we get the lift of the flat plate in the subsonic airflow under the small angle of attack.

The attack angle is considered to be affected by a periodic disturbance $\alpha = \alpha_0 + \alpha_1 \cos \Omega_2 t$. Taking the periodic perturbation into the aerodynamic force, the expression of the aerodynamic force containing the perturbation term is obtained

$$L = L_0 + L_1 \cos \Omega_2 t \quad (5)$$

3 Formulation

In this section, the dynamic equation of the laminated composite cantilever plate is derived, which is subjected to the interaction between the plane excitation and the subsonic aerodynamic load. As shown in Fig. 3, x is the spanwise direction, y is the direction of the chord, and z is the vertical direction of the plate. The plate is clamped at $x = 0$. the ply stacking sequence is $[0^\circ / 90^\circ]_S$, and the layer number is N . The in-plane excitation is $F = F_0 + F_1 \cos \Omega_1 t$, which is distributed along the chord direction of the plate. The vertical of the plate along spanwise direction is excited by subsonic aerodynamic force L .

The nonlinear governing equations are established in Cartesian coordinate system. The Reddy's third-order shear deformation plate theory is used, and the von Karman nonlinear strain-displacement relation is introduced, so the displacements and strain-displacement relation are given

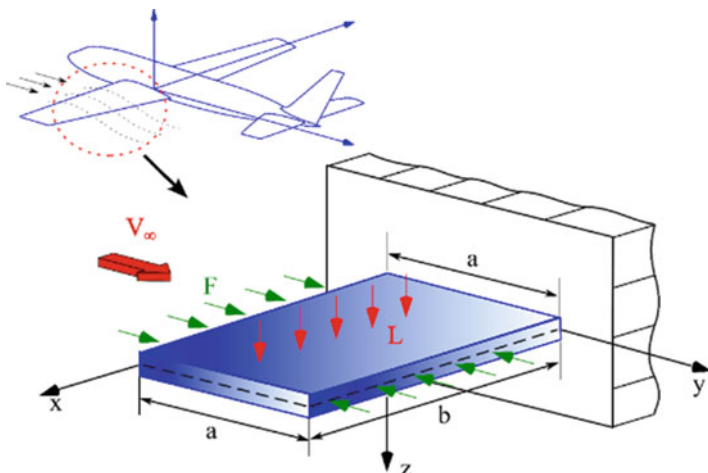


Fig. 3 Mechanical model of cantilever laminated composite plate

$$u(x, y, t) = u_0(x(t), y, t) + z\varphi_x(x(t), y, t) - z^3 \frac{4}{3h^2} \left(\varphi_x + \frac{\partial w_0}{\partial x} \right) \quad (6a)$$

$$v(x, y, t) = v_0(x(t), y, t) + z\varphi_y(x(t), y, t) - z^3 \frac{4}{3h^2} \left(\varphi_y + \frac{\partial w_0}{\partial y} \right) \quad (6b)$$

$$w(x, y, t) = w_0(x(t), y, t) \quad (6c)$$

According to the Hamilton's principle,

$$\int_0^T (\delta K - \delta U + \delta W) dt = 0 \quad (7)$$

The nonlinear governing equations of motion are given as follows:

$$N_{xx,x} + N_{xy,y} = I_0 \ddot{u}_0 + (I_1 - c_1 I_3) \ddot{\phi}_x - c_1 I_3 \frac{\partial \ddot{w}_0}{\partial x} \quad (8a)$$

$$N_{yy,y} + N_{xy,x} = I_0 \ddot{v}_0 + (I_1 - c_1 I_3) \ddot{\phi}_y - c_1 I_3 \frac{\partial \ddot{w}_0}{\partial y} \quad (8b)$$

$$\begin{aligned} & N_{yy,y} \frac{\partial w_0}{\partial y} + N_{yy} \frac{\partial^2 w_0}{\partial y^2} + N_{xy,x} \frac{\partial w_0}{\partial y} + N_{xy,y} \frac{\partial w_0}{\partial x} + 2N_{xy} \frac{\partial^2 w_0}{\partial x \partial y} + N_{xx,x} \frac{\partial w_0}{\partial x} + N_{xx} \frac{\partial^2 w_0}{\partial x^2} \\ & + c_1 (P_{xx,xx} + 2P_{xy,xy} + P_{yy,yy}) + (Q_{x,x} - c_2 R_{x,x}) + (Q_{y,y} - c_2 R_{y,y}) + L - \gamma \dot{w}_0 \\ & = c_1 I_3 \left(\frac{\partial \ddot{u}_0}{\partial x} + \frac{\partial \ddot{v}_0}{\partial y} \right) + c_1 (I_4 - c_1 I_6) \left(\frac{\partial \ddot{\phi}_x}{\partial x} + \frac{\partial \ddot{\phi}_y}{\partial y} \right) + I_0 \ddot{w}_0 - c_1^2 I_6 \left(\frac{\partial^2 \ddot{w}_0}{\partial x^2} + \frac{\partial^2 \ddot{w}_0}{\partial y^2} \right) \end{aligned} \quad (8c)$$

$$\begin{aligned} M_{xx,x} + M_{xy,y} - c_1 P_{xx,x} - c_1 P_{xy,y} - (Q_x - c_2 R_x) &= (I_1 - c_1 I_3) \ddot{u}_0 \\ &+ (I_2 - 2c_1 I_4 + c_1^2 I_6) \ddot{\phi}_x - c_1 (I_4 - c_1 I_6) \frac{\partial \ddot{w}_0}{\partial x} \end{aligned} \quad (8d)$$

$$M_{yy,y} + M_{xy,x} - c_1 P_{yy,y} - c_1 P_{xy,x} - (Q_y - c_2 R_y) \quad (8e)$$

where γ is the damping coefficient.

The discrete equation is derived by Galerkin method, and the discrete function adopts the following expression

$$w_0 = w(t)_1 X_1(x) Y_1(y) + w(t)_2 X_2(x) Y_2(y) \quad (9)$$

where

$$X_i(x) = \sin \frac{\lambda_i}{a} x - \sinh \frac{\lambda_i}{a} x + \alpha_i \left(\cosh \frac{\lambda_i}{a} x - \cos \frac{\lambda_i}{a} x \right) \quad (10a)$$

$$Y_j(y) = \sin \frac{\beta_m}{b} y + \sinh \frac{\beta_m}{b} y - \alpha_m \left(\cosh \frac{\beta_m}{b} y + \cos \frac{\beta_m}{b} y \right) \quad (10b)$$

Similarly, the aerodynamic force is discretized by using the modal function.

$$L = l_1 X_1(x) Y_1(y) + l_2 X_2(x) Y_2(y) \quad (11)$$

where l_1 and l_2 represent the amplitudes of the aerodynamic force corresponding to the two transvers modes, and they contain perturbed items.

The governing differential equation of transverse motion of the system is derived as follows:

$$\ddot{w}_1 + \gamma_{11}\dot{w}_1 + \omega_1^2 w_1 + \gamma_{12}f_1 \cos \Omega_1 t w_1 + \gamma_{13}w_2 \\ - \gamma_{14}w_1^3 - \gamma_{15}w_1^2 w_2 - \gamma_{16}w_1 w_2^2 - \gamma_{17}w_2^3 = \gamma_{18}l_1 \quad (12a)$$

$$\ddot{w}_2 + \gamma_{21}\dot{w}_2 + \omega_2^2 w_2 + \gamma_{22}f_1 \cos \Omega_1 t w_2 + \gamma_{23}w_1 \\ - \gamma_{24}w_2^3 - \gamma_{25}w_2^2 w_1 - \gamma_{26}w_2 w_1^2 - \gamma_{27}w_1^3 = \gamma_{28}l_2 \quad (12b)$$

In order to study the relationship between different resonances of the laminated composite plate, the finite element model of the cantilever laminated composite plate is established.

The ply stacking sequence is $[0^\circ / 90^\circ]_3s$. The thickness of each layer is h_i ($i = 1, \dots, 6$). The different model with span-chord ratio c is calculated, where $c = 1, 2, \dots, 4$. The natural frequencies of bending vibration of laminated composite cantilever plate with different span-chord ratio and different layer thickness are calculated, and the results are shown in Fig. 4.

Based on the results of numerical simulations shown in Fig. 4, the first six orders natural frequencies of the laminated composite cantilever plate are obtained. It is obviously observed that there is a proportional relation between the frequencies of bending vibration of each order, such as relation 1:1 in area c of Fig. 4, relation 1:2 and relation 1:3. We select 1:2 internal resonance relationship between two bending mode, the nonlinear bending vibrations of the laminated composite cantilever plate are considered in the following analysis.

We make $\dot{a}_1 = \dot{a}_2 = \dot{\varphi}_1 = \dot{\varphi}_2 = 0$ and $\varphi_1 = \frac{\pi}{4}$, $\varphi_2 = \frac{3\pi}{4}$. The frequency-response functions of the system are given as follow

$$0 = \gamma_{11}a_1 - 2\sigma_1a_1 - \gamma_{12}a_1 f_1 + \frac{3}{2}\gamma_{14}a_1^3 + \gamma_{16}a_1 a_2^2 \quad (13a)$$

$$0 = \gamma_{21}a_2 + \sigma_2a_2 - \frac{3}{4}\gamma_{24}a_2^3 + \frac{1}{2}\gamma_{26}a_2 a_1^2 + \sqrt{2}\gamma_{28}l_2 \quad (13b)$$

From the Eq. (13), we can find that the amplitude a_1 and amplitude a_2 are coupled, the weak coupled form is considered here. Through introducing the

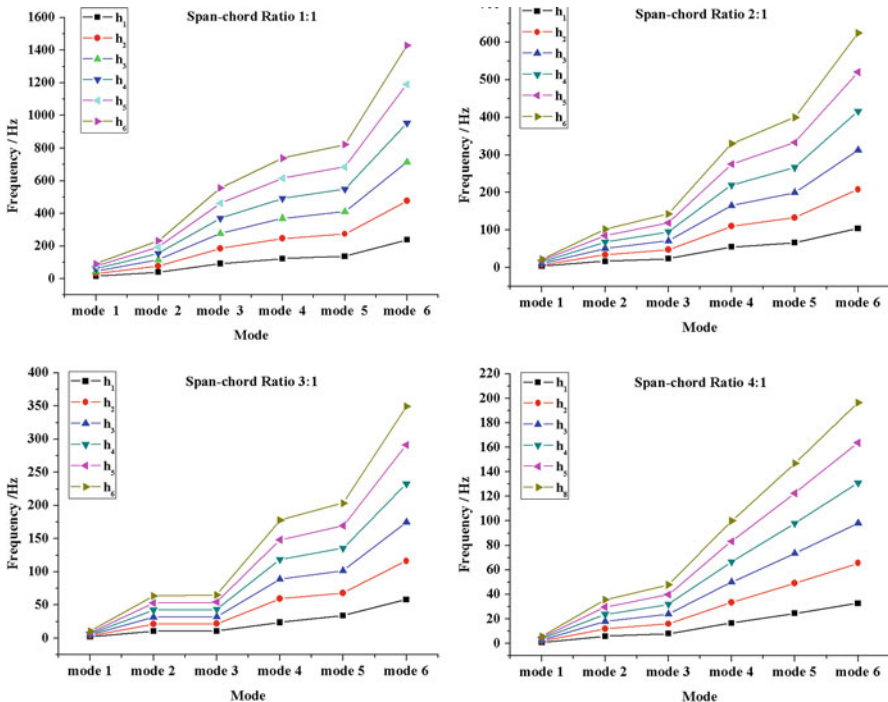


Fig. 4 Natural frequencies with different thickness under the Span-chord ratio 1:1,2:1,3:1,4:1

proportional relation $a_1/a_2 = \varepsilon$, and analyze the frequency-responses between the amplitudes and the tuning parameters.

According to the geometries and the material properties of the nonlinear system, the basic parameters are chosen as $\gamma_{11} = 0.2$, $\gamma_{12} = -6$, $\gamma_{14} = 5$, $\gamma_{16} = -5$, $\gamma_{21} = 0.6$, $\gamma_{24} = 9$, $\gamma_{26} = 9$, $\gamma_{28} = -2$. The relationship between amplitude and tuning parameter in different excited condition can be obtained. Figure 5 gives the relationship between amplitude a_1 and tuning parameter σ_1 in different internal force amplitude f_1 , and Fig. 6 gives relationship between amplitude a_2 and tuning parameter σ_2 in different aerodynamic amplitude l_2 .

Next, the geometries and the material properties of the nonlinear system are fixed, and the effects of different decoupling parameter ε are calculated and the relationship between amplitude and tuning parameter can be found in Fig. 5.

The stiffness hardening phenomenon can be seen in the relationship between the tuning parameters and the amplitude. With the increase of external excitation amplitude, the stiffness hardening phenomenon of the system is gradually strengthened. The typical jump phenomenon of the nonlinear oscillations is also happened in the system. The jump phenomenon appears in the frequency-response curves at point A* and point B* with the increase of the tuning parameters in Fig. 5.

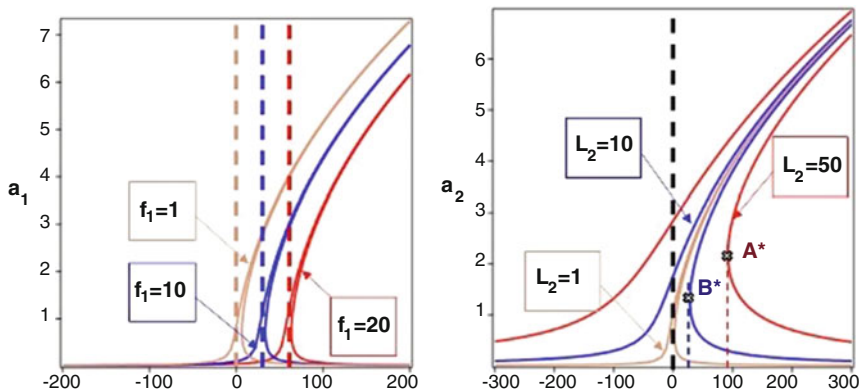


Fig. 5 The relationship between amplitude and tuning parameter in different excited condition

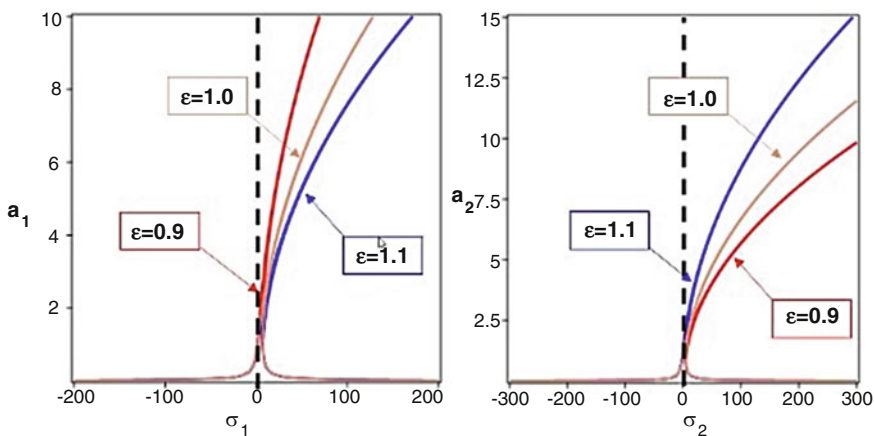


Fig. 6 The relationship between amplitude and tuning parameter

The frequency-response curves have the wider resonance interval and the larger oscillation amplitudes under the stronger external excitation amplitude l_2 .

4 Conclusion

The nonlinear dynamics of the laminated composite cantilever plate under subsonic air flow are investigated in this chapter. The subsonic air flow around the three-dimensional cantilever rectangle laminated composite plate is considered based on the lifting surface. The subsonic aerodynamic lift on the three-dimensional finite length flat wing is calculated by using the Vortex Lattice method. Then, the finite length flat wing is modeled as a laminated composite cantilever plate based on the

Reddy's third-order shear deformation plate theory, and the von Karman geometry nonlinearity is introduced. The nonlinear partial differential governing equations are established via Hamilton's principle. The Galerkin method is used to separate the partial differential equations and the 1:2 internal resonance is considered here. Corresponding to several selected parameters, the frequency-response curves are obtained. The hardening-spring-type behaviors and jump phenomena are exhibited with the tuning parameters changing.

References

1. Mehri, M., Asadi, H., Kouchakzadeh, M.A.: Computationally efficient model for flow-induced instability of CNT reinforced functionally graded truncated conical curved panels subjected to axial compression. *Comput. Methods Appl. Mech. Eng.* **318**, 957–980 (2017)
2. Chia, C.Y.: Nonlinear Analysis of Plates. McGraw-Hill, New York (1980)
3. Chia, C.Y.: Geometrically nonlinear behavior of composite plates: a review. *Appl. Mech. Rev.* **41**, 439–451 (1988)
4. Sathyamoorthy, M.: Nonlinear vibration analysis of plates: a review and survey of current developments. *Appl. Mech. Rev.* **40**, 1553–1561 (1987)
5. Noor, A.K., Burton, W.S.: Assessment of shear deformation theories for multilayered composite plates. *Appl. Mech. Rev.* **42**, 1–13 (1989)
6. Noor, A.K., Burton, W.S.: Stress and free vibration analyses of multilayered composite plates. *Compos. Struct.* **11**, 183–204 (1989)
7. Noor, A.K., Starnes Jr., J.H., Peters, J.M.: Thermomechanical buckling and postbuckling of multilayered composite panels. *Compos. Struct.* **23**, 233–251 (1993)
8. Abe, A., Kobayashi, Y., Yamada, G.: Two-mode response of simply supported, rectangular laminated plates. *Int. J. Nonlinear Mech.* **33**, 675–690 (1998)
9. Abe, A., Kobayashi, Y., Yamada, G.: Three-mode response of simply supported, rectangular laminated plates. *JSME Int. J. Ser. C Mech. Syst. Machine Elements Manuf.* **41**, 51–59 (1998)
10. Abe, A., Kobayashi, Y., Yamada, G.: Analysis of subharmonic resonance of moderately thick antisymmetric angle-ply laminated plates by using method of multiple scales. *J. Sound Vib.* **217**, 467–484 (1998)
11. Oh, K., Nayfeh, A.H.: Nonlinear combination resonances in cantilever composite plates. *Nonlinear Dyn.* **11**, 143–169 (1996)
12. Pai, P.F., Nayfeh, A.H.: A nonlinear composite plate theory. *Nonlinear Dyn.* **2**, 445–477 (1991)
13. Pai, P.F., Nayfeh, A.H.: A unified nonlinear formulation for plate and shell theories. *Nonlinear Dyn.* **6**, 459–500 (1994)

Adaptation of Energy Dissipation in a Laminated Module with Tunable Twin Wells



Dejian Li and Hui Fang

Abstract Vibration energy dissipation in structural components has specific requirements, and the low damping of structural metal favors a lasting dynamic response. This chapter proposes a hysteresis damper realized with a specifically designed laminated metal module consisting of a preloaded beam bimorph and linear springs. Through continuous vibration modeling and simplification, the dynamic governing equations of the laminated module are obtained. In the solution process of the multiple scales method, we focus on the interwell motion characteristics that bring about an order of magnitude increase in energy dissipation compared to a linear module. Our studies employ analytical and numerical findings to probe how the parameters of the system affect energy dissipation. When carefully designed, a twin-well metal module can provide significant damping even for a small excitation amplitude.

Keywords Hysteresis dissipation · Continuous module · Snap-buckling

1 Introduction

Dynamic excitation acting on an engineering structure can produce additional stresses. An effective stiffness able to bear the stress and high energy dissipation are indispensable for dynamic response reduction [1]. Conventionally, structural damping can be achieved via high-damping material layers, typically polymers, and the resulting composite structures have effective properties that are intermediate between the properties of the base constituents. Energy dissipation of the damper will be insufficient if the macroscopic displacement/strain varies locally or finitely due to a high stiffness.

D. Li · H. Fang (✉)

Institute of Coastal and Ocean Engineering, School of Engineering,

Ocean University of China, Qingdao, China

e-mail: lidejian@stu.ouc.edu.cn; fanghui@ouc.edu.cn

High damping in a metal module is desirable for vibration energy dissipation in marine structures. Negative stiffness components have shown potential for significant damping, primarily due to the energetic transitions between stable equilibrium modes. Based on the shift in the elastic buckling mode of a uniform straight rod, Dong et al. [2] tested a hysteretic member in which a displacement induced a force in the opposite direction. A dissipation system with snap-through buckling features can passively and drastically change depending on the response dynamics excited by the input [3]. Kidambi et al. [4] optimized the relationship of snap-through components combined with a positive stiffness structure, and experimental results indicated that energy dissipation is improved under near resonance conditions. However, these modules were deliberately designed as discrete systems, while continuous modules are necessary for engineering structures.

A continuous metal module with an internal snap-buckling mechanism, consisting of a preloaded beam bimorph and a linear spring layer laminated together, is proposed. Through continuous vibration modeling and simplification, the governing equations of the module subjected to transverse excitations will be derived. Numerical simulations are utilized to identify how the various dynamic states can be leveraged to achieve large and adaptable dissipation properties. The module's potential function and axial preload are altered to delineate their important roles in the damping behavior.

2 Model Development

Figure 1a shows that the proposed metal module consists of a preloaded beam bimorph and a linear elastic layer laminated together. One side of the elastic layer is constrained and connected to a vibration object. The constrained side is considered non-deformable. The displacement excitation is $Z(t)$, and the qualitative character of the reaction force $f(t)$ is evaluated on the constrained side of the linear elastic layer. The elastic layer's other side is bonded to the preloaded clamped-clamped beam,

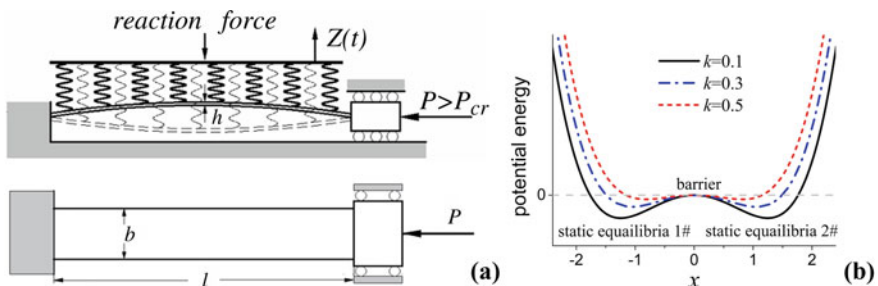


Fig. 1 (a) Archetypal mechanical model that integrates a bimorph and an elastic layer, showing a side view ($P > P_{cr}$) and the top view. (b) Twin-well potential of the modules

which is directly subjected to a static axial loading P and subjected to a transverse dynamic excitation via the elastic layer. When load P is beyond the critical buckling load (P_{cr}), the bending beam exhibits two stable equilibrium positions (S_{p1} and S_{p2}). The laminated model may exhibit very different properties compared to the individual elements.

According to the Euler-Bernoulli beam theory, the total strain at a point located a distance z_0 from the neutral axis can be written as follows:

$$\varepsilon(s, t, z_0) = \left(u' + \frac{w'^2}{2} - \frac{w'^4}{8} - \frac{u'w'^2}{2} \right) - z_0 \left(w'' - 2u'w'' - u''w' - \frac{3}{2}w'^2w'' \right) \quad (1)$$

where s is the arc length, u is the longitudinal displacement, and w is the transversal displacement. Hamilton's principle is utilized to develop the governing equations of the system. The potential energy U and kinetic energy T can be written as:

$$U = \frac{1}{2} \int_0^l \sigma \varepsilon ds, \quad T = \int_0^l \frac{1}{2} \rho (\dot{u}^2 + \dot{w}^2) ds \quad (2)$$

where ρ is the mass density the stress $\sigma = E\varepsilon$ in Eq. (2), and E is the Young's modulus of the beam. The nonconservative virtual work term can be expressed as follows:

$$\delta W^{nc} = \int_0^l K_l [Z - w(s, t)] \delta w(s, t) ds + \int_0^l c \dot{w} \delta w(s, t) ds - P \delta u(l, t) \quad (3)$$

where c is the mechanical viscous damping coefficient, $Z(t) = \bar{z} \cos(\bar{\Omega}t)$ is the external excitation, P is the preloaded beam's axial load, and δ is a variational operator. Substituting Eqs. (1)–(3) into Hamilton's principle, the relationship between the longitudinal and transversal deflections is solved as $u'(s, t) = -\frac{P}{EA} - \frac{w'^2}{2}$, which can be used to eliminate the longitudinal dynamics $u(s, t)$ from the governing equations. Based on Galerkin's method, we assume $w(s, t)$ to be in the form $w(s, t) = \sum_{i=1}^{\infty} \phi_i(s) \bar{x}_i(t)$, where $\bar{x}_i(t)$ are generalized temporal coordinates and $\phi_i(s)$ are chosen as a set of orthonormal admissible functions. The system response in terms of the first modal frequency is obtained as follows:

$$\bar{M}_1 \ddot{\bar{x}}_1 + \bar{c}_1 \dot{\bar{x}}_1 + \bar{K}_1 (1 - r) \bar{x}_1 + \bar{\Lambda}_{1111} \bar{x}_1^3 = \bar{K}_l \bar{z} \cos(\bar{\Omega}t) - \bar{K} \bar{x}_1 \quad (4)$$

$$\begin{aligned} \bar{M}_1 &= \int_0^l m \phi_1^2 ds, \quad \bar{c}_1 = \int_0^l c \phi_1^2 ds, \quad \bar{K}_1 = \int_0^l EI \phi_1''^2 ds, \quad \bar{\Lambda}_{1111} = \int_0^l \left(EI \phi_1'^2 \phi_1''^2 - \frac{P}{2} \phi_1'^4 \right) ds, \\ \bar{K}_l &= K_l \int_0^l \phi_1^2 ds, \quad \bar{K} = K_l \int_0^l \phi_1^2 ds, \quad r = \alpha P, \quad \alpha = \frac{1}{\bar{K}_1} \int_0^l \phi_1'^2 ds. \end{aligned}$$

Then, the dimensionless equation can be written as follows:

$$x_1'' + 2\mu_1 x_1' + (1 - r + k) x_1 + \lambda_{1111} x_1^3 = k_l z \cos(\Omega\tau) \quad (5)$$

Table 1 Physical parameters

E [GPa]	P [kg·m ⁻³]	l [mm]	b [mm]	h [mm]
190	8100	250	15	0.5

Table 2 Analytical model parameters

k_l	r	μ	λ	k
0.25	1.8	0.05	0.45	0.3

$$x_1 = \bar{x}_1/r_g, z = \bar{z}/r_g, \tau = \omega_1 t, \Omega = \bar{\Omega}/\omega_1, r_g = \sqrt{K_1/EAl}, (\bullet)' = d(\bullet)/d\tau, \mu_1 = \frac{\bar{c}_1}{2M_1\omega_1}, \lambda_{1111} = \frac{\bar{\lambda}_{1111}r_g^2}{M_1\omega_1^2}, k_l = \frac{\bar{K}_l}{\bar{K}_1}, k = \frac{\bar{K}}{\bar{K}_1}, \omega_1 = \sqrt{K_1/M_1}.$$

In the following, numerical subscripts on the different variables will be omitted for simplicity.

According to Eq. (5), the potential of this continuous laminated module has two stable equilibria separated by a potential barrier. Modules with the same beam bimorph and different linear springs are considered. The model parameters are presented in Tables 1 and 2. When the stiffness per length of the spring layer is 1141 N/m, the equivalent stiffness is normalized as $k = 0.3$. The linear spring contributes the primary term to the system's stiffness, which dramatically affects the distance between the wells as well as the height of the potential barrier (Fig. 1b).

3 Approximate Approaches

3.1 Intrawell Oscillations

By introducing $x_\tau = x - x_s$ into Eq. (5), we can expand the governing equation around the stable nodes to obtain the single-well dynamics ($x_s = \pm\sqrt{(r-1-k)/\lambda}$):

$$x_\tau'' + 2\mu x_\tau' + \omega^2 x_\tau + \gamma x_\tau^2 + \lambda x_\tau^3 = k_l z \cos(\Omega\tau) \quad (6)$$

where $\omega = \sqrt{2(r-1-k)}$ represents the linearized oscillation frequency within a single potential well, $\gamma = 3\sqrt{(r-1-k)/\lambda}$ is the quadratic coefficient, and x_τ represents the dynamic trajectories around the nontrivial equilibria. We expand the time dependence into multiple time scales with the following form:

$$T_n = \varepsilon^n \tau \quad (7)$$

where ε is a bookkeeping parameter. The time derivatives are expressed as follows:

$$\frac{d}{d\tau} = D_0 + \varepsilon D_1 + \varepsilon^2 D_2 + \dots, \quad \frac{d^2}{d\tau^2} = D_0^2 + 2\varepsilon D_0 D_1 + \varepsilon^2 D_1^2 + 2\varepsilon^2 D_0 D_2 + \dots \quad (8)$$

where $D_n = \partial/\partial T_n$. Then, we can expand x_τ into the following form:

$$x_\tau(\tau) = x_0(T_0, T_1, T_2) + \varepsilon x_1(T_0, T_1, T_2) + \varepsilon^2 x_2(T_0, T_1, T_2) + \dots \quad (9)$$

Equation (6) is rescaled with a small parameter, ε . The rescaled form is as follows:

$$x_\tau'' + 2\varepsilon^2 \mu x_\tau' + \omega^2 x_\tau + \varepsilon \gamma x_\tau^2 + \varepsilon^2 \lambda x_\tau^3 = \varepsilon^2 k_l z \cos(\Omega\tau) \quad (10)$$

To express the excitation frequency near the first modal frequency of a single potential well, we let $\Omega = \omega + \varepsilon^2 \sigma$, where σ is a small detuning parameter. For the sake of brevity, the solution process of the classical multiple scales method is omitted. The final nonlinear frequency response equation is obtained as follows:

$$(\mu a_0)^2 + \left[\sigma a_0 + \left(\frac{5\gamma^2}{12\omega^3} - \frac{3\lambda}{8\omega} \right) a_0^3 \right]^2 = \frac{(k_l z)^2}{4\omega^2} \quad (11)$$

where a_0 represents the steady-state amplitude. Equation (11) can be analytically solved for the steady-state amplitude and any given displacement z .

3.2 Interwell Oscillations

Since the effective local stiffness about the unstable saddle is negative, we scale the damping and external excitation at order ε [5]:

$$x'' + (1 - r + k)x + \lambda x^3 = O(\varepsilon) \quad (12)$$

We assume that the first-order harmonic solution is $x = \bar{A} \cos(\Omega\tau)$ and obtain:

$$-\Omega^2 x + (1 - r + k)x + \lambda x^3 = O(\varepsilon) \quad (13)$$

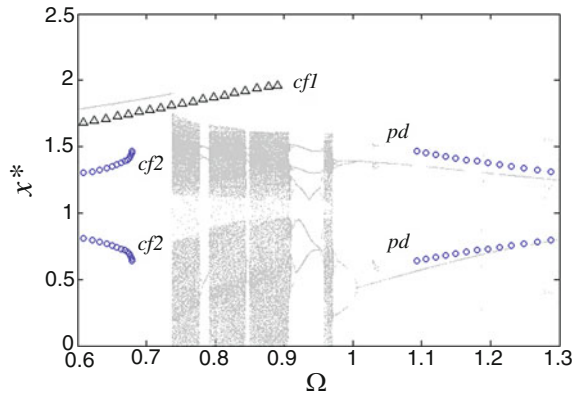
This result implies that the left-hand side of the previous equation can be scaled at order ε . Adding the term $\Omega^2 x$ to the left-hand side of Eq. (5) and using the scaling of Eq. (12), we obtain:

$$x'' + 2\varepsilon \mu x' + \Omega^2 x + \varepsilon \left(-\Omega^2 x + (1 - r + k)x + \lambda x^3 \right) = \varepsilon k_l z \cos(\Omega\tau) \quad (14)$$

We can now apply the method of multiple scales in the traditional way and obtain the following nonlinear frequency response equation:

$$(\mu a_0)^2 + \left(\frac{\Omega^2 - (1 - r + k)}{2\Omega} a_0 - \frac{3\lambda}{8\Omega} a_0^3 \right)^2 = \left(\frac{k_l z}{2\Omega} \right)^2 \quad (15)$$

Fig. 2 Bifurcation diagram for a twin-well module with the parameters shown in Table 1



where a_0 represents the steady-state amplitude. Equation (15) is used to analytically construct the frequency response curve (Fig. 2) of the system.

4 Frequency Response Curves and Dissipation Investigation

A bifurcation diagram (i.e., the gray dotted line in Fig. 2) is generated by integrating Eq. (6) for many different excitation frequency values ($0.6 \leq \Omega \leq 1.3$). The model parameters are presented in Tables 1 and 2, with $k = 0.3$; the normalized excitation amplitude z is 0.7. Figure 2 shows that a large-amplitude solution branch appears near the lower end of the frequency range, which represents the periodic interwell responses. For the frequency range considered, this large-amplitude branch disappears in a cyclic-fold bifurcation and exhibits complex multiple-period responses. As the frequency decreases, a cyclic-fold bifurcation occurs on the introwell branch, disappears and is replaced by a period-doubling bifurcation. As the frequency further decreases, a cascade of period-doubling bifurcations occurs, leading to a window of chaotic motions, which disappears in a boundary crisis. Using the equations in the last section, intra- and interwell analytical solutions are obtained, which are presented as the blue circle and black triangle lines, respectively, in Fig. 2. The analytical solution overestimates the frequency when bifurcation occurs, which can be attributed to the fact that the prediction method for the bifurcation point involves approximating the stability loss through variational equations that are linearized assuming small perturbations.

4.1 Excitation Frequency

When the normalized excitation frequency is relatively high, $\Omega = 1.2$, the dynamic trajectories (blue curve in Fig. 3a) remain confined to a single equilibrium position,

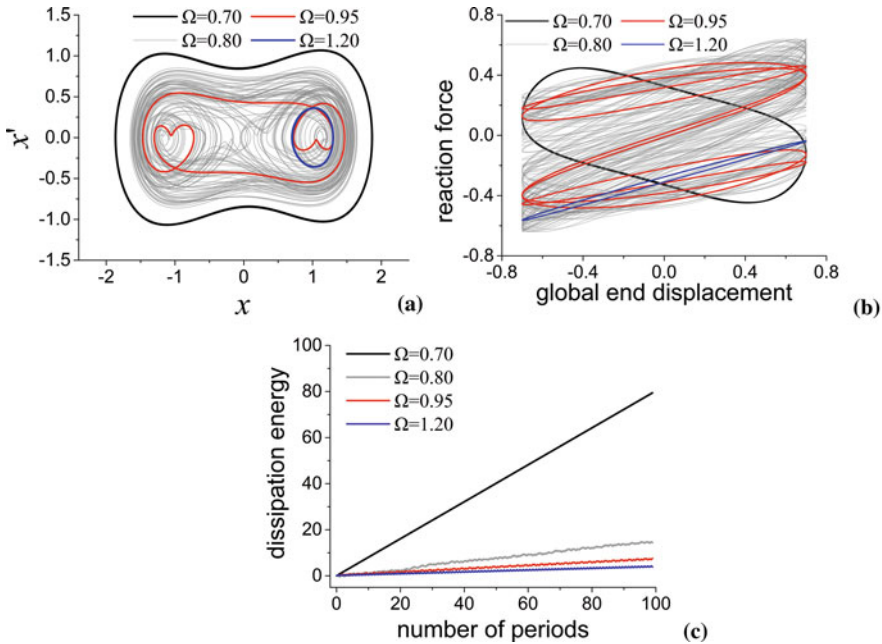


Fig. 3 Dynamic and dissipation features when the excitation frequency is varied: (a) phase plots, (b) force-displacement curve, (c) dissipation energy

which means that the system's potential energy is too low to escape from the well. The module's reaction force ($F = \bar{K}_z \cos(\bar{\Omega}t) - \bar{K}\bar{x}_1$ in Eq. (5))-global end displacement curve behaves linearly (blue curve in Fig. 3b). Using $W = \int F dz$, the reaction force's work W is calculated over excitation periods. The energy dissipation in 100 periods ($\Omega = 1.2$) is the lowest (blue curve in Fig. 3c). As the frequency decreases, a period-doubling bifurcation occurs. When $\Omega = 0.95$, the module has a larger force-displacement range than when $\Omega = 1.2$ because a large trajectory (red curve in Fig. 3a) between the two potential wells occurs. Although the amplitude is much larger than that when $\Omega = 1.2$, the energy dissipation only slightly increases because the reaction force and end displacement phase difference remains small (red curve in Fig. 3b). As the frequency further decreases, a cascade of period-doubling bifurcations occurs, leading to a window of interwell chaotic motions (Fig. 2). The reaction force-end displacement curve ($\Omega = 0.8$ for instance) becomes chaotic (gray curve in Fig. 3b), which is consistent with the phase plot (gray curve in Fig. 3a) and causes greater hysteresis damping than when $\Omega = 0.95$. In such situations, the amplitudes notably increase, but the curve slopes are positive, which means that viscous damping (μ) still dominates the energy dissipation. When the excitation is decreased to a critical frequency (cf1), a large-amplitude solution branch appears (Fig. 2), which represents the periodic interwell responses ($\Omega = 0.7$, black curve in Fig. 3a). Since the excitation and response are periodic, the force-

displacement trajectory forms a large loop, resulting from snap-through hysteresis, with a negative mean slope (black curve in Fig. 3b). The snap-through behavior is clearly confined to a large hysteresis loop, consequently resulting in a dozens of times higher energy dissipation than that in the chaotic situation with a similar amplitude (black curve in Fig. 3c). High energy dissipation is achieved for relatively fixed excitation amplitudes due to the internal snap-buckling mechanism in the bandwidth of periodic interwell oscillations.

4.2 Potential Function

Equation (6) is numerically integrated for modules with different linear springs ($k = 0.1, 0.3$, and 0.5) (Fig. 4). The module ($k = 0.1$) with the deepest well (Fig. 1b) restricts the oscillator to intrawell periodic motion with a wide bandwidth because the potential energy cannot overcome the potential barrier. A periodic motion ($\Omega = 0.9$) with a small amplitude (Fig. 5a) cannot produce effective energy dissipation. As shown in Eq. (6), an axial compressive load can permit tuning of the module at the same frequency for different configurations. The simulated module (Table 2 and $k = 0.3$) has an oscillation frequency of 39 Hz in the twin-well configuration and in the monostable configuration when $P = 5.8$ N. Here, the cubic term of Eq. (5) is neglected. The dissipation performance of the linear system

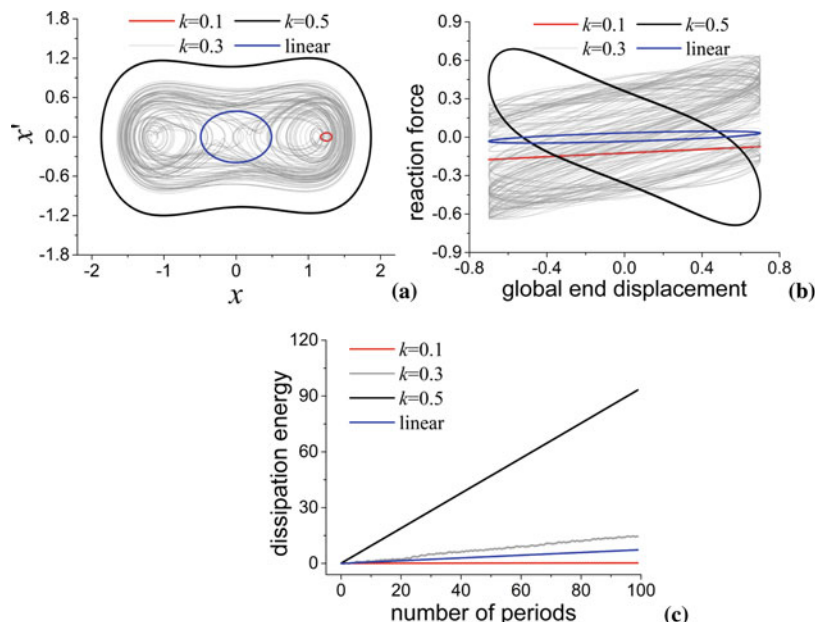


Fig. 4 Dynamic and dissipation features of models with different k values: (a) phase plots, (b) force-displacement curve, (c) dissipation energy

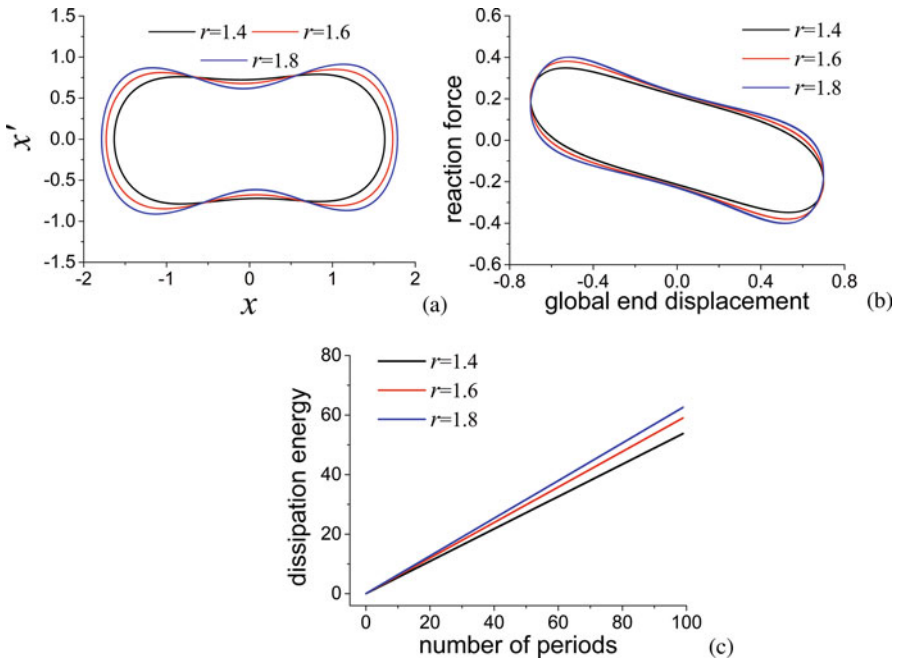


Fig. 5 Dynamic and dissipation features of models with different axial compressive loads (P): (a) phase plots, (b) force-displacement curves, (c) dissipation energy

is compared to that of the twin-well system with the same resonance frequency, and less energy is dissipated in the linear system than in the chaotic situation because of the smaller amplitude. The potential wells of the module with $k = 0.5$ are shallow and close, which can help generate and maintain interwell motion of the oscillator (Fig. 5a). As expected, the interwell oscillations result in very large energy dissipation compared to the single-well, linear and chaotic situations. Equation (6) is numerically integrated for modules ($k = 0.3$) with different constant compressive loads ($P = 27.0, 30.9, 34.7$ N; $r = \alpha P = 1.4, 1.6, 1.8$). When applying the same excitation ($\Omega = 0.6$), the module with the largest preload exhibits the highest energy dissipation (Fig. 5). A higher preload reasonably results in a larger equilibrium position value. More details about the role of the preload will be discussed in the future.

5 Conclusion

This chapter explores the adaptable energy dissipation characteristics of a continuous laminated metal module of a beam bimorph and a linear elastic layer based on the snap-buckling mechanism. This continuous module exhibits a reaction force in

the opposite direction to the displacement due to the internal snap-buckling behavior of the interwell oscillator, which brings about an order of magnitude increase in energy dissipation compared to the single-well and chaotic situations within a certain bandwidth.

References

1. Liu, C.C., Jing, X.J., Daley, S.F., Li, M.: Recent advances in micro-vibration isolation. *Mech. Syst. Signal Process.* **56–57**, 55–80 (2015)
2. Dong, L., Lakes, R.: Advanced damper with high stiffness and high hysteresis damping based on negative structural stiffness. *Int. J. Solids. Struct.* **50**, 2416–2423 (2013)
3. Johnson, D.R., Thota, M., Semperlotti, F., Wang, K.W.: On achieving high and adaptable damping via a bistable oscillator. *Smart Mater. Struct.* **22**, 115027 (2013)
4. Kidambi, N., Harne, R.L., Wang, K.W.: Adaptation of energy dissipation in a mechanical metastable module excited near resonance. *J. Vib. Acoust.* **138**, 011001 (2016)
5. Panyam, M., Masana, R., Daqaq, M.F.: On approximating the effective bandwidth of bi-stable energy harvesters. *Int. J. Nonlinear. Mech.* **67**, 153–163 (2014)

The Duffing–Mathieu Equation Arising from Dynamics of Post-Buckled Beams



Enrico Babilio

Abstract The nonlinear dynamics of a beam embedded in a viscoelastic continuous medium is considered. The beam undergoes large deflections induced by an axial harmonic excitation. The non-dimensional equation of motion describing the problem is approximated by a Duffing–Mathieu equation. Some analytical and numerical results are reported.

Keywords Duffing–Mathieu equation · Straight beams · Post-buckling behavior · Single-mode approximation · Bifurcation scenario

1 Introduction

The present short contribution deals with nonlinear dynamics of a beam embedded in a viscoelastic medium and follows previous works, whose results are partially reported in [1–5]. Beams resting on, or embedded in, deformable media are suitable models to describe different problems, starting from classical examples in the field of civil engineering [6] up to modern applications in the emerging nanotechnology science [7]. The beam we are dealing with undergoes moderately large deflections in post-buckled regimes, induced by an axial harmonic excitation. To derive a reduced-order model, the corresponding partial differential equation of motion, in non-dimensional form, is discretized with a single-mode approximation. The resulting equation is of Duffing–Mathieu type that is indeed a nonlinear version of the celebrated Mathieu equation. This latter plays a central role in a number of problems in engineering and physics [8], as vibration in elliptic membranes, motion of an inverted pendulum with vertically vibrating suspension point, stability of floating bodies, elastic oscillations of a ferromagnetic material, and many others, whose dynamics is induced by a parametric excitation. It is well-known that in the

E. Babilio (✉)

Department of Structures for Engineering and Architecture (DiSt), University of Naples “Federico II”, Naples, Italy
e-mail: enrico.babilio@unina.it

linear case parametric excitation may induce unbounded oscillations, even for small exciting terms, while, on the contrary, in the nonlinear case, the system response may remain bounded, thanks to the detuning effect of the nonlinearities [9].

2 The Mechanical Model and Equation of Motion

Let us consider a slender, straight beam embedded in a viscoelastic medium, excited by an axial harmonic load. Taken a Cartesian triad x , y , and z as reference frame, the beam centerline of length L lays down with x , where principal cross-sectional axes are along y and z . We consider planar, twistless deformed states into xy -plane, with the rigid cross sections, of area A and second moment of area I , preserving normality to deformed beam axis, which implies that the beam is unshearable. Right and left edges of the beam are simply supported and the surrounding medium exerts reaction forces along y -direction

$$R(x, t) = k_1 v - k_2 v_{,xx} + c v_{,t}, \quad (1)$$

being k_1 and k_2 elastic stiffnesses and c the linear viscous dissipation parameter. Here and hereafter, we use the comma notation for derivatives, meaning that a subscript comma followed by letters stands for the partial derivative with respect to (w.r.t.) the variables indicated by those letters.

A buckled configuration of the beam is shown in Fig. 1, where at a given abscissa x , the transverse displacement $v(x, t)$ and the internal generalized stresses, namely axial force $N(x, t)$, shear force $T(x, t)$, and bending moment $M(x, t)$, are reported.

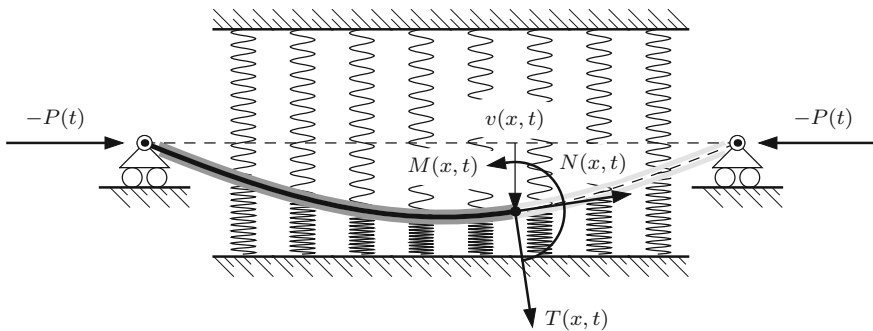


Fig. 1 The buckled beam. Transverse displacement and internal generalized stresses at a generic abscissa are shown. Notice that since restraints on boundary edges ($x = 0$ or $x = L$) of the beam imply simply supported boundary conditions, forces at $x = 0$ and $x = L$, acting along x -direction, must be equal. Hence, since we are solely interested in transversal motion (i.e. along y -direction), we do not need to make explicit where the axial restraint is located, nor distinguish if the force on the left edge is the external excitation and that on the right is the reaction of boundary restraint or *vice versa*

The axial time-dependent harmonic load $P(t)$, responsible for the beam vibrations is also shown. The transversal equation of motion (i.e., along y -direction) is

$$\rho A v_{,tt} - F_{y,x} + R = 0, \quad (2)$$

where the internal force $F_y = F_y(x, t)$ is given by $F_y = T + N v_{,x}$ and R is defined in Eq. (1).

Being the beam unshearable, T is an internal reaction for which no constitutive assumption can be assigned. However, the balance of moments of an infinitesimal slice of the beam allows getting $T = M_{,x}$. Furthermore, because of the boundary conditions we are dealing with, $N = P + T v_{,x} = P + M_{,x} v_{,x}$ holds. Therefore, we must consider a constitutive hypothesis only for the bending moment, for which we assume the linear relationship $M = -EI v_{,xx}$, where $E = E(x)$ is the Young's modulus of the material.

Thus, the transversal motion equation is finally written as

$$\rho A v_{,tt} + c v_{,t} + (EI v_{,xx})_{,xx} - (P + k_2)v_{,xx} + k_1 v = -2(EI v_{,xx})_x v_{,x} v_{,xx}, \quad (3)$$

where $\rho = \rho(x)$ is the mass density of the material.

2.1 The Dimensionless Equation of Motion

A dimensionless version of Eq. (3) is deduced as

$$\mu \ddot{w} + 2\zeta \dot{w} + (\mathcal{E} w'')'' - \pi^2(\mathcal{P} + \kappa_2)w'' + \kappa_1 w = -2(\mathcal{E} w'')' w' w'', \quad (4)$$

after the introduction of rescaled length, time, displacement, and force as

$$\xi = \frac{x}{L}, \quad \tau = \frac{t}{L^2} \sqrt{\frac{E_0 I}{\rho_0 A}}, \quad w = \frac{v}{L}, \quad \mathcal{P} = \frac{PL^2}{\pi^2 E_0 I} = \frac{P}{P_{\text{crit}}}, \quad (5)$$

and dimensionless mass density, Young's modulus, foundation parameters, and damping ratio as

$$\mu = \frac{\rho}{\rho_0}, \quad \mathcal{E} = \frac{E}{E_0}, \quad \kappa_1 = \frac{k_1 L^4}{E_0 I}, \quad \kappa_2 = \frac{k_2}{P_{\text{crit}}}, \quad \zeta = \frac{c L^2}{2\sqrt{\rho_0 A E_0 I}}, \quad (6)$$

where ρ_0 and E_0 are suitable reference parameters, P_{crit} is the first buckling load, and overdot and prime stand for partial differentiation of w w.r.t. τ and ξ .

Since attacking nonlinear partial differential equation can be very complicated both analytically, even with perturbation methods, and numerically, in what follows we consider a low-dimensional Galerkin discretization.

2.2 The Galerkin Discretization and Duffing–Mathieu Equation

In order to get a single-mode approximation of Eq.(4), we apply the standard Galerkin method, after selecting as tentative solution

$$w(\xi, \tau) = \varphi(\tau) \sin(\pi\xi), \quad (7)$$

which resembles the first linear buckling mode shape, being φ a generalized coordinate representing the transversal dimensionless displacement of the mid-span cross section of the beam.

By substituting for Eq.(7) in Eq.(4), multiplying everything by $\sin(\pi\xi)$ and integrating in the unit interval, after a rearrangement of terms, we get

$$\ddot{\varphi}(\tau) + 2\frac{\zeta}{M}\dot{\varphi}(\tau) + \left(\frac{K}{M} + \frac{\pi^4 \mathcal{P}}{M}\right)\varphi(\tau) = -\frac{\Gamma}{M}\varphi^3(\tau), \quad (8)$$

where

$$M = 2 \int_0^1 \sin^2(\pi\xi) \mu(\xi) d\xi, \quad (9)$$

$$\begin{aligned} K = & \kappa_1 + \pi^4 \kappa_2 + 2\pi^4 \int_0^1 \sin^2(\pi\xi) \mathcal{E}(\xi) d\xi \\ & - 2\pi^3 \int_0^1 \sin(2\pi\xi) \mathcal{E}'(\xi) d\xi - 2\pi^2 \int_0^1 \sin^2(\pi\xi) \mathcal{E}''(\xi) d\xi, \end{aligned} \quad (10)$$

$$\Gamma = \pi^6 \int_0^1 \sin(2\pi\xi)^2 \mathcal{E}(\xi) d\xi + 4\pi^5 \int_0^1 \cos(\pi\xi) \sin(\pi\xi)^3 \mathcal{E}'(\xi) d\xi. \quad (11)$$

It is worth noting that Eq.(8), because of the single-mode Eq.(7), is a rough approximation of Eq.(4), since it ignores higher modes. Instead, such modes, also called passive modes, may be relevant to the dynamics, due to nonlinear couplings. The way to represent higher modes by means of the lower ones is the essential step in dimension reduction methods more sophisticated than the standard Galerkin method that however proved to be efficient in constructing approximated solutions for many continuous systems. Being beyond the scopes of this brief contribution, we leave further investigation on this aspect for future work and we refer to [10] for some detail on the subject. Here, we further manipulate Eq.(8). Indeed, by setting

$$\omega = \sqrt{\frac{K}{M}}, \quad v = \frac{\zeta}{\omega M}, \quad \epsilon = -\frac{\pi^4 \mathcal{P}}{2M}, \quad \gamma = \frac{\Gamma}{M}, \quad (12)$$

and choosing the exciting force as

$$\mathcal{P} = \cos(2\Omega\tau),$$

Eq. (8) turns out to be the Duffing–Mathieu equation

$$\ddot{\varphi} + 2v\omega\dot{\varphi} + (\omega^2 - 2\epsilon \cos(2\Omega\tau))\varphi = -\gamma\varphi^3. \quad (13)$$

For $\gamma = 0$, we get the (linear) Mathieu equation, whose solution has the form

$$\varphi = e^{-v\omega\tau} \left(\eta_1 C\left(\frac{\omega_d^2}{\Omega^2}, \frac{\epsilon}{\Omega^2}, \Omega\tau\right) + \eta_2 S\left(\frac{\omega_d^2}{\Omega^2}, \frac{\epsilon}{\Omega^2}, \Omega\tau\right) \right), \quad (14)$$

where $C(\cdot, \cdot, \cdot)$ and $S(\cdot, \cdot, \cdot)$ are the even and odd Mathieu functions, $\omega_d = \omega\sqrt{1-v^2}$ is the damped frequency, η_1 and η_2 are constants defined as

$$\eta_1 = \frac{S_0(\dot{\varphi}_0 + v\omega\varphi_0) - \dot{S}_0\varphi_0}{S_0\dot{C}_0 - \dot{S}_0C_0}, \quad \eta_2 = -\frac{C_0(\dot{\varphi}_0 + v\omega\varphi_0) - \dot{C}_0\varphi_0}{S_0\dot{C}_0 - \dot{S}_0C_0}, \quad (15)$$

being C_0 , S_0 , \dot{C}_0 , and \dot{S}_0 the Mathieu functions and their derivatives w.r.t. τ evaluated at $\tau = 0$.

Mathieu functions, and therefore the solution (14), are only periodic in τ for certain so-called *characteristic values* of the ratio ω_d^2/Ω^2 , for $\epsilon \neq 0$. Such characteristic values are denoted, in what follows, as $a_r(\epsilon/\Omega^2)$, first argument of the even C function, and $b_r(\epsilon/\Omega^2)$, first argument of the odd S function, with r an integer or, more in general, although not used in what follows, a rational number. Furthermore, Eq. (14) may be bounded or not, that is, stable or unstable, respectively. In the undamped case ($v = 0$), the transition curves between stable and unstable domains are related to the characteristic values a_r and b_r , as functions that here we call f_r and g_r , respectively. In the damped case, f_r and g_r do not play anymore the role of stability boundaries and are completely included in the stable region. Relations between f_r and a_r and between g_r and b_r are stated as

$$f_r^{(\Omega, v)}(\epsilon) = \frac{\Omega^2}{1-v^2} a_r\left(\frac{\epsilon}{\Omega^2}\right), \quad r = 0, 1, 2, \dots \quad (16)$$

$$g_r^{(\Omega, v)}(\epsilon) = \frac{\Omega^2}{1-v^2} b_r\left(\frac{\epsilon}{\Omega^2}\right), \quad r = 1, 2, 3 \dots \quad (17)$$

and they will be computed through the harmonic balance method [11] in Sect. 3.

3 On the Stability Charts and a Bifurcation Diagram

Stability charts for the Mathieu equation, which is, as already stated, indeed the linear version of Eq. (13), are reported in Fig. 2, for the undamped case ($\nu = 0$) and two different values of the damping (namely ν set to 0.1 and 0.5). The gray-shaded regions correspond to sets of parameters leading to unstable solutions. The functions f_r and g_r can be computed, by exploiting a result from Floquet theory assuring that periodic solutions exist along the transitions curves. Hence, the general periodic solution is found substituting the trial Fourier expansion

$$\varphi(\tau) = A_0 + \sum_{r=1}^{\infty} A_r \cos(r\Omega\tau) + B_r \sin(r\Omega\tau), \quad (18)$$

in a linear, undamped version of Eq. (13), namely

$$\ddot{\varphi} + (\omega_d^2 - 2\epsilon \cos(2\Omega\tau))\varphi = 0, \quad (19)$$

where ω_d (indeed, the already defined damped frequency) replaces ω , as a dummy variable. Actually, here we use ω_d instead of ω in order to get results valid in both the undamped and damped cases and, needless to say, ω_d takes value ω whenever ν vanishes. Upon inserting Eq. (18) in Eq. (19) and collecting coefficients of each $\cos(r\Omega\tau)$ and $\sin(r\Omega\tau)$ (which is the rationale of the harmonic balance method [11]), it becomes evident that to satisfy Eq. (19), apart the trivial solution, all those coefficients must vanish. This leads to an infinite set of linear, homogeneous equations for the coefficients A_r and B_r , that is

$$\omega_d^2 A_0 - \epsilon A_2 = 0, \quad (20)$$

$$(\omega_d^2 - 4\Omega^2) A_1 - \epsilon A_3 = 0, \quad (21)$$

$$(\omega_d^2 - 4\Omega^2) A_2 - \epsilon (A_4 - 2A_0) = 0, \quad (22)$$

$$(\omega_d^2 - 4\Omega^2) A_{2+r} - \epsilon (A_r + A_{4+r}) = 0, \quad r = 1, 2, 3, \dots \quad (23)$$

$$(\epsilon + \omega_d^2 - \Omega^2) B_1 - \epsilon B_3 = 0, \quad (24)$$

$$(\omega_d^2 - 4\Omega^2) B_2 - \epsilon B_4 = 0, \quad (25)$$

$$(\omega_d^2 - (2+r)^2 \Omega^2) B_{2+r} - \epsilon (B_r + B_{4+r}) = 0, \quad r = 1, 2, 3, \dots \quad (26)$$

To obtain f_0, f_2, f_4, \dots , we must require that the determinant of coefficients of a system made with Eqs. (20), (22), and (23), $r = 2, 4, 6, \dots$, vanishes. Similarly, from Eqs. (21) and (23), with $r = 1, 3, 5, \dots$, we get f_1, f_3, f_5, \dots ; from Eqs. (24)

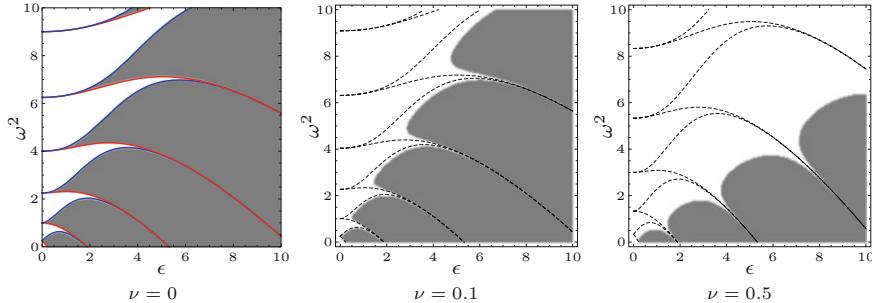


Fig. 2 Stability charts of Mathieu equation for different damping values. The curves f_r and g_r , respectively blue- and red-colored in the undamped diagram, are computed retaining 15 terms in Eq. (18). The loading frequency is set to $\Omega = 0.5$ in all the graphs. In the considered damped cases, regions of parameters leading to stable or unstable solutions have been numerically evaluated, by checking if, at a sufficiently large time (here, $5 \times 10^3 \pi / \Omega$), Eq. (14) goes to zero (stable solution) or diverges (unstable solution). By setting $\varphi_0 = 0.0$, $\dot{\varphi}_0 = 0.1$, η_1 and η_2 , given by Eqs. (15), are determined for any ω

and (26), with $r = 1, 3, 5 \dots$, we compute g_1, g_3, g_5, \dots ; and finally g_2, g_4, g_6, \dots are obtained by operating on Eqs. (25) and (26), $r = 2, 4, 6 \dots$. Approximated f_r and g_r can be obtained by limiting the number of terms in Eq. (18) to that allowing the desired precision. Results are reported in Fig. 2 and show the stabilizing role of the damping: indeed, for the occurrence of the instability ϵ must be greater than zero, while in the undamped case, the solution can be unstable even if $\epsilon = 0$, for given values of the frequency. However, in the linear case unbounded solutions can take place in both damped and undamped cases. This situation changes in the nonlinear case, as can be seen from Fig. 3, where the stability chart for the linear case, taken up from Fig. 2, in the rectangle $(0 \leq \epsilon \leq 10) \times (2.0 \leq \omega^2 \leq 4.5)$ as part of the diagram for $\nu = 0.1$ (top panel) is compared with the bifurcation diagram of Eq. (13) (bottom panel), which summarizes the results of numerical computations performed through a brute force integration algorithm. Numerical integrations are made over time interval from $\tau_0 = 0$ to $\tau_f = 3000\pi/\Omega$, as the bifurcation parameter ϵ varies in the interval from 0 to 10, forward and backward, with a step equal to 0.025. The other mechanical data take values $\omega = \sqrt{3}$, $\Omega = 0.5$, $\nu = 0.1$, and $\gamma = 1$. Initial conditions at the first computational stage are set as $\varphi_0^{(1)} = 0.0$, $\dot{\varphi}_0^{(1)} = 0.1$, while at any stage $i > 1$, $\varphi_0^{(i)} = \varphi_f^{(i-1)}$ and $\dot{\varphi}_0^{(i)} = \dot{\varphi}_f^{(i-1)}$ (for further details on the code, see [2]). Up to $\epsilon \approx 1.6$ the solution approaching zero is stable in both the linear and nonlinear cases. After such a value, the linear solution is unbounded (apart for very narrow intervals of ϵ), while the solution for the nonlinear problem remains bounded and exhibits various bifurcations and transition to chaos (see, among others, the doubling period cascade starting at $\epsilon \approx 2.4$). The finite amplitude is an effect of the fact that as the amplitude of motion increases, the frequency increases and the system falls out of resonance [9, 11]. Indeed, the period–amplitude relationship, due to the nonlinearity, detunes the resonance. Finally, in Fig. 3, red (black) dots

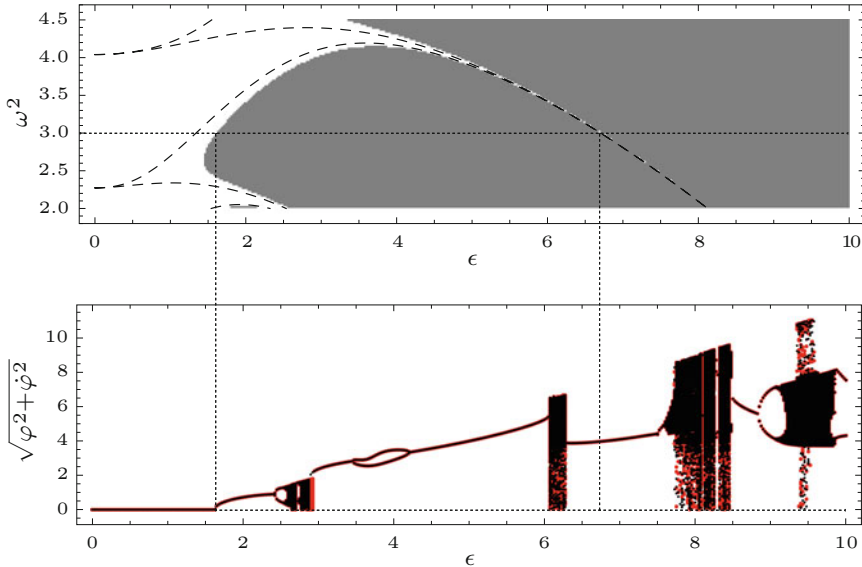


Fig. 3 A detail of stability chart reported in Fig. 2 for the damped linear equation, with $\nu = 0.1$ (top panel), compared to the bifurcation diagram for the Mathieu-Duffing equation (bottom panel). Notice that, up to $\epsilon \approx 1.6$ (see the first vertical dashed line between the two panels) the solution approaching zero is stable in both the linear and nonlinear cases. After such a value, the linear solution is unbounded (apart for very narrow intervals of ϵ , as that in correspondence with the second vertical dashed line between the two panels), while the solution for the nonlinear problem remains bounded, due to the detuning effect of nonlinearity. Red (black) dots refer to solutions got for the bifurcation parameter ϵ varying forward (respectively, backward)

refer to solutions for forward (respectively, backward) varying ϵ . Forward and backward paths appear very close to each other, although some little differences can be found. For instance, a transition from chaotic to periodic behavior occurs at $\epsilon^* \in (2.925, 2.95)$, when ϵ increases, while when it decreases the periodic response remains stable up to $\epsilon^* \in (2.875, 2.9)$. Here, the size of both open intervals in which the transition values are detected depends on the step chosen for the bifurcation parameter.

4 Conclusions

The present contribution is focused on the study of nonlinear dynamics of a straight beam embedded in a viscoelastic medium. The beam, assumed undergoing large deflections, is axially loaded by a harmonic excitation. The results of a number of numerical simulations are collected in a bifurcation diagram, qualitatively compared with the stability chart for the linear case.

References

1. Babilio, E.: Dynamics of an axially graded beam on elastic foundation. In: Lenci, S., Warminski, J. (eds.) Proceedings of Euromech Colloquium N. 541: New Advances in the Nonlinear Dynamics and Control of Composites for Smart Engineering Design, Senigallia, Ancona, June 3–6 (2013). ISBN: 978-88-87965-72-8
2. Babilio, E.: Nonlinear dynamics of buckling-restrained braces with axially graded core in elastic regime. In: Amabili, M., Alijani, F. (eds.) Proceedings of the 4th Canadian Conference on Nonlinear Solid Mechanics (CanCNSM 2013), Montréal, July 23–26 (2013), vol. 1, pp. 191–196. Monograph compiled by E. M. Croitoro and E. Babilio. ISBN: 978-1-55058-533-9
3. Babilio, E.: Dynamics of functionally graded beams on viscoelastic foundation. *Int. J. Struct. Stab. Dyn.* **14**(8), Article No. 1440014 (2014). <https://doi.org/10.1142/S0219455414400148>
4. Babilio, E.: On the effect of axial material gradation on the dynamics of a slender beam in a viscoelastic medium. In: Proceedings of ICCE-25: 25th International Conference on Composites/Nano-Engineering, Rome, July 16–22 (2017)
5. Babilio, E.: Nonlinear dynamics of a slender axially graded beam embedded in a viscoelastic medium. Proc. ASME Des. Eng. Tech. Conf. **6**. <https://doi.org/10.1115/DETC2017-68464>. Cleveland, OH, August 6–9 (2017)
6. Wang, Y.H., Tham, L.G., Cheung, Y.K.: Beams and plates on elastic foundations: a review. *Prog. Struct. Eng. Mater.* **7**(4), 174–182 (2005)
7. Li, Z., Dharap, P., Nagarajaiah, S., Nordgren, R.P., Yakobson, B.: Nonlinear analysis of a SWCNT over a bundle of nanotubes. *Int. J. Solids. Struct.* **41**(24–25), 6925–6936 (2004)
8. Ruby, L.: Applications of the Mathieu equation. *Am. J. Phys.* **64**(1), 39–44 (1996)
9. Zoures, R.S., Rand, R.H.: Global behavior of a nonlinear quasiperiodic Mathieu equation. *Nonlinear Dyn.* **27**, 87–105 (2002)
10. Rega, G., Troger, H.: Dimension reduction of dynamical systems: methods, models, applications. *Nonlinear Dyn.* **41**, 1–15 (2005)
11. Rand, R.H.: Lecture Notes on Nonlinear Vibrations. [Online] <http://hdl.handle.net/1813/28989>, Version 53 (2012)

Resonance-Induced Energy Localization in Weakly Dissipative Anharmonic Chains



Agnessa Kovaleva 

Abstract This chapter studies the emergence of resonance and resonance-induced localization in a weakly dissipative anharmonic chain subjected to a harmonic force applied at one end. The system does not possess a linear spectrum, and resonance is imposed by external forcing. It is shown that weak dissipation may be a key factor preventing large-amplitude resonance. The resulting process in the dissipative system represents resonant oscillations in a part of the chain adjacent to the source of energy and escape from resonance of the distant oscillators. Conditions of the emergence of resonance and energy localization are derived. An agreement between the analytical and numerical results is demonstrated.

Keywords Nonlinear oscillations · Asymptotic methods · Localization

1 Introduction

Localization of responses in oscillator arrays has been of interest for recent decades, with special attention to the role of nonlinearity and discreteness in the formation of localized structures (see, e.g., [1–5] and references therein). However, the influence of dissipation has not been addressed in the literature. The attention was drawn to the so-called dissipative roto-breathers in pendulum-like models forced by a constant torque [6], as well as to localized responses of harmonically excited dissipative oscillators, such as coupled optical resonators [7] or micro- and macroscale cantilever arrays [5, 8–11]. The recent work [12] studied the emergence of resonance and resonantly induced localization in a weakly dissipative quasi-linear chain, wherein intense energy transport is sustained by the cumulative effect of internal and external resonances.

A. Kovaleva (✉)
Space Research Institute, Moscow, Russia
e-mail: agnessa_kovaleva@hotmail.com

In the present chapter, we extend the procedures presented in [12] to anharmonic chains. The dynamics of the chain is studied assuming 1:1 (fundamental) resonance, when the response of each nonlinear oscillator has a dominant harmonic with frequency close to the frequency of the external excitation. It is shown that weak dissipation may prevent the emergence of resonance in the entire array even if its non-dissipative analogue is totally captured in resonance. Capture into resonance and escape from resonance are illustrated by numerical simulations.

2 Equations of the Resonant Dynamics

We analyze the chain consisting of n identical weakly linearly coupled cubic oscillators subjected to a harmonic force applied at one edge of the chain. The equations of motion are given by

$$\frac{d^2U_r}{dt^2} + \chi \frac{dU_r}{dt} + \gamma U_r^3 + \kappa [\eta_{r,r-1}(U_r - U_{r-1}) + \eta_{r,r+1}(U_r - U_{r+1})] = A_r \sin \omega t. \quad (1)$$

In Eq. (1), the variable U_r denotes the absolute displacement of the r th oscillator from its rest state, $r \in [1, n]$; γ is the cubic stiffness coefficient; κ denotes stiffness of linear coupling; χ is the coefficient of dissipation; all parameters are reduced to the unit mass. The coefficients $\eta_{r,k} = \{1, k \in [1, n]; 0, k = 0, k = n + 1\}$ indicate that the end oscillators are unilaterally coupled with the adjacent elements. Since the harmonic excitation is applied to the first oscillator, we let $A_1 = A$, $A_r = 0$ at $r \geq 2$. The chain is assumed to be initially at rest, i.e., $U_r = 0$, $V_r = dU_r/dt = 0$ at $t = 0$ for all oscillators.

Equation (1) is reduced to the dimensionless form, which has a simpler structure than the original system. Assuming weak coupling, we introduce the dimensionless coupling parameter $\varepsilon = \kappa/(2\omega^2) \ll 1$. Taking into consideration weak nonlinearity and weak dissipation, we define the rescaled parameters $\chi/\omega = 2\varepsilon\delta$; $\alpha^{1/2}A_r/\omega^2 = 2\varepsilon f_r$; the dimensionless coefficient of nonlinearity is given by $\gamma/\omega^2 = 4\alpha/3$. Besides, the dimensionless space variables $u_r = \alpha^{1/2}U_r$ and the dimensionless fast and slow time variables $\tau_0 = \omega t$ and $\tau = \varepsilon\tau_0$ are introduced. Although the generating nonlinear system $\frac{d^2u_r}{d\tau_0^2} + \frac{4}{3}u_r^3 = 0$ does not possess a spectrum independent of energy of oscillations, energy transport can be studied under the assumption of 1:1 (fundamental) resonance, i.e., under the condition that the responses of the coupled oscillators have a dominant harmonic component with a frequency close to the excitation frequency. Under these assumptions, Eq. (1) is rewritten in the form

$$\begin{aligned} & \frac{d^2 u_r}{d\tau_0^2} + 2\varepsilon\delta \frac{du_r}{d\tau_0} + u_r \\ & + 2\varepsilon \left[\sigma \left(\frac{4}{3}u_r^3 - u_r \right) + \eta_{r,r-1} (u_r - u_{r-1}) + \eta_{r,r+1} (u_r - u_{r+1}) \right] = 2\varepsilon f_r \sin \tau_0, \end{aligned} \quad (2)$$

where $2\varepsilon\sigma = 1$. Since only the dominant harmonic with frequency 1 remains in the asymptotic analysis of the resonant system (2), it is convenient to introduce the following single-frequency change of variables:

$$\Psi_r = \left(\frac{du_r}{d\tau_0} + iu_r \right) e^{-i\tau_0}, \quad \Psi_r^* = \left(\frac{du_r}{d\tau_0} - iu_r \right) e^{i\tau_0}. \quad (3)$$

Substitution of Eq. (3) into Eq. (2) yields the following equations for the envelopes Ψ_r :

$$\begin{aligned} \frac{d\Psi_r}{d\tau_0} = & -\varepsilon\delta\Psi_r + i\varepsilon \left[\sigma \left(|\Psi_r|^2 - 1 \right) \Psi_r + \eta_{r,r-1} (\Psi_r - \Psi_{r-1}) \right. \\ & \left. + \eta_{r,r+1} (\Psi_r - \Psi_{r+1}) - f_r + G_r(\tau_0, \Psi) \right] \end{aligned} \quad (4)$$

and similar equations for the complex-conjugate variables Ψ_r^* , $r \in [1, n]$, with initial conditions $\Psi_r(0) = \Psi_r^*(0) = 0$. The coefficients $G_r(\tau_0, \Psi)$ include higher harmonics in τ_0 from all components Ψ_r , Ψ_r^* but explicit expressions of these coefficients are insignificant for further analysis.

The asymptotic analysis is produced with the help of the multiple-scale expansion:

$$\psi_r(\tau_0, \tau, \varepsilon) = \psi_r(\tau) + \varepsilon\psi_r^{(1)}(\tau_0, \tau) + O(\varepsilon^2), \quad (5)$$

where the main slow approximations $\psi_r(\tau)$ satisfy the averaged equations [13, 14]:

$$\begin{aligned} \frac{d\psi_r}{d\tau} = & -\delta\psi_r \\ & + i \left[\sigma \left(|\psi_r|^2 - 1 \right) \psi_r + \eta_{r,r-1} (\psi_r - \psi_{r-1}) + \eta_{r,r+1} (\psi_r - \psi_{r+1}) - f_r \right] \end{aligned} \quad (6)$$

with initial conditions $\psi_r(0) = 0$. The change of variables $\psi_r = a_r e^{i\Delta_r}$, $a_r = |\psi_r|$, $\Delta_r = \arg_r$ transforms Eqs. (6) into the differential equations for the real-valued amplitudes a_r and phases Δ_r

$$\begin{aligned} \frac{da_r}{d\tau} &= -\delta a_r + [\eta_{r,r-1} a_{r-1} \sin(\Delta_{r-1} - \Delta_r) + \eta_{r,r+1} a_{r+1} \sin(\Delta_{r+1} - \Delta_r)] \\ &\quad - f_r \sin \Delta_r, \\ a_r \frac{d\Delta_r}{d\tau} &= \sigma(a_r^2 - 1) a_r + [\eta_{r,r-1} (a_r - a_{r-1} \cos(\Delta_{r-1} - \Delta_r)) \\ &\quad + \eta_{r,r+1} (a_r - a_{r+1} \cos(\Delta_{r+1} - \Delta_r)) - f_r \cos \Delta_r]. \end{aligned} \quad (7)$$

The accuracy of asymptotic approximations (5) is discussed in [13, 14]. Omitting details, we recall that the error of approximations tends to zero as $\varepsilon \rightarrow 0$.

3 Resonance in Non-dissipative Chains

In this section, we examine the emergence of resonance in the non-dissipative chain at $\delta = 0$. The first parametric threshold can be found assuming resonance in the excited oscillator accompanied by small oscillations of the attachment. Under these assumptions, the equations of the excited oscillator are approximated as follows:

$$\begin{aligned} \frac{da_1}{d\tau} &= -f \sin \Delta_1, \\ a_1 \frac{d\Delta_1}{d\tau} &= \sigma(a_1^2 - 1) a_1 + a_1 - f \cos \Delta_1, \end{aligned} \quad (8)$$

with initial conditions $a_1(0) = 0$, $\Delta_1(0) = -\pi/2$, which determine the so-called *Limiting Phase Trajectory* (LPT) corresponding to maximum possible energy transfer from a source of energy to a receiver [15]. Referring to [15], we obtain the following parametric boundaries between small and large oscillations of oscillator (8):

$$(a) : f = f_{1\varepsilon} = \sqrt{(1 - 2\varepsilon)^3 / 54\varepsilon^2}; \quad (b) : f_{2\varepsilon} = \sqrt{(1 - 2\varepsilon)^3 / 27\varepsilon^2} = \sqrt{2} f_{1\varepsilon}. \quad (9)$$

It was shown [15] that at $f < f_{1\varepsilon}$ the LPT of small oscillations represents an outer boundary for a set of closed trajectories encircling the stable center on the axis $\Delta_1 = -\pi$, while at $f > f_{1\varepsilon}$ the LPT of large oscillations depicts an outer boundary for trajectories encircling the stable center on the axis $\Delta_1 = 0$. The transition from small-amplitude to large-amplitude oscillations for a particle being initially at rest occurs due to the loss of stability of the LPT of small oscillations at $f = f_{1\varepsilon}$.

In the next step, motion of an n -particle chain is analyzed. Given that the excited oscillator is captured into resonance, large-amplitude resonant oscillations of the attachment may occur if the coupling strength is large enough to transfer the required amount of energy. In order to evaluate the lower bound of the coupling parameter ε , we calculate the steady states of Eqs. (7) at $\delta = 0$. Since the steady

states $\bar{a}_r, \bar{\Delta}_r$ satisfy the conditions $d\bar{a}_r/d\tau = 0, d\bar{\Delta}_r/d\tau = 0$, the stationary phases $\bar{\Delta}_r$ at $\delta = 0$ are defined by the equations: $\sin\bar{\Delta}_1 = 0, \sin(\bar{\Delta}_{r+1} - \bar{\Delta}_r) = 0, r \in [1, n]$. In analogy to the results obtained for the Duffing oscillators [15, 16] and the quasi-linear oscillator chain [12], one can verify both analytically and numerically that the solution $\bar{\Delta}_r = 0$ corresponds to the maximum stationary amplitude of stable resonance for any $r \in [1, n]$. The corresponding equations for stationary amplitudes are given by

$$\begin{aligned}\sigma(a_1^2 - 1)a_1 + (a_1 - a_2) &= f, \\ \sigma(a_r^2 - 1)a_r + 2(2a_r - a_{r-1} - a_{r+1}) &= 0, \quad r \in [2, n-1], \\ \sigma(a_n^2 - 1)a_n + (a_n - a_{n-1}) &= 0.\end{aligned}\tag{10}$$

The maximum solutions of Eqs. (10) at $\sigma = \frac{1}{2}$ are approximated as

$$\begin{aligned}\bar{a}_1 &= 1 + \varepsilon f + O(\varepsilon^2 f), \\ \bar{a}_r &= 1 + O(\varepsilon^r f), \quad r \in [2, n].\end{aligned}\tag{11}$$

Solutions (11) formally exist even if the coupling strength 2ε is nearly negligible. Now we define the coefficient ε , which yields the coupling response sufficient to sustain resonance in the r th oscillator under the condition of resonance in the preceding $(r-1)$ th oscillator and small-amplitude oscillations of the succeeding $(r+1)$ th oscillator.

Assuming resonance in the $(n-1)$ th oscillator and ignoring higher-order correction terms, the n th equation in Eqs. (10) is reduced to the following form:

$$a_n^3 - (1 - 2\varepsilon)a_n = 2\varepsilon\bar{a}_{n-1},\tag{12}$$

where $\bar{a}_{n-1} = 1$. The roots of Eq. (12) are analyzed through the properties of the discriminant $D_n = 4[27\varepsilon^2 - (1 - 2\varepsilon)^3]$ [17]. If $D_n < 0$, then Eq. (12) has three different real roots; if $D_n = 0$, two real roots merge; if $D_n > 0$, then there exists a single real and two complex-conjugate roots. The condition $D_n > 0$ is transformed into the inequality

$$\varepsilon > \varepsilon_{\text{cr}} = 0.125.\tag{13}$$

Next, we analyze the r th oscillator ($2 \leq r \leq n-1$) assuming large-amplitude resonant response of the preceding $(r-1)$ th oscillator accompanied by negligibly small oscillations of the $(r+1)$ th oscillator. Under these assumptions, the equation for a_r takes the form

$$a_r^3 - (1 - 4\varepsilon)a_r = 2\varepsilon\bar{a}_{r-1},\tag{14}$$

where $\bar{a}_{r-1} = 1$. The roots of Eq. (14) are analyzed through the properties of the corresponding discriminants $D_r = 4[27\varepsilon^2 - (1 - 4\varepsilon)^3]$, $r \in [2, n - 1]$. It can be verified that $D_r > 0$ if $\varepsilon > \varepsilon_{\text{cr}}^{(1)} = 0.0945$, that is, $\varepsilon_{\text{cr}}^{(1)} < \varepsilon_{\text{cr}}$.

Finally, the first equation in Eqs. (10) is analyzed. Assuming small oscillations of the second oscillator, the equation under consideration is given by

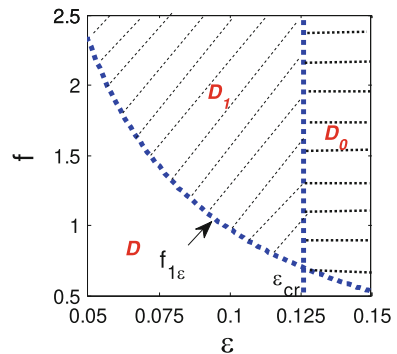
$$a_1^3 - (1 - 2\varepsilon)a_1 = 2\varepsilon f \quad (15)$$

with the discriminant $D_1 = 4[27\varepsilon^2 f^2 - (1 - 2\varepsilon)^3]$. The condition $D_1 > 0$ is equivalent to the inequality $f > f_{1\varepsilon} = \sqrt{(1 - 2\varepsilon)^3 / 27\varepsilon^2} > f_{1\varepsilon}$ corresponding to the vanishing of the stable center on the axis $\Delta_1 = -\pi$ [15]. As shown above, the transition from small oscillations about the center at $\Delta_1 = -\pi$ to large oscillations about the center at $\Delta_1 = 0$ occurs under the weaker condition $f > f_{1\varepsilon}$. This implies that the admissible parametric domain for the emergence of resonance in the entire multiparticle chain is determined by the conditions: $f > f_{1\varepsilon}$, $\varepsilon > \varepsilon_{\text{cr}}$ (see Fig. 1).

As discussed above, oscillators with the parameters $(\varepsilon, f) \in D$ execute small quasi-linear oscillations; the entire chain with the parameters $(\varepsilon, f) \in D_0$ is captured into resonance; if the parameters $(\varepsilon, f) \in D_1$, then the forced oscillator is captured into resonance but the dynamics of the attachment should be investigated separately.

Numerical results for the 4-particle chain are presented in Fig. 2. Numerical simulations demonstrate small oscillations of the chain with parameters $(\varepsilon = 0.07, f = 0.7) \in D$ and large-amplitude resonant oscillations of the chains with parameters $(\varepsilon = 0.07, f = 2) \in D_1$ and $(\varepsilon = 0.13, f = 0.7) \in D_0$. Since all particles in the chain with parameters from D exhibit small oscillations, the only amplitude $a_1(\tau)$ is depicted in Fig. 2a. Figure 2b, c indicate that at large times the resonant amplitude of the excited oscillator fluctuates near $\bar{a}_1 = 1.13$ at $\varepsilon = 0.07, f = 2.5$ and near $\bar{a}_1 = 1.08$ at $\varepsilon = 0.13, f = 0.7$, respectively, while the amplitudes of the attached oscillators in both systems remain close to 1. Note that the numerical solutions agree with formulas (11).

Fig. 1 Parametric thresholds (9) and (13)



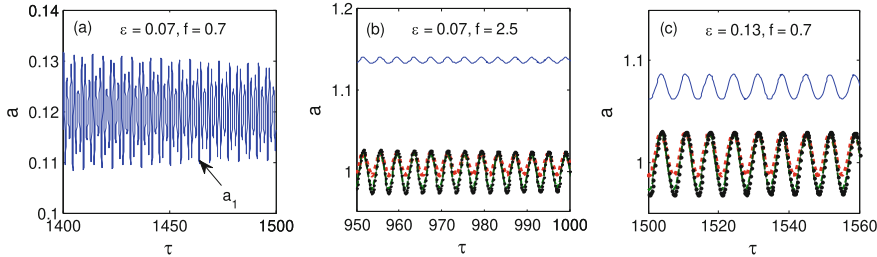


Fig. 2 Slowly-varying amplitudes in the 4-particle chain: —: a_1 ; ·······: a_2 ; - - -: a_3 ; -•-: a_4

4 Energy Localization in Weakly Dissipative Chains

In this section, we demonstrate that a weakly dissipative short-length chain may be totally captured into resonance but the growth of dissipation as well as an increase of the chain length may cause escape from resonance of the oscillators far removed from the source of energy.

In order to evaluate the limiting dissipation coefficients, we calculate the steady states \bar{a}_r , $\bar{\Delta}_r$ of system (7). If dissipation is small enough, and the entire chain is captured into resonance, then Eqs. (11) remain approximately valid for the dissipative chain. In this case, the leading-order approximations to the stationary phases $\bar{\Delta}_r$ may be found from the following equations:

$$\begin{aligned} -\delta + \sin(\Delta_2 - \Delta_1) - f \sin \Delta_1 &= 0, \\ -\delta + [\sin(\Delta_{r-1} - \Delta_r) + \sin(\Delta_{r+1} - \Delta_r)] &= 0, \quad r \in [2, n-1], \\ -\delta + \sin(\Delta_{n-1} - \Delta_n) &= 0 \end{aligned} \quad (16)$$

provided that $\delta \ll 1$, $|\sin \bar{\Delta}_1| \ll 1$, $|\sin(\bar{\Delta}_r - \bar{\Delta}_{r-1})| \ll 1$. Solving Eqs. (16), we find that

$$\sin \bar{\Delta}_1 = -\delta n / f, \quad \sin \bar{\Delta}_r = -\left[n/f + (r-1)(2n-r)/2\right], \quad (17)$$

provided that $|\sin \bar{\Delta}_r| \ll 1$, $r \in [1, n]$. Let

$$\delta_r = [n/f + (r-1)(2n-r)/2]^{-1} \quad (18)$$

be the critical coefficients of dissipation such that $\delta_1 > \delta_2 > \dots > \delta_n$. It follows from Eqs. (17) and (18) that the entire chain is captured into resonance if $\delta \leq \delta_n < \delta_1$.

Expressions (17) demonstrate that, although the chain consists of identical oscillators, the value of $|\sin \bar{\Delta}_r|$ increases with an increase of the oscillator index r as well as with an increasing number n of oscillators in the chain. These observations suggest large-amplitude resonance either in a relatively short chain or in an initial

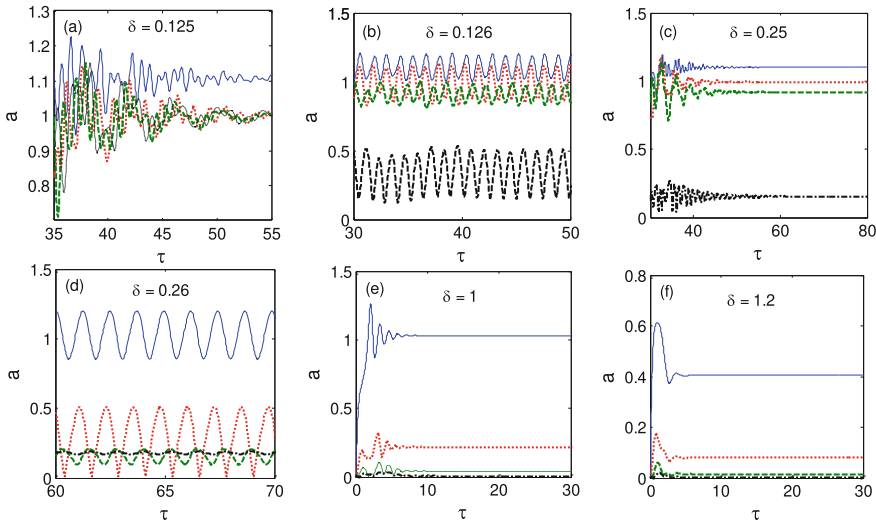


Fig. 3 Oscillations of the 4-particle arrays with parameters $(\varepsilon = 0.07, f = 2) \in D_1$ and different coefficients of dissipation: —: a_1 ; ·····: a_2 ; - - -: a_3 ; -•-: a_4

part of a protracted chain involving $l < n$ particles, together with small oscillations of the distant oscillators. In this case, the parameter l determines *localization length*.

Figure 3 illustrates oscillations of the 4-particle chain with parameters $(\varepsilon = 0.07, f = 2) \in D_1$; the critical coefficients of dissipation are $\delta_1 = 0.5, \delta_4 = 0.125$. It is seen from Fig. 3a that the entire chain remains captured into resonance up to $\delta = 0.125 = \delta_4$; this corresponds to $l = 4$. In the next step, at $\delta = 0.126$, the last (forth) oscillator escapes from resonance ($l = 3$); this effect holds up to $\delta = 0.25$ (Fig. 3b, c). At $0.26 \leq \delta \leq 1$ resonant energy localization occurs only in the forced oscillator ($l = 1$) while all attached oscillators escape from resonance (Fig. 3d, e). Finally, at $\delta = 1.2 \gg \delta_1$, the entire chain escapes from resonance (Fig. 3f).

5 Concluding Remarks

In this chapter, the emergence of resonance-induced energy localization in a weakly dissipative nonlinear chain has been investigated for the first time. The chain under consideration comprises n identical weakly linearly coupled cubic oscillators; an external harmonic force is applied to the first oscillator. The dynamics of the chain is studied under the assumption of 1:1 (fundamental) resonance, when the response of each nonlinear oscillator has a dominant harmonic component with a frequency close to the excitation frequency. As in the quasi-linear case, the equations for the slow variables have been obtained with the help of the multiple-scale and averaging procedures. The approximate solution defines parametric conditions of

the emergence of resonance in the non-dissipative chain. Furthermore, the obtained solutions indicate that the maximal concentration of energy in the excited oscillator occurs together with equipartition of energy among other resonant oscillators. The second part of the paper discusses resonant processes in a weakly dissipative chain. It has been demonstrated that dissipation may prevent the emergence of resonance in the entire array, even though its non-dissipative counterpart is totally captured in resonance. The resulting process in the weakly damped chain represents localization of energy in the initial segment against small-amplitude oscillations in rest of the chain. Close agreement between the analytical and numerical results has been demonstrated.

References

1. Vazquez, L., MacKay, R., Zorzano, M.P.: *Localization and Energy Transfer in Nonlinear Systems*. World Scientific, Singapore (2003)
2. Dauxois, T., Litvak-Hinenzon, A., MacKay, R., Spanoudaki, A.: *Energy Localization and Transfer*. World Scientific, Singapore (2004)
3. Vakakis, A.F., Gendelman, O., Bergman, L.A., McFarland, D.M., Kerschen, G., Lee, Y.S.: *Passive Nonlinear Targeted Energy Transfer in Mechanical and Structural Systems*. Springer, Berlin (2008)
4. May, V., Kühn, O.: *Charge and Energy Transfer Dynamics in Molecular Systems*. Wiley-VCH, Weinheim (2011)
5. Sato, M., Hubbard, B.E., Sievers, A.J.: Nonlinear energy localization and its manipulation in micromechanical oscillator arrays. *Rev. Mod. Phys.* **78**, 137–157 (2006)
6. Flach, S., Gorbach, A.V.: Discrete breathers with dissipation. *Lect. Notes Phys.* **751**, 289–320 (2008)
7. Egorov, O., Peschel, U., Lederer, F.: Mobility of discrete cavity solitons. *Phys. Rev. E* **72**, 066603 (2005)
8. Sato, M., Hubbard, B.E., Sievers, A.J., Ilic, B., Czaplewski, D.A., Craighead, H.G.: Observation of locked intrinsic localized vibrational modes in a micromechanical oscillator array. *Phys. Rev. Lett.* **90**, 044102 (2003)
9. Kimura, M., Hikihara, T.: Coupled cantilever array with tunable on-site nonlinearity and observation of localized oscillations. *Phys. Lett. A* **373**, 1257–1260 (2009)
10. Dick, A., Balachandran, B., Mote Jr., C.D.: Localization in micro-resonator arrays: influence of natural frequency tuning. *J. Comput. Nonlinear Dyn.* **5**, 011002 (2009)
11. Balachandran, B., Perkins, E., Fitzgerald, T.: Response localization in micro-scale oscillator arrays: influence of cubic coupling nonlinearities. *Int. J. Dyn. Control.* **3**, 183–188 (2015)
12. Kovaleva, A.: Energy localization in weakly dissipative resonant chains. *Phys. Rev. E* **94**, 022208 (2016)
13. Bogoliubov, N.N., Mitropolski, Y.A.: *Asymptotic Methods in the Theory of Non-linear Oscillations*. Gordon and Breach, New York (1961)
14. Sanders, J.A., Verhulst, F., Murdock, J.: *Averaging Methods in Nonlinear Dynamical Systems*. Springer, Berlin (2007)
15. Manevitch, L.I., Kovaleva, A., Shepelev, D.S.: Non-smooth approximations of the limiting phase trajectories for the Duffing oscillator near 1:1 resonance. *Phys. D* **240**, 1–12 (2011)
16. Kovaleva, A.: Capture into resonance of coupled Duffing oscillators. *Phys. Rev. E* **92**, 022909 (2015)
17. Korn, G.A., Korn, T.M.: *Mathematical Handbook for Scientists and Engineers*, 2nd edn. Dover, New York (2000)

Part IV

**Experimental Dynamics, System
Identification and Monitoring**

Torsional Analysis of Transmission Line Cables



Nilson Barbieri, Marcos José Mannala, Renato Barbieri, and Gabriel de Sant'Anna Vitor Barbieri

Abstract In this work, torsion parameter values are experimentally derived as a function of the tensile load for three commercial cables used in electric power transmission lines. The analyzes were conducted using the experimental data obtained from a test bench of transmission line components using samples with a length of 54 m and subjected to different mechanical tension. The cables were excited by a lever positioned at different positions along the samples and subjected to dynamic forces. The tests were performed by varying the angular displacement clockwise and counterclockwise. The results showed nonlinear variations according to the applied load, position of the load application, and direction of rotation of the lever. The experimental data will be used to adjust nonlinear mathematical models of dynamic simulation of cables of electric transmission lines.

Keywords Cable · Torsion · Experimental data · Nonlinear parameters

1 Introduction

Many works have been developed in the attempt to analyze the effect of axial tension and torsion coupling in transmission line cables. Some pioneering works were developed by McConnell and Chang [1] and McConnell and Zemke [2]. In the works, the behavior of ACSR (aluminum conductor steel reinforced) electrical conductors were analyzed. At the same time [3], the mechanical behavior of ACSR

N. Barbieri (✉) · G. de Sant'Anna Vitor Barbieri
Pontifícia Universidade Católica do Paraná-PUCPR, Curitiba, Paraná, Brazil

Universidade Tecnológica Federal do Paraná-UTFPR, Curitiba, Paraná, Brazil
e-mail: nilson.barbieri@pucpr.br

M. J. Mannala
Instituto de Tecnologia para o Desenvolvimento-LACTEC, Curitiba, Paraná, Brazil

R. Barbieri
Universidade do Estado de Santa Catarina-UDESC, Joinville, Santa Catarina, Brazil

conductors under static-loading conditions which may comprise any combination of tension, torsion, and bending was investigated.

The behavior of nine different mathematical models [4] taking into account the effects of traction and torsion for dynamic analysis of cables was implemented. The analytical models give satisfactory estimations of the elastic stiffness constants for lay angles below 20°. For cables with larger lay angles, it was recommended the use of 3D FE models for dynamic analyses of the system.

Nonlinear response of elastic cables with flexural-torsional stiffness was studied in [5, 6]. Recently [6] the nonlinear dynamic analysis of high-voltage overhead transmission lines using generalized Hamilton's principle, three-dimensional (3D) mathematical models, was used to analyze the vibration in-plane and out-of-plane.

Recursive models, based on Love's general thin rod theory, for dynamic analysis of cables, subjected to traction and torsion, can be used [7].

Barbieri et al. [8–10] investigated the dynamic behavior of transmission cables. In these cases, several aspects were addressed: modal analysis using linear models, reduced damping matrix adjustment and dynamic analysis using nonlinear models. The analyses involved the acquisition of experimental data in cable test benches and numerical data obtained through computational simulation of mathematical models using the finite element method. The Irvine parameter and frequency response function adjustment were used in the nonlinear analysis.

2 Material and Method

In this work, the tests were performed on a test bench of electrical transmission line components shown schematically in Fig. 1. The lever was placed at positions $L/16$, $L/8$, $L/4$, $3L/8$, and $L/2$ (A1–A5) in the sample of length L . Three different transmission line cables (Fig. 2) were used (CAA Tern, CAL Phosphorus, and CAL

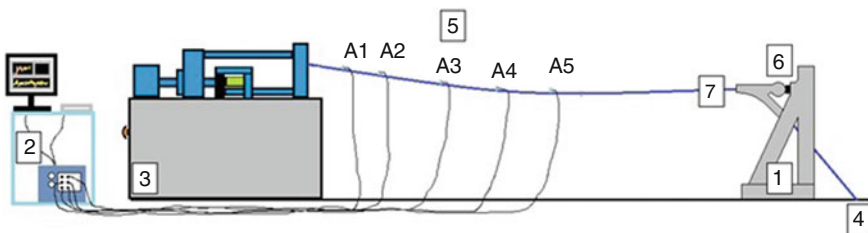


Fig. 1 Schematic representation of the test bench. (1) Rigid structure, (2) data acquisition system and load control, (3) load cell and mechanical load control, (4) anchorage (fixation) system, (5) lever positioning (A1–A5), (6) anchorage, (7) cable sample

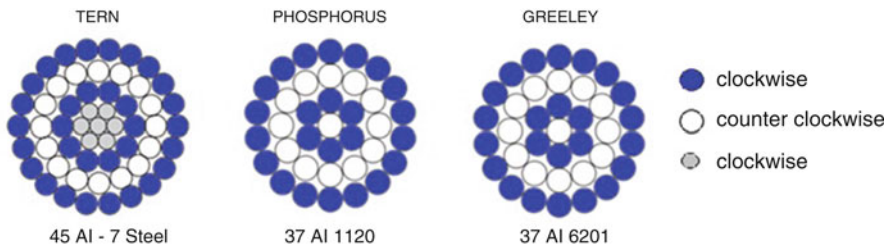


Fig. 2 Transmission line cables

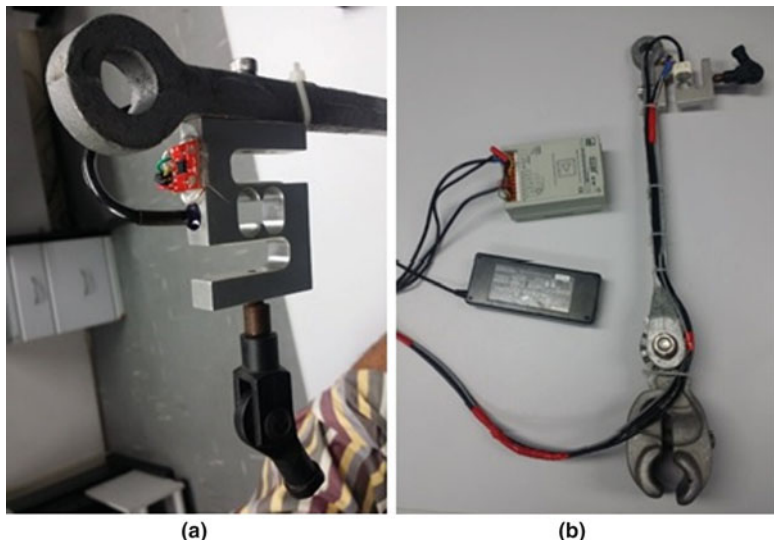


Fig. 3 The excitation system. (a) The position of loading coupled load cell and triaxial accelerometer and (b) the lever with the instrumentation

Greeley) with variable mechanical load (9–30% of the ultimate tensile strength—UTS).

The excitations were manually introduced using a lever as shown in Fig. 3.

The torsion lever consists of a metal part containing a cable connector up to 30 mm of diameter and a lug at the opposite end of the metal part, where there is a Z-type (tension and compression) load cell with a capacity of 98.07 N (10 kgf) and gain of 2 mV/V, with a hinged piece used for traction.

The traction was performed manually at the end of the lever, allowing the torsional strain to be transferred to the cable. Under the load cell there is a triaxial accelerometer, whose purpose is to measure the angle in relation to the vertical axis.

The accelerometer has an acceleration range of 3 g on each of the three axes and is powered by 3 V (2.4–3.6 V range), the x and y axis with a voltage range of 1.35–1.65 V (± 1 g) and the z axis from 1.2 to 1.8 V (± 1 g). The load cell is powered by a

conditioner (HBM AE301) with a carrier frequency of 600 Hz and a supply voltage of the 5 V bridge. The data acquisition rate of each channel is 4000 samples per second. As the measurement is performed every 50 ms, each indicator is the result of an average of 200 readings. The resolution of each channel is from 18 bits to ± 5000 mV, that is, 38.15 μ V for the accelerometer, whereas for the load cells it is 374.1 μ N.

Figure 4 shows schematically the cable sample (deformed cable) with the coupled lever and the reference system.

Figure 5 shows the initial position of the lever (solid line) and the position with applied load (dashed line). In this figure, L represents the position of the load application, a represents the position of the CG of the lever, p the gravitational force, and F the applied load.

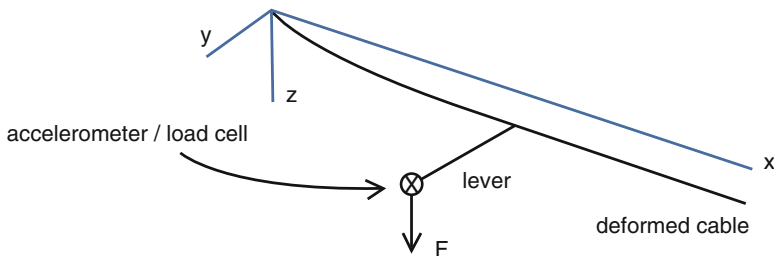


Fig. 4 Schematic representation of cable sample with lever attached

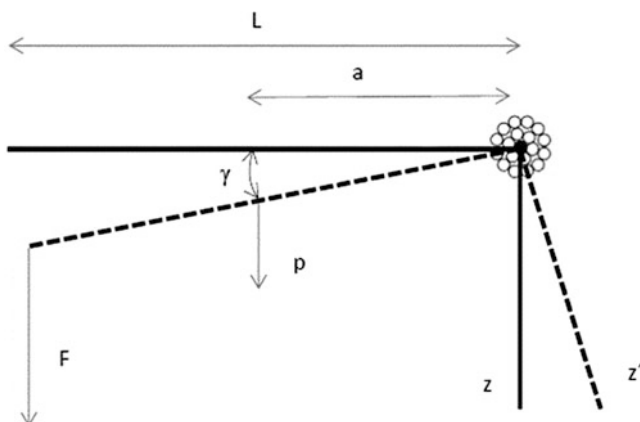


Fig. 5 Reference system with lever coupled with and without load application

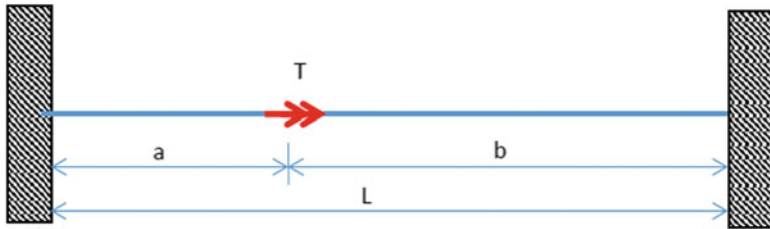


Fig. 6 Schematic representation of the torque applied in the sample

Based on the acceleration measurement on the three axes of the triaxial accelerometer, the angle is obtained around the z axis. The torsion angle measurement is detailed in the reference [11] and the torque in the cable is given by:

$$T = L F \cos(\gamma) + pa \cos(\gamma) \quad (1)$$

Figure 6 shows the torque applied in the sample.

As the point of placement of the lever varies across half of the sample (Fig. 1), it is necessary to obtain the torque value acting on the left and right ends of the sample. Considering the torque acting on the left end of the sample and making the balance with respect to the right end and considering the torsion angle null on the right end support:

$$\Delta\phi = \frac{TL}{GJ} = \frac{T_e L}{GJ} - \frac{Tb}{GJ} = 0 \quad (2)$$

$$T_e = \frac{Tb}{L} \quad (3)$$

where T_e is the torque acting on the left side of the lever.

3 Results

The curves were adjusted by interpolation through third order polynomial fit. Figure 7 shows the experimental and adjusted curves obtained for the Greeley cable and the lever positioned in the middle of the sample with 9.2% of UTS.

Figure 8 shows the adjusted curves for five different tensile loads of the Greeley cable and the lever positioned in the middle of the sample. Note that there is a trend of slope variation as the tensile load increases. In the extreme conditions of loading (9.2% and 30% UTS), the curves present different behaviors from the others.

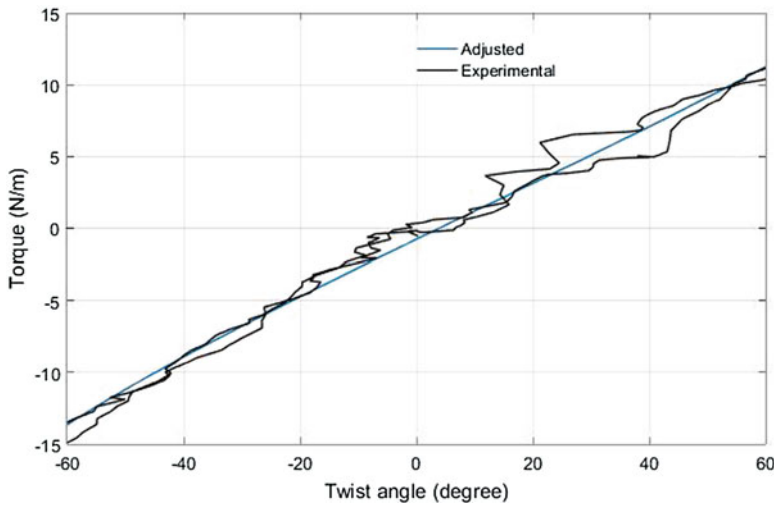


Fig. 7 Torque versus twist angle curves (experimental and adjusted curves)

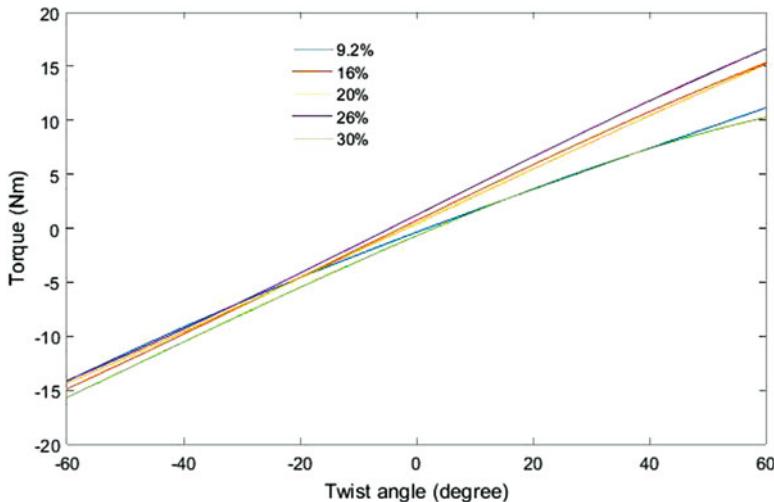


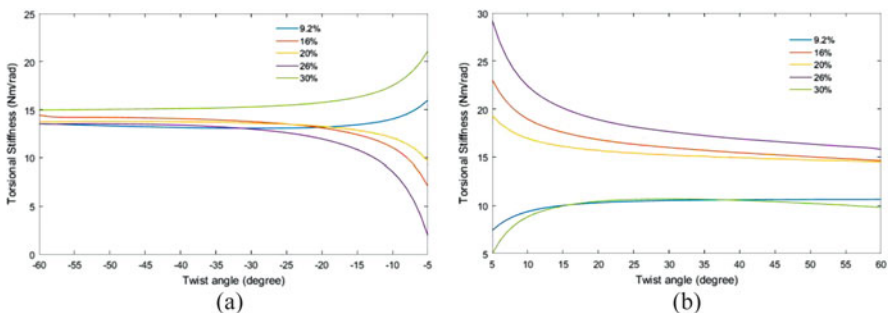
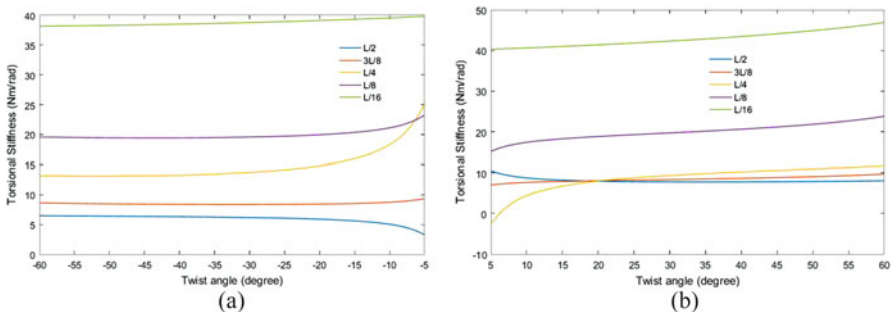
Fig. 8 Torque versus twist angle curves

The adjusted curves (third order polynomial) for the five loading conditions shown in Fig. 8 are shown in Table 1. The curves were adjusted using the *polyfit* routine of Matlab. The adjusted curves are of the form:

$$T = a_1 \theta^3 + a_2 \theta^2 + a_3 \theta + a_4 \quad (4)$$

Table 1 The curve parameters

Loading (UTS) (%)	Parameters			
	<i>a</i> 1	<i>a</i> 2	<i>a</i> 3	<i>a</i> 4
9.2	0.2999	-0.9373	10.9917	-0.7031
16	-0.4643	-0.2438	14.2861	-0.8924
20	-0.2667	0.0739	13.1519	-1.1790
26	-0.5815	0.3101	14.0847	-1.0241
30	-0.6062	-1.6589	12.3791	-0.4549

**Fig. 9** Variation of torsional stiffness as a function of twist angle and variation of tensile load. (a) clockwise and (b) counterclockwise**Fig. 10** Variation of torsional stiffness as a function of twist angle and lever position. (a) clockwise and (b) counterclockwise

The torsional stiffness was adjusted according to the slope of the torque curve versus twist angle. The values found considering the load variation are shown in Fig. 9 and considering the variation of the positioning of the lever are shown in Fig. 10. Note that there are differentiated behaviors for small angular displacements and for the extreme conditions of loading. In addition, the stiffness varies according to the torque application position.

Figure 11 shows the torque curves as a function of the twist angle for the three different cables and the lever at position $L/2$. Note that the curve for the Greeley cable has a different slope than the curves of the other two cables that are similar.

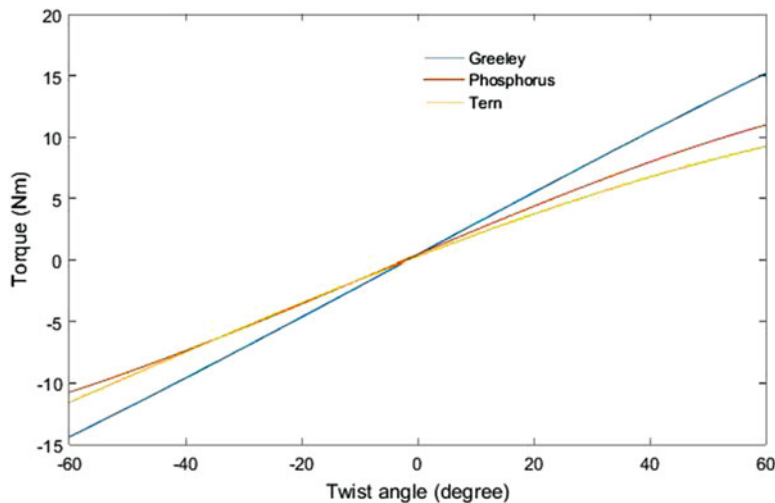


Fig. 11 Torque versus twist angle curves for three different cables

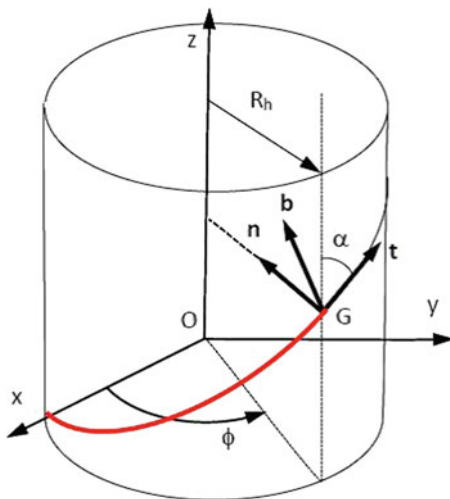


Fig. 12 Helical representation of wire

4 Conclusions

In this work, the results of torsional tests of transmission line cables are presented. Although the results shown are for the Greeley cable, similar results were observed for the Tern and Phosphorus cables. It was noticed that there are variations of the torsional parameters according to the direction of rotation of the cable, the

mechanical load of traction, and the position of application of the load. The nonlinear behavior of the torsional parameters was evidenced.

In order to improve the nonlinear mathematical models [10], the combined axial tension-torsion effect must be included through the isolated modeling of the wires, taking the helical shape of the wires [4] (Fig. 12) or modeling the cable as a single body [5].

References

1. McConnell, K.G., Chang, C.-N.: A study of the axial-torsional coupling effect on a sagged transmission line. *Exp. Mech.* **26**, 324–329 (1986)
2. McConnell, K.G., Zemke, W.P.: A model to predict the coupled axial torsion properties of ACSR electrical conductors. *Exp. Mech.* **22**, 237–244 (1982)
3. Lanteigne, J.: Theoretical estimation of the response of helically armored cables to tension, torsion, and bending. *J. Appl. Mech.* **52**, 423–432 (1985)
4. Ghoreishi, S.R., Messagera, T., Cartraud, P., Davies, P.: Validity and limitations of linear analytical models for steel wire strands under axial loading, using a 3D FE model. *Int. J. Mech. Sci.* **49**, 1251–1261 (2007)
5. Arena, A., Pacitti, A., Lacarbonara, W.: Nonlinear response of elastic cables with flexural-torsional stiffness. *Int. J. Solids Struct.* **87**, 267–277 (2016)
6. Zhang, M., Zhao, G., Li, J.: Nonlinear dynamic analysis of high-voltage overhead transmission lines. *Shock Vib.* **2018**, 35p (2018)
7. Usabiaga, H., Pagalday, J.M.: Analytical procedure for modelling recursively and wire by wire stranded ropes subjected to traction and torsion loads. *Int. J. Solids Struct.* **45**, 5503–5520 (2008)
8. Barbieri, N., Souza Junior, O.H., Barbieri, R.: Dynamical analysis of transmission line cables. Part 1—linear theory. *Mech. Syst. Signal Process.* **18**, 659–669 (2004)
9. Barbieri, N., Souza Junior, O.H., Barbieri, R.: Dynamical analysis of transmission line cables. Part 2—damping estimation. *Mech. Syst. Signal Process.* **18**, 671–681 (2004)
10. Barbieri, R., Barbieri, N., Souza Junior, O.H.: Dynamical analysis of transmission line cables. Part 3—nonlinear theory. *Mech. Syst. Signal Process.* **22**, 992–1007 (2008)
11. <https://www.digikey.com/en/articles/techzone/2011/may/using-an-accelerometer-for-inclination-sensing>

Application of a Stochastic Version of the Restoring Force Surface Method to Identify a Duffing Oscillator



Luis G. G. Villani, Samuel da Silva, and Americo Cunha Jr.

Abstract A stochastic version of the restoring force surface method is proposed and used to identify the parameters of a clamped-free beam with nonlinear effects induced by the presence of a magnet near to the free extremity. This system recalls a Duffing oscillator, which is used as a single-degree-of-freedom mathematical model to represent the mechanical system. Experimental and theoretical responses are compared taking into account a probabilistic band of confidence. The results show that the stochastic model identified can predict the beam's vibration responses, which ensure the robustness of the stochastic identification method.

Keywords Nonlinear dynamics · Stochastic model · Restoring force surface · Duffing oscillator

1 Introduction

It is known that many engineering structures can present nonlinear behavior caused by geometric effects, operating conditions, materials with complex structure, and others. So, to perform a reliable analysis of a structure, the nonlinear effects have to be taken into account [1]. In this sense, Masri and Caughey [2] presented the method of restoring force surface (RFS) that showed to be effective [3]. Many other approaches can be used to describe nonlinear systems, such as Hilbert transform, NARMAX models, high-order frequency response functions [4, 5], Volterra series [6], harmonic balance, or artificial neural network [7]. However,

L. G. G. Villani · S. da Silva (✉)

UNESP – Universidade Estadual Paulista, Faculdade de Engenharia, Departamento de Engenharia Mecânica, São Paulo, Brasil

e-mail: luis.villani@unesp.br; samuel.silva13@unesp.br

A. Cunha Jr.

UERJ – Universidade do Estado do Rio de Janeiro, NUMERICO – Nucleus of Modeling and Experimentation with Computers, Rio de Janeiro, Brasil

e-mail: americoo@ime.uerj.br

once the approaches described above are deterministic, they are neither robust to variations in the system parameters nor offer a confidence interval to the identified model. Since any real system is uncertain with regard to the nominal project values (due to material imperfections, noise, etc. [8]), a reliable system identification technique must take into account the model parameters uncertainties, also known as *data uncertainties*.

Techniques of stochastic system identification are available in the literature, for instance, using convex analysis [9], Bayesian statistics [10–15] or a nonparametric probabilistic approach [16–18]. These methods are very sophisticated and powerful tools, generally used to identify a mechanical system with a large number of degrees-of-freedom (DoFs). Although these techniques can be used to identify systems with one or a few DoFs, the low dimension of these systems allows one to develop a more simple framework for stochastic identification. It is proposed to use a stochastic version of the RSF method to identify a single degree-of-freedom (DoF) system, developed in a probabilistic framework, which models the system parameters as random variables assuming underlying uncertainties. In this way, the main contribution is to propose a stochastic version of the RFS method, where the probability density functions (PDFs) of model parameters are identified, instead of the parameters deterministic values, as made by conventional RFS methods. The conclusions show that the method is simple and reaches useful results, so that it is suitable for application in simple systems, with low order, where the use of more sophisticated techniques may be complicated.

2 Experimental Apparatus

The experimental setup is composed of a clamped-free beam ($300 \times 18 \times 3$ [mm³]) with a steel mass glued in the free extremity, which is connected to cause a magnetic interaction between the beam and a magnet (Fig. 1). A shaker is used to excite the structure considering different levels of voltage amplitude. A vibrometer laser is utilized to measure the beam free extremity velocity. It is important to note that

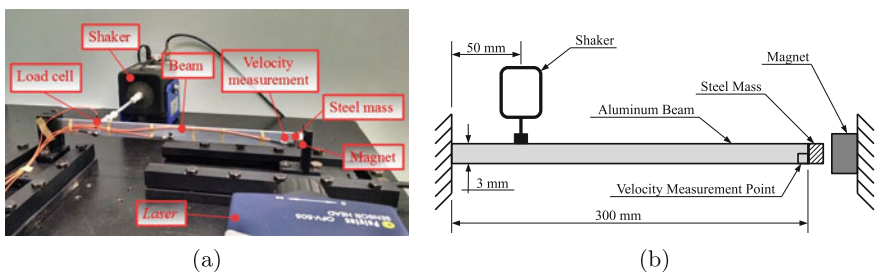


Fig. 1 Illustration of the experimental apparatus used. **(a)** Experimental apparatus. **(b)** Schematic representation

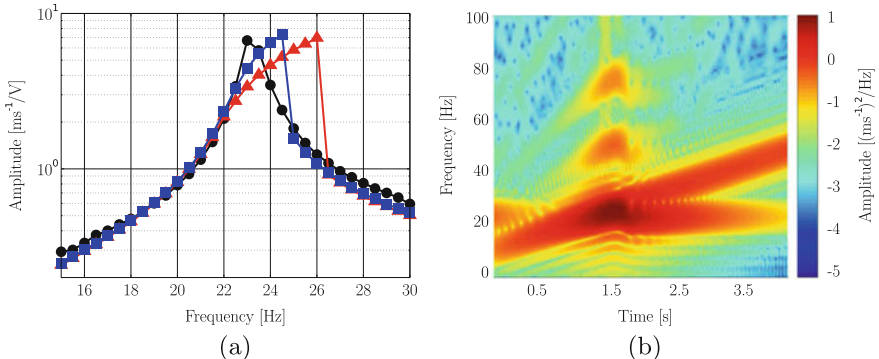


Fig. 2 Illustration of the system nonlinear behavior: **(a)** stepped sine test for different levels of voltage applied in the shaker. Filled circle -0.01 V, blue filled square -0.10 V and red filled triangle -0.15 V; **(b)** spectrogram of the system response

the input signal considered in this work is the voltage applied to the shaker. By using this strategy, the input signal is kept constant over a range of frequencies. The magnetic interaction of the system generates a hardening nonlinear behavior showed in Fig. 2a, which presents the jump phenomenon that is represented by a sudden drop in the amplitude of the response with a low increment in the excitation frequency. Additionally, the spectrogram of the system response can be seen in Fig. 2b where it is observed the presence of the second and third order harmonics in the response.

3 Mechanical–Mathematical Modeling

The experimental setup presents nonlinear behavior only for large displacements, so a Duffing oscillator can well approximate its dynamic behavior [19]

$$m \ddot{x}(t) + c \dot{x}(t) + k x(t) + k_2 x(t)^2 + k_3 x(t)^3 = U(t), \quad (1)$$

where m is the system equivalent mass, c is the damping coefficient, k is the linear stiffness, k_2 is the quadratic stiffness, k_3 is the cubic stiffness, and $U(t)$ is the external force. The displacement, velocity, and acceleration in the free extremity of the beam are represented, respectively, by $x(t)$, $\dot{x}(t)$ and $\ddot{x}(t)$. Once in the application of the RFS method no form for the restoring force is assumed initially, Eq. (1) is rewritten in terms of the restoring force $\mathcal{F}(x, t)$ as

$$m \ddot{x}(t) + c \dot{x}(t) + \mathcal{F}(x, t) = U(t). \quad (2)$$

The parameters uncertainties are induced by measurement noise, variation in the boundary conditions, the position of the shaker, sensor, and magnet, uncertainties related to the methods of parameters estimation [8]. Thus, the model parameters are

random variables or random processes, defined on the probability space $(\Theta, \Sigma, \mathbb{P})$, where Θ is sample space, Σ is a σ -algebra over Θ , and \mathbb{P} is a probability measure. Thus, the stochastic equivalent of Eq. (2) is given by

$$m(\theta) \ddot{x}(\theta, t) + c(\theta) \dot{x}(\theta, t) + F(x(\theta, t), t) = U(t), \quad (3)$$

where the random processes $(\theta, t) \in \Theta \times \mathbb{R} \mapsto x(\theta, t)$, $(\theta, t) \in \Theta \times \mathbb{R} \mapsto \dot{x}(\theta, t)$, and $(\theta, t) \in \Theta \times \mathbb{R} \mapsto \ddot{x}(\theta, t)$, respectively, represent the displacement, velocity, and acceleration in the beam free extremity. The stochastic model of Eq. (3) is used to describe the nonlinear random dynamics of the mechanical system emulated by the experimental apparatus.

4 Stochastic System Parameters Identification

Two types of experimental tests were performed. The first one excites the mechanical system with a chirp signal with a low level (0.01 V) of the constant voltage amplitude, while in the second test, the level is high (0.15 V). The two tests were executed in sequence, so that chirp signal range of frequencies varied with a rate of 10 Hz/s, from 10 to 50 Hz. Each test was repeated 200 times on different days.

The identification of system parameters m and c uses the underlying linear dynamics of the beam assuming the low level of input amplitude. The system equivalent mass and damping coefficients are estimated using the impulse response function. After, identifying several realizations of these parameters (200 in fact), their PDFs are nonparametrically estimated through histograms and kernel smoothed curves [20].

Then, using the nonlinear dynamics of the beam, obtained when the input signal has a high level of amplitude (0.15 V), the restoring force $F(x(\theta, t), t)$ is estimated to each realization θ . In this case, the RFS method defines the restoring force from the equation

$$F(x(\theta, t), t) = U(t) - [m \ddot{x}(\theta, t) + c \dot{x}(\theta, t)], \quad (4)$$

where all objects of the equation right-hand side are known. Note that the nonlinear function F is a stochastic process, once it is defined as the difference between the excitation U and the stochastic process $m \ddot{x} + c \dot{x}$. In practice, realizations of F are constructed utilizing realizations of the system parameters as well as from velocity and acceleration time series. Additionally, the reader can observe that, for a fixed time t , each experimental realization of F defines a three-dimensional surface, i.e., $F = g(x, \dot{x})$ for some scalar map $g : \mathbb{R}^2 \rightarrow \mathbb{R}$. Thus, the polynomial coefficients (k_1 , k_2 and k_3), to each realization, can be estimated through the polynomial regression based on the minimization of the squared error (least squares method). As performed with the mass and damping, the PDFs of k_1 , k_2 , and k_3 are nonparametrically estimated.

5 Results and Discussion

The nonparametric estimations for mass and damping coefficient PDFs can be seen in Fig. 3. The figures show PDFs of normalized random variables, i.e., random variables with zero mean and unit standard deviation, in addition to the nominal values. The PDFs show that both parameters have unimodal behavior. It is possible to observe that m has mean value of $\mu_m = 0.233$ [kg] with low dispersion around the nominal value. The coefficient of variation, standard deviation divided by the mean, is $\delta_m = 2.44\%$. The damping coefficient c has concentration across the mean value $\mu_c = 1.226$ [Ns/m] and $\delta_c = 1.77\%$.

With the surfaces $\mathcal{F} = g(x, \dot{x})$ nonparametric estimated, a parametric identification of this force to fit a function whose shape resembles the curve raised by RFS method. A polynomial form was chosen to describe the nonlinear force, as described in the Duffing equation of Eq. (1). Since the nonlinear restoring force is random, it should be assumed that the stiffnesses are also aleatory, being modeled by random variables. The nonparametric estimations for the PDFs of k , k_2 , and k_3 are present in Fig. 4. It can be seen in Fig. 4a the PDF of the linear stiffness. The behavior is unimodal with the values concentrated around the mean value $\mu_k = 4.954 \times 10^3$ N/m and $\delta_k = 2.21\%$. Figure 4b shows the PDF of the quadratic stiffness. The mean value is equal to $\mu_{k_2} = -30.867$ N/m² and $\delta_{k_2} = 2.72\%$. The PDF of the cubic stiffness, presented in Fig. 4c, has also unimodal distribution with $\mu_{k_3} = 39.859 \times 10^7$ [N/m³] and $\delta_{k_3} = 4.06\%$. The large variation of these parameters is related with the uncertainties present in the RFS method applied considering underlying variabilities (e.g., noise, the magnet, shaker and sensor position, etc.). Finally, Fig. 4d shows the experimental F and the polynomial modeling identified with 99% of confidence bands. The results are satisfactory considering that the model can predict the behavior of the restoring force, mainly when it has high amplitude.

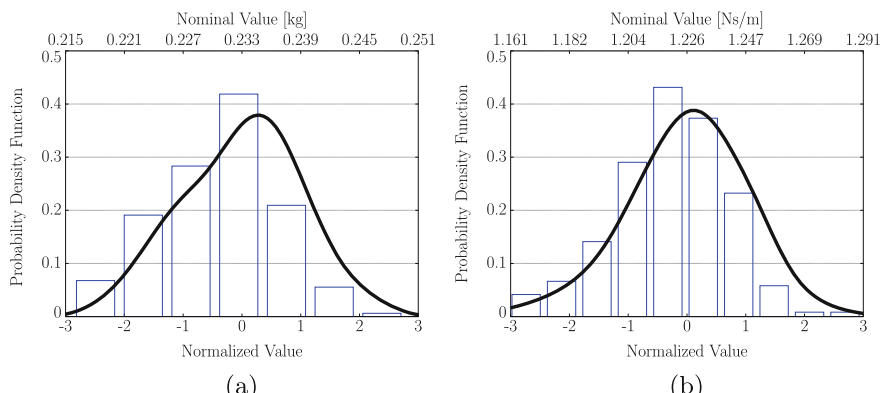


Fig. 3 PDFs for mass and damping parameters of the mechanical system. The PDF is represented by the solid line and the histogram by the bars. **(a)** Estimated PDF for m . **(b)** Estimated PDF for c

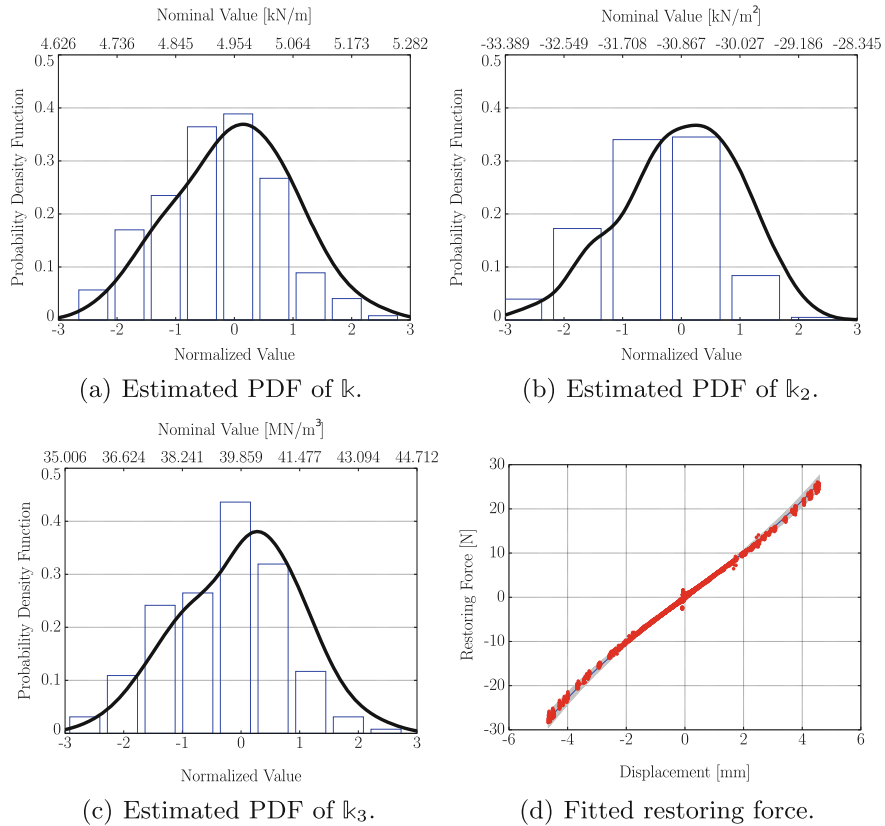


Fig. 4 PDFs for mechanical system stiffnesses and the fitted restoring force. **(a, b, and c)** The PDF is represented by the solid line and the histogram by the bars; **(d)** The model mean is presented as blue lines, the confidence band as gray shown, and the experimental realization as red filled circle

Once the stochastic model of Eq. (3) is identified, it can be used to make predictions about the beam nonlinear dynamics behavior, offering probabilistic limits of confidence in the response. The calculation of the model response is done using Monte Carlo (MC) method [21]. First of all, the experimental nonparametric PDFs estimated are used to generate samples of the system parameters. In the procedure, the Metropolis–Hastings Markov Chain Monte Carlo (MCMC) algorithm is applied [21]. Additionally, the sampling is made considering the correlation between the random variables, through the Cholesky decomposition of the correlation matrix. Comparisons between experimental and simulated beam velocity, in the time domain, can be seen in Fig. 5, considering the same chirp signal used in the model identification process. One can observe that the experimental response is inside the limits with 99% of confidence that indicates the adequate performance of the stochastic model.

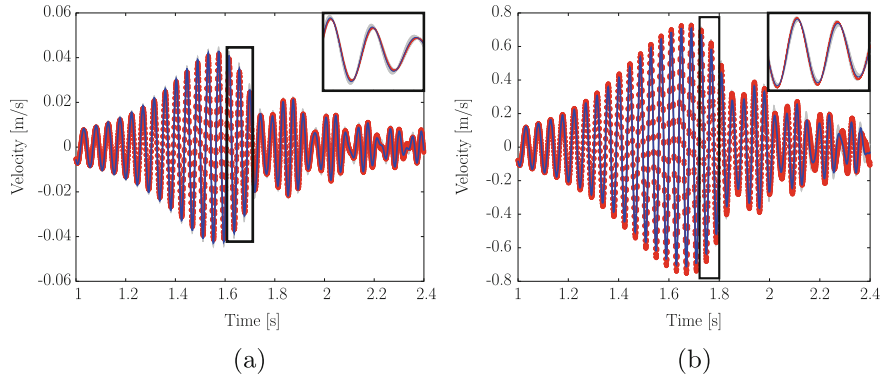


Fig. 5 System response comparison. The model mean is presented as blue lines, the confidence band as gray fill, and the experimental realization as red line-red circle-red line. **(a)** Low level of input (linear). **(b)** High level of input (nonlinear)

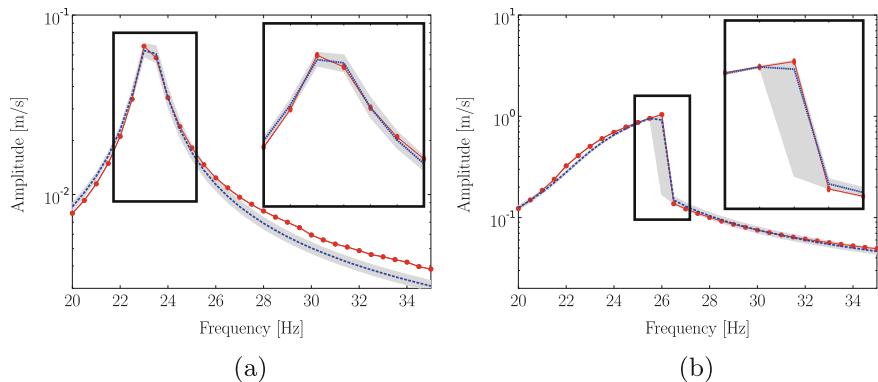


Fig. 6 Stepped sine curves comparison. The model mean is presented as —, the confidence band as gray fill, and the experimental realization as —○—. (a) Low level of input (linear). (b) High level of input (nonlinear)

The model validation was performed considering the stepped sine test, and the results are shown in Fig. 6. It is possible to see that the stochastic model describes well the system behavior, both in linear as nonlinear regime of motion. The difference between the curves seen in the linear case is related to the difficulty of conducting the stepped sine test with very low excitation amplitude and the possible influence of the second vibration mode shape; this can be confirmed observing Fig. 2(a). In the nonlinear case, the stochastic model is also able to describe the experimental behavior. The large data dispersion in the nonlinear regime of motion, in consequence of the nonlinear restoring force variation, makes the nonlinear stiffness varies, as seen in Figs. 4b, c.

6 Final Remarks

A stochastic version of the restoring force surface method was proposed to identify the parameters of a Duffing oscillator. The formulation of this method was done in terms of a stochastic process and able to take into account the intrinsic variability of the system parameters. In the analysis of non-complex nonlinear systems, the proposed method can be applied without the use of more sophisticated mathematical tools. The effectiveness of this methodology was tested and verified in the parameters estimation of a clamped-free beam, presenting nonlinear behavior. The results showed that the identified stochastic model is robust, once it describes well the structure behavior and specifies a reliability envelope.

Acknowledgements The authors are thankful for the financial support provided by São Paulo Research Foundation (FAPESP) grant number 2012/09135-3, 2015/25676-2 and 2017/15512-8, Carlos Chagas Filho Research Foundation of Rio de Janeiro State (FAPERJ) under grants E-26/010.002.178/2015 and E-26/010.000.805/2018 and Coordenação de Aperfeiçoamento de Pessoal de Nível Superior—Brasil (CAPES)—Finance Code 001 and CNPq grant number 307520/2016-1.

References

1. Virgin, L.N.: *Introduction to Experimental Nonlinear Dynamics: A Case Study in Mechanical Vibration*. Cambridge University Press, Cambridge (2000)
2. Masri, S., Caughey, T.: A nonparametric identification technique for nonlinear dynamic problems. *J. Appl. Mech.* **46**(2), 433–447 (1979)
3. Noël, J., Renson, L., Kerschen, G.: Complex dynamics of a nonlinear aerospace structure: experimental identification and modal interactions. *J. Sound Vib.* **333**(12), 2588–2607 (2014)
4. Kerschen, G., Worden, K., Vakakis, A.F., Golinval, J.C.: Nonlinear system identification in structural dynamics: current status and future directions. In: 25th International Modal Analysis Conference, Orlando (2007)
5. Worden, K., Kerschen, G., Vakakis, A.F., Golinval, J.C.: Nonlinear system identification in structural dynamics: a short (and biased) history. In: 25th International Modal Analysis Conference, Orlando (2007)
6. Scussel, O., da Silva, S.: Output-only identification of nonlinear systems via Volterra series. *J. Vib. Acoust.* **138**, 041012 (2016)
7. Bussetta, P., Shiki, S.B., da Silva, S.: Nonlinear updating method: a review. *J. Braz. Soc. Mech. Sci. Eng.* **39**(11), 4757–4767 (2017)
8. Soize, C.: *Uncertainty Quantification: An Accelerated Course with Advanced Applications in Computational Engineering*. Springer International Publishing, New York (2017)
9. Papadimitriou, C., Katafygiotis, L.S., Beck, J.L.: Approximate analysis of response variability of uncertain linear systems. *Probab. Eng. Mech.* **10**(4), 251–264 (1995)
10. Beck, J.L., Katafygiotis, L.S.: Updating models and their uncertainties. i: Bayesian statistical framework. *J. Eng. Mech.* **124**(4), 455–461 (1998)
11. Beck, J.L.: Bayesian system identification based on probability logic. *Struct. Control. Health Monit.* **17**(7), 825–847 (2010)
12. Beck, J.L., Taflanidis, A.: Prior and posterior robust stochastic predictions for dynamical systems using probability logic. *Int. J. Uncertain. Quantif.* **3**(4), 271–288 (2013)

13. Yan, W.J., Katafygiotis, L.S.: A novel Bayesian approach for structural model updating utilizing statistical modal information from multiple setups. *Struct. Saf.* **52**(Part B), 260–271 (2015). *Engineering Analyses with Vague and Imprecise Information*
14. Behmanesh, I., Moaveni, B., Lombaert, G., Papadimitriou, C.: Hierarchical Bayesian model updating for structural identification. *Mech. Syst. Signal Process.* **64**, 360–376 (2015)
15. Ritto, T., Sampaio, R., Aguiar, R.: Uncertain boundary condition Bayesian identification from experimental data: a case study on a cantilever beam. *Mech. Syst. Signal Process.* **68**, 176–188 (2016)
16. Capiez-Lernout, E., Soize, C.: Robust updating of uncertain damping models in structural dynamics for low- and medium-frequency ranges. *Mech. Syst. Signal Process.* **22**(8), 1774–1792 (2008). <http://www.sciencedirect.com/science/article/pii/S0888327008000393>
17. Soize, C., Capiez-Lernout, E., Ohayon, R.: Robust updating of uncertain computational models using experimental modal analysis. *AIAA J.* **46**(11), 2955–2965 (2008)
18. Batou, A., Soize, C., Audebert, S.: Model identification in computational stochastic dynamics using experimental modal data. *Mech. Syst. Signal Process.* **50**, 307–322 (2015)
19. Kovacic, I., Brennan, M.J.: *The Duffing equation: nonlinear oscillators and their behaviour*. John Wiley & Sons, Hoboken (2011)
20. Wassermann, L.: *All of Nonparametric Statistics*. Springer, Berlin (2006)
21. Rubinstein, R.Y., Kroese, D.P.: *Simulation and the Monte Carlo Method*. 3rd edn. Wiley, Hoboken (2016)

Modeling of the Hysteretic Behavior of Wire Rope Isolators Using a Novel Rate-Independent Model



Nicolò Vaiana, Francesco Marmo, Salvatore Sessa, and Luciano Rosati

Abstract This paper presents a novel rate-independent model to predict the hysteretic response of Wire Rope Isolators along their two principal transverse directions, namely Roll and Shear directions. Employing the proposed model, the device restoring force can be evaluated by solving an algebraic equation that requires a set of only five parameters directly related to specific graphical features of the hysteresis loop. To verify such a model, some experimental results, obtained during several experimental tests recently performed at the Department of Industrial Engineering of the University of Naples Federico II, are predicted analytically.

Keywords Wire rope isolator · Hysteretic behavior · Rate-independent model

1 Introduction

Wire Rope Isolators are devices manufactured by embedding a stainless steel cable, having a helix shape, into two metal retainer bars [1].

These devices generally exhibit a kinematic hardening hysteretic behavior when a displacement time history is applied along one of their two principal transverse directions, denominated Roll and Shear directions, respectively. Indeed, the distance between the two parallel curves, that typically limit their hysteresis loops, remains constant during the entire deformation process and the device restoring force increases when a transverse displacement with increasing amplitude is applied.

Several differential rate-independent models are currently available in the literature to accurately reproduce the complex transverse response characterizing such metal devices [2–6]. Unfortunately, these phenomenological models suffer from some limitations such as the unclear mechanical significance of the adopted

N. Vaiana (✉) · F. Marmo · S. Sessa · L. Rosati
Department of Structures for Engineering and Architecture,
University of Naples Federico II, Naples, Italy
e-mail: nicolo.vaiana@unina.it

parameters and the limited computational efficiency due to the need of numerically solving a differential equation to predict the device response.

This paper presents a novel rate-independent model, formulated by specializing a general class of models recently proposed by Vaiana et al. [7–9], to reproduce the response of Wire Rope Isolators along the Roll and Shear directions. In particular, this model offers several advantages, such as the use of a small number of parameters, which have a precise mechanical significance, as well as a significant computational efficiency due to the solution of an algebraic equation, rather than a differential one, to compute the device restoring force.

2 Proposed Hysteretic Model

The Proposed Hysteretic Model (PHM) has been formulated by specializing a recently developed family of uniaxial models [7–9].

Such a general formulation assumes the generalized displacement u (generalized rate-independent hysteretic force f_{ri}) as input (output) variable, and describes a generalized rate-independent force-displacement hysteresis loop by adopting four different curves: the upper c_u and the lower c_l limiting curves and the generic loading c^+ and unloading c^- curves.

Figure 1 illustrates the four curves describing a hysteresis loop limited by two parallel curves; note that the generic loading (unloading) curve, defined by a positive (negative) sign of the generalized velocity \dot{u} , is identified by an arrow plotted on the curve.

As shown in Fig. 1, the upper (lower) limiting curve intersects the vertical axis at the point with coordinates 0 and \bar{f} ($-\bar{f}$). Furthermore, the generic loading (unloading) curve intersects the lower (upper) limiting curve at a point having

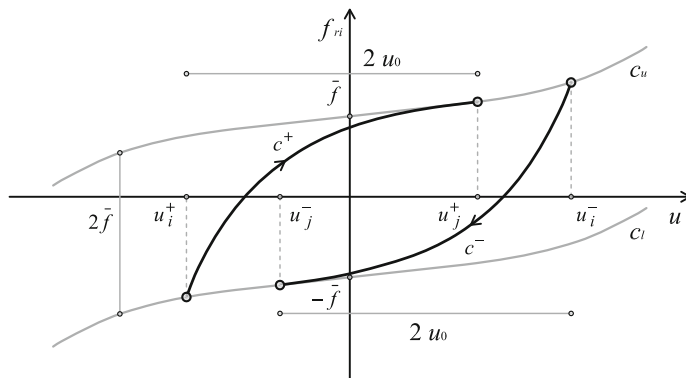


Fig. 1 An example of hysteresis loop described by the curves c_u , c_l , c^+ , and c^-

abscissa u_i^+ (u_i^-), and the upper (lower) limiting curve at a point having abscissa u_j^+ (u_j^-), with $u_i^+ = u_j^+ - 2u_0$ ($u_i^- = u_j^- + 2u_0$).

In the following subsections, we first describe the PHM formulation by introducing the proposed expressions of the generalized rate-independent hysteretic force and of the history variable; then, we show how each PHM parameter affects the size and/or the shape of a hysteresis loop.

2.1 PHM Formulation

The PHM requires the calibration of only five parameters, that is, k_a , k_b , α , β_1 , and β_2 . In addition, it also adopts two additional parameters, namely $u_0 > 0$ and $\bar{f} > 0$, that can be computed after selecting k_a , k_b , α taking into account the following conditions: $k_a > k_b$, $k_a > 0$, $\alpha > 0$, and $\alpha \neq 1$.

2.1.1 Generalized Rate-Independent Force

According to Fig. 1, during a generic loading (unloading) phase, $f_{ri} = c^+$ ($f_{ri} = c^-$) if $u_i^+ \leq u < u_j^+$ ($u_j^- < u \leq u_i^-$), whereas $f_{ri} = c_u$ ($f_{ri} = c_l$) if $u > u_j^+$ ($u < u_j^-$).

In particular, in the PHM, the expressions of c_u and c_l are

$$c_u(u) = \beta_1 u^3 + \beta_2 u^5 + k_b u + \bar{f}, \quad (1)$$

$$c_l(u) = \beta_1 u^3 + \beta_2 u^5 + k_b u - \bar{f}, \quad (2)$$

whereas the ones of c^+ and c^- are

$$\begin{aligned} c^+(u, u_j^+) &= \beta_1 u^3 + \beta_2 u^5 + k_b u \\ &+ (k_a - k_b) \left[\frac{(1 + u - u_j^+ + 2u_0)^{(1-\alpha)}}{1 - \alpha} - \frac{(1 + 2u_0)^{(1-\alpha)}}{1 - \alpha} \right] + \bar{f}, \end{aligned} \quad (3)$$

$$\begin{aligned} c^-(u, u_j^-) &= \beta_1 u^3 + \beta_2 u^5 + k_b u \\ &+ (k_a - k_b) \left[\frac{(1 - u + u_j^- + 2u_0)^{(1-\alpha)}}{\alpha - 1} - \frac{(1 + 2u_0)^{(1-\alpha)}}{\alpha - 1} \right] - \bar{f}. \end{aligned} \quad (4)$$

Furthermore, the expression of \bar{f} , required in Eqs. (1)–(4), is

$$\bar{f} = \frac{k_a - k_b}{2} \left[\frac{(1 + 2u_0)^{(1-\alpha)} - 1}{1 - \alpha} \right]. \quad (5)$$

Since $k_a > k_b$, $\alpha \neq 1$, and $u_0 > 0$, Eq. (5) gives a positive value of \bar{f} .

2.1.2 History Variable

In the PHM, the expression of u_j^+ is

$$u_j^+ = 1 + u_P + 2u_0 - \left\{ \frac{1 - \alpha}{k_a - k_b} \left[f_P - \beta_1 u_P^3 - \beta_2 u_P^5 - k_b u_P \right. \right. \\ \left. \left. - \bar{f} + (k_a - k_b) \frac{(1 + 2u_0)^{(1-\alpha)}}{1 - \alpha} \right] \right\}^{\left(\frac{1}{1-\alpha}\right)}, \quad (6)$$

whereas the one of u_j^- is

$$u_j^- = -1 + u_P - 2u_0 + \left\{ \frac{\alpha - 1}{k_a - k_b} \left[f_P - \beta_1 u_P^3 - \beta_2 u_P^5 - k_b u_P \right. \right. \\ \left. \left. + \bar{f} + (k_a - k_b) \frac{(1 + 2u_0)^{(1-\alpha)}}{\alpha - 1} \right] \right\}^{\left(\frac{1}{1-\alpha}\right)}. \quad (7)$$

2.2 Parameter Sensitivity Analysis

Figure 2 shows how the size and (or) the shape of hysteresis loops, obtained by imposing a full sinusoidal cycle of generalized displacement having amplitude of 1, change(s) due to the variation of each PHM parameter. In particular, it can be noted that:

- k_a affects the hysteresis loop size (Fig. 2a);
- k_b produces a rotation of the hysteresis loop and a slight variation of its size (Fig. 2b);
- α affects the hysteresis loop size (Fig. 2c);
- β_1 affects the hysteresis loop shape (Fig. 2d).

Since the variation of the hysteresis loop shape due to β_2 is similar to the one produced by β_1 , the related figure is not presented for brevity.

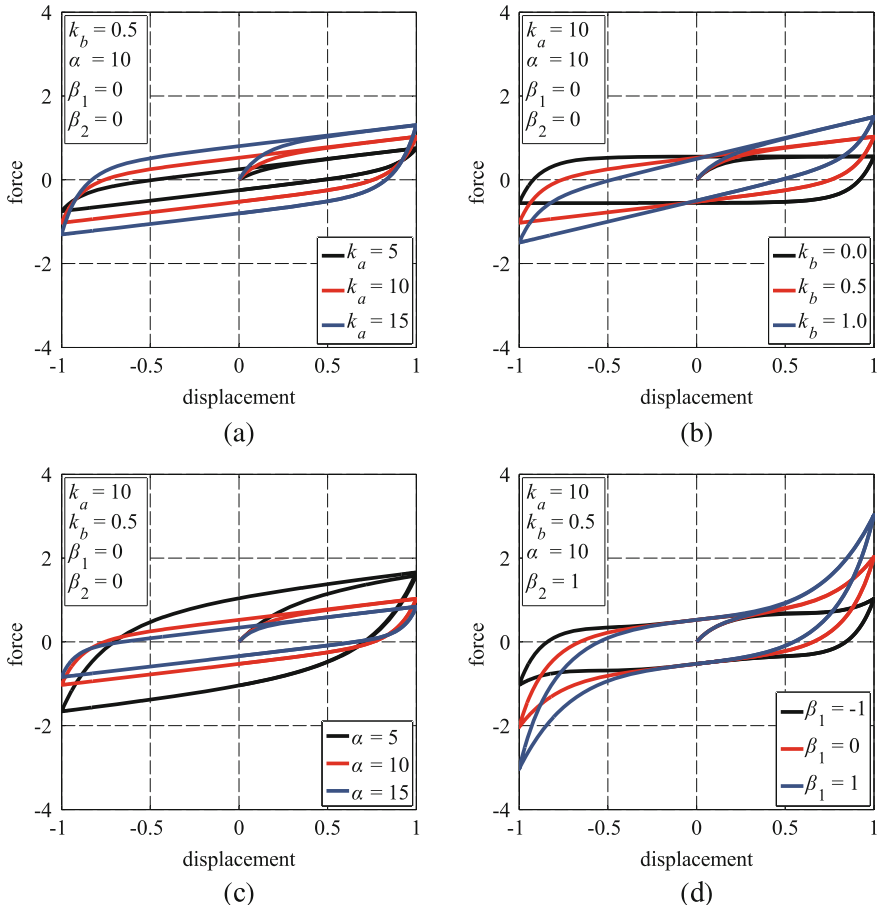


Fig. 2 Variation of the hysteresis loop size and/or shape associated with each PHM parameter

3 Experimental Verification

In this section the PHM, illustrated in Sect. 2, is validated by comparing the analytical results with those obtained from several dynamic tests performed on a Wire Rope Isolator (WRI) at the Department of Industrial Engineering of the University of Naples Federico II (Italy) by Vaiana et al. [10].

3.1 Tested Wire Rope Isolator

Figure 3a shows the geometrical characteristics of the tested WRI having two principal transverse directions, denominated Roll and Shear directions. Such a metal

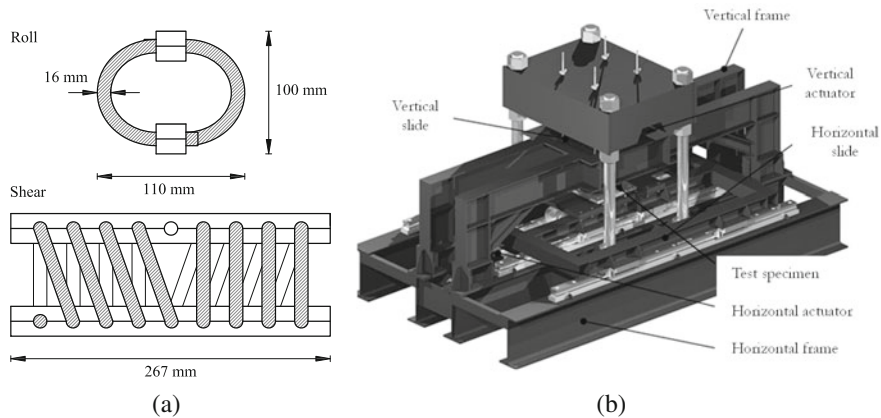


Fig. 3 Tested wire rope isolator (a) and adopted testing machine (b)

device, manufactured by Powerflex S.r.l. (Limatola, Italy), has been constructed by assembling two types of elements: a Stainless Steel Type 316 wire rope and two aluminum alloy retainer bars. Specifically, the wire rope, constituted by six strands wrapped around a central one, has been wound in the shape of a helix and embedded into the two retainer bars. Each external strand of the wire rope is made of 25 steel wires, whereas the inner one is made of 49 steel wires.

Figure 3b shows the Testing Machine (TM) adopted to perform the experimental tests. Such a machine allows one to impose a transverse displacement or force, by means of a horizontal hydraulic actuator, under the effect of a constant axial compressive force, applied by means of a vertical hydraulic actuator [11–13]. The tested WRI has been installed by fixing its retainer bars to the lower and upper rigid steel plates of the TM.

During the experimental tests, conducted at room temperature, the time history of the relative transverse displacement between the TM lower and upper plates and the time histories of the axial and transverse forces have been measured by sampling the data at 250 Hz.

3.2 *Simulation of the Experimental Behavior*

Figure 4 (5) illustrates both the analytical and experimental hysteresis loops that have been obtained by imposing, to the tested WRI, five cycles of sinusoidal transverse displacement, having frequency of 1 Hz; in particular, such results have been obtained for three different amplitude levels, that is, 0.25, 0.50, and 1 cm, and by applying a constant axial compressive force, f_v , of 0 kN (2 kN). Note that Figs. 4a and 5a show the results along the Roll direction, whereas Figs. 4b and 5b present the results along the Shear direction.

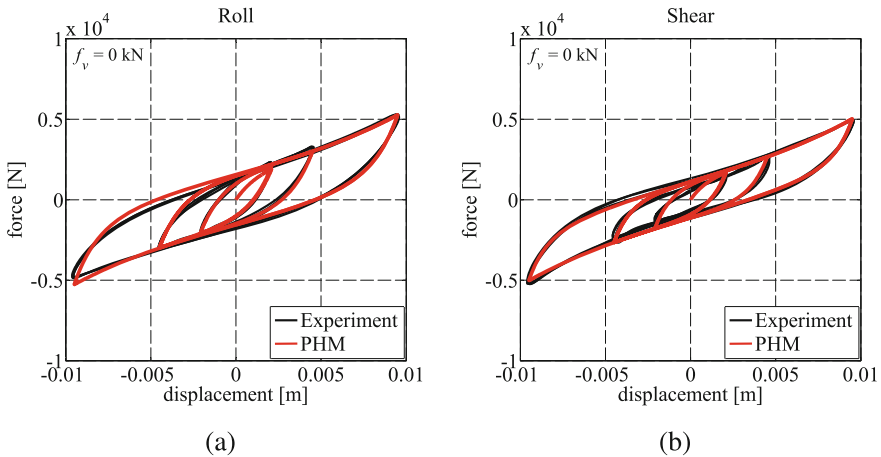


Fig. 4 Analytical and experimental hysteresis loops obtained in roll (a) and shear (b) directions for $f_v = 0 \text{ kN}$

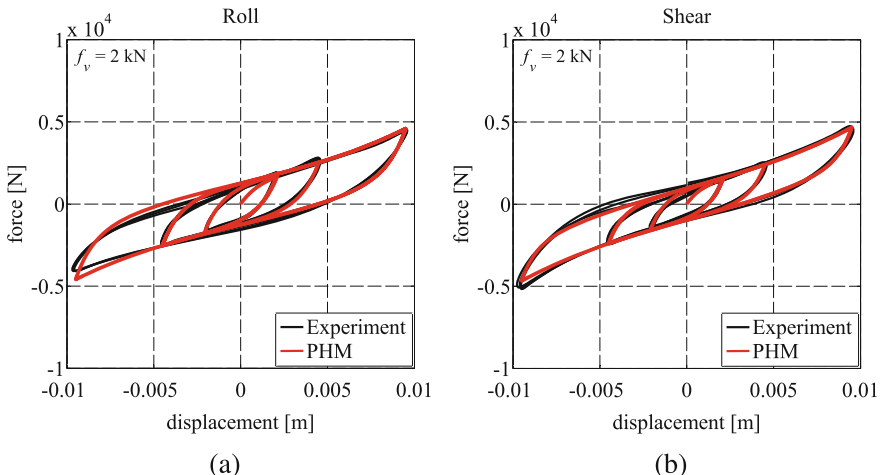


Fig. 5 Analytical and experimental hysteresis loops obtained in roll (a) and shear (b) directions for $f_v = 2 \text{ kN}$

A satisfactory agreement can be observed between the experimental hysteresis loops and the analytical ones, simulated by adopting the PHM parameters listed in Table 1 (2). Such model parameters have been calibrated through a simple analytical fitting of the experimental data. Note that, although in this case it has been possible setting $\beta_2 = 0$, all five model parameters are typically required for accuracy reasons.

Thus, it has been demonstrated that the PHM can well reproduce the stiffening behavior occurring in the tested WRI and that it requires only one set of parameters

Table 1 PHM parameters used for reproducing the hysteresis loops in Fig. 4

$f_v = 0\text{ kN}$	$k_a [\text{Nm}^{-1}]$	$k_b [\text{Nm}^{-1}]$	α	$\beta_1 [\text{Nm}^{-3}]$	$\beta_2 [\text{Nm}^{-5}]$
(a) Roll	28×10^5	30×10^4	8×10^2	10×10^8	0
(b) Shear	28×10^5	32×10^4	11×10^2	10×10^8	0

Table 2 PHM parameters used for reproducing the hysteresis loops in Fig. 5

$f_v = 2\text{ kN}$	$k_a [\text{Nm}^{-1}]$	$k_b [\text{Nm}^{-1}]$	α	$\beta_1 [\text{Nm}^{-3}]$	$\beta_2 [\text{Nm}^{-5}]$
(a) Roll	28×10^5	26×10^4	10×10^2	10×10^8	0
(b) Shear	28×10^5	30×10^4	13×10^2	10×10^8	0

to simulate the device response obtained at various levels of amplitude in the presence of a constant axial compressive force.

Finally, the comparison of Tables 1 and 2 shows that the set of model parameters has to be suitably calibrated, based on the experimental results, in order to account for a different value of the applied constant axial compressive force.

4 Conclusions

We have illustrated a novel rate-independent model capable of predicting the hysteretic response of WRIs along their Roll and Shear transverse directions in the presence of a constant axial compressive force.

Adopting the PHM, the device restoring force can be computed by solving an algebraic equation requiring a set of only five parameters which are characterized by a clear mechanical significance, as shown in Sect. 2.2.

According to the experimental verification, it can be concluded that:

- the WRIs hysteretic behavior obtained at various amplitude levels, including the stiffening behavior, can be simulated by means of the PHM using only one set of parameters;
- the WRIs hysteretic behavior obtained for a different value of the constant axial compressive force can be simulated by conveniently recalibrating the set of five model parameters.

Forthcoming papers will show the numerical accuracy as well as the computational efficiency of the PHM by performing nonlinear time history analyses [14] on hysteretic mechanical systems and comparing the results with those obtained by using the celebrated Bouc–Wen model [15, 16] or its modified version [3, 4].

References

1. Ko, J.M., Ni, Y.Q., Tian, Q.L.: Hysteretic behavior and empirical modeling of a wire-cable vibration isolator. *Int. J. Anal. Exp. Modal Anal.* **7**(2), 111–127 (1992)
2. Demetriades, G.F., Constantinou, M.C., Reinhorn, A.M.: Study of wire rope systems for seismic protection of equipment in buildings. *Eng. Struct.* **15**(5), 321–334 (1993)
3. Ni, Y.Q., Ko, J.M., Wong, C.W., Zhan, S.: Modelling and identification of a wire-cable vibration isolator via a cyclic loading test. Part 1: experiments and model development. *J. Syst. Control Eng.* **213**(3), 163–171 (1999)
4. Ni, Y.Q., Ko, J.M., Wong, C.W., Zhan, S.: Modelling and identification of a wire-cable vibration isolator via a cyclic loading test. Part 2: identification and response prediction. *J. Syst. Control Eng.* **213**(3), 173–182 (1999)
5. Wang, H-X., Gong, X-S., Pan, F., Dang, X-J.: Experimental investigations on the dynamic behaviour of O-type wire-cable vibration isolators. *Shock Vib.* **2015**, Article ID 869325, 12 pp. (2015)
6. Chang, C-M., Strano, S., Terzo, M.: Modelling of hysteresis in vibration control systems by means of the Bouc-Wen model. *Shock Vib.* **2016**, Article ID 3424191, 14 pp. (2016)
7. Vaiana, N., Sessa, S., Marmo, F., Rosati, L.: A class of uniaxial phenomenological models for simulating hysteretic phenomena in rate-independent mechanical systems and materials. *Nonlinear Dyn.* **93**(3), 1647–1669 (2018)
8. Vaiana, N., Sessa, S., Marmo, F., Rosati, L.: An accurate and computationally efficient uniaxial phenomenological model for steel and fiber reinforced elastomeric bearings. *Compos. Struct.* **211**, 196–212 (2019)
9. Vaiana, N., Sessa, S., Marmo, F., Rosati, L.: Nonlinear dynamic analysis of hysteretic mechanical systems by combining a novel rate-independent model and an explicit time integration method. *Nonlinear Dyn.* (2019). <https://doi.org/10.1007/s11071-019-05022-5>
10. Vaiana, N., Spizzuoco, M., Serino, G.: Wire rope isolators for seismically base-isolated lightweight structures: experimental characterization and mathematical modeling. *Eng. Struct.* **140**, 498–514 (2017)
11. Strano, S., Terzo, M.: Actuator dynamics compensation for real-time hybrid simulation: an adaptive approach by means of a nonlinear estimator. *Nonlinear Dyn.* **85**(4), 2353–2368 (2016)
12. Losanno, D., Madera Sierra, I.E., Spizzuoco, M., Marulanda, J., Thomson, P.: Experimental assessment and analytical modeling of novel fiber-reinforced isolators in unbounded configuration. *Compos. Struct.* **212**, 66–82 (2019)
13. Madera Sierra, I.E., Losanno, D., Strano, S., Marulanda, J., Thomson, P.: Development and experimental shear behavior of HDR seismic isolators for low-rise residential buildings. *Eng. Struct.* **183**, 894–906 (2019)
14. Greco, F., Luciano, R., Serino, G., Vaiana, N.: A mixed explicit-implicit time integration approach for nonlinear analysis of base-isolated structures. *Annals Solid Struct. Mech.* **10**, 17–29 (2018)
15. Bouc, R.: Modele mathematique d'hysteresis. *Acustica* **24**, 16–25 (1971)
16. Wen, Y.K.: Method for random vibration of hysteretic systems. *J. Eng. Mech. Div. ASCE* **102**(2), 249–263 (1976)

A Non-linear Model of Rubber Shear Springs Validated by Experiments



Sanpeng Gong, Sebastian Oberst, and Xinwen Wang

Abstract Vibrating flip-flow screens provide an effective solution for screening highly viscous or fine materials. However, only linear theory has been applied to their design. Yet, to understand deficiencies and to improve performance an accurate model especially of the rubber shear springs equipped in screen frames is critical for its dynamics to predict, e.g. frequency- and amplitude-dependent behaviour. In this chapter, the amplitude dependency of the rubber shear spring is represented by employing a friction model in which parameters are fitted to an affine function rather than constant values used for the classic Berg's friction model; the fractional derivative model is used to describe its frequency dependency and compared to conventional dashpot and Maxwell models with its elasticity being represented by a non-linear spring. The experimentally validated results indicate that the proposed model with a non-linear spring, friction and fractional derivative model is able to more accurately describe the dynamic characteristics of a rubber shear spring compared with other models.

Keywords Non-linear dynamic model · Rubber shear spring · Stiffness · Damping

1 Introduction

Rubber shear springs (RSS) are widely used in numerous places as important components in structures or machines to transmit vibrations. One example RSS are

S. Gong · X. Wang

School of Chemical and Environmental Engineering, China University of Mining and Technology, Beijing, China

Center for Audio, Acoustics and Vibration, University of Technology, Sydney, NSW, Australia

S. Oberst (✉)

Center for Audio, Acoustics and Vibration, University of Technology, Sydney, NSW, Australia
e-mail: sebastian.oberst@uts.edu.au

commonly used is in vibrating flip-flow screens (VFFS) which play an important role in the dry screening of wet and fine materials such as gold deposited rocks, iron or coal ore. One of the key aspects in VFFS is that the RSS can exhibit frequency- and amplitude-dependent behaviour. Due to the frequency dependency, an increase in frequency can result in an increased stiffness. The non-linear behaviour underlying non-linear spring characteristics may, however, largely affect the vibration characteristics of VFFS, which is responsible for a screen's performance [1–3] but has rarely been studied in detail. The most widely used model when considering frequency-dependent behaviour is that of the Kelvin-Voigt (KV) model in which a linear spring is installed in parallel to a viscous dashpot [4]. Yet, even though widely used, this model overestimates damping in the higher frequency regimes [5, 6]. Placing a spring in series with a viscous dashpot, a three-parameter Maxwell model can be obtained [7]; while underestimating the damping, it better approximates the dynamic stiffness at high frequencies. To improve the prediction of the frequency-dependent dynamics, the use of a fractional derivative model has therefore been suggested by Sjöberg [8], which is composed of not only a fractional derivative element but also a linear spring and Berg's friction element to better approximate the dynamic behaviour of rubber springs. Berg [7] presented in 1998 a smooth friction model with two constants, this simple analytical model describes the non-linear relationship between friction force and displacement (frictional hysteresis curve) in rubber materials using a “smooth Coulomb friction force”, and it can better approximate the smoothness of measured curves than e.g. the stick-slip component model [8]. However, this friction model underestimates stiffness and damping relative to the measurements when the excitation amplitude is too small. Zhu et al. [9] enhanced Berg's friction model using a parameter estimation via statistical methods and remedied the effect the friction force had on the amplitude-dependent behaviour.

This chapter presents a novel RSS model composed of an elastic, an amplitude- and a frequency-dependent model. For improved accuracy, a non-linear spring replaces the linear spring. The friction model uses fitted parameters dependent on an affine function by maintaining Berg's smooth friction model philosophy. The viscoelastic property is described as a fractional derivative model using only two parameters. Experimental cyclic tests of RSS are carried out to verify the reasonability of the proposed model.

2 Model Development

Based on the specific experimental results, the overall structure of the proposed model consists of three different branches (see Fig. 1). An elastic sub-model (F_e) represents the static non-linear stiffness characteristic, the friction model (F_f) accounts for the hysteresis and the amplitude dependency, and the viscous model

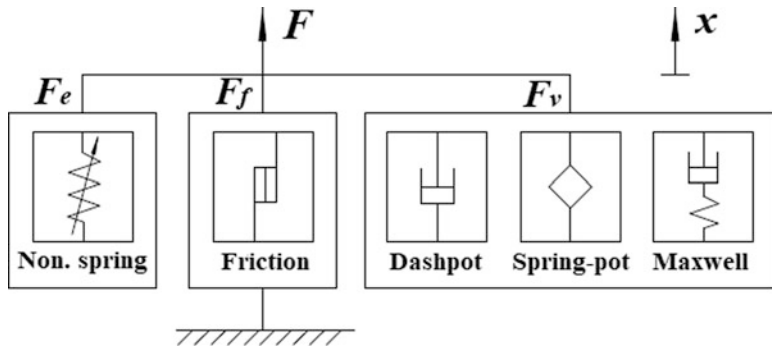


Fig. 1 Model with viscous sub-models

(F_v) is responsible for the frequency-dependent dynamics. Hence, the total force F is the combined results of these three elements and is given by

$$F = F_e + F_f + F_v. \quad (1)$$

2.1 Elastic Model

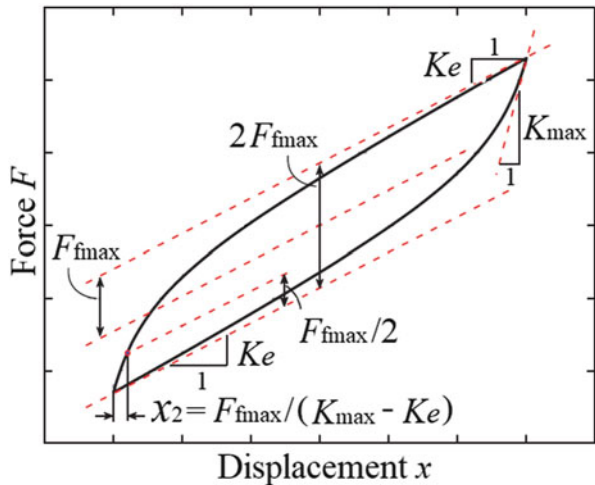
The elastic model consists of a non-linear algebraic relationship between the instantaneous displacement $x = x_0 \sin(\omega t)$ and the resulting elastic force $F_e = K_e x$, where ω and t represent the angular frequency and the time, respectively. The elastic stiffness K_e is identified by analysing the hysteresis loop obtained in the quasi-static test (see Fig. 2) and fitted to an affine formula (constant and linear part) using different amplitudes: $K_e = a + bx_0$ with x_0 [mm] being the excitation amplitude. The parameters a [N/mm] and b [N/mm²] are obtained by the method of curve fitting using the available experimental data.

2.2 Friction Model

The friction model used here is not that of Berg, which provides erroneous results especially when the excitation amplitudes are small. It rather uses the friction model with the relationship between the displacement x and the corresponding friction force F_f and can be mathematically described by:

For $x = x_s$

$$F_f = F_{fs}, \quad (2a)$$

Fig. 2 Hysteresis loop

for $x > x_s$

$$F_f = F_{fs} + \frac{x - x_s}{x_2(1 - \varepsilon) + (x - x_s)} (F_{fmax} - F_{fs}), \quad (2b)$$

for $x < x_s$

$$F_f = F_{fs} + \frac{x - x_s}{x_2(1 + \varepsilon) - (x - x_s)} (F_{fmax} + F_{fs}). \quad (2c)$$

Here, the reference displacement x_s and force F_{fs} form the starting points $(x_s, F_{fs}) = (0,0)$ of an iterative process which is updated whenever the direction of excitation velocity changes. The maximum friction force F_{fmax} and the displacement x_2 are identified through the hysteresis loop (Fig. 2) and fitted to an affine function using different amplitudes x_0 : $F_{fmax} = (c + dx_0)$ and $x_2 = (e + fx_0)$; c [N], d [N/mm], e [mm], and f [mm²] are obtained via curve fitting using the available experimental data. The parameters F_{fmax} and x_2 in the Berg's friction model are constants with its friction force being described by formula (2). The instantaneous friction coefficient $\varepsilon = F_{fs}/F_{fmax}$ ranges from -1 to 1 .

2.3 Viscous Model

There are several ways to model the viscous properties of rubber elements. One method of modelling the viscous properties is to introduce a linear viscous damper with parameter c and viscous force $c\dot{x}$. However, this model can neither accurately represent the non-linear behaviour of rubber springs, nor can it accurately represent

the frequency dependency of the energy loss mechanisms. An improved formulation of viscous forces uses a Maxwell module, which is represented by a viscous damper placed in series to a linear spring. The viscoelastic force amplitude is expressed as $F_{vM} = \omega C_M x_0 / \sqrt{1 + (\omega C_M / K_M)^2}$, where K_M , C_M are the stiffness of the linear spring and the damping of the linear damper, respectively. Due to the Maxwell module underestimating the damping at higher frequencies, a so-called fractional derivative model has been proven to be useful in describing the viscoelastic property of a rubber spring over a larger frequency range [9]. To define F_v the fractional derivative model generalizes the operation of differentiation to non-integer orders

$$F_v = b D^\alpha x = b \frac{d^\alpha x}{dt^\alpha}. \quad (3)$$

Here, non-integer $\alpha \in]0, 1[$ and $b > 0$ are model constants, which represent the order of the time derivative as well as the coefficient of the viscoelastic force, respectively. For $\alpha = 0$ or $\alpha = 1$ the model becomes that of a linear spring or a viscous damper, respectively. The fractional derivative can be simplified through a fractional Riemann–Liouville integration as

$$\frac{d^\alpha x(t)}{dt^\alpha} = \frac{1}{\Gamma(1-\alpha)} \frac{d}{dt} \int_{\alpha}^t \frac{x(\tau)}{(t-\tau)^\alpha} d\tau \quad (4)$$

with the Gamma function being defined as [8]

$$\Gamma(\beta) = \int_0^\infty t^{\beta-1} \exp(-t) dt. \quad (5)$$

Here, \exp denotes the exponential function. For numerical approximation of the fractional derivative, a more convenient form can be given using the Grünwald–Letnikov definition [8]:

$$F_{vf}(t_n) = b D^\alpha x_n \approx b \frac{(\Delta t)^{-\alpha}}{\Gamma(-\alpha)} \sum_{j=0}^{n-1} \frac{\Gamma(j-\alpha)}{\Gamma(j+1)} x_{n-j} \quad (6)$$

with $t_n = n\Delta t$, $x_n = x(t_n)$; and Δt , n are a constant time step and the truncation number, respectively.

3 Experimental Cyclic Tests of Shear Rubber Springs

Two experiments were conducted using quasi-static and harmonic dynamic tests. In the quasi-static test, harmonic displacement excitations of 1–6 mm amplitude in 1 mm step at 0.01 Hz were applied to the actuator, respectively. The viscous force

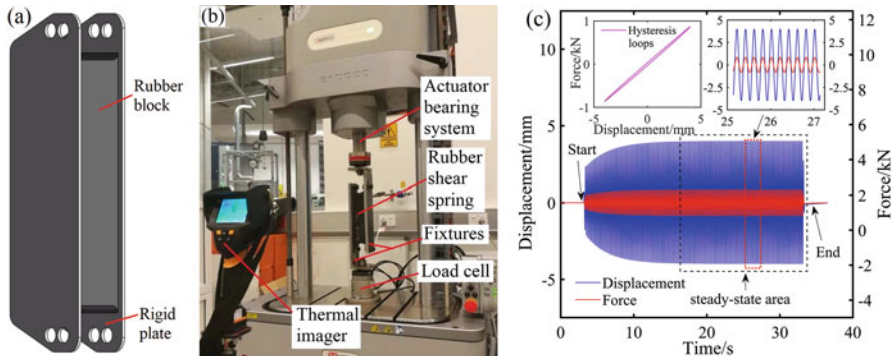


Fig. 3 Dynamic stiffness and damping tests of the RSS: (a) schematic drawing of the RSS; (b) experimental test; (c) experimental data

can be neglected as the frequency is rather low (0.01 Hz). This allows to extract from hysteresis loops K_e in elastic model, $F_{f\max}$ as well as x_2 in the friction model (see Fig. 2) [7]. The harmonic dynamic tests use different frequencies ranging from 1 to 15 Hz in 1 Hz steps at 4 mm to vary the viscous force. The parameters α and β of the spring-spot, c of the dashpot, K_M and C_M of the Maxwell model are retrieved through numerically fitting the results of the harmonic dynamic tests [11]. The quasi-static and harmonic dynamic tests were also used to verify the proposed model.

In this study, the RSS (Tiangong, size $203 \times 70 \times 48$ mm, China, Fig. 3a) was tested on a dynamic testing machine (Instron, Type E10000, accuracy $\pm 0.5\%$, Massachusetts, USA) (Fig. 3b). During the measurement, two fixtures were used to connect the tested rubber spring and the test instrument. One fixture was fixed with the actuator bearing system with maximum displacement and velocity being 30 mm and 500 mm/s, respectively. Another fixture was installed on the load cell (Instron, type 2527, capacity 10 kN, accuracy $\pm 0.005\%$, Massachusetts, USA) and used to measure the force signal. Force and the displacement signals were recorded using the Instron testing software (Instron, Type WaveMatrix, America). A thermal imager (Testo, Type 875, sensitivity < 50 mK, accuracy $\pm 2\%$ °C, Baden-Württemberg, Germany) was used to test the temperature of RSS. We guaranteed several minutes break between two consecutive measurements to make sure that every test was carried out at a constant temperature of 23 °C. To test the dynamic stiffness and damping, a controlled sine wave was imposed on the structure, and the resulting force was measured. One hundred and fifty cycles of data of all cases were recorded and only steady-state data of force and displacement were used to form the hysteresis loops (see Fig. 3c); the dynamic stiffness K (storage and loss stiffness) and the damping ratio ζ can be calculated from the measured hysteresis loops:

$$K = \frac{1}{n} \sum_{j=1}^n \frac{F_{\max,j} - F_{\min,j}}{x_{\max,j} - x_{\min,j}} \quad \text{and} \quad \zeta = \frac{1}{n} \sum_{j=1}^n \frac{E_j}{\pi (F_{\max,j} - F_{\min,j}) (x_{\max,j} - x_{\min,j}) / 4}, \quad (7)$$

where $F_{\max,j}$ and $F_{\min,j}$ are the maximum and minimum force of each force-displacement hysteresis plot, respectively, $x_{\max,j}$ and $x_{\min,j}$ are defined as the related displacement of forces, n is the number of hysteresis loops evaluated to obtain an average value, and $E_j = \oint F dx$ represents the energy loss and is a closed integration along the hysteresis loop.

4 Results and Discussion

Parameters for the elastic and the force model are identified through the method described in Sect. 2. Parameters for the viscous model can be obtained using the least-squares technique discussed in [11], and the parameters for the newly proposed model as well as that of Sjöberg's model are presented in Table 1. Here, R^2 is the coefficient of determination (squared Pearson correlation coefficient). Parameter values for the elastic and the force model in Sjöberg's model are shown by their values of mean \pm standard deviation. The Sjöberg's model as it is widely used to describe the dynamic behaviour of rubber springs [8, 10] is compared here with our proposed model.

The simulated results of the proposed RSS model and Sjöberg's model were compared with experimental data in the quasi-static conditions, see Figs. 4 and 5. It can be found in Fig. 4 that the hysteresis loops of the simulation results of the proposed model better match the experimental results than those of Sjöberg's model when the excitation amplitude is small (1 mm), especially at large displacements of the hysteresis loops. In addition, the amplitude-dependent behaviour of RSS can be seen in Fig. 5: with an initial increase of the amplitude, the measured stiffness decreases while the damping increases, before it starts decreasing for amplitudes ranging from 1 to 6 mm. The description of the amplitude dependency in the experiments can be enhanced using the proposed model instead of Sjöberg's model (Fig. 5). In detail, the mean squared error (MSE) between the experimental and the numerical stiffness of the proposed and Sjöberg's model are 0.68 and 23.80,

Table 1 Parameters for the proposed model and Sjöberg's model

Symbol	Proposed model	Sjöberg's model	Unit
K_e	$205.9 - 3.28x_0$ ($R^2 = 0.998$)	186.45 ± 0.43	[N/mm]
F_{\max}	$4.31 + 10.56x_0$ ($R^2 = 0.995$)	68.3 ± 0.26	[N]
x_2	$0.45x_0 - 0.09$ ($R^2 = 0.993$)	2.64 ± 0.04	[mm]
α	0.16	0.16	[–]
β	9.9	9.9	[Ns $^\alpha$ /mm]

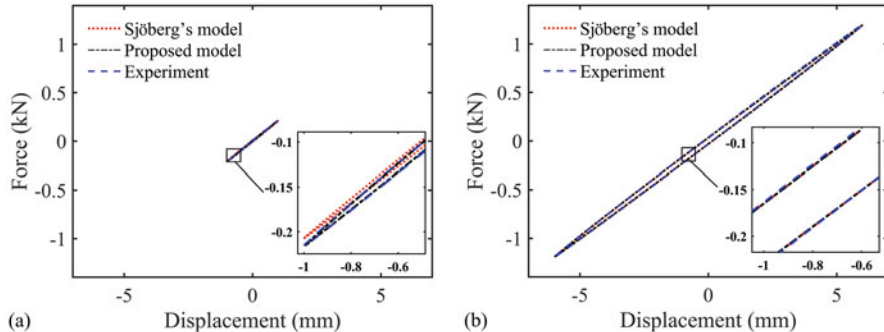


Fig. 4 Hysteresis loops compared between experiment and simulation with frequency of 0.01 Hz for different amplitudes: (a) 1 mm, (b) 6 mm

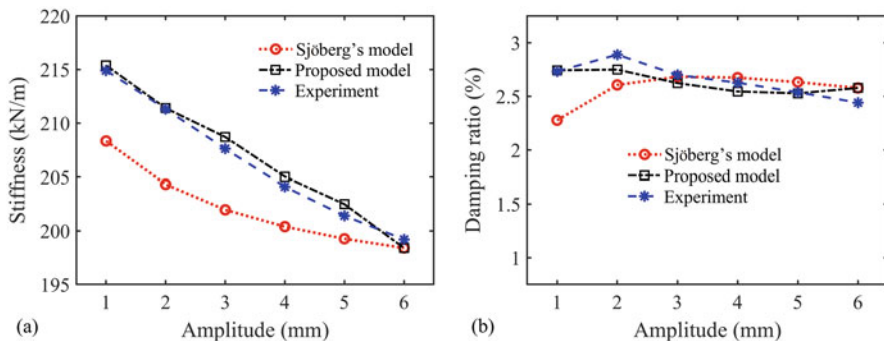


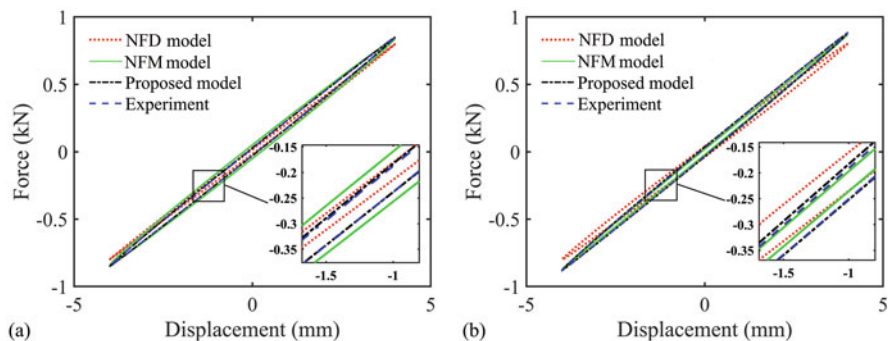
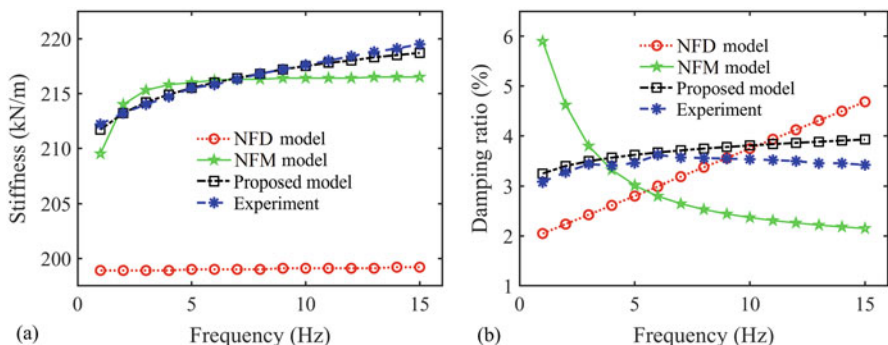
Fig. 5 Dynamic behaviour versus excitation amplitude with frequency of 0.01 Hz: (a) stiffness, (b) damping ratio

respectively, and the MSE of damping between experiment and simulation of the proposed model and the Sjöberg's model are 0.0085 and 0.053, respectively.

A displacement of excitation amplitude $x_0 = 4$ mm was chosen for frequencies from 1 to 15 Hz. Similarly, using the parameter identification method, parameters for NFD model (non-linear spring + friction + dashpot model) and NFM model (non-linear spring + friction + Maxwell model) can be obtained (Table 2). Parameters for the newly proposed model (non-linear spring + friction + fractional derivative model) are listed in Table 1. Plotting the hysteresis loops and frequency-dependent results of the experiments and for these three models produces Figs. 6 and 7, respectively. The hysteresis loop of the experimental results is more accurately described by our newly proposed model compared to that of NFD model and NFM model. This is especially the case for large displacements (Fig. 6). It can be found in Fig. 7 that NFD model performs poorly in approximating either the measured stiffness or the damping. Using NFM model results in an enhanced fit of the stiffness, but the damping is far off from the experiments. The newly

Table 2 Parameters for the proposed Model 1 and Model 2

NFD model	Unit	NFM model	Unit
$K_e = 205.9 - 3.28x_0$ ($R^2 = 0.998$)	[N/mm]	$K_e = 205.9 - 3.28x_0$ ($R^2 = 0.998$)	[N/mm]
$F_{fmax} = 4.31 + 10.56x_0$ ($R^2 = 0.995$)	[N]	$F_{fmax} = 4.31 + 10.56x_0$ ($R^2 = 0.995$)	[N]
$x_2 = 0.45x_0 - 0.09$ ($R^2 = 0.993$)	[mm]	$x_2 = 0.45x_0 - 0.09$ ($R^2 = 0.993$)	[mm]
$C = 0.06$	[Ns/mm]	$C_M = 3.45$	[Ns/mm]
		$K_M = 17.73$	[N/mm]

**Fig. 6** Hysteresis loops compared between experiment and simulation with amplitude of 4 mm for different frequency: (a) 1 Hz, (b) 15 Hz**Fig. 7** Dynamic behaviour versus excitation frequency with amplitude of 4 mm: (a) stiffness, (b) damping ratio

proposed model shows the best fit of both the measured stiffness and the damping compared with NFD and NFM models. In detail, the mean squared errors (MSE) of stiffness and damping between experiment and simulation of NFD and NFM models and the proposed model are 308.36 and 2.75 and 0.12, and 0.59, 1.52 and 0.079, respectively.

5 Conclusion

In this study, we developed a non-linear model of a RSS to illustrate the dependency of the rubber friction to the amplitude and the frequency dependency as consequence of the viscoelastic properties of the rubber. The model is validated experimentally using quasi-static and harmonic tests. The elastic element in the proposed model is represented by a non-linear spring, and the friction model uses fitted parameters depending on an affine function by maintaining Berg's smooth friction. The fractional derivative model is then used to describe the viscoelastic property of the RSS. Several models for the investigated rubber spring are compared with experimental results under quasi-static and harmonic excitation tests. The newly proposed model is capable in describing the amplitude and the frequency dependency more accurately than the models, which are conventionally used. The research work presented here not only forms the first step to study the dynamic of VFFS but also potentially contributes to better understand the dynamic behaviour of RSS. How the dynamics will be influenced by the stress-strain relationship in rubber materials using e.g. the Ramberg-Osgood or the extended Masing model needs to be studied in the future.

References

1. Xiong, X., Niu, L., Gu, C., Wang, Y.: Vibration characteristics of an inclined flip-flow screen panel in banana flip-flow screens. *J. Sound Vib.* **411**, 108–128 (2017)
2. Akbari, H., Ackah, L., Mohanty, M.: Performance optimization of a new air table and flip-flow screen for fine particle dry separation. *Int. J. Coal Preparation Util.* **0**, 1–23 (2017)
3. Gong, S., Wang, X., Oberst, S.: Non-linear analysis of vibrating flip-flow screens. *MATEC Web of Conferences*, vol. 221, 04007 (2018)
4. Knothe, K.L., Grassie, S.L.: Modelling of railway track and vehicle/track interaction at high frequencies. *Vehicle Syst. Dyn.* **22**(3–4), 209–262 (1993)
5. Babitsky, V.I., Veprik, A.M.: Universal bumpered vibration isolator for severe environment. *J. Sound Vib.* **218**(2), 269–292 (1998)
6. Fenander, A.: Frequency dependent stiffness and damping of railpads. *Proc. Inst. Mech. Eng. F J. Rail Rapid Transit.* **211**(1), 269–292 (1997)
7. Berg, M.: A non-linear rubber spring model for rail vehicle dynamics analysis. *Vehicle Syst. Dyn.* **30**(3–4), 197–212 (1998)
8. Sjöberg, M.: Nonlinear isolator dynamic at finite deformations: an effective hyperelastic, fractional derivative, generalized friction model. *Nonlin. Dyn.* **33**, 323–336 (2003)
9. Zhu, H., Yang, J., Zhang, Y., Feng, X.: A novel air spring dynamic model with pneumatic thermodynamics, effective friction and viscoelastic damping. *J. Sound Vib.* **408**, 87–104 (2017)
10. Sedlaczek, K., Dronka, S., Rauh, J.: Advanced modular modelling of rubber bushing for vehicle simulations. *Vehicle Syst. Dyn.* **49**, 741–759 (2011)
11. Shi, H., Wu, P.: A nonlinear rubber spring model containing fractional derivatives for use in railroad vehicle dynamic analysis. *Proc. Inst. Mech. Eng. F J. Rail Rapid Transit.* **230**(7), 1745–1759 (2016)

Operational Modal Analysis on a Six-Degree-of-Freedom Parallel Manipulator: Reproducibility, Excitation and Pose Dependency



Kasper Ringgaard and Ole Balling

Abstract In machining applications knowledge of structural response is key when optimizing the productivity. For six degrees of freedom parallel kinematic manipulators the response can be highly pose dependent. Mapping the response throughout the workspace becomes excessively labour intensive using traditional techniques, such as experimental modal analysis and so far accurate structural dynamic models are not convincing. This contribution covers experimental work using operational modal analysis with shaker excitation to map the response in multiple poses in the workspace of a 6-UTU parallel manipulator. The future prospects of applying output-only modal analysis are better and faster modal analysis which can support correct modelling of vibrational response. This contribution provides insight regarding reproducibility of operational modal analysis results, how excitation with shakers affect the results and whether pose dependent structural response is measurable using the technique.

1 Introduction

Parallel kinematic manipulators are receiving increasing attention in the field of robotic machining due to superior stiffness and accuracy compared to serial manipulators [1]. Knowledge of the structural dynamics of the manipulator is required to efficiently manufacture high precision parts, but the structural response of the manipulator can be highly dependent on the kinematic configuration of the manipulator, i.e., the pose. The pose dependent dynamic response is caused by multiple non-linear phenomena such as [2]: position dependent inertia properties due to relative motion of bodies; changing stiffness- and damping-properties of prismatic actuators with changing joint coordinates; non-linearity of contacts and friction in joints. Modelling of position dependent inertia properties is manageable,

K. Ringgaard (✉) · O. Balling

Mechanical and Materials Engineering, Department of Engineering, Aarhus University, Aarhus, Denmark

e-mail: kri@eng.au.dk

but modelling of complicated contact and friction phenomena in structural dynamics is cumbersome. The non-linear nature of the models yields high computational cost, and the models often struggle to accurately represent the physics of the systems [3].

In machining applications the general trend is to approximate the non-linear structural response of the system with linear dynamics for different states of static equilibrium of the structure, i.e., for different poses of the parallel manipulator. Two approaches are found in machining literature: Mapping of the structural response experimentally in the workspace and using dynamic models of the structure for prediction of the structural response for different poses. An example of the former is Tunc et al. [4] who obtained the dynamic response of a parallel manipulator in the workspace through experimental modal analysis (EMA) for a grid of manipulator poses. Mapping of structural response using EMA is labour intensive and lacks details between grid points. Tunc et al. also focused solely on response of the tool tip, thereby excluding the opportunity of understanding the physics of the structure through the normal mode shapes. The latter is not well covered in machine tool literature, but an example is Law et al. [5], who modelled a serial-parallel kinematic machine tool using flexible multibody dynamics and applied EMA for one specific pose for validation. The modelled response is not in good agreement with experimental results, and the model is only compared to experimental results for one specific pose; hence, validation of the non-linear pose dependent dynamic response is not addressed.

Experimental modal data for more poses is required to better understand the physics of the pose dependent dynamic response. This contribution proposes application of Operational Modal Analysis (OMA) to overcome the labour intensiveness of EMA. OMA is an output-only modal analysis technique, i.e., the method only requires measurement of structural response using, e.g., accelerometers which simplify the experimental work tremendously. The method is widely applied to identification for large structures such as bridges and buildings [6], but applications to machine structures are sparse. Recent trends in modal analysis drift towards development of automated OMA, where an automatic algorithm identifies modal parameters of the structure at hand [7]. If applied for parallel manipulators the methods can identify modal properties for a large selection of poses without requiring large amounts of manual labour during both experimental work and identification.

The scope of this contribution is application of OMA on a six degree of freedom parallel manipulator of the 6-UTU type. Experimental results from an extensive experimental campaign are presented, and answer questions related to application of OMA on parallel manipulators such as are the experiments reproducible, is excitation using shakers feasible and is it possible to gain knowledge about how the dynamic response changes with varying manipulator pose.

2 Experimental Setup

A six-degree-of-freedom motion simulation system from MOOG INC. of the type MB-E-6DOF, shown in Fig. 1a, is experimentally investigated in this contribution. The system consists of one steel tube hexagon frame and six identical struts, each comprised of two universal joints and one linear ball screw actuator. The non-linearities of the system can be caused by non-linear changes of the inertia of the system with pose, non-linear variations of strut stiffness with length and friction and contact phenomena in both universal joints and the screw spindle drives and motors. Two *LDS V406* shakers, mounted on the structure, are activated using a white noise signal and a set of accelerometers attached to the steel frame are used to record the response. The signals are recorded using a National Instruments data acquisition system connected to a PC. Each experiment lasts approximately two minutes and data is collected with a sampling frequency of 10 kHz. The duration of the measurement campaigns are based on recommendations stated in [7]. A total of 20 *B&K 4508-B* uni-axial accelerometers are attached to the steel frame of the motion base using polycarbonate clips glued to the surface. The accelerometer measuring range is up to 8 kHz, with a sensitivity of 10 mV/g, a weight of 4.8 g and a residual noise level of 250 μ g. Sensors are distributed with focus on making deflection modes of the steel platform observable. Six different manipulator poses shown in Fig. 1b are selected for experimental analysis.

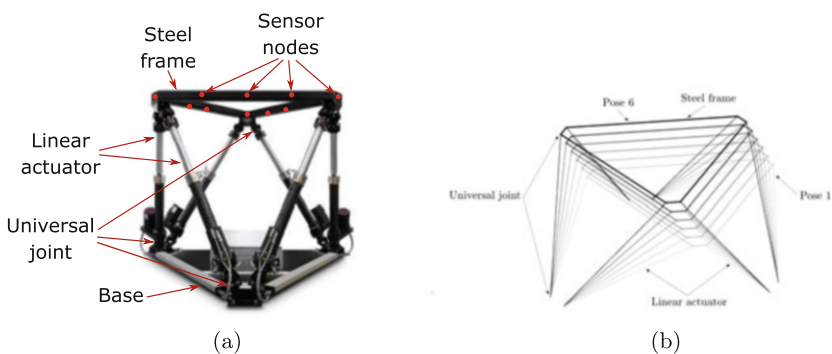


Fig. 1 (a) MOOG motion base MB-E-6DOF with sensor nodes indicated by red dots. Two accelerometers are mounted for each node. (b) Illustration of the six poses investigated. The steel frame is the thick line, the universal joints are the circles and actuators are thin lines. Each pose is plotted with a different shade of grey/black

3 Results and Discussion

The randomness of the recorded time signals, which is a prerequisite for application of OMA identification, is validated through comparison to Gaussian normal distributions prior to modal analysis. The time signals are transformed to the frequency domain, and the poles and mode shapes are identified using the Frequency Domain Decomposition (FDD) [10] identification method. The FDD technique decomposes the signal using Singular Value Decomposition (SVD) and the peaks in singular values are identified as poles of the system. The singular vectors associated with singular value peaks are representative of structural mode shapes.

3.1 Reproducibility

A series of experiments are conducted to clarify whether experiments are reproducible. Two successive experiments are conducted for each of the six poses. Figure 2 sums up results regarding reproducibility of experiments. Frequencies are

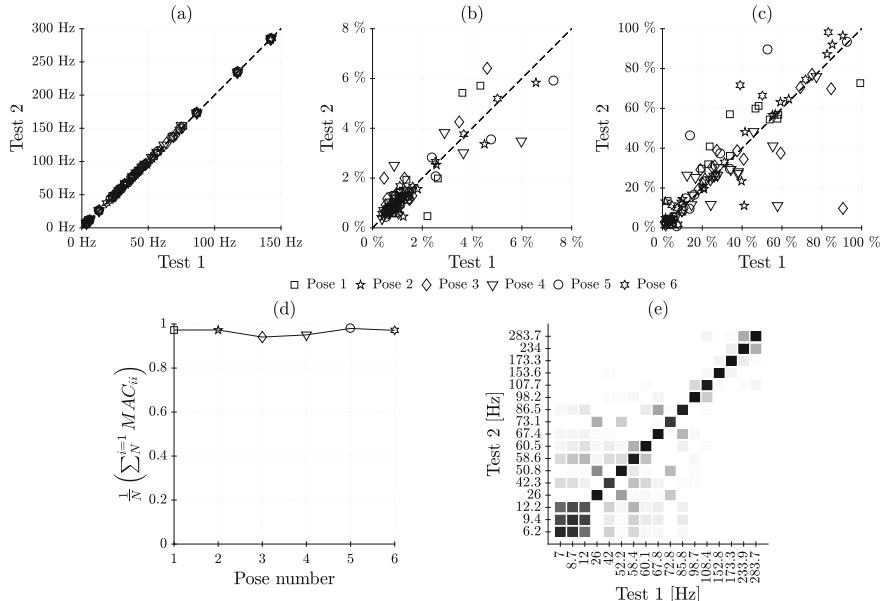


Fig. 2 Identification results for all reproducibility experiments. (a) Frequency comparison, (b) damping ratio comparison, (c) mode complexity factor comparison [8], (d) sum of MAC diagonal for each pose, (e) MAC plot [9] for the two tests in pose 1. For (a), (b) and (c) the identifications correlate perfectly if all markers are on diagonal line. For (d) the modes correlate fully if a value of one is obtained, and (e) shows full correlation if the diagonal is black and all off-diagonal elements are white

in general well re-identified. The damping ratios are re-estimated with considerable variance, as is the mode complexity factors. The real part of the mode shapes is well re-identified for all six poses. An example MAC [9] is shown in Fig. 2e. This indicates that the three first modes in the 5–15 Hz region might be the same mode and not three separate modes. In the 40–100 Hz region the off-diagonal elements show considerable correlation.

3.2 Shaker Reorientation and Relocation

Attaching shakers to the structure changes the physics of the system by alternating the mass distribution. The orientation of the shakers determine directions of excitation forces applied to the structure. A series of test for one specific manipulator pose is conducted to gain insight into the effect. Figure 3 presents results of shaker manipulation tests. All three manipulation tests are compared to the same reference test. Frequencies are in general well correlated, damping ratios are more widespread and modal complexity factor have very little correlation. Mode shapes are not well re-estimated except for a few cases. The results indicate that relocation of an exciter changes the real parts (frequency and MAC) more than reorientation alone. The results also show that reorientation of the excitation forces causes large changes in complex parts of the signals (damping ratios and mode complexity factors).

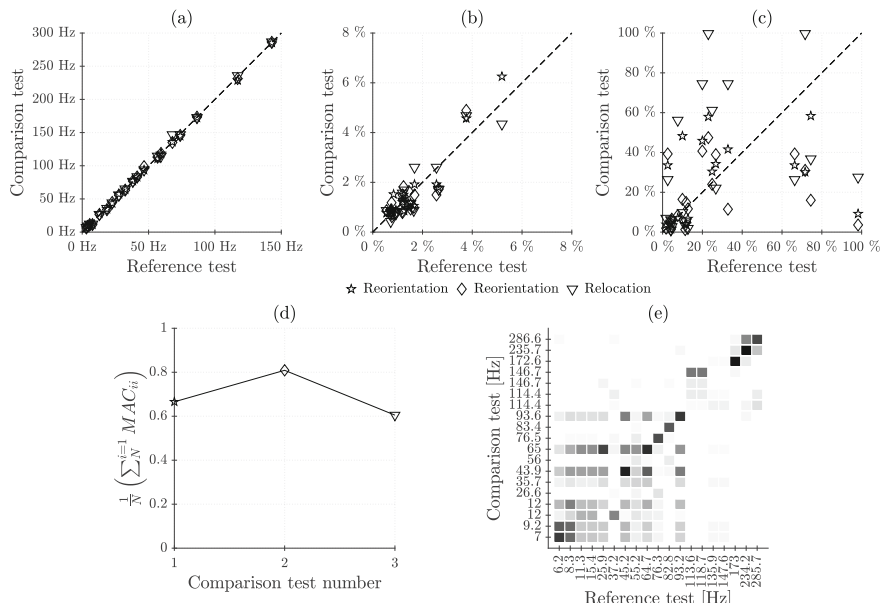


Fig. 3 Identification results for shaker reorientation and relocation. See Fig. 2 for explanation of plot content

3.3 Pose Dependency

Pose dependency of the dynamic response is analysed through the identified modal parameters for pose 1 to pose 6. The mode shapes identified for pose 1 are compared to the mode shapes of pose 6 using MAC and six modes having MAC values above 0.80 are deemed comparable. Figure 4 illustrates how the identified frequencies changes for the six modes for pose 1 to 6. Polynomial functions are fitted to the data points to evaluate the nature of the variations, and for two modes the best fit is non-linear (second order polynomial). By inspection Fig. 4 shows that modes 1, 2, 4 and 5 vary less than 1 Hz across the six poses, whereas mode 3 changes approximately 6 Hz and mode 6 changes approximately 2 Hz. Thus, the only modes varying significantly with the pose of the manipulator are mode 3 and mode 6 which are visualized in Fig. 5.

By inspection of the mode shapes for mode 3 in Fig. 5a, b the mode can be interpreted as bending of the steel platform and some level of axial deflection of the struts. Thus, changing the strut stiffness will impose changes boundary conditions on the platform and therefore change the frequency. The strut lengths increase going from pose 1 to 6, which causes both axial and lateral stiffness of the struts to decrease. Considering the fact that the lateral stiffness of a simply supported beam, which is comparable to the UTU struts, decreases non-linearly with increasing beam length could be the source of the non-linear decrease of the frequency for mode number 3. The mode shapes of mode 6 in Fig. 5c, d show that mode shape 6 does not involve large axial deflections of the struts, but some larger bending deflections of the platform. In Fig. 4 the frequency of mode 6 is increasing, which is opposite to the behaviour of mode 3. Based on this the change in frequency might be measurement

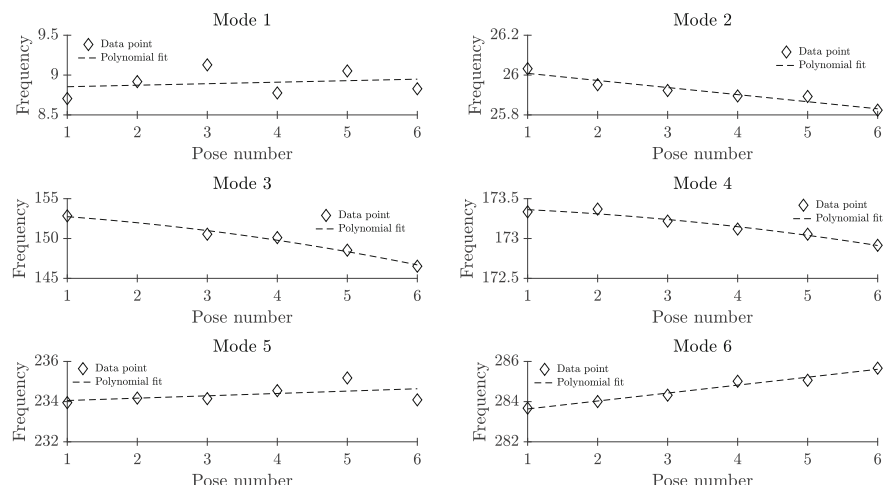


Fig. 4 Frequency variation with varying pose for six correlated modes. Modes 1, 2, 5 and 6 fitted using first order polynomials and modes 3 and 4 are second order polynomials

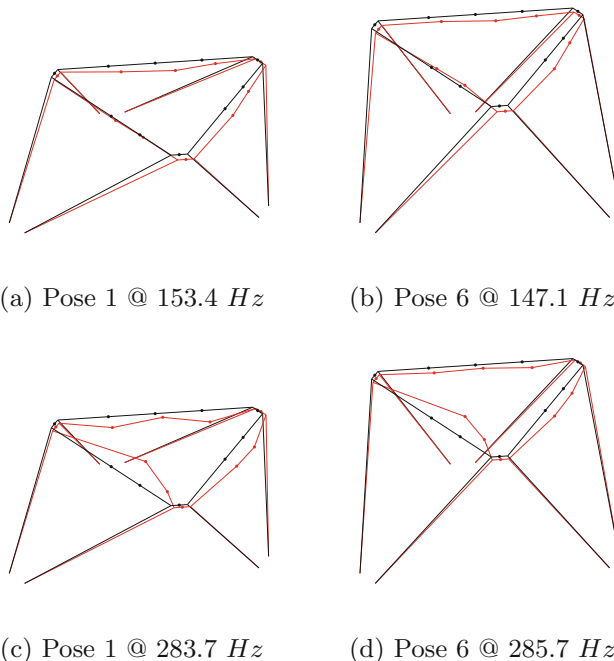


Fig. 5 Mode shape visualizations for (a), (b) mode 3 and (c), (d) mode 6, respectively. Black lines represent the undeformed structure and red lines represent the deformed structure. Dots indicate measured points

uncertainty. The remaining frequencies are independent of pose for the scenarios tested in this case. This indicates that the modes are either related to, e.g., vibration of the base of the manipulator, i.e., vibration of the entire manipulator, or that the strut stiffnesses do not vary sufficiently with pose for any significant change to be measured on the platform.

4 Conclusion

This contribution presents the findings of applying operational modal analysis with shaker excitation to a MOOG MB-E-6DOF parallel manipulator. As presented in the introduction the study is stepping stone for obtaining automated extraction of modal parameters for large number of poses for parallel manipulators which can aid studies on non-linear changes of modal parameters and modelling of systems. A set of poles and mode shapes are found to be stable throughout the experiments, but some variations are present in the complex parts of the parameters. Mounting shakers alters the response significantly, and complex parts of the identified parameters are sensitive to excitation directions and positions. The sensitivity of the parameters

are caused by high correlation of the measured response and the excitation signal. A subset of identifiable poles are traced across six different poses. Majority of the modes do not vary with pose and are therefore concluded to either be related to, e.g., base vibration or simply not affected by varying strut stiffnesses to a measurable extent for the poses investigated. One mode varies significantly and is concluded to vary non-linearly with pose based on polynomial regression. The origin of the non-linearity is assumed to be the changing length of the struts, which can physically be interpreted as simply supported beams which has a non-linear change of lateral stiffness with length.

The experimental results presented spurs continuation of research towards application of automated operational modal analysis on parallel manipulators. The application of shaker excitation needs re-evaluation based on the findings of the extensive experimental campaign presented in this paper. A new excitation scheme which does not interfere with the structure, and excites the structure more randomly in space has to be developed. This has the potential of lowering the complexity of the mode shapes, i.e., obtain normal mode descriptions instead of operational mode shapes. Additionally, increasing the signal-to-noise ratio could aid clarification of the results in the 40–100 Hz region, along with making other poles more clear and less complex. Further studies of the non-linearities should be conducted through investigation of more poses which causes larger changes of strut lengths and inertia properties. Furthermore, an investigation of the lateral vibration of the struts is proposed to clarify whether the lateral vibration modes of the struts are in fact a part of the modes of vibration.

References

1. Patel, Y., George, P.: Parallel manipulators applications survey. *Mod. Mech. Eng.* **2**(03), 57 (2012)
2. Shabana, A.A.: Dynamics of multibody systems. Cambridge University Press, Cambridge (2013)
3. Taghirad, H.D.: Parallel Robots: Mechanics and Control. CRC Press, Boca Raton (2013)
4. Tunc, L., Shaw, J.: Investigation of the effects of Stewart platform-type industrial robot on stability of robotic milling. *Int. J. Adv. Manuf. Technol.* **87**(1–4), 189–199 (2016)
5. Law, M., Ihlenfeldt, S., Wabner, M., Altintas, Y., Neugebauer, R.: Position-dependent dynamics and stability of serial-parallel kinematic machines. *CIRP Annals* **62**(1), 375–378 (2013)
6. Rainieri, C., Fabbrocino, G.: Operational Modal Analysis of Civil Engineering Structures, vol. 142, p. 143. Springer, New York (2014)
7. Brincker, R., Ventura, C.: Introduction to Operational Modal Analysis. John Wiley & Sons, Hoboken (2015)
8. Imregun, M., Ewins, D.: Complex modes-origins and limits. In: Proceedings-SPIE The International Society for Optical Engineering, SPIE International Society for Optical, pp. 496–496 (1995)
9. Allemand, R.J., Brown, D.L.: A correlation coefficient for modal vector analysis. In: Proceedings of the 1st International Modal Analysis Conference, vol. 1, pp. 110–116. SEM, Orlando (1982)
10. Brincker, R., Zhang, L., Andersen, P.: Modal identification of output-only systems using frequency domain decomposition. *Smart Mater. Struct.* **10**(3), 441 (2001)

Shaking Table Investigation on the Masonry Structures Behaviour to Earthquakes with Strong Vertical Component



Nicola Cavalagli, Matteo Ciano, Gianluca Fagotti, Massimiliano Gioffrè, Vittorio Gusella, and Chiara Pepi

Abstract In this paper an experimental investigation on the dynamic response of masonry structures due to the combined effects of vertical and horizontal seismic components is presented. The motivation of this study started with on-site observations of a special damage state affecting some masonry buildings after the Central Italy earthquake in 2016, which can be ascribed to the interaction of vertical and horizontal components of the seismic action. For this purpose, experimental tests on a two-storey building masonry structure were performed using a shaking table in order to investigate its behaviour to earthquakes with strong vertical component.

Keywords Masonry structures · Shaking table test · Seismic action · Vertical acceleration

1 Introduction

In 2016 Central Italy and Umbria Region have been struck by a seismic sequence of significance intensity highlighting the necessity to improve the knowledge regarding the nonlinear dynamic response of masonry structures subjected to horizontal and vertical loads. In particular, several buildings located in a restricted area near the city of Norcia have shown special damage patterns that can be related to the vertical component of the seismic action. It is well known that the understanding of the nonlinear dynamic behaviour and damage accumulation process of masonry

N. Cavalagli (✉) · M. Ciano · M. Gioffrè · V. Gusella · C. Pepi

Department of Civil and Environmental Engineering, University of Perugia, Perugia, Italy

e-mail: nicola.cavalagli@unipg.it; matteo.ciano@unipg.it; massimiliano.gioffre@unipg.it; vittorio.gusella@unipg.it; chiara.pepi@unipg.it

G. Fagotti

Ufficio Speciale Ricostruzione Umbria, Foligno, Italy

e-mail: fagotti@regione.umbria.it

material, under seismic sequences, is a very important topic [1, 2]. Nevertheless, despite the important role played by the vertical acceleration, a few contributions focused on it can be found in literature [3, 4].

In this context, a research programme aimed at improving the dynamic performance of masonry structures by using confined masonry technique was started. An experimental campaign on shaking table has been carried out at the ENEA laboratory in Casaccia, Rome, on both unreinforced and confined masonry buildings, in order to compare the dynamic response provided by the two different construction typologies. In order to highlight the significant role of the vertical component, this paper is focused only to the case of unreinforced model. The main experimental observations are presented and the preliminary results given by an analytical model are shown.

2 Description of the Experimental Tests

2.1 Tested Masonry Building Model

The tested masonry building model is characterized by two storeys, having 3.00×3.50 m plan dimensions and 2.20 m height for each storey (Fig. 1a and b). The model shape and dimensions are similar to previous experimental tests available in literature carried out on the same shaking table [5]. The masonry consists of bearing clay blocks with 45% of core percentage, 25 × 18 cm size and 16 cm thickness. The first floor is a hollow-core slab with reinforced concrete elements, while the roof is made of steel frames designed in order to facilitate the positioning of additional masses at both the levels. The façades of the model are characterized

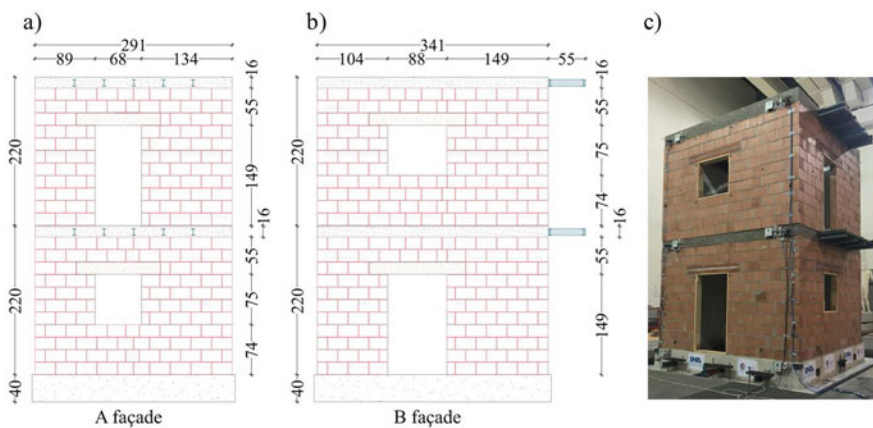


Fig. 1 (a) and (b) Geometrical details of two model façades. (c) Two-storey masonry building model tested on the shaking table

by several openings having different dimensions and positioning, in order to confer eccentricity to the global stiffness. Figure 1 reports the details of two model façades (Fig. 1a and b) and an image of the model on the shaking table (Fig. 1c). For more details about geometrical description and other characteristics see [6].

2.2 Experimental Setup

The experimental tests were carried out on a shaking table of $4 \times 4 \text{ m}^2$ in dimensions and characterized by six degrees of freedom, a frequency range of [0–50] Hz, maximum acceleration of 3.0 g, maximum velocity of 0.5 m/s and a maximum allowed displacement of 0.25 m. The earthquake of October 30th 2016, called in the following as N , recorded by a station of the national accelerometric network (Italian Civil Protection Department) in the city of Norcia was used as input, being characterized by a high intensity in all directions. Figure 2 shows the acceleration time histories of the three components and the related acceleration spectra. The shaking table tests have been carried out by applying all of the three components of the seismic signals reported in Fig. 2 simultaneously and increasing/decreasing the intensity level in three steps: $0.25 N$, N and $1.2 N$. Other intermediate steps with intensity lower than N have not been used to avoid damage accumulation.

The dynamic response of the model during the test is evaluated by an acceleration acquisition system and a 3D motion capture system. The first one consists of 10 uniaxial MEMS (Micro Electrical Mechanical Systems) accelerometers, installed in seven points of the model (Fig. 3a): three at each level including the base and

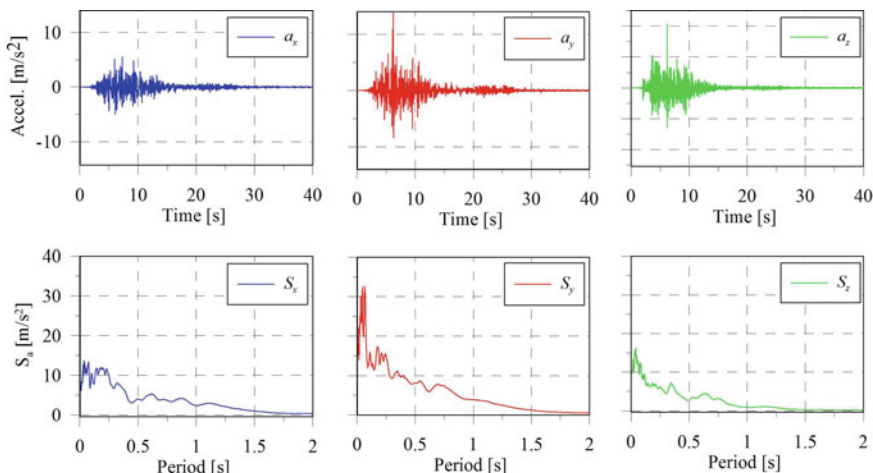


Fig. 2 Acceleration time histories recorded at the base of the model corresponding to 100% of the seismic intensity level (upper panels) and corresponding spectra (lower panels)

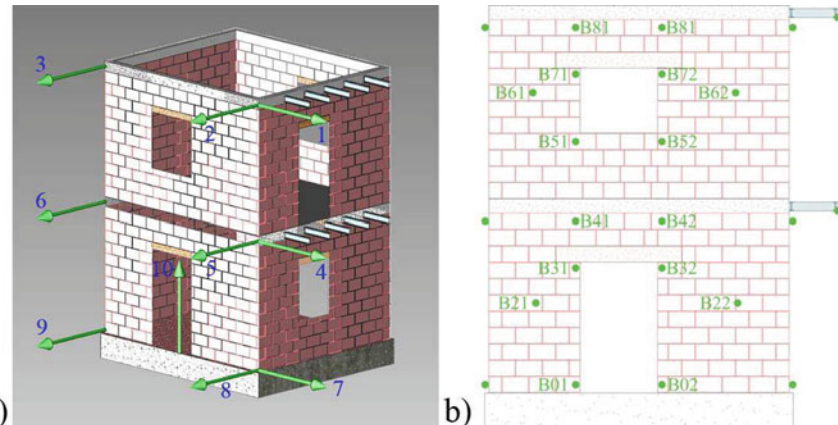


Fig. 3 (a) Position scheme of uniaxial MEMS accelerometers during the tests. (b) Marker positions on B façades

one for the vertical component. The sensors used are uniaxial accelerometers with a sensitivity of $1 \text{ V}/\text{g}$, a measuring range of $\pm 2\text{ g}$ and equipped with a linear analogue output.

The motion capture system is a 3D light-based system consisting of 9 Near InfraRed digital cameras for data acquisition [7]. The target points are identified by several markers fixed on the model surfaces. The displacement data processing has been carried out through specific procedures developed by the ENEA research group. The markers are positioned in several points, particularly 66, on the walls surfaces and used as three-dimensional single point optical displacement measurements. The green dots in Fig. 3b indicate the positions of the markers.

2.3 Experimental Results

As previously described (Sect. 2.2), the dynamic input N has been applied at the base of the model with three incremental scale factors: $0.25 N$, N and $1.2 N$. Each dynamic test has been followed by a random noise input base acceleration to allow for structural identification. For more details see [6].

The first dynamic test ($0.25 N$) did not cause any visible damage to the structure. On the other hand, the test with 100% seismic intensity level caused a significant damage scenario, mainly located in the lower part of the structure, due to combined effects of the horizontal and vertical components of the seismic load. Figure 4 shows two out of four elevation views of the model with the observed damage.

During the test, a vertical detachment of the crack B-1 and B-2 has been clearly observed, followed by a small residual sliding between the upper and the lower parts of the structure. As a consequence, a mixed mode of fracture has been observed on the B façade: Mode I fracture, as the vertical opening if solid along a bed joint;

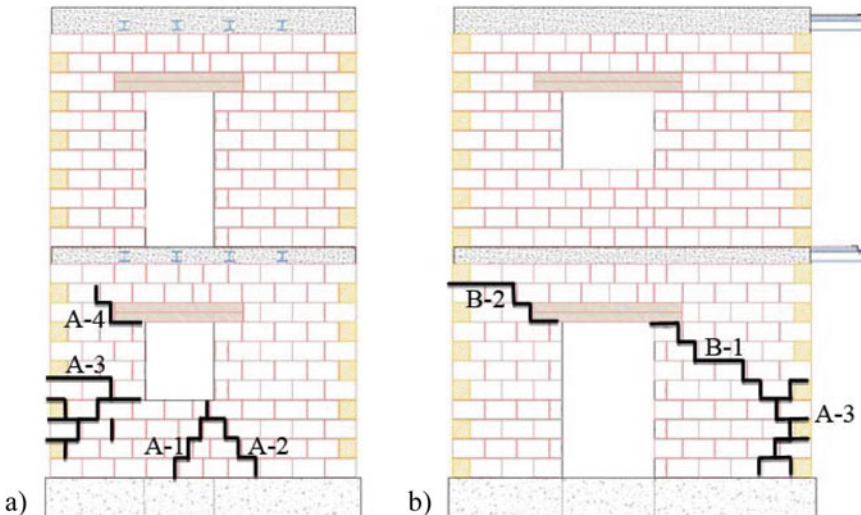


Fig. 4 Damage scenario for 100% of the seismic intensity level input: (a) A façade Fig. 1a; (b) B-façade Fig. 1b

Mode II fracture with a sliding on the bed joints due to shear loads. This aspect is also highlighted by the displacement time series recorded during the tests by the 3D motion capture system. Figure 5 shows the vertical (Δz) and horizontal (Δx) relative displacement time series extracted from the markers B61-B21, B51-B31, B52-B32 and B62-B22. The vertical opening of fracture is highlighted by the peak values in Δz graph, which reach almost 7 mm, while the residual sliding observed in the Δx graph is of about 2 mm. It is worth noting that the input acceleration data (Fig. 2) and the output displacement observations (Fig. 5) are not recorded with the same acquisition system so that they appear asynchronous.

Finally, the test with 120% seismic intensity level did not cause any further visible cracks in the model.

3 Simplified Rocking Model

The dynamic response of masonry structures is in some cases suitable to be analysed through nonlinear dynamics of rigid bodies [8–11]. In this context, other papers can be found in literature concerning the influence of the vertical acceleration on the dynamics of rectangular rigid bodies [12, 13], in which the different motion possibilities of liftoff and/or slip are explained.

In order to evaluate the influence of the vertical component in the described shaking table test, a preliminary analytical rocking model has been investigated. Starting from the observed damage, the idea is to verify the possibility of rocking

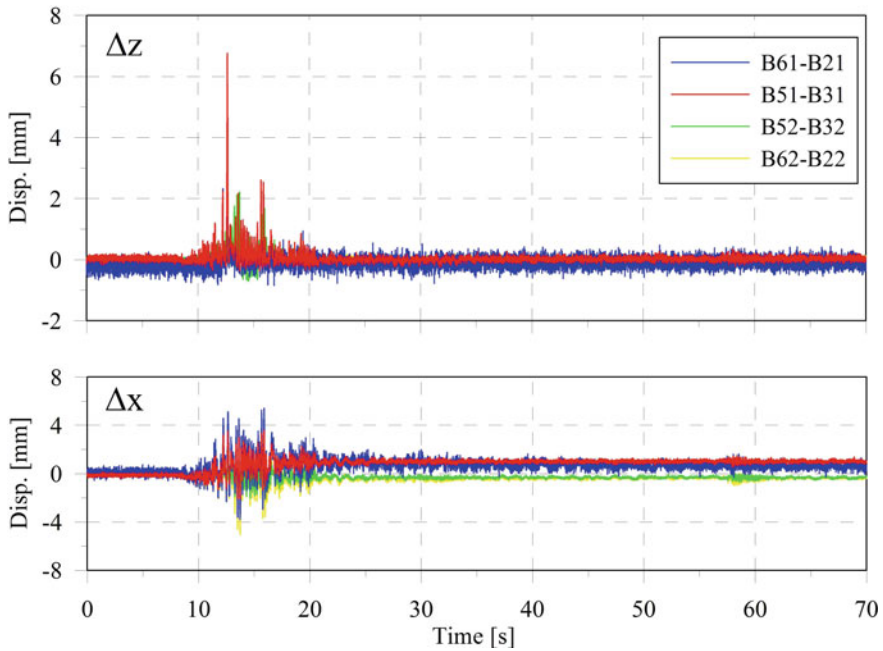


Fig. 5 Dynamic measurement of Δx and Δz displacements between the targets B61-B21, B51-B31, B52-B32 and B62-B22 of Fig. 1b for 100% of the seismic intensity level input

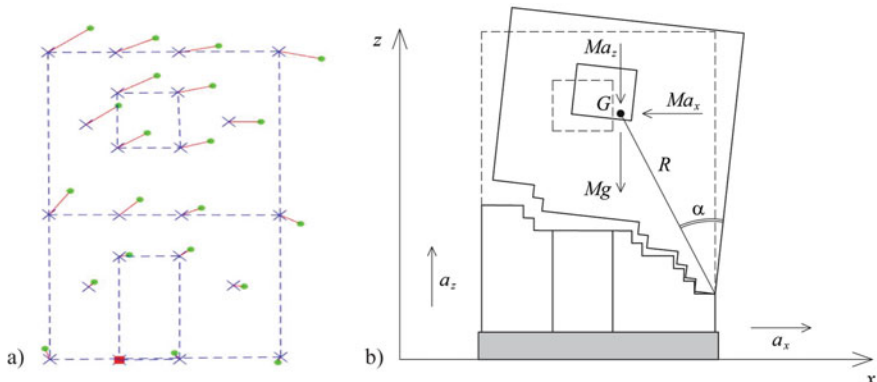


Fig. 6 (a) Displacements field detected by the 3D motion capture measurement system in the instant frame related to rocking motion of the model upper part. (b) Reference scheme for the rocking analysis of B-façade

motion activation with and without the presence of vertical action. The portion of structure participating which was moved in rocking has been identified through the analysis of the dynamic displacements field detected by the 3D motion capture measurement system, together with the observation of the damage pattern (Fig. 6a).

The model is referred only to the B-façade of the masonry building and is analysed in its plane. With reference to Fig. 6b, the liftoff activating conditions of the detached rigid body to horizontal and vertical ground motion are derived from the equilibrium of the overturning moment and stabilizing moment around the indicated pivoting edge

$$M(g + a_z)R \sin \alpha < M|a_x|R \cos \alpha, \quad (1)$$

where M is the mass of the block, g is the gravity acceleration, a_x and a_z are the horizontal and vertical ground acceleration, respectively. The values of a_x are taken in their absolute values to be in the safe side. Being the model analysed only in the B-façade plane, the mass M has been estimated considering the right ratio of the slabs' weights, comprising the constituent materials and the additional masses fixed on them. Finally, the relation (1) can be reduced in the following ratios ρ_1 and ρ_2 related to the activation conditions of liftoff motion, with and without considering the vertical acceleration, respectively,

$$\rho_1 = |a_x| / [(g + a_z) \tan \alpha] > 1 \quad (2)$$

$$\rho_2 = |a_x| / [g \tan \alpha] > 1 \quad (3)$$

Figure 7 shows the values of the ratios ρ_1 and ρ_2 evaluated from the acceleration time series and the geometrical properties of the model. The overcoming of the threshold $\rho_1 = 1$ in Fig. 7a points out the activation of the rocking motion in presence of the vertical acceleration, while in Fig. 7b the value $\rho_2 = 1$ is not reached. Finally, it is conceivable to believe that the particular dynamic response of the masonry building model on shaking table can be ascribed to the presence of the vertical component of the seismic action.

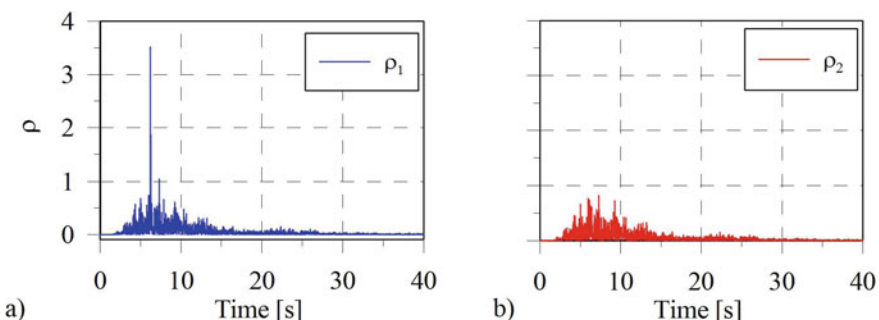


Fig. 7 Evaluation of the ratios ρ_1 (a) and ρ_2 (b) in presence and in absence of the vertical acceleration, respectively.

4 Conclusions

In this paper the first results obtained by shaking table experimental tests on a two-storey masonry building model have been presented. The dynamic tests have been performed using all three seismic input accelerations time series in order to investigate the influence of the vertical component on the dynamic structural response. A preliminary analysis of the experimental results has pointed out the influence of the vertical acceleration component on the dynamic response. A simplified analytical model based on the rocking behaviour of rigid bodies has confirmed this result.

Acknowledgements The Authors gratefully acknowledge the financial support of the “Fondazione Cassa di Risparmio di Perugia” that funded this study through the project “Casa Sicura: tecniche antisismiche innovative nella tradizione delle costruzioni” (Project Code 2017.0233.021).

References

1. Addessi, D., Gatta, C., Vestroni, F.: Dynamic response of a damaging masonry wall. *Procedia Eng.* **199**, 152–157 (2017)
2. Toti, J., Gattulli, V., Sacco, E.: Nonlocal damage propagation in the dynamics of masonry elements. *Comput. Struct.* **152**, 215–227 (2015)
3. Breccolotti, M., Materazzi, A.L.: The role of the vertical acceleration component in the seismic response of masonry chimneys. *Mater. Struct.* **49**(1–2), 29–44 (2016)
4. Bayraktar, A., Hökelekli, E., Meral Halifeoğlu, F., Mosallam, A., Karadeniz, H.: Vertical strong ground motion effects on seismic damage propagations of historical masonry rectangular minarets. *Eng. Fail. Anal.* **91**, 115–128 (2018)
5. Dolce, M., Ponzo, F.C., Moroni, C., Nigro, D., Goretti, A., Giordano, F., De Canio, G., Marnetto, R.: 3D dynamic tests on 2/3 scale masonry buildings retrofitted with different systems. In: Proceedings of the 14th World Conference on Earthquake Engineering, Beijing, pp. 12–17 (2008)
6. Meoni, A., D’Alessandro, A., Cavalagli, N., Gioffrè, M., Ubertini, F.: Shaking table tests on a masonry building monitored using smart bricks: damage detection and localizations. *Earthquake Engng. Struct. Dyn.* **48**(8), 910–928 (2019)
7. Mongelli, M., Roselli, I., De Canio, G., Ambrosino, F.: Quasi real-time FEM calibration by 3D displacement measurements of large shaking table tests using HPC resources. *Adv. Eng. Soft.* **120**, 14–25 (2016)
8. Azevedo, J., Sincraian, G., Lemos, J.V.: Seismic behaviour of blocky masonry structures. *Earthq. Spectra* **16**(2), 337–365 (2000)
9. Al Shawa, O., de Felice, G., Mauro, A., Sorrentino, L.: Out-of-plane seismic behaviour of rocking masonry walls. *Earthquake Engng. Struct. Dyn.* **41**, 949–968 (2012)
10. Makris, N., Vassiliou, M.F.: Planar rocking response and stability analysis of an array of free-standing columns capped with a freely supported rigid beam. *Earthquake Engng. Struct. Dyn.* **42**(3), 431–449 (2013)
11. Severini, L., Cavalagli, N., DeJong, M., Gusella, V.: Dynamic response of masonry arch with geometrical irregularities subjected to a pulse-type ground motion. *Nonlinear Dynam.* **91**(1), 609–624 (2018)

12. Taniguchi, T.: Non-linear response analyses of rectangular rigid bodies subjected to horizontal and vertical ground motion. *Earthquake Engng. Struct. Dyn.* **31**, 1481–1500 (2002)
13. Hao, H., Zhou, Y.: Dynamic response of rigid blocks to simultaneous horizontal and vertical ground shock. *Adv. Struct. Eng.* **15**(7), 1069–1082, (2012)

Quantifying Rate-Dependence of a Nonlinear Hysteretic Device



Marco Antonelli, Biagio Carboni, Walter Lacarbonara Davide Bernardini, and Tamás Kalmár-Nagy

Abstract Hysteretic systems are extensively used in vibration control and in a wide range of mechanical problems. The first issue is to know whether the system is rate-dependent or not. In order to address the problem for a specific device employed for vibration isolation, laboratory measurements using a uniaxial testing machine are performed. The device is represented by a wire rope spring. Different types of tests are conducted in displacement control acquiring the device restoring force: cyclic ramps with increasing amplitudes and displacement time histories reobtained applying simple and random homeomorphisms to the ramp histories. The rate-dependence is evaluated comparing the restoring forces measured for the different tests and estimating a quantitative parameter which is chosen to measure the rate-dependence degree.

Keywords Experimental hysteresis · Rate-dependence · Nonlinear device · Wire rope testing · Asymmetric restoring force

1 Introduction

The hysteretic cycles exhibited by short wire ropes subject to coupled bending tensile loads are currently exploited for applications in the field of vibration control [7]. An important aspect consists in establishing the rate-dependence of the restoring force to properly address the device modeling. By definition, a system is rate-independent if the restoring force does not depend on the loading rate and its responses are invariant with respect to invertible transformations of the

M. Antonelli · B. Carboni · W. Lacarbonara · D. Bernardini

Department of Structural and Geotechnical Engineering, Sapienza University of Rome, Rome, Italy

e-mail: antonelli.133537@studenti.uniroma1.it; biagio.carboni@uniroma1.it

T. Kalmár-Nagy

Department of Fluid Mechanics, Faculty of Mechanical Engineering, University of Technologies and Economics, Budapest, Hungary

time scale [1]. A survey of rate-independent systems can be found in various sources [2]. The selection of a rate-dependent or rate-independent model is very important for hysteretic systems [3, 4]. A quantification of rate-dependence is crucial to understand the system behavior and which type of constitutive model best represents its response. In order to check the rate-dependence of a system, a general transformation of the time scale t is denoted by $t_{\text{new}} = \phi(t)$. According to [5], a rate-dependence measure can be defined as follows:

$$\varepsilon = \left| \left| \beta_t [\mathbf{u}(\phi(t)) ; x_0] - \alpha_{\phi(t)} [\mathbf{u}(t) ; x_0] \right| \right|. \quad (1)$$

In Eq. (1), ε represents a rate-dependence parameter, which lies in a neighborhood of zero if the system is rate-independent, while $\alpha_t [\mathbf{u}(t) ; x_0]$ and $\beta_t [\mathbf{u}(\phi(t)) ; x_0]$ indicate the original experimental output of the system and that obtained applying the time transformation, respectively (i.e., the homeomorphism), or vice versa. The rate-dependence parameter may be evaluated on the basis of two different experimental outputs, by which another parameter is varied (i.e., velocity). Whereas in [5] analytical and numerical tests about the accuracy of the measure (1) were discussed, in this paper a possible way to estimate ε by means of experimental data is proposed.

2 Test Apparatus and Experimental Campaign

The system under consideration is shown in Fig. 1a and it consists of two plates connected at their edges with two steel continuous wire ropes. The device is manufactured by Enidine [6] and is used for isolation purposes for vertical or horizontal base excitations. The tests are performed with a Zwick Roell testing machine under displacement control and are arranged in 4 groups for this study.

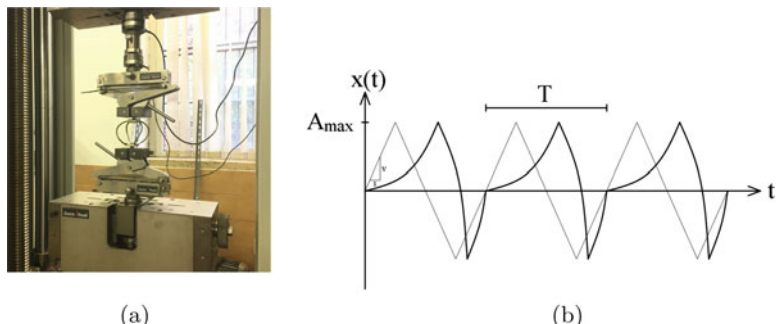


Fig. 1 (a) The specimen initial configuration and (b) Displacement time histories: the thin line shows the ramp-periodic input, while the thick line shows the input displacement history obtained with the simple homeomorphism applied to a single cycle and then repeated

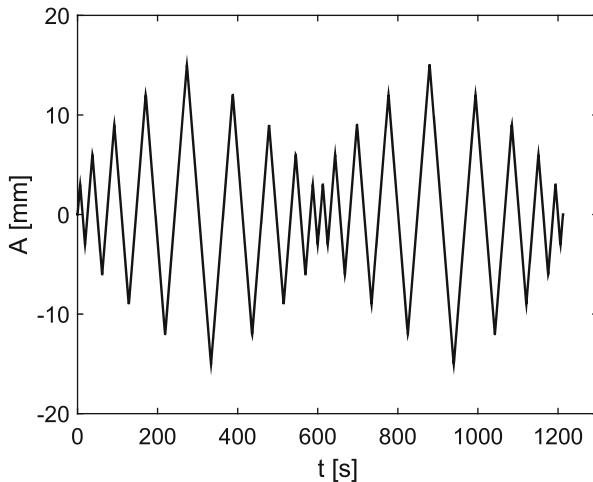


Fig. 2 Input displacement vs. time of Test18 in Group D

Table 1 Tests of Group A and B

Group ID	A			B					
Test ID	Test01	Test02	Test03	Test04	Test05	Test06	Test07	Test08	Test09
A_{\max} [mm]	5	10	15	5	10	15	5	10	15
v [mm/s]	0.5	0.5	0.5	1.0	1.0	1.0	10.0	10.0	10.0

Group A consists of cyclic ramps with different amplitudes $A_{\max} = \{5, 10, 15\}$ mm and constant velocity $v = 0.5$ mm/s (Fig. 1b thin line). Group B consists of ramps with amplitudes $A_{\max} = \{5, 10, 15\}$ mm and velocities $v = \{1.0, 10.0\}$ mm/s which are obtained by applying simple linear homeomorphisms to the loading histories of Group A. Group C consists of cycles obtained applying linear (Fig. 1b thick line) and random homeomorphisms on the third test of Group A, which is associated with $A_{\max} = 15$ mm. Finally, Group D contains cyclic increasing-decreasing ramp tests, characterized by different increment-decrement ΔA_{\max} at each cycle and velocities v (see Fig. 2).

2.1 Results of Group A and Group B Tests

The tests of Group A are assumed as reference tests and are listed, together with Group B, in Table 1. The maximum velocity and displacement are chosen according to the Zwick Roell machine and the device limits. Group B represents very simple homeomorphisms applied to the reference tests of Group A.

The results of the Group A tests are presented in Fig. 3, for the three different amplitudes. The outcomes show that the device has a strong hardening behavior

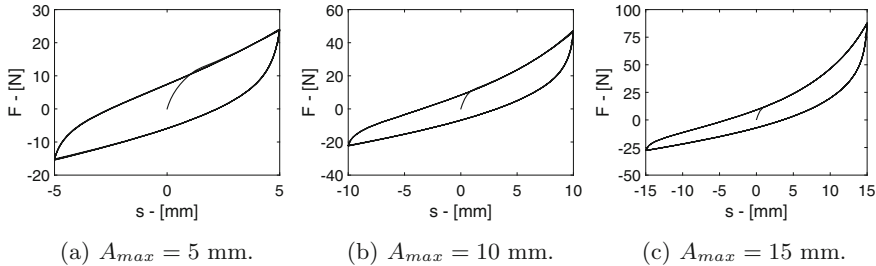


Fig. 3 Experimental force-displacement cycles for Group A tests. (a) $A_{\max} = 5$ mm. (b) $A_{\max} = 10$ mm. (c) $A_{\max} = 15$ mm

Table 2 Tests of Group C

Test ID	Test10	Test11	Test12	Test13	Test14
Homeomorphism	Simple	Simple	Simple	Simple	Random
Coefficient α	0.2	0.4	0.6	0.8	—

for positive displacements (i.e., coupled tensile and bending forces on the ropes) which becomes more pronounced at larger amplitudes. For negative displacements (i.e., coupled compression and bending forces on the ropes) the device exhibits a softening behavior. The nonsymmetric restoring force is expected to provide a global softening behavior for low amplitudes that evolves in hardening when a threshold amplitude is exceeded.

2.2 Results of Group C

Tests of type C (see Table 2) are homeomorphic transformations of Test03 (see Table 1) defined by the following time rescaling:

$$t_{\text{new}} = t_{i+1} - \frac{t_{i+1} - t_i}{1 + \frac{1-a}{a} \frac{t-t_i}{t_{i+1}-t}}. \quad (2)$$

It turns out that when $a < 0.5$, the new transformed time is such that the displacement history is stretched along the positive loading direction and it is contracted in the remaining part of the cycles, while for $a > 0.5$ the opposite behavior occurs. If $a = 0.5$, Eq. (2) reduces to the identity transformation, thus the test reduces to the reference one.

All transformations are applied to the first cycle and then repeated 5 times as for the tests of Group A. Figure 1b (thick line) shows the homeomorphism defined by Eq. (2) for $a = 0.2$. Besides the simple homeomorphisms defined by (2), more refined random homeomorphisms are used to test the rate-dependence. The random homeomorphisms are defined by Eq. (3) where the reference time of Test03 is

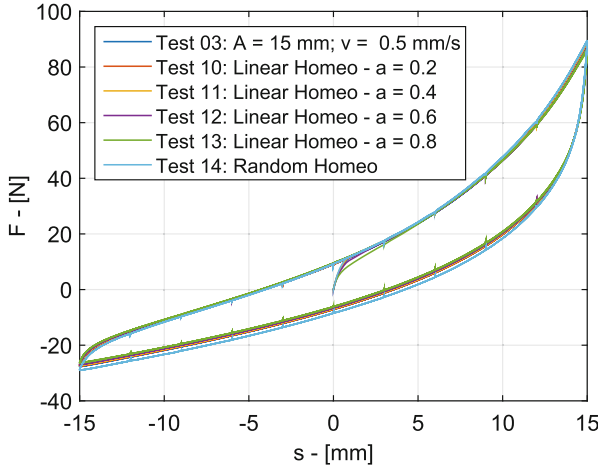


Fig. 4 Experimental force-displacement cycles for Group C tests

denoted by t and the rescaled time is \tilde{t} . Vector r contains $N - 1$ scalars where N represents the number of recorded time instants. The values assumed by r are chosen according to a Gaussian distribution in the range $[0, 1]$, so that the resulting homeomorphisms are Gaussian random homeomorphisms:

$$\tilde{t}_{i+1} = \tilde{t}_i + 2 r_i (t_{i+1} - t_i), \quad i = 1, \dots, N - 1 \quad (3)$$

Concerning the test results, as shown in Fig. 4, the restoring force histories obtained with the simple homeomorphisms are very similar anticipating an essential rate-independent behavior. Only the measurements performed taking into account the random homeomorphism look a little different from the others.

2.3 Results of Group D

The tests within Group D are performed using an increasing-decreasing ramp displacements time history. They are characterized by a number of growing cycles with a constant amplitude variation ΔA at each cycle (see Fig. 2). All tests reach the maximum amplitude of 15 mm and then reduce their amplitude with the same ΔA . These displacement histories are repeated twice or five times. They are also performed for different speeds according to Table 3.

The results of the Group D tests are presented in Fig. 5. Significant differences of the restoring force between the homeomorphic tests cannot be appreciated by the visual inspection of the plots. Whereas visual inspection of the plots which describe the experimental results roughly suggests a rate-independent behavior of the system under consideration, the problem of a precise, quantitative assessment

Table 3 Tests of group D

Test ID	Test15	Test16	Test17	Test18	Test19	Test20	Test21
ΔA [mm]	2.5	2.5	2.5	3	3	3	3
v [mm/s]	0.5	1.0	10.0	0.5	1.0	10.0	10.0
Repetitions	2	2	2	2	2	2	5

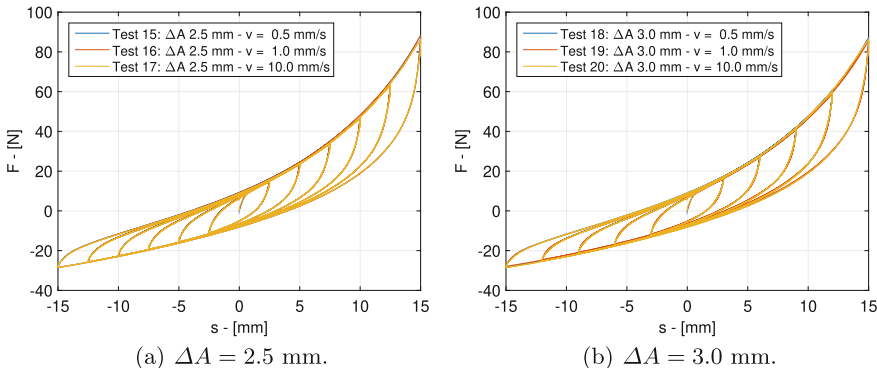


Fig. 5 Experimental force-displacement cycles for the tests of Group D. (a) $\Delta A = 2.5\text{ mm}$. (b) $\Delta A = 3.0\text{ mm}$

according to measure (1), based on use of experimental data is addressed next. This is thus a natural sequel of the approach presented in [5] which made use of numerical simulations only.

3 Rate-Dependence Matrices

Having carried out several experimental tests, a rate-dependence test can be performed for each pair of tests whose loading histories are related by a given homeomorphism. A possible rate-dependence measure of the experimental tests (i , j) can be defined according to:

$$\varepsilon_{ij} = \frac{1}{N} \sum_{k=1}^N \frac{F_i(s_k) - F_j(s_k)}{\max(|F_i(s_k)|, |F_j(s_k)|)}, \quad (4)$$

where N is number of points in which the force-displacement records are interpolated, s_k represents the k th input displacement to which the force $F_i(s_k)$ of the i th test is acquired. Interpolations are necessary to have vectors of the same length and the restoring forces F_i and F_j must be computed at the same displacement s_k .

Computing (4) for each pair of tests, the *rate-dependence matrix* ε is obtained. Given the strong asymmetry between tensile and compressive responses of this system, it is useful to compute the following two similar matrices:

$$\varepsilon_{ij}^{C,T} = \frac{1}{N} \sum_{k=1}^N \frac{F_i(s_k) - F_j(s_k)}{\max(|F_i(s_k)|, |F_j(s_k)|)}, \quad s_k < 0, \quad s_k \geq 0. \quad (5)$$

In Eq. (5) the displacement sign convention for s_k assumes that they are positive when the deformations are extending the wire ropes and vice versa. Therefore the matrices ε_{ij}^C and ε_{ij}^T define the *compression rate-dependence matrix* and the *tension rate-dependence matrix*, respectively (notice that the evaluation of rate-dependence is done in terms of restoring forces). It turns out that all these matrices are skew-symmetric by definition. Tables 4, 5 and 6 show the matrices computed from the experimental results. Moreover, the tables show also an additional row defined according to:

$$E_j = \frac{\sum_{i=1}^m |\varepsilon_{ij}|}{m}, \quad j = 1, \dots, m, \quad (6)$$

where m denotes the number of tests considered in the comparison.

Table 4 Rate-dependence matrix containing the parameters ε_{ij} : F_i, F_j interpolated with $N = 2851$; the matrix norm is equal to 6.16%

Test ID	T03	T06	T09	T10	T11	T12	T13	T14
T03	0	0.049	0.014	-0.019	-0.044	-0.063	-0.100	0.083
T06		0	-0.028	-0.060	-0.081	-0.097	-0.130	0.044
T09			0	-0.027	-0.056	-0.075	-0.111	0.061
T10				0	-0.031	-0.051	-0.090	0.095
T11					0	-0.028	-0.071	0.113
T12						0	-0.053	0.126
T13							0	0.156
T14								0
$E [\%]$	4.9	6.1	4.7	4.7	5.3	6.2	8.9	8.5

Table 5 Compression rate-dependence matrix containing the parameters ε_{ij}^C : F_i, F_j interpolated with $N = 2851$; the matrix norm is equal to 5.91%

Test ID	T03	T06	T09	T10	T11	T12	T13	T14
T03	0	0.058	0.046	-0.019	-0.042	-0.060	-0.101	0.054
T06		0	-0.005	-0.069	-0.089	-0.105	-0.141	-0.004
T09			0	-0.058	-0.077	-0.093	-0.129	0.006
T10				0	-0.028	-0.048	-0.090	0.071
T11					0	-0.025	-0.069	0.093
T12						0	-0.052	0.110
T13							0	0.150
T14								0
$E [\%]$	4.7	5.9	5.2	4.8	5.3	6.2	9.1	6.1

Table 6 Tensile rate-dependence matrix containing the parameters ε_{ij}^T : F_i , F_j interpolated with $N = 2851$ points; the matrix norm is equal to 6.41%

Test ID	T03	T06	T09	T10	T11	T12	T13	T14
T03	0	0.041	-0.015	-0.019	-0.045	-0.065	-0.099	0.109
T06		0	-0.048	-0.053	-0.075	-0.090	-0.120	0.088
T09			0	0.000	-0.037	-0.059	-0.096	0.109
T10				0	-0.034	-0.054	-0.089	0.117
T11					0	-0.032	-0.072	0.130
T12						0	-0.054	0.140
T13							0	0.161
T14								0
E [%]	4.9	6.4	4.6	4.6	5.3	6.2	8.6	10.7

The mean values E_j of the parameters ε_{ij} indicate a norm of the rate-dependence behavior. In fact, Eq. (6) provides the percent mean difference in terms of restoring force of a given displacement history with respect to the associated homeomorphic time transformed histories. The final norm of the rate-dependence matrix is defined as the mean of the values E_j which turns out to be equal to 6.16%, 5.91%, and 6.41% for matrices Tables 4, 5 and 6, respectively. The averages of the parameters ε show an upper bound close to 10%. The values obtained for the tensile branches are slightly larger denoting a sensible rate-dependent behavior when the device becomes hardening due to the coupled bending and tensile forces arising in the ropes. However, in the range of the investigated velocities, the behavior of the system can be considered practically rate-independent since the difference in terms of restoring force is negligible for the overall system dynamics.

4 Conclusions

In this work the problem of obtaining a quantitative measure of the possible rate-dependence behavior of a given system by means of experimental tests has been addressed. The average value of E_j in (6) can be considered an experimental counterpart of the measure (1) proposed in [5]. The application of this procedure to the tension-compression tests of a wire rope device has shown that the method can be successfully applied to other real systems. Refinements of the analysis by focusing attention to restricted parts of the response (i.e., tension as opposed to compression) were also explored. Further applications of this procedure to other systems will be described in future works.

Acknowledgments The research reported in this paper was partially supported by the PRIN Program of the Italian Ministry of Science and Education (Grant N. 2017L7X3CS_002) and by the Higher Education Excellence Program of the Ministry of Human Capacities in the frame of the Water Sciences & Disaster Prevention research area of BME (BME FIKP-VÍZ), and by

the National Research, Development and Innovation Fund (TUDFO/51757/2019-ITM, Thematic Excellence Program).

References

1. Pokrovskii, A., Sobolev, V.: A naive view of time relaxation and hysteresis. In: Singular Perturbations and Hysteresis, vol. 117. Society for Industrial and Applied Mathematics, Philadelphia (2005)
2. Mielke, A.: Evolution of rate-independent systems. *Evol. Equ.* **2**, 461179 (2005).
3. Bernardini, D., Rega, G.: Evaluation of different SMA models performances in the nonlinear dynamics of pseudoelastic oscillators via a comprehensive modeling framework. *Int. J. Mech. Sci.* **130**, 458–475 (2017)
4. Carboni B., Lacarbonara W., Brewick, P.T., Masri, S.F.: Dynamical response identification of a class of nonlinear hysteretic systems. *J. Intell. Mater. Syst. Struct.* **29**, 2795–2810 (2018). <https://doi.org/10.1177/1045389X18778792>
5. Kalmár-Nagy, T., Bernardini, D., Carboni, B., Lacarbonara, W.: Quantifying rate dependence of hysteretic systems. *Procedia Eng.* **199**, 1447–1453 (2017)
6. Latvis Jr, M.P.: U.S. Patent No. 6,244,579. Washington, DC: U.S. Patent and Trademark Office (2001)
7. Lacarbonara, W.: Nonlinear Structural Mechanics: Theory, Dynamical Phenomena and Modeling. Springer, New York (2013)

Application of Photoelasticity to Some Nonlinear Dynamic Problems and Stress State Analysis in Dams: A Brief Overview Inspired by the Results of Prof. Vlatko Brčić



Katica R. (Stevanović) Hedrih, Stanko V. Brčić, and Stepa Paunović

Abstract Photoelasticity is a useful method for experimental testing of structures, which can provide a direct visual insight into the stress state in a tested model. Photoelastic method has been used in various types of problems, and this chapter provides a brief overview of the development and application of this method, from its early stages and static applications, to some problems of nonlinear dynamics and stress state analysis in dams. Since there is relatively obscure literature on experimental dam testing, and prof. V. Brčić (1919–2000) has published several papers regarding this topic, although done several decades ago, these papers provide a solid basis for photoelastic dam testing and are referenced here briefly. The improvements of the method from its beginnings to its current state are also summarized, and many recent researches on practical applications of the photoelastic method to some nonlinear dynamics problems are pointed out.

Keywords Photoelastodynamics · Photoelastic testing · Dams

1 Introduction

Photoelasticity is one of the few methods for experimental testing of structures, which provides a direct visual insight into the stress state in a tested specimen. It is a very useful method with a broad application field. The aim of this chapter is to give a brief overview of the development of the photoelasticity and its application to the stress state analysis in some nonlinear dynamics problems, with a special emphasis

K. R. (Stevanović) Hedrih · S. Paunović (✉)

Department of Mechanics, Mathematical Institute of the Serbian Academy of Sciences and Arts, Belgrade, Serbia

e-mail: khedrih@sbb.rs

S. V. Brčić

Faculty of Civil Engineering, University of Belgrade, Belgrade, Serbia

on testing of dams, since it has played an important role in dam design in the past and it is still a useful method for experimental testing of dams even today.

However, experimental testing and construction of dams are very costly and relatively rare, thus the literature on this subject is relatively obscure. Still, in the second half of the twentieth century many dams were built in Yugoslavia (now the Western Balkans region) and many of them were designed and/or tested by prof. Vlatko Brčić, a prominent researcher and engineer of that time, who afterwards published several papers regarding experimental testing of dams, which have influenced the development of the photoelastic method and its practical application. Prof. Brčić was also one of the first researchers to combine photoelastic method with holographic interferometry, but nevertheless, all these papers are only concerned with *static* stress analysis, due to technical limitations of that time.

However, over the last several decades there has been a tremendous technological advancement which has also enabled the improvement of photoelastic method. For instance, now the maps of isoclinics and isochromatics can be captured in much more detail [1] and also some new optically active materials are used [2], but the main difference is that now digital polariscope is used and image acquisition and processing is done automatically. Therefore, testing process has become much more precise, significantly faster and almost completely automated through the use of image acquisition and processing, RGB interferometry, and 3D printing (e.g., [3]). These advances, combined with the development of high-speed cameras, made photoelastic analysis of dynamic problems possible.

In this chapter, a brief overview of the development and application of the photoelastic method to the stress state analysis in dynamic problems is presented, including the dynamic analysis of dams. However, although prof. Brčić published papers regarding only static analysis of dams, these papers are also referenced here because they present valuable material on the photoelastic dam testing. Therefore, the chapter is organized as follows: first the key points of the invention and the development of the method are presented, from its early stages and static stress analysis applications, to its more recent state, pointing out the main advancements and improvements. In the subsequent section the application to dynamics problems including some complex phenomena and dynamic dam testing is presented, and at the end the concluding remarks are given.

2 Photoelasticity: Development and Dam Testing Applications

2.1 *Invention and Early Development of Photoelasticity*

Photoelasticity (in its current form) has been invented at the beginning of the twentieth century, and it is based on birefringence and stress-optical activity of some translucent materials. Since it is a very convenient experimental testing method,

it quickly became widely used and developed in the middle of the last century. However, since the image acquisition technology was relatively limited at that time, the application of the photoelasticity was restricted to static analysis only. Nevertheless, many practical applications of this method arose, one of which was in the process of design and experimental testing of dams. And as it has been already mentioned, many dams in Western Balkans were designed and tested by Professor V. Brčić around the middle of the twentieth century.

2.2 Static Photoelastic Analysis of Dams and Prof. Brčić's Contribution

Prof. Dr. Eng. Sci. and Dipl. Math. Vlatko Brčić (September 16, 1919, Varaždin, Croatia, Yugoslavia—August 22, 2000, Belgrade, Serbia) was a renowned and very active mathematician, engineer, professor, researcher, and scientist, and he was acknowledged worldwide (for instance, he held a course in holographic interferometry at the International Centre for Mechanical Sciences in Udine, Italy, in 1974). Prof. Brčić has conducted numerous researches of dams and published some of these results, providing a solid foundation for dam research and design. A more detailed review of these papers can be found in [4], while only the key points of some of them are presented here.

In the beginning of his professional career, Prof. Brčić used photoelastic analysis to investigate the stress concentrations in dams with openings, depending on the opening position in the dam body [5]. The analyzed models and the corresponding isochromatics are shown in Fig. 1a [4]. Afterwards he broadened this research to analyze the influence of the foundation soil on the stress concentrations, while treating the soil as a homogeneous elastic continuum [6]. Isochromatics are presented in Fig. 1b.

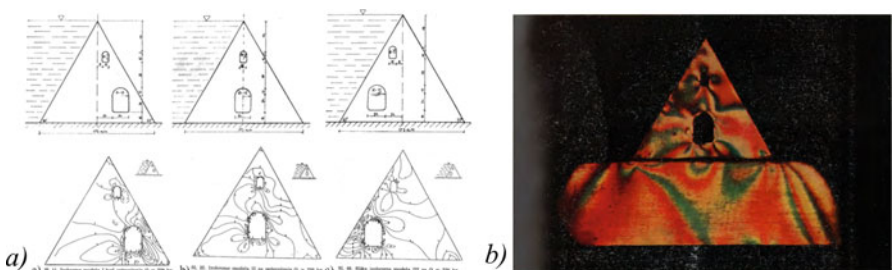


Fig. 1 (a) The variant positions of the openings in a gravity dam and the corresponding maps of isochromatics [4], (b) The isochromatics for the model of the dam and the elastic soil [6]

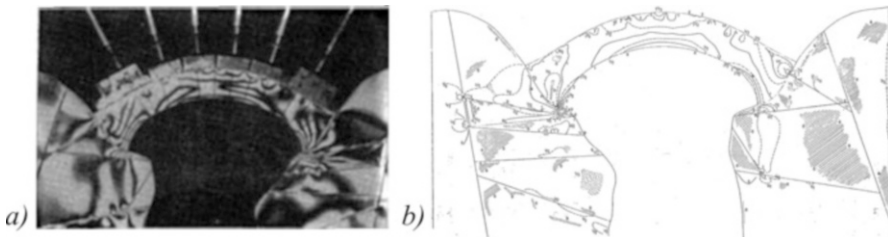


Fig. 2 Isochromatics for Mratinje dam models; (a) photograph, (b) scheme [8]

Later on, he used the acquired knowledge to analyze the stress state in the buttress dam of the hydroelectric power plant Bajina Bašta in detail [7]. This analysis gave valuable insight in stress state inside the dam buttresses and improved the dam design process. Later still, prof. Brčić used photoelasticity to investigate the influence of discontinuities in bedrock supporting a dam [8]. Therein, two cases were studied—the Grančarevo dam and the Mratinje dam (220 m high). The main focus was modeling and examination of cracked (discontinuous) supporting bedrock and its influence on the stress state inside the dams. The resulting isochromatics are shown in Fig. 2.

As it can be seen, even in its beginnings, photoelasticity was successfully used in solving some very complex engineering problems, including the design and testing of several types of dams. However, these investigations were restricted to static analysis in early stages of the method development, and it was only after technological advancements took place that the photoelastic testing could be broadened to dynamic problems.

2.3 *Improvements of the Method and Its Contemporary State*

Over the second half of the last century, photoelasticity was much improved, mainly by combining it with other optical methods and incorporating some technological advancements and inventions of that time, regarding materials as well as the image capturing and processing methods. For instance, prof. Brčić contributed to combining the holographic interferometry with the photoelastic testing, thus overcoming one of its main drawbacks [9]. Also, new artificial materials such as different plastics, resins or alloys, even glass [2], made it possible to investigate some more complex phenomena. This has led to the development of photoviscoelasticity and photoplasticity [4], or even to the photoelastic testing of the influence of structures' self-weight [10].

However, the main advances were made in the field of computer aided testing, image acquisition and processing, greatly improving the quality and precision of the results and efficiency of the testing process, which is now almost completely automated [11]. Also, 3D printing is now used for model production, which enabled

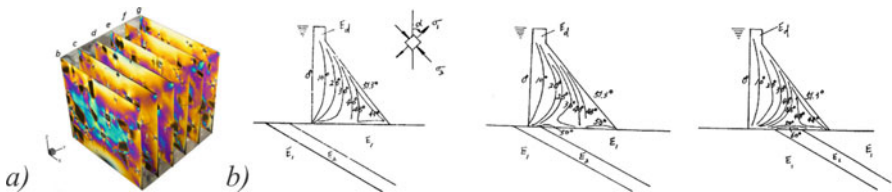


Fig. 3 (a) Isochromatics in a 3D printed specimen of concrete tested by stress freezing photoelastic method [3], (b) isoclinics in the tested gravity dam for the three considered positions of a discontinuity in the foundation soil [14]

detailed testing of highly complex structures, thus overcoming another major drawback of early photoelasticity. This has been done for instance in [11], or in [3], presented in Fig. 3a, where the photoelastic testing of a 3D model of highly heterogeneous material such as concrete was conducted. All these improvements made it possible to use photoelastic analysis in both materially and geometrically nonlinear problems. It has been successfully applied to some complex problems regarding fracture mechanics [12], composite and porous materials stress analysis [13], but also dam testing—as has been done in [14] for instance, results of which are shown in Fig. 3b. In that paper the influence of a bedrock on the stress state in one gravity dam in China was investigated. Although done recently (2012), this research highly resembles the work of Prof. Brčić done several decades ago. Photoelastic method can also be used for nondestructive stress analysis of structures *in situ*, by using some optically active coatings, which combined with modern computer equipment allows for a real-time stress analysis of structures [15].

However, the main broadening of the field of application of the photoelastic method was due to the invention of high-speed cameras, which enabled the application of this method to dynamic and transient problems, while still having the capacity to deal with both material and geometrical nonlinearities. This has made photoelasticity an indispensable method for experimental stress testing in nonlinear dynamics problems.

3 Contemporary Use of Photoelasticity in Nonlinear Dynamics

In this century, photoelasticity has been used in different fields of dynamics. One application example is the investigation of stress wave propagation in solids, as has been done in [16–18] for instance. Figure 4a shows how a stress wave propagates through a medium with discontinuities [11], and Fig. 4b shows how a stress wave propagates through a series of disks [18]. Photoelasticity was also used to investigate the dynamic fracture and crack propagation in material, as reported in [19] or in [20]

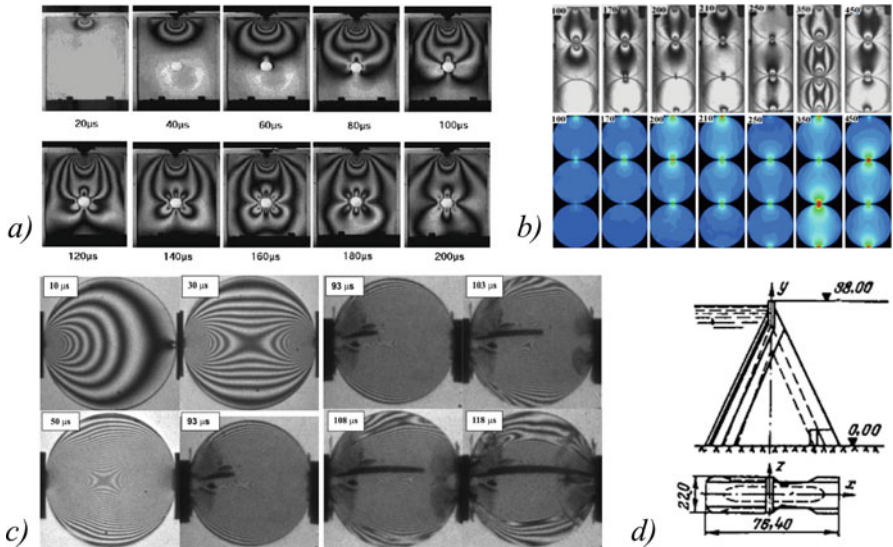


Fig. 4 (a) Stress wave propagation in an elastic medium with a discontinuity (a hole), in the first 200 μs [11], (b) Stress wave propagation analysis in a chain of 3 disks, from 100 to 450 μs [18], (c) the crack formation and its propagation in a concrete cylinder under dynamic load [20], (d) Analysis of vibration and stress wave propagation in a massive concrete dam [21]

and presented in Fig. 4c. There were also photoelastic studies on how seismic waves propagate through a gravity dam body (e.g., [21], presented in Fig. 4d).

Another complex nonlinear problem that photoelasticity has successfully been applied to is the contact analysis. In fact, photoelastic testing is the only available method to directly experimentally determine the contact stresses. Many forms of contact analysis were performed with photoelastic method. For instance, in [22] the influence of inclusions of different shapes on stress field in the surrounding matrix of a composite material was investigated (Fig. 5a)). Also, simultaneous multiple body contact can be analyzed by the photoelastic method, as shown in [23] (Fig. 5b)). Moreover, photoelastic analysis has been used to solve the problems of gear contact, one of very complex and highly nonlinear dynamic problems. There are many papers on its application to the design process and model testing (e.g., [7, 15]), but through the use of reflexive polariscope, also *the real parts and gears* can be tested by the photoelastic method, as has been reported in [24], for instance (Fig. 5c, d)). In addition, photoelasticity can be used to investigate some even more complex phenomena such as contact stress analysis of cracked gears, where contact analysis of elements with complex geometry is coupled with fracture mechanics effects [25] (Fig. 5e)). There have even been reported investigations on the seismic effects on a multistory building [26] (Fig. 5f)).

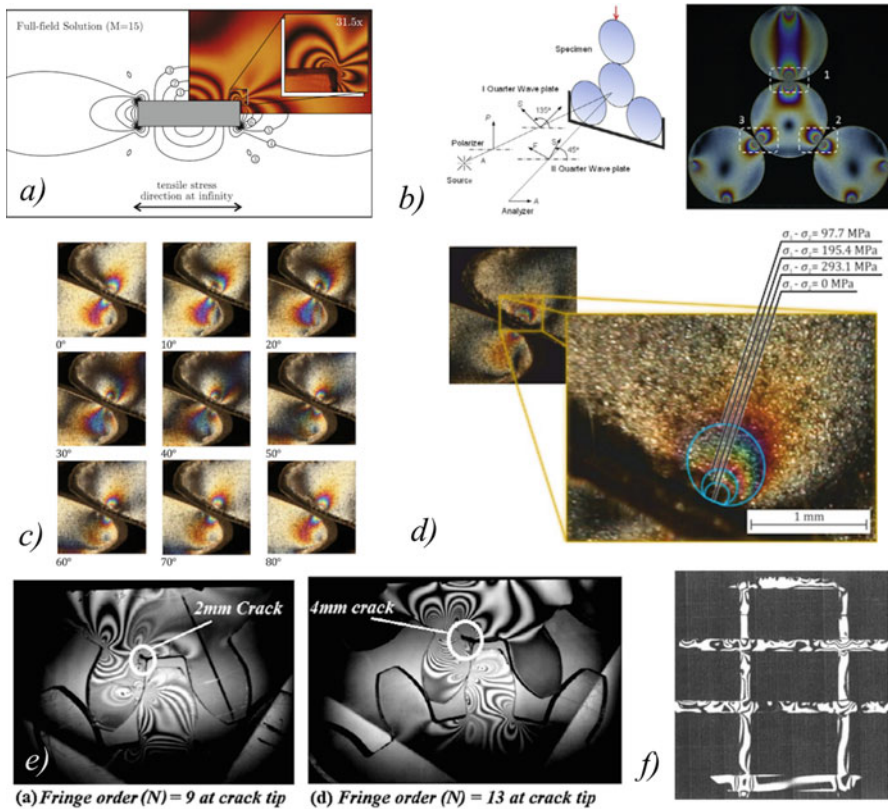


Fig. 5 (a) Stress concentration in composite matrix around a stiff inclusion [22], (b) multiple body contact stress analysis [23], (c) contact stresses in gears analyzed by reflexive polariscope [24], (d) a detail of contact stresses in gears [24], (e) contact stresses in cracked gears [25], (f) photoelastic testing of seismic impact on a part of a multistory building [26]

4 Concluding Remarks

From everything presented, it can be concluded that photoelasticity is a powerful and reliable tool for experimental testing of structures and can greatly contribute to solving some complex problems of nonlinear dynamics, as well as to validate theoretical analyses of those problems. New technologies regarding materials and 3D printing enable its application to problems with both material and geometrical nonlinearities. However, dynamic photoelastic testing is possible only in the case of plane stress state, but with further advances in technology, this limitation could also be overcome, broadening the method's field of application even more.

On the other hand, recently, most attention is directed towards detailed numerical modeling of structures, mostly by the finite element method (FEM). However, numerical modeling cannot replace experimental testing entirely. There are some

phenomena too complex or still not known and investigated enough for which there are yet no appropriate mathematical models, and photoelasticity is irreplaceable when it comes to the whole field evaluation and stress analysis of structures. Therefore, photoelasticity and FEM should be used as complement methods, and the same goes for other methods for experimental testing of structures, such as digital image correlation technique. In this combination of experimental testing methods lies another application potential. Namely, in DIC the deformations are measured and stresses are deduced by applying the constitutive relations. On the contrary, in photoelastic testing, stresses are obtained directly, while deformations should be deduced based on the applied constitutive relations. Therefore, combining these two methods provides a tool for validating the proposed constitutive relations, again proving the efficiency and applicability of the photoelastic method in the process of both experimental and theoretical analysis of structures.

Acknowledgments Parts of this research were supported by the Ministry of Sciences and Technology of Republic of Serbia, through Mathematical Institute SASA, Belgrade, and Grant ON174001 “Dynamics of hybrid systems with complex structures. Mechanics of materials” and Faculty of Mechanical Engineering, University of Niš.

References

1. Ajovalasit, A., Petrucci, G., Scafidi, M.: Review of RGB photoelasticity. *Opt. Lasers Eng.* **68**, 58–73 (2015)
2. Ramesh, K., Ramakrishnan, V.: Digital photoelasticity of glass: a comprehensive review. *Opt. Lasers Eng.* **87**, 59–74 (2016)
3. Ju, Y., et al.: Visualization of the three-dimensional structure and stress field of aggregated concrete materials through 3D printing and frozen-stress techniques. *Constr. Build. Mater.* **143**, 121–137 (2017)
4. (Stevanović) Hedrih, K.R., Paunović, S.: Photoelasticity and its application to structural analysis. a review based on Professor Vlatko Brčić achievements. *J. Serbian Soc. Comput. Mech.* **12**(1), 144–168 (2018)
5. Brčić, V.: Fotoelastično ispitivanje naponskog stanja kod gravitacionih brana sa otvorima, Saopštenja Instituta “Jaroslav Černi”, vol. 12, pp. 1–22 (1958)
6. Brčić, V., Vidaković, M.: Fotoelastično ispitivanje brane sa otvorima na elastičnoj podlozi, Saopštenja Instituta “Jaroslav Černi”, vol. 17, pp. 25–28 (1960)
7. Brčić, V.: Fotoelastično ispitivanje modela brane HE Bajina Bašta., Saopštenja Instituta “Jaroslav Černi”, vol. 29, pp. 1–15 (1963)
8. Brčić, V., Nešović, M.: Fotoelastično ispitivanje dikontinualnih stena, Saopštenja Instituta “Jaroslav Černi”, pp. 31–49 (1970)
9. Brčić, V. Prilog teoriji holografske interferometrije primenjene u fotoelastičnosti, Saopštenja Instituta “Jaroslav Černi”, pp. 5–10 (1969)
10. Brčić, V., Nešović, M. Primena niskomodulnih materijala kod ispitivanja uticaja sопstene težine, Saopštenja Instituta “Jaroslav Černi”, pp. 23–36 (1968)
11. Asundi, et al.: Dynamic photoelasticity using TDI imaging. *Opt. Lasers Eng.* **38**, 3–16 (2002)
12. Patil, P., Vyasarayani, C.P., Ramji, M.: Linear least squares approach for evaluating crack tip fracture parameters using isochromatic and isoclinic data from digital photoelasticity. *Opt. Lasers Eng.* **93**, 182–194 (2017)

13. Liebig, W.V., Leopold, C., Schulte, K.: Photoelastic study of stresses in the vicinity of a unique void in a fibre-reinforced model composite under compression. *Compos. Sci. Technol.* **84**, 72–77 (2013)
14. Feng, W., et al.: Research on the effect of bedrock upon the stress of a gravity dam bulk by the photoelastic method. *J. Mater. Process. Technol.* **123**, 236–240 (2002)
15. Calvert, G., Lesniak, J., Honlet, M.: Applications of modern automated photoelasticity to industrial problems. *Insight* **44**(4), 1–4 (2002)
16. Lagarde, A.: Static and Dynamic Photoelasticity and Caustics. Springer, New York (1987)
17. Glam, B., et al.: Dynamics of stress wave propagation in a chain of photoelastic discs impacted by a planar shock wave; part I, experimental investigation. *Shock Waves* **17**, 1–14 (2007)
18. Goldenberg, A., et al.: Dynamics of stress wave propagation in a chain of photoelastic discs impacted by a planar shock wave: part II, numerical investigation. *Shock Waves* **17**, 15–27 (2007)
19. Lee, S., Ravichandran, G.: An investigation of cracking in brittle solids under dynamic compression using photoelasticity. *Opt. Lasers Eng.* **40**, 341–352 (2003)
20. Gomez, J.T., Shukla, A., Sharma, A.: Static and dynamic behavior of concrete and granite in tension with damage. *Theor. Appl. Fract. Mech.* **36**, 37–49 (2001)
21. Khesin, L., et al.: Investigation of dynamic stresses in models of hydraulic structures by the photoelastic method. *Gidrotekhnicheskoe Stroitel'stvo* **1**, 23–29 (1973)
22. Misseroni, D., Dal Corso, F., Shahzad, S., Bigoni, D.: Stress concentration near stiff inclusions: Validation of rigid inclusion model and boundary layers by means of photoelasticity. *Eng. Fract. Mech.* **121–122**, 87–97 (2014)
23. Hariprasad, M.P., Ramesh, K.: Analysis of contact zones from whole field isochromatics using reflection photoelasticity. *Opt. Lasers Eng.* **105**, 86–92 (2018)
24. Frankovsky, P., et al.: Methodology of contact stress analysis of gearwheel by means of experimental photoelasticity. *Appl. Opt.* **55**(18), 4856–4864 (2016)
25. Pandya, Y., Parey, A.: Experimental investigation of spur gear tooth mesh stiffness in the presence of crack using photoelasticity technique. *Eng. Fail. Anal.* **34**, 488–500 (2013)
26. Hayasi, R., et al.: Photoelastic analysis of stress waves in building subjected to vertical impact under laboratory earthquake experiments. *Int. J. Impact Eng.* **36**, 1150–1155 (2009)

Part V

**Fluid–Structure Interaction, Multibody
System Dynamics**

Levitated and Parametrically Excited Sphere Dynamics in a Single-Axis Ultrasonic Levitator



Amit Dolev and Izhak Bucher

Abstract The dynamics of an acoustically levitated rigid small sphere subjected to a parametric excitation is investigated analytically, experimentally, and numerically. An axisymmetric single-axis ultrasonic (~ 28.56 kHz) levitator comprising an emitter and a matching concave reflector was designed and built, and the complex acoustic field generated by the emitter's unique oscillation mode is estimated by the boundary element method. The generated acoustic radiation forces counteracting gravity are approximated using Gor'kov potential and are modulated by varying the emitter oscillation amplitude. In addition, it is assumed that energy is dissipated by a drag force acting on the smooth sphere. By fitting the nonlinear conservative and dissipative forces, an analytical model was derived and analytically solved using the method of multiple scales. The analytical solution, in case of principal parametric resonance (PPR), predicts a softening behavior with a good agreement to the numerical simulations. Moreover, it predicts the existence of up to three solutions at a given frequency, where the trivial and a nontrivial solution are stable. In addition, experimental results of a levitated sphere made of polystyrene foam subjected to PPR are shown.

Keywords Acoustic levitation · Parametric excitation · Multiple scales

1 Introduction

The standing wave-based levitation phenomenon attracts much interest, and various methods were developed over the years to allow free floatation of solid and liquid matter [1] (e.g., magnetic, electric, optical, and acoustic levitation). Acoustic levitation differs from other methods because it is materials-independent (i.e., it can be used to levitate any solids, liquids, and even heavy gases). In recent years, there is a growing interest in technologies allowing contactless levitation

A. Dolev · I. Bucher

Faculty of Mechanical Engineering, Technion—Israel Institute of Technology, Haifa, Israel
e-mail: amitd@technion.edu

and manipulation of particles, droplets, and small specimens. Apparatuses whose underlying mechanism is standing wave acoustic levitation are already in use in different fields (e.g., microassembly [2], analytical chemistry [3], and materials science [4]). These acoustic levitation devices (ALDs) are mainly used to suspend particles in fixed positions in space; however, there is a growing interest in ALDs capable of particle manipulation. Currently, most particle manipulations are done quasi-statically [5], i.e., particles are manipulated by slowly varying the acoustic trap position while ignoring the dynamics.

To design faster and more accurate ALDs capable of particle manipulation, a better understanding of the dynamics is required. In this work, an axisymmetric single-axis ultrasonic levitator suspends a small rigid sphere, and its dynamics is investigated when subjected to a PPR. The derived analytical model assumes that energy is dissipated by the drag force, and the levitation forces are modeled using Gor'kov potential [6].

2 Derivation of the Governing Equations of Motion

Acoustic radiation forces are generated by nonlinear phenomena occurring in strong acoustic fields and can be used to counteract gravity and generate propulsion. These forces can be expressed analytically for numerous cases; herein they are approximated by computing the Gor'kov potential gradient (Eq. (1)). Gor'kov used the linear acoustic wave equation solution to estimate the acoustic radiation forces acting on a small rigid sphere. Given the potential, the force vector acting on the sphere can be computed.

$$U_G = 2\pi r_s^3 \left[\frac{1}{3\rho_0 c_0^2} \left(1 - \frac{\rho_0 c_0^2}{\rho_s c_s^2} \right) \langle p_1^2 \rangle - \rho_0 \left(\frac{\rho_s - \rho_0}{2\rho_s + \rho_0} \right) \langle \mathbf{u}_1 \cdot \mathbf{u}_1 \rangle \right], \quad \mathbf{F} = -\nabla U_G. \quad (1)$$

where $\rho_{0/s}$ are the air and sphere densities, $c_{0/s}$ are the sound speeds in the air and sphere, r_s is the sphere's radius, p_1 is the linear pressure in the sphere's location, \mathbf{u}_1 is the particle velocity at the location of the sphere, and $\langle \bullet \rangle$ is the time average of \bullet .

Assuming the ALD in Fig. 1 is axisymmetric, the governing equations in the presence of gravity without dissipation are derived by employing Hamilton's principal. Considering only movement along the ALD z -axis as shown in Fig. 2, and adding the drag force ad hoc (F_d see Eq. (2)), the governing equation is:

$$m\ddot{z} - F_d(\dot{z}) + \frac{\partial U_G}{\partial z} = -mg, \quad F_d(\dot{z}) = -\frac{\rho\pi r_s^2}{2} |\dot{z}| \dot{z} C_D(\text{Re}), \quad \text{Re} = \frac{2r_s \rho_0}{\mu} |\dot{z}|. \quad (2)$$

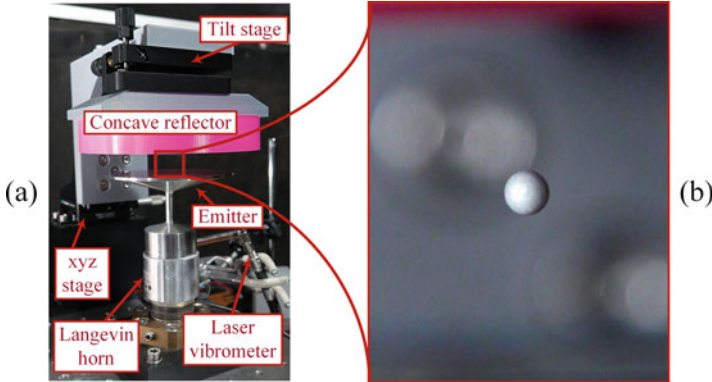


Fig. 1 (a) The single-axis ultrasonic levitator experimental system. (b) An acoustically levitated rigid sphere (1.5 mm diameter) made of polystyrene foam

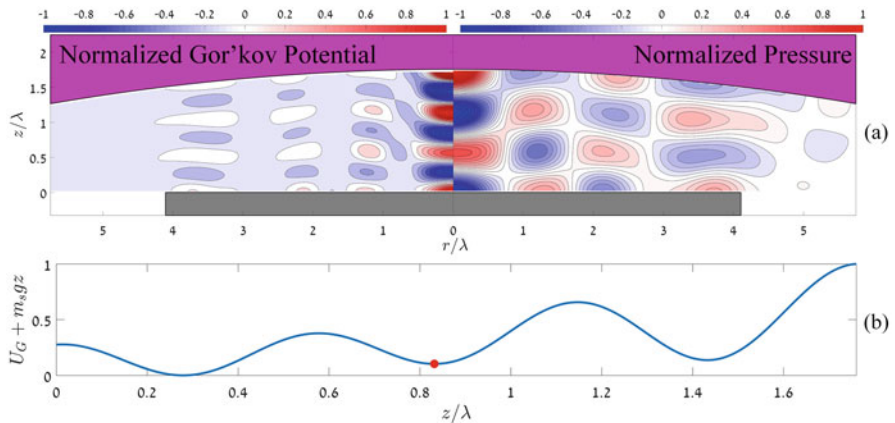


Fig. 2 (a) The single-axis ultrasonic levitator section view. The normalized pressure field and matching normalized Gor'kov potential were numerically computed using the boundary elements method. (b) The total normalized potential energy on the symmetry line along the z -axis and a marker highlighting the selected equilibrium point z_{eq}

Here μ is the air dynamic viscosity. Moreover, U_G is linearly related to the second power of the emitter's velocity. Hence, by modulating it, the parametric excitation is introduced into Eq. (2), which can be written in the following form:

$$\begin{aligned} u'' + \frac{c_1}{m\omega_n}u' + \frac{c_2}{m}\lambda\varepsilon u'^2 + \frac{c_3}{m}\lambda^2\varepsilon^2\omega_n u'^3 \\ + [1 + \alpha \cos(\Omega\tau)] \left(u + \frac{k_2}{k_1}\lambda\varepsilon u^2 + \frac{k_3}{k_1}\lambda^2\varepsilon^2 u^3 \right) = -\frac{v_0^2\alpha k_0}{m\omega_n^2\lambda\varepsilon} \cos(\Omega\tau), \end{aligned} \quad (3)$$

whereas

$$\begin{aligned}
 -F_d(\dot{z})|_{\dot{z}=0} &\approx c_1\dot{z} + c_2\dot{z}^2 + c_3\dot{z}^3 + \dots, \quad \frac{\partial U_G}{\partial z}\Big|_{z_{\text{eq}}} \\
 &\approx v^2 \left(k_0 + k_1\Delta z + k_2\Delta z^2 + k_3\Delta z^3 + \dots \right), \\
 \Delta z = z - z_{\text{eq}} &= \varepsilon\lambda u, \quad \tau = \omega_n t, \quad \frac{\partial \bullet}{\partial \tau} = \bullet' \omega_n = v_0 \sqrt{\frac{k_1}{m}}, \quad v = v_0 \sqrt{1 + \alpha \cos(\Omega\tau)}. \tag{4}
 \end{aligned}$$

Here, ε is a small positive parameter related to the linear damping, λ is the acoustic wavelength, $\Omega = \omega_p/\omega_n$ is the scaled parametric excitation frequency, $\alpha < 1$ is the parametric excitation magnitude, and z_{eq} is the equilibrium position (shown in Fig. 2b). The numerically computed conservative and drag forces were curves fitted, and the parameters are in accordance with the experimental system. Once the parameters were estimated, Eq. (3) in its dimensionless form reduces to:

$$u'' + 2\varepsilon\zeta_1 u' + \varepsilon^2\zeta_3 u'^3 + [1 + \varepsilon\gamma \cos(\Omega\tau)] \left(u + \varepsilon\kappa_2 u^2 + \varepsilon^2\kappa_3 u^3 \right) = \varepsilon\gamma F \cos(\Omega\tau), \tag{5}$$

whereas

$$\begin{aligned}
 \zeta_1 &= \frac{c_1}{2\varepsilon m \omega_n} = 2.96, \quad \zeta_3 = \frac{c_3 \lambda^2 \omega_n}{m} = 0.57, \quad c_2 \approx 0, \quad \gamma = \frac{\alpha}{\varepsilon} = 14.2 \approx 1.2(4\zeta_1), \\
 \kappa_2 &= \frac{k_2}{k_1} \lambda = 1.41, \quad \kappa_3 = \frac{k_3}{k_1} \lambda^2 = -18.78, \quad F = -\frac{v_0^2 k_0}{m \omega_n^2 \lambda \varepsilon} = -11.46, \quad \varepsilon \sim O(10^{-3}). \tag{6}
 \end{aligned}$$

3 Approximate Analytical Solution

In this section, the asymptotic solution is approximated using the method of multiple scales [7]. A second-order uniform solution in the following form is sought:

$$u(\varepsilon, \tau) = u_0(\tau_0, \tau_1, \tau_2) + \varepsilon u_1(\tau_0, \tau_1, \tau_2) + \varepsilon^2 u_2(\tau_0, \tau_1, \tau_2), \quad \tau^i = \varepsilon^i t. \tag{7}$$

The fast time scale is associated with changes occurring at frequency close to ω_n , which is scaled to unity. The other slow time scales are associated with amplitude and phase modulations due to damping, resonances, and nonlinearities. Eliminating u from Eq. (5) using Eq. (7), and collecting terms in the same order of magnitude in ε , leads to:

$$\underline{\varepsilon^0} : D_0^2 u_0 + u_0 = 0 \quad (8)$$

$$\underline{\varepsilon^1} : D_0^2 u_1 + u_1 = \gamma F \cos(\Omega\tau) - 2D_0 D_1 u_0 - 2\zeta_1 D_0 u_0 - \kappa_2 u_0^2 - \gamma u_0 \cos(\Omega\tau) \quad (9)$$

$$\underline{\varepsilon^2} : D_0^2 u_2 + u_2 = -D_1^2 u_0 - 2D_0 D_2 u_0 - 2D_0 D_1 u_1 - 2\zeta_1 (D_1 u_0 + D_0 u_1) - \zeta_3 (D_0 u_0)^3 - 2\kappa_2 u_0 u_1 - \kappa_3 u_0^3 - \gamma \cos(\Omega\tau) (u_1 + \kappa_2 u_0^2) \quad (10)$$

The zero-order solution, expressed in complex form is $u_0 = A(\tau_1, \tau_2) e^{i\tau_0} + cc$, where cc stands for the complex conjugate of the proceeding terms. Next, u_0 is eliminated from Eq. (9). When the pumping frequency is approximately twice the natural frequency, yielding PPR, the particular solution of Eq. (9) contains secular and small divisor terms, hence the following detuning parameter, σ , is defined as $\Omega = 2 + \varepsilon\sigma$. Therefore, the terms producing secular terms in u_1 can be eliminated by solving:

$$-2i D_0 A - 2i \zeta_1 A - \frac{1}{2} \gamma \bar{A} e^{i\sigma\tau_1} = 0, \quad (11)$$

where \bar{A} is the complex conjugate of A , and the particular solution is:

$$u_1 = \frac{\gamma A}{2\Omega(2+\Omega)} e^{i(1+\Omega)\tau_0} + \frac{\kappa_2}{3} A^2 e^{2i\tau_0} - \kappa_2 A \bar{A} - \frac{\gamma F}{2(\Omega^2-1)} e^{i\Omega\tau_0} + cc. \quad (12)$$

Now, both u_0 and u_1 are eliminated from Eq. (10), and the terms $D_1 A$ and $D_1^2 A$ are eliminated via Eq. (11). Eliminating the secular terms yields:

$$\begin{aligned} & \left\{ \zeta_1^2 - \gamma^2 \left[\frac{1}{16} + \frac{1}{4(2+\varepsilon\sigma)(4+\varepsilon\sigma)} \right] \right\} A + \frac{\gamma}{4} \left[\sigma + \frac{4F\kappa_2}{(2+\varepsilon\sigma)^2-1} \right] \bar{A} e^{i\varepsilon\sigma\tau_0} \\ & + \frac{1}{3} \left(10\kappa_2^2 - 9\kappa_3 - 9i\zeta_3 \right) A^2 \bar{A} - 2i D_2 A = 0 \end{aligned} \quad (13)$$

It can be shown that Eqs. (11) and (13) are the first two terms in a multiple scale analysis of:

$$\begin{aligned} & -2i (A' + \varepsilon\zeta_1 A) - \frac{\gamma\varepsilon}{2} \bar{A} e^{i\varepsilon\sigma\tau_0} + \frac{\varepsilon^2}{96} \\ & \times [3(32\zeta_1^2 A - 3\gamma^2) A + 8(4F\gamma\kappa_2 + 3\gamma\sigma) \bar{A} e^{i\varepsilon\sigma\tau_0} \\ & + 32(10\kappa_2^2 - 9(\kappa_3 + i\zeta_3)) A^2 \bar{A}] = 0 \end{aligned} \quad (14)$$

Substituting the polar form $A(\tau) = 0.5a(\tau)e^{i\phi(\tau)}$ into Eq. (14), separating to real and imaginary, and transforming the latter equation set to an autonomous system, by defining $\psi = \varepsilon\sigma\tau - 2\phi$, the steady-state solution (i.e., $a' = \psi' = 0$) can be computed:

$$u = a_0 \cos\left(\frac{\omega_p}{2}t - \frac{\psi_0}{2}\right) + O(\varepsilon) \quad (15)$$

where a_0 and ψ_0 are the steady state amplitude and phase, accordingly.

It can be shown that γ should be larger than $4\xi_1$ to achieve a nontrivial solution [8, 9]; therefore, it was set approximately as $4.8\xi_1$ (see Eq. (6)).

4 Numerical Simulation Verification

The approximate analytical solution is verified by comparing the dominant harmonic amplitude of the responses a_0 , whose frequency is close to ω_n . In what follows, the analytically computed amplitudes are compared with four different numerical simulations, during which the amplitude and velocity stayed in bounds of the curve fitting (see Sect. 2). The simulations differ by the stiffness and damping models that were used. The two stiffness models and two damping models are according to Eq. (2) and Eq. (4). The appropriate models that were used in each simulation are summarized in the table in Fig. 3, and the results are depicted in Fig. 3. Lines show the analytically computed amplitudes, and markers show the numerically computed results. Continuous and dashed lines show the stable and unstable solution branches accordingly. The results shown in the Fig. 3 verify the predicted softening behavior, which is due to the quadratic stiffness and negative cubic stiffness [9, 11, 12].

The steady-state solution stability was determined in a standard procedure [7]. Good agreement between the analytical solution and numerical simulations was obtained; however, at $\sigma \approx -45$ the simulations depart from the analytical solution, as the nontrivial solution is no longer stable in practice. It can be deduced from the results that the simplified model suffices to capture the dynamics with high accuracy.

5 Preliminary Experimental Results

Using the experimental rig shown in Fig. 1a, a small rigid sphere made of polystyrene foam ($r_s \approx 1.5$ mm, $\lambda \approx 1.2$ cm) was levitated steadily (Fig. 1b).

As a first step towards parametric excitation, the natural frequency was estimated from a step response (Fig. 4). The motion of the sphere was captured using a high-speed camera, and the instantaneous frequency was estimated by applying Hilbert transform [10], as shown in Fig. 4. The average value, which approximates

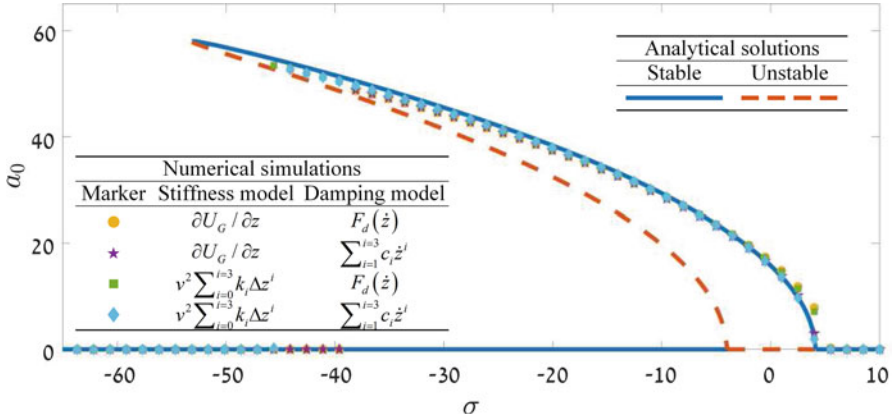


Fig. 3 The dominant harmonic amplitude a_0 vs. the detuning parameter σ . Continuous (dashed) lines depict the stable (unstable) analytical solution, and markers depict the simulated results

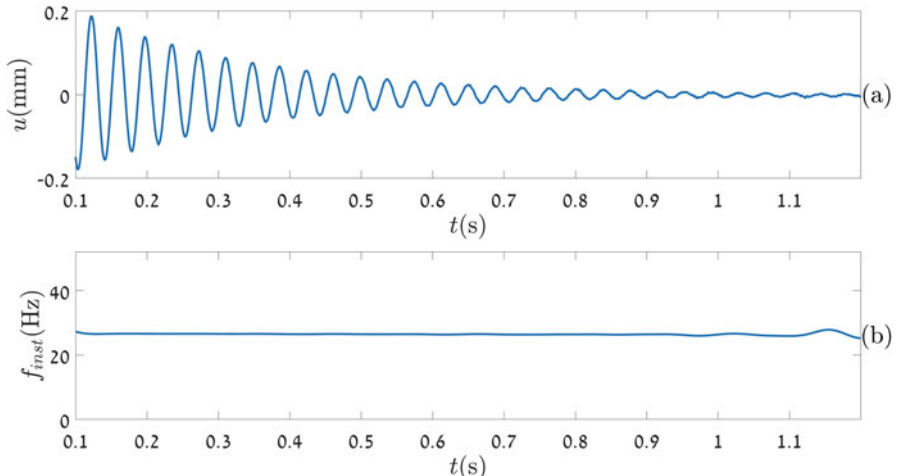


Fig. 4 Measured step response. (a) The sphere's displacement in the z direction. (b) The instantaneous frequency, computed using the Hilbert transform [10]

the natural frequency, is $\omega_n = 26.5$ Hz. Once the natural frequency was known, the velocity amplitude of the emitter was modulated according to Eq. (4), at $\Omega = 52.3$ Hz. The two leading terms of the Hilbert vibration decomposition (HVD) [10] were extracted, and their average instantaneous frequencies are $f_1 = 26.13$ Hz and $f_2 = 52.3$ Hz. It is shown in Fig. 5a that the first component is more than an order of magnitude larger than the second term, and its frequency (Fig. 5b) is half of the excitation frequency, while the frequency of the second term equals the excitation frequency. Therefore, it can be deduced that the first component is due to principal parametric resonance, and the second is due to the direct forcing (see Eq. (3)).

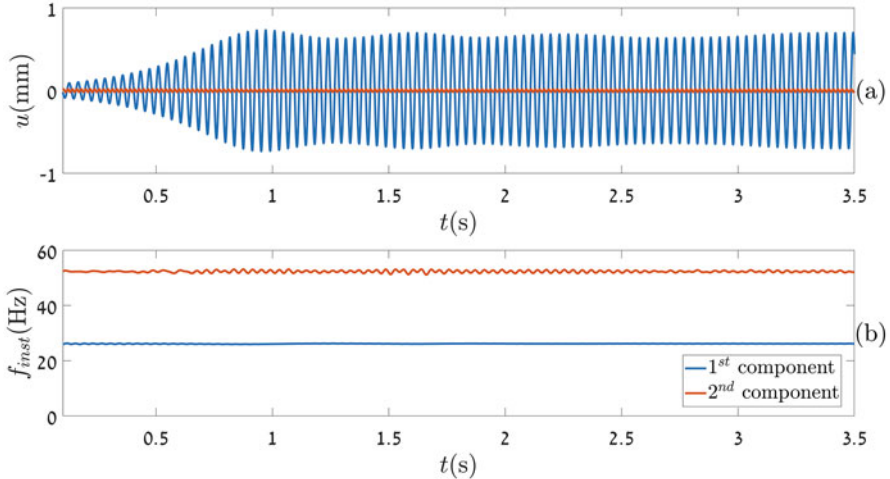


Fig. 5 Measured response to PPR. (a) The two leading HVD (see [10]) components of the displacements of the sphere in the z direction. (b) The instantaneous frequency of each component

6 Summary and Conclusions

The dynamics of a small rigid acoustically levitated sphere subjected to principal parametric resonance was studied analytically and numerically. Moreover, the ability to parametrically excite it was shown experimentally. The parameters for the analytical models were estimated according to an experimental setup in the laboratory (Fig. 1). This study is a preliminary stage prior to conducting experiments and validating the derived results. According to the setup, a numerical simulation was carried out to estimate the generated pressure field, from which the sound radiation forces were computed (Fig. 2). The conservative acoustic force and drag force were fitted in the close neighborhood of the equilibrium position, by which a simplified nonlinear equation of motion was derived. The equation of motion was analytically solved using the method of multiple scales, and the solution was numerically verified (Fig. 3), as the numerical results are in good agreement with analytical solution. According to the model, the system has a softening behavior due to the quadratic stiffness and negative cubic stiffness terms. Moreover, up to three solutions may coexist at a given frequency, where one is unstable, another is the trivial solution, and the last one is nontrivial.

In the last section, experimental results of an acoustically levitated sphere subjected to PPR were shown, hence validating the theory. However, these are preliminary results, and further research is required. It is important to estimate the stiffness and damping models as accurately as possible, in order to tune the parametric excitation frequency and magnitude properly to yield principal parametric resonance.

Acknowledgment The first author would like to acknowledge the generous financial support of the Israeli Ministry of Science and Technology (3-13336) for the Applied Science scholarship for engineering PhD students 2016.

References

1. Brandt, E.H.: Levitation in physics. *Science*. **243**, 349–355 (1989)
2. Vandaele, V., Lambert, P., Delchambre, A.: Non-contact handling in microassembly: acoustical levitation. *Precis. Eng.* **29**, 491–505 (2005)
3. Santesson, S., Nilsson, S.: Airborne chemistry: acoustic levitation in chemical analysis. *Anal. Bioanal. Chem.* **378**, 1704–1709 (2004)
4. Gao, J.R., Cao, C.D., Wei, B.: Containerless processing of materials by acoustic levitation. *Adv. Space Res.* **24**, 1293–1297 (1999)
5. Andrade, M.A.B., Pérez, N., Adamowski, J.C.: Review of progress in acoustic levitation. *Braz. J. Phys. Ther.* **48**, 190–213 (2018)
6. Gor'kov, L.P.: Forces acting on a small particle in an acoustic field within an ideal fluid. *Dokl. Akad. Nauk SSSR* **140**, 88–91 (1961)
7. Nayfeh, A.H., Mook, D.T.: *Nonlinear Oscillations*. Wiley-VCH, Weinheim (2008)
8. Dolev, A., Bucher, I.: Tuneable, non-degenerated, nonlinear, parametrically-excited amplifier. *J. Sound Vib.* **361**, 176–189 (2016)
9. Dolev, A., Bucher, I.: Optimizing the dynamical behavior of a dual-frequency parametric amplifier with quadratic and cubic nonlinearities. *Nonlinear Dyn.* **92**(4), 1955–1974 (2018). <https://link.springer.com/article/10.1007/s11071-018-4174-5>
10. Feldman, M.: Hilbert transform applications in mechanical vibration. In: Wiley (2011)
11. Zavodney, L.D., Nayfeh, A.H., Sanchez, N.E.: The response of a single-degree-of-freedom system with quadratic and cubic non-linearities to a principal parametric resonance. *J. Sound Vib.* **129**, 417–442 (1989)
12. Zavodney, L.D., Nayfeh, A.H.: The response of a single-degree-of-freedom system with quadratic and cubic non-linearities to a fundamental parametric resonance. *J. Sound Vib.* **120**, 63–93 (1988)

Modelling VIV of Transversally Oscillating Rigid Structures Using Nonlinear Fluid Oscillators



Victoria Kurushina, Ekaterina Pavlovskaya, Andrey Postnikov,
Guilherme Rosa Franzini, and Marian Wiercigroch

Abstract This work is aimed to develop a series of wake oscillator models to predict displacements of the single degree-of-freedom (1DOF) rigid structure for a range of mass ratio. The work includes modification of the model with alternative damping terms, calibration of the models with the “medium” mass ratio (around 6.0), validation with the same experimental arrangement, validation with the different set-up and definition of the application range.

Keywords Vortex-induced vibration · Wake oscillator · Rigid structure · Calibration · Validation

1 Introduction

Although a lot of work has been done on modelling of vortex-induced vibrations (VIV) for both rigid and flexible structures, there is still a need to improve the prediction accuracy of the existing models. The current study is focused on the problem of the transversally oscillating rigid structure modelled using the semi-empirical wake oscillator method. This class of models implies that fluctuations of

V. Kurushina (✉)

Department of Transport of Hydrocarbon Resources, Institute of Transport, Industrial University of Tyumen, Tyumen, Russia

Centre for Applied Dynamics Research, School of Engineering, University of Aberdeen, Kings' College, Aberdeen, Scotland, United Kingdom

e-mail: v.kurushina@outlook.com

E. Pavlovskaya · M. Wiercigroch

Centre for Applied Dynamics Research, School of Engineering, University of Aberdeen, Kings' College, Aberdeen, Scotland, United Kingdom

A. Postnikov

School of Engineering, University of Lincoln, Lincoln, United Kingdom

G. R. Franzini

Offshore Mechanics Laboratory, Escola Politécnica, University of São Paulo, São Paulo, Brazil

the fluid drag and lift forces on the structure can be predicted using self-excited limit cycle oscillators, and a number of empirical constants should be employed in order to establish a link with the real phenomenon.

Wake oscillator method was developed primarily to model VIV during the resonance (or lock-in state) between the fluid and the structure. Lock-in can be observed in terms of the cross-flow/in-line displacement amplitudes depending on the reduced velocity of the flow. Jauvtis and Williamson [1] proposed the terminology for the elements of the lock-in peak: the lock-in of the low mass ratio (below 6.0) 2DOF structures consists of the initial, super-upper and lower branches, and the lock-in of the high mass ratio (above 6.0) 2DOF structures and all 1DOF structures is formed by the initial, upper and lower branches. This classification is based on the difference in both developed amplitudes and the peak shape. At the present time, the mathematical apparatus of wake oscillator method for lock-in modelling includes the relationship between the drag and lift coefficients [2]; coupling terms between the structural and the fluid equation [3]; frequency-dependent coefficients [4]; nonlinear structural equation [5]; various nonlinear damping terms in the fluid equation [6, 7]; relationship between the mean drag and the transverse oscillation amplitude [8, 9]. The calibration of empirical coefficients using the constrained nonlinear minimization tool was developed in [10] to establish a strong connection of the semi-empirical wake oscillator and the experimental data.

Comparing 1DOF and 2DOF rigid structures' oscillations during lock-in, it is possible to notice both similarities and differences. Lock-in of both 1DOF and 2DOF rigid structures is sensitive to the Reynolds number, mass and damping ratios, as explicitly shown in the experimental study [11], and to other set-up parameters, such as the influence of the aspect ratio [12] or the angle between the flow and the structure [13].

The work [9] has observed the evolution of the super-upper branch of the 2DOF rigid structures. Lock-in at the low mass ratio of 2.36 has the angular shape, and there is the abrupt drop from the top displacement amplitude, that is significantly higher than the one for 1DOF structure, to the lower branch. Increase in the mass ratio leads to the almost circular upper branch at the mass ratio of 10.63 observed for the 2DOF rigid structure, very close to the amplitudes of the 1DOF structure. It is also possible to observe in [9] the similarity between the 1DOF and 2DOF lock-in: the initial branch shifts to the higher values of the reduced velocity with the growing mass ratio for both structures.

The study [10] shows that the beginning of lock-in in terms of the reduced velocity for a 2DOF rigid structure is similar throughout a few different experimental arrangements, if the mass ratio is kept in the range of approximately from 2.0 to 4.0. Other case parameters, including Reynolds number and damping ratio, are significantly different across the considered set-ups. On the contrary, the work [14] shows that the shape of lock-in peak and the start point of lock-in in the reduced velocity range of a transversally oscillating rigid structure (1DOF) is quite sensitive to the experimental arrangement, especially to the end conditions.

In the current research, the authors aim to investigate the prediction accuracy of the wake oscillator models in the case of a transversally oscillating rigid structure

(1DOF). The research objectives include modification of the existing wake oscillator model [3] with various nonlinear damping types; calibration with the experimental data [9] for the mass ratio 6.54 which can be defined as “medium” mass ratio according to the classification in [1]; identification of the most accurate model options with the corresponding sets of coefficients and the approximate applicability range, based on the comparison with the data for “low” and “high” mass ratios in [9].

The rest of the paper is structured as follows: Section 2 describes the considered nonlinear damping terms for the wake oscillator model of a 1DOF rigid structure oscillating in the uniform flow and the strategy for calibration. Section 3 presents the calibration results and their discussion, and, finally, a summary of the conducted research is given in Sect. 4.

2 Mathematical Model: Modification and Calibration

The influence of fluid nonlinearities on the quality of the VIV prediction is studied in this work using the base model of a 1DOF rigid structure oscillating in the fluid flow, as in [3, 15]. The model is designed to predict free vibrations of an elastically mounted rigid cylinder oscillating in the cross-flow direction and restricted in the in-line direction. The structure is shown in Fig. 1. It is characterized by structural mass m_s , diameter D , structural damping r_s and stiffness of elastic support k in the cross-flow (\bar{Y}) direction.

In the mathematical description of this system, the following non-dimensional parameters are used:

$$\omega_{st} = \frac{\omega_n}{\omega_0}; \quad \xi = \frac{r_s}{2\omega_0 m_*}; \quad \mu = \frac{4m_s}{\pi\rho_f D^2}, \quad (1)$$

where ω_n is the natural frequency of the structure in still water according to experimental data [9], ω_0 is the reference frequency, ρ_f is the fluid density, ξ is

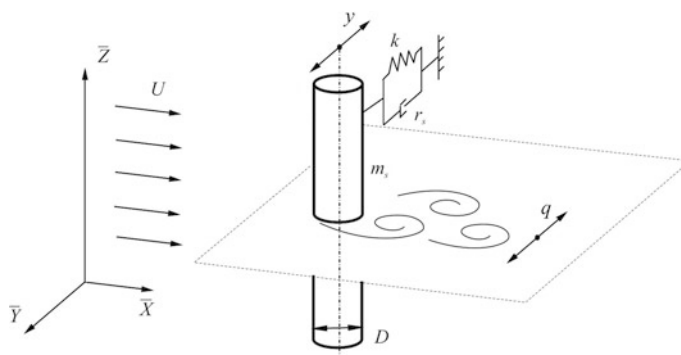


Fig. 1 One degree-of-freedom elastically supported rigid structure interacting with the uniform flow of velocity U

the dimensionless damping ratio, ω_{st} is the dimensionless natural frequency of the structure and μ is the mass ratio.

In all calculations conducted in this study, the reference frequency ω_0 is kept equal to the natural frequency of the structure ω_n , therefore, the dimensionless frequency is $\omega_{st} = \frac{\omega_n}{\omega_0} = 1$. Mass m_* includes the structural mass and the fluid added mass as $m_* = 0.25(\mu + C_A)\pi\rho_f D^2$, where C_A is the fluid added mass coefficient. The coefficient C_A is assumed to be equal to 1 in the majority of VIV studies. However, in the current research the coefficient C_A will be calibrated together with the other dimensionless coefficients.

The time t and the cross-flow displacement y of the centre of the structure are non-dimensionalized as $\tau = \omega_0 t$ and $Y = y/D$, respectively.

The fluid flow is assumed to be uniform, with the velocity U and the vortex shedding frequency Ω_f . In the dimensionless form of the model, the reduced velocity $U_R = (2\pi U) / (\omega_n D)$ and the vortex shedding frequency $\Omega_R = \Omega_f / \omega_0 = (2\pi StU) / (\omega_0 D)$ are applied.

The reduced velocity from the experimental data available in the literature is used in all calculations performed in this work. The Strouhal number St is assumed to be constant and equal to 0.2 in this study for all considered cases.

The lift force acting on the cylinder is calculated using the fluctuating lift coefficient C_L which is represented as non-dimensional cross-flow wake coefficient $q = 2C_L/C_{L0}$. The amplitude of the lift coefficient observed for a fixed cylinder C_{L0} and the initial drag coefficient C_{D0} are included in the dimensionless coefficients $d = (C_{L0}\rho_f D^2) / (16\pi^2 St^2 m_*)$ and $e = (C_{D0}\rho_f D^2) / (4\pi St m_*)$, respectively.

The base equations of motion are

$$\ddot{Y} + 2\xi\dot{Y} + \omega_{st}^2 Y = d\Omega_R^2 q - e\Omega_R \dot{Y}; \quad (2)$$

$$\ddot{q} + \varepsilon_y \Omega_R (q^2 - 1) \dot{q} + \Omega_R^2 q = A_y \ddot{Y}. \quad (3)$$

Here, A_y is the empirical coefficient in the acceleration coupling term proposed in [3], and the Van der Pol oscillator is employed to model fluctuations of the lift force, with the nonlinear damping $\varepsilon_y \Omega_R (q^2 - 1) \dot{q}$.

There are a few versions of damping in the fluid equation employed throughout the history of the wake oscillator method, as proposed by Rayleigh, Van der Pol, Landl [6] and Krenk and Nielsen [7]. The current study focuses on investigating the effects of these options on the accuracy of prediction of the base model. The equations of oscillators replacing Eq. (3) are presented in Table 1. In addition to the classic Van der Pol and Rayleigh equations, it is suggested to investigate also Modified Van der Pol and Modified Rayleigh equations where the damping coefficient ε_y is split into separate coefficients for each damping term as ε_{y1} and ε_{y2} . Landl and Krenk-Nielsen equations contain also coefficient ε_{y3} to regulate the contribution of the third damping term of wake oscillator. Therefore, this study considers the base model and 5 models with modified fluid oscillators, with 6–8 calibrated empirical coefficients.

Table 1 Wake oscillator equations considered instead of Eq. (3) for one degree-of-freedom model

Oscillator	Cross-flow equation
Modified Van der Pol	$\ddot{q} - \varepsilon_{y1}\Omega_R\dot{q} + \varepsilon_{y2}\Omega_R\dot{q}^2 + \Omega_R^2 q = A_y \ddot{Y}$
Classic Rayleigh	$\ddot{q} - \varepsilon_y\Omega_R\dot{q} + \frac{\varepsilon_y}{\Omega_R}\dot{q}^3 + \Omega_R^2 q = A_y \ddot{Y}$
Modified Rayleigh	$\ddot{q} - \varepsilon_{y1}\Omega_R\dot{q} + \frac{\varepsilon_{y2}}{\Omega_R}\dot{q}^3 + \Omega_R^2 q = A_y \ddot{Y}$
Landl	$\ddot{q} + \Omega_R\dot{q}(\varepsilon_{y1} - \varepsilon_{y2}q^2 + \varepsilon_{y3}q^4) + \Omega_R^2 q = A_y \ddot{Y}$
Krenk-Nielsen	$\ddot{q} - \varepsilon_{y1}\Omega_R\dot{q} + \varepsilon_{y2}\Omega_R\dot{q}^2 + \frac{\varepsilon_{y3}}{\Omega_R}\dot{q}^3 + \Omega_R^2 q = A_y \ddot{Y}$

Calibration of the considered models is performed using four different calibration schemes as proposed in [10] utilising nonlinear minimization tool from the Matlab Optimization Toolbox. To obtain the amplitudes of displacement for a range of the flow velocities, the equations of motion described in this section are integrated using the Matlab ode45 solver applying zero initial conditions to all variables apart from the wake coefficient which initial value is set up to be small but non-zero.

Models are calibrated using the experimental data [9] for the mass ratio of 6.54, the damping ratio of 0.006 and the Reynolds number ranging from 18,300 to 83,800. The data are presented in [9] for the mass ratios from 2.36 to 12.96 and allow validation with the same experimental arrangement. The structure has the diameter of 0.0554 m, the aspect ratio of 8 and the natural frequency of 1.261 Hz for the mass ratio of 6.54. The experimental data [9] are focused on the evolution of the upper branch with the systematic variation of the mass ratio, implying that other case parameters are kept the same throughout all the experiments. The same as in the experimental study [9], the calculations were done independently for each flow velocity value, and the effects of following the obtained solution with increasing or decreasing flow velocity were not considered.

The preliminary calibrations of this set of 1DOF models allow to conclude that the prediction of the initial branch can be significantly improved by introducing the lock-in delay coefficient K , which is similar to the observations presented in [10]. The coefficient K is the difference between the velocities of the lock-in start according to the experimental data used for calibration U_{Rexp} and according to the model U_{Rm} , or $K = U_{Rexp} - U_{Rm}$. Hence, the 1DOF rigid structure model with, for example, Rayleigh damping is as follows:

$$\ddot{Y} + 2\xi\dot{Y} + \omega_{st}^2 Y = d(\Omega_R - StK)^2 q - e(\Omega_R - StK)\dot{Y}; \quad (4)$$

$$\ddot{q} + \varepsilon_y(\Omega_R - StK)(\dot{q}^2 - 1)\dot{q} + (\Omega_R - StK)^2 q = A_y \ddot{Y}, \quad (5)$$

where StK corrects the frequency of vortex formation in order to tune the initial branch of lock-in as in the experimental data.

The influence of a simple substitution of damping while keeping the same set of coefficients is illustrated in Fig. 2. Here, $C_{L0} = 0.84$, $C_{D0} = 2.03$, $\varepsilon_y = \varepsilon_{y1} = \varepsilon_{y2} = \varepsilon_{y3} = 0.019019$, $A_y = 5.28$, $C_A = 0.87$, $K = 1.04$. The classic Van der Pol equation allows the modelled structure to develop the highest amplitudes of displacement, and the Landl damping results in the lowest amplitudes. Also, the

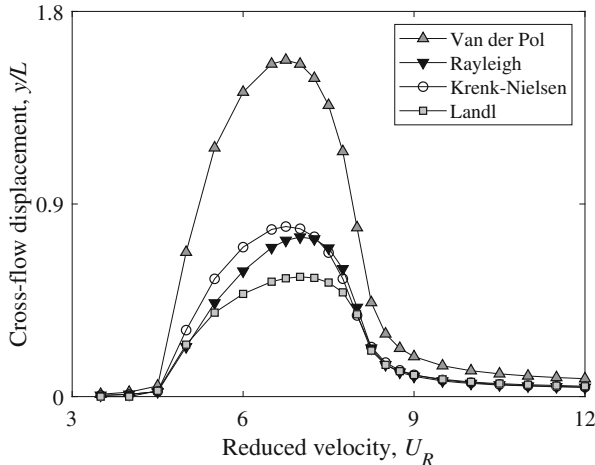


Fig. 2 Influence of fluid nonlinearities on prediction of the amplitude of cross-flow oscillations through the lock-in region of velocity of the flow, if the empirical coefficients are kept the same: $C_{L0} = 0.84$, $C_{D0} = 2.03$, $\varepsilon_y = \varepsilon_{y1} = \varepsilon_{y2} = \varepsilon_{y3} = 0.019019$, $A_y = 5.28$, $C_A = 0.87$, $K = 1.04$

highest displacement amplitude occurs at a slightly higher reduced velocity when the Rayleigh or Landl oscillator is applied.

The calibration results presented in Sect. 3 with the target data [9] are obtained with the 6 models modified with the lock-in delay coefficient K .

3 Results and Discussion

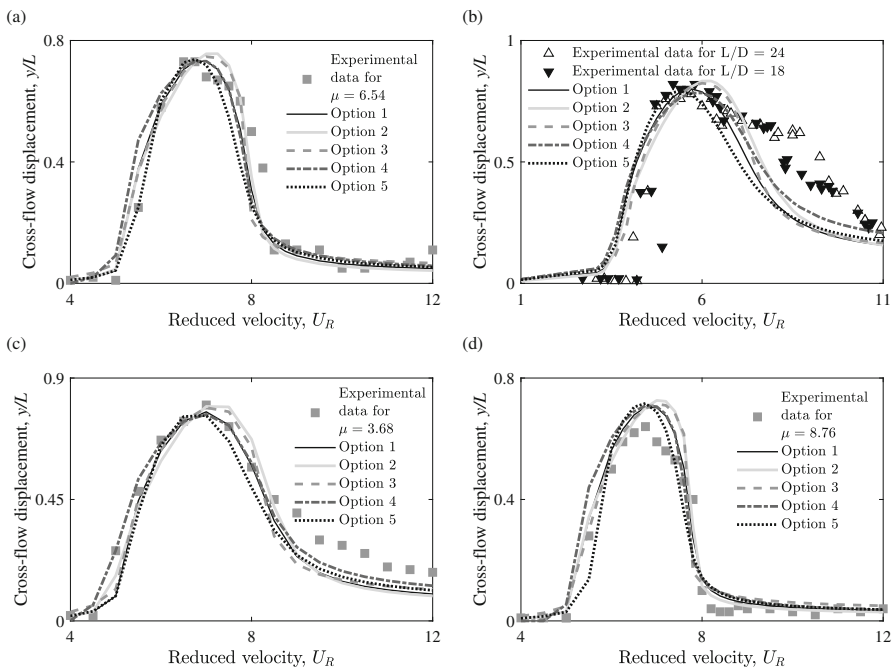
Results of the calibration with the medium mass ratio of 6.54 are summarized in Table 2. These models with the corresponding sets of coefficients are short-listed based on the lowest objective function obtained during the optimization. Table 2 does not reveal a preferable oscillator, but it shows that the simple Van der Pol and Rayleigh oscillators are not at the top of the list in terms of the prediction accuracy.

The calibration results are presented in Fig. 3a. Here, Option 5 gives the most accurate highest displacement amplitudes and a suitable initial branch, but the peak predictions in the reduced velocity interval from 7.0 to 8.0 are much better with the other model variations.

The validation of models from Table 2 with the experimental data from a different set-up [12] is shown in Fig. 3b. This experimental case is very close to [9] in terms of the mass and damping ratio, however, the Reynolds number range is significantly lower. The calibrated models presented in Fig. 3b allow accurate prediction of the upper branch, but they underestimate the lower branch of the lock-in peak. The lock-in delay coefficient K , calibrated with the set-up [9], appears not applicable for the set-up [12]. This suggests that the coefficient K should be calibrated for each facility.

Table 2 Calibrated coefficients for different models obtained using experimental results [9] for the mass ratio of 6.54

Option number	Option	Signal statistics	C_{L0}	C_{D0}	ε_y	A_y	C_A	K
1	Krenk-Nielsen	Standard deviation	0.61	1.75	0.081990, 0.016313, 0.012551	5.49	1.12	1.34
2	Modified Rayleigh	Standard deviation	0.69	1.70	0.038019, 0.016162	5.14	0.95	1.22
3	Modified Van der Pol	Maximum	0.58	1.22	0.696500, 0.367820	3.85	0.97	1.17
4	Landl	Maximum	0.67	1.90	0.008562, 0.009240, 0.008891	5.08	1.00	1.17
5	Modified Van der Pol	Maximum	0.48	2.22	0.035601, 0.026508	6.28	1.13	1.40

**Fig. 3** Displacement amplitudes generated by the considered model versions from Table 2 against the experimental records [9]: (a) calibration results obtained for the mass ratio of 6.54 [9], including K ; (b) validation results obtained for the mass ratio of 2.5 [12], with $K = 0$; (c) validation results obtained for the mass ratio of 3.68 [9], including K ; (d) validation results obtained for the mass ratio of 8.76 [9], including K . For the set-up [9], the damping ratio is $\xi = 0.006$, the Reynolds number range is 18,300–83,800. For the set-up [12], the damping ratio is $\xi = 0.005$, the Reynolds number range is 1320–6660

The validation of calibrated models has also been conducted with the data from the same experimental arrangement [9] for the mass ratios of 2.36–12.96. Figure 3c and d provide the samples of these validation results for the low mass ratio of 3.68 and the high mass ratio of 8.76, respectively. Here, displacements are calculated using already identified sets of coefficients (as given in Table 2), including the lock-in delay coefficient K . It is possible to see that the calibrated models hold a suitable quality of prediction for the mass ratio range from 3.68 to 8.76, which is consistent with the results from [16] for the 2DOF rigid structure models calibrated with the medium mass ratio.

Results for the mass ratio of 3.68 in Fig. 3c reveal that Option 4 provides a relatively good estimate of the peak width. Options 2 and 3 can capture the maximum of the displacement amplitude. For the mass ratio 8.76, the most advantageous fit is provided by Options 1–3.

Based on the validations in Fig. 3b–d, it is possible to recommend Model 3 (Modified Van der Pol) for the practical application in the mass ratio range of 3.68–8.76. The lock-in delay coefficient K should be calibrated for each experimental facility for the medium mass ratio around 6.0. This would allow a suitable range of the mass ratio to be covered, that brings the wake oscillator models closer to the design practice.

4 Conclusions

The study presented in this paper included: modification of an already existing model [3] of the transversally oscillating rigid structure with 5 alternative damping types; calibration with the published experimental data [9] for the mass ratio of 6.54; collection of the most accurate options with the corresponding sets of coefficients; validation of the most accurate options with experimental data from the same set-up [9] they were calibrated with; validation with the data [12].

This study shows that the results are consistent with the data presented in [16] for the rigid structure with two degrees-of-freedom: wake oscillator models calibrated with the medium mass ratio demonstrate a reasonably wide application range. The models of 1DOF structure presented in Table 2 are applicable for the set-up [9] for the mass ratios from 3.68 to 8.76, with no need for change of the calibrated coefficients, including the coefficient K . If the models are applied to predict VIV for a different arrangement, the lock-in delay coefficient K should be recalibrated with the medium mass ratio around 6.0. This is different from the results for the 2DOF structure models calibrated with the low mass ratio [10] that are applicable for other set-ups with no changes in K and from the results for the 2DOF structure models calibrated with the medium mass ratio [16] that are applicable for the same arrangement only.

Among the model options listed in Table 2, Model 3 (with the Modified Van der Pol damping term) could be recommended as the most suitable for the practical application.

Acknowledgements V.K. would like to acknowledge the support of the Industrial University of Tyumen, Tyumen, Russia, and the State Program “Global Education”, Russia. This work has been performed using the Maxwell High Performance Computing Cluster funded by the University of Aberdeen. Authors would like to express their gratitude to Dr Andrew Starkey for advices regarding optimization procedures and to Naveed Khan for technical advices on accelerating computations.

G.R.F. acknowledges the Brazilian National Council of Scientific and Technological Development (CNPq) for the grant 310595/2015-0.

References

1. Jauvtis, N., Williamson, C.H.K.: The effect of two degrees-of-freedom on Vortex-induced vibration at low mass and damping. *J. Fluid. Mech.* **509**, 23–62 (2004)
2. Nayfeh, A.H., Owis, F., Hajj, M.R.: A model for the coupled lift and drag on a circular cylinder. In: ASME 2003 International Design Engineering Technical Conferences and Computers and Information in Engineering Conference, pp. 1289–1296 (2003)
3. Facchinetto, M.L., De Langre, E., Biolley, F.: Coupling of structure and wake oscillators in Vortex-induced vibrations. *J. Fluid. Struct.* **19**(2), 123–140 (2004)
4. Ogink, R.H.M., Metrikine, A.V.: A wake oscillator with frequency dependent coupling for the modeling of Vortex-induced vibration. *J. Sound Vib.* **329**(26), 5452–5473 (2010)
5. Srinil, N., Zanganeh, H.: Modelling of coupled cross-flow/in-line Vortex-induced vibrations using double Duffing and Van der Pol oscillators. *Ocean Eng.* **53**, 83–97 (2012)
6. Lendl, R.: A mathematical model for Vortex-excited vibrations of bluff bodies. *J. Sound Vib.* **42**(2), 219–234 (1975)
7. Krenk, S., Nielsen, S.R.K.: Energy balanced double oscillator model for Vortex-induced vibrations. *J. Eng. Mech.* **125**(3), 263–271 (1999)
8. Postnikov, A.: Wake oscillator and CFD in modelling of VIVs, PhD thesis, University of Aberdeen (2016)
9. Stappenbelt, B., Lalji, F.: Vortex-induced vibrations super-upper response branch boundaries. *Int. J. Offshore Polar Eng.* **18**(02), 99–105(2008)
10. Kurushina, V., Pavlovskaya, E., Postnikov, A., Wiercigroch, M.: Calibration and comparison of VIV wake oscillator models for low mass ratio structures. *Int. J. Mech. Sci.* **142–143**, 547–560 (2018)
11. Blevins, R.D., Coughran, C.S.: Experimental investigation of Vortex-induced vibration in two-dimensions. In: The Eighteenth International Offshore and Polar Engineering Conference (2008)
12. Franzini, G.R., Fujarra, A.L.C., Meneghini, J.R., Korkischko, I., Franciss, R.: Experimental investigation of Vortex-induced vibration on rigid, smooth and inclined cylinders. *J. Fluid. Struct.* **25**(4), 742–750 (2009)
13. Franzini, G.R., Gonçalves, R.T., Meneghini, J.R., Fujarra, A.L.C.: One and two degrees-of-freedom Vortex-induced vibration experiments with yawed cylinders. *J. Fluid. Struct.* **42**, 401–420 (2013)
14. Kinaci, O.K., Lakka, S., Sun, H., Bernitsas, M.M.: Effect of tip-flow on Vortex-induced vibration of circular cylinders. *Ocean Eng.* **117**, 130–142 (2016)
15. Postnikov, A., Pavlovskaya, E., Wiercigroch, M.: 2DOF CFD calibrated wake oscillator model to investigate Vortex-induced vibrations. *Int. J. Mech. Sci.* **127**, 176–190 (2017)
16. Kurushina, V., Pavlovskaya, E.: Fluid nonlinearities effect on wake oscillator model performance. In: MATEC Web of Conferences ICoEV, Paper No. 148–04002, pp. 1–6 (2018)

Asymptotic Analysis of a Dynamical System for Vortex-Induced Vibration and Galloping



Claudio Mannini

Abstract The present work presents an asymptotic analysis of a wake-oscillator model for the transverse oscillation of a rectangular cylinder in a cross airflow due to the interference of galloping instability and vortex shedding. Periodic synchronized solutions of the dynamical system are sought with the method of Krylov–Bogolyubov. The semi-analytical solutions are compared with the numerical solutions for several values of the mass-damping parameter of the system, showing a general agreement. Nevertheless, the study highlights the important role of the strong nonlinearity of the wake equation and the quasi-periodicity of the solution in some flow-velocity ranges. These features are not accounted for in the asymptotic analysis and are responsible for the shortcomings of the semi-analytical solutions.

Keywords Galloping · Wake-oscillator model · Autonomous system · Synchronization · Asymptotic analysis

1 Introduction

Many slender bluff bodies immersed in a cross flow are prone to both vortex-induced vibration (VIV) and the purely self-excited instability known as galloping. In the ideal case, the two phenomena occur in different flow speed ranges and do not interact with each other. Nevertheless, it has been shown in [1] that in many practical situations the two excitation mechanisms interfere giving rise to the so-called unsteady galloping instability, showing peculiar features that cannot be captured by the theories of VIV and galloping taken separately.

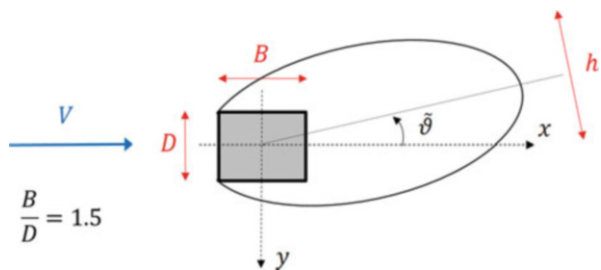
C. Mannini (✉)

CRIACIV-Department of Civil and Environmental Engineering, University of Florence,
Florence, Italy

e-mail: claudio.mannini@unifi.it

<https://www.unifi.it/p-doc2-2017-0-A-2c303b303228-0.html>

Fig. 1 Schematic of the near-wake oscillator



On this basis, a wake-oscillator model has been applied to the paradigmatic case of a rectangular cylinder with a sectional side ratio of 1.5 [2] (Fig. 1). The model is a modified version of the one proposed at the end of the 1970s by Prof. Y. Tamura for the vortex-induced vibration of a circular cylinder and subsequently applied to the case of a square cylinder [3]. It simply relies on the linear superposition of unsteady forces due to the oscillation of the near wake and producing vortex-induced vibration, and quasi-steady forces responsible for galloping. The major contribution of the work in [2] was the removal of a crucial assumption to estimate one of the model's parameters, increasing significantly the amount of nonlinearity in the wake equation and promoting the tendency of mechanical and wake oscillators to synchronize. This allowed overcoming the major drawbacks of the results obtained in [3]. The numerical solution of the equations revealed a rich nonlinear behavior, confirmed by the experimental data in [4], showing supercritical and subcritical bifurcations, periodic and quasi-periodic solutions, and hysteresis loops [2].

To shed some light on the behavior of the dynamical system and understand the role of the fairly strong nonlinearity of the wake equation, the use of asymptotic methods can be very useful. As a first step, the simple method of Krylov–Bogolyubov is employed here to search for synchronized steady-state solutions. A similar analysis has recently been carried out in [5] for a wake-oscillator model for the vortex-induced vibration of a circular cylinder. In contrast, the method of multiple scales was employed in [6] to study a different model for the combined effect of vortex shedding and galloping.

2 Wake-Oscillator Model

The wake-oscillator model used to study unsteady galloping represents an autonomous system of two coupled nonlinear equations; the nondimensional transverse vibrations of the body (normalized with the cross-flow section dimension D of the prism) are described by a linear oscillator subjected to a nonlinear force, while a van der Pol equation is employed for the wake:

$$y'' + (2\zeta + \mu U)y' + y = \beta U^2 \vartheta + U^2 C_{QS} \quad (1)$$

$$\vartheta'' + \epsilon U(\vartheta^2 - 1)\vartheta' + \delta^2 U^2 \vartheta = \gamma y'' + \sigma U y' \quad (2)$$

With reference to Fig. 1, it has been posed $\vartheta = 2f\tilde{\vartheta}/C_{L0}$, where f represents the slope of the unsteady nondimensional transverse force with the wake inclination, and C_{L0} the amplitude of such a force when the prism is stationary. $U = V/\omega_0 D$ is the reduced flow speed and represents the control parameter (V is the dimensional flow speed and ω_0 the natural circular frequency of the mechanical oscillator). ζ is the mechanical critical damping ratio. The prime denotes derivative with respect to the nondimensional time $\tau = \omega_0 t$. μ represents the linear aerodynamic damping coefficient due to unsteady wake forces, β is the force coefficient due to the coupling with the near wake oscillation, ϵ is the nonlinear damping coefficient of the wake oscillator, δ represents the ratio of the natural frequency of the wake oscillator to the one of the mechanical oscillator for unit reduced flow speed; finally, γ and σ account for the feedback effect of the body oscillation on the wake dynamics (acceleration and velocity coupling):

$$\mu = \frac{f}{m^*} \quad \beta = \frac{C_{L0}}{2m^*} \quad \epsilon = 16\sqrt{2}\text{St}^3 h^* f \quad (3)$$

$$\delta = 2\pi\text{St} \quad \gamma = \frac{16\pi\text{St}^2 h^* f}{C_{L0}} \quad \sigma = \frac{8\pi^2\text{St}^2 f}{C_{L0}} \quad (4)$$

$$C_{QS}(\alpha) = -\frac{\sec\alpha}{m^*} [C_L(\alpha) + C_D(\alpha) \tan\alpha] = \sum_{k=1}^4 (-1)^{k+1} A_{2k-1} \left(\frac{y'}{U} \right)^{2k-1} \quad (5)$$

where $\tan\alpha = y'/U$ denotes the relative angle of attack, $m^* = 2m/\rho D^2 \cong 1500$ (m is the oscillator mass per unit length and ρ the air density) is the mass ratio; $h^* = h/D$, being h the depth of the near wake (see Fig. 1); St is the Strouhal number, *i.e.*, the nondimensional vortex-shedding frequency for the stationary body. C_{QS} is the quasi-steady force coefficient, defined as the projection in the transverse direction of static lift, C_L , and drag, C_D , coefficients. In the dynamic case, it is a nonlinear function of y' and is assumed here as a seventh-order odd-power polynomial (Fig. 2a). It is to note that this polynomial is a sharp simplification of the more complicated experimental pattern reported in [2, 4]. According to experimental evidences [2], C_{L0} is a function of the Reynolds number and therefore of the nondimensional flow speed U (see Fig. 2b). Except for C_{QS} , the values assumed for the other aerodynamic parameters are the same as those employed in [2] ($\text{St} = 0.106$, $f = 9$, $h^* = 1.8$). All the details concerning the model and its parameters can be found in [2].

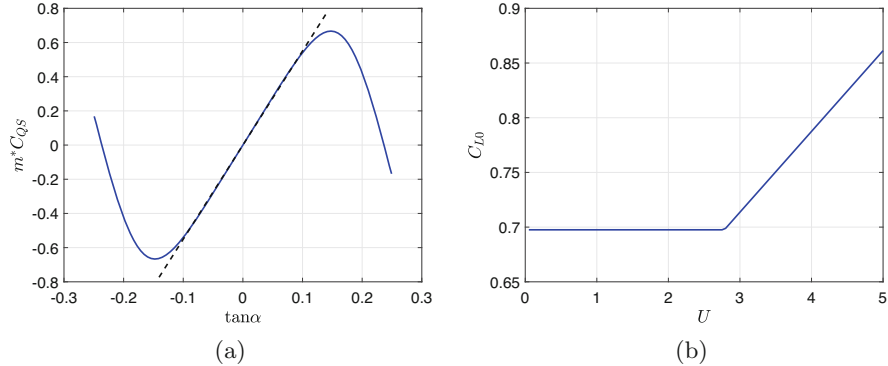


Fig. 2 (a) C_{QS} and its linear approximation; (b) dependence of C_{L0} on reduced flow velocity. $m^*A_1 = 5.50$, $m^*A_3 = -31.93$, $m^*A_5 = -4342.4$, $m^*A_7 = -35,878$

3 Asymptotic Analysis

Harmonic functions with fast-time frequency ω and slowly varying amplitude and phase are assumed for the dependent variables in Eqs. (1)–(2):

$$\begin{bmatrix} y(\tau) \\ \vartheta(\tau) \end{bmatrix} = \begin{bmatrix} Y(\tau) \\ \Theta(\tau) \end{bmatrix} e^{i\omega\tau} + \begin{bmatrix} \bar{Y}(\tau) \\ \bar{\Theta}(\tau) \end{bmatrix} e^{-i\omega\tau} \quad (6)$$

where Y and Θ are the slowly varying complex amplitudes, the overbar denotes complex conjugate and i is the imaginary unity. Substituting Eq. (6) and its derivatives into Eqs. (1)–(2) and averaging over the period $2\pi/\omega$, one obtains

$$\begin{aligned} Y' = & \left[i \frac{1 - \omega^2}{2\omega} - \zeta_1 \right] Y - \frac{3}{2} \frac{\omega^2}{U} A_3 |Y|^2 Y + 5 \frac{\omega^4}{U^3} A_5 |Y|^4 Y \\ & - \frac{35}{2} \frac{\omega^6}{U^5} A_7 |Y|^6 Y - i \frac{\beta U^2}{2\omega} \Theta \end{aligned} \quad (7)$$

$$\Theta' = - \left[\frac{1}{2} \epsilon U \left(|\Theta|^2 - 1 \right) + i \frac{\omega^2 - \delta^2 U^2}{2\omega} \right] \Theta + \frac{1}{2} (\sigma U + i \gamma \omega) Y + \gamma Y' \quad (8)$$

where $\zeta_1 = \zeta + \frac{1}{2} (\mu - A_1) U$.

Then, considering the polar form of the dependent variables, $Y = \frac{1}{2} r_y e^{i\phi_y}$ and $\Theta = \frac{1}{2} r_\theta e^{i\phi_\theta}$, posing $\omega = 1$ (thereby accounting for frequency variation with respect to the natural frequency of the mechanical oscillator through the derivative of the slowly varying phases ϕ_y and ϕ_θ), and introducing the phase difference $\psi = \phi_\theta - \phi_y$, one ends up with the following real-variable equations:

$$r'_y = -\zeta_1 r_y - \frac{3}{8} \frac{A_3}{U} r_y^3 + \frac{5}{16} \frac{A_5}{U^3} r_y^5 - \frac{35}{128} \frac{A_7}{U^5} r_y^7 + \frac{1}{2} \beta U^2 r_\theta \sin \psi \quad (9)$$

$$r'_\theta = -\frac{1}{8} \epsilon U (r_\theta^2 - 4) r_\theta - \frac{1}{4} \beta \gamma U^2 r_\theta \sin 2\psi + \frac{1}{2} r_y (\sigma U \cos \psi + \gamma \sin \psi) + \gamma r'_y \cos \psi \quad (10)$$

$$\begin{aligned} \psi' &= \frac{\delta^2 U^2 - 1}{2} + \frac{1}{2} \frac{r_y}{r_\theta} (\gamma \cos \psi - \sigma U \sin \psi) \\ &\quad + \frac{1}{2} \beta U^2 \frac{r_\theta}{r_y} \cos \psi - \frac{1}{2} \beta \gamma U^2 \cos^2 \psi - \gamma \frac{r'_y}{r_\theta} \sin \psi \end{aligned} \quad (11)$$

The fixed points of Eqs. (9)–(11) can be found by setting $r'_y = 0$, $r'_\theta = 0$, $\psi' = 0$, and represent synchronized steady-state periodic solutions of the system. To find these equilibrium solutions with a simple procedure, in a first step the higher-order powers of r_y in the steady-state version of Eq. (9) are neglected:

$$r_y = \frac{\beta U^2}{2\zeta_1} r_\theta \sin \psi \quad (12)$$

This is equivalent to a linearization of the force coefficient C_{QS} , which is a very accurate approximation up to $\tan \alpha \cong 0.1$ (Fig. 2a). Equation (12) is then substituted into the steady-state equations derived from Eqs. (10)–(11), yielding

$$r_\theta = 2 \left[1 - \frac{\beta \gamma U}{2\epsilon} \sin 2\psi + \frac{\beta U}{2\epsilon \zeta_1} \sin \psi (\sigma U \cos \psi + \gamma \sin \psi) \right]^{\frac{1}{2}} \quad (13)$$

$$\begin{aligned} &\left[\beta \sigma U^3 + 2\zeta_1 (1 - \delta^2 U^2) \right] \tan^3 \psi - \left(\beta \gamma U^2 + 4\zeta_1^2 \right) \tan^2 \psi \\ &\quad + 2\zeta_1 \left(1 - \delta^2 U^2 + \beta \gamma U^2 \right) \tan \psi - 4\zeta_1^2 = 0 \end{aligned} \quad (14)$$

Once the solutions of Eqs. (12)–(14) have been determined, these can be considered exact up to the line $\tan \alpha = (2\omega - 1)r_y/U \cong 0.1$ reported in Fig. 3a. To improve the accuracy of the solution beyond this limit, the higher-order terms in r_y are reintroduced. The previously mentioned results for $(r_y \ r_\theta \ \psi)^T$ are taken as initial guess, and the solutions are refined iteratively up to convergence (relative difference in the values of ψ , r_θ and r_y between two consecutive iterations lower than 10^{-4}). It has also been verified that no additional solution appears for $\tan \alpha = (2\omega - 1)r_y/U \leq 0.25$, which represents the limit beyond which no experimental data are available for C_{QS} (see Fig. 2a). Finally, the circular frequency of the synchronized steady-state solution can be obtained by

$$\omega = 1 + \phi'_y = 1 + \phi'_\theta = 1 - \frac{1}{2} \beta U^2 \frac{r_\theta}{r_y} \cos \psi \quad (15)$$

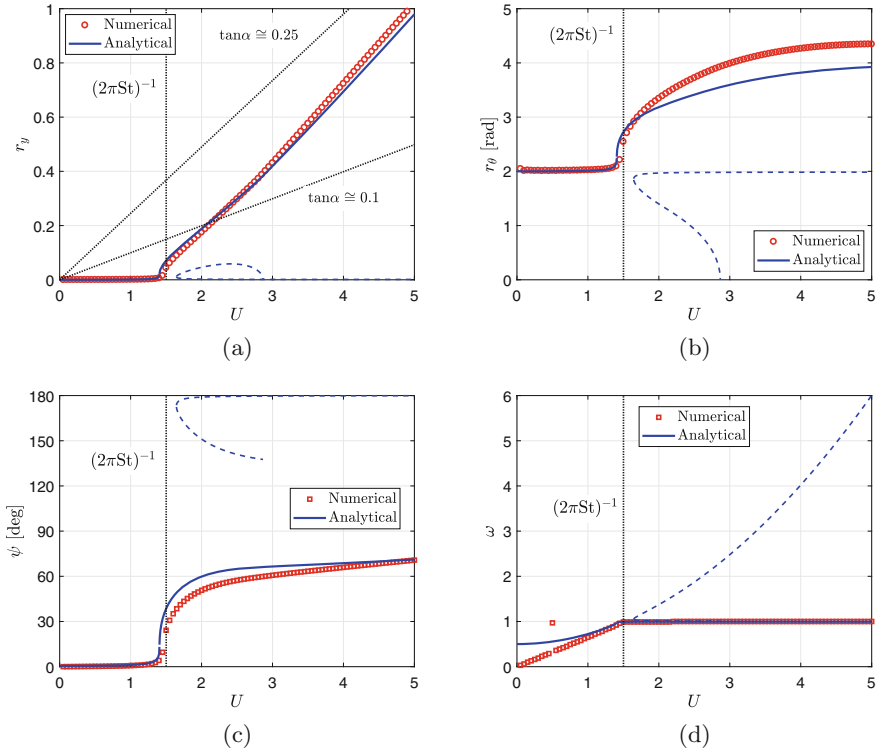


Fig. 3 Equilibrium solutions of Eqs. (9)–(11) and (15) for $2\pi\xi m^* = 42.2$ (solid and broken lines denote, respectively, stable and unstable solutions): (a) nondimensional oscillation amplitude of the cylinder; (b) oscillation amplitude of the wake oscillator; (c) phase difference between body and wake oscillations; (d) synchronized oscillation frequency

4 Discussion of Results

For large mass ratios, the steady-state oscillations of a given cylindrical body due to VIV and galloping are ruled by a mass-damping parameter $2\pi\xi m^*$, often known as Scruton number [1]. For a reference value of $2\pi\xi m^* = 42.2$, for which the interaction of VIV and galloping is strong, Fig. 3 reports the semi-analytical equilibrium solutions of Eqs. (9)–(11), compared with the numerical solutions of the equations, obtained through a Runge–Kutta algorithm, as explained in [2]. The agreement is good in terms of amplitude of the transverse oscillation (Fig. 3a), though some small discrepancies can be observed, especially for large vibrations. Larger deviations of the semi-analytical solution from the numerical one can be detected for the wake oscillation amplitude (Fig. 3b) and for the phase lag of prism to wake motion (Fig. 3c). These differences can be ascribed to the strong

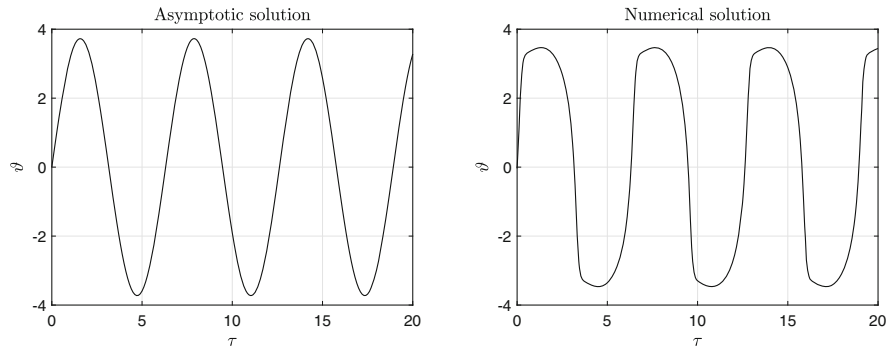


Fig. 4 Time history of wake oscillations for $2\pi\zeta m^* = 42.2$ and $U = 3.5$: comparison between semi-analytical and numerical solutions

nonlinear nature of wake oscillations, where the contribution of odd superharmonics is significant, as explained in [2] and emphasized in Fig. 4. As for the synchronized frequency, it can be noticed that after the instability onset at the vortex-resonance velocity $(2\pi St)^{-1}$ both the prism and the wake oscillate nearly at the natural frequency of the mechanical oscillator ($\omega \cong 1$), as is typical for fluid-structure interaction problems with large mass ratios. In contrast, for values of U below the bifurcation, the semi-analytical result is significantly different from the numerical solution. This is caused by the limitation of having imposed a synchronized solution, while the real behavior of the equations (and also the experimental evidence) shows a small-amplitude forced oscillation of the body at the wake natural frequency (and its odd superharmonics), except for the mild third-order superharmonic resonance at $U \cong 0.5$.

Figure 5 shows the results in terms of oscillation amplitude of the prism for lower and higher values of the mass-damping parameter. For low values of $2\pi\zeta m^*$, the semi-analytical solution is slightly less accurate for small vibration amplitudes, slightly after the bifurcation close to $U = (2\pi St)^{-1}$ (Fig. 5a). The opposite behavior is observed for large values of the mass-damping parameter (Fig. 5b–d). Nevertheless, the most interesting discrepancy concerns the intermediate-amplitude branch revealed by the numerical solution of system equations for $2\pi\zeta m^* = 62.2$ and 77.2 . While this remains unstable according to the asymptotic solution, conversely it is stable in certain velocity ranges according to the numerical solution (Fig. 5b and c). The oscillations along this branch are known to be quasi-periodic [2] (Fig. 6), a feature that is not accounted for in the present simplified approach. In addition, a key role is probably played by the strong nonlinearity of the wake equation, which is neglected here. The latter issue is also likely to explain why, for $2\pi\zeta m^* = 90$, the semi-analytical approach does not exhibit the upper branch solution in the range $2.5 \lesssim U \lesssim 4$ but, instead, an amplitude death after the vortex-resonance region (Fig. 5d).

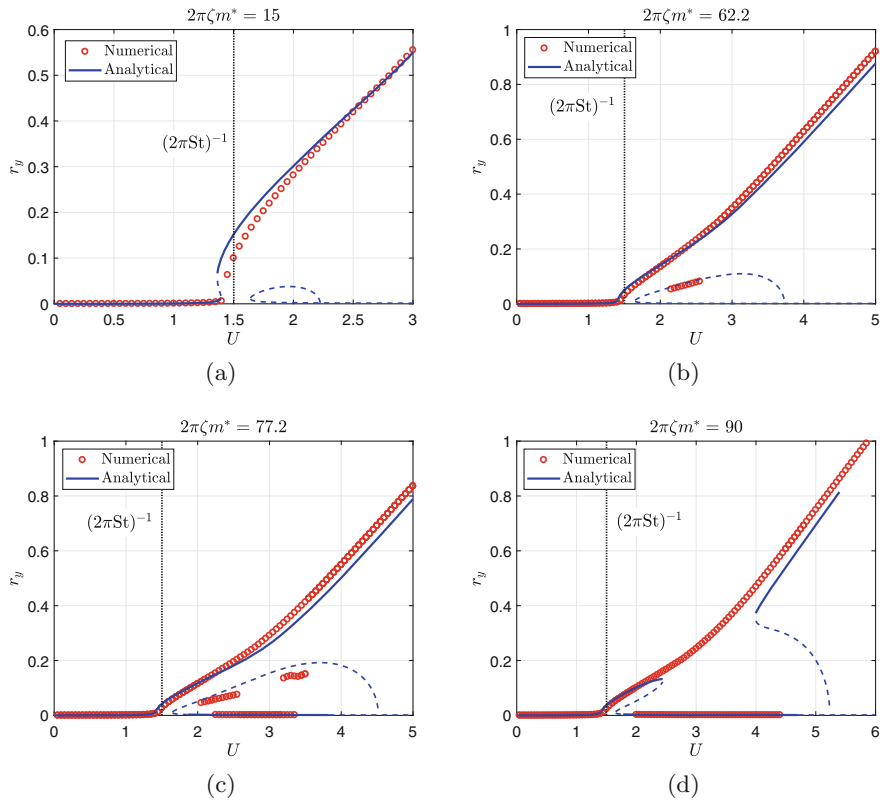


Fig. 5 Equilibrium solutions of the dynamical system in terms of vibration amplitude for different values of the mass-damping parameter of the system

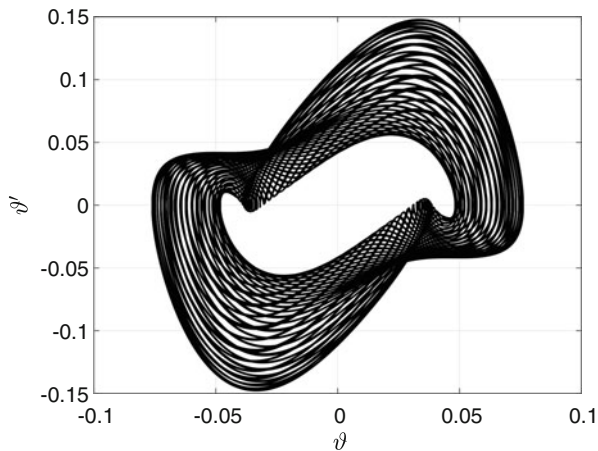


Fig. 6 Phase-space plot of the asymptotic solution for $2\pi\zeta m^* = 77.2$ and $U = 3.5$

5 Concluding Remarks

The asymptotic analysis with the method of Krylov–Bogolyubov of the considered nonlinear wake-oscillator dynamical system provided approximate synchronized steady-state solutions of the equations for several values of the mass-damping parameter. The semi-analytical solutions reproduce with reasonable accuracy some important features of this complicated nonlinear system without the drawback of the high computational cost of a numerical solution. Nevertheless, the analysis also underscores the limitations of such an approach, which does not account for the fact that the wake equation is not weakly nonlinear and that the solution in the intermediate-amplitude branch is quasi-periodic instead of perfectly synchronized.

References

1. Mannini, C., Marra, A.M., Bartoli, G.: VIV-galloping instability of rectangular cylinders: review and new experiments. *J. Wind Eng. Ind. Aerod.* **132**, 109–124 (2014). <https://doi.org/10.1016/j.jweia.2014.06.021>
2. Mannini, C., Massai, T., Marra, A.M.: Modeling the interference of vortex-induced vibration and galloping for a slender rectangular prism. *J. Sound Vib.* **419**, 493–509 (2018). <https://doi.org/10.1016/j.jsv.2017.12.016>
3. Tamura, Y., Shimada, K.: A mathematical model for the transverse oscillations of square cylinders. In: 1st International Conference on Flow Induced Vibrations, Bowness-on-Windermere, pp. 267–276 (1987)
4. Mannini, C., Marra, A.M., Massai, T., Bartoli, G.: Interference of vortex-induced vibration and transverse galloping for a rectangular cylinder. *J. Fluid. Struct.* **66**, 403–423 (2016). <https://doi.org/10.1016/j.jfluidstructs.2016.08.002>
5. Shoshani, O.: Deterministic and stochastic analyses of the lock-in phenomenon in vortex-induced vibrations. *J. Sound Vib.* **434**, 17–27 (2018). <https://doi.org/10.1016/j.jsv.2018.07.023>
6. Corless, R.M., Parkinson, G.V.: Mathematical modelling of the combined effects of vortex-induced vibration and galloping. part II. *J. Fluid. Struct.* **7**, 825–848 (1993). <https://doi.org/10.1006/jfls.1993.1050>

A Quasi-Steady 3-DoFs Sectional Aerodynamic Model: Preliminary Results



Cristoforo Demartino, Giulia Matteoni, and Christos T. Georgakis

Abstract A generalized quasi-steady three-degrees-of-freedom analytical model, capable of predicting the aerodynamic instability of a cylinder with a generic cross-section, is proposed. The three degrees-of-freedom refer to the two orthogonal displacements, perpendicular to the body's axis, plus the rotation about the longitudinal body axis. It allows for the variation of the force coefficients, i.e., drag, lift, and moment, with Reynolds number based on the relative flow velocity, with relative angle-of-attack, and relative cable-wind angle. The aerodynamic forces acting on the structure are linearized around the static equilibrium configuration. Based on the analytical solution of the eigenvalue problem, an expression of the galloping-and static divergence-type instability condition is derived. Finally, an application of the model is proposed to study the galloping of a full-scale dry inclined/yawed cable.

Keywords Bluff body · Aerodynamic damping · Three degrees-of-freedom · Quasi-steady · Instability criterion

C. Demartino (✉)

Department of Energy, Environment, and Infrastructure Sciences, Zhejiang University-University of Illinois (ZJUI), Zhejiang University, Haining, China

e-mail: cristoforo.demartino@me.com

G. Matteoni

Arup, London, UK

e-mail: giulia.matteoni@arup.com

C. T. Georgakis

Department of Engineering-Structural Monitoring and Dynamics, Aarhus University, Aarhus, Denmark

e-mail: cg@eng.au.dk

1 Introduction

When a structure oscillates in steady flow, the flow field relative to the structure also oscillates, thus producing fluctuating aerodynamic force components, which can be coupled either linearly or non-linearly, to the body's structural acceleration, velocity, or displacement/rotation [1]. For wind engineering applications, the first case is generally negligible since the air density is too low. In the second and third cases, a variation of the body's effective damping and an effective stiffness (frequency) occur, respectively. This can eventually vanish when the flow field generates negative aerodynamic damping, equal in absolute value to the structural damping. The first phenomenon can initiate instabilities of dynamic types, such as galloping, which is characterized by the occurrence of large amplitude vibrations, mostly in the cross-wind direction, at low frequencies. The second is related to the static divergence.

Bluff-body aerodynamic instabilities of galloping-type have been modeled, based on the Quasi-Steady (QS) theory. QS models are quite important in the Bridge Engineering field to predict the instability conditions of bridge cables. Three key issues play a major role in the assessment of inclined cable galloping when using the quasi-steady approach [2]: (1) the complex inclined flow aerodynamics, (2) the geometric irregularities characterizing real stay cables, and (3) the sectional quasi-steady stability galloping modeling in inclined flow conditions.

In real applications, circular cross-sections are never perfect. A cylinder featuring small deviations from a perfect circular one can be defined a nominally circular cylinder. These deviations, or irregularities, are classified into cylinder irregularities or flow irregularities, and the former are further subdivided into surface irregularities, section irregularities, and spanwise irregularities [3, 4]. Operating bridge cables proved to feature all these irregularities both in dry conditions [2, 5, 6] and in iced conditions [4, 7–10], which heavily affect aerodynamics and aerodynamic stability. These types of vibration were also observed during full-scale ambient vibration measurements [11].

Following the QS theory, a number of models have been derived accounting for the characteristics of the vibration phenomenon, such as: (1) flow conditions (cross or inclined), (2) directions of vibration of the structure (acrosswind, alongwind and/or torsional), (3) variation of the mean aerodynamic coefficients with Reynolds number, angle of attack and yaw angle, and (4) dynamic conditions (tuning and inertial coupling). These were reviewed and compared in Demartino and Ricciardelli [10] and in Piccardo et al. [12]. Recently, a probabilistic framework for the assessment of the minimum structural damping required to prevent galloping of dry bridge hangers using a 2-DoFs model was proposed accounting for the irregularities in a probabilistic way [13]. The available models are not proposing a closed form solution of the stability for the generic 3-DoFs case being usually based on the assessment of the eigenvalues. The proposed model overcomes this problem by applying the Routh–Hurwitz criterion and the Lienard–Chipart criterion and providing an expression of the galloping- and static divergence-type instability.

2 Aeroelastic Model

The equations of motion for the cylinder are (see Fig. 1)

$$\mathbf{M}_s \ddot{\mathbf{q}}(t) + \mathbf{C}_s \dot{\mathbf{q}}(t) + \mathbf{K}_s \mathbf{q}(t) = \mathbf{F}_a(\dot{\mathbf{q}}(t), \theta(t), U) \quad (1)$$

where \mathbf{M}_s , \mathbf{C}_s , \mathbf{K}_s are the structural mass, damping and stiffness matrices, respectively, and $\mathbf{F}_a(\dot{\mathbf{q}}(t), \theta(t), U)$ represents the aerodynamic force vector. $\mathbf{q}(t)$ is the vector containing the sectional displacements: $\eta_x(t)$ and $\eta_y(t)$, the two orthogonal displacements belonging to the cross-section plane and $\theta(t)$ the rotation about the cylinder's longitudinal axis. \mathbf{U} is the vector containing mean wind speed.

For the purpose at hand, it is necessary to define different reference systems. (X, Y, Z) is the global reference system with \mathbf{U} oriented parallel to the X -axis and Z the vertical, upward axis. The attitude to the flow of a cylinder is described by the inclination Θ , i.e., the angle between the body's longitudinal axis and its projection in the horizontal plane, and the yaw angle β , i.e., the angle between the free-stream velocity \mathbf{U} and the projection of the body's axis in the horizontal plane. (x', y', z) is the wind reference system with the axis x' parallel to the direction of the normal wind velocity U_N and y' perpendicular to it; z is parallel to the cylinder axis. (x, y, z) is the dynamic reference system where x , y belong to the cross-sectional plane of the cylinder and the DoFs $\eta_x(t)$ and $\eta_y(t)$ are in these two directions, respectively. x , y is rotated with respect to x' , y' of an angle α_s that is defined structural angle.

The aerodynamic forces in the (x, y, z) reference system are expressed as

$$\mathbf{F}_a(\dot{\mathbf{q}}(t), \theta(t), U) = \frac{1}{2} \rho D U_R^2(\dot{\mathbf{q}}(t), U) \mathbf{R}_z(\dot{\mathbf{q}}(t), \theta(t), U) \mathbf{C}(\dot{\mathbf{q}}(t), \theta(t), U) \quad (2)$$

where ρ is the air density (usually 1.25 kg/m^3), D is a characteristic size of the cross-section, U_R is the relative wind speed (accounting for $\dot{\mathbf{q}}(t)$), \mathbf{R}_z is the rotation

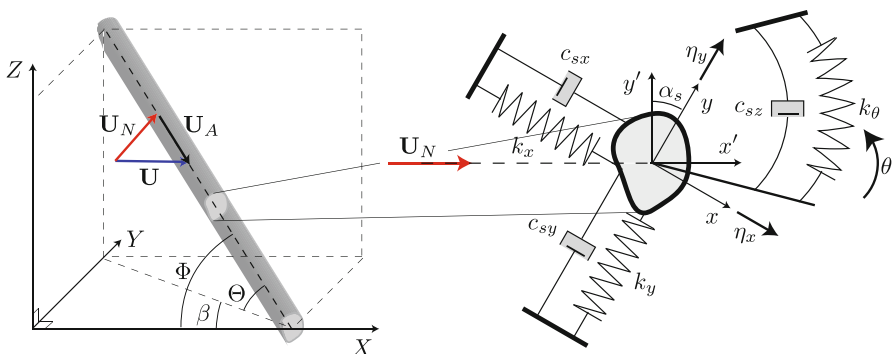


Fig. 1 Sectional aeroelastic model

matrix around the cable axis and $\mathbf{C}(\dot{\mathbf{q}}(t), \theta(t), U)$ is the vector containing $C_{x'}$ and $C_{y'}$ (the aerodynamic coefficients in x' and y' directions, respectively) and C_{Mz} (torsional moment aerodynamic coefficient). U is the modulus of \mathbf{U} .

The aerodynamic forces are non-linear functions of $\dot{\mathbf{q}}(t)$ and $\theta(t)$. A first order Taylor expansion of the aerodynamic forces about $\dot{\mathbf{q}}(t) = \mathbf{0}$ and $\mathbf{q}(t) = \mathbf{0}$ (i.e., $\theta(t) = 0$) is performed:

$$\mathbf{F}_a(\dot{\mathbf{q}}(t), \theta(t), U) = \mathbf{F}_a|_{(\mathbf{0}, \mathbf{0})} + \nabla_{\dot{\mathbf{q}}(t)} \mathbf{F}_a|_{(\mathbf{0}, \mathbf{0})} \dot{\mathbf{q}}(t) + \nabla_{\mathbf{q}(t)} \mathbf{F}_a|_{(\mathbf{0}, \mathbf{0})} \mathbf{q}(t) \quad (3)$$

The first term of Eq.(3), $\mathbf{F}_a|_{(\mathbf{0}, \mathbf{0})}$, contains the steady components of the aerodynamic forces per unit length and is neglected in the stability analysis and, accordingly, it is not provided. The second and third terms of Eq.(3) are the aerodynamic damping, and stiffness forces per unit length, respectively, and can be rearranged as

$$\begin{aligned} \nabla_{\dot{\mathbf{q}}(t)} \mathbf{F}_a|_{(\mathbf{0}, \mathbf{0})} &= \frac{\rho v^2}{2D} \left\{ \left[(\mathbf{R}_z(\alpha_s) \mathbf{C}) \otimes \left(\left(2Re \frac{D}{v} \right) \nabla_{\dot{\mathbf{q}}(t)} U_R \right) \right] \right. \\ &\quad \left. + Re^2 \left[(\mathbf{F} \mathbf{C} \otimes \nabla_{\dot{\mathbf{q}}(t)} \alpha_s) + \mathbf{R}_z(\alpha_s) [(\nabla_{\mathbf{d}} \mathbf{C}) (\nabla_{\dot{\mathbf{q}}(t)} \mathbf{d})] \right] \right\}|_{(\mathbf{0}, \mathbf{0})} \\ \nabla_{\mathbf{q}(t)} \mathbf{F}_a|_{(\mathbf{0}, \mathbf{0})} &= \frac{\rho v^2}{2D} \left\{ \overbrace{\left[(\mathbf{R}_z(\alpha_s) \mathbf{C}) \otimes \left(\left(2Re \frac{D}{v} \right) \nabla_{\dot{\mathbf{q}}(t)} U_R \right) \right]}^{0} \right. \\ &\quad \left. + Re^2 \left[(\mathbf{F} \mathbf{C} \otimes \nabla_{\dot{\mathbf{q}}(t)} \alpha_s) + \mathbf{R}_z(\alpha_s) [(\nabla_{\mathbf{d}} \mathbf{C}) (\nabla_{\dot{\mathbf{q}}(t)} \mathbf{d})] \right] \right\}|_{(\mathbf{0}, \mathbf{0})} \end{aligned} \quad (4)$$

where Re is the Reynolds number and v is the air viscosity. \mathbf{F} is a matrix defined as

$$\mathbf{F} = \begin{bmatrix} -\sin(\bar{\varphi}) & -\cos(\bar{\varphi}) & 0 \\ \cos(\bar{\varphi}) & -\sin(\bar{\varphi}) & 0 \\ 0 & 0 & 0 \end{bmatrix} \text{ with } \bar{\varphi} = -\left(\arctan \frac{\tan \beta}{\sin \Theta} \right) \quad (5)$$

\mathbf{d} is a vector defined as

$$\mathbf{d}(\dot{\mathbf{q}}(t), \theta(t), U) = [Re(\dot{\mathbf{q}}(t), \theta(t), U)) \alpha(\dot{\mathbf{q}}(t), \theta(t), U)) \Phi(\dot{\mathbf{q}}(t), \theta(t), U))]^T \quad (6)$$

where Φ is the wind-cable angle defined as $\Phi = \text{atan}(\tan \Theta / \sin \beta)$.

3 Stability Conditions

In order to find the eigenvalues, the characteristic equation is solved by posing the system in the state-space form (using Eq. (1) and substituting Eq. (4)) and by neglecting the steady components:

$$\det \left(\begin{bmatrix} \mathbf{0} & \mathbf{I} \\ -\mathbf{M}_s^{-1} \mathbf{K}_s & -\mathbf{M}_s^{-1} \mathbf{C}_s \end{bmatrix} + \begin{bmatrix} \mathbf{0} & \mathbf{0} \\ \mathbf{M}_s^{-1} \nabla_{\mathbf{q}(t)} \mathbf{F}_a|_{(\mathbf{0}, \mathbf{0})} & \mathbf{M}_s^{-1} \nabla_{\dot{\mathbf{q}}(t)} \mathbf{F}_a|_{(\mathbf{0}, \mathbf{0})} \end{bmatrix} - \lambda \mathbf{I} \right) = 0 \quad (7)$$

where \mathbf{I} is the identity matrix and λ are the eigenvalues. Equation (7) is a monic polynomial of 6th degree of the form:

$$p(\lambda) = \lambda^6 + p_1 \lambda^5 + p_2 \lambda^4 + p_3 \lambda^3 + p_4 \lambda^2 + p_5 \lambda + p_6 = 0 \quad (8)$$

where $p_1 - p_6$ are the coefficients of the characteristic polynomial. The eigenvalues found using the Eq. (8) are either real values or complex conjugate pairs. The system is stable if the real parts of all eigenvalues are negative.

The Routh–Hurwitz criterion [14] allows to check the stability of the system without solving the characteristic equation. The criterion establishes that a system is stable, i.e., all roots of the characteristic polynomial have negative real parts, if and only if all the leading principal minors of the Hurwitz matrix H , are positive. The Hurwitz matrix is defined by

$$H = \begin{bmatrix} p_1 & 1 & 0 & 0 & 0 & 0 \\ p_3 & p_2 & p_1 & 1 & 0 & 0 \\ p_5 & p_4 & p_3 & p_2 & p_1 & 1 \\ 0 & p_6 & p_5 & p_4 & p_3 & p_2 \\ 0 & 0 & 0 & p_6 & p_5 & p_4 \\ 0 & 0 & 0 & 0 & 0 & p_6 \end{bmatrix} \quad (9)$$

The principal diagonal minors of the Hurwitz matrix are

$$\begin{aligned} \Delta_0 &= (p_1 p_4 - p_5) & \Delta_1 &= p_1 \\ \Delta_2 &= p_1 p_2 - p_3 & \Delta_3 &= p_3 \Delta_2 - p_1 \Delta_0 \\ \Delta_4 &= p_4 \Delta_3 + (p_1 p_6 - p_2 p_5) \Delta_2 + p_5 \Delta_0 & \Delta_5 &= p_5 \Delta_4 - p_6 \\ \Delta_6 &= p_6 \Delta_5 \end{aligned} \quad (10)$$

If $\Delta_1 - \Delta_5$ are positive, the stability condition on Δ_6 reduces to imposing $p_6 > 0$. The condition $\Delta_6 = 0$ represents a boundary of stability, then there are two options:

- $p_6 = 0$. This condition corresponds to the case when one of the eigenvalues is zero without imaginary part. The system is on the boundary of the aperiodic stability. In fact, $p_6 = 0$ corresponds to the case in which the aerodynamic and structural stiffness are the same. This is the critical condition for static divergence.
- $\Delta_5 = 0$. In this case, a complex conjugate pair of the eigenvalues at a fixed point becomes purely imaginary. This is the critical condition for galloping. A single Hopf bifurcation occurs.

If $\Delta_1 - \Delta_5$ are not positive, in the 3-DoFs system the Hopf bifurcation can be single, double, or triple. This is the critical condition for galloping.

In order to simplify the computational problem of the stability analysis, the Lienard–Chipart criterion [17] can be used. The criterion has the advantage of providing a test for the system instability by means of a lower number of determinants to be computed. According to the criterion, the system (necessary and sufficient condition) is stable if

$$p_2, p_4, p_6 > 0 \text{ and } \Delta_1 = p_1, \Delta_3, \Delta_5 > 0 \quad (11)$$

Also in this case, the critical condition for static divergence is $p_6 = 0$. In the following, this criterion will be used in the application.

4 Application to a Full-Scale Dry Inclined/Yawed Cable

Quasi-steady drag, lift, and moment coefficients were measured by means of static wind tunnel tests [9], for a model of a full-scale bridge stay cable, made of a plain-surfaced HDPE tube, provided by bridge cable suppliers, with a nominal diameter of 160 mm. Tests were performed for varying yaw angles, β , in the range of 0 to 180°, and mean wind speeds, U , in the range of 8 to 29 m/s. In all the tests, the cable model was oriented at a vertical inclination, $\Theta = 30^\circ$. The aerodynamic coefficients are depicted in Fig. 2.

Figure 3 shows the map of the galloping instability as a function of Re and Φ . Table 1 illustrates the geometrical and structural properties of the cable model adopted in the analysis. The grey areas represent the region of predicted stability and the red areas represent the region of predicted instability. The galloping instability is predicted for $Re > 2.5 \times 10^5$ and in the range of $\Phi = 60$ to 120°. This is in good agreement with predictions of Macdonald and Larose [18] done with a 1-DoF model with similar characteristics validating the proposed model.

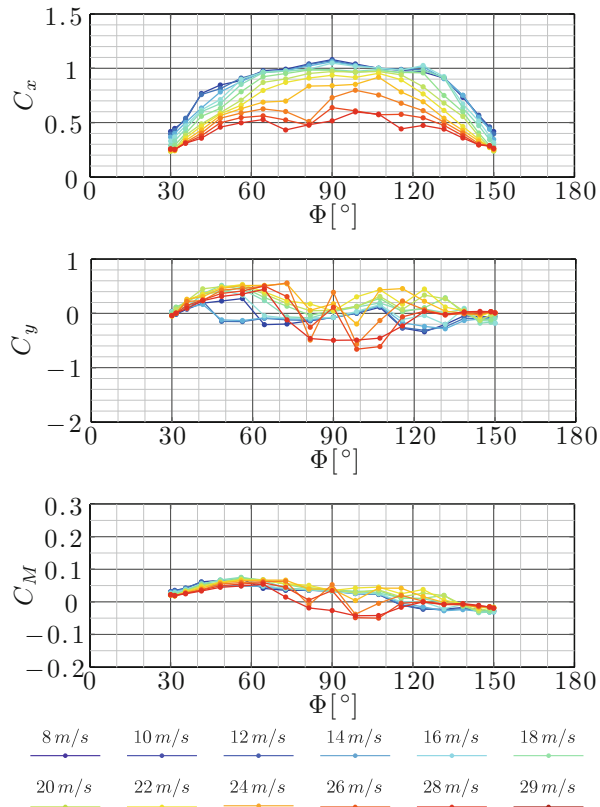


Fig. 2 Aerodynamic force coefficients for a dry cable in inclined flow. (Details about the wind tunnel tests are reported in [15, 16])

Fig. 3 Predicted galloping instability region (red: instability; gray: stability)

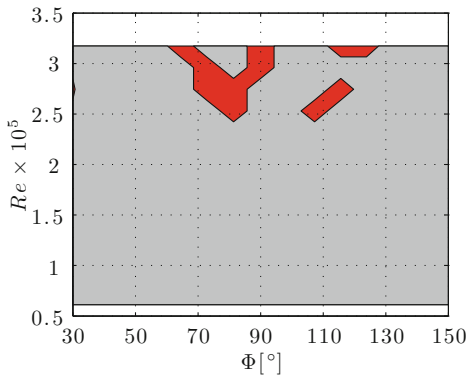


Table 1 Structural and aerodynamic parameters chosen to investigate the stability

Parameter	Value	Parameter	Value	Parameter	Value
m [kg/m]	100	ω_x [rad/s]	6.28	ξ_x [%]	0.02
D [m]	0.16	ω_y [rad/s]	6.28	ξ_y [%]	0.02
J [kg m]	0.32	ω_θ [rad/s]	50.2	ξ_θ [%]	0.02

m is the mass per unit length, J is the mass moment of inertia per unit length, ω is the angular frequency, ξ is the damping ratio

5 Conclusions

A generalized quasi-steady 3-DoFs analytical model, capable of predicting the galloping and static divergence instability of a cylinder with a generic cross-section, was proposed. Based on the analytical solution of the eigenvalue problem, an expression of the galloping- and static divergence-type instability condition is derived. An application of the 3-DoFs analytical model was proposed in order to study the galloping stability conditions of a full-scale dry inclined/yawed cable. It was found that for selected ranges of angle-of-attack and Reynolds number, the dry cable can undergo in galloping. The results of the proposed model are in agreement with the findings of previous models for similar conditions providing a validation of the proposed model. Future work should therefore include the evaluation of the stability considering a complete parametric study in order to identify the main influencing variables.

References

1. Blevins, R.D.: Flow-Induced Vibration, vol. 1, p. 377. Van Nostrand Reinhold, New York (1977)
2. Demartino, C., Ricciardelli, F.: Assessment of the structural damping required to prevent galloping of dry HDPE stay cables using the quasi-steady approach. *J. Bridge Eng.* **23**(4), 04018004 (2018)
3. Demartino, C.: Aerodynamics and Aeroelastic Behaviour of Ice-Accreted Bridge Cables. PhD thesis, University of Naples Federico II University of Naples Federico II–Department of Structures for Engineering and Architecture (2014)
4. Demartino, C., Ricciardelli, F.: Aerodynamics of nominally circular cylinders: A review of experimental results for civil engineering applications. *Eng. Struct.* **137**, 76–114 (2017)
5. Matteoni, G., Georgakis, C.T.: Effects of bridge cable surface roughness and cross-sectional distortion on aerodynamic force coefficients. *J. Wind Eng. Ind. Aerodynam.* **104**, 176–187 (2012)
6. Matteoni, G., Georgakis, C.T.: Effects of surface roughness and cross-sectional distortion on the wind-induced response of bridge cables in dry conditions. *J. Wind Eng. Ind. Aerodynam.* **136**, 89–100 (2015)
7. Koss, H.H., Gjelstrup, H., Georgakis, C.T.: Experimental study of ice accretion on circular cylinders at moderate low temperatures. *J. Wind Eng. Ind. Aerodynam.* **104**, 540–546 (2012)
8. Gjelstrup, H., Georgakis, C.T., Larsen, A.: An evaluation of iced bridge hanger vibrations through wind tunnel testing and quasi-steady theory. *Wind & Struct.* **15**(5), 385–407 (2012)

9. Demartino, C., Koss, H.H., Georgakis, C.T., Ricciardelli, F.: Effects of ice accretion on the aerodynamics of bridge cable. *J. Wind Eng. Ind. Aerodynam.* **138**, 98–119 (2015)
10. Demartino, C., Ricciardelli, F.: Aerodynamic stability of ice-accreted bridge cables. *J. Fluid. Struct.* **52**, 81–100 (2015)
11. Acampora, A., Macdonald, J.H.G., Georgakis, C.T., Nikitas, N.: Identification of aeroelastic forces and static drag coefficients of a twin cable bridge stay from full-scale ambient vibration measurements. *J. Wind Eng. Ind. Aerodynam.* **124**, 90–98 (2014)
12. Piccardo, G., Pagnini, L.C., Tubino, F.: Some research perspectives in galloping phenomena: critical conditions and post-critical behavior. *Continuum Mech. Therm.* **27**(1–2), 261–285 (2015)
13. Demartino, C., Ricciardelli, F.: Probabilistic vs. deterministic assessment of the minimum structural damping required to prevent galloping of dry bridge hangers. *J. Struct. Eng.* **145**, 04019078 (2019)
14. Hurwitz, A.: Ueber die bedingungen, unter welchen eine Gleichung nur Wurzeln mit negativen reellen Theilen besitzt. *Math. Ann.* **46**, 273–284 (1895)
15. Demartino, C., Koss, H., Ricciardelli, F.: Experimental study of the effect of icing on the aerodynamics of circular cylinders-Part I: cross flow. In 6th European and African Conference on Wind Engineering, Robinson College, Cambridge (2013)
16. Demartino, C., Georgakis, C.T., Ricciardelli, F.: Experimental study of the effect of icing on the aerodynamics of circular cylinders-Part II: inclined flow. In 6th European and African Conference on Wind Engineering, Robinson College, Cambridge, UK (2013)
17. Liénard, A., Chipart, M.H.: Sur le signe de la partie réelle des racines d'une équation algébrique. *J. Math. Pures Appl.* **10**(4), 291–346 (1914)
18. Macdonald, J.H.G., Larose, G.L.: A unified approach to aerodynamic damping and drag/lift instabilities, and its application to dry inclined cable galloping. *J. fluid. Struct.* **22**(2), 229–252 (2006)

Lie Group Dynamics of Multibody System in Vortical Fluid Flow



Zdravko Terze, Viktor Pandža, and Dario Zlatar

Abstract This paper describes a computationally efficient method for simulating dynamics of the coupled multibody-fluid system that utilizes symplectic and Lie-Poisson reductions in order to formulate fully coupled dynamical model of the multi-physical system by using solid variables only. The multibody system (MBS) dynamics is formulated in Lie group setting and integrated with the pertinent Lie group integration method that operates in MBS state space. The effects of fluid flow on MBS dynamics are accounted for by the added masses to the submerged bodies, calculated by boundary element method. The case study of coupled dynamics of three rigid ellipsoid (blunt) bodies in fluid flow without circulation is presented. In order to take into account additional viscous effects and include fluid vorticity and circulation in the system dynamics (when motion of the kinematical chain with sharp edges is considered), vortex shedding mechanism is incorporated in the overall model by numerically enforcing Kutta condition.

Keywords Lie groups · Multibody dynamics · Fluid-structure interaction

1 Introduction

The conventional approach to simulating dynamics of multibody system (MBS) moving in ambient fluid most commonly includes discretization of the large fluid domain, using separate meshes for the fluid and solid part of the system. This leads to the calculation of large amount of fluid data, that are usually not of the prime interest, since we are mostly concerned with effects that the fluid exerts on the MBS motion. In order to circumvent these deficiencies and obtain numerically more efficient method for simulating system coupled dynamics, we adopt a geometric modeling approach of fully coupled MBS-fluid system, incorporating boundary

Z. Terze · V. Pandža (✉) · D. Zlatar

Chair of Flight Vehicle Dynamics, Faculty of Mechanical Engineering and Naval Architecture, University of Zagreb, Zagreb, Croatia
e-mail: zdravko.terze@fsb.hr

integral method for calculating added masses, and time integrator in Lie group setting.

The configuration space of an unconstrained multibody system (MBS) comprising k rigid bodies is modeled as a Lie group $G = \mathbb{R}^3 \times SO(3) \times \cdots \times \mathbb{R}^3 \times SO(3)$ (k copies of $\mathbb{R}^3 \times SO(3)$) with the elements of the form $p = (\mathbf{x}_1, \mathbf{R}_1, \dots, \mathbf{x}_k, \mathbf{R}_k)$. G is a Lie group of the dimension $n = 6k$, where k is the number of the rigid bodies. The left multiplication in the group is given as $L_p : G \rightarrow G$, $p \rightarrow p \cdot p$, where origin of the group G is given as $e = (\mathbf{0}_1, \mathbf{I}_1, \dots, \mathbf{0}_k, \mathbf{I}_k)$. With G so defined, its Lie algebra is given as $g = \mathbb{R}^3 \times so(3) \times \cdots \times \mathbb{R}^3 \times so(3)$ with the elements of the form $v = (\mathbf{v}_1, \tilde{\boldsymbol{\omega}}_1, \dots, \mathbf{v}_k, \tilde{\boldsymbol{\omega}}_k)$, \mathbf{v}_i being velocity of i th body mass center and $\tilde{\boldsymbol{\omega}}_i$ i th body angular velocity in skew symmetric matrix form [1].

By assuming inviscid and incompressible fluid, the configuration space of the coupled MBS-fluid system is reduced by eliminating fluid variables via symplectic and Lie-Poisson two stages reduction [2], without compromising any accuracy. The first reduction exploits particle relabeling symmetry, associated with the conservation of circulation: fluid kinetic energy, fluid Lagrangian, and associated momentum map are invariant with respect to this symmetry [3]. Consequently, the equations of motion for the submerged MBS are formulated without explicitly incorporating the fluid variables, while effect of the fluid flow to MBS overall dynamics is accounted for by the added masses to the submerged bodies [4, 5]. In such approach, the added masses are expressed as boundary integral functions of the fluid density and the flow velocity potential. Further reduction of the system is associated with the symmetry based on invariance of the dynamics under superimposed rigid motion [6]. The similar approach is taken in [4], however, with an additional assumption of zero vorticity, and applied to the multibody system consisting solely of smooth bodies without sharp edges.

Here, in order to allow for simulations of bodies with non-smooth boundaries (that include sharp edges), the point vortex shedding and evolution mechanism is incorporated in the fluid-structure dynamical model. The vortices are assumed to be irrotational, and are being shed in a way to ensure the satisfaction of the Kutta condition at the sharp edges. By using the proposed framework it is possible to include an arbitrary combination of smooth and sharp-edged bodies in a coupled multibody-fluid system, as long as the major viscosity effects of the fluid on the body can be described by shedding and evolution of the irrotational point vortices. This broadens the possibilities for utilization of the presented method by removing the necessity of having smooth shape of the moving bodies immersed in the ambiental fluid, such as in the case of the models described in [4].

2 Multibody System Dynamics in Fluid Flow

We consider system of k articulated, constrained, and submerged bodies in ideal fluid, which is at rest at the infinity. In other words, at any time t , the system consisting of the solid bodies and the fluid occupies an open connected region \mathcal{M} of

the Euclidean space, which we identify with \mathbb{R}^3 . More specifically, the solid bodies occupy regions \mathcal{B}_i , $i = 1, \dots, k$ and the fluid occupies a connected region $\mathcal{F} \subset \mathcal{M}$ such that \mathcal{M} can be written as a disjoint union of open sets as $\mathcal{M} = \mathcal{B}_1 \cup \dots \cup \mathcal{B}_k \cup \mathcal{F}$. Configuration space \mathcal{Q} of such a system is the set of all appropriately smooth maps from \mathcal{M} to \mathcal{M} , where fluid part $\mathcal{Q}_f \in \text{Diff}_{\text{vol}}(\mathcal{F})$ —Lie group $\text{Diff}_{\text{vol}}(\mathcal{F})$ is the set of volume-preserving diffeomorphisms of \mathcal{F} that are the identity at infinity—represents position field of the fluid particles. Bodies part \mathcal{Q}_{Bi} , $i = 1, 2, \dots, k$, represents rigid body motion of the i -th solid body $\mathcal{B}_i \subset \mathcal{M}$ with boundary $\partial\mathcal{B}_i$, meaning that the configuration space of an unconstrained multibody system (MBS) comprising k rigid bodies is modeled as Lie group G introduced in Sect. 1.

To this end, the MBS state space is introduced as $S = G \times g$, i.e., $S = \mathbb{R}^3 \times SO(3) \times \dots \times \mathbb{R}^3 \times SO(3) \times \mathbb{R}^3 \times so(3) \times \dots \times \mathbb{R}^3 \times so(3) \cong TG$ with the elements $x = (\mathbf{x}_1, \mathbf{R}_1, \dots, \mathbf{x}_k, \mathbf{R}_k, \mathbf{v}_1, \tilde{\omega}_1, \dots, \mathbf{v}_k, \tilde{\omega}_k)$ [1]. S is the left-trivialization of the tangent bundle TG . This is a Lie group itself that possesses the Lie algebra $S = \mathbb{R}^3 \times so(3) \times \dots \times \mathbb{R}^3 \times so(3) \times \mathbb{R}^3 \times \mathbb{R}^3 \times \dots \times \mathbb{R}^3 \times \mathbb{R}^3$ with the element $z = (\mathbf{v}_1, \tilde{\omega}_1, \dots, \mathbf{v}_k, \tilde{\omega}_k, \dot{\mathbf{v}}_1, \dot{\omega}_1, \dots, \dot{\mathbf{v}}_k, \dot{\omega}_k)$.

It can be shown that—if kinematical constraints are imposed on the system bodies—MBS dynamics in fluid flow can be expressed as DAE-index-1 problem formulated as

$$\begin{bmatrix} \mathbf{M} & \mathbf{C}^T \\ \mathbf{C} & \mathbf{0} \end{bmatrix} \begin{bmatrix} \dot{\mathbf{z}} \\ \lambda \end{bmatrix} = \begin{bmatrix} \mathbf{Q} \\ \xi \end{bmatrix}, \quad (1)$$

where \mathbf{M} represents inertia matrix and \mathbf{Q} is the force vector. Inertia matrix \mathbf{M} contains standard inertial properties of the MBS in vacuum [1], supplemented by added mass that the MBS perceives due to interaction with the fluid. The added mass effects are calculated by BEM (described in the Sect. 3), after symplectic reduction on \mathcal{Q} is performed, see below.

The force vector \mathbf{Q} can be written as

$$\mathbf{Q} = \mathbf{Q}_{\text{ext}} + \mathbf{Q}_{\text{ideal}} + \mathbf{Q}_{\text{vort}}, \quad (2)$$

where \mathbf{Q}_{ext} represents a vector of general external forces and torques acting on a body, $\mathbf{Q}_{\text{ideal}}$ represents a vector of forces and torques that potential and inviscid fluid would exert on the MBS, while \mathbf{Q}_{vort} represents a vector of forces and torques acting on a body due to the presence of the point vortices.

Other parts of the equation stem from the kinematical generalized position constraint equation

$$\Phi(q) = \mathbf{0}, \quad (3)$$

which is differentiated to obtain a constraint equation at the velocity level

$$\mathbf{C}(q)\mathbf{z} = \mathbf{0}, \quad (4)$$

where \mathbf{C} represents constraint Jacobian, and λ associated Lagrange multipliers, see [1]. Further differentiation yields constraint equation at the acceleration level

$$\mathbf{C}(q)\dot{z} = \xi(q, z).$$

By inspecting (1) it is clear that dynamics of the coupled system MBS-fluid-flow, expressed in this way, is basically governed by the MBS variables only, i.e., fluid terms vanish from the model, except for the vector \mathbf{Q}_{vort} ($\mathbf{Q}_{\text{ideal}}$ can also be expressed in terms of MBS variables and added mass effects).

Indeed, if vorticity effects are excluded from the analysis, it can be shown that symplectic reduction at zero vorticity yields

$$J_{\mathcal{F}}^{-1}(0)/\text{Diff}_{\text{vol}}(\mathcal{F}) = T^*(\mathcal{Q}/\text{Diff}_{\text{vol}}(\mathcal{F})) = T^*G \quad (5)$$

indicating that the whole dynamics of the system evolves in T^*G (no fluid variables!) and fluid influence on the MBS dynamics is reduced to added mass effect only [4]. In (5), $J_{\mathcal{F}}$ is momentum map associated with the action of $\text{Diff}_{\text{vol}}(\mathcal{F})$ on \mathcal{Q} .

Similarly as it is shown in [1], Lie group integrator that operates in S can be utilized to obtain system velocities z , while constraint violation stabilization algorithm for both constraint Eqs. (3) and (4) needs to be simultaneously performed as well as BEM procedure (Sect. 3) for the added mass determination. After obtaining system velocities, a reconstruction of the system translation is a trivial task, while rotational part requires a non-linear (Lie group) update.

To this end, Munthe-Kaas Lie group method [7] is utilized, where kinematic reconstruction is performed by seeking an incremental rotation vector θ in each time step by integrating ODE equation in Lie algebra

$$\dot{\theta} = \text{dexp}_{-\theta}^{-1}(\omega), \quad \theta(0) = \mathbf{0}.$$

The rotation matrix in time step $i + 1$ is then reconstructed as

$$\mathbf{R}_{i+1} = \mathbf{R}_i \exp(\theta_{i+1}),$$

where \exp represents exponential mapping on $SO(3)$ and $\text{dexp}_{-\theta}^{-1}$ represents inverse differential exponential operator (more details can be found in [1]).

3 Boundary Element Method

In the context of the coupled MBS-fluid-flow formulation described in Sect. 2, the added mass effect is to be determined by BEM. This is due to the fact that bodies in MBS are generally hydrodynamically coupled and added mass effect on each body is the function of the motion of the whole MBS.

As an example, the system of three ellipsoid rigid bodies linked by revolute joints moving in a fluid is chosen. The domain of rigid bodies is defined as $\mathcal{B} = \mathcal{B}_1 \cup \mathcal{B}_2 \cup \mathcal{B}_3$, and the fluid domain is denoted as \mathcal{F} . As the region \mathcal{F} is connected, if the flow is irrotational, the velocity field \mathbf{u} can be written in terms of a potential $\mathbf{u} = \nabla\phi$. Incompressibility now implies that the Laplacian of ϕ is zero [3], i.e.:

$$\Delta\phi = 0 \quad \text{in } \mathcal{F}.$$

After applying non-penetrating boundary condition, i.e., the condition that fluid cannot pass through the boundary of the rigid body, but may slip freely along the edges, the Neumann conditions for the boundary value problem are obtained:

$$\nabla\phi \cdot \mathbf{n}_i = \mathbf{v}_i \cdot \mathbf{n}_i \quad \text{on } \partial\mathcal{B}_i, \quad \text{for } i = 1, 2, 3. \quad (6)$$

This, together with condition that the fluid is at rest at infinity, i.e.:

$$\nabla\phi = 0 \quad \text{at } \infty$$

completes the full description of the exterior Laplace boundary value problem with the Neumann boundary conditions. Following approach proposed in [8], the boundary value problem can be formulated as

$$H \cdot \gamma_0^{\text{ext}}\phi = -\left(\frac{1}{2}I + K'\right) \cdot \gamma_1^{\text{ext}}\phi, \quad (7)$$

where H represents hypersingular boundary Laplace operator, $\gamma_0^{\text{ext}}\phi$ represents unknown Dirichlet boundary condition, I is the identity boundary operator, K' is the adjoint double layer boundary Laplace operator, and $\gamma_1^{\text{ext}}\phi$ represents Neumann boundary conditions defined in (6).

The Eq. (7) can be solved by discretizing the surface of the MBS with boundary elements. In the paper, the MBS is meshed with triangular elements by using an open source software Gmsh [9]. The open source platform BEM++ [10] is used for solving the above defined boundary element problem. BEM++ is an efficient code that uses the hierarchical matrix technique to significantly speed up the process of assembling the boundary operators in (7), which is one of the most time-consuming operations in the formulation. In addition to that, the number of variables in the model is reduced by the multiple orders of magnitude due to the solid boundary discretization, as opposed to the conventional full 3D fluid domain discretization, leading to significant reductions in computational time.

The Neumann boundary function (6) is described via discontinuous piecewise constant values across the boundary elements, while the unknown Dirichlet function is described as a continuous piecewise linear function across the elements. The kinetic energy of the fluid, and subsequently the added mass effects in Eq. (1), can be computed from the calculated values of the Dirichlet boundary conditions.

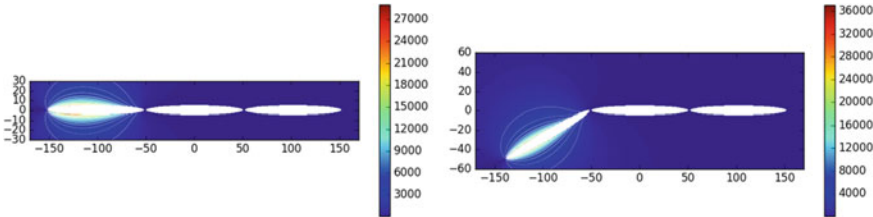


Fig. 1 The velocity potential field for MBS consisting of 3 rigid bodies, with the leftmost body rotating at 100 rad/s in ambient fluid. The images show the results for two different configurations. In the left figure, leftmost body is in initial configuration, while the right figure depicts system with leftmost body rotated by $\pi/6$ from initial configuration

If needed, the resulting velocity potential field can be reconstructed from the Dirichlet and Neumann data as

$$\phi = \phi_\infty - S_{LP} \cdot \gamma_1^{\text{ext}} \phi + DLP \cdot \gamma_0^{\text{ext}} \phi, \quad (8)$$

where ϕ_∞ represents value of the velocity potential at infinity, S_{LP} is the single layer Laplace potential operator, and DLP is the double layer Laplace potential operator.

As a test case, the multibody system consisting of three rigid 3D ellipsoid bodies, submerged in an incompressible and inviscid fluid and connected by a revolute joints, is considered. The leftmost body of the MBS is articulated with an angular velocity of 100 rad/s and the computation is performed for a boundary value problem as defined in (7). The velocity potential is reconstructed from the Dirichlet and Neumann data by using (8), and the results for the midplane through the ellipsoids are shown in Fig. 1.

4 Point Vortices

By using the approach described up to this point in the paper, dynamics of MBS in ambiental potential flow can be solved. This means that vorticity effects, represented by Q_{vort} in (1), are not considered in the analysis so far and—consequently—no fluid variables (apart from BEM added mass determination) are included in the solution. To this end, the discretization is required only at the boundary of the MBS, as opposed to the conventional approach, which requires discretization of the large fluid domain. However, by following this path, the extent of the applications to which this method can be applied is limited, mainly due to the inviscid fluid assumption. On the other hand, there is a number of application where viscosity plays an important role, but can be reasonably well approximated by shedding and evolution of the irrotational point vortices. One example of such applications are insect-type flapping micro aerial vehicles, as described in [11] and [12].

Modeling of viscosity effects via irrotational point vortices is especially useful for the multibody systems with sharp edges, since such a shedding can be modeled by applying Kutta condition at the edges, enforcing physical meaningfulness of the velocities, i.e., velocity at the tip must be equal in magnitude and direction, when analyzed from any surface [13]. However, calculation of the shed vortex initial position, appropriate circulation and subsequent evolution and interaction of the vortices with the environment presents a non-trivial task.

In the paper, the approach taken in [14] is followed, where the vortices are shed at each time step, at the approximate midpoint between edge positions at two time steps. The circulation of the vortex is taken to ensure a satisfaction of the Kutta condition. Unlike test cases described in [14], where 2D problems are solved, in this paper the simulation is performed in three dimensions, by assuming that the vortex is constant along the direction colinear with the edge.

Since there are no external forces acting on the fluid-solid system the overall linear \mathbf{P} and angular momentum $\boldsymbol{\Pi}$ have to be preserved. Mathematically, this can be formulated as (by following approach in [15] and [16])

$$\begin{aligned}\frac{d\mathbf{P}}{dt} &= \frac{d}{dt} \left(\sum_{i=1}^k m_i \mathbf{v}_i + \oint_{\partial\mathcal{B}} \mathbf{x} \times (\mathbf{n} \times \mathbf{u}) ds + \int_{\mathcal{F}} \mathbf{x} \times \boldsymbol{\Omega} da \right) = 0, \\ \frac{d\boldsymbol{\Pi}}{dt} &= \frac{d}{dt} \left(\sum_{i=1}^k \mathbf{J}_i \boldsymbol{\omega}_i - \frac{1}{2} \oint_{\partial\mathcal{B}} \|\mathbf{x}\|^2 (\mathbf{n} \times \mathbf{u}) ds - \frac{1}{2} \int_{\mathcal{F}} \|\mathbf{x}\|^2 \boldsymbol{\Omega} da \right) = 0,\end{aligned}$$

where m_i and \mathbf{J}_i represent i -th body mass and inertia matrix, \mathbf{x} and \mathbf{n} represent position vector with respect to the inertial frame and normal to the surface of the body, while $\boldsymbol{\Omega} = \nabla \times \mathbf{u}$ is the fluid vorticity.

In the case of the irrotational point vortices as introduced in our model, the vorticity is equal to zero everywhere except at the centerline of the vortex. In that case, the expressions for the linear and angular momentum of the fluid-solid system can be simplified and written in the form

$$\begin{aligned}\mathbf{P} &= \mathbf{P}_{\text{loc}} + \mathbf{P}_{\text{vort}} \\ \boldsymbol{\Pi} &= \boldsymbol{\Pi}_{\text{loc}} + \boldsymbol{\Pi}_{\text{vort}}.\end{aligned}\tag{9}$$

Here \mathbf{P}_{loc} and $\boldsymbol{\Pi}_{\text{loc}}$ account for the linear and angular momenta due to the locomotion of the MBS in the ideal fluid, while \mathbf{P}_{vort} and $\boldsymbol{\Pi}_{\text{vort}}$ correspond to the linear and angular momenta caused by the presence of point vortices. By taking derivative of the Eq. (9) and equaling it with zero, the system of Eq. (1), that also includes \mathbf{Q}_{vort} , is obtained and solved as described in Sect. 2.

Apart from following approach in [14], the different techniques for modeling vortical effects on the MBS motion can be incorporated in the presented framework. When justified by the nature of the flow, the vortices can be shed in pair, with equal magnitude of circulation, but opposite sign [16]. This ensures satisfaction of

the Kelvin circulation theorem inherently, without any additional treatment. When required, the models that more precisely describe the vortex dynamics can also be utilized. One example of such model is presented in [17], where the numerical procedure for computing a continuous vortex sheet is proposed. The procedure is derived by enforcing satisfaction of the Kelvin's circulation theorem, continuity of the normal velocity across the body and the boundedness of the velocity field. The future work will include comparison of the results for different treatments of the vortical effects on the MBS motion.

5 Conclusions

By using approach described in this work it is possible to model the coupled MBS-fluid system by discretizing boundary of the bodies, instead of conventional discretization of the whole fluid domain, which reduces the numerical burden significantly. In the case of potential flow with zero circulation, this leads to the description of the coupled MBS-fluid system without explicit fluid variables. In the case of MBS comprised of bodies with sharp edges, the fluid variables are needed only to describe vortical effects. Because of the improved efficiency compared to the conventional models which discretize large fluid domain, this model is well suited for application in design optimization of the complex systems motion that includes fluid flow.

Acknowledgement This work has been fully supported by Croatian Science Foundation under the project IP-2016-06-6696.

References

- Terze, Z., Müller, A., Zlatar, D.: Lie-group integration method for constrained multibody systems in state space. *Multibody Sys. Dyn.* **34**, 275–305 (2015)
- Bloch, A.M.: Nonholonomic Mechanics and Control. Springer, Berlin (2003)
- Arnold, V.I., Khesin, B.A.: Topological Methods in Hydrodynamics. Springer, Berlin (1998)
- Kanso, E., Marsden, J.E., Rowley, C.W., Melli-Huber, J.B.: Locomotion of articulated bodies in a perfect fluid. *J. Nonlinear Sci.* **15**, 255–289 (2005)
- Leonard, N.E.: Stability of a bottom-heavy underwater vehicle. *Automatica* **33**(3), 331–346 (1997)
- Vankerschaver, J., Kanso, E., Marsden, J.: The geometry and dynamics of interacting rigid bodies and point vortices. *J. Geom. Mech.* **1**(2), 223–266 (2009)
- Munthe-Kaas, H.: Runge–Kutta methods on Lie groups. *BIT Numer. Math.* **38**, 92–11 (1998)
- Steinbach, O.: Numerical Approximation Methods for Elliptic Boundary Value Problems. Springer, Berlin (2008)
- Geuzaine, C., Remacle, J.F.: Gmsh: a three-dimensional finite element mesh generator with built-in pre- and post-processing facilities. *Int. J. Numer. Meth. Eng.* **79**(11), 1309–1331 (2009)
- Śmigaj, W., Arridge, S., Betcke, T., Phillips, J., Schweiger, M.: Solving boundary integral problems with BEM++. *ACM T. Math. Software* **41**(2), 6:1–6:40 (2015)

11. Yu, Y., Tong, B., Ma, H.: An analytic approach to theoretical modeling of highly unsteady viscous flow excited by wing flapping in small insects. *Acta Mech. Sinica* **19**(6), 508–516 (2003)
12. Terze, Z., Pandza, V., Zlatar, D., Gagnon, L., Masarati, P.: Vortical flow airfoil dynamics in lie group setting: Geometric reduction and numerical analysis. In: ASME 2018 International Design Engineering Technical Conferences and Computers and Information in Engineering Conference (IDETC/CIE 2018) (2018)
13. Anderson, J.D.: Fundamentals of Aerodynamics, 6th edn. McGraw-Hill Education, New York (2017)
14. Tallapragada, P., Kelly, S.D.: Integrability of velocity constraints modeling vortex shedding in ideal fluids. *J. Comput. Nonlinear Dyn.* **12**(2), 021008 (2017)
15. Saffmann, P.G.: Vortex Dynamics. Cambridge University Press, Cambridge (1992)
16. Kanso, E.: Swimming in an inviscid fluid. *Theo. Comput. Fluid. Dyn.* **24**, 201–207 (2010)
17. Shukla, R.K., Eldredge, J.D.: An inviscid model for vortex shedding from a deforming body. *Theo. Comput. Fluid. Dyn.* **21**, 343 (2007)

Damping Models in Aircraft Flutter Analyses



Marco Eugeni, Franco Mastroddi, and Francesco Saltari

Abstract This paper aims to introduce a first-principle-based viscoelastic damping formulation to be applied to aeroelastic systems describing highly flexible aircraft in order to critically assess its influence into linear flutter and response analyses.

Keywords Viscoelastic damping · Aeroelasticity

1 Introduction

The modeling of viscoelastic materials is critical for aerospace industrial applications, Ref.[1, 2]. The damping behavior of viscoelastic materials depends on the entire strain history [3]. Indeed, the relation between the viscous portion of the stress tensor \mathbf{T} , denoted by \mathbf{T}_{vis} , and the strain rate tensor $\dot{\mathbf{E}}$, where \mathbf{E} is the strain tensor and the dot denotes the derivative with respect to time t , can be written as (Ref. [3])

$$\mathbf{T}_{vis}(t) = \int_0^{+\infty} \boldsymbol{\Phi}(\tau) \dot{\mathbf{E}}(t - \tau) d\tau, \quad \lim_{\tau \rightarrow +\infty} \boldsymbol{\Phi}(\tau) = 0 \quad (1)$$

where $\boldsymbol{\Phi}(\tau)$ is known as stress relaxation function that satisfies the fading property in the second relationship of Eq. (1) and the causality condition $\boldsymbol{\Phi}(\tau) = 0$ for $\tau < 0$. Moreover it is assumed that $\boldsymbol{\Phi}(\tau) = 0$ for $\tau < 0$, Ref.[4]. Usually numerical calculation uses a frequency-domain characterization of the damping, which even if easily evaluated experimentally requires a careful modeling in order to provide a causal response. The aim of the present paper is to assess the damping performances of different damping models when introduced into an advanced aeroelastic framework.

M. Eugeni · F. Mastroddi (✉) · F. Saltari

Department of Mechanical and Aerospace Engineering, Sapienza University of Rome,
Rome, Italy

e-mail: marco.eugeni@uniroma1.it; franco.mastroddi@uniroma1.it;
francesco.saltari@uniroma1.it

2 Theoretical Issues on Linear Viscoelastic Models and Their Performances

A viscoelastic material is characterized by a stress state dependent on the entire strain history. For a solid material, the stress tensor \mathbf{T} can be split into a conservative elastic term \mathbf{T}_E and a dissipative viscous term \mathbf{T}_{vis} . The elastic portion of the stress tensor is function of the strain tensor only, that is, it is given by the constitutive elastic law $\mathbf{T}_E = \mathbf{T}_E(\mathbf{E})$. The viscous portion depends on the strain rate history according to Eq. (1), where $0 \leq \tau < \infty$ and the relaxation function $\Phi(\tau)$ is a fourth-order tensor [3]. The strain and strain rate tensors are assumed to be linearized and are written as $\mathbf{E} = Sym(\nabla \mathbf{u})$ and $\dot{\mathbf{E}} = Sym(\nabla \dot{\mathbf{u}})$, respectively, where \mathbf{u} is the displacement vector. Once the relation in Eq. (1) is assigned, the problem can be solved for generic bodies using a FEM space discretization where the displacement field is assumed to be a Hilbert space \mathcal{H} spanned by a basis of independent vector field shape functions $\phi^{(i)}$ ($i = 1, \dots, \infty$), see Eq. (2).

$$\mathbf{u}(\mathbf{x}; t) \cong \sum_{i=1}^N q_i(t) \phi^{(i)}(\mathbf{x}) \quad (2)$$

where the quantities q_i ($i = 1, \dots, N$) are nodal generalized displacement. In the present work is assumed that, Ref. [4], the principal directions of \mathbf{T}_E and \mathbf{T}_{vis} keep parallel at any time is used. Thus,

$$\dot{\Phi}(\tau) = \eta(\tau) \mathbf{C} \quad \text{with} \quad \eta(\tau) = 0 \quad \text{for} \quad \tau < 0 \quad (3)$$

where $\eta(\tau)$ is a scalar function describing the material memory satisfying the causality condition. The above assumption brings to the general formulation of the viscoelastic discretized problem:

$$\mathbf{M}\ddot{\mathbf{q}}(t) + \mathbf{K}\mathbf{q}(t) + \sum_{e=1}^{N_e} \mathbf{K}_e \int_0^{+\infty} \eta_e(\tau) \mathbf{q}(t - \tau) d\tau = \mathbf{f}(t) \quad (4)$$

where \mathbf{q} is the FEM nodal generalized displacement vector, \mathbf{M} and \mathbf{K} the corresponding $N \times N$ mass, and stiffness matrices, \mathbf{K}_e the $N \times N$ element stiffness matrix, $\eta_e(\tau)$ the element fading function, and \mathbf{f} the generalized force vector. A frequency-domain model can be obtained by applying the Borel theorem and the Fourier transform to the time-domain model in Eq. (4), which for zero initial conditions gives $\tilde{\mathbf{q}}(\omega) = \mathbf{H}(\omega)\tilde{\mathbf{f}}(\omega)$, where ω is the Fourier variable and, using $\mathbf{K} = \sum_{e=1}^{N_e} \mathbf{K}_e$, the system FRF is written as

$$\mathbf{H}(\omega) := \left\{ -\omega^2 \mathbf{M} + \sum_{e=1}^{N_e} \mathbf{K}_e [1 + \tilde{\eta}_e(\omega)] \right\}^{-1} \quad (5)$$

with

$$\tilde{\eta}_e(\omega) := \mathcal{F}[\eta_e(\tau)] = \mathcal{R}_e(\omega) + j\mathcal{X}_e(\omega) \quad (6)$$

where j is the imaginary unit and \mathcal{R}_e and \mathcal{X}_e are, respectively, the real and imaginary part of the Fourier transform of the element fading function. Note that the system is Hermitian since the original time-domain response is real and $\mathcal{R}_e(\omega)$ and $\mathcal{X}_e(\omega)$ are a Hilbert pair, since the second relationship in Eq. (3) implies that the system has a causal time-domain response.

In experimental practice, viscoelastic materials are characterized by measuring $\tilde{\eta}_e(\omega)$ rather than $\eta_e(\tau)$. Therefore, when using FEM models, damping is typically modeled in the frequency domain in terms of a complex stiffness matrix. However, the constitutive damping model in the frequency domain needs to be assigned such that the corresponding time-domain model be causal. This condition requires that the real and imaginary parts of $\tilde{\eta}_e$ form a Hilbert pair, Refs. [5, 6]. Next, a general performance indicator of the energy dissipated in the several damping models is introduced in order to evaluate its effectiveness when introduced in a general aeroelastic system. For that purpose, let us consider the energy dissipated in a cycle $T = 2\pi/\omega$ of a permanent fully developed harmonic motion with angular frequency ω for a continuum solid. Because of this position, the displacement field is

$$\mathbf{u}(\mathbf{x}, t) = \mathbf{f}(\mathbf{x}) \sin(\omega t) \quad (7)$$

where $\mathbf{f}(\mathbf{x})$ represents an arbitrary assumed displacement field for the solids satisfying its boundary conditions, and, consequently,

$$\mathbf{E}(\mathbf{x}, t) = \text{Sym}(\nabla \mathbf{f}(\mathbf{x})) \sin(\omega t) \quad \dot{\mathbf{E}}(\mathbf{x}, t) = \omega \text{Sym}(\nabla \mathbf{f}(\mathbf{x})) \cos(\omega t) \quad (8)$$

Thus, the following dissipation index \mathcal{I}_D associated with the solid and with the given angular frequency ω can be defined, by considering Eq. (1), the hypothesis of linearly parallel-elastic viscosity, and Eq. (8),

$$\mathcal{I}_D(\omega) := \iiint_{\mathcal{V}} \int_0^{2\pi/\omega} \mathbf{T}_{vis} : \dot{\mathbf{E}} dt d\mathcal{V} = \mathcal{F}_\eta(\omega) \mathcal{F}_{\mathcal{B}} \quad (9)$$

with

$$\mathcal{F}_\eta(\omega) := \omega \int_0^{2\pi/\omega} \int_0^\infty \eta(\tau) \sin[\omega(t - \tau)] d\tau \cos(\omega t) dt, \quad (10)$$

$$\mathcal{F}_{\mathcal{B}} := \iiint_{\mathcal{V}} \text{Sym}(\nabla \mathbf{f}) \text{CSym}(\nabla \mathbf{f}) d\mathcal{V} \quad (11)$$

It is worth noting that the factor $\mathcal{F}_\eta(\omega)$ depends only by the damping characterization of Eq. (3) linearly parallel-viscous material as given by the time function $\eta(\tau)$,

whereas the factor $\mathcal{F}_{\mathcal{B}}$ by the elastic energy stored by the body as associated with the displacement field $\mathbf{f}(\mathbf{x})$. Indeed, the factor $\mathcal{F}_{\eta}(\omega)$ can also be expressed using a frequency-domain description given by $\tilde{\eta}(\omega)$ by applying the Borel theorem to Eq. (10) so obtaining:

$$\begin{aligned}\mathcal{F}_{\eta}(\omega) &= \omega \int_0^{2\pi/\omega} \mathfrak{F}^{-1} \left[\tilde{\eta}(\bar{\omega}) \frac{\pi}{j} [\delta(\bar{\omega} - \omega) - \delta(\bar{\omega} + \omega)] \right] \cos(\omega t) dt \\ &= \pi \mathcal{I}m [\tilde{\eta}(\omega)]\end{aligned}\quad (12)$$

where the symbol \mathfrak{F}^{-1} indicates the inverse Fourier transform. It is worth pointing out that in the definition of the indicator of the energy dissipated $\mathcal{I}_D(\omega)$ in Eq. (9), the factor $\mathcal{F}_{\eta}(\omega)$ (see Eq. (10)) is independent from the solid geometry and gives a direct measure of the dissipative effectiveness of material. Here in the following three different expressions for the indicator $\mathcal{I}_D(\omega)$ will be presented for three widely used damping models.

- *Linearly viscous damping materials*

In this case one has

$$\tilde{\eta}_V(\omega) = 2 \frac{j\omega\xi}{\bar{\omega}} \quad (13)$$

where ξ is the so-called damping ratio and $\bar{\omega}$ is a reference angular frequency. Since $|\tilde{\eta}_V(\omega)| = 2\xi\omega/\bar{\omega}$ and $\varphi_{\tilde{\eta}_V}(\omega) = \pi/2$ (where $|\bullet|$ and φ_{\bullet} are the magnitude and the phase of the complex number \bullet , respectively), one has, applying Eq. (12),

$$\mathcal{I}_D(\omega) = \frac{2\pi\xi}{\bar{\omega}} \omega \mathcal{F}_{\mathcal{B}} \quad (14)$$

- *Standard hysteretic damping*

In this case one has

$$\tilde{\eta}_H(\omega) = j \bar{\eta}_h \operatorname{sgn}(\omega) \quad (15)$$

where $\bar{\eta}_h$ is the so-called loss factor denoting the hysteretic damping. Since $|\tilde{\eta}_H(\omega)| = \bar{\eta}_h$ and $\varphi_{\tilde{\eta}_H}(\omega) = \pi/2$, one has, applying Eq. (12),

$$\mathcal{I}_D(\omega) = \pi \bar{\eta}_h \mathcal{F}_{\mathcal{B}} \quad (16)$$

- *Biot damping model*

Biot model [7] is a two-parameter model ($\bar{\eta}_b$ and ε_b) defined in frequency domain as

$$\tilde{\eta}_B(\omega) = \frac{2}{\pi} \bar{\eta}_b \left[\log \sqrt{1 + \frac{\omega^2}{\varepsilon_b^2}} + j \operatorname{atan} \left(\frac{\omega}{\varepsilon_b} \right) \right] \quad (17)$$

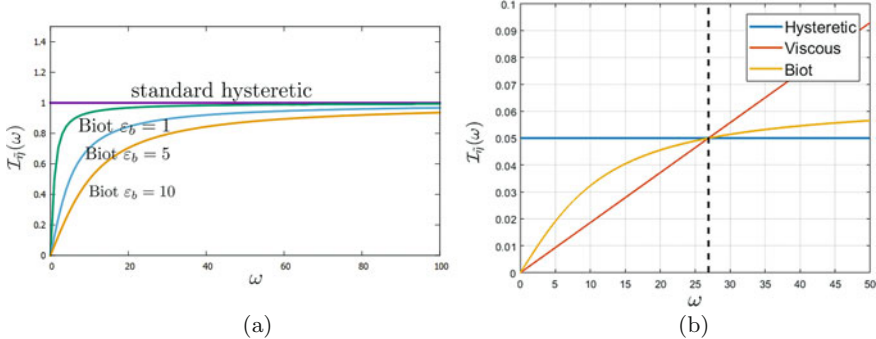


Fig. 1 Comparison among different damping performances $I_D(\omega)$. (a) Hysteretic vs Biot with $\bar{\eta}_h = \bar{\eta}_b$. (b) Models as in Eq. (25) and Table 1

Thus, applying Eq. (12), one has

$$I_D(\omega) = \frac{2}{\pi} \bar{\eta}_b \operatorname{atan}\left(\frac{\omega}{\varepsilon_b}\right) \mathcal{F}_{\mathcal{B}} \quad (18)$$

In Fig. 1b a comparison among different damping performance for the viscous, hysteretic, and Biot damping models is shown.

3 Aero viscoelastic Model

In the previous sections the discretized equations of a viscoelastic continuum (see Eq. (4)) have been obtained. These equations can be easily extended to the aeroelastic case by including the aerodynamic and inertial forces. In order to consider the effects of inertial and aerodynamic coupling, the rigid-body motion \mathbf{u}_R and elastic motion \mathbf{u}_E can be studied separately, such that $\mathbf{u} = \mathbf{u}_R + \mathbf{u}_E$. Consequently, the elastic displacements can be expressed by means of the natural mode shapes of the free-free structure $\bar{\phi}^{(n)}$ and the elastic modal coordinates ξ_n . Let us assume $\bar{\mathbf{q}} = \{\Delta x^T \Delta \Theta^T \Delta \xi^T\}^T$ the vector collecting the perturbation of the components of center of mass position and attitude of the aircraft with respect to the *inertial frame of reference* and modal coordinates, and $\bar{\mathbf{v}} = \{\Delta v^T \Delta \omega^T \Delta \dot{\xi}^T\}^T$, the vector of the perturbation of components of center of mass velocity and angular velocity expressed with respect to the *non-inertial frame of reference* [8] and modal velocities. The relationship between these two vectors is generally a nonlinear function of the Euler angles, that can be linearized about level flight such as having $\dot{\bar{\mathbf{q}}} = \mathbf{T} \bar{\mathbf{v}}$ (see [8] for the definition of matrix \mathbf{T}).

Under the additional assumption of homogeneity of $\tilde{\eta}$ throughout the structure, the integro-differential system in Eq. (4) specialized for the aero viscoelastic case is

thus recast by including the aerodynamic forces produced by the dynamics of the aircraft \mathbf{e} , and the perturbation of the projection of gravity on the reference frame \mathbf{f}_w given by the aircraft attitude:

$$\bar{\mathbf{M}}\dot{\bar{\mathbf{q}}}(t) + \bar{\mathbf{D}}\bar{\mathbf{v}}(t) + \bar{\mathbf{K}}\bar{\mathbf{q}}(t) + \bar{\mathbf{K}} \int_0^{+\infty} \eta(\tau)\bar{\mathbf{q}}(t-\tau)d\tau = \bar{\mathbf{f}}(t) + \mathbf{e}(t) + \mathbf{f}_w(t) \quad (19)$$

where $\bar{\mathbf{M}}$ is the generalized mass matrix including inertial effects between rigid-body and elastic modes, $\bar{\mathbf{D}}$ is a damping matrix that includes only inertial effects, $\bar{\mathbf{K}}$ is the generalized stiffness matrix, and $\bar{\mathbf{f}}$ is the vector of the generalized external forces, such as given by the gust. The aerodynamic forces (both given by aircraft motion and gust) are expressed by means of the generalized aerodynamic forces matrix in reduced frequency domain $k = \omega b/U_\infty$ (where b is generally the half-chord and U_∞ is the aircraft speed) as a function of the dynamic pressure q_D and Mach number M_∞ .

$$\tilde{\mathbf{e}} = q_D \mathbf{E}(k, M_\infty) \tilde{\bar{\mathbf{q}}} \quad (20)$$

$$\tilde{\mathbf{f}} = q_D \mathbf{E}_g(k, M_\infty) \tilde{w}_g \quad (21)$$

where \mathbf{E} is the generalized aerodynamic forces (GAF) matrix and w_g is the vertical gust component velocity. Furthermore, the projection of the gravity can be expressed such as $\tilde{\mathbf{f}}_w = -\mathbf{K}_w \tilde{\bar{\mathbf{q}}}$, where \mathbf{K}_w is a further stiffness contribution given to the rigid-body DoFs by the weight projection. All the contributions above can be summarized to express the aeroviscoelastic equations of motion in Laplace domain:

$$\left(s^2 \bar{\mathbf{M}} \mathbf{T}^{-1} + s \bar{\mathbf{D}} + (1 + \tilde{\eta}(\omega)) \bar{\mathbf{K}} + \mathbf{K}_w - q_D \mathbf{E}(k, M_\infty) \right) \tilde{\bar{\mathbf{q}}}(s) = q_D \mathbf{E}_g(k, M_\infty) \tilde{w}_g \quad (22)$$

It is apparent that the obtained aeroviscoelastic equation is a transcendent function of Laplace variable s . Nonetheless, the homogeneous solution of Eq. (22) can still be expressed in time domain as:

$$\bar{\mathbf{q}}(t) = \sum_{n=1}^N c_n \mathbf{w}^{(n)} e^{s_n t} \quad (23)$$

where $\mathbf{w}^{(n)}$ and s_n ($n = 1, \dots, 2N_{modes}$) are, respectively, the n -th complex eigenvector and n -th pole of the aeroviscoelastic system above. The stability of the system can thus be studied by solving a *non-standard* eigenvalue problem where the relationships $\omega = Im(s)$ and $k = Im(s)b/U_\infty$ allow to close the iterative numerical procedure (generally p - k method) to obtain the system poles and eigenvectors. On the other hand, the frequency response function to gust input \tilde{w}_g is given by

$$\mathbf{h}_g(\omega) = q_D \left(-\omega^2 \bar{\mathbf{M}} \mathbf{T}^{-1} + j\omega \bar{\mathbf{D}} + (1 + \tilde{\eta}(\omega)) \bar{\mathbf{K}} + \mathbf{K}_w - q_D \mathbf{E}(\omega) \right)^{-1} \mathbf{E}_g(\omega) \quad (24)$$

4 Results

The effects of different damping models on stability and response analyses of a Body-Freedom-Flutter (BFF) type aircraft (Ref. [8]) are presented. For a complete aeroelastic analysis the reader may refer to Ref. [8]. The first bending and torsional elastic mode shapes of the unrestrained structure are equal to $f_1 = 5.830$ Hz and $f_5 = 20.093$ Hz. The root locus of the undamped aircraft in steady rectilinear flight carried out for $U_\infty = 15 \rightarrow 30$ m/s, $M_\infty = 0$, and sea level conditions showed a body-freedom flutter speed equal to $U_F = 19.85$ m/s [8] (see Fig. 2a). Moreover, the flutter critical mode has a frequency of $\omega_F = 26.82$ Hz. All the considered damping models (i.e., viscous, hysteretic, and Biot) have been tuned to have the same value of $\tilde{\eta}$ at flutter speed and angular frequency, thus having

$$\mathcal{I}_{\tilde{\eta}_V}(\omega_F) = \mathcal{I}_{\tilde{\eta}_H}(\omega_F) = \mathcal{I}_{\tilde{\eta}_B}(\omega_F) \quad (25)$$

The parameters used for this analysis are listed in Table 1. The relative functions $\tilde{\eta}(\omega)$ are shown in Fig. 1b for each damping model, whereas the stability scenarios of all different aeroviscoelastic models are shown in Fig. 2b. It can be noticed that: (1) the flutter speed does not differ too much between the different models, thus having U_F equal to 20.04, 20.1, and 20.78 m/s, respectively, for the viscous, hysteretic, and Biot damping models (despite the damping is the same for flutter frequency, the different damping models modify the system behavior globally so

Table 1 Parameters used for the different damping models

ζ	$\bar{\omega}$	$\tilde{\eta}_h$	$\tilde{\eta}_b$	ε_b
0.025	26.82	0.05	0.0646	10.

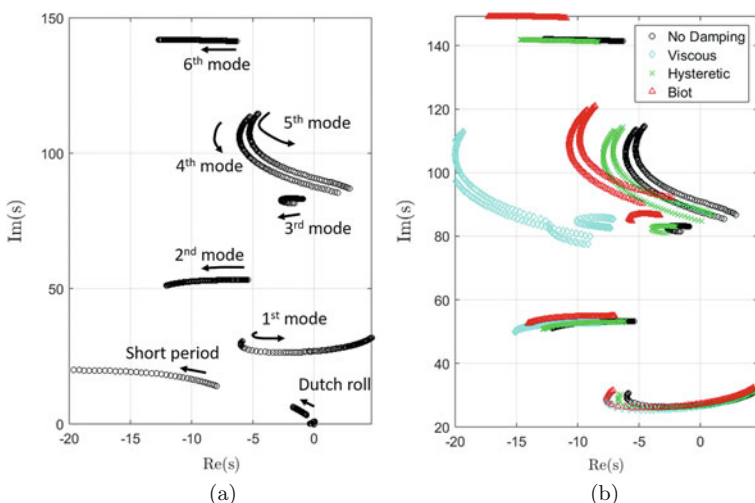


Fig. 2 Root loci of damped and undamped systems. (a) Without damping. (b) With damping

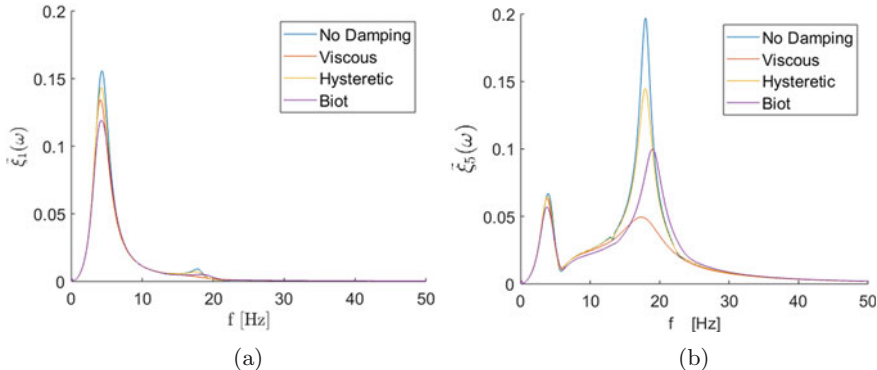


Fig. 3 FRFs associated with modes 1 and 5 at speed 16.35 m/s at sea level condition. **(a)** $\tilde{\xi}_1(\omega)$. **(b)** $\tilde{\xi}_5(\omega)$

perturbing in different way the flutter margins); (2) viscous damping results in an increase damping at higher frequencies due to its increasing damping effectiveness with frequency; (3) Biot damping model results in an increase of both damping and frequencies with respect to the hysteretic case. This behavior is due to the real part of $\hat{\eta}_B$ that produces an increase of stiffness as the frequency increases. Differences between the aeroviscoelastic systems with different damping models arise also in the frequency response functions to the vertical gusts at the speed $U_\infty = 16.35$ m/s at sea level conditions (see Fig. 3 for FRF of mode 1 and 5). In particular, the fifth structural mode response denotes great differences at higher frequencies. Especially, as it is shown from root locus, the Biot model produces a shift of the second peaks at higher frequencies.

5 Concluding Remarks

In this paper different first-principle-based damping models have been introduced into an aeroelastic framework to compare their effects to the stability and response of flexible aircraft. In order to assess their performances, a parameter to evaluate their effectiveness has been introduced based on the dissipation associated with a fixed shaped mono-frequency motion. The aeroviscoelastic analysis involved a non-standard study of the stability and response of a BFF flexible aircraft configuration by tuning the different viscoelastic models to behave similarly at the flutter margin of the undamped configuration. The stability scenarios and the gust frequency responses marked the different behaviors of the investigated damping models when included in the aeroelastic framework.

References

1. Riso, C., Fransen, S., Mastroddi, F., Coppotelli, G., Trequattrini, F., De Vivo, A.: Experimental validation of solid rocket motor damping models. *CEAS Space J.* **10**(2), 213–230 (2018)
2. Mastroddi, F., Martarelli, F., Eugeni, M., Riso, C.: Time- and frequency-domain linear viscoelastic modeling of highly damped aerospace structures. *Mech. Syst. Signal Process.* **122**, 42–45 (2019)
3. Coleman, B.D., Noll, W.: Foundations of linear viscoelasticity. *Rev. Mod. Phys.* **33**(2), 239 (1961)
4. Mastroddi, F., Eugeni, M., Erba, F.: On the modal diagonalization of viscoelastic mechanical systems. *Mech. Syst. Signal Process.* **96**, 159–175 (2017)
5. Nashif, A.D., Jones, D.I.G., Henderson, J.P.: *Vibration Damping*. Wiley, New York (1985)
6. Makris, N.: Frequency-independent dissipation and causality. In: *Third International Conference on Computational Stochastic Mechanics*, Santorini (1998)
7. Biot, M.A.: Linear thermodynamics and the mechanics of solids. In: *Proceedings of the Third U.S. National Congress of Applied Mechanics*. ASME, New York (1958)
8. Saltari, F., Riso, C., De Matteis, G., Mastroddi, F.: Finite-element based modeling for flight dynamics and aeroelasticity of flexible aircraft. *J. Aircr.* **54**(6), 2350–2366 (2017)

Dynamic Response of a Morphing Wing



Patrizio Rosatelli, Walter Lacarbonara ID, Andrea Arena,
and Daniel J. Inman

Abstract This work aims to develop a computational framework to predict the dynamic response of a morphing wing. Unlike conventional aerodynamic surfaces, the investigated wing has the capability of continuously morphing its trailing edge shape in order to improve the wing aerodynamic performance. The computational tool here developed incorporates a structural wing linear model whose dynamics are coupled with the unsteady aerodynamics generated by the wing interaction with an incompressible airflow. The wing equations of motion are derived from the theory of thin plates, while the airflow dynamics are described through an unsteady formulation and solved by the vortex lattice method (VLM). The fluid–structure interaction is then obtained by performing iterative simulation loops in which, starting from a reference wing and airflow configuration, the mechanical unknowns (i.e., the wing deflections and velocities) are used as input to modify the reference geometry of the aerodynamic surface and thus to modify accordingly the airflow dynamics around it. This allows the determination of the equivalent aerodynamic loads acting on the wing and the calculation of its dynamic response. The critical airflow speed leading to the flutter instability is evaluated for several trailing edge shapes of the morphing wing and compared with the critical speed attained in the unmorphed case.

Keywords Aeroelasticity · Morphing wing · Flutter · VLM

P. Rosatelli ()

Sapienza University of Rome, Rome, Italy

e-mail: rosatelli.1556643@studenti.uniroma1.it

W. Lacarbonara · A. Arena

Department of Structural and Geotechnical Engineering, Sapienza University of Rome,
Rome, Italy

e-mail: andrea.arena@uniroma1.it

D. J. Inman

Department of Aerospace Engineering, University of Michigan, Ann Arbor, MI, USA

1 Introduction

Since the beginning of the aviation history, the capability of aircraft to adapt themselves to several flight conditions was one of the main concerns for aeronautical engineers. As a matter of fact, the idea of shape modification of the aerodynamic surfaces was often employed in aircraft to accommodate the changes in the aerodynamic effects so as to increase their efficiency over a variety of flight conditions. In particular, the trailing edge is the portion of the wing whose motion is the most commonly used to modify the aerodynamic loads, and over the years this morphing capability has been exploited to get a wide range of favorable effects on the aerodynamic performance of a wing.

The spanwise morphing trailing edge (SMTE) concept was realized for the first time at the AIMS Laboratory of the University of Michigan [1]. The morphing strategy aimed to vary locally the trailing edge camber of a wing or control surface in order to work as a modular replacement for conventional ailerons without altering the wing spar box.

Moosavian et al. [2] investigated the aerodynamic effects associated with the change in geometry of morphing wings inspired by the wave-like camber variation in the trailing edge feathers of large birds (just as the SMTE wing) and the endurance capability was chosen as the measure of the flight efficiency ($c_L^{3/2}/c_D$) (here c_L and c_D indicate the lift and drag coefficients). The unmorphed NACA 0012 wing, including a variable angle of attack, is able to match the performance of the best morphed configurations at lower c_L values, although the morphed configurations outperform the unmorphed profile for $c_L > 0.6$. Given that this kind of configuration for the wing showed better aerodynamic performance, a preliminary structural and aeroelastic analysis for the finite half-wing is the subject of this study.

Several papers over the years addressed aeroelastic analysis of morphing wings; in [3] the aeroelastic roll performance of a morphing wing was studied by adopting a one-dimensional (1D) beam model, discretized by means of the finite element method (FEM), coupled with unsteady aerodynamics modeled via the vortex lattice method (VLM). The VLM was used also in [4] to simulate the unsteady aerodynamics of wings in order to evaluate the roll performance, although the wing structural behavior was modeled by an equivalent plate whose equation of motion was solved by the Ritz method. In [5] the dynamic aeroelastic stability of a morphing wing was evaluated by employing both CFD and FEM analyses. In the present study, a novel Matlab-based numerical tool is proposed to study the aerodynamic stability of morphing wings including parametric studies to evaluate the effects of the wing trailing edge shape towards improving the flutter speed. To this end, the wing structure is modeled as an equivalent thin plate whose equation of motion is solved via the Galerkin approach, while the aerodynamics of the airflow are modeled via an unsteady, non-standard VLM including the wake effect.

2 Problem Formulation

Before delving into the details of the aerodynamic and structural modeling, it is important to provide some context on the type of morphing employed for the studied SMTE wing. The shape changing of the trailing edge of the SMTE is parameterized via a sinusoidal law, and the position of the wing trailing edge in the vertical direction z is described as a function of its location y along the wing span expressed as $z(y) = A \sin(2k\pi y + \varphi)$, where A is the constant amplitude of the wave, k is the spatial frequency, and φ is the phase shift. By assuming an incompressible, non-viscous, non-detached, initially irrotational and isentropic airflow, the aerodynamic loads generated by the flow–structure interaction can be evaluated starting from the well-known potential flow theory. In particular, by introducing the potential function φ , such that the airflow velocity vector \mathbf{v} can be expressed as $\mathbf{v} = \nabla\varphi$, the continuity equation in the airflow space domain (x, y, z) , away from the wing surface, can be written as

$$\nabla^2\varphi = 0, \quad (1)$$

together with the boundary conditions $\frac{\partial\varphi}{\partial n} = \mathbf{v} \cdot \mathbf{n}$ at the wing surface (with \mathbf{n} being the unit vector normal to the wing surface), $\varphi = 0$ at the far field (i.e., at $x, y \rightarrow \pm\infty$), and the Kutta condition at the trailing edge.

It is well known that in incompressible potential flows the points in contact with the aerodynamic surface represent a singularity for the Kelvin theorem. Moreover, the flow field near the wing surface is necessarily characterized by the presence of the wake which is a surface of discontinuity in the velocity potential φ . In this context, a singularity in the solution of Eq. (1) is given by the so-called vortex line. An ideal, infinite vortex line spins the flow around the line itself and the velocity of each material point of the flow decreases its intensity in a way inversely proportional to the distance from the vortex line. One of the most interesting applications of this singular solution is that many vortices can be generated so as to simulate more realistic flow dynamics in the wake [6]. Using vortex rings, the flow boundary conditions can be satisfied on the wing reference surface (i.e., on some “control points” over the surface) and the wake mechanism can be described. A three-dimensional thin lifting surface problem can be solved by using vortex ring elements.

The present study aims at capturing the aeroelastic interaction between the dynamics of the wing and those of the flow across the aerodynamic surface. To this end, the unsteady formulation within the VLM is based on a different expression for the boundary conditions, the addition of the wake mechanism, and the utilization of the unsteady Bernoulli equation.

On the other hand, the mechanical behavior of the wing is described using the classical thin plate theory. In this context, the wing structure (i.e., the wingbox)

is modeled as an equivalent Kirchhoff–Love cantilever plate whose inertial and stiffness properties are determined so as to reflect the static and dynamic flexural–torsional behavior of the actual (truss-like) wing structure. In the fixed Cartesian frame ($\mathbf{e}_x, \mathbf{e}_y, \mathbf{e}_z$) having its origin in the leading edge corner of the fixed boundary, the position vector $\mathbf{x} = x\mathbf{e}_x + y\mathbf{e}_y$ is adopted to describe the reference planar configuration of the plate mid-surface, while $w(\mathbf{x}, t)$ represents the out-of-plane flexural displacement of the plate. The geometry of the plate reference configuration is provided by the length l , the width b , and the thickness h of the equivalent cantilever plate. Denoting by $D = E h^3/12(1 - \nu^2)$ the plate flexural stiffness, with E and ν being the equivalent Young modulus and Poissons ratio, respectively, and denoting by ρ the equivalent mass density of the plate, the Kirchhoff–Love equation describing the plate bending is cast as

$$\rho h \ddot{w}(\mathbf{x}, t) + c \dot{w}(\mathbf{x}, t) + D \nabla^4 w(\mathbf{x}, t) = f(\mathbf{x}, w, \dot{w}; t), \quad (2)$$

together with the cantilever-type boundary conditions (zero deflection and slopes on the clamped edge and zero moment and shear force on the stress-free edges) and the initial conditions. In Eq. (2), the overdot indicates time differentiation and $f(\mathbf{x}, w, \dot{w}; t)$ is the force per unit surface acting on the plate, including the aerodynamic loads.

The Galerkin approach is adopted to solve the partial differential equation governing the motion of the wing by choosing the eigenfunctions $\phi_n(\mathbf{x})$ of the equivalent cantilever thin plate as the basis of orthogonal trial functions. The following expression of the plate transverse deflection $w(\mathbf{x}, t)$ is adopted:

$$w(\mathbf{x}, t) = \sum_{n=1}^N q_n(t) \phi_n(\mathbf{x}), \quad (3)$$

where q_n are the generalized coordinates and N is the number of trial functions in the Galerkin discretization. It is easy to show that only the lowest mode shapes provide significant contributions since the flutter instability is generated from an interaction between the lowest bending mode and the lowest torsional mode. To obtain a more accurate analysis, also the second torsional mode and the second and third bending modes are chosen to be included in the deflection description. By substituting Eq. (3) into Eq. (2) and enforcing the minimization of the residual force per unit area across the wing midplane, the following discrete form of the wing equation of motion is obtained:

$$\mathbf{M} \ddot{\mathbf{q}} + \mathbf{C} \dot{\mathbf{q}} + \mathbf{K} \mathbf{q} = \mathbf{f}(\mathbf{q}, \dot{\mathbf{q}}, t), \quad (4)$$

where \mathbf{M} , \mathbf{C} , and \mathbf{K} are the mass, damping, and stiffness matrices, respectively, and \mathbf{q} is the vector collecting the generalized coordinates q_n . On the other hand, the $N \times 1$ vector $\mathbf{f}(\mathbf{q}, \dot{\mathbf{q}}, t)$ represents the generalized forces associated with the aerodynamic loads provided by the VLM.

The Newmark-beta method (a generalized modification of the original Newmark method [7]) for time integration of a forced differential system is used in this study. The Newmark-beta method is based on substituting expressions for velocity and acceleration at each time step, thus generating an easier linear system to solve for obtaining the deflections. A Matlab-based VLM code was developed in collaboration with the University of Michigan [8], tailored to take into account morphing capabilities of the trailing edge. The time-dependent, fluid–structure interaction is implemented via a CSS procedure [9]. The algorithm consists in the following steps performed at each time step: (1) the motion of the wet boundary is transferred, by extrapolation, to the aerodynamic mesh which is then updated; (2) the fluid subsystem advances to the next time step and the new pressure field is computed; (3) the pressure field is then converted into a new load and transferred to the structure by interpolation; (4) the dynamic response of the structural subsystem is evaluated and the simulation moves to the next time step. All of these coupling capabilities were developed from scratch using the VLM code described in [8] as the starting point. As a result, a novel optimized tool was obtained in Matlab to perform calculations for coupled, structural, and aerodynamic analyses on wings with the possibility of arbitrarily varying the trailing edge shape. The code executes several functions written “ad hoc” in a loop and described next. First, the wing shape, the aerodynamic mesh, and the flow properties are given as input: the wing span, the chord length, the incidence, sweep, taper ratio, dihedral, as well as the number of panels to discretize the wing, and the free stream velocity are some of the parameters that can be changed to carry out parametric analyses. Then, the routine for structural analysis calculates the plate mesh deflection. The plate transversal deflection is then extrapolated to find the displacements of the aerodynamic mesh and to compute the orientation of each flow panel (taking into account the morphing capabilities). A routine implementing the unsteady VLM is then used to calculate the flow potential across the field and also the wake is first generated and its position is advanced at each time step. Finally, the forces acting over the wing are computed before applying them over the structural mesh, thus starting a new step of the loop.

3 Numerical Results

The equivalent plate has the following properties: chord=0.3 m, half-span= 0.912 m, E=5.1 GPa, thickness=0.005 m, density=38.15 kg/m³. The aeroelastic flutter condition is found by observation of the dynamic response of the wing lying in a free stream flow. First of all, the behavior of the wing with non-morphing capabilities is investigated to obtain a general starting point for comparison with the subsequent results. Most importantly, the main goal of the study is to highlight the different aeroelastic performance of a conventional wing as opposed to a SMTE morphing wing. As discussed in this section, important differences are found which may represent the starting point of more refined analyses and experimental testing

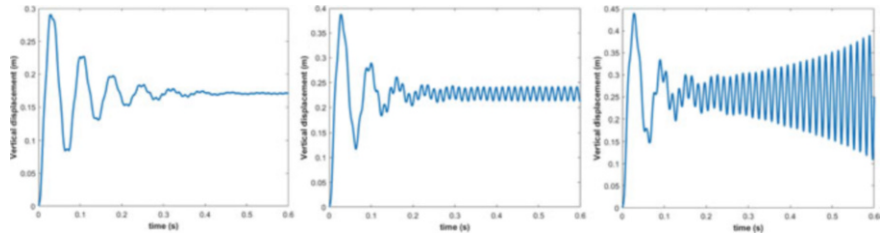


Fig. 1 Aeroelastic response of the wing at different airflow speeds: (left) $U_{\infty} < U_F$ (stable behavior), (center) $U_{\infty} = U_F$ (flutter critical condition), (right) $U_{\infty} > U_F$ (unstable behavior)

Table 1 Flutter speeds for different morphing configurations

k	φ	U_F	k	φ	U_F
0.15	315°	26 m/s	0.1	315°	28 m/s
0.05	315°	32 m/s	0.25	225°	34 m/s

campaigns. A representative set of dynamic responses of the conventional wing vibrating in different regimes is reported in the following figures.

In particular, the vertical deflections of the mid-chord point of the cross section at the wing tip and of an off-center point are evaluated at each time step to understand the overall dynamic behavior of the wing. The off-center point is chosen such that its motion well represents the initial bending of the wing; moreover, at later times, it is possible to observe the interaction between bending and torsional motion, a crucial aspect to understand aeroelastic phenomena. When damping is large enough to reduce the amplitude of this coupled motion, the wing achieves a deflected equilibrium after a transient behavior (Fig. 1 (left)). If this motion cannot be damped out, flutter occurs as shown in Fig. 1 (center) (Hopf bifurcation) and in Fig. 1 (right). The free stream velocity leading to this unstable behavior is the flutter speed. Specifically, for the non-morphing configuration, an unbounded growth of the response can be obtained at the lowest speed $U_{\infty} = U_F = 24.5$ m/s. The flutter speed is also computed for some of the morphing configurations which yield the best performance as discussed in [2]. All behaviors found in these cases are similar to the behavior observed for the unmorphed configuration, but the flutter speeds for the morphed configurations are considerably different. Table 1 gives the flutter speeds for the wing configurations depicted in Fig. 2; in particular, the trailing edge was morphed according to the shape provided by the expression $z(y) = A \sin(2k\pi y + \varphi)$, where $A = 0.019$ m and the extension of the trailing edge shape morphing along the chord-wise direction x is assumed to be one-fourth of the chord length.

Figure 3 shows the vertical aerodynamic pressure distribution on the morphing wing when $k=0.15$ and $\varphi=315^{\circ}$ at an airflow speed below the flutter speed. As expected, the vertical pressure exhibits its peak value at the wing root and along the leading edge and is increased with respect to the unmorphed case because of the presence of the morphing trailing edge. A remarkable result is that morphing has a

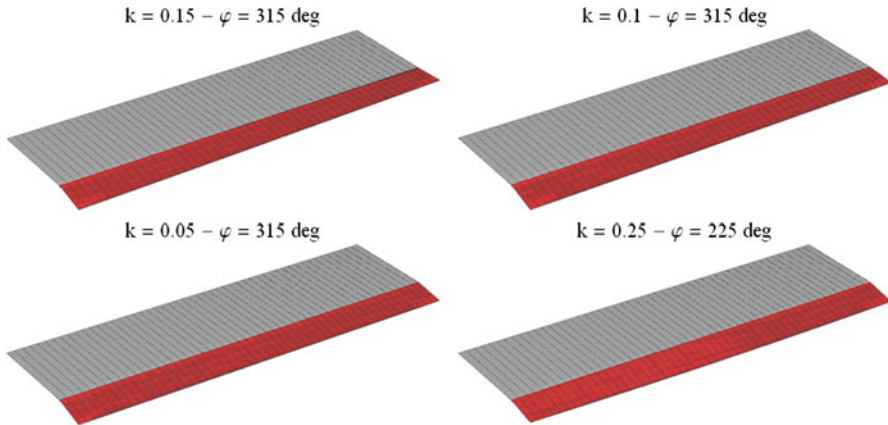


Fig. 2 Wing morphing configurations: in red the morphed trailing edge

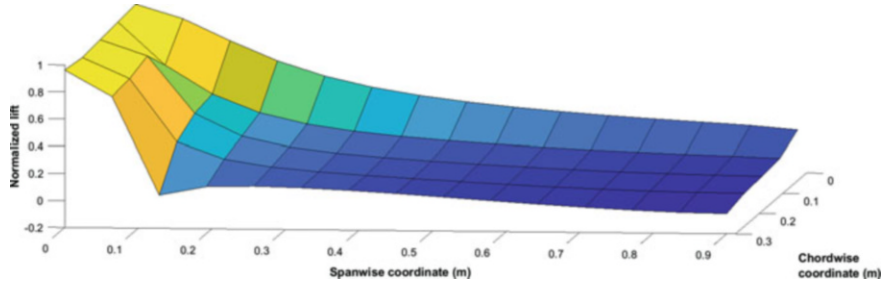


Fig. 3 Vertical aerodynamic pressure acting on the morphing wing for $k=0.15$ and $\varphi=315^\circ$ at the airflow speed $U \approx 10 \text{ m/s}$

considerable, nontrivial effect on the flutter speed. As a general rule, the flutter speed is lower for morphing wings as opposed to the conventional non-morphing designs. Moreover, in the present case, morphing is effected by deflecting an aileron, thus increasing lift on the wing because of the increased curvature of the wing profile. For these reasons a lower flutter speed for this morphing wing was expected, but the opposite trend is observed. Indeed, the more the aileron increases lift, the more aerodynamic forces in percentage are applied on the rear chord-wise part of the wing. Also, the elastic center of the plate-like wing is exactly in the mid-chord (unlike most of the aircraft wings). The combination of increased forces acting on the rear part of the wing and the collocation of the elastic center seems to be the reason why the more the SMTE increases lift, the higher the flutter speed. In fact, if the forces are increased in the rear part of the wing, the “center of the chord-wise lift distribution” moves backwards. In this way the “torsional” lever arm is reduced and the twisting moment is reduced accordingly. Actually, the chord-wise center of lifting forces acting on the inner part of the wing (the first four panels chord-wise

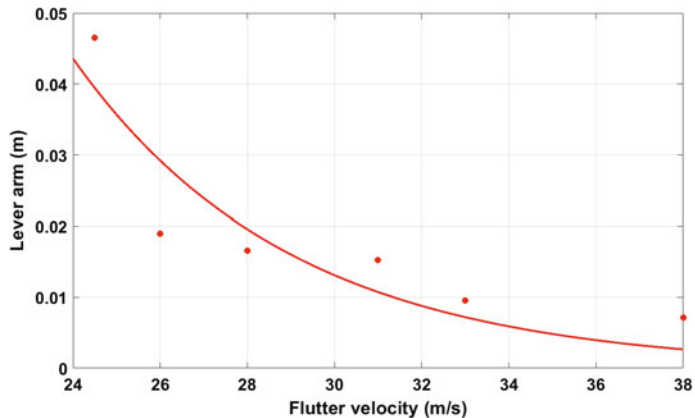


Fig. 4 Forces are applied away from the elastic center for lower flutter speeds

near the wing root) was evaluated for a stationary load at the flutter speed for each of the above configurations. The results showed that the flutter speed increases if the center of forces is closer to the mid-chord (see Fig. 4). Since lower twisting moments are generated, this may be the explanation for increased flutter speeds.

It should be noted that the described phenomenon is strictly connected to the plate-like representation of the wing. For more realistic wing geometries, the elastic center of the wing is placed near the aerodynamic center so that the effect described above may influence flutter differently.

4 Conclusions

FEM models of the wing, wingbox, and plate were constructed to validate the Matlab code tackling the wing equivalent plate problem. The Newmark-beta method was employed for time integration. Concerning the aerodynamics, flow unsteadiness and morphing capabilities were implemented in the context of a VLM approach. Fluid–structure interaction was tackled by accounting for displacements and aerodynamic load transfer. Several analyses allowed the flutter speed to be calculated for the morphing and non-morphing wing configurations. Moreover, an interesting explanation for the flutter speed variation for different morphing configurations was provided.

Acknowledgements This work is supported in part by the US Air Force Office of Scientific Research under Grant Number FA9550-16-1-0087, titled Avian-Inspired Multifunctional Morphing Vehicles monitored by Dr. BL Lee.

References

1. Pankonien, A.M.: Smart material wing morphing for unmanned aerial vehicles. PhD dissertation, Department of Aerospace Engineering, University of Michigan (2015)
2. Moosavian, A., Chae, E.J., Pankonien, A.M., Lee, A.J., Inman, D.J.: A parametric study on a bio-inspired continuously morphing trailing edge. In: Proceedings of SPIE 10162, Bioinspiration, Biomimetics, and Bioreplication (2017)
3. Sanders, B., Eastep, F.E., Forster, E.: Aerodynamic and aeroelastic characteristics of wings with conformal control surfaces for morphing aircraft. *J. Aircr.* **40**(1), 94–99 (2003)
4. Gern, F.H., Inman, D.J., Kapanin, R.K.: Structural and aeroelastic modeling of general planform UCAV wings with morphing airfoils. In: 42nd AIAA/ASME/ASCE/AHS/ASC Structures, Structural Dynamics, and Materials Conference and Exhibit (2001)
5. Finchman, J.H.S., Friswell, M.I., Inman, D.J.: Aeroelastic modelling of morphing wings. In: 4th Aircraft Structural Design Conference, Belfast (2014)
6. Katz, J., Plotkin, A.: Low-Speed Aerodynamics, 2nd edn. Cambridge University Press, Cambridge (2001)
7. Newmark, N.M.: A method of computation for structural dynamics. In: Proceedings of ASCE, vol. 85, pp. 67–94 (1959)
8. Mishra, A., Davoudi, B., Duraisamy, K.: Multiple fidelity modeling of interactional aerodynamics. *J. Aircr.* **55**(5), 1839–1854 (2018)
9. Farhat, C., Van der Zee, K.G., Geuzaine, P.: Provably second-order time-accurate loosely-coupled solution algorithms for transient nonlinear computational aeroelasticity. *Comput. Methods Appl. Mech. Eng.* **195**, 1973–2001 (2006)

Helicopter Pilot Biomechanics by Multibody Analysis



Pierangelo Masarati, Andrea Zanoni, Vincenzo Muscarello, Rita Paolini, and Giuseppe Quaranta

Abstract Helicopter handling qualities can be affected by the voluntary and involuntary interaction between the vehicle dynamics and the human body biomechanics. To investigate the possible couplings, a first-principles approach has been taken: biomechanical multibody models of the pilot upper limbs and spine have been developed along with generation procedures that can be used to represent human bodies of broadly varying anthropometric parameters. The models have been used both for the identification of the linearized behavior about arbitrary steady conditions and for full nonlinear analysis of helicopter transient maneuvers, through direct and inverse dynamics analyses.

Keywords Rotorcraft · Biomechanics · Multibody

1 Introduction and Motivation

The standard layout of helicopter control inceptors comprises the *cyclic* stick, the *collective* lever, and the pedals. The helicopter pilot's control action on the cyclic and collective inceptors (Fig. 1, left) is exerted through the action of their hands, commanded by the activity of their muscles in the upper limbs and torso. At the same time, their bodies are subjected to the inertial effects of the rotorcraft dynamics. The resulting induced motion of the control inceptors, which actuates the control surfaces, thus producing loads that amplify the motion of the vehicle, is at the roots of several possible adverse interactions between the voluntary and involuntary action of the pilot and the handling qualities of rotorcraft [1–3]. These problems are well known and have been investigated in the past with reference to fixed wing aircraft [3]. However, there is a lack of understanding of specific problems arising in rotorcraft [1]. Although relatively sophisticated, yet lumped

P. Masarati (✉) · A. Zanoni · V. Muscarello · R. Paolini · G. Quaranta
Department of Aerospace Science and Technology, Politecnico di Milano, Milano, Italy
e-mail: pierangelo.masarati@polimi.it

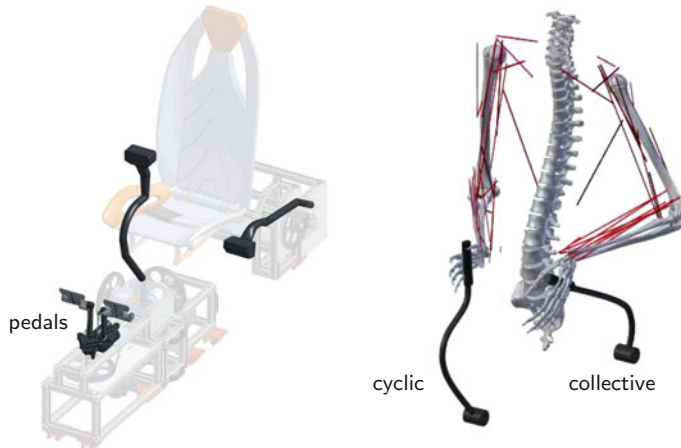


Fig. 1 Schematic view of helicopter control inceptors (left), and upper limbs and trunk multibody models (right)

parameter biomechanical models were developed [4], the typical approach is based on using transfer functions of the pilot's biodynamics, obtained experimentally, often in flight [1]. Such approach limits the validity of the analysis to existing cockpit and control inceptor configurations, and hides the influence of fundamental biomechanics. To investigate these phenomena, generally collected under the acronym (RPCs, Rotorcraft Pilot Couplings) from a first-principles perspective, an enduring effort has been carried out at Politecnico di Milano Department of Aerospace Science and Technology towards the development, implementation, and validation of biomechanical multibody models of the human upper body. They are implemented in the general-purpose, free multibody analysis software MBDyn [5] (<https://www.mbdyn.org/>), which is also developed by the authors. This work presents an overview of the research activities carried out in this field during the last several years, and an outlook into envisaged development.

2 Multibody Models

2.1 Upper Limb Model

The model of each upper limb is composed of 6 rigid bodies representing the scapula, clavicle, humerus, ulna, radius, and hand, constrained by 7 ideal kinematic constraints that model the sternoclavicular, acromioclavicular, glenohumeral, humeroulnar, humeroradial, radioulnar, and radiocarpal joints. The scapulothoracic joint is modeled through a deformable element. Twenty-eight muscle bundles act on the remaining 13 degrees of freedom. Each is modeled using a nonlinear viscoelastic

element that can be actuated, following the model proposed by Pennestrì et al. in [6], that falls in the general scheme of Hill-type muscular actuators (Fig. 2). The internal force produced by each single muscle bundle is in the form

$$\tilde{f}_m(\hat{l}, \hat{v}, a) = F_0 \left(f_1(\hat{l}) f_2(\hat{v}) a + f_3(\hat{l}) \right) \quad (1)$$

where F_0 is the peak isometric contraction force of the muscle bundle, $\hat{l} = l/l_0$ is its nondimensional length, including the portion related to tendons, $\hat{v} = \dot{l}/v_0$ is its elongation velocity divided by a reference velocity that can be set to $4l_0 \text{ ms}^{-1}$ for skeletal muscles [7], a is the activation level, varying between 0 and 1. The nonlinear functions f_1 and f_2 therefore describe the dependency of the active contribution, while f_3 is related to the passive contribution, largely represented by the axial strain response of the tendons.

Each limb can be considered as a kinematically underdetermined, overactuated manipulator. To cope with the kinematic indeterminacy, the problem is solved directly at the position level. The motion of the degrees of freedom of the model, \mathbf{q} , is restrained by (nonlinear) “ergonomics” springs that impose a penalty on the motion of the relative degrees of freedom, $\theta(\mathbf{q})$, they connect. The problem is equivalent to a nonlinear optimization problem, seeking the minimization of a cost function J_p represented by the potential energy of the ergonomics springs, subjected to the kinematic constraints, both scleronomic, $\phi(\mathbf{q}) = \mathbf{0}$, and rheonomic, $\psi(\mathbf{q}) = \alpha(t)$, the latter used to prescribe the motion of parts through the function $\alpha(t)$,

$$J_p(\theta) = \frac{1}{2} (\theta - \theta_{\text{ergo}})^T \mathbf{K} (\theta - \theta_{\text{ergo}}) + \lambda^T \phi(\mathbf{q}) + \mu^T (\psi(\mathbf{q}) - \alpha(t)) \quad (2)$$

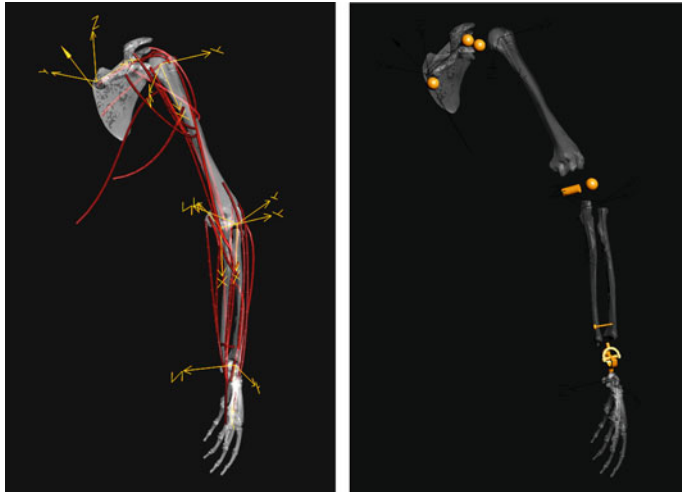


Fig. 2 The upper limb multibody model: location of the nodes on the respective bones (left); schematic representation of the kinematic constraints (right)

where \mathbf{K} is the matrix of joint rotations ergonomic penalization, λ and μ are Lagrange multipliers vectors, θ is the joint angles vector, and θ_{ergo} are assumed equal to the average of the minimum and maximum angle of the individual articular joint.

At the velocity and acceleration levels, the underdeterminacy is solved by minimizing the error between the actual velocity/acceleration and reference values, obtained by differentiating the solution at the position level:

$$J_v(\dot{\mathbf{q}}) = \frac{1}{2} (\dot{\mathbf{q}} - \dot{\mathbf{q}}_0)^T \mathbf{M} (\dot{\mathbf{q}} - \dot{\mathbf{q}}_0) + \lambda^T \phi_{/\mathbf{q}} \dot{\mathbf{q}} + \mu^T (\psi_{/\mathbf{q}} \dot{\mathbf{q}} - \dot{\alpha}(t)) \quad (3a)$$

$$\begin{aligned} J_a(\ddot{\mathbf{q}}) = & \frac{1}{2} (\ddot{\mathbf{q}} - \ddot{\mathbf{q}}_0)^T \mathbf{M} (\ddot{\mathbf{q}} - \ddot{\mathbf{q}}_0) + \lambda^T (\phi_{/\mathbf{q}} \ddot{\mathbf{q}} + (\phi_{/\mathbf{q}} \dot{\mathbf{q}})_{/\mathbf{q}} \dot{\mathbf{q}}) \\ & + \mu^T (\psi_{/\mathbf{q}} \ddot{\mathbf{q}} + (\psi_{/\mathbf{q}} \dot{\mathbf{q}})_{/\mathbf{q}} \dot{\mathbf{q}} - \ddot{\alpha}(t)) \end{aligned} \quad (3b)$$

where \mathbf{M} is the mass matrix.

Once the complete kinematics of the problem is determined, the joint torques required to produce it can be directly found, since at this level the problem is fully determined. To estimate the muscular forces required to produce the computed torques, a constrained minimization problem must be solved, seeking the activations a_i that minimize a cost function (e.g., the total norm, among the many that have been proposed in the literature) that can vary according to the task, constrained by the admissibility conditions $0 \leq a_i \leq 1$, i.e., the *saturation* limits for the muscle bundles [8]. The problem can be stated as

$$\mathbf{c} = (\theta_{/\mathbf{q}}^+)^T \mathbf{B} \tilde{\mathbf{f}}_m(\hat{l}, \hat{v}, a) = (\theta_{/\mathbf{q}}^+)^T (\mathbf{M} \ddot{\mathbf{q}} - \mathbf{f}) \quad (4)$$

where \mathbf{B} is the matrix of the moment arms of muscle forces with respect to the rigid bodies they are attached to, \mathbf{f} is the external forces resultant, and the “+” superscript denotes pseudoinversion. Please note however that the two problems are currently solved independently, i.e., the muscular activations are computed after the joint torques are known. Furthermore, the first equivalence represents a linear underdetermined problem in the activations; therefore, to the minimal contribution coming from the minimization of the objective function, an additional contribution can be added, using combinations of activations that do not produce a change in joint torques. These torque-less activation modes (TLAM) can be found decomposing matrix $\mathbf{A} = (\theta_{/\mathbf{q}}^+)^T \mathbf{B}$ [8]. The resulting activations are associated with the passive pilot input. To them, a *reflexive* (voluntary) contribution is added, considering a quasi-steady approximation of the activation dynamics, and introducing an activation contribution proportional to the variation of length and contraction velocity of the muscle actuator:

$$a = a_0 + k_p \left(\frac{l}{l_0} - \frac{l_{\text{ref}}}{l_0} \right) + k_d \left(\frac{\dot{l}}{v_0} \right) \quad (5)$$

where l_{ref} is the reference length of the muscle from inverse kinematics. This latter procedure can also be used to simulate complete maneuvers.

2.2 Trunk Model

In several cases, the dynamics of the pilot body mid-section has been proven important to adequately model the biodynamic interaction between the body and the vehicle. For this purpose, also a complete model of the trunk has been developed [9] (Fig. 3, left). The model comprises 34 rigid bodies, associated with vertebrae from S1 to C1, the head, and 8 bodies in which visceral masses are lumped. Each vertebral mass is connected to the neighboring ones by algebraic constraints that do not constrain rotation, but only allow relative displacement along the local longitudinal axis of the spine, and by 3D viscoelastic elements acting on the remaining linear and angular degrees of freedom. The head and the sacrum, to which the masses of the pelvis and a portion of the masses of the thighs are associated, are modeled as rigid bodies and are also connected, respectively, to C1 and L5 by algebraic joints and viscoelastic elements. The visceral masses are connected to the respective vertebrae through linear viscoelastic elements as well (Fig. 3).

The model is adapted for both direct and inverse dynamics analyses, following the same procedure outlined in the previous section for the upper limb model. In this case, the elastic elements that connect the vertebrae bodies are used to impose the penalty coefficients on the corresponding relative degrees of freedom when inverting the model kinematics. The model is generally used to identify reduced order models (ROMs) that are then combined with the upper limb models in the form of component mode synthesis (CMS) elements, but can also be used in full joint simulations, effectively reproducing the entire upper body dynamics of the pilot.



Fig. 3 The upper limbs and torso multibody models (left) and the intervertebral (middle) and vertebra-viscera constraints (right) in the torso model

2.3 Models Parameterization

Since the context in which the models are used does not require subject-specific tailoring—as is often the case, for example, in biomechanical simulations aimed at predicting the outcome of surgical procedures—the geometrical, inertial, and structural parameters of the two models are generated following a generalized procedure, starting from just four anthropometric parameters (age, gender, height, and weight). From these input data, the most probable geometry of the subject's rib cage is generated relying on a statistical model published by Shi et al. [10]. The positions of thoracic vertebrae and of the center of the glenoid fossa (the center of the glenohumeral joint) are directly estimated on the rib cage model. Geometric and inertial parameters for the upper limb segments are then estimated using regression coefficients, while structural parameters (stiffnesses, damping factors) are scaled making use of geometrical scaling coefficients derived from the comparison between the generated rib cage geometry and the reference one.

3 Examples

The models can be utilized to estimate activation patterns during entire maneuvers: Fig. 4 shows the results of a simple simulation based on Eqs. (2–3), in which a reference sinusoidal motion has been applied to the collective lever. The corresponding activation patterns of selected muscular fascicles in the upper limb are reported alongside the lever rotation. It can be noted that synergic muscles are activated with similar patterns.

Experiments, including the acquisition of limb motion via motion capture and of muscular activation via electromyography (EMG) in a flight simulator, have been recently carried out. The most recent experimental activity was carried out considering a ship landing task (Fig. 5), performed by an experienced test pilot [11]. The workload of the pilot was varied modifying the ship motion according to the sea state, between 0 (calm) and 5 (rough). EMG signals of two left forearm muscles, the *Extensor Carpi Radialis* and the *Flexor Carpi Ulnaris*, and two upper arm muscles, the *Biceps Brachii* and the *Triceps Brachii* are shown in Fig. 6 (top row).

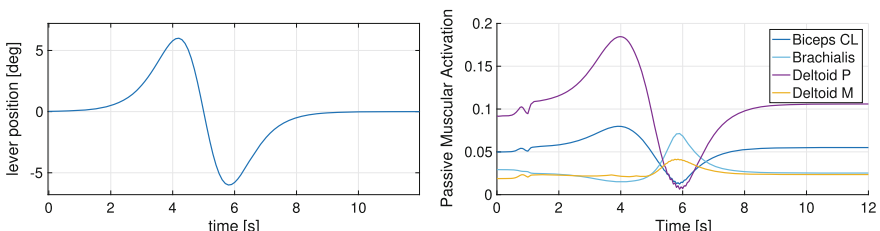


Fig. 4 Imposed collective lever rotation (left) and corresponding muscular activations in the upper arm (right)

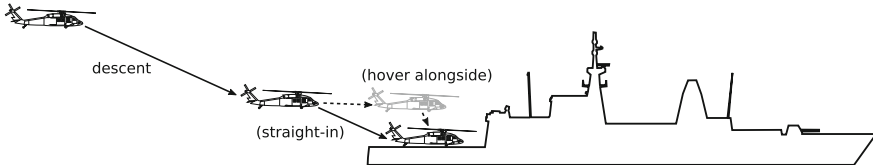


Fig. 5 Example of ship-landing maneuvers executed during simulator tests: descent towards the ship is followed by straight-in landing when the ship motion allows it. Otherwise, hovering alongside the naval unit is performed, waiting for quiescence

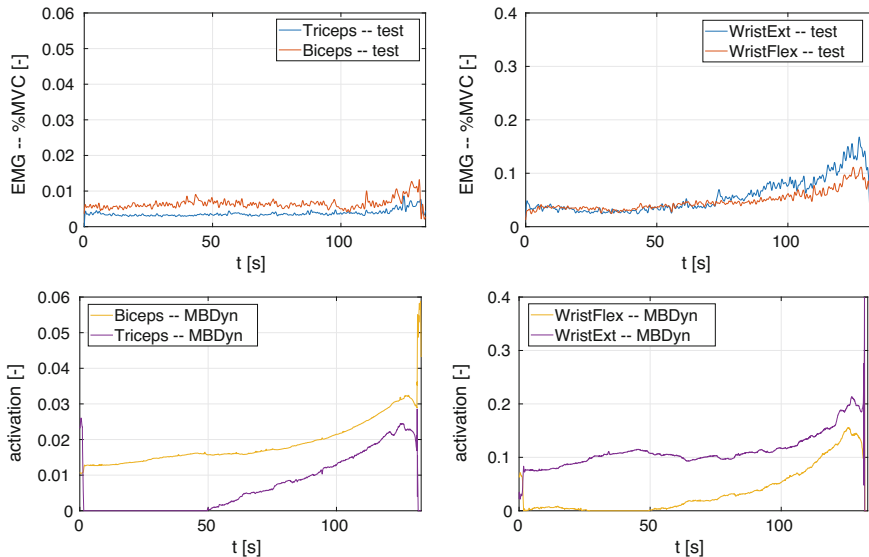


Fig. 6 Measured EMG signals (top row) and predicted activation levels (bottom row) of two upper arm and two forearm muscles during a ship landing simulator test

The forearm muscles show an increasing level of co-contraction during the descent and in particular in the final approach phase, signaling an increasing effect of the workload on the stiffness of wrist flexion–extension articulation. The upper arm muscles, instead, show very low level of EMG activity throughout the test. The levels of activation predicted by the multibody models are shown in the bottom row graphs of Fig. 6. While the absolute values of EMG and activation should not be directly compared [12], it can be noted that the order of magnitude of the computed activations compares favorably with the registered value. The time variation of the activation levels of the forearm muscles was captured to a certain degree enriching the baseline activation with a contribution proportional to TLAMs. However, at this very preliminary stage of the analysis, the effect of TLAMs is also important in the muscles of the upper portion of the limb, a behavior that was not observed during experiments. Further investigations are therefore needed to better understand how to

correctly reproduce the observed patterns. More test, involving pilots with different levels of experience, are also needed to assess the variability of the EMG patterns.

4 Conclusions

There is practical evidence of adverse RPC phenomena that evolve in diverging oscillations, often culminating in limit cycles, at frequencies that are too high for a human operator to control. Sources of nonlinearities can be found in the kinematics and constitutive properties of the limbs, in friction and nonlinear constitutive properties intentionally designed in the control inceptors, and in the aeromechanics and servodynamics of the vehicle. These phenomena typically surface during flight testing; they can be rather dangerous as well as elusive, as their appearance is often related to subjective characteristics of the pilots. A better understanding of RPCs, and the capability to model and anticipate their insurgence, can be of extraordinary importance in terms of safety and, from an industrial standpoint, of savings in development time and resources.

References

1. Pavel, M.D., Jump, M., Dang-Vu, B., Masarati, P., Gennaretti, M., Ionita, A., Zaichik, L., Smaili, H., Quaranta, G., Yilmaz, D., Jones, M., Serafini, J., Malecki, J.: Adverse rotorcraft pilot couplings — past, present and future challenges. *Prog. Aerosp. Sci.* **62**, 1–51 (2013). <https://doi.org/10.1016/j.paerosci.2013.04.003>
2. Pavel, M.D., Masarati, P., Gennaretti, M., Jump, M., Zaichik, L., Dang-Vu, B., Lu, L., Yilmaz, D., Quaranta, G., Ionita, A., Serafini, J.: Practices to identify and preclude adverse aircraft-and-rotorcraft-pilot couplings — a design perspective. *Prog. Aerosp. Sci.* **76**, 55–89 (2015). <https://doi.org/10.1016/j.paerosci.2015.05.002>
3. McRuer, D.T.: Aviation Safety and Pilot Control: Understanding and Preventing Unfavourable Pilot-Vehicle Interactions. National Research Council, National Academy Press, Washington (1997)
4. Jex, H.R., Magdaleno, R.E.: Biomechanical models for vibration feedthrough to hands and head for a semisupine pilot. *Aviat. Space Environ. Med.* **49**(1–2), 304–316 (1978)
5. Masarati, P., Morandini, M., Mantegazza, M.: An efficient formulation for general-purpose multibody/multiphysics analysis. *J. Comput. Nonlinear Dyn.* **9**(4), 041001 (2014). <https://doi.org/10.1115/1.4025628>
6. Pennestri, E., Stefanelli, R., Valentini, P.P., Vita, L.: Virtual musculo-skeletal model for the biomechanical analysis of the upper limb. *J. Biomech.* **40**(6), 1350–1361 (2007). <https://doi.org/10.1016/j.jbiomech.2006.05.013>
7. Lichtwark, G.A., Wilson, A.M.: A modified hill muscle model that predicts muscle power output and efficiency during sinusoidal length changes. *Indian J. Exp. Biol.* **208**, 2831–2843 (2005)
8. Masarati, P., Quaranta, G., Zanoni, A.: Dependence of helicopter pilots' biodynamic feedthrough on upper limbs' muscular activation patterns. *Proc. IMechE Part K J. Multi-Body Dyn.* **227**(4), 344–362 (2013). <https://doi.org/10.1177/1464419313490680>

9. Zanoni, A., Masarati, P.: Direct and inverse analysis of human spine for helicopter comfort assessment. In: 5th Joint International Conference on multibody Dynamics, Lisboa (2018)
10. Shi, X., Cao, L., Reed, M.P., Rupp, J.D., Hoff, C.N., Hu, J.: A statistical human rib cage geometry model accounting for variations by age, sex, stature and body mass index. *J. Biomech.* **47**(10), 2277–2285 (2014)
11. Quaranta, G., Paolini, R., Zanoni, A., Masarati, P., Galli, M., Zago, M., Frigerio, L., Maisano, G., Ragazzi, A.: Biodynamic testing for the prediction of rotorcraft-pilot couplings. In: 75th Annual Forum of the Vertical Flight Society, Philadelphia (2019)
12. Hicks, J.L., Uchida, T.K., Seth, A., Rajagopal, A., Delp, S.L.: Is my model good enough? Best practices for verification and validation of musculoskeletal models and simulations of movement. *J. Biomech. Eng.* **137**(2), 020905-020905-24. <https://doi.org/10.1115/1.4029304>

Derivation of Non-dimensional Equation of Motion for Thin Plate in Absolute Nodal Coordinate Formulation



Kun-Woo Kim, Jae-Wook Lee, Jin-Seok Jang, Ji-Heon Kang,
and Wan-Suk Yoo

Abstract The absolute nodal coordinate formulation was developed in the mid-1990s to express large deformations and large rotations in flexible multi-body dynamics. It is a non-incremental finite-element procedure wherein the mass matrix is expressed as a constant while the stiffness matrix carries highly nonlinear features. The formulation for a thin plate can be developed on the basis of continuum or structural mechanics similar to that for a beam. Absolute nodal coordinate formulation necessarily uses the global slope vector, and this results in an increase in the degree of freedom. In this study, to reduce analysis time, the non-dimensional equation of motion of a thin plate is derived from the dimensional equation of motion using non-dimensional variables. An example of a thin cantilever plate is used to present the improved efficiency of analysis due to the non-dimensional equation of motion, and the simulations are shown with various numbers of elements. The non-dimensional equation of motion is thus verified by demonstrating the similarities of the solutions for both the dimensional and non-dimensional equations of motion.

Keywords Absolute nodal coordinate formulation · Non-dimensional equation of motion · Thin plate

1 Introduction

The absolute nodal coordinate formulation (ANCF) was developed in the mid-1990s to express large deformations and large rotations in flexible multi-body dynamics [1]. The ANCF is a non-incremental finite-element procedure wherein

K.-W. Kim (✉) · J.-W. Lee · J.-S. Jang
Korea Institute of Industrial Technology, Daegu, South Korea
e-mail: kwkim@kitech.re.kr

J.-H. Kang · W.-S. Yoo
Pusan National University, Busan, South Korea

the mass matrix is expressed as a constant while the stiffness matrix contains highly nonlinear features. The mass matrix that is expressed as a constant suggests the absence of a transformation matrix. This is distinguishable from the floating frame of reference formulation in which the mass matrix is expressed as a nonlinear object while the stiffness matrix is expressed as a constant [1, 2]. As one of the studies concerning ANCF, Kim et al. [3] have proposed a non-dimensional equation of motion to reduce the time required for analysis. Their proposed method converts the dimensional equation of motion into the non-dimensional equivalent by introducing non-dimensional variables [4]. The solution to the converted equation was verified with an example of a cantilever beam whose exact solution exists, its applicability to equations of motion based on continuum and structural mechanics was also presented.

The formulation for a plate in ANCF was also developed in the mid-1990s [1]. For a fully parameterized element based on continuum mechanics, there are 12 degrees of freedom for each node, resulting in a total of 48 degrees of freedom per element with four nodal points [5]. This is disadvantageous as the time required for analysis increases [1]. Further, the time for analysis increases compared to the equation of motion based on structural mechanics, which uses the gradient-deficient element [6]. This study intends to convert the equation of motion studied by Dufva and Shabana [6] into its non-dimensional equivalent using non-dimensional variables to reduce the time required for analysis. To demonstrate the improved efficiency of analysis and to verify the non-dimensional equation of motion, a thin cantilever plate will be used as an example. Its analysis efficiency is expected to increase with increasing number of elements. The originality of the present study would be ascribable to following points:

- An introduction of the newly defined non-dimensional shape function and nodal coordinate for the thin plate in absolute nodal coordinate formulation.
- Derivation of the non-dimensional equation of motion for a thin plate using non-dimensional variables.
- Verification of the non-dimensional equation of motion and improved efficiency of analysis.

2 Derivation of Non-dimensional Equation of Motion

Non-dimensionalization of the equation of motion can be achieved using the variable T_{ND} , which non-dimensionalizes the dimension of time, as shown in Eq. (1).

$$t = T_{ND} t^* \left(T_{ND} = L_{ND}^2 \sqrt{\frac{\rho}{F_{ND}}} \right) \quad (1)$$

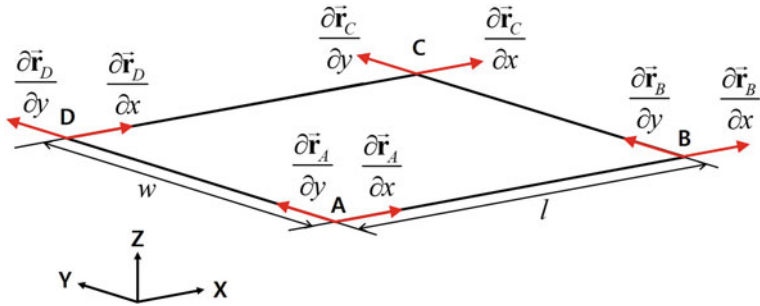


Fig. 1 Four-node rectangular thin plate in ANCF

Here, t and ρ denote the time and density. L_{ND} and F_{ND} denote the arbitrary length and force on the thin plate. The symbol “*” is the non-dimensionalized variable.

As shown in Fig. 1, the general coordinates used to express the position vectors of four nodes with a total of 36 degrees of freedom for a rectangular thin plate can be expressed as combinations of the global position vectors and in-plane global slope vectors. In Fig. 1, the subscripts A, B, C, and D signify anticlockwise nodal points. x and y are the coordinates along the plane of the thin plate before deformation. l and w denote the length and width of the thin plate, respectively. In this study, the shape function $\hat{\mathbf{S}}$ was determined to be non-dimensional, whereas the nodal coordinate $\hat{\mathbf{e}}$ was defined as a dimension of length. Therefore, the non-dimensional position vector \vec{r}^* is defined as Eq. (2), from the dimensional position vector \vec{r} .

$$\vec{r} = \hat{\mathbf{S}} \hat{\mathbf{e}} = L_{ND} \hat{\mathbf{S}} \hat{\mathbf{e}}^* \rightarrow \vec{r}^* = \hat{\mathbf{S}} \hat{\mathbf{e}}^* \quad (2)$$

where $\hat{\mathbf{e}}^*$ is the newly defined non-dimensional nodal coordinate. Therefore, the non-dimensional equation of motion can be derived as in Eq. (3).

$$\mathbf{M}^* \left(\frac{d^2 \hat{\mathbf{e}}^*}{dt^{*2}} \right) + \mathbf{K}^* (\hat{\mathbf{e}}^*) \hat{\mathbf{e}}^* = \vec{\mathbf{F}}_C^* \quad (3)$$

where \mathbf{M}^* and \mathbf{K}^* are the non-dimensional mass and stiffness matrices. $\vec{\mathbf{F}}_C^*$ is the non-dimensional conservative force vector.

2.1 Non-dimensional Mass Matrix

Using the non-dimensional variables, the kinetic energy can be written as Eq. (4).

$$\begin{aligned} T &= \frac{1}{2} \int_V \rho \left(\frac{\partial \vec{r}}{\partial t} \right)^T \left(\frac{\partial \vec{r}}{\partial t} \right) dV \\ &= \frac{L_{ND}^5}{T_{ND}^2} \frac{1}{2} t^* \int_0^{l^*} \int_0^{w^*} \rho \left(\frac{\partial \vec{r}^*}{\partial t^*} \right)^T \left(\frac{\partial \vec{r}^*}{\partial t^*} \right) dy^* dx^* \end{aligned} \quad (4)$$

From Eq. (4), the non-dimensional kinetic energy can be expressed as Eq. (5).

$$\begin{aligned} T^* &= \frac{1}{2} t^* \int_0^{l^*} \int_0^{w^*} \left(\frac{\partial \vec{r}^*}{\partial t^*} \right)^T \left(\frac{\partial \vec{r}^*}{\partial t^*} \right) dy^* dx^* \\ &= \left(\frac{\partial \hat{\vec{\epsilon}}^*}{\partial t^*} \right)^T \frac{1}{2} h^* \int_0^{l^*} \int_0^{w^*} \hat{\mathbf{S}}^T \hat{\mathbf{S}} dy^* dx^* \left(\frac{\partial \hat{\vec{\epsilon}}^*}{\partial t^*} \right) \end{aligned} \quad (5)$$

Therefore, the non-dimensional mass matrix can be defined as Eq. (6).

$$\mathbf{M}^* = h^* \int_0^{l^*} \int_0^{w^*} \hat{\mathbf{S}}^T \hat{\mathbf{S}} dy^* dx^* \quad (6)$$

2.2 Non-dimensional Stiffness Matrix

The strain energy can be defined as Eq. (7) using the Kirchhoff shell theory based on structural mechanics [6]. The first term in Eq. (7) is related to membrane stretch and shear. The second term is associated with bending and twisting along the plane of the element.

$$U = \frac{1}{2} \int_{-h/2}^{h/2} \int_0^l \int_0^w \vec{\epsilon}^T \mathbf{E} \vec{\epsilon} dy dx dz + \frac{1}{2} \int_{-h/2}^{h/2} \int_0^l \int_0^w \vec{\kappa}^T \mathbf{E} \vec{\kappa} dy dx dz \quad (7)$$

where $\vec{\epsilon}$ is the non-linear Green-Lagrange strain vector, \mathbf{E} is the matrix of coefficients for linearly elastic isotropic materials, and $\vec{\kappa}$ is the curvature vector. The strain energy can be defined as a non-dimensional strain energy, as given in Eq. (8).

$$\begin{aligned} U &= (F_{ND} L_{ND}) U^* \\ \rightarrow U^* &= \underbrace{\frac{1}{2} \int_{-h^*/2}^{h^*/2} \int_0^{l^*} \int_0^{w^*} \vec{\epsilon}^{*T} \mathbf{E}^* \vec{\epsilon}^* dy^* dx^* dz^*}_{U_1^*} \\ &\quad + \underbrace{\frac{1}{2} \int_{-h^*/2}^{h^*/2} \int_0^{l^*} \int_0^{w^*} \vec{\kappa}^{*T} \mathbf{E}^* \vec{\kappa}^* dy^* dx^* dz^*}_{U_2^*} \end{aligned} \quad (8)$$

Stiffness Matrix for the First Term U_1^* . The stiffness matrix for the first term U_1^* can be derived using the non-dimensional strain vector and the matrix of coefficients. In the plane stress problem, the non-dimensional strain vector can be expressed as Eq. (9).

$$\hat{\boldsymbol{\varepsilon}}^* = \begin{bmatrix} \varepsilon_{x^*x^*}^* & \varepsilon_{y^*y^*}^* & 2\varepsilon_{x^*y^*}^* \end{bmatrix}^T \text{ where } \varepsilon_{ij}^* = \frac{1}{2} \left(\hat{\boldsymbol{\varepsilon}}^{*T} \hat{\mathbf{S}}_i^T \hat{\mathbf{S}}_j \hat{\boldsymbol{\varepsilon}}^* - \delta_{ij} \right) \quad (i, j = x^*, y^*) \quad (9)$$

The matrix of coefficients can be expressed as Eq. (10).

$$\mathbf{E}^* = \frac{E^*}{1-\nu^2} \begin{bmatrix} 1 & \nu & 0 \\ \nu & 1 & 0 \\ 0 & 0 & \frac{1-\nu}{2} \end{bmatrix} \quad (10)$$

where E^* is the non-dimensional modulus of elasticity, and ν is the Poisson's ratio. From Eqs. (9) and (10), U_1^* can be expressed as Eq. (11).

$$U_1^* = \frac{1}{2} h^* \frac{E^*}{1-\nu^2} \int_0^{l^*} \int_0^{w^*} \left(\varepsilon_{xx}^* \varepsilon_{xx}^* + \nu \varepsilon_{xx}^* \varepsilon_{yy}^* + \nu \varepsilon_{yy}^* \varepsilon_{xx}^* + \varepsilon_{yy}^* \varepsilon_{yy}^* + \frac{1-\nu}{2} \gamma_{xy}^* \gamma_{xy}^* \right) dx^* dy^* \quad (11)$$

Using Eq. (11), the non-dimensional stiffness matrix can be defined as Eq. (12).

$$\frac{\partial U_1^*}{\partial \hat{\boldsymbol{\varepsilon}}^*} = \hat{\boldsymbol{\varepsilon}}^{*T} \mathbf{K}_1^* \left(\hat{\boldsymbol{\varepsilon}}^* \right) \quad (12)$$

Stiffness Matrix for the Second Term U_2^* . To derive the stiffness matrix for the second term U_2^* , the non-dimensional curvature vector can be derived as in Eq. (13).

$$\hat{\boldsymbol{\kappa}}^* = z^* \begin{bmatrix} \kappa_{x^*x^*}^* & \kappa_{y^*y^*}^* & 2\kappa_{x^*y^*}^* \end{bmatrix}^T \text{ where } \kappa_{ij}^* = \frac{\left(\hat{\boldsymbol{\varepsilon}}^{*T} \hat{\mathbf{S}}_{ij}^T \right)^T \mathbf{n}^*}{\|\mathbf{n}^*\|^3} \quad (i, j = x^*, y^*) \quad (13)$$

where the vertical vector \mathbf{n}^* is perpendicular to the plane of the element, and $\|\mathbf{n}^*\|$ is defined as $\|\mathbf{n}^*\| = \sqrt{\mathbf{n}^{*T} \mathbf{n}^*}$. From Eqs. (10) and (13), U_2^* can be expressed as Eq. (14).

$$U_2^* = \frac{h^{*3} E^*}{24(1-\nu^2)} \times \int_0^{l^*} \int_0^{w^*} \left(\kappa_{xx}^* \kappa_{xx}^* + \nu \kappa_{xx}^* \kappa_{yy}^* + \nu \kappa_{yy}^* \kappa_{xx}^* + \kappa_{yy}^* \kappa_{yy}^* + 2(1-\nu) \kappa_{xy}^* \kappa_{xy}^* \right) dx^* dy^* \quad (14)$$

The partial derivatives of the curvature vector with respect to the non-dimensional nodal coordinate can be expressed as Eq. (15).

$$\frac{\partial \kappa_{ij}^*}{\partial \hat{\mathbf{e}}^*} \approx \frac{1}{\|\bar{\mathbf{n}}^*\|^3} \bar{\mathbf{n}}^{*T} \hat{\mathbf{S}}_{ij} \quad (i, j = x^*, y^*) \quad (15)$$

where $\bar{\mathbf{n}}^*$ denotes the average value of the vertical vector perpendicular to the plane of the element, as obtained from each nodal point. Therefore, the non-dimensional stiffness matrix can be defined as Eq. (16).

$$\frac{\partial U_2^*}{\partial \hat{\mathbf{e}}^*} = \hat{\mathbf{e}}^{*T} \mathbf{K}_2^* \left(\hat{\mathbf{e}}^* \right) \quad (16)$$

2.3 Non-dimensional Force Vector

The gravity corresponding to the conservative force can be derived from the principle of virtual work using Eq. (17).

$$\delta W_C = h \int_0^l \int_0^w \rho \vec{\mathbf{G}}^T \hat{\mathbf{S}} dy \ dx \delta \hat{\mathbf{e}} \quad (17)$$

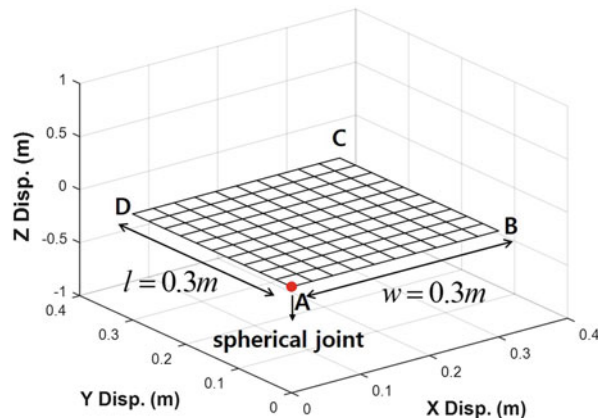
where $\vec{\mathbf{G}} = [0 \ 0 \ -g]^T$ denotes the vector containing the gravitational acceleration g in the z direction. Therefore, from Eq. (17), the non-dimensional conservative force vector can be defined as Eq. (18).

$$\vec{\mathbf{F}}_C^{*T} = \frac{1}{F_{ND}} h \int_0^l \int_0^w \rho \vec{\mathbf{G}}^T \hat{\mathbf{S}} dy \ dx \quad (18)$$

3 Numerical Solution of Non-dimensional Equation of Motion

The efficiency of the non-dimensional equation of motion will be presented through a comparison with the dimensional equation of motion by using an example of thin cantilever plate, as shown in Fig. 2. The properties of the thin cantilever plate are presented in Table 1. Based on Table 1 and Eq. (1), the value of T_{ND} increases with an increasing number of elements. The specification of the personal computer used for the analysis and information regarding the commercial software used are shown in Table 2.

The simulation time of the dimensional and non-dimensional equation of motion to physical time of 0.3 s are presented in Fig. 3. When the number of elements

Fig. 2 Thin cantilever plate**Table 1** Properties of thin cantilever plate

Density (kg/m^3)	7810
Young's modulus (N/m^2)	1.0E + 05
Poisson's ratio (.)	0.3
Length and width (m)	0.3
Thickness (m)	0.001

Table 2 Workstation performance for the analysis

CPU	Intel(R) Xeon(R) CPU E5-2697 v3 @ 2.60 GHz
Memory capacity	64 GB
Commercial software	MATLAB R2019a—64bit

is 3^2 or greater, the non-dimensional equation of motion is more efficient than the dimensional equation of motion. In particular, the efficiency of analysis increases with an increasing number of elements. The positions of point C at the physical time of 0.3 s are presented in Fig. 4, in which the solutions converge in accordance with the increasing number of elements.

To validate the efficiency of the non-dimensional equation of motion, the solution of the non-dimensional equation of motion should be identical to that of the dimensional equation of motion. The positions of point C in the case of 1^2 element and 8^2 elements are presented in Figs. 5 and 6, respectively. The positions in both the cases correspond to each other, and the numerical results obtained from both the dimensional and non-dimensional equations of motion also correspond. Therefore, the correct transformation of the non-dimensional equation of motion from the dimensional equation of motion is validated, and the analysis efficiency can be secured.

Based on the results presented in Figs. 5 and 6, the three-dimensional behaviors of the thin cantilever plate are presented in Figs. 7 and 8. The black solid line represents the position of point C plotted along the time. By considering the

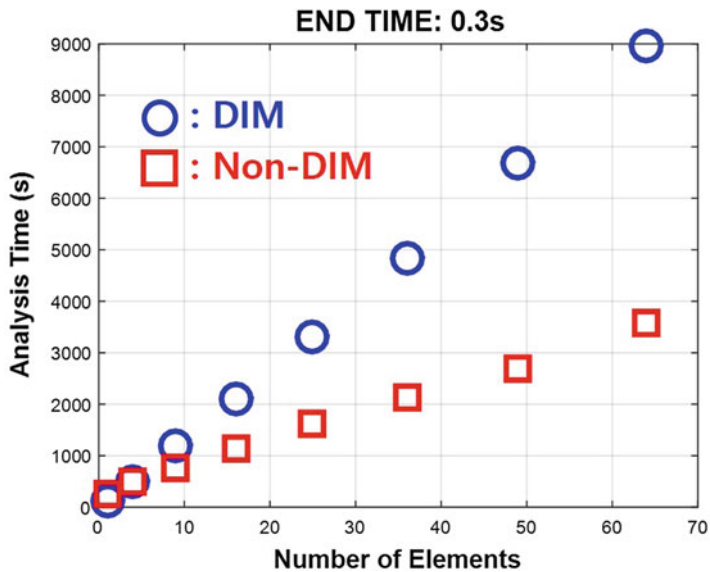


Fig. 3 Simulation time

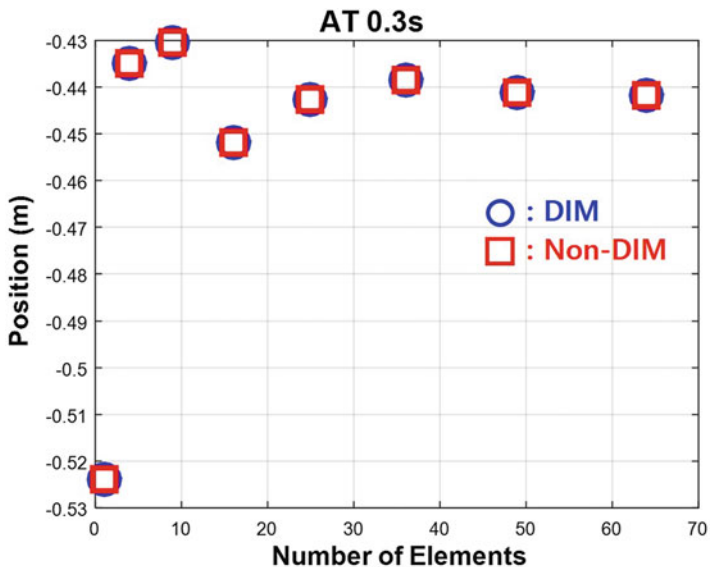


Fig. 4 Position of point C at 0.3 s

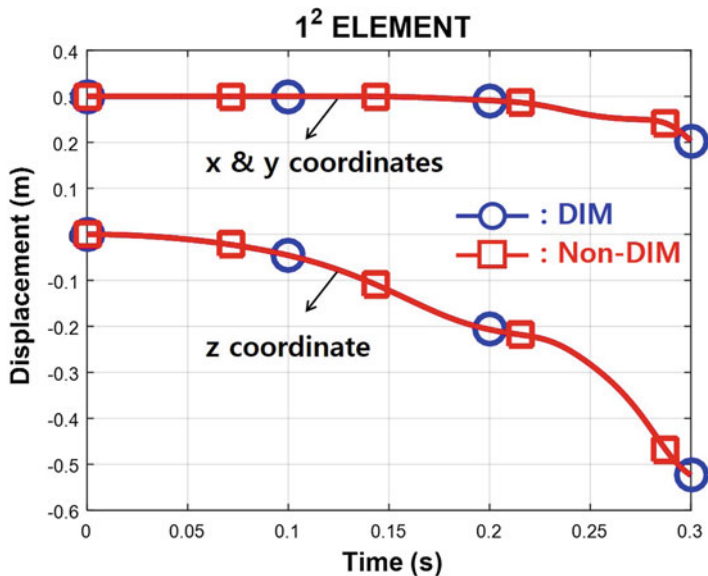


Fig. 5 Position of point C with 1² element

Fig. 6 Position of point C with 8² elements

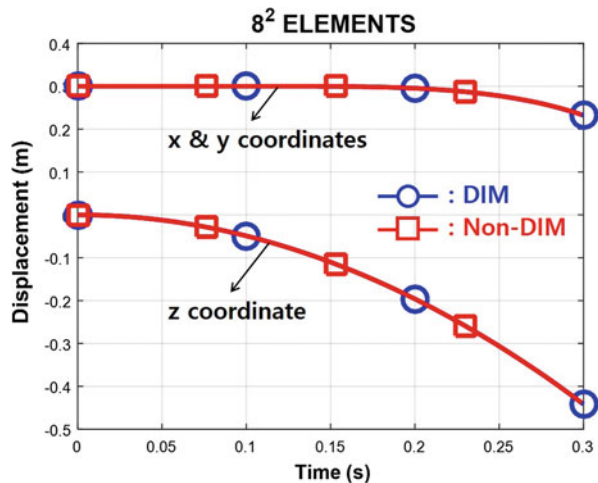


Fig. 7 Three-dimensional motion with 1^2 element

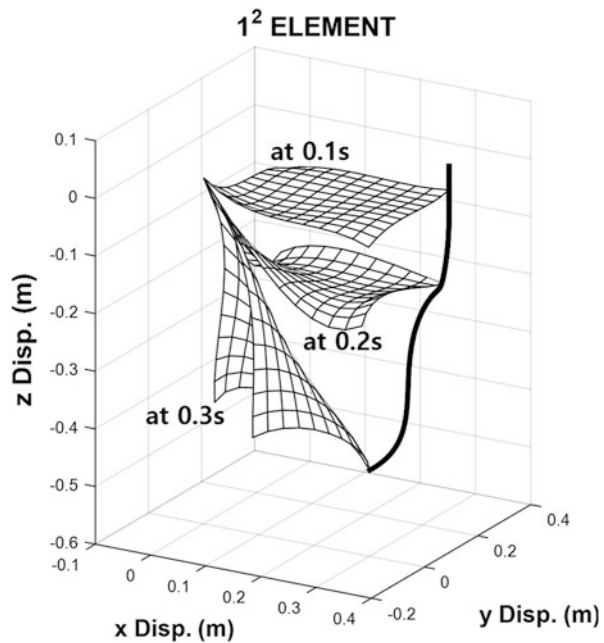
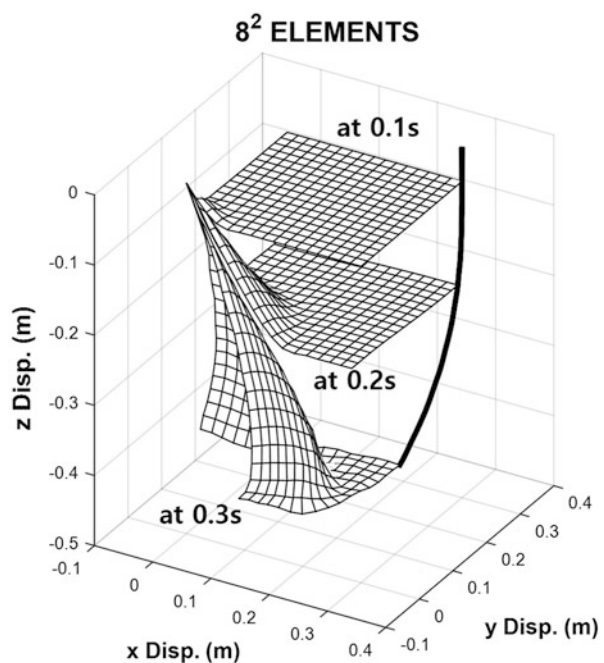


Fig. 8 Three-dimensional motion with 8^2 elements



solutions of the finite element analysis that would converge in accordance with an increasing number of elements, it can be inferred that the solution resulting from the analysis of 8^2 elements is more correct than those resulting from the analysis of 1^2 element.

4 Conclusions

The absolute nodal coordinate formulation to express large deformations and large rotations in flexible multi-body dynamics necessarily uses the global slope vector, and this results in an increase in the degree of freedom. The increase in the time required for analysis because of an increase in the number of degrees of freedom in thin plate has been regarded to be disadvantageous in absolute nodal coordinate formulation. In this study, the dimensional equation of motion studied by Dufva and Shabana [6] was converted into the non-dimensional equation of motion by using non-dimensional variables. A thin cantilever plate was used to validate the non-dimensional equation of motion. An improvement in the analysis speed in accordance with an increase in the number of elements was presented.

Acknowledgments This research was supported by Korea Institute of Industrial Technology (KITECH) and by National Research Foundation of Korea (No. 2018R1D1A1A09083567).

References

1. Gerstmayr, J., Sugiyama, H., Mikkola, A.: An overview on the developments of the absolute nodal coordinate formulation. The 2nd Joint International Conference on Multibody System Dynamics (2012)
2. Dibold, M., Gerstmayr, J., Irshik, H.: A detailed comparison of the absolute nodal coordinate and the floating frame of reference formulation in deformable multibody systems. *J. Comput. Nonlinear Dyn.* **4**(2), 021006 (2009)
3. Kim, K.W., Lee, J.W., Jang, J.S., Oh, J.Y., Kang, J.H., Kim, H.R., Yoo, W.S.: Efficiency of non-dimensional analysis for absolute nodal coordinate formulation. *Nonlinear Dyn.* **87**, 1139–1151 (2017)
4. Kawaguti, K., Terumich, Y., Takehara, S., Kaczmarczyk, S., Sogabe, K.: The study of the tether motion with time-varying length using the absolute nodal coordinate formulation with multiple nonlinear time scales. *J. Syst. Des. Dyn.* **1**(3), 491–500 (2007)
5. Dmitrochenko, O., Pogorelov, D.: Generalization of plate finite elements for absolute nodal coordinate formulation. *Multibody Syst. Dyn.* **10**, 17–43 (2003)
6. Dufva, K., Shabana, A.A.: Analysis of thin plate structures using the absolute nodal coordinate formulation. *J. Multibody Dyn.* **219**, 345–355 (2005)

Part VI

**Turning Processes, Rotating Systems, and
Systems with Time Delays**

Approximated Dynamics of Chatter in Turning Processes



Bence Beri and Gabor Stepan

Abstract The nonlinear behaviour of the turning process is analysed, which is described by a one degree-of-freedom dynamical system. The model takes the form of a delay differential equation that is non-smooth when the cutting tool leaves contact with the surface. The delay equation is approximated by means of a power series with respect to the delay to reveal the geometric structure of the relevant dynamics in a low dimensional phase space. The bifurcation diagram of the non-smooth system is calculated and compared to the existing theoretical and experimental results of the literature.

Keywords Chatter · Turning · Relevant dynamics · Lorenz map

1 Motivation

During machining, unexpected vibrations called chatter might occur due to the regeneration effect especially at high material removal rates. This is because either the cutting tool or the workpiece (or both) are compliant and the chip thickness varies due to the relative vibrations of the tool and the workpiece. Chatter generally results in noise or tool breakage and leads to poor surface quality, so in practice, there is a need to prescribe boundaries on technological parameters such as spindle speed and chip width. During chatter, the tool repeatedly loses contact with the surface and soon restores the contact again. In case of turning, the regeneration effect is modelled by a time delay system. The tool cuts the surface that was formed in the previous cut and the chip thickness is defined by the difference of the current and the previous positions of the tool. The time delay between two succeeding cuts corresponds to reciprocal value of the period of the workpiece rotation [1].

B. Beri (✉) · G. Stepan

Department of Applied Mechanics, Budapest University of Technology and Economics,
Budapest, Hungary

e-mail: beri@mm.bme.hu

The objective of this study is to describe the geometric structure of a three-dimensional phase space of a non-smooth dynamical model that is reduced from the original infinite dimensional time delay system. Experiments demonstrate that large-amplitude chattering motions may appear above a certain value of chip width [2]. There have been some related results in the literature: Stepan and Kalmar-Nagy [3] investigated the nonlinear delay system of turning by means of analytical tools and gave an estimation for the parameter point where the cutting tool loses contact with the workpiece. The authors of [4] analysed the global dynamics of chatter in orthogonal cutting by taking into account the loss of contact between the tool and the workpiece and constructed a non-smooth mechanical model.

In this paper, the non-smoothness is considered but the delayed term is approximated by a power series with respect to the time delay. Since this Taylor expansion is not uniformly convergent, the stability analysis shows that the approximate system is valid only at the higher spindle speed range. According to the bifurcation diagram of the system, the global behaviour of the low dimensional system represents essential similarities with the delayed model.

2 Modelling and Analysis

2.1 Model Formulation

A simple model developed for turning operations can demonstrate the chattering phenomenon. The motion of the tool is described by a one degree-of-freedom dynamical model. As it is shown in Fig. 1a, the tool vibrates in the y direction and F_y is the normal component of the cutting force (see Fig. 1b). Here, m , c_y and k_y are the modal mass, modal damping and modal stiffness, respectively. The dimensionless governing equation of motion is given by

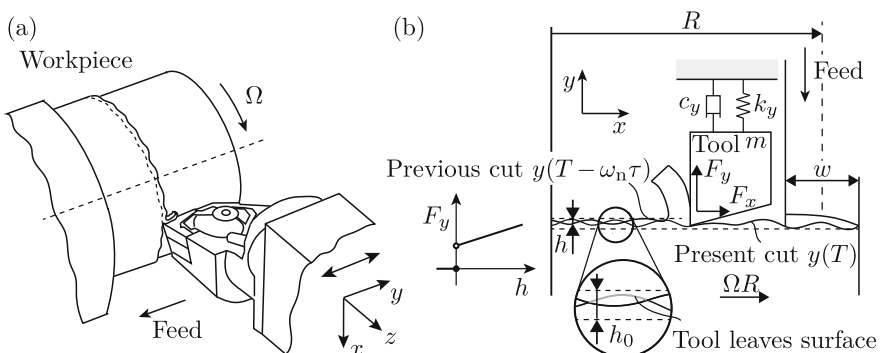


Fig. 1 Panel (a) shows the chip removal in turning processes in case of a compliant tool. Panel (b) depicts the surface regeneration

$$y''(T) + 2\zeta y'(T) + y(T) = \frac{F_y(T)}{\omega_n^2}, \quad (1)$$

where $\zeta = c_y/(2m\omega_n)$ is the damping ratio, $\omega_n = \sqrt{k_y/m}$ is the natural angular frequency of the undamped system and $T = \omega_n t$ is the dimensionless time. In practice, we find that the cutting force is linearly proportional to the chip width w but there is a nonlinear dependence on the chip thickness h . Thus, it is given by the empirical formula

$$F_y(T) = K_y w h^q(T), \quad (2)$$

where K_y is the cutting force parameter and q is the cutting force exponent. This represents a nonlinearity that highly influences the evolving large-amplitude motion. In the literature, many suggestions can be found related to the cutting force exponent q to accurately estimate the cutting force characteristics [5, 6]. A simple but still reasonable approximation is suggested by [7] for $h > 0$, the cutting force is linearised at the desired chip thickness h_0 :

$$F_y(T) = K_y w h_0^q + q K_y w h_0^{q-1} (h(T) - h_0) + \mathcal{O}(h^2(T)). \quad (3)$$

When surface regeneration effect develops, the chip thickness h is defined by the present and the previous positions of the tool (see Fig. 1b)

$$h(T) = h_0 + y(T - \omega_n \tau) - y(T), \quad (4)$$

where $\tau = 2\pi/\Omega$ is the time delay given by the spindle speed Ω .

In this model, the tool loses contact with the surface of the workpiece when $h = 0$ and moves as a free damped oscillator until it reaches the workpiece again. The governing equation of motion of the piecewise-linearised smooth system is given by the linearised equation

$$\eta''(T) + 2\zeta \eta'(T) + \eta(T) = \begin{cases} \frac{k_1}{\omega_n^2}(\eta(T - \omega_n \tau) - \eta(T)) & h > 0 \\ 0 & h \leq 0, \end{cases} \quad (5)$$

where $k_1 = q K_y w h_0^{q-1}/m$ is the specific cutting force coefficient and $\eta(T) = y(T) - y_0$ is the small perturbation around the equilibrium position y_0 . The switching function takes the form $h_0 = \omega_n^2 \tau^2 \eta(T)/2 + \omega_n \tau (1 + \omega_n \tau \zeta) \eta'(t)$ at $h = 0$. Equation (5) describes that the tool is in cut when the chip thickness $h > 0$ and it starts flying when $h \leq 0$. By using Taylor expansion with respect to the time delay τ , the dimensional reduction of Eq. (5) for $h > 0$ gives

$$\begin{aligned} \frac{1}{6}k_1\tau^3\omega_n^3\eta'''(T) + \left(1 - \frac{1}{2}k_1\tau^2\right)\omega_n^2\eta''(T) + (2\xi\omega_n + \tau k_1)\omega_n\eta'(T) \\ + \omega_n^2\eta(T) = 0. \end{aligned} \quad (6)$$

Insperger [8] analysed the stability properties and the validity of Taylor expansion of the time delayed terms with respect to the time delay. It is stated that Taylor expansion properly approximates the asymptotic nature of the system till the order of the expansion does not exceed the leading order of the equation by two.

Note that Eq. (6) is coupled to a second-order differential equation that describes a free damped oscillator (see Eq. (5) for $h \leq 0$).

2.2 Stability

In the industry, the technological parameters w and Ω are assumed to be the most relevant. Thus, if there is an intention to approach the prescribed surface quality, stable parameter region of cutting needs to be calculated. The stability chart of the approximate system can be determined by using the Routh–Hurwitz criterion for Eq. (6). The stability boundary of the cutting operation is shown in Fig. 2a

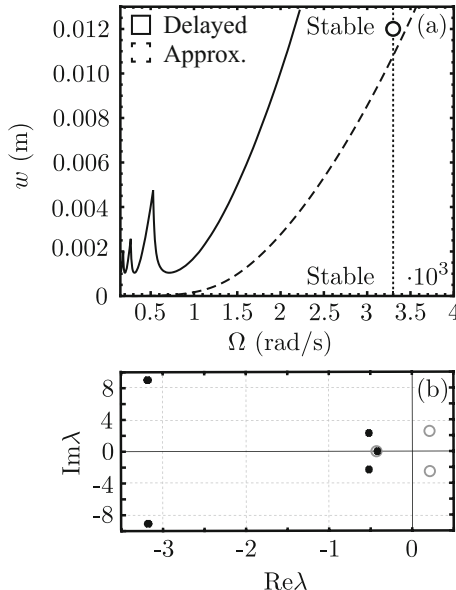


Fig. 2 Panel (a) shows the stability diagrams of Eq. (1) for $h > 0$ and Eq. (2). Panel (b) illustrates the spectrum of the delay and the approximate system at the parameter point denoted by a circle in Panel (a). The dots correspond to the roots of the delay equation (see Eq. (5) for $h > 0$) and the circles belongs to the three-order system described by Eq. (6). The numerical values that were used: $h_0 = 0.001$ m, $q = 3/4$, $K_y = 10^8$ N/m $^{1+q}$, $\zeta = 0.08$, $m = 10$ kg, $\omega_n = 515.5$ rad/s

by the dashed line. Since Taylor expansion is not uniformly convergent, further investigation is restricted only to small time delays τ that correspond to higher spindle speeds Ω .

Equation (6) allows us to investigate the problem in the three-dimensional phase space. It has roots of a complex conjugate pair and a real root in contrast to the infinite number of roots of the delay system. The investigation of the roots of the delay equation (for $h > 0$) has been accomplished by using the MatLab package called DDE-BIFTOOL [9]. In the vicinity of the stability boundary of the third-order model, the value of the real root and the imaginary part of the complex conjugate pair of the approximate system matches within 6% with the corresponding roots of the delay system (see Fig. 2b). Since the stability boundary of the delay system is approached from below by the approximate system, the real parts of the corresponding complex conjugate pairs show somewhat larger deviation.

This means that in case of unstable cutting operation when the tool may lose contact with the surface of the workpiece, the large-amplitude oscillations can be represented in a three-dimensional phase space. The corresponding eigenvector of the real root of Eq. (6) defines a one-dimensional stable subspace of \mathbb{R}^3 and the eigenvectors belonging to the complex conjugate pair span an unstable two-dimensional subspace of \mathbb{R}^3 . So the trajectory starts spiralling outwards till it meets the switching surface $h = 0$, then it suddenly jumps down to a two-dimensional subspace spanned by the corresponding eigenvectors of Eq. (5) for $h \leq 0$. Since this subspace is stable, the tool gets back to cutting after a while, that is, the switching surface is crossed again (see Fig. 3) and this process is repeated again and again.

2.3 Bifurcation Analysis

As it was mentioned in Sect. 2.2, the stability of the system is frequently given as a function of the chip width w and the spindle speed Ω . To perform the bifurcation analysis of the system, a certain value of the spindle speed Ω is fixed and the effect of

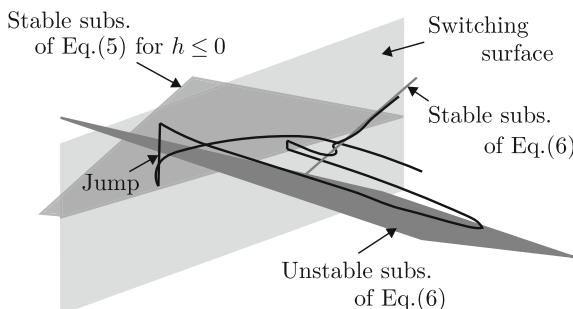


Fig. 3 Three-dimensional phase space where the motion of the cutting tool is illustrated

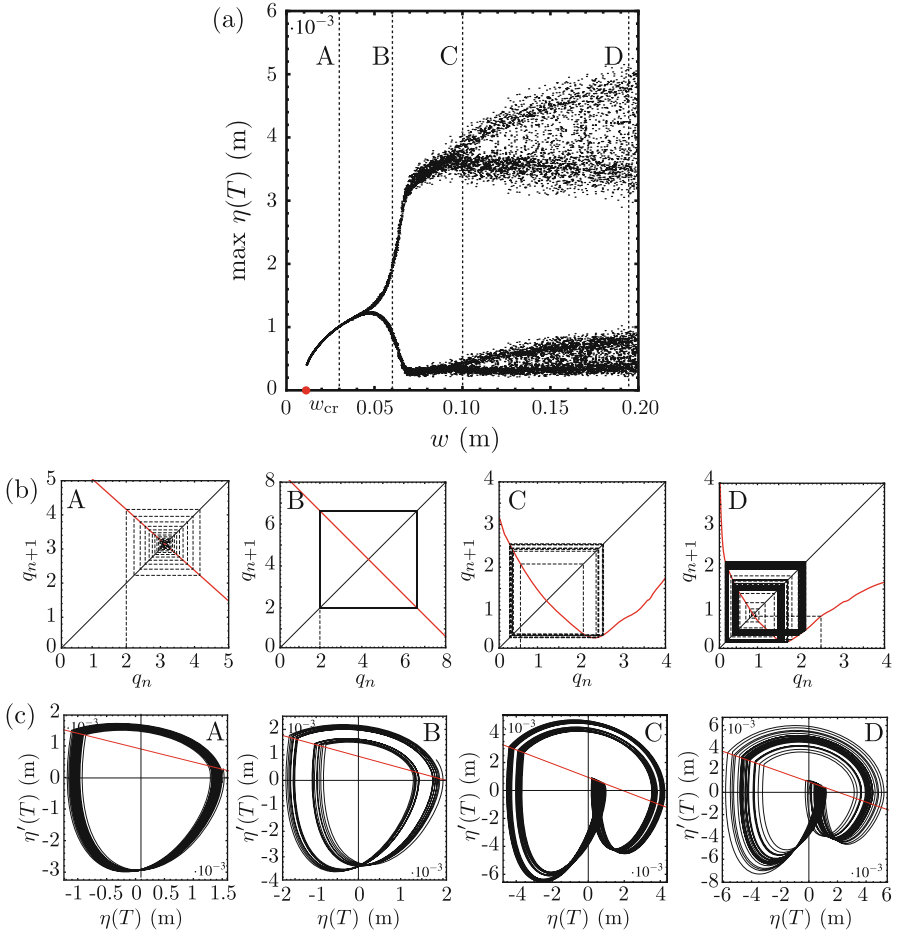


Fig. 4 Panel (a) shows the bifurcation diagram calculated by numerical integration of the approximated non-smooth system. Panel (b) depicts Lorenz maps corresponding to the given sections and panel (c) shows the corresponding trajectories in the phase space where the switching function is denoted by the red line

the variation of the chip width w on the global dynamics of the system is observed. The bifurcation diagram is shown in Fig. 4a where w_{cr} means the bifurcation point that corresponds to the stability boundary at $\Omega = 3300$ rad/s (see Fig. 2a).

As long as the cutting process is stable, that is, the technological parameters are chosen from the stable parameter region $w < w_{cr}$ shown in Fig. 2a, no vibrations arise. As the bifurcation point w_{cr} (stability boundary) is approached, large-amplitude oscillations occur. The tool may lose contact with the surface at $w_{cr} = 0.01$ m (see the bifurcation diagram of Fig. 4a) and starts the chattering motion with amplitude at P as it was observed and proved by measurements shown in [2]. These vibrations can highly affect the quality of the surface of the

workpiece by leaving a wavy pattern behind. Since linear cutting force characteristic is considered, there is a sudden jump in the amplitude at w_{cr} without any additional transition such as subcritical Hopf-bifurcation in [2, 4]. By increasing the chip width w , stable periodic solution occurs, which continues to chaotic motion through the sequence of period-doubling bifurcations (see Fig. 4b, c).

Since the attractor is very flat in the direction of the stable subspace of Eq. (6) (see Fig. 3), the so-called Lorenz map can be constructed with one-dimensional projection. Based on this one-dimensional mapping, the different periodic attractors can be also identified as shown in Fig. 4b. At section A, period-1 window exists that bifurcates at around $w = 0.04$ m. Section B and C depict further periodic windows, a period-2 solution and a period-4 solution. As the bifurcation parameter w increases, chaotic motion can also be identified by using the Lorenz map (see the cobweb diagrams at section D in Fig. 4b). The corresponding state space trajectories are projected to the (η, η') plane and shown in Fig. 4c.

3 Conclusion

This paper deals with the approximated dynamics of chatter in turning processes. The problem can be described by a one degree-of-freedom damped oscillator that models the motion of the cutting tool. The tool is excited by the cutting force that also introduces the so-called surface regeneration effect. So, the cutting tool meets the surface that was formed in the past. In case of unstable cutting, because of the waviness of the surface of the workpiece, it can happen that the tool loses contact with the surface and moves as a free damped oscillator. This phenomenon introduces non-smoothness in the governing delay equations.

To achieve dimensional reduction, Taylor expansion has been used with respect to the time delay τ . This allows us to investigate the dynamical model in a three-dimensional phase space. By using the so-called Lorenz map, periodic windows can be identified, which leads to chaotic motion by increasing the bifurcation parameter.

The results showed qualitative correspondence to the global dynamical behaviour of the delay system and the measurements [2, 4].

Acknowledgements The research leading to these results has received funding from the European Research Council under the European Unions Seventh Framework Program (FP/2007–2013)/ERC Advanced Grant Agreement No. 340889.

References

1. Stepan, G.: Retarded Dynamical Systems: Stability & Characteristic Functions. Longman Scientific & Technical, New York (1989)
2. Shi, H., Tobias, S.: Theory of finite-amplitude machine-tool instability. Int. J. Mach. Tools Manuf. **24**(1), 45–69 (1984). [https://doi.org/10.1016/0020-7357\(84\)90045-3](https://doi.org/10.1016/0020-7357(84)90045-3)

3. Stepan, G., Kalmar-Nagy, T.: Nonlinear regenerative machine tool vibrations. In: Paper No. DETC97/VIB-4021. ASME Design Engineering Technical Conferences, Sacramento (1997)
4. Dombovari, Z., Barton, D.A.W., Wilson, R.E., Stepan, G.: On the global dynamics of chatter in the orthogonal cutting model. *Int. J. Non-Linear Mech.* **46**(1), 330–338 (2011). <https://doi.org/10.1016/j.ijnonlinmec.2010.09.016>
5. Taylor, F.W.: On the art of cutting metals. *Trans. Am. Soc. Mech. Eng.* **28**, 31350 (1907)
6. Kienzle, O.: Spezifische schnittkrafte bei der metallbearbeitung. *Werkstattstechnik und Maschinenbau* **47**, 224225 (1957)
7. Altintas, Y.: Manufacturing Automation. Cambridge University Press, New York (2012)
8. Insperger, T.: On the approximation of delayed systems by Taylor series expansion. *J. Comput. Nonlinear Dyn.* **10**, 024503 (2015)
9. Engelborghs, K., Luzyanina, T., Samaey, G.: DDE-Biftool v.2.00: a Matlab package for bifurcation analysis of delay differential equations. Technical Report TW330, Department of Computer Science 10, 024503 (2001)

Chaotic Dynamics in Spinning Shafts with Non-constant Rotating Speed Described by Variant Lyapunov Exponents



Fotios Georgiades 

Abstract The dynamics of spinning shafts with nonconstant rotating speed is described by a nonlinear system that under certain conditions might exhibit also chaotic behavior. In this chapter, chaotic dynamics of the spinning shaft is examined. Initially, the trajectories in phase space around the equilibrium manifolds are determined. Then by choosing a set of initial conditions, nearby to an equilibrium, corresponding to eigenvalues of the Jacobian with a nonzero real part, identification of chaos is examined. Approximations of the trajectory, with the linearization curves around the equilibria, are defined and they are good in a region very close to the associated equilibrium point. It is shown that the eigenvalues, as Lyapunov exponent indicators, are not parameter dependent but state dependent. The eigenvalues of the linearized system within an orbit are varying from positive to zero; therefore, the Lyapunov exponent is not defined through this limit as an explicit number but variant. The existence of eigenvalues with positive real parts in certain parts of the orbit is an indication of chaos since it shows a divergence of nearby orbits. One orbit starting from an initial condition which corresponds to eigenvalues with positive real part is crossing the threshold and pass to points that the eigenvalues with zero real parts; therefore, this “threshold” is not discriminating chaotic with regular regions as expected. The variant positive Lyapunov exponents have been examined also with numerical investigations, and it is an indication of chaos. The Poincare section indicates irregular motion and the approximated information entropy is relatively high, and both are indicating chaos. It should be highlighted that this is a mechanical system with variant real parts of eigenvalues as Lyapunov exponents within one orbit, and the threshold is insufficient to distinguish chaotic from regular regions. Further work is needed to determine the chaotic regions of the spinning shaft. Further developments in the mathematics of nonlinear dynamical systems associated with the equilibrium manifolds are needed to examine the significance of variant Lyapunov exponents for this kind of systems. Also, the necessity to

F. Georgiades (✉)

School of Engineering, College of Science, University of Lincoln, Lincoln, UK

e-mail: fgeorgiadis@lincoln.ac.uk

reexamine the validity of existing algorithms and the development of new ones for the determination of variant Lyapunov exponents become evident.

Keywords Variant Lyapunov exponent · Chaos · Spinning shaft

1 Introduction

A number of articles have focused on dynamics of rotating structures with constant rotating speed, but the examination of dynamics of rotating structures with a non-constant rotating speed which occurs during spin-up/down operation is very limited [1–5]. In Ref. [4], the equations of motion of a spinning shaft as Euler–Bernoulli isotropic beam has been derived, and dynamic analysis is performed. This model has a similar form with the one obtained in Ref. [3] about rotating blades. In Ref. [5] the equilibrium manifolds (EMs) have been determined with their associated normal modes, and stability is examined. Also, there are a vast number of articles examining chaotic dynamics near specific equilibrium points, but articles relevant to equilibrium manifolds with the examination of points that the linearized solution is changing nature with state space-dependent eigenvalues are very limited, and few relevant comments can be found in Ref. [6].

This chapter is a continuation of the work done in Ref. [5], focused on chaotic motions in the nonlinear dynamics of the spinning shaft, using typical technique applied in nonlinear dynamics which is the linearization around EM. First, the trajectories arising from linearization around some EMs are determined, and second, using direct numerical integration, the validity of the solutions with the associated eigenvalues is examined. Also using numerical methods, the notion of variant Lyapunov exponent and the chaotic behavior in the dynamics of the spinning shaft are examined by means of the determination of Poincare section, the Lyapunov exponents (LE), and the approximated information entropy for a specific set of initial conditions (ICs).

2 Trajectories Around Equilibrium Manifolds

A spinning shaft (with length L , internal D_i and external diameter D_o) with a non-constant rotating speed made of isotropic material (with density ρ , Young's and Shear modulus being E and G , respectively) modeled as Euler–Bernoulli beam is considered. The equations of motion describing the dynamics are given in Refs [4] and [5] by neglecting the equation of rigid body angular position, then a restricted system arises. The restricted system does not correspond to the specific energy function; therefore, even if a linear counterpart of the restricted system exists, the examination of chaotic orbits through Melnikov theory would be rather complicated [7–9]. So, in this chapter, as the first investigation of chaotic orbits on the restricted

system, linearization through perturbations around EM and examination of the associated real parts of the eigenvalues as indicators of LE is used.

Herein the analysis will be restricted around the following EM:

$$y_0^{(1)} = (y_{0,1}, y_{0,2}, y_{0,3}, y_{0,4}, y_{0,5}, y_{0,6}, y_{0,7}) = (0, 0, 0, \dot{\theta}_0, 0, 0, 0) \quad \text{with } \dot{\theta}_0 \in \mathbb{R} \quad (1)$$

and

$$y_0^{(3)} = (y_{0,1}, y_{0,2}, y_{0,3}, y_{0,4}, y_{0,5}, y_{0,6}, y_{0,7}) = (0, 0, q_{0,\phi}, \pm\omega_T, 0, 0, 0) \quad \text{with } q_{0,\phi} \in \mathbb{R} \quad (2)$$

namely first and third EM as mentioned in Ref. [5], whereas y_1 , y_2 , and y_3 , are the modal displacements in lateral bending motions and torsion, respectively, y_4 is the rigid body angular velocity, and the rest are the associated velocities of the modal displacements in the same order. Considering ξ_i (ζ_i) perturbations for each generalized i -coordinate on the equilibriums for the first EM (third EM) and then after linearization, the system will be examined in the region of phase space that is defined by rigid body angular velocity of $\dot{\theta}_0 \in (\omega_b \sqrt{1-M}, \frac{\omega_b(1-M)}{\sqrt{-M}})$. The constants are given by

$$m = \pi \rho \left(\frac{D_o^2 - D_i^2}{4} \right), \quad I_1 = \rho I = \rho \pi \left(\frac{D_o^4 - D_i^4}{64} \right), \quad \omega_b = \sqrt{\frac{\pi^4 EI}{L^2 \pi^2 I_1 + L^4 m}}, \quad (3a-c)$$

$$\omega_T = \frac{\pi}{2L} \sqrt{\frac{G}{\rho}}, \quad F = \frac{2}{\pi} \sqrt{2I_1 L}, \quad M = -\frac{I_1 \pi^2}{m L^2}. \quad (4a-c)$$

The linearization around the first EM $(y_0^{(1)})$ leads to two fully decoupled systems of differential equations, one describing the two lateral bending motions and the other one describing the coupled torsional with rigid body motions which will be considered herein [5]. The linearization around the third EM $(y_0^{(3)})$ [5] leads to three systems of differential equations, one describing the two lateral bending motions fully decoupled from the equations that are describing the torsional with rigid body motions which will be considered herein [5].

The eigenvalues of the linearized system around the first EM are given by [5]

$$\{\lambda_j\} = \left[-\sqrt{\frac{I_1 L (\dot{\theta}_0^2 - \omega_T^2)}{(I_1 L - F^2)}}, 0, \sqrt{\frac{I_1 L (\dot{\theta}_0^2 - \omega_T^2)}{(I_1 L - F^2)}} \right]^T, \quad j = 1, 2, 3 \quad (5)$$

which are real in case of $\dot{\theta}_0 > \omega_T$. Therefore, based on the existing theory, there is a “threshold” of $\dot{\theta}_0 = \omega_T$, whereas for higher angular velocities, the LE from zero becomes positive [9]. The existence of the chaotic region for $\dot{\theta}_0 > \omega_T$ and the transition to chaos around the region $\dot{\theta}_0 = \omega_T$ will be examined. For $\dot{\theta}_0 = \omega_T$, the first EM is approaching the third EM which justifies that the examination must be performed considering both EM. The eigenvalues of the linearized system around third EM are purely imaginary or zero and they are given by [5]

$$\{\mu_j\} = \left[-i \frac{2\omega_T y_{0,3}}{\sqrt{(I_1 L - F^2 + y_{0,3}^2)}}, 0, i \frac{2\omega_T y_{0,3}}{\sqrt{(I_1 L - F^2 + y_{0,3}^2)}} \right]^T, \quad j = 1, 2, 3. \quad (6)$$

The systems of differential equations which describe the motions around the first and third EM will be used for the projection to the phase space by parametrizing time with respect to the perturbation in torsional position (ξ_3 and ζ_3 , respectively) [5].

Using the linearized equations arising with ξ_i perturbations around the first EM lead to [5]

$$\frac{d\xi_4}{d\xi_3} = \frac{F(\dot{\theta}_0^2 - \omega_T^2)\xi_3}{(I_1 L - F^2)\xi_7}, \quad (7)$$

$$\frac{d\xi_7}{d\xi_3} = \frac{I_1 L (\dot{\theta}_0^2 - \omega_T^2)\xi_3}{(I_1 L - F^2)\xi_7} \iff \xi_7^2 - \frac{I_1 L (\dot{\theta}_0^2 - \omega_T^2)}{(I_1 L - F^2)}\xi_3^2 = A, \quad (8)$$

neglecting $\xi_7 \neq 0$ which corresponds to the local extrema of perturbation of torsional position (ξ_3), then in phase space, the curves are given by

$$\xi_7^2 - \frac{I_1 L (\dot{\theta}_0^2 - \omega_T^2)}{(I_1 L - F^2)}\xi_3^2 = A \iff y_7^2 - \frac{I_1 L (\dot{\theta}_0^2 - \omega_T^2)}{(I_1 L - F^2)}y_3^2 = A, \quad (9)$$

where the case of $\dot{\theta}_0 > \omega_T$ corresponds to a family of hyperbolas with center (0,0) in phase space, the case of $\dot{\theta}_0 = \omega_T$ leads to a constant perturbation in torsional velocity (ξ_7), and the last case of $\dot{\theta}_0 < \omega_T$ corresponds to a family of ellipses with center (0,0) in phase space. Using Eq. (9), the constant of integration A can be determined. Rearrangement of Eq. (9) leads to

$$\xi_7 = \pm \sqrt{\frac{I_1 L (\dot{\theta}_0^2 - \omega_T^2)}{(I_1 L - F^2)}\xi_3^2 + A} \iff y_7 = \pm \sqrt{\frac{I_1 L (\dot{\theta}_0^2 - \omega_T^2)}{(I_1 L - F^2)}y_3^2 + A}, \quad (10)$$

Then using Eq. (10) in Eq. (7) and after integration considering original system state space variables lead to,

$$y_4 = \dot{\theta}_0 \pm \frac{F}{I_1 L} \sqrt{\frac{I_1 L (\dot{\theta}_0^2 - \omega_T^2)}{(I_1 L - F^2)} y_3^2 + A + B}, \quad (11)$$

which corresponds to the following families of orbits:

$$\frac{(I_1 L)^2 (y_4 - \dot{\theta}_0 - B)^2}{F^2 A} - \frac{I_1 L (\dot{\theta}_0^2 - \omega_T^2)}{A (I_1 L - F^2)} y_3^2 = 1, \quad (12)$$

where $\dot{\theta}_0 > \omega_T$ corresponds to a family of hyperbolas with center $(\dot{\theta}_0 + B, 0)$, $\dot{\theta}_0 = \omega_T$ leads to a constant rigid body angular velocity (y_4), and finally $\dot{\theta}_0 < \omega_T$ leads to a family of ellipses with center $(\dot{\theta}_0 + B, 0)$ in phase space.

In Ref. [5], the linearized third EM which corresponds to $\dot{\theta}_0 = \omega_T$ is surrounded by periodic orbits; therefore, the constant perturbations in torsional and rigid body angular velocities obtained from Eqs. (10) and (11) respectively are not describing the orbits in this region. In this region of the orbit, a better approximation of the orbits can be obtained from the linearization of the third EM. The orbits associated with the third EM around ζ_i perturbations, by parametrizing time with the perturbation in torsional position (ζ_3) using equations obtained in Ref. [5], are determined. First, the differential equation,

$$\frac{d\zeta_4}{d\zeta_7} = \frac{F\zeta_4 - \zeta_7}{(I_1 L + y_{0,3}^2) \zeta_4 - F\zeta_7} \quad (13)$$

neglecting the points of $(I_1 L + y_{0,3}^2) \zeta_4 \neq F\zeta_7$ which corresponds to the local extrema of perturbation of torsional velocity (ζ_7), is solved to obtain

$$\zeta_4 = \frac{F\zeta_7}{(I_1 L + y_{0,3}^2)} \pm \frac{\sqrt{- (I_1 L - F^2 + y_{0,3}^2) \zeta_7^2 + C}}{(I_1 L + y_{0,3}^2)}. \quad (14)$$

The constant of integration C can be determined using any pair of values in the following rearranged equation:

$$(I_1 L + y_{0,3}^2)^2 \zeta_4^2 + (I_1 L + y_{0,3}^2) \zeta_7^2 - 2(I_1 L + y_{0,3}^2) F\zeta_4\zeta_7 - C = 0, \quad (15)$$

which is a second-degree equation, and it forms an ellipse [10].

The other equation (considering $\zeta_7 \neq 0$) is given by

$$\frac{d\zeta_7}{d\zeta_3} = 2\omega_T y_{0,3} \left(\frac{(I_1 L + y_{0,3}^2)}{(I_1 L - F^2 + y_{0,3}^2)} \frac{\zeta_4}{\zeta_7} - \frac{F}{(I_1 L - F^2 + y_{0,3}^2)} \right) \quad (16)$$

and using (Eq. 14) and direct integration lead to

$$\zeta_3 = \mp \frac{1}{2\omega_T y_{0,3}} \sqrt{- (I_1 L - F^2 + y_{0,3}^2) \zeta_7^2 + C + D} \quad (17)$$

or using state space variables of the original system and rearrangement lead to the following family of curves in phase space:

$$[2\omega_T y_{0,3} (y_3 - y_{0,3} - D)]^2 + (I_1 L - F^2 + y_{0,3}^2) y_7^2 = C, \quad (18)$$

which is an ellipsis centered at $(y_3, y_7) = (y_{0,3} + D, 0)$ [10].

Solving Eq. (18) for perturbation of modal torsional velocity with respect to perturbation of modal torsional position leads

$$\zeta_7 = \pm \sqrt{\frac{C - [2\omega_T y_{0,3} (\zeta_3 - D)]^2}{(I_1 L - F^2 + y_{0,3}^2)}} \iff y_7 = \pm \sqrt{\frac{C - [2\omega_T y_{0,3} (y_3 - y_{0,3} - D)]^2}{(I_1 L - F^2 + y_{0,3}^2)}}, \quad (19)$$

and replacing (Eq. 19) in (Eq. 14) considering state space variables of the original system lead to

$$y_4 = \omega_T \pm \frac{F}{(I_1 L + y_{0,3}^2)} \sqrt{\frac{C - [2\omega_T y_{0,3} (y_3 - y_{0,3} - D)]^2}{(I_1 L - F^2 + y_{0,3}^2)}} \pm \frac{2\omega_T y_{0,3} (y_3 - y_{0,3} - D)}{(I_1 L + y_{0,3}^2)} \quad (20)$$

and if it is written as a second-order equation, it becomes evident that it forms a family of ellipsis with center at $(y_3, y_4) = (y_{0,3} + D, \omega_T)$ [10].

3 Numerical Results and Discussion

A 1-m length shaft with internal and external radii $r_i = 0.028$ m and $r_o = 0.03$ m, respectively, is considered. It is made of stainless steel with density $\rho = 7850$ kg/m³, Young modulus $E = 200$ GPa, shear modulus $G = 76.9$ GPa, and Poisson's ratio $\nu = 0.3$.

The ICs are $(y_1, y_2, y_3, y_4, y_5, y_6, y_7) = (0, 0, 0, 4996.41, 0, 0, 0.1)$ and correspond to a perturbation of the first EM for $y_{0,4} = \dot{\theta}_0 = \omega_T + 80$ rad/s, whereas the trajectory around this point can be approximated by hyperbolas given by Eqs. (9) and (12). The total restricted system has been numerically integrated with time step ($1.5e^{-5}$) for approximated 3997 orbits (approximating average orbital period 0.01251 s). The full manifold superimposed with the plot of the EMs is depicted in Fig. 1a, noting that the lateral bending motions are zero, and therefore in Fig. 1a the total manifold is depicted. In Fig. 1a the four points that the trajectory is approaching the third EM ($\dot{\theta}_0 = \omega_T = 4916.41$ rad/s) are also indicated. The points are defined by the following sets of values: $(y_3, y_4, y_7) = (0.001374, 4916.411021, -2.686653)$ for the first point, $(y_3, y_4, y_7) = (0.006003, 4916.411603, 2.686645)$ for the second point, $(y_3, y_4, y_7) = (-0.001374, 4916.411674, -2.686633)$ for the third point, and $(y_3, y_4, y_7) = (-0.006003, 4916.411329, 2.686636)$ for the fourth point, which are not the singular points of first EM since $y_7 \neq 0$. Around these points, the trajectory can be approximated by ellipsis given by Eqs. (18) and (20).

In Fig. 2, the projection of the trajectory in (y_3, y_4) plane superimposed with the analytical solutions around the ICs (using Eqs. 10 and 11) and around the four points that the trajectory is approaching the third EM (using Eqs. 17 and 20) is depicted.

Examining Fig. 2b becomes evident that the trajectory around the ICs is very well approximated by hyperbolas (Fig. 2b), and the linearized system has real eigenvalues (Eq. 5). When the trajectory is approaching points 2 and 4, the trajectory is very well approximated with ellipses (Fig. 2d, f) which correspond to purely complex eigenvalues given by Eq. (6). In cases that the trajectory is approaching points 1 and 3, the trajectory is approximated in a very small region around them (Fig. 2c, e) with ellipses, again with zero LE.

The definition of Lyapunov exponent for an equilibrium of an autonomous dynamical system is given by [9]

$$\text{LE}_j = \lim_{t \rightarrow \infty} \frac{1}{t} \text{Re}(\sigma_j t), \quad (21)$$

where the real part of σ_j which is the j eigenvalue of the linearized system around the equilibrium is considered, and this limit exists when they are monotonic. In the considered case, the eigenvalues are dependent on states. When the part of the orbit is close to ICs (first EM), then the linearized system has pure real eigenvalues (λ_j), and when part of the orbit nearby the points 1–4 (third EM) is considered, then the eigenvalues (μ_j) are pure complex. Therefore, the real part of the σ_j eigenvalues from the linearized systems approximating the original nonlinear system are varying within one orbit $\sigma_1 \in \left[0, \sqrt{\frac{I_1 L (\dot{\theta}_0^2 - \omega_T^2)}{(I_1 L - F^2)}} \right]$, and the limit of Eq. (21) has no specific value but since the trajectory is approximated well locally with different curves which corresponds to different eigenvalues, it can be claimed that the LE is variant within an orbit. The existence of positive real eigenvalues in some parts of the orbit means nearby orbits at this region are diverging, and it is an indication of chaos.

Examining Fig. 2a on the right-hand side with the indication of the eigenvalues of the first EM and based on the standard stability theory then the point of $\dot{\theta}_0 = \omega_T$,

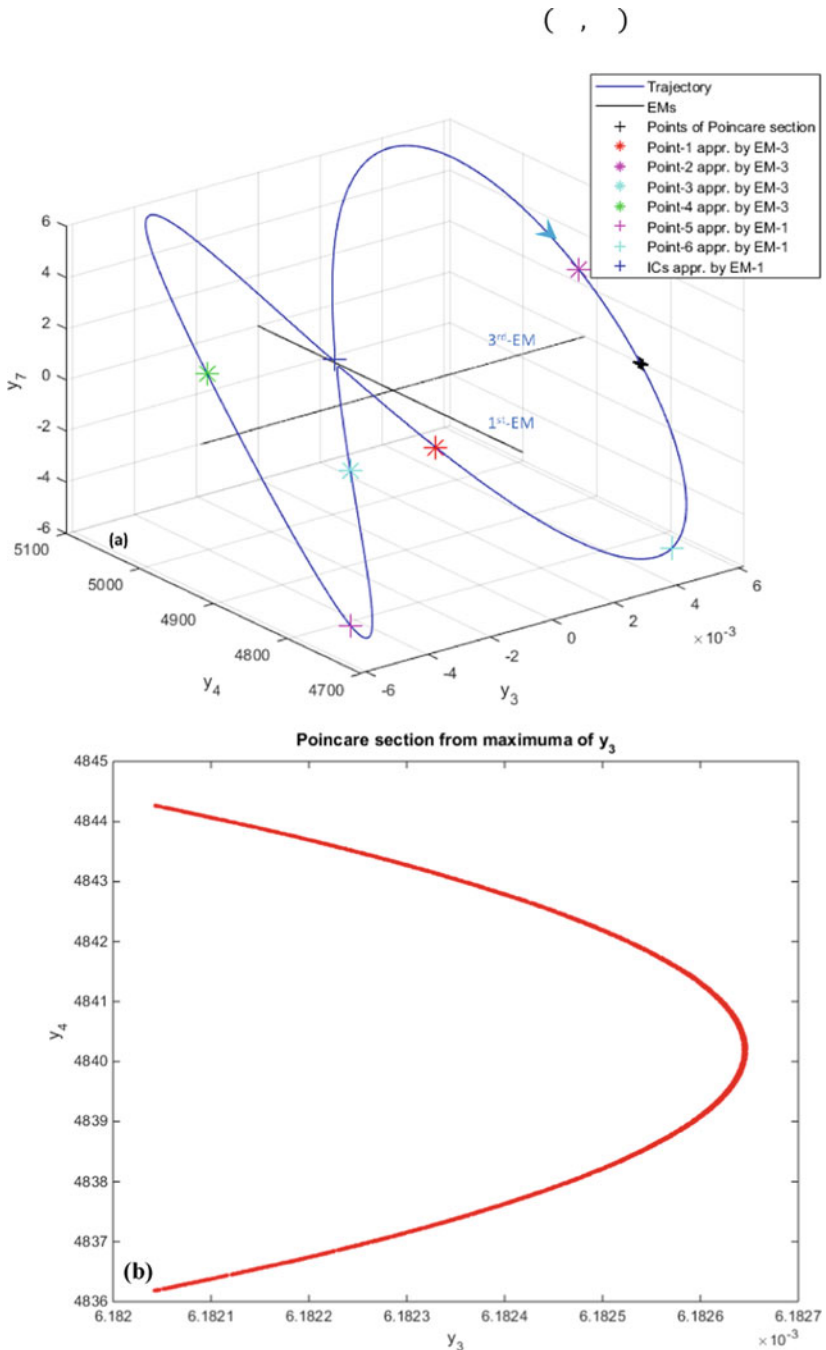


Fig. 1 (a) The total trajectory in phase space superimposed with the EMs. (b) Poincare section with maxima of torsional angle

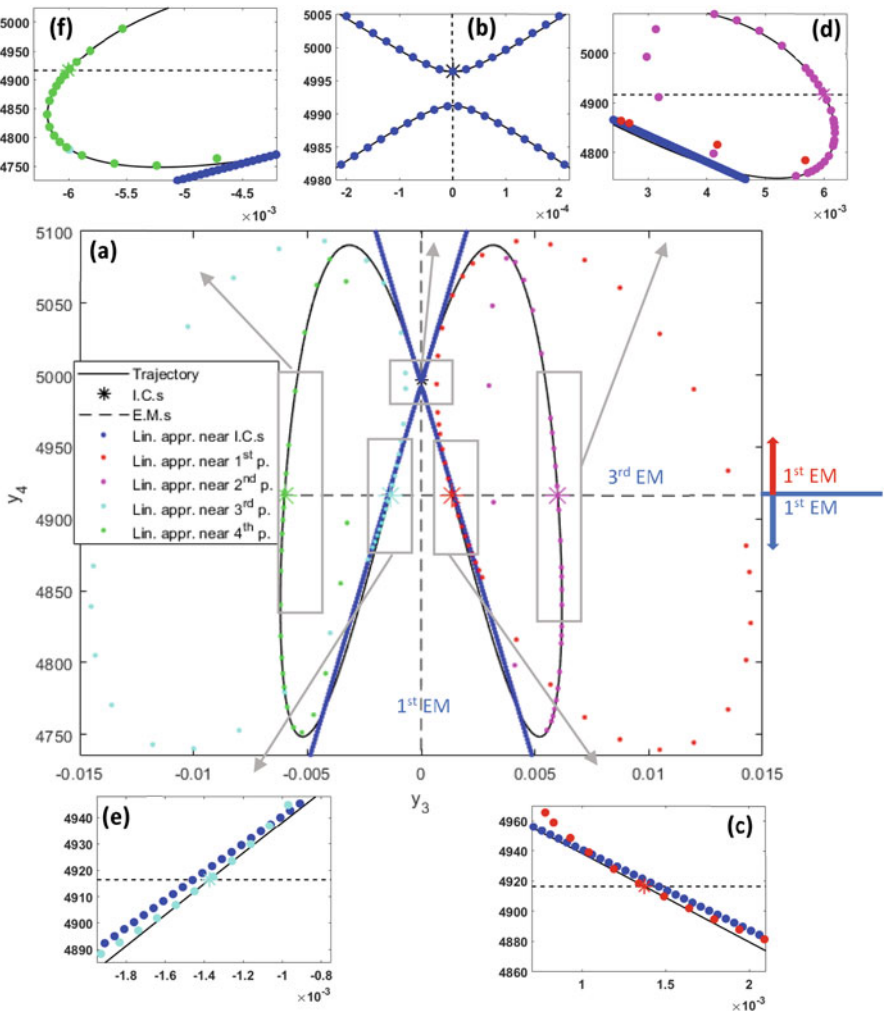


Fig. 2 (a) Projection of the trajectory in (y_3, y_4) plane superimposed with the analytical solutions around ICs and four points, whereas the region of first EM indicated with red arrow (right-hand side) is associated with real nonzero eigenvalues, and the blue arrow indicates the region with pure complex eigenvalues; (b) zoom out near the point of the ICs with eigenvalues $\lambda_1 = 0, \lambda_{2,3} = \pm 2406.6$ (real); (c) zoom out near the first point (red star indication) that the trajectory is approaching the third EM with eigenvalues $\mu_1 = 0, \mu_{2,3} = \pm i890.91$ (imag.); (d) near the second point (magenta star indication) that the trajectory is approaching the third EM with eigenvalues $\mu_1 = 0, \mu_{2,3} = \pm i3631.59$ (imag.); (e) near the third point (green star indication) that the trajectory is approaching the third EM with eigenvalues $\mu_1 = 0, \mu_{2,3} = \pm i890.91$ (imag.); (f) near the fourth point (cyan star indication) that the trajectory is approaching the third EM with eigenvalues $\mu_1 = 0, \mu_{2,3} = \pm i3631.59$ (imag.)

whereas the eigenvalues from purely complex becomes real, can be considered as the “threshold” to discriminate the chaotic ($\dot{\theta}_0 > \omega_T$) with regular regions ($\dot{\theta}_0 < \omega_T$). Herein this is not the case. If the initial conditions are taken from the same trajectory but from the “lower region” ($\dot{\theta}_0 < \omega_T$) whereas the eigenvalues are purely complex, these initial conditions correspond to the regular region, but they follow a chaotic trajectory.

The analysis of the projection of the trajectory to (y_3, y_7) plane superimposed with the analytical solutions provided similar results.

In Fig. 1b the Poincare section obtained with zero crossings of torsional velocity (y_7) restricted to the maxima of torsional angle (y_3) is depicted. The **absence of periodic and quasiperiodic motion** due to the existence of **irregular points in the Poincare section** is evident.

The numerical determination of the LE has been done by three methods, in first one using direct integration of the system, the Lyapunov spectrum with the re-orthonormalization Gram-Schmidt (G-S) method is determined [11]. In the other two methods only the maximum LE is determined, and in the second, the direct integration of the system with rescaling to the neighboring trajectory as described by Seydel in Ref. [12] is used, and in the last one, the maximum LE is obtained from data series after direct numerical integration of the system using a Matlab tool [13]. The first two methods are well explained in the literature [11, 12], and they are well known so it will not be explained further on. Both the methods provide reliable results as long as the elementary volume expansion or contraction (an indication of LE) in the considered direction of the dynamical system is monotonic with time [15]. In Ref. [15], in the implementation of the different numerical schemes, there is an emphasis on how to implement the different schemes to avoid the non-monotonicity in time of the used estimators.

In the third method, a Matlab tool to determine the LE has been used [13]. Using the data series, the lag (estimated from the same tool), and the embedded dimension of the phase space as input, then the analysis can be performed with a tool figure to obtain the largest LE. It is based on the practical method developed in Ref. [16], and the algorithm used for the determination is explained very well in Ref. [13].

Briefly, the method and the algorithm are based on curve fitting of the divergence of nearby points (Y_n and Y_{n^*}) [13]

$$\text{LDIV} = \ln \frac{\|Y_{n+K} - Y_{n^*+K}\|}{\|Y_n - Y_{n^*}\|} \quad (22)$$

by considering the values of them at several time instants (K) belonging to a certain expansion range $[K_{\min}, K_{\max}]$, with a plot of the average divergence, then the LE estimation is done through a curve fitting in selected expansion ranges, which is based on the following formula:

$$\text{LE}(n) = \frac{1}{K_{\max} + K_{\min} + 1} \sum_{K=K_{\min}}^{K_{\max}} \frac{1}{K \cdot dt} \ln \frac{\|Y_{n+K} - Y_{n^*+K}\|}{\|Y_n - Y_{n^*}\|}. \quad (23)$$

In case that the LE is variant, for different time instants (K), the logarithm in Eqs. (22) and (23) can have a positive or negative value (slope), since the ratio of the initial difference (denominator) with the considered time instant difference (nominator) throughout the expansion range is decreasing or increasing. Also this method is developed for monotonic values of divergence.

All the codes for LE determination have been tested successfully to obtain the benchmark values for many systems indicated in Ref. [14].

The determination of the LE has been done using approximately 1500 orbits for the first two methods and approximately 1000 orbits for the last one. In the presenting results for the first method, $1.25e^{-3}$ s time step has been used, in the second $4.17e^{-5}$ s with initial perturbation $1e^{-9}$ (limited only to torsional velocity), and in the third $2.502e^{-5}$ s.

The LE spectrum obtained using the G-S method is summarized in Table 1, where the largest value is positive. The accuracy of the G-S method is dependent on the number of orthonormalizations and the choice of the finite-time step for each orthonormalization. In Hamiltonian systems, the validity of LE spectrum can be checked by the sum of LE which should be equal to zero, and this is the case for the spectrum in Table 1. Therefore, under the monotonic assumption of the elementary volume expansion or contraction and based on the current knowledge, the selected time step and number of orbits (for a specific time step is an indicator of the number of orthonormalizations) are leading to “reliable” results.

Table 2 presents a positive value of the maximum LE using the second method. According to Refs [12, 14], based on the reported experiments, in the second method of LE estimation, in case of monotonic divergence of nearby trajectories and if the perturbation is very small ($1e^{-9}$ in this case), the maximum LE is determined independently of the choice of time steps.

Also, in the plots of identifying the plateaus of the LE values in first and second methods, there are small fluctuations within an orbit.

Matlab tool in the third method provides the opportunity to examine whether there are enough data points by reconstructing the phase space, which has been done successfully. Figure 3 depicts the plot as a Matlab tool to determine the slopes of the divergence of nearby points with respect to the expansion steps which defines the maximum LE using this method. In Fig. 3, there are four different slopes at different expansion ranges based on the divergence of nearby points throughout the

Table 1 Lyapunov spectrum using G-S method

\ln	1	2	3	4	5	6	7
LE_n (bits/orbit)	87.6	3.9	1.9	0	-1.9	-3.9	-87.6

Table 2 Maximum LE (bits/orbit) using the three different methods

	G-S	Seydel [12]	Range 1 (35–96) [13]	Range 2 (157–224)	Range 3 (275–342)	Range 4 (413–474)
LE	87.6	13.7	-8.1	11.3	-9.8	10.3

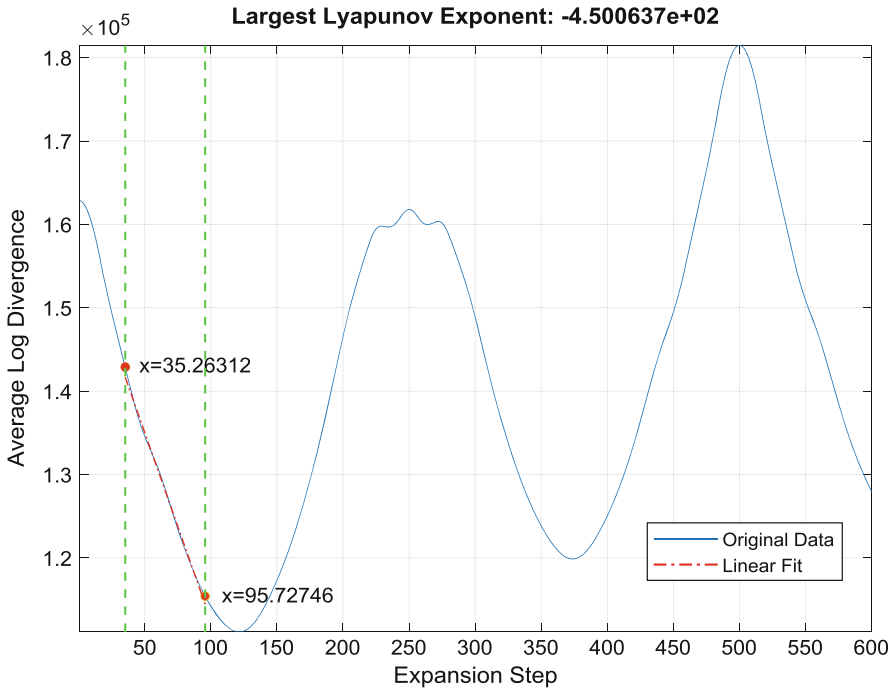


Fig. 3 Matlab tool (third method), divergence of nearby points with respect to expansion steps

considered total expansion range (600). The estimated slopes are summarized in Table 2, and they have positive and negative values.

The values of the largest LE obtained from the three methods are summarized in Table 2 which are different. In the first two methods, the maximum LE is positive but different to each other because the two methods use different ways to obtain a representative value of LE throughout the total range since the LE is variant within an orbit.

In the third method, depending on the selected expansion range (time instants), the LE have positive and negative values. The variant Lyapunov exponent arising from the theoretical analysis is also justified with this third method, whereas the different ranges correspond to different time instants that the exponent of the divergence of the orbits varies from negative to positive.

The Matlab tool from Ref. [13] applied in the data series estimates that the approximated information entropy is 0.155. Therefore, the **irregularity is high**, and the **information loss is significant which is an indication of chaos**.

4 Conclusions

In this chapter, chaotic dynamics of a spinning shaft with non-constant rotating speed is examined through linearization around the EM. The analytical approximation of the orbit is approximated well, only locally, nearby the different equilibria, and, in that respect, it is shown that there are positive and zero eigenvalues which are indicative of the Lyapunov exponent. Although the limit does not exist, the Lyapunov exponent can be considered as variant within one orbit. Also, it is shown that the in-principle threshold of the change of nature of the eigenvalues whereas from purely complex become real which it should be expected to separate chaotic with regular regions in a given orbit is not valid. Therefore, a more advanced theory is needed to identify the thresholds of the chaotic motion in case of the spinning shaft. Examination of the Poincare section indicates irregular motion. The LE has been determined numerically with three methods, and they are very different. In the first two cases, they are positive. In the third method, they are clearly state-dependent with the largest being positive which certifies the variant theoretical Lyapunov exponent. Also, the approximated information entropy is relatively high which is an indication of chaos. Since the Lyapunov exponent is varying within an orbit the methods of calculating *LE* that are relying on monotonicity and they are based on the sampling of state-space variables values at certain time instants they cannot provide reliable results. This work is a first attempt to identify chaotic motions in spinning shafts using analytical and numerical methods, but further work is needed. It highlights the need for further development in the mathematics of nonlinear dynamical systems associated with EMs and the significance of the variant Lyapunov exponent examination for this kind of system. Also, generate the need to reexamine the cases of the validity of algorithms to estimate variant LE within an orbit, since most of them are based on the constant value assumption; therefore, there is a need of the development of new ones considering variant LE.

5 Acknowledgments

I would like to thank and express my gratitude to Prof. Yuri V. Mikhlin for providing me valuable feedback and to Prof. Giuseppe Rega for his valuable comments, both on a draft manuscript.

I would like to thank and express my gratitude to the Organization Committee of fifth Summer School of Nonlinear Dynamical Systems (1992) at University of Crete (Greece) and especially to Prof. Tassos Bountis and Prof. Spyros Pnevmatikos that they accepted my participation, although I was still an undergraduate student in engineering. Since then, I followed several of them in Greece, and the knowledge that I gained, thanks to the instructors, was my induction to chaos which is substantial to write this chapter.

References

1. Natsiavas, S.: On the dynamics of rings rotating with variable spin speed. *Nonlinear Dyn.* **7**, 345–363 (1995)
2. Warminski, J., Balthasar, J.M., Brasil, R.M.L.R.F.: Vibrations of a non-ideal parametrically and self-excited model. *J. Sound Vib.* **245**, 363–374 (2001)
3. Georgiades, F., Latalski, J., Warminski, J.: Equations of motion of rotating composite beam with a non-constant rotation speed and an arbitrary preset angle. *Meccanica*. **49**, 1833–1858 (2014). <https://doi.org/10.1007/s11012-014-9926-9>
4. Georgiades, F.: Nonlinear dynamics of a spinning shaft with non-constant rotating speed. *Nonlinear Dyn.* **93**, 89–118 (2018). <https://doi.org/10.1007/s11071-017-3888-0>
5. Georgiades, F.: Equilibrium points with their associated normal modes describing nonlinear dynamics of a spinning shaft with non-constant rotating speed. *J. Vibr. Test. Syst. Dyn.* **2**, 327–373 (2018)
6. Liebscher, S.: *Bifurcation Without Parameters*. Springer, Geneva (2015)
7. Guckenheimer, J., Holmes, P.: *Nonlinear Oscillations, Dynamical Systems, and Bifurcations of Vector Fields*. Springer, New York (1983)
8. Wiggins, S.: *Introduction to Applied Nonlinear Dynamical Systems and Chaos*. Springer, New York (2003)
9. Nayfeh, A.H., Balachadran, B.: *Applied Nonlinear Dynamics*. Wiley-VCH, Weinheim (2004)
10. Vittal, P.R.: *Analytical Geometry 2D and 3D*. Dorling Kindersley (India) Pvt Ltd, Chennai (2013)
11. Benettin, G., Galgani, L., Giorgilli, A., Strelcyn, J.-M.: Lyapunov characteristic exponents for smooth dynamical systems and for hamiltonian system; a method for computing all of them. *Meccanica*. **15**, 21–30 (1980)
12. Seydel, R.: *Practical Bifurcation and Stability Analysis*. Springer, New York (2010)
13. Mathworks, Matlab R2018b, Predictive maintenance toolbox, <http://www.mathworks.com/products/> (2018)
14. Wolf, A., Swift, J.B., Swinney, H.L., Vastano, J.A.: Determining Lyapunov exponents from a time series. *Phys. D*. **16**, 285–387 (1985)
15. Geist, K., Parlitz, U., Lauternborn, W.: Comparison of different methods for computing Lyapunov exponents. *Prog. Theor. Phys.* **83**, 875–893 (1990)
16. Rosenstein, M.T., Collins, J.J., De Luca, C.J.: A practical method for calculating largest Lyapunov exponents from small data sets. *Phys. D*. **65**, 117–134 (1993)

Post-Resonance Backward Whirl in a Jeffcott Rotor with a Breathing Crack Model



Mohammad A. Al Shudeifat and C. Nataraj

Abstract Propagation of fatigue cracks is one of the major causes for catastrophic damage in rotor systems. Such cracks have an unusual property in that they can open and close continuously and synchronously with the shaft rotational speed which was termed as a breathing mechanism. This problem has not been adequately analyzed from nonlinear and rotor dynamic perspectives in the literature in spite of a large number of papers that have appeared over the last two decades. Separately from this, backward whirl (where the precession is opposite to the rotational direction) can be dangerous and can lead to catastrophic failures in rotor systems. Interestingly, a new backward whirl phenomenon at start-up and coast down operations in cracked rotor systems with open crack models was observed in a recent publication. This phenomenon has been numerically and experimentally verified with an open crack to directly appear after the passage through the critical speed. Building on these recent findings, there is an imperative need to further investigate this phenomenon in rotor systems associated with open and breathing crack models from nonlinear and rotor dynamic perspectives. For start-up and coast down operations at constant angular acceleration, the model of the cracked rotor system with open or breathing crack models becomes a linear time-varying (LTV) system. Here, we also numerically verify the existence of this new backward whirl (BW) phenomenon in a cracked rotor with a breathing crack model via numerical simulation. Results indicated that a wide zone of BW rotational speeds is observable after the passage through the critical speed due to appearance of the breathing crack in the considered Jeffcott rotor system.

Keywords Cracked rotor · Backward whirl · Jeffcott rotor

M. A. Al Shudeifat

Department of Aerospace Engineering, Khalifa University,
Abu Dhabi, UAE

e-mail: mohd.shudeifat@ku.ac.ae

C. Nataraj

Department of Mechanical Engineering, Villanova University, Villanova, PA, USA

1 Introduction

Several of real-life rotor systems are usually exposed to recurrent passage through critical forward whirl speeds during start-up and coast down operations that are associated with constant angular acceleration. Therefore, as cracks propagate, it is important to diagnose their presence and their effect on the backward whirl excitation at start-up and coast down operations to be able to shut down the machinery before catastrophic failures occur.

In most of the published literature, it has been believed that the backward whirl phenomena might be only excited before passing through critical forward whirl speeds at elevated vibration amplitudes. This assumption is usually based on the related Campbell diagrams of such rotor systems in which the frequency curves are obtained at discrete constant angular velocities of the system (i.e., steady-state operation at zero angular acceleration).

Few studies in the literature have considered the effect of the angular acceleration on rotor systems response during the passage through the critical rotational speeds. In Ref. [1], the equations of motion which incorporate the angular acceleration effect and their analytical solutions were obtained for slender rotating shafts. Accordingly, it was analytically verified that the critical speeds were higher for the accelerating shaft and lower for the decelerating shaft compared with those obtained at constant angular velocity of similar systems. Moreover, the analytical solution of an accelerating shaft at start-up operations was obtained in Ref. [2] where the response was found incorporating different frequency components. In another series of publications [3–6], the angular acceleration effect on the whirl response of the considered systems was also investigated. However, in all of these available studies, the effect of the angular acceleration on capturing the backward whirl response in intact and cracked rotor systems was not investigated. The Jeffcott rotor model has been extensively used in the literature for studying the underlying nonlinear dynamics in the whirl response of cracked rotor systems. For example, in Refs [7–9], the appearance of the backward whirl phenomena in nonlinear cracked rotor systems using the simple two-degree-of-freedom Jeffcott model has been studied.

In a recent publication in Ref. [10], new backward whirl phenomena associated with angular acceleration of rotor systems has been found to exist immediately after passing through the critical forward whirl speed for start-up and coast down operations of cracked rotors with an open crack model. These findings contradict with Campbell diagram analysis of such systems since incorporating the angular acceleration in modeling and equations of motions converts these systems into linear time-varying systems (LTVs) which are considered as nonlinear in nature. Accordingly, this work is to further explore this new backward whirl phenomena in a cracked Jeffcott rotor system with a breathing crack model. The combined effect of the angular acceleration during start-up operations and the unbalance force vector orientation of the considered cracked rotor system on the new backward whirl excitation is investigated here.

2 Mathematical Model

2.1 Jeffcott Rotor Model

The simple two-degree-of-freedom Jeffcott rotor disk model in Fig. 1 with the physical parameters in Table 1 is considered here. In this model, a rigid disk of mass m is attached to a simply supported massless shaft.

$$\mathbf{M}\ddot{\mathbf{q}} + \mathbf{C}\dot{\mathbf{q}} + \mathbf{K}_C(t)\mathbf{q} = \mathbf{F}_u(t) + \mathbf{F}_g \quad (1)$$

where $\mathbf{q} = [u(t) \ v(t)]^T$ is the vector of the horizontal $u(t)$ and vertical $v(t)$ oscillations of the center of the rigid disk with respect to the fixed X and Y axes, respectively, \mathbf{F}_u is the unbalance force excitation vector, and \mathbf{F}_g is the gravity force vector. The 2×2 matrices of the mass \mathbf{M} and the time-varying stiffness $\mathbf{K}_C(t)$ are given as

$$\mathbf{M} = \begin{bmatrix} m & 0 \\ 0 & m \end{bmatrix}, \quad \mathbf{K}_C(t) = \frac{48E}{L^3} \begin{bmatrix} I_Y(t) & I_{XY}(t) \\ I_{YX}(t) & I_X(t) \end{bmatrix} \quad (2)$$

where $I_X(t)$, $I_Y(t)$, and $I_{XY}(t)$ are the time-varying moments of area of the cracked cross section which are computed according to the new breathing functions in Refs [11, 12] by replacing Ωt in these functions by the angle of rotation $\theta(t)$ of the accelerated rotor system where $\theta(t) = 0.5\alpha t^2$ and α is the constant angular acceleration of the shaft. Note that they can be complicated functions of time; note also that if the crack opening is modeled as depending on the local flexural curvature, the stiffness becomes nonlinear. The damping matrix is assumed to be proportional to the mass and stiffness matrices of the intact shaft as $\mathbf{C} = \gamma\mathbf{M} + \zeta\mathbf{K}$, where $\gamma = 0.01 \text{ s}^{-1}$ and $\zeta = 0.001 \text{ s}$. The components of the unbalance force

Fig. 1 The considered rotor disk system

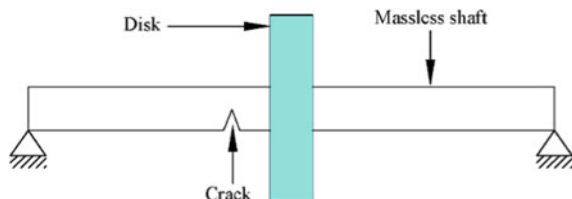


Table 1 Physical parameters of the theoretical model

Description	Value
Length of the rotor, L	700 mm
Radius of the rotor, R	9.5 mm
Density of rotor, ρ	7850 kg/m ³
Modulus of elasticity, E	$2.1 \times 10^{11} \text{ N/m}^2$
me	$1 \times 10^{-4} \text{ kg.m}$

excitation vector in the fixed X and Y axes at the angular velocity of $\Omega(t) = \alpha t$ are written, respectively, as [13]

$$\begin{aligned} f_X(t) &= me\alpha^2 t^2 \cos(\theta(t)) + me\alpha \sin(\theta(t)) \\ f_Y(t) &= me\alpha^2 t^2 \sin(\theta(t)) - me\alpha \sin(\theta(t)) \end{aligned} \quad (3)$$

where e is the eccentricity of the unbalance mass in Jeffcott rotor. Since $\alpha \ll \omega(t)^2$ for the considered range of rotational speeds of the system, the second terms in $f_X(t)$ and $f_Y(t)$ can be ignored and dropped from the equations of motion. The crack depth in the radial direction is normalized to the radius of the shaft and expressed by μ while the resultant vibration whirl amplitude is represented by

$$Z = \sqrt{u^2 + v^2} \quad (4)$$

During start-up and coast-down operations at constant angular acceleration, a parametrically excited system (and hence a linear time-varying one) is obtained which is excited by the resulting nonlinear unbalance force in Eq. (3). Note that this parametrically excited system is not necessarily periodic (of the Hill's type) and needs detailed analysis. Here, our objective is to investigate whether the new BW zones captured in cracked rotor systems with an open crack model in Ref. [1] can also be captured for such systems with a breathing crack model.

2.2 Numerical Simulation Results

Numerical simulations for the equations of motions at the given parameters in Table 1 were carried out for varying angular acceleration and rotational speeds of start-up operations. The results are shown in Fig. 2 for two different crack depths at zero unbalance force vector angle with the fixed X -axis. The fundamental critical whirl amplitude is followed with local whirl amplitudes as shown which get elevated as the angular acceleration is increased. Similar to Ref. [1], the backward whirl

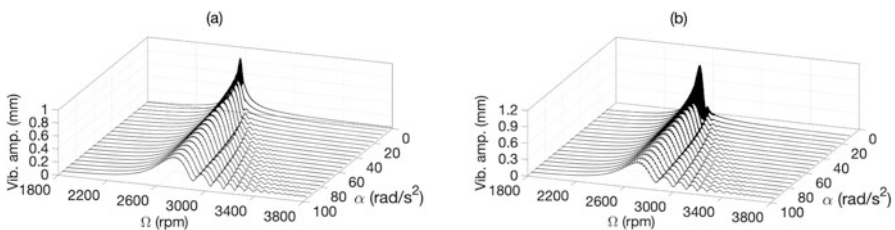


Fig. 2 Numerical simulation response of the resultant whirl amplitude Z versus the start-up rotational speed and the angular acceleration of the cracked rotor system in (a) for $\mu = 0.15$ and $\beta = 0$ rad in (b) for $\mu = 0.25$ and $\beta = 0$ rad

zone is mainly expected to appear between the fundamental whirl amplitude and the directly following one. This zone of backward whirl rotational speeds is strongly affected by the angular acceleration and the crack propagation in the system.

For $\alpha = 10 \text{ rad/s}^2$, the effect of the unbalance force vector orientation is explored in Fig. 3 where changing the angle of the unbalance force vector from zero to other values shows some change in the whirl response. However, this behavior does not significantly affect the backward whirl zones of rotational speeds. The results depicted in Fig. 4 show the vibration whirl amplitude plots for the intact and cracked systems at $\alpha = 10 \text{ rad/s}^2$. The effect of the crack on the whirl response is clear where the zones of rotational speeds at which backward whirl orbits are captured are shown. Accordingly, the whirl orbits preceding this backward whirl zone, within the zone, and after passing this zone are plotted in Fig. 5 for the cracked system. Similar to the cracked rotor system with an open crack model in Ref. [1], the new

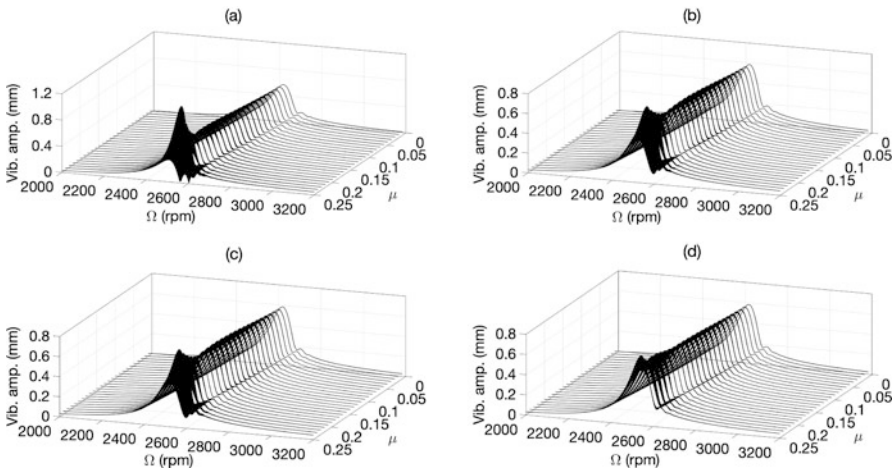


Fig. 3 Numerical simulation response of the resultant whirl amplitude Z versus the start-up rotational speed and the normalized crack depth at $\alpha = 10 \text{ rad/s}^2$ and unbalance force angles of $\beta = 0 \text{ rad}$ in (a), $\beta = \pi/3 \text{ rad}$ in (b), $\beta = 5\pi/6 \text{ rad}$ in (c), $\beta = 3\pi/2 \text{ rad}$ in (d)

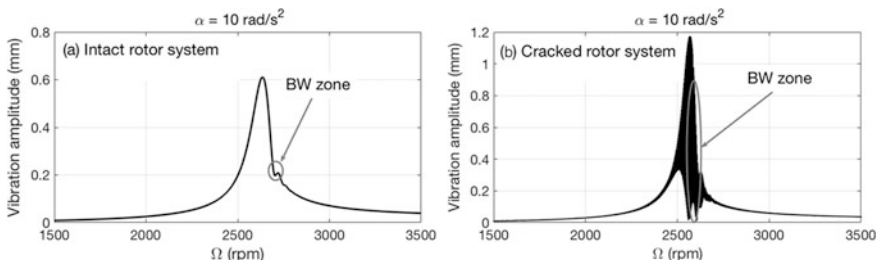


Fig. 4 Numerical simulation response of the resultant whirl amplitude Z versus the start-up rotational speed for the intact rotor system in (a) and the cracked rotor in (b) at $\mu = 0.25$

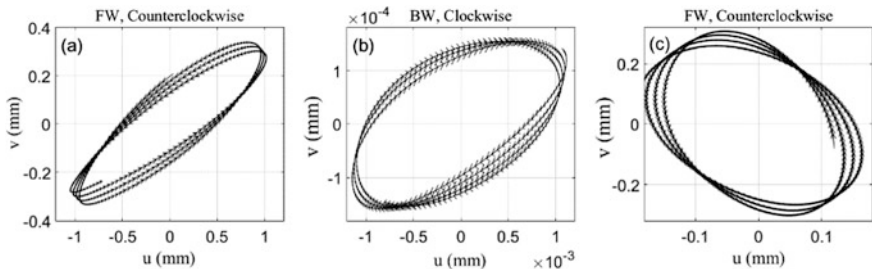


Fig. 5 Numerical simulation whirl orbits of the cracked rotor system for start-up running in the neighborhood of the BW zone at $\mu = 0.25$

backward whirl zone for the considered system with the breathing crack model is also captured here directly after the passage through the critical forward whirl speed under the effect of breathing crack appearance.

3 Conclusions

The singularly puzzling appearance of backward whirl (BW) zones after the passage through the critical speed is investigated for a cracked rotor system with a breathing crack model during start-up operations at constant angular acceleration. It is found here that the BW zone is immediately captured after the passage through the critical FW speed. It is also observed that this BW zone is associated with abrupt *reduction* in whirl amplitudes rather than an elevation in amplitudes. Therefore, we hypothesize that the effect of the crack damage on the appearance of this new BW phenomenon could be employed as an indicator for detecting a propagating breathing crack.

References

1. F. Howitt: The influence of angular acceleration through critical speeds on amplitudes of whirl of a rotating shaft. PhD thesis, McGill University. <http://digitool.library.mcgill.ca/thesisfile113412.pdf> (1961)
2. Zhou, S., Shi, J.: The analytical imbalance response of Jeffcott rotor during acceleration. *J Manuf Sci Eng.* **123**(2), 299–302 (2001)
3. Henson, G.: Response of an oscillating system to harmonic forces of time-varying frequency. *AIAA J.* **46**(8), 2033–2041 (2008)
4. Millsaps, K., Reed, G.: Reducing lateral vibrations of a rotor passing through critical speeds by acceleration scheduling. *J. Eng. Gas Turbine Power.* **120**(3), 615–620 (1998)
5. Fleming, D., Sawicki, J., Poplawski, J.: Unbalance response prediction for accelerating rotors with load-dependent nonlinear bearing stiffness. *Tech. Rep. NASA/TM-213801, E-15159*, NASA (2005)

6. Fan, C.-C., Syu, J.-W., Pan, M.-C., Tsao, W.-C.: Study of start-up vibration response for oil whirl, oil whip and dry whip. *Mech. Syst. Signal Process.* **25**(8), 3102–3115 (2011)
7. Gasch, R.: A survey of the dynamic behavior of a simple rotating shaft with a transverse crack. *J Sound Vib.* **160**, 313–332 (1993)
8. Sekhar, A., Prabhu, B.: Vibration and stress fluctuation in cracked shafts. *J Sound Vib.* **169**, 655–667 (1994)
9. Ishida, Y., Hirokawa, K.: Internal resonances of a cracked rotor: Major critical speed and critical speeds in precritical range. *JSME Int. J. Ser C Dyn. Control Robot. Des. Manuf.* **39**, 225–233 (1996)
10. Al Shudeifat, M.: New backward whirl phenomena in intact and cracked rotor systems. *J Sound Vib.* **443**, 124–138 (2019)
11. Al-Shudeifat, M., Butcher, E.: New breathing functions for the transverse breathing crack of the cracked rotor system: approach for critical and subcritical harmonic analysis. *J Sound Vib.* **330**(3), 526–544 (2011)
12. Guo, C., Al-Shudeifat, M., Yan, J., Bergman, L., McFarland, D., Butcher, E.: Application of empirical mode decomposition to a Jeffcott rotor with a breathing crack. *J Sound Vib.* **332**(16), 3881–3892 (2013)
13. Friswell, M., Penny, J., Garvey, S., Lees, A.: Dynamics of rotating machines. Cambridge University Press, Cambridge (2010)

Proper and Smooth Orthogonal Decompositions for Detection of Inner Race Defects in Rolling Element Bearings with Variable Rotational Speeds



Turki H. Mohamad, Shahab Ilbeigi, and C. Nataraj

Abstract Rolling element bearings represent one of the prominent sources of nonlinearity in rotating systems, which makes fault diagnostics one of the most challenging tasks. This paper presents the application of proper and smooth orthogonal decomposition methods as feature extraction techniques for rolling bearing diagnostics under variable operating conditions. Multiple operation configurations are investigated using proper and smooth orthogonal-based features in order to characterize bearings with inner race defects. Results demonstrate the effectiveness of the proposed techniques for optimal detection of inner race defects under variable rotational speeds.

Keywords Condition-based maintenance · Bearing diagnostics · Feature extraction · Machine learning · Orthogonal decomposition · Inner race defects

1 Introduction

Condition-based maintenance (CBM), which is also known as predictive maintenance, is based on performing online assessments of the current machine condition without interrupting the normal machine operation. CBM provides insight into a potential breakdown, which can help take the necessary actions to fix the problem while minimizing downtime as much as possible.

Rolling element bearings are the load carrying components of a rotating system and consist of rolling elements such as balls or rollers that sit between two bearing rings called races. They represent one of the prominent sources of nonlinearity in rotating systems due to the nonlinear restoring forces between various curved surfaces in contact, radial clearance between the races, and defects. One of the common modes of failure in a rolling element bearing is a point defect on the inner race or the outer race of the bearing. Of these, the inner race defect is more

T. H. Mohamad (✉) · S. Ilbeigi · C. Nataraj

Villanova Center for Analytics of Dynamic Systems, Villanova University, Villanova, PA, USA
e-mail: thajmoha@villanova.edu; <http://vcads.org>

difficult to detect using the traditional diagnostic techniques which rely heavily on accelerometer sensors that are usually installed on the bearing case. Because of this configuration, the vibration signal is transmitted through multiple components, which affects the signal quality.

The nonlinearity of rolling element bearings makes the development of robust fault diagnostic approaches one of the most challenging tasks in health management of rotating machines. In general, the prevailing diagnostic methods in industry do not take into account critical nonlinearities of systems, resulting in a lack of general applicability and ineffectiveness for complex multidisciplinary systems, which are increasingly the norm of modern technology. This can crucially risk the safety of operations in practical applications in addition to compromising the cost effectiveness of maintenance. Therefore, there is a pressing need to continuously develop and improve current maintenance algorithms to ensure safe and efficient day-to-day operations.

Diagnostic problems can be formulated as a classification problem that involves extracting features from measured signals and then using classifiers or learning algorithms such as artificial neural networks (ANN) and support vector machines (SVM) to predict the health condition. The robustness of the classifier's performance depends significantly on the extracted feature set that represents the system's health over a wide range of conditions such as speed, load, and fault level. Almost all existing diagnostics methods are based on extracting statistical features of a system in time or frequency domain, and supervised learning methods. These include work in [1–3] just to mention a few.

Our previous work investigated rolling bearing diagnostics using various techniques [4–8]. Domain dependency was investigated in some of our work [5, 9] but is still currently an unsolved problem. Therefore, there is a need to develop techniques that can be applied and adapted to different operation domains of the system. In this paper, we consider features directly related to the subspace on which the dynamical system evolves. In order to identify this subspace, we use a multivariate analysis of the system's scalar field using *proper orthogonal decomposition* (POD), and a newly developed method called *smooth orthogonal decomposition* (SOD).

The rest of this paper is organized as follows: in Sect. 2, the experimental setup is described. Section 3 presents the proposed feature extraction method. In Sect. 4, the fault detection results are presented for three operating condition cases. Finally, Sect. 5 summarizes and concludes the paper.

2 Experimental Setup and Data Collection

The proposed method in this study was implemented on a rotating fault simulator machine shown in Fig. 1. It consists of a motor-driven shaft mounted on two bearings. The tests in this study were conducted with a balanced shaft and a mass load of 5 kg applied to it. The vertical and horizontal vibration displacements of the shaft were measured using GE/Bently Nevada 7200 series proximity probe sensors

installed close to the bearing housing. The data were then processed through the corresponding conditioning units and were digitized using a National Instruments NI USB 6363 data acquisition system as shown in Fig. 1. The vibration data of the shaft was collected for two bearing conditions including healthy bearings (H) and those with inner race defects (IR) at 19 different speeds ranging from 300 rpm to 3000 rpm with alternating increments of 120 and 180 rpm (e.g., 300, 420, 600, 720, 900, . . . , 3000), at a sampling rate of 10 kHz, and for a time length of 5 s. In order to obtain sufficient data, 10 sets of data were collected at each rotating speed for a total number of 380 sampled signals.

3 Diagnostic Method

An overview of the fault detection method used in this paper is summarized in Fig. 2 and is described as follows. The proximity probe sensors in two orthogonal directions measured the vibration of the shaft for two bearing conditions such as healthy and inner race defect for variable operating speeds.

For each data set, two feature sets, which will be explained later, were extracted using POD and SOD methods. Various speed domains were considered for training and testing a classification model using an artificial neural network (ANN). In the following subsections, we provide a brief mathematical overview of proper and smooth orthogonal decomposition methods for completeness; for more details please refer to [10–12].

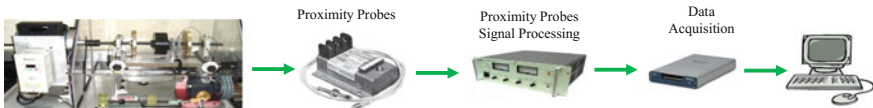


Fig. 1 Data collection process

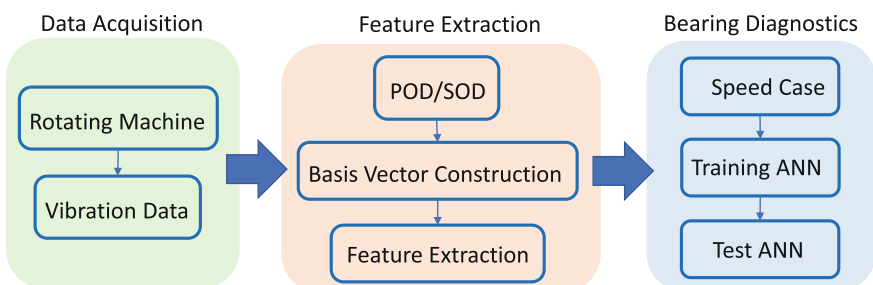


Fig. 2 Diagnostic approach

3.1 Proper Orthogonal Decomposition

Proper orthogonal decomposition (POD) [10, 11], also known as principal component analysis (PCA), is a statistical method used to represent multi-dimensional data as orthogonal basis vectors in which the data projection onto these basis vectors has maximum variance. Let us assume that matrix $\mathbf{Y} \in \mathbb{R}^{r \times n}$ is composed of r snapshots of n measurements of a system or phenomenon, and $\dot{\mathbf{Y}} \in \mathbb{R}^{r \times n}$ is the derivative of \mathbf{Y} , containing the rate of changes in data or information. Provided that \mathbf{Y} and $\dot{\mathbf{Y}}$ have zero mean, the corresponding auto-covariance matrices can be formed by

$$\Sigma_{yy} = \frac{1}{r-1} \mathbf{Y}^T \mathbf{Y}, \quad \Sigma_{\dot{y}\dot{y}} = \frac{1}{r-1} \dot{\mathbf{Y}}^T \dot{\mathbf{Y}}. \quad (1)$$

In POD, we seek a basis vector $\phi \in \mathbb{R}^n$ such that a projection of the data matrix onto this vector has maximal variance. The description of POD translates into the following constrained maximization problem:

$$\max_{\phi} \|\mathbf{Y}\phi\|^2 \quad \text{subject to} \quad \|\phi\| = 1. \quad (2)$$

We obtain the solution to the POD problem by solving the eigenvalue problem of the auto-covariance matrix Σ_{yy} :

$$\Sigma_{yy}\phi_k = \lambda_k\phi_k, \quad (3)$$

where λ_k are proper orthogonal values (POVs), $\phi_k \in \mathbb{R}^n$ are proper orthogonal modes (POMs), and proper orthogonal coordinates (POCs) are columns of $\mathbf{Q} = \mathbf{Y}\Phi$, in which $\Phi = [\phi_1, \phi_2, \dots, \phi_n] \in \mathbb{R}^{n \times n}$. POVs are ordered such that $\lambda_1 \geq \lambda_2 \geq \dots \geq \lambda_n$, and reflect the variances in \mathbf{Y} data along the corresponding POMs.

3.2 Smooth Orthogonal Decomposition

Smooth orthogonal decomposition (SOD) [11, 12] can be viewed as an extension to POD in which multi-dimensional data are represented with basis vectors (not necessary orthogonal) in which the data projection onto these basis vectors has maximum variance and minimum roughness, or in other words, maximum smoothness. In SOD, we are looking for a basis vector $\psi \in \mathbb{R}^n$ such that a projection of the data matrix onto this vector has both maximal variance and minimal roughness (i.e., maximal smoothness.) Roughness can be defined as squared L_2 norm of rate of change of data. Thus, the roughness of a scalar field \mathbf{Y} is equal to $\|\dot{\mathbf{Y}}\psi\|$. Therefore, the description of SOD can be stated as maximizing the following function:

$$\lambda(\psi) = \frac{\|\mathbf{Y}\psi\|^2}{\|\dot{\mathbf{Y}}\psi\|^2}. \quad (4)$$

We rewrite the above equation by considering Eq. (1) in the following form:

$$\lambda(\psi) = \frac{\psi^T \Sigma_{yy} \psi}{\psi^T \Sigma_{\dot{y}\dot{y}} \psi}. \quad (5)$$

In order to maximize $\lambda(\psi)$, we set the first derivative equal to zero:

$$\frac{\partial \lambda(\psi)}{\partial \psi} = \frac{2(\psi^T \Sigma_{\dot{y}\dot{y}} \psi) \Sigma_{yy} \psi - 2(\psi^T \Sigma_{yy} \psi) \Sigma_{\dot{y}\dot{y}} \psi}{(\psi^T \Sigma_{\dot{y}\dot{y}} \psi)^2} = 0. \quad (6)$$

As a result, Eq. (6) can be simplified using Eq. (5):

$$\Sigma_{yy} \psi_k = \lambda_k \Sigma_{\dot{y}\dot{y}} \psi_k. \quad (7)$$

Equation (7) is the generalized eigenvalue problem of the matrix pairs Σ_{yy} and $\Sigma_{\dot{y}\dot{y}}$ which yields the solution to the SOD problem. In this equation, scalars λ_k are smooth orthogonal values (SOVs), and vectors $\psi_k \in \mathbb{R}^n$ are *smooth projection modes* (SPMs). A matrix that contains all the SPMs has the form $\Psi = [\psi_1, \psi_2, \dots, \psi_n] \in \mathbb{R}^{n \times n}$, and a matrix that contains all the SOVs has the form $\Lambda = \text{diag}([\lambda_1, \lambda_2, \dots, \lambda_{2n}]) \in \mathbb{R}^{n \times n}$. Using these definitions, Eq. (7) can be summarized into the following matrix form:

$$\Sigma_{yy} \Psi = \Sigma_{\dot{y}\dot{y}} \Psi \Lambda. \quad (8)$$

The degree of smoothness of the coordinates is described by the magnitude of the corresponding SOV. Thus, the greater in magnitude the SOV, the smoother in time is the corresponding coordinate. It should be noted that, if we were to replace $\Sigma_{\dot{y}\dot{y}}$ with the identity matrix, the formulation would yield POD.

In summary, POD and SOD are techniques used to map multi-dimensional data into basis vectors. POD considers the spatial or geometric consequences of this mapping and neglects the temporal structure of the state evolution. In contrast, SOD considers both the geometrical features of states and their time evolution in terms of overall spatial variation and temporal smoothness of the corresponding coordinate.

3.3 Feature Extraction and Supervised Learning

The advantage of both POD and SOD techniques is their capacity of characterizing nonlinear dynamical systems and identifying trends in the data by *preserving the nonlinearity* of the original data flow in its projection onto the basis vectors. In

this work, POD and SOD methods were used as feature extraction techniques for detection of inner race bearing defects using the shape of orbits plots. Orbit plots are a visualization of the shaft path that it takes as it vibrates during rotation. They are created by two simultaneous orthogonal displacement measurements of the rotational shaft.

The shape of the orbit plots characterizes the response of the rotating system in a qualitative fashion, which can be vitally important in analysis and diagnostics of rotating machinery. Extracting meaningful information of this qualitative visualization is a challenging task and requires expert knowledge. Thus, quantitative characterization of the orbit plots could offer valuable information in describing the condition of the system without having to involve an expert. Therefore, our chief concern here is to extract a set of features that can quantify the orbit plots.

Figure 3 depicts samples of the orbit plots for a healthy bearing and a bearing with inner race defect. The figure also shows the proper and smooth orthogonal modes for the corresponding data. For each data sample, the POD and SOD were performed to the orbit plot. A feature set was then extracted including (1) the angle lying between each proper orthogonal mode and the positive x -axis, (2) each proper orthogonal value, (3) the angle lying between each smooth projection mode and the positive x -axis, (4) each smooth orthogonal value, and (5) shaft rotational speed. This represents a set of five features for each technique.

An ANN was then developed in order to find the relationship between the extracted features (input) and the bearing condition (output). A two-layer neural network with a single hidden layer was chosen to map those features in order to predict the bearing health condition at various rotational speeds. The total number of selected neurons was twenty and the backpropagation algorithm was used to train the artificial neural network. In the trained ANNs, the activation functions for the neurons of hidden and output layers were Tansig and Softmax, respectively.

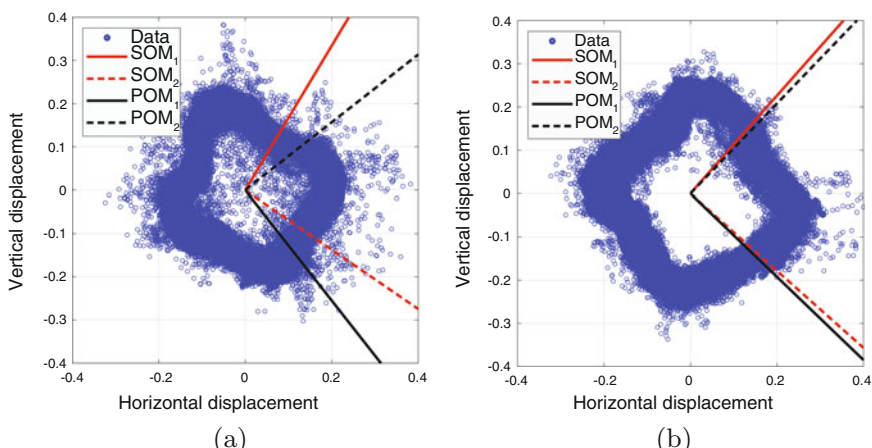


Fig. 3 Orbit plots of the rotational shaft at 300 rpm along with the orthogonal modes for (a) healthy bearing and (b) bearing with inner race defect

4 Fault Detection Results

The current study investigated different speed configurations between the training and testing sets of the classification model: (Case A) known speed domains, (Case B) bounded speed domains, and (Case C) unknown speed domains.

In order to attain this goal, Case A investigated the classification model by training and testing the classifier on the same set of speeds. This case is important when we have sufficient knowledge about the system and its operating conditions. Case B involved generalizing the diagnostic approach to variable operating speeds within a predefined speed range where the test set domain is different from the training set but it is bounded by the training speeds. This approach is useful for applications where the operating range is known, i.e., maximum and minimum operating speeds, but not the exact operating speed. Finally, Case C studied the effect of training and testing on entirely different speed domains where the test speeds were unknown to the user and the trained model. This is a difficult problem but is commonly encountered in industry.

The performance of the classification models can be analyzed using certain evaluation matrices such as the overall model accuracy, the fault prediction precision, and sensitivity. The definition of these metrics along with some examples can be found in our previous work [13]. Considering multiple metrics in building the classification model is a very important practice, especially, to avoid biased or conservative models. A high sensitivity and low precision for a certain class indicates a biased classifier and the opposite indicates a conservative classifier. Ideally, a classifier with high recall and high precision is what we seek. Finally, the overall accuracy of the classifier is the rate of the correct prediction.

Results in Table 1 demonstrate the effectiveness of the SOD technique in the diagnostics of inner race bearings under certain speed conditions. An overall accuracy of 100% was achieved under cases (A) and (B). This indicates the high significance of the SOD-based features in characterizing the dynamic behavior of the bearing system operating under an identical speed domain and variable speed domains bounded with a known range. However, the SOD-based features performed poorly in Case (C), which indicates that there was inadequate information extracted to detect the inner race defect. The POD-based features provided valuable information for the detection of inner race defects for all the three speed cases (A, B, and C). An overall accuracy of 100% was achieved for Case (A), 97% was

Table 1 Classification results for various speed cases using POD and SOD techniques

Technique	Case	Accuracy	Precision	Sensitivity
POD	A	100.0%	100.0%	100.0%
	B	97.2%	94.4%	100.0%
	C	84.4%	82.5%	85.7%
SOD	A	100.0%	100.0%	100.0%
	B	100.0%	100.0%	100.0%
	C	50.0%	62.5%	50.0%

achieved for Case (B), and 84% was achieved for Case (C). This indicates the superiority of POD-based features over SOD-based features as it has the capability to be generalized to different speed domains.

5 Conclusions

This work introduced the application of POD and SOD as feature extraction techniques for the detection of inner race bearing defects under variable operating conditions. Various features were extracted using estimated proper and smooth modes and values. We showed that the POD and SOD based features effectively characterized the behavior of the system by *preserving the nonlinearity* of the original data flow, and can also be applied to various dynamical system domains with minimum knowledge about the signatures of the response under various bearing conditions. In the case of rotating machinery diagnostics, these results are significant due to the shaft rotational speed's strong influence on the dynamic system behavior. The results in general are quite impressive considering that only five features were extracted from the shaft displacement data in order to diagnose bearings with inner race defects under variable rotational speeds. This work has very good potential in the field of machinery diagnostics. In general, the current work has potential for unsupervised domain adaptation, where these kind of problems are mostly unsolved. In addition, results show the superiority of POD-based features compared with SOD-based features, particularly for the case of unknown speed domains.

References

- Stepanic, P., Latinovic, I.V., Djurovic, Z.: A new approach to detection of defects in rolling element bearings based on statistical pattern recognition. *Int. J. Adv. Manuf. Technol.* **45**(1–2), 91–100 (2009)
- De Moura, E., Souto, C., Silva, A., Irmao, M.: Evaluation of principal component analysis and neural network performance for bearing fault diagnosis from vibration signal processed by RS and DF analyses. *Mech. Syst. Signal Process.* **25**(5), 1765–1772 (2011)
- Yuan, R., Lv, Y., Song, G.: Fault diagnosis of rolling bearing based on a novel adaptive high-order local projection denoising method. *Complexity* **2018**, 3049318 (2018)
- Mohamad, T.H., Kitio Kwuiyim, C.A., Nataraj, C.: Discrimination of multiple faults in bearings using density-based orthogonal functions of the time response. In: ASME 2017 International Design Engineering Technical Conference (IDETC), Cleveland (2017)
- Mohamad, T.H., Samadani, M., Nataraj, C.: Rolling element bearing diagnostics using extended phase space topology. *ASME J. Vib. Acoust.* **140**(6), 061009 (2018)
- Kitio Kwuiyim, C.A., Mohamad, T.H., Nataraj, C.: Using the Gottwald and Melbourne's 0–1 test and the Hugichi fractal dimension to detect chaos in defective and healthy ball bearings. *MATEC Web Conf.* **241**, 01017 (2018)
- Mohamad, T.H., Nataraj, C.: An overview of PST for vibration based fault diagnostics in rotating machinery. *MATEC Web Conf.* **211**, 01004 (2018)

8. Mohamad, T.H., Kitio Kuwimy, C.A., Nataraj, C.: Multi-speed multi-load bearing diagnostics using extended phase space topology. MATEC Web Conf. **241**, 01011 (2018)
9. Kappagantu, K., Nataraj, C.: Nonlinear modeling and analysis of a rolling element bearing with a clearance. Commun. Nonlinear Sci. Numer. Simul. **16** (10), 4134–4145 (2011)
10. Lu, K., Jin, Y., Chen, Y., Yang, Y., Hou, L., Zhang, Z., Li, Z., Fu, C.: Review for order reduction based on proper orthogonal decomposition and outlooks of applications in mechanical systems. Mech. Syst. Signal Process. **123**, 264–297 (2019)
11. Chelidze, D., Zhou, W.: Smooth orthogonal decomposition-based vibration mode identification. J. Sound Vib. **292**(3), 461–473 (2006)
12. Ilbeigi, S., Chelidze, D.: A new approach to model reduction of nonlinear control systems using smooth orthogonal decomposition. Int. J. Robust Nonlinear Control **28**(15), 4367–4381 (2018)
13. Mohamad, T.H., Chen, Y., Chaudhry, Z., Nataraj, C.: Gear fault detection using recurrence quantification analysis and support vector machine. J. Softw. Eng. Appl. **11**(5), 181 (2018)

Effect of the Compliance of the Part on the Double-Turning Process



Alexander Gouskov , Grigory Panovko , and Dinh Duc Tung

Abstract The report studies the influence of the processing parameters on the vibration excitation at two-cut turning of an extended cylindrical workpiece. The design scheme of the process and the acting forces are described. The model of the part is represented in the form of the Bernoulli–Euler beam. The solution of the obtained equations with a retarded argument is constructed using the Galerkin method. Based on the results of the numerical solution, the influence of the main parameters of processing is analyzed. It is shown that for a deformable workpiece, the presence of two symmetrically located cutters due to the flexibility of the workpiece in an unstable mode does not provide symmetric processing without vibration.

Keywords Stability · Delay · Cutting process · Nonlinear dynamics · Numerical simulation

1 Introduction

Turning process of workpieces is often accompanied by the occurrence of self-oscillations in the system “machine-tool-workpiece” [1, 2], which negatively affect the quality of manufactured parts and equipment wear. The various causes of their occurrence are described and studied in sufficient detail in the modern literature, in particular, those that are caused by the nonlinearity of the characteristics of the cutting forces [3], by the pliability of machine elements or of the part, by the conditions for fixing the cutting tool [4], by turning over the surface formed in the previous turn of the workpiece, etc. [5, 6]. However, in relation to the

A. Gouskov · G. Panovko ()

Mechanical Engineering Research Institute of Russian Academy of Sciences, Moscow, Russia
e-mail: gouskov_am@mail.ru; gpanovko@yandex.ru

D. D. Tung

Bauman Moscow State Technical University, Moscow, Russia
e-mail: tungdinhx48@gmail.com

development of various progressive cutting schemes with the simultaneous use of several cutting tools, a great deal of new problems arises related to the analysis of the dynamics of the multi-cutter process [7–9]. This chapter studies the influence of processing parameters on the excitation of vibration in the two-cutter turning process of an extended cylindrical part with finite flexural rigidity. The turning is made by two rigid cutters, which are symmetrically disposed on the cross section of the workpiece [10, 11]. Similar processing scheme allows one to eliminate the use of intermediate support elements, while simultaneously increasing the depth of cut.

2 Design Scheme and Dynamic Models

The workpiece is a cylinder with a constant cross section of radius R along its length L . The left end of the workpiece is rigidly fixed in the spindle of the lathe; the right end of the workpiece rests on the freely rotating center of the machine's tailstock. The workpiece rotates at a constant speed ω relative to its longitudinal axis Oz , the beginning of which (see Fig. 1) is combined with the center of the section located at the spindle exit (the axis Ox is vertical, the plane yOz is horizontal). When describing the dynamics of the process, the part is presented in the form of a Bernoulli–Euler beam, the material of which is considered linearly elastic.

Processing is simultaneously performed by two cutters at points C_1 and C_2 , located at the opposite ends of the diameter ($x = 0, z = z_C$) of the workpiece parallel to the horizontal axis Oy . It is assumed that both cutters are rigidly fixed on a common support which moves along the workpiece at a constant speed V_0 . The positions of the cutting points $C_1(0, R_{C1}, z_C(t))$, $C_2(0, -R_{C2}, z_C(t))$ are determined

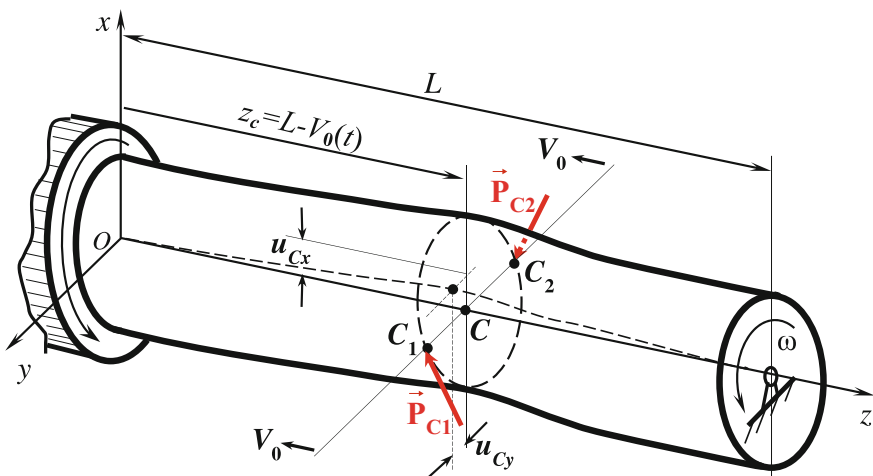


Fig. 1 Design scheme of the workpiece

by the radius of the cylindrical surface of the workpiece R_C and the axial coordinate $z_C(t) = L - V_0 t$ depending on time t . Cutting starts from the free end of the workpiece $z_C(0) = L$. At points C_1 and C_2 cutting forces $\vec{\mathbf{P}}_{C1}, \vec{\mathbf{P}}_{C2}$ are applied to the workpiece, under the action of which the workpiece bends in the direction of the axes Ox and Oy with displacements u_{Cx}, u_{Cy} (see Fig. 1).

The main objective of this study is to determine the effect of the deformability of the workpiece under the action of cutting forces $\vec{\mathbf{P}}_{C1}, \vec{\mathbf{P}}_{C2}$ on the stability of the continuous cutting (without chip breaking).

Vectors of cutting forces $\vec{\mathbf{P}}_{Ck}$ ($k = 1, 2$) retain their orientation with respect to the surface being treated, which does not depend on the longitudinal coordinate of the point z_C : $\vec{\mathbf{P}}_{Ck} = P_{Ck} \vec{\mathbf{e}}_k$ ($|\vec{\mathbf{e}}_k| = 1$). Usually in practice, cutting forces are expressed as:

$$\vec{\mathbf{P}}_{Ck} = \gamma_k \sigma_L B_k h_k \cdot f(h_k, r_k, c_k) \vec{\mathbf{e}}_k. \quad (1)$$

Here, the dimensionless coefficient γ_k depends on the geometry of the cutting edges (takes values from several units to several tens $\sim 10-10^2$); B_k is the cutting depth; h_k is the thickness of the removed layer; σ_L is the characteristic stress of the material being processed (for ductile materials they usually take the yield strength); nonlinear function characterizing the dependence of the cutting force on the thickness of the removed layer can be written in the form: $f(h_k, r_k, c_k) = (c_k + r_k h_k)/(c_k + h_k)$, where c_k, r_k are the experimental coefficients [11]. We assume that both cutters have the same geometry, i.e., $\gamma_1 = \gamma_2 = \gamma$, $c_1 = c_2 = c$, $r_1 = r_2 = r$ and present the nonlinear part of the cutting law as

$$f_k = f(h_k, r, c) = (c + r h_k) / (c + h_k), \quad [h_k] = [c] = m, \quad [r] = [f_k] = 1. \quad (2)$$

Define the vectors of the cutting forces $\vec{\mathbf{P}}_{C1}, \vec{\mathbf{P}}_{C2}$ by the projection on the tangential (t), radial (r), and axial (z) directions as: $\vec{\mathbf{P}}_{C1} = P_{t1} \vec{\mathbf{i}}_x - P_{r1} \vec{\mathbf{i}}_y - P_{z1} \vec{\mathbf{i}}_z$, $\vec{\mathbf{P}}_{C2} = -P_{t2} \vec{\mathbf{i}}_x + P_{r2} \vec{\mathbf{i}}_y - P_{z2} \vec{\mathbf{i}}_z$. Accordingly, the tangential, radial, and axial components of the cutting forces (1) can be presented in a single form, taking into account:

$$\begin{aligned} P_{Xk} &= k_X B_k h_k f_k; \quad k_X = l_X \gamma \sigma_L; \quad X = t, r, z; \\ l_{1t} &= \vec{\mathbf{e}}_1 \cdot \vec{\mathbf{i}}_x; \quad l_{1r} = -\vec{\mathbf{e}}_1 \cdot \vec{\mathbf{i}}_y; \quad l_{1z} = -\vec{\mathbf{e}}_1 \cdot \vec{\mathbf{i}}_z; \quad l_{2t} = -\vec{\mathbf{e}}_2 \cdot \vec{\mathbf{i}}_x, \\ l_{2r} &= \vec{\mathbf{e}}_2 \cdot \vec{\mathbf{i}}_y; \quad l_{2z} = -\vec{\mathbf{e}}_2 \cdot \vec{\mathbf{i}}_z; \\ l_t &= |l_{1t}| = |l_{2t}|; \quad l_r = |l_{1r}| = |l_{2r}|; \quad l_z = |l_{1z}| = |l_{2z}|. \end{aligned} \quad (3)$$

We reduce the task of the study to the detection of the influence of compliance of the part on the excitation of its vibrations depending on the processing parameters

and the position of the cutters along the length of the part. The feature of this system is that the dynamic compliance of the part depends on the coordinates of the cutting forces points of application along the length and the excitation of vibrations of the part changes during the process of turning.

For the further formulation of the oscillation of workpiece as a Bernoulli–Euler beam, we bring both the cutting forces to the point $C(0, 0, z_C)$. As a result we get the resultant force and moment located on the axis of the workpiece:

$$\begin{aligned}\overrightarrow{\mathbf{P}}_C &= (P_{t1} - P_{t2}) \overrightarrow{\mathbf{i}}_x + (P_{r2} - P_{r1}) \overrightarrow{\mathbf{i}}_y - (P_{z1} + P_{z2}) \overrightarrow{\mathbf{i}}_z; \\ \overrightarrow{\mathbf{M}}_C &= -(R_{C1}P_{t1} + R_{C2}P_{t2}) \overrightarrow{\mathbf{i}}_z + (R_{C2}P_{z2} - R_{C1}P_{z1}) \overrightarrow{\mathbf{i}}_x.\end{aligned}\quad (4)$$

We will consider only the components of the cutting forces in the plane of the cross section along the axes Ox , Oy and neglect the torque. In the future we set the radii $R_{C1} = R_{C2} \approx R$. In the matrix form Eq. (4) for the projections on the axes Ox , Oy :

$$\mathbf{P}_C = \begin{Bmatrix} P_{t1} - P_{t2} \\ P_{r2} - P_{r1} \end{Bmatrix}, \quad \mathbf{M}_C = \begin{Bmatrix} R & (P_{z2} - P_{z1}) \\ 0 & 0 \end{Bmatrix}. \quad (5)$$

In the symmetric operation of both cutters, the generalized forces (5) are equal to zero. In case of symmetry breaking due to deformations of the part, shear force and bending moments arise. The oscillations of the part will be considered in two mutually perpendicular planes. The cylindrical part is considered as the Bernoulli–Euler beam:

$$\begin{aligned}m\ddot{u}_x + (Au_x'')'' &= P_{Cx}\delta(z - z_C), \\ m\ddot{u}_y + (Au_y'')'' &= P_{Cy}\delta(z - z_C) + M_{Cx}\delta'(z - z_C),\end{aligned}\quad (6)$$

where m is the mass per unit length of beam, A is the flexural stiffness, $u_x(z, t)$, $u_y(z, t)$ are the components of deflection of z axis of beam and $\delta(z - z_C)$ is the Dirac delta-function. The derivative with respect to the axial coordinate is denoted by u'_j , $j = \{x, y\}$, and \dot{u}_j is the time derivative.

When symmetrically machining of an ideal cylinder, the cutting depth and thickness of the removed layer for both cutters will be the same ($B_1 = B_2 = B^0$, $h_1 = h_2 = h^0$) and the corresponding components of the cutting forces P_{Xk} (see Eq. (1)) will be nominal:

$$P_X{}^0 = k_X B^0 h^0 f^0; \quad X = t, r, z; \quad f^0 = f(h^0, r, c) = (c + rh^0) / (c + h^0). \quad (7)$$

When vibrations appear, the symmetry is broken, and the sections of the chips will change due to the radial movement of the axis of the workpiece $u_y(t)$ and cross-section rotation θ_x :

$$\begin{aligned} B_1 &= B^0 - u_y(t) + u_y(t - T_0/2), \quad B_2 = B^0 + u_y(t) - u_y(t - T_0/2), \\ h_1 &= h^0 + R^0[\theta_x(t) - \theta_x(t - T_0/2)], \quad h_2 = h^0 - R^0[\theta_x(t) - \theta_x(t - T_0/2)], \end{aligned} \quad (8)$$

where R^0 is the nominal radius of the cylindrical surface being processed (we assume that $R = R^0$); $T_0 = 2\pi R^0/V_C$ is the period of rotation of the part that will determine the delay $T_0/2$ in the sequential operation of diametrically located cutters; V_C is a cutting velocity; B^0 is the difference between the radii of the initial cylindrical surface and the treated one. The nominal thickness of the removed layer h^0 is determined by the axial speed of the tool V_0 and is equal to $h^0 = V_0 T_0/2$.

The appearance and development of vibrations of a part is caused by the regenerative effect associated with delay. The increase in vibrations reduces the instability of the cutting process. The determination of the increase in vibration can be found by considering the small deviations of the part in time. In the following, linearized equations of oscillations of a deformable workpiece will be considered; therefore, cutting forces (7) with (8) will take the form:

$$\begin{aligned} B_{kj}hf(h, r, c) &\approx B^0 h^0 f^0 + h^0 f^0 \Delta B_k + B^0 g^0 \Delta h_k, \\ g^0 &= \partial(hf)/\partial h|_{h=h^0} = r + (1-r)c^2/(c+h^0)^2, \end{aligned} \quad (9)$$

where the increments of the cutting depth ΔB_k and thickness of the removed chips Δh_k linearly depend on the change in the position of the processed section of the part:

$$\Delta B_1 = u_y(t) - u_y(t - T_0/2), \quad \Delta h_1 = -R^0[u'_y(t) - u'_y(t - T_0/2)]. \quad (10)$$

In the symmetric case $\Delta B_2 = -\Delta B_1$, $\Delta h_2 = -\Delta h_1$ (if we ignore the influence of torque in the section plane of the part and the axial force from the action of the cutting forces on the part). However, the breaking of symmetry or transverse perturbations leads to the excitation of vibrations, by the nature of which one can judge the stability and instability of the turning process. After using the values (9) in (10), we will rewrite the workpiece flexural oscillations equations (6) in a dimensionless form. To do this, we introduce the scaling: $T_* : t = T_* \tau$; $Z_* : z = Z_* \zeta$; $U_* : u = U_* \xi$. Select the following scale values: $T_* = L^2 \sqrt{\rho \pi (R^0)^2 / A^0}$; $Z_* = L$; $U_* = 1$, where ρ is the mass per unit length. Furthermore, we assume that the stiffness of the bending section varies slightly when turning $A^0 = A = \pi E (R^0)^4 / 4$, where E is Young's modulus. Then we have $T_* = 2R^0 / (\varepsilon^2 V_S)$, where $V_S = \sqrt{E/\rho}$ is a speed of sound in the material. Now Eq. (6) has the form:

$$\begin{aligned} \ddot{\xi}_x + \dot{\xi}_x''' &= +\frac{K\Delta}{\varepsilon^3} \delta(\zeta - \zeta_C); \\ \ddot{\xi}_y + \dot{\xi}_y''' &= -\frac{\dot{K}\Delta}{\varepsilon^3} \kappa_r \delta(\zeta - \zeta_C) - \frac{K\Delta}{\varepsilon^2} \kappa_z \delta'(\zeta - \zeta_C), \end{aligned} \quad (11)$$

where

$$\Delta = \eta f^0 \xi_y(\tau, \zeta) - \xi_y(\tau - T, \zeta) + \beta \varepsilon g^0 \xi'_y(\tau, \zeta) - \xi'_y(\tau - T, \zeta).$$

The dimensionless delay is equal to $T = T_0/2T_*$. We also use the designations:

$$\begin{aligned} \beta &= \frac{B^0}{R^0}, \quad \varepsilon = \frac{R^0}{L}, \quad \eta = \frac{h^0}{R^0}, \quad \kappa_r = \frac{k_r}{k_t}, \quad \kappa_z = \frac{k_z}{k_t}, \\ K &= \frac{8\gamma\sigma_L}{\pi E}, \quad T = \frac{\pi\varepsilon^2 V_S}{2V_C}, \quad \Omega = \frac{\pi}{T}. \end{aligned} \quad (12)$$

A further solution is constructed by the Galerkin method. We represent the solution of problem (11) in the following form:

$$\xi_x(\tau, \zeta) \approx q_1(\tau) p_1(\zeta) + q_2(\tau) p_2(\zeta), \quad \xi_y(\tau, \zeta) \approx q_3(\tau) p_1(\zeta) + q_4(\tau) p_2(\zeta). \quad (13)$$

The linearized system (11) presents the vibrations in two planes—vertical and horizontal. The vibrations in horizontal plane $\xi_y(\tau, \zeta)$ can be studied independently of vibration in vertical plane. After substituting the expression for ξ_y from (13) into the second equation of the system (11) and orthogonalizing the residual coordinate functions $p_i(\zeta)$, $i = 1, 2$, we obtain two equations that we write in the matrix form:

$$\ddot{\mathbf{q}}(\tau) + 2n_d \mathbf{D}\dot{\mathbf{q}}(\tau) + (\boldsymbol{\alpha} + \mathbf{C})\mathbf{q}(\tau) = \mathbf{C}\mathbf{q}(\tau - T), \quad (14)$$

where the following designations are used:

$$\mathbf{C}(\zeta_C) = \frac{K}{\varepsilon^3} \left(\eta f^0 \mathbf{A} + \beta \varepsilon g^0 \mathbf{B} \right), \quad \boldsymbol{\alpha} = \begin{bmatrix} \alpha_1^4 & 0 \\ 0 & \alpha_2^4 \end{bmatrix}, \quad \mathbf{D} = \begin{bmatrix} \alpha_1^2 & 0 \\ 0 & \alpha_2^2 \end{bmatrix}, \quad \mathbf{q} = \begin{bmatrix} q_3 \\ q_4 \end{bmatrix},$$

where \mathbf{A} and \mathbf{B} are the functions on cutting-edge position $\mathbf{p}^T = \{p_1(\zeta_C), p_2(\zeta_C)\}$:

$$\mathbf{A}(\zeta_C) = \kappa_r \mathbf{p} \mathbf{p}^T - \varepsilon^2 \kappa_z \left(\mathbf{p} \mathbf{p}'^T + \mathbf{p} \mathbf{p}^T \right), \quad \mathbf{B}(\zeta_C) = \kappa_r \mathbf{p} \mathbf{p}'^T - \varepsilon^2 \kappa_z \left(\mathbf{p} \mathbf{p}''^T + \mathbf{p}' \mathbf{p}'^T \right).$$

The coordinate functions $p_i(\zeta)$ will be chosen as the eigen functions of the transverse vibrations for the Bernoulli–Euler beam as:

$$p_n''' - \alpha_n^4 p_n = 0, \quad \zeta = 0 : p_n = 0, p'_n = 0; \quad \zeta = 1 : p_n = 0, p'_n = 0, \|p_n\| = 1. \quad (15)$$

Equation (15) is a system of linear ordinary differential equations with two degrees of freedom for a system without delay, and the natural frequency of n th mode is equal to α_n^2 . The matrices \mathbf{A} , \mathbf{B} depend on the current position of the cutting tools coordinate $\zeta_C(\tau) = 1 - (\tau V_C)/(2\varepsilon V_S)$. A linear viscous damping matrix \mathbf{D} is introduced in Eq. (15), n_D is the damping coefficient. As the cutters move from the

right end $\zeta = 1$ to the left one (that is fixed in the spindle) $\zeta = 0$, the dynamic compliance in the cutting forces application places changes. The modules of linear and angular dynamic compliance of the part $|\hat{\xi}_y(f, \zeta_C)|$ and $|\hat{\xi}'_y(f, \zeta_C)|$ defined as:

$$\left| \hat{\xi}_y(f, \zeta_C) \right| = \left| \mathbf{p}^T(\zeta_C) \hat{\mathbf{q}}(f) \right|, \quad \left| \hat{\xi}'_y(f, \zeta_C) \right| = \left| \mathbf{p}'^T(\zeta_C) \hat{\mathbf{q}}(f) \right|, \quad (16)$$

where vector $\hat{\mathbf{q}}(f)$ is the solution of the following linear algebraic system:

$$\left[(2\pi if)^2 + 2n_d(2\pi if)\mathbf{D} + \boldsymbol{\alpha} \right] \hat{\mathbf{q}}(f) = \mathbf{p}(\zeta_C), \quad i = \sqrt{-1}.$$

The natural frequencies are equal to $f_1 = \alpha_1^2/2\pi \approx 2.45$, $f_2 = \alpha_2^2/2\pi \approx 7.95$.

3 Analysis of the Calculation Results

Numerical integration of the system of equations with a lagging argument was used by the program dde23 of the computing environment MATLAB. All calculations were carried out with the following parameters and values of the system and taking into account the adopted notation for dimensionless complexes in (12): $R^0 = 0.02$ m, $L = 0.5$ m, $\rho = 7.8 \cdot 10^3$ kg · m⁻³, $E = 2 \cdot 10^{11}$ Pa, yield strength of the material of the part $\sigma_L = 3 \cdot 10^8$ Pa, $c = 2.5 \cdot 10^{-4}$ m, $r = 0.65$, $\gamma = 50$, cutting velocity $V_C = 2$ m · s⁻¹, $\beta = 0.1$, $\eta = 0.02$, $n_d = 0.01$, $\kappa_r = 0.25$; $\kappa_z = 0.5$ [1]. We consider the spatial representation for the calculations in nine different cutter positions $\zeta_C = \{0.1, 0.2, \dots, 0.9\}$. Figure 2 compares the two turning processes and the nature of the growth of perturbations with $\eta = 0.02$ (see Fig. 2a) and with

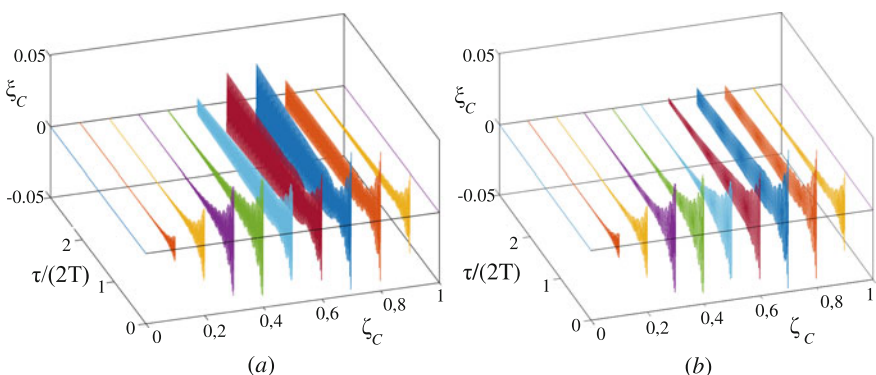


Fig. 2 Development of vibrations at $\eta = 0.02$ (a), and $\eta = 0.005$ (b)

a decrease in the chip thickness four times $\eta = 0.005$ (see Fig. 2b). In the first case ($\eta = 0.02$), the emerging vibrations that appear will increase—unstable turning in the middle of workpiece. The growth of perturbations leads to the appearance of intermittent cutting corresponds to the Hopf bifurcation [7, 10].

Reducing the feed per revolution by four times ($\eta = 0.02 \rightarrow \eta = 0.005$) stabilizes the turning process over the entire length of the workpiece. Analogous results can be shown with time delay (cutting velocity) and cutting depth—parameter β .

4 Conclusion

A nonlinear model for turning a cylindrical part with finite flexural rigidity has been developed. The linearized model shows that vibrations occur in a horizontal plane regardless of vibrations in a vertical plane. Vibrations in the vertical plane are generated by oscillations in the horizontal plane. The peculiarity of this system is that the dynamic compliance of the system at the cutting points depends on its position along the length of the workpiece: the excitation changes during the turning process. The highest sensitivity of the system to vibrations is provided by cutting speed and feed per revolution. It is shown that it is possible to choose such values of the turning conditions that during the whole process the emerging vibrations will attenuate. It is shown that for a deformable workpiece, the presence of two symmetrically located cutters due to the flexibility of the workpiece in an unstable mode does not provide symmetric processing without vibration.

Acknowledgments The work has been realized under the support of the Russian Science Foundation, project № 18-19-00708.

References

- Smith, G.T.: Cutting Tool Technology. Industrial Handbook. Springer, London (2008)
- Chen, C.K., Tsao, Y.M.: A stability analysis of regenerative chatter in turning process without using tailstock. *Int J Adv Manuf Technol.* **29**, 648–654 (2006)
- Dassanayake, A.V., Suh, C.S.: On nonlinear cutting response and tool chatter in turning operation. *Commun. Nonlinear Sci. Numer. Simul.* **13**, 979–1001 (2008)
- Otto, A., Khasawneh, F.A., Radons, G.: Position-dependent stability analysis of turning with tool and workpiece compliance. *Int J Adv Manuf Technol.* **79**(9–12), 1453–1463 (2015)
- Gerasimenko, A., Guskov, M., Duchemin, J., Lorong, P., Gouskov, A.: Variable compliance-related aspects of chatter in turning thin-walled tubular parts. *Proc. CIRP.* **31**, 58–63 (2015)
- Brissaud, D., Gouskov, A., Paris, H., Tichkiewitch, S.: The fractional model for the determination of the cutting forces. *Asian Int. J. Sci. Technol. Production Manuf.* **1**, 17–25 (2008)
- Reith, M.J., Bachrathy, D., Stepan, G.: Improving the stability of multi-cutter turning with detuned dynamics. *Machining Sci. Technol.* **20**(3), 440–459 (2016)
- Ozlu, E., Budak, E.: Comparison of one-dimensional and multi-dimensional models in stability analysis of turning operations. *Int J Mach Tool Manuf.* **47**, 1042–1047 (2009)

9. Avzar M., Budak E.: Multi-dimensional modeling of chatter stability in parallel turning operation. In: 17th International Conference on Machine Design and Production, Bursa, Turkey (2016)
10. Ozturk, E., Comak, A., Budak, E.: Tuning of tool dynamics for increased stability of parallel (simultaneous) turning processes. *J Sound Vib.* **6**(360), 17–30 (2016)
11. Guskov, A.M., Voronov, S.A., Paris, H., Batzer, S.A.: Nonlinear dynamics of a machining system with two interdependent delays. *Commun. Nonlinear Sci. Numer. Simul.* **7**, 207–221 (2002)

Effect of the Regenerative and Frictional Force on Chatter in Turning Process



An Wang, Wuyin Jin, and Qian Lin

Abstract Based on a new proposed single-degree-of-freedom turning process model, in this work, the effects of the regenerative and the frictional force on cutting tool nonlinear behaviors are investigated by bifurcation analysis and numerical simulation. The Hopf bifurcation usually generates large amplitude vibration and even causes chaotic vibration in the cutting process; hence, it is used in the prediction of chatter onset. We have concluded that the vibration amplitude of the cutting tool increases and the chatter vibration happened earlier as the regenerative force increases. Meanwhile, the vibration amplitude of the cutting tool is reduced due to the increase of the frictional force; however, it affects the original equilibrium position of the cutting tool.

Keywords Chatter · Bifurcation analysis · Hopf bifurcation · Turning process

1 Introduction

With the rapid development of science and technology, chatter has drawn much more attention in the fields of precision machining in the past time. As we all know, chatter is strongly relative to the vibration of the cutting process, especially between the cutting tool and the workpiece, and it is also an important reason for surface quality and tool breakage. In order to eliminate the chatter in the cutting process, the vibration mechanism and vibration response must be studied. Three mechanisms known as frictional chatter, regeneration chatter, and mode coupling chatter are the major reasons for chatter. Various methods were used to explore the chatter phenomena and reveal their vibrational properties, such as analytical

A. Wang · W. Jin (✉)

School of Mechanical and Electronical Engineering, Lanzhou University of Technology,
Lanzhou, China

e-mail: wangan1981@126.com; wuyinjin@hotmail.com

Q. Lin

Editorial Department of Journal of Lanzhou University of Technology, Lanzhou University of
Technology, Lanzhou, China

© Springer Nature Switzerland AG 2020

W. Lacarbonara et al. (eds.), *Nonlinear Dynamics of Structures, Systems and Devices*, https://doi.org/10.1007/978-3-030-34743-0_51

513

methods [1, 2], numerical techniques [3–7], and experimental tests [8, 9]. All of these methods are important means of understanding the mechanism and dynamic response of chatter. There are many factors that influence the chatter system including cutting variables, tool geometry, and other nonlinearity factors. Rusinek proposes a model that considers both frictional and regenerative mechanisms, since the friction phenomenon exists in the cutting process. Simultaneously, the effects of frictional force and regenerative force on the cutting stability region were studied [10]. Recently, a similar model considering frictional and regenerative force was established by Weremczuk, and the multi-time scale method was used to study the effects of friction and regeneration factors on the chatter system [11]. In this chapter, the influence of frictional force and regenerative force on the dynamic characteristics of the cutting system is studied by using the bifurcation analysis method.

2 Model

In this section, a simple single-degree-of-freedom model of turning process is developed. The model mainly considers the influence of regenerative force and frictional force. The focus of this chapter is to propose the effect of regenerative force and frictional force on the orthogonal turning system. Therefore, other nonlinear factors are not considered in our model, for example, nonlinear spring, loss of tool-workpiece contact, and other nonlinearity factors.

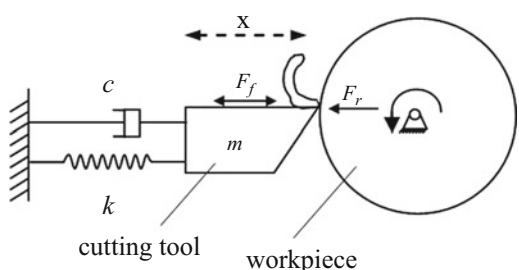
Here, the cutting process of the cutting tool is modeled as a vibrator which can be vibrated in x direction as shown in Fig. 1. Hence, the governing equation of cutting tool vibration is

$$m\ddot{x} + c\dot{x} + kx = F_r + F_f \quad (1)$$

where x is the vibration displacement of cutting tool in x direction, m is an equivalent mass of the cutting tool, c is the equivalent damping, and k is the equivalent stiffness.

The cutting force is made up of regenerative force F_r and frictional force F_f [11–16]. They have the form as follows:

Fig. 1 Schematic model of orthogonal turning process



$$\begin{aligned} F_r &= K_f w (x(t - \tau) - x(t)) \\ F_f &= K_t (\operatorname{sgn}(v_r) - av_r + bv_r^3) \end{aligned} \quad (2)$$

in which K_f is the cutting coefficient, w is the chip width, $x(t)$ and $x(t - \tau)$ are the current cutting tool position and its delayed position, time delay τ is inversely proportional to the spindle velocity and, for the turning process, it is the period of one revolution, K_t is the component of the frictional force, a and b are the coefficients of the frictional force, v_r is the relative velocity between the cutting tool and the chip, and it is connected with the workpiece diameter d and time delay τ

$$v_r = \pi d / \tau - \dot{x} \quad (3)$$

Substituting Eq. (2) into Eq. (1) and introducing nondimensional variables defined by $\tilde{x} = x/L$, $\tilde{t} = \omega_0 t$, $\tilde{w} = w/L$, $\tilde{\tau} = \omega_0 \tau$, $\tilde{d} = d/L$, $\alpha = K_f \tilde{w} L / m \omega_0^2$, $\beta = K_t / m \omega_0$, it can be cast into the dimensionless form as

$$\ddot{x} + \delta \dot{x} + x = \alpha (x(t - \tau) - x(t)) + \beta (\operatorname{sgn}(v_r) - av_r + bv_r^3) \quad (4)$$

where x is the dimensionless vibration displacement of cutting tool and δ is a viscous damping coefficient. We note that both the regenerative force and the frictional force are considered in our model. Meanwhile, the cutting force mainly depends on the dimensionless parameters α and β in the model.

3 Effect of the Regenerative Force and Frictional Force

In the present study, a bifurcation analysis is performed to investigate the effects of the regenerative force and the frictional force on cutting tool nonlinear behaviors. Particularly, the main purpose is to research the type of Hopf bifurcation, which is very important to cutting system, because the Hopf bifurcation can generate large amplitude vibration and even cause chaotic vibration in the cutting process. In addition, the bifurcation diagrams were determined using the software package KNUT [17], which is a continuation and bifurcation software for delay differential equations.

The bifurcation diagram represents the vibration amplitude of the cutting tool as function of time delay for different α and β combination. Based on our dynamic model, the increase of α and β means the increase of regenerative force and frictional forces, respectively. In addition, fix $\delta = 0.1$, $d = 1$, $a = 0.5$, and $b = 0.1$ in Eq. (4).

Figures 2, 3, and 4 show the bifurcation diagrams obtained for $\alpha = 0.1, 0.5, 1, 2$ and fixed $\beta = 0.01, 0.1, 1$, respectively, using dimensionless time delay τ as a bifurcation parameter. In the bifurcation diagrams, Hopf bifurcation point is denoted

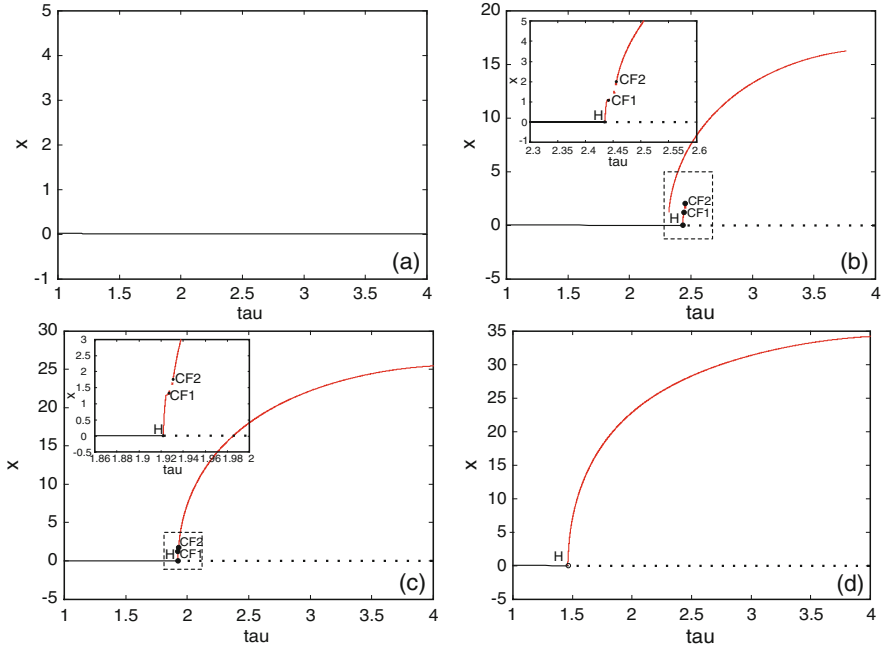


Fig. 2 The bifurcation diagrams of the dimensionless vibration displacement of cutting tool in x direction vs. delay time τ , with $\beta = 0.01$ and different values of α : (a) $\alpha = 0.1$, (b) $\alpha = 0.5$, (c) $\alpha = 1$, (d) $\alpha = 2$. The black solid line denotes stable trivial motion of the cutting tool, black dotted line denotes unstable trivial motion of the cutting tool, red solid line denotes stable periodic motion of the cutting tool, and red dotted line denotes unstable periodic motion of the cutting tool. H stands for Hopf bifurcation point, CF stands for cyclic fold bifurcation point

by H , CF refers to fold bifurcation point, and CH stands for chaos. In addition, black solid line denotes stable trivial motion of the cutting tool, black dotted line denotes unstable trivial motion of the cutting tool, red solid line denotes stable periodic motion of the cutting tool, and red dotted line denotes unstable periodic motion of the cutting tool.

It is quite evident from Fig. 2a that the response of the cutting tool is always stable while $\beta = 0.01$ and $\alpha = 0.1$, whereas when the value of α is 0.5, 1, and 2, the stable limit cycle emanates from the supercritical Hopf bifurcation points H ($H = 2.44$, 1.92, and 1.46 respectively) as shown in Fig. 2b-d, meaning that the cutting tool chatter vibration appears. In addition, in the neighborhood of the Hopf bifurcation point H , there are three branches: one is a stable trivial motion of the cutting tool at the left of the point H , one is an unstable trivial motion of the cutting tool at right of the point H , and one is a stable (and partial unstable) limit cycle motion of the cutting tool at the top right of the point H . It is clear that the position of the Hopf bifurcation point H is affected by the regenerative force. The Hopf bifurcation point H moves toward the left as α is increased, which indicated that the parameter range of tool stability response is also reduced. In other words, the cutting tool chatter

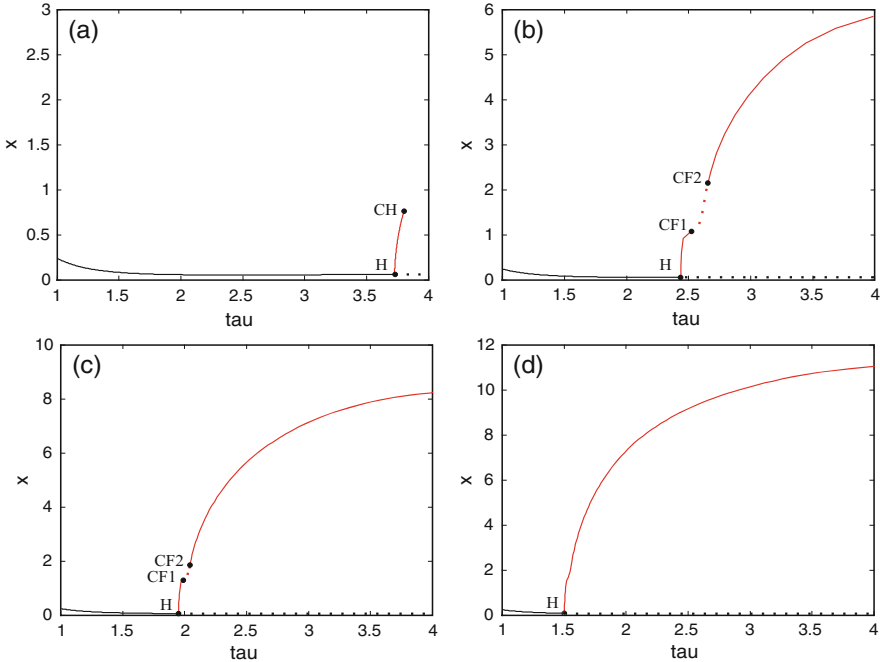


Fig. 3 The bifurcation diagrams of the dimensionless vibration displacement of cutting tool in x direction vs. delay time τ , with $\beta = 0.1$ and different values of α : (a) $\alpha = 0.1$, (b) $\alpha = 0.5$, (c) $\alpha = 1$, (d) $\alpha = 2$. The black solid line denotes stable trivial motion of the cutting tool, black dotted line denotes unstable trivial motion of the cutting tool, red solid line denotes stable periodic motion of the cutting tool, and red dotted line denotes unstable periodic motion of the cutting tool. H stands for Hopf bifurcation point, CF stands for cyclic fold bifurcation point, and CH stands for chaos

vibration is more likely to occur due to increase in regenerative force. Moreover, we also note that the amplitude of the limit cycle becomes larger while the regenerative force is increased.

It is obvious that there is another bifurcation point: cyclic fold bifurcation point (CF1 and CF2) in Fig. 2b, c, where CF1 is subcritical cyclic fold bifurcation point and CF2 is supercritical cyclic fold bifurcation point. The stability of the limit cycle is changed at the cyclic fold bifurcation point. At the same time, the amplitude of the limit cycle will change abruptly at the cyclic fold bifurcation point. This phenomenon has a great influence on the stability of the cutting process.

As shown in Fig. 3 while $\beta = 0.1$ and $\alpha = 0.1, 0.5, 1, 2$, respectively, the branches bifurcate from the supercritical Hopf bifurcation point H ($H = 3.73, 2.44, 1.95$, and 1.50), which indicates stable limit cycle of the response of the cutting tool. The branches expand to the upper left as α increases. This means the vibration amplitude of the cutting tool gradually increases and the chatter vibration happened earlier as the regenerative force increases (α increased from 0.1 to 2). In comparison with

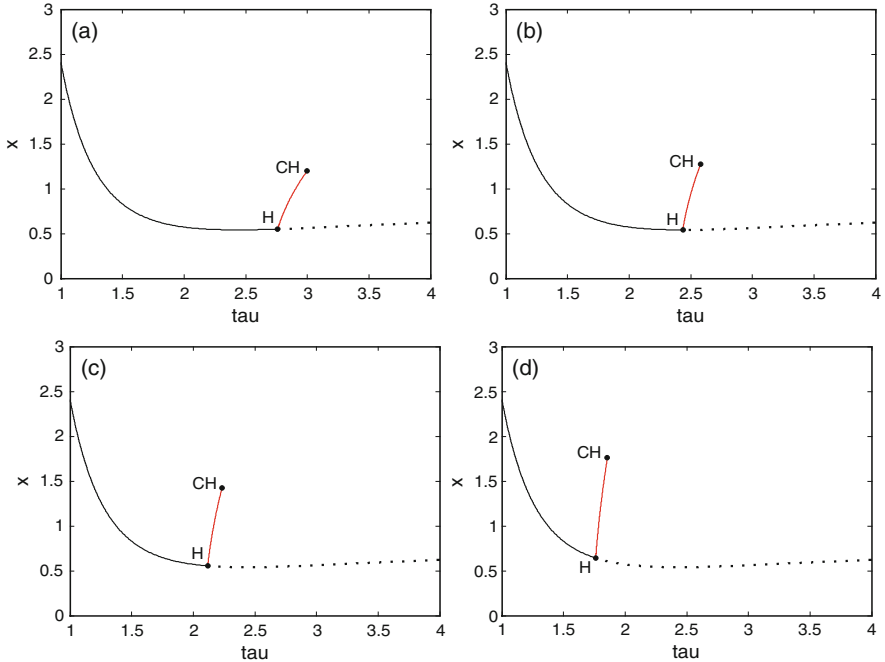


Fig. 4 The bifurcation diagrams of the dimensionless vibration displacement of cutting tool in x direction vs. delay time τ , with $\beta = 1$ and different values of α : **(a)** $\alpha = 0.1$, **(b)** $\alpha = 0.5$, **(c)** $\alpha = 1$, **(d)** $\alpha = 2$. The black solid line denotes stable trivial motion of the cutting tool, black dotted line denotes unstable trivial motion of the cutting tool, red solid line denotes stable periodic motion of the cutting tool, and red dotted line denotes unstable periodic motion of the cutting tool. H stands for Hopf bifurcation point, CH stands for chaos

Figs. 2b, c and 3b, c, there are also subcritical cyclic fold bifurcation point and supercritical cyclic fold bifurcation point.

Here is an interesting phenomenon that the stable trivial motion and the unstable trivial motion of the cutting tool begin to deviate from the equilibrium position while frictional force increases (β increased from 0.01 to 0.1), this phenomenon is more obvious especially when the time delay is relatively a small value. Moreover, in contrast to Fig. 2b-d, the structure of the bifurcation diagrams are very similar, but the vibration amplitude of the cutting tool in Fig. 3b-d decreases significantly with increasing frictional force. Especially, in Fig. 3a, when the time delay exceeds CH point, the response of the cutting tool appears chaotic vibration. Subsequently, it will be validated by numerical simulation method.

As can be observed in Fig. 4, while $\beta = 1$ and $\alpha = 0.1, 0.5, 1, 2$, respectively, the stable limit cycle of the response of the cutting tool bifurcates from different supercritical Hopf bifurcation points H (2.76, 2.43, 2.12, and 1.76). With the increase of regenerative force, the amplitude of the limit cycle increases rapidly, and the cutting tool response presents a chaotic vibration after CH point. In contrast to Figs. 2 and 3, the stable trivial motion and the unstable trivial motion of the cutting

tool is obviously deviated from the equilibrium position, similar to Fig. 3, especially when the time delay is relatively a small value. In addition, subcritical cyclic fold bifurcation point and supercritical cyclic fold bifurcation point in Figs. 2b, c and 3b, c do not appear in Fig. 3.

Compared with Figs. 2 and 3, the vibration amplitude of the cutting tool in Fig. 4 is further reduced due to the increase of frictional force. In addition, the range of the limit cycle branch is obviously reduced and the chaotic vibration of the cutting tool appears after the point CH.

In the following simulations, the largest Lyapunov exponent (LLE) and Poincaré section are used to analyze the dynamic motions of the cutting tool with the help of the numerical simulation method. The Poincaré section defined as those trajectories which pierce the hyper-surface $\dot{x} = 0$ at negative velocity of the tool in the three-dimensional space composed of $\{x, \dot{x}, x(t - \tau)\}$. For the case of $\beta = 0.1, \alpha = 0.1$ and $\beta = 1, \alpha = 0.1$ (Corresponding to Figs. 3a and 4a respectively), the LLE and Poincaré section of the tool dynamic response are shown in the Fig. 5. It can be found that LLE (Fig. 5a, b) are consistent with bifurcation diagrams (Figs. 3a and 4a). In addition, the Poincaré section (Fig. 5c, d) further confirms that the dynamic response of the tool is chaotic motion.

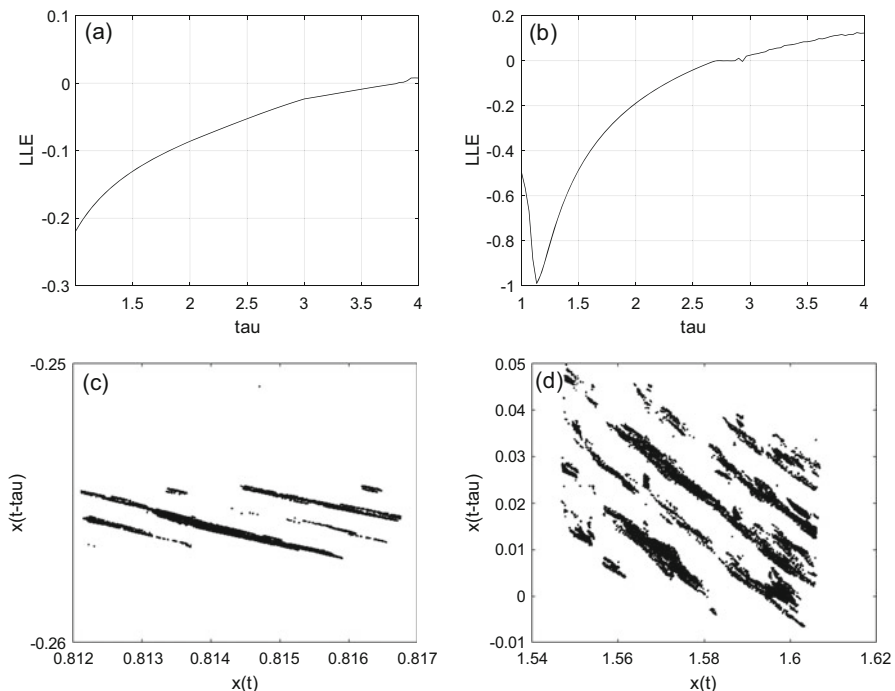


Fig. 5 The largest Lyapunov exponent (LLE) (a, b) and Poincaré section (c, d) of the dimensionless vibration displacement of cutting tool. (a) $\alpha = 0.1, \beta = 0.1$, (b) $\alpha = 0.1, \beta = 1$, (c) $\alpha = 0.1, \beta = 0.1, \tau = 4$, (d) $\alpha = 0.1, \beta = 1, \tau = 4$

4 Conclusions

In this chapter, a single-degree-of-freedom model for turning process is examined where the dynamic cutting force consists of frictional force and regenerative force. The influence of regenerative force and frictional force on the dynamic characteristics of cutting tool is analyzed by using bifurcation analysis and numerical simulation methods in this work. It can be found that regenerative force will induce chatter and large amplitude vibration, while frictional force can effectively suppress vibration amplitude; however, frictional force will cause the cutting tool to deviate from the original equilibrium position. Therefore, it is possible to suppress the chatter by reasonable control of frictional force in the cutting process.

Acknowledgments This research is supported by the National Natural Science Foundation of China (No. 11372122) and Science and Technology Program of Gansu Province of China (No. 1610RJYA020).

References

1. Davies, M.A., Pratt, J.R., Dutterer, B., Burns, T.J.: Stability prediction for low radial immersion milling. *J Manuf Sci Eng.* **124**(2), 217–225 (2002)
2. Insperger, T., Mann, B.P., Stepan, G., Bayly, P.V.: Stability of up-milling and down-milling, part 1: alternative analytical methods. *Int J Mach Tool Manuf.* **43**(1), 25–34 (2003)
3. Balachandran, B.: Nonlinear dynamics of milling processes. *Philos Transact A Math Phys Eng Sci.* **359**(1781), 793–819 (2001)
4. Schmitz, T.L.: Automatic trimming of machining stability lobes. *Int J Mach Tool Manuf.* **42**(13), 1479–1486 (2002)
5. Dombrovári, Z., Barton, D.A.W., Wilson, R.E., Stepan, G.: On the global dynamics of chatter in the orthogonal cutting model. *Int. J. Nonlinear Mech.* **46**(1), 330–338 (2011)
6. Wang, A., Jin, W., Wang, G., Li, X.: Analysis on dynamics of a cutting tool with the thermal distortion in turning process. *Nonlinear Dyn.* **2**, 1183–1191 (2016)
7. Wang, A., Jin, W., Chen, W., Feng, R., Xu, C.: Bifurcation and chaotic vibration of frictional chatter in turning process. *Adv Mech Eng.* **10**(4), 168781401877126 (2018)
8. Mann, B.P., Insperger, T., Bayly, P.V., Stépán, G.: Stability of up-milling and down-milling, part 2: experimental verification. *Int J Mach Tool Manuf.* **43**(1), 35–40 (2003)
9. Honeycutt, A., Schmitz, T.: A numerical and experimental investigation of period-n bifurcations in milling. *J. Manuf. Sci. Eng.* **139**(1), 011003-1-011003-11 (2017)
10. Rusinek, R., Kecik, K., Warminski, J., Weremczuk, A.: Dynamic model of cutting process with modulated spindle speed. *Am. Inst. Phys. Conf. Ser.* **1493**, 805–809 (2012)
11. Weremczuk, A., Rusinek, R.: Influence of frictional mechanism on chatter vibrations in the cutting process—analytical approach. *Int J Adv Manuf Technol.* **89**, 2837–2844 (2016)
12. Awrejcewicz, J.: Chaos in simple mechanical systems with friction. *J Sound Vib.* **109**(1), 178–180 (1986)
13. Awrejcewicz, J.: Analysis of self-excited vibration in mechanical system with four degrees of freedom. *Sci. Bull. Lodz Tech. Univ.* **72**, 5–27 (1987)
14. Awrejcewicz, J.: Chaotic motion in a nonlinear oscillator with friction. *J. Mech. Sci. Technol.* **2**(2), 104–109 (1988)

15. Awrejcewicz, J.: A route to chaos in a nonlinear oscillator with delay. *Acta Mech.* **77**(1–2), 111–120 (1989)
16. Awrejcewicz, J., Wojewoda, J.: Observation of chaos in a nonlinear oscillator with delay: a numerical study. *KSME J.* **3**(1), 15 (1989)
17. Robert, S.: Knut: a continuation and bifurcation software for delay-differential equations. <http://gitorious.org/knut> (2005–2013)

Noise-Induced Transitions and Resonances in a Delayed Triple-Well Potential System



Yanfei Jin and Pengfei Xu

Abstract The noise-induced transitions and resonances are studied in a delayed triple-well potential system driven by correlated Gaussian white noises and a harmonic signal. The analytical expressions for the stationary probability density (SPD) and the spectral amplification (SA) are derived by using the small time delay approximation and the linear response theory. The results show rich transition and resonance phenomena. It is found that the time delay induces an occurrence of the transitions of the system. Both the reentrance phenomena in noise-induced transitions and the double stochastic resonance (SR) are observed when the multiplicative and additive noises are correlated. Under the condition of large noise intensity, the noise-induced resonance effect can be enhanced with the assistance of the cross-correlation between noises. Moreover, the noise-induced resonance phenomenon notably depends on the cooperative effects of time delay and correlated noises. The appropriate choice of noise intensities and time delay can improve the response of the system to an external forcing.

Keywords Noise-induced transition and resonance · Correlated noises · Time delay

1 Introduction

Numerous physical systems are associated with random fluctuating environment or noise, which is usually considered as a source of disorder and chaos. In some circum-

Y. Jin (✉)

Department of Mechanics, Beijing Institute of Technology, Beijing, China
e-mail: jinyf@bit.edu.cn

P. Xu

Department of Mechanics, Beijing Institute of Technology, Beijing, China
Department of Mathematics, Changzhi University, Changzhi, China

stance, noise may play a constructive role and induce new ordering phenomena, such as noise-induced transition [1], noise enhanced stability [2], resonant activation [3], and stochastic and coherence resonances (SR and CR) [4]. These counterintuitive phenomena attracted the interests of people and have been extensively investigated in theory and applications [5, 6]. However, the majority of works on noise-induced transition and resonance considered bi-stable and mono-stable systems, only a few publications involved multi-stable systems [7, 8]. Nicolis [7] extended the theory of SR to explain noise-induced transitions between an initial and a final stable state in multi-stable systems. Xu et al. [8] studied the SR in multi-stable coupled systems subjected to two different driving signals. They observed the stochastic multi-resonance phenomenon in the subsystem driven by low frequency signal. Moreover, time delays always exist and play an important role in physics [9], biology [10], and engineering [11]. Especially, the combined effects of both noise and time delay are necessary to consider in the modeling of the practical dynamical systems [12–15]. For example, Frank [12] studied the nonlinear stochastic systems with time-delayed feedback by using the approximate Fokker–Planck method. Jin [13, 14] explored the effects of noise on the delay-independent stability and noise-induced resonances in the time-delayed systems. To the best knowledge of authors, less attention has been paid to the nonlinear dynamics of the delayed multi-stable system with correlated noises.

In Ref. [15], a general nonlinear dynamical system that contains time-delayed feedback and noise are proposed as follows:

$$\dot{x}(t) = f(x(t), x(t - \tau)) + \varepsilon \sin(\omega t) + x(t)\xi(t) + \eta(t), \quad (1)$$

where τ is the time delay, ε and ω represent the amplitude and the frequency of a harmonic signal, respectively. The multiplicative noise $\xi(t)$ and additive noise $\eta(t)$ are cross-correlated Gaussian white noises with zero mean and Dirac correlation functions, which are characterized as follows:

$$\begin{aligned} \langle \xi(t)\xi(t') \rangle &= 2D\delta(t - t'), & \langle \eta(t)\eta(t') \rangle &= 2Q\delta(t - t'), \\ \langle \xi(t)\eta(t') \rangle &= \langle \xi(t')\eta(t) \rangle = 2\lambda\sqrt{DQ}\delta(t - t'). \end{aligned} \quad (2)$$

where D and Q are the multiplicative and additive noise intensity, respectively. λ is the cross-correlation strength between multiplicative and additive noises.

The triple-well potential systems can model many real systems and have many applications in various fields, such as parallel reaction [16], quantum mechanics [17], and energy harvesting [18]. Particularly, a triple-well potential is found to improve the broadband performance of energy harvesting. Thus, the delayed nonlinear function has taken the following form, i.e., $f(x, x_\tau) = ax_\tau^5 - b(1+c)x^3 + cx$, where a , b , and c are the parameters of the potential function. The triple-well potential function corresponding to Eq. (1) has three stable states s_i ($i = 1, 2, 3$) and two unstable states u_j ($j = 1, 2$) for fixed $a = 1/30$, $b = 1/5$, and $c = 3/10$.

The chapter is organized as follows. In Sect. 2, the stationary probability density (SPD) is obtained through the Fokker–Planck equation with small time delay. The phase diagram of the system is plotted to indicate the noise-induced transition. Section 3 is devoted to derive the spectral amplification to characterize noise-induced resonance. Finally, some conclusions are drawn in Sect. 4.

2 Noise-Induced Transition

Using the small time delay approximation proposed in Ref. [19], the Fokker–Planck equation corresponding to Eq. (1) with Eq. (2) can be derived as follows:

$$\frac{\partial}{\partial t} p(x, t) = \left\{ -\frac{\partial}{\partial x} \left[\alpha(x) + \beta(x) \frac{d\beta(x)}{dx} \right] + \frac{\partial^2}{\partial x^2} \beta^2(x) \right\} p(x, t), \quad (3)$$

where

$$\alpha(x) = [-ax^5 + b(1+h)x^3 - hx + \varepsilon \sin(\omega t)] (1 + 5a\tau x^4),$$

$$\beta(x) = [Dx^2 + 2\lambda(DQ)^{1/2}x + Q]^{1/2} (1 + 5a\tau x^4).$$

Setting the left-side of Eq. (3) to zero leads to the following quasi SPD:

$$p_{st}(x) = N\beta(x)^{-1} \exp \left[-D^{-1} \tilde{V}(x, t) \right], \quad (4)$$

where N is the normalization constant. The modified potential $\tilde{V}(x, t)$ is derived as

$$\tilde{V}(x, t) = -D \int [\alpha(x)/\beta^2(x)] dx = V_0(x) - \varepsilon g(x) \sin(\omega t), \quad (5)$$

with

$$V_0(x) = \int^x [au^5 - b(1+h)u^3 + hu] \left[(u^2 + 2\lambda\sqrt{R}u + R)(1 + 5a\tau u^4) \right]^{-1} du,$$

$$g(x) = \int^x \left[(u^2 + 2\lambda\sqrt{R}u + R)(1 + 5a\tau u^4) \right]^{-1} du,$$

where $R = Q/D$ is the noise intensity ratio.

The extrema of SPD (4) are determined by the following equation:

$$\alpha(x) - \beta(x) \frac{d\beta(x)}{dx} = 0. \quad (6)$$

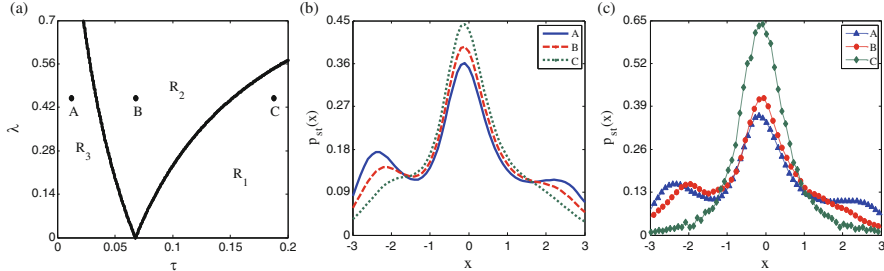


Fig. 1 (a) Phase diagram of the system. R_1 denotes the mono-stable one, R_2 the bi-stable one, and R_3 the tri-stable phase. The representative points A, B, C are marked in each region. (b) The SPD (4) about the points A, B, C are shown, respectively. (c) The results of Monte Carlo simulations are presented. Other parameters are chosen as $D = 0.11$ and $Q = 0.12$

According to Eqs. (4) and (6), the phase diagram and the SPD are plotted in Fig. 1 for observations of phase transitions. The cross-correlation strength between multiplicative and additive noises λ as a function of time delay τ is shown in Fig. 1a. The phase diagram makes it apparent that for fixed value of λ and for small values of τ , the system is found in the tri-stable phase. After increasing τ beyond some threshold values, the system undergoes a transition to a bi-stable phase. With further increasing τ , the system finally reaches a mono-stable phase in the range $0 < \lambda < 0.57$. That is, the system undergoes a succession of two delay-induced transitions. For example, these points A, B, C (see Fig. 1a) correspond to a path of a succession of two transitions. In order to verify the transitions predicted in the phase diagram, the SPD of the points A, B, C are presented in Fig. 1b. It is seen that the right-side peak disappears first and then the left-side peak disappears with an increase in τ . The reason is that the cross-correlation between noises leads to a symmetry-breaking effect on the SPD. However, the symmetry-breaking effect for small λ is suppressed by the increasing time delay. As a result, there is a single peak in SPD for large time delay. It also indicates that the system can jump easily from the left or right potential well to the middle one with the assistance of time delay, but it is difficult for it to return back to the two lateral potential wells. Meanwhile, the Monte Carlo simulations (MCS) of SPD are performed from original system (1) in Fig. 1c. It is obvious that the MCS confirms the effectiveness of the theoretical analyses obtained in Fig. 1a, b.

The cooperative effects of multiplicative noise intensity D and additive noise intensity Q on the transition phenomenon are analyzed for different values of cross-correlation strength λ in Fig. 2. It is clearly observed from Fig. 2a that for fixed small λ and for any value of Q , an increasing D leads to a transition from the tri-stable phase to a bi-stable one and then to a mono-stable one. However, as λ increases from 0.2 up to 0.8, the reentrance phenomena in noise-induced transitions occur in Fig. 2b. For example, the horizontal line makes it apparent that, for some regions of values of additive noise intensity ($0.62 < Q < 1$) and for zero and small values of D , the system is found in a tri-stable phase. With the increment of D , the system toggles

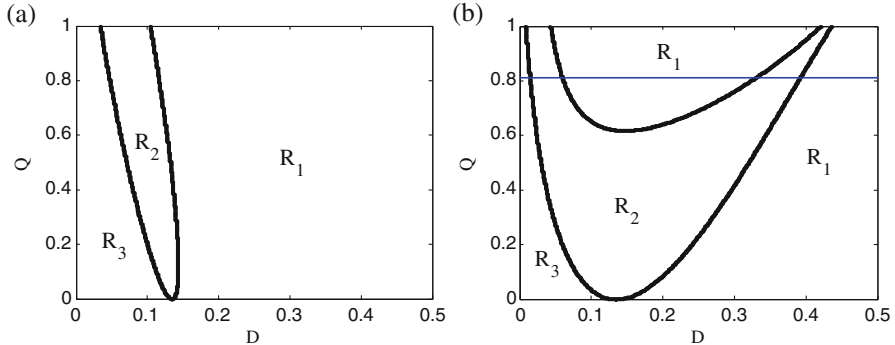


Fig. 2 Phase diagram with fixed $\tau = 0.05$ for different values of (a) $\lambda = 0.2$ and (b) $\lambda = 0.8$. R_1 denotes the mono-stable one, R_2 the bi-stable one, and R_3 the tri-stable phase. Note the horizontal line in (b) implying an occurrence of reentrance phenomena

into the bi-stable region immediately. Then, after D is increased beyond some threshold values, the system undergoes a transition from the bi-stable phase to a mono-stable one. However, if one further increases the multiplicative noise intensity, the system goes back to the bi-stable phase first and then to a mono-stable one again. Namely, the system undergoes a succession of two noise-induced reentrant transitions. Since the noise correlation strongly affects the stationary probability distribution of the system. The multiplicative and additive noises play different roles in the transition of the system. Thus, the reentrance phenomena in noise-induced transitions are quite sensitive to the correlated noises in the triple-well potential system.

3 Noise-Induced Resonance

In the adiabatic limit, Eq. (3) can be mapped into a discrete-state Markov process describing the transfer of probability masses $p_i(i = 1, 2, 3)$ between the attraction basins of the stable states s_i . The corresponding kinetic equation is written as

$$\dot{\mathbf{P}} = \mathbf{WP}, \quad (7)$$

where $\mathbf{P} = (p_1 \ p_2 \ p_3)^T$ and the superscript T denotes the transpose of matrix. The transfer matrix \mathbf{W} has the following form:

$$\mathbf{W} = \begin{pmatrix} -W_{1,2} & W_{2,1} & 0 \\ W_{1,2} & -(W_{2,1} + W_{2,3}) & W_{3,2} \\ 0 & W_{2,3} & -W_{3,2} \end{pmatrix}. \quad (8)$$

Here the individual transition rates in Eq. (8) are calculated from Eq. (5) by Kramers' formula [5]:

$$W_{m,m+1} = (2\pi)^{-1} \sqrt{V_0''(s_m) | v |} \exp \left\{ D^{-1} \left[\tilde{V}(s_m) - \tilde{V}(u_m) \right] \right\}, \quad (m = 1, 2),$$

$$W_{n,n-1} = (2\pi)^{-1} \sqrt{V_0''(s_n) | V_0''(u_{n-1}) |} \exp \left\{ D^{-1} \left[\tilde{V}(s_n) - \tilde{V}(u_{n-1}) \right] \right\}, \quad (n=2, 3).$$

Expanding the ε -dependent terms in Eq. (7) and remaining the first nontrivial order can lead to the following equations:

$$\Delta \dot{\mathbf{P}} = \mathbf{W}^{(0)} \Delta \mathbf{P} + \boldsymbol{\varphi}^{(0)} \sin(\omega t), \quad (9)$$

where $\mathbf{P} = \mathbf{P}^{(0)} + \varepsilon \Delta \mathbf{P}$ and $\mathbf{W} = \mathbf{W}^{(0)} + \varepsilon \Delta \mathbf{W}$. According to Eq. (7), the time-dependent average response to an external weak periodic forcing can be obtained as

$$\langle x(t) | x_0, t_0 \rangle = \int x P(x, t | x_0, t_0) dx, \quad (10)$$

with $P(x, t | x_0, t_0) = \sum_{i=1}^3 p_i(t) \delta(x - s_i)$. By substituting the asymptotic response $\Delta p_i = A_i \sin(\omega t + \psi_i)$ in Eq. (9) into Eq. (10), the average response in the long time limit is of the following forms:

$$\langle x(t) \rangle_{\text{as}} = \lim_{t_0 \rightarrow -\infty} \langle x(t) | x_0, t_0 \rangle = \sum_{i=1}^3 s_i \left[p_i^{(0)} + \varepsilon_0 A_i \sin(\omega t + \psi_i) \right], \quad (11)$$

where $A_i = \sqrt{\mu_i^2 + \nu_i^2}$ and $\psi_i = \arctan(\nu_i/\mu_i)$. The analytical expressions of the elements μ_i and ν_i can be derived from Eq. (9) as follows:

$$\mu_i = - \sum_{k=1}^3 (\gamma_k a_k \xi_{k,i}) / (\gamma_k^2 + \omega^2), \quad \nu_i = - \sum_{k=1}^3 (\omega a_k \xi_{k,i}) / (\gamma_k^2 + \omega^2),$$

where γ_k and ξ_k are the eigenvalues and eigenvectors of $\mathbf{W}^{(0)}$ in Eq. (9). The $\boldsymbol{\varphi}^{(0)}$ of Eq. (9) is expanded as $\boldsymbol{\varphi}^{(0)} = \sum_{k=1}^3 a_k \xi_k$.

As an important candidate commonly used for characterizing the nature of noise-induced resonance, the spectral amplification (SA) can be obtained from Eq. (11):

$$\eta_1 = \sum_{j=1}^3 (s_j A_j)^2 + 2s_1 s_2 A_1 A_2 \cos(\theta_1) + 2s_3 A_3 \cos(\theta_2) \Lambda, \quad (12)$$

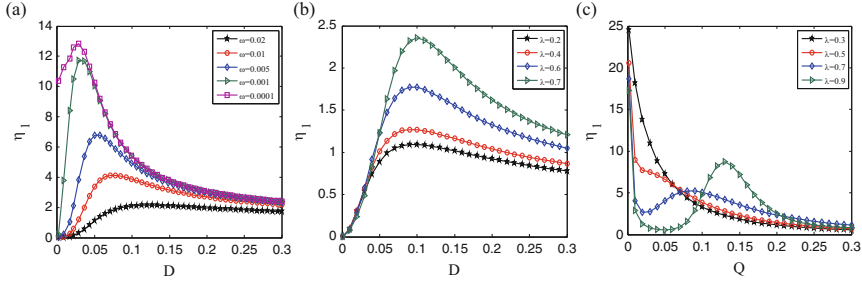


Fig. 3 The effects of driving frequency ω and cross-correlation strength λ on spectral amplification η_1 with fixed $\tau = 0.05$. (a) η_1 versus D with $\lambda = 0.5$, $Q = 0.1$, and different ω . (b) η_1 versus D with $\omega = 0.01$, $Q = 0.2$, and different λ . (c) η_1 versus Q with $\omega = 0.01$, $D = 0.1$, and different λ

where

$$\Lambda = \sqrt{(s_1 A_1)^2 + 2s_1 s_2 A_1 A_2 \cos(\theta_1) + (s_2 A_2)^2}, \quad \theta_1 = \psi_2 - \psi_1,$$

$$\theta_2 = \psi_3 - \psi_1 - \kappa_1, \quad \kappa_1 = \arctan \{ [s_2 A_2 \sin(\theta_1)] / [s_1 A_1 + s_2 A_2 \cos(\theta_1)] \}.$$

According to Eq. (12), the dependence of SA η_1 on the driving frequency ω is analyzed in Fig. 3a. It is seen from Fig. 3a that there is a single peak in these curves. This is a typical phenomenon of stochastic resonance (SR). As ω is decreased, the peak value increases obviously and the optimal noise intensity for resonance decreases. In fact, the height of the peak can reach a finite limiting value as ω tends to zero. In other words, the increasing frequency can weaken the effect of resonance and suppress the role of noise in this system. The reason for this phenomenon is that if the driving frequency is much higher than the inverse of the system's intrinsic time scales, the response of the system to a harmonic signal can be weakened or even vanish. In Fig. 3b, the variation of η_1 versus D is presented with different values of cross-correlation strength λ . It is found that the height of resonant peak ascends while the position of the peak keeps almost invariable with the enlargement of λ . Namely, the resonance effect is enhanced with increasing λ at the fixed optimal noise intensity ($Q = 0.2$), the system has sufficient energy to cross the potential barrier and hop among the three wells back and forth in accordance with the harmonic signal. The cross-correlation between noises plays a positive role in the enhancement of SR. Moreover, for $D = 0.1$ and small values of λ in Fig. 3c, η_1 decreases monotonously with an increase in Q and the noise-induced resonance disappears. However, when λ becomes sufficiently large (e.g., $\lambda \geq 0.7$), the curve of η_1 exhibits a suppression first and then a typical resonance with pronounced peak. The SR effect can be improved as the cross-correlation strength is further increased.

The effect of time delay τ on SA η_1 is shown in Fig. 4. It is found from Fig. 4a that these curves present a double-peak characteristic, which is called the double SR phenomena. The reason behind this observation is that the correlated noises cause the symmetry breaking of the system (see Fig. 1). The system driven by weak noise

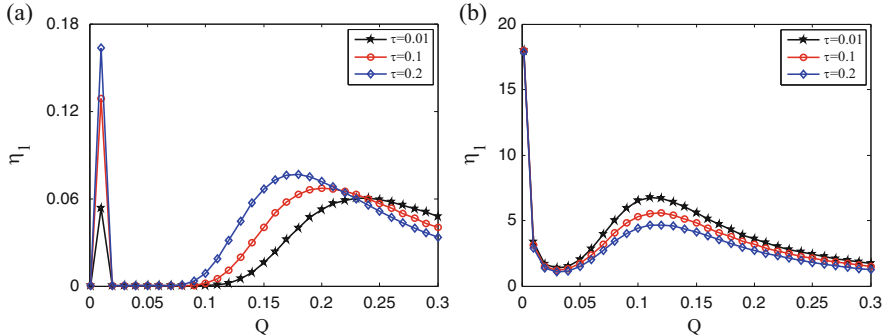


Fig. 4 Spectral amplification η_1 versus additive noise intensity Q for different values of time delay τ . Other parameters are chosen as $\omega = 0.01$, $\lambda = 0.8$, (a) $D = 0.01$ and (b) $D = 0.1$

($D = 0.01$) can continuously jump between one side well and middle well. As a result, the noise-induced resonance between two adjacent wells occurs. With the further increase of Q , the system has sufficient energy to induce the transition of the resonance from two adjacent wells to two lateral wells. So, the double SR can be observed in the triple-well potential subjected to correlated noises. Interestingly, the heights of the two peaks are both increased with an increase in τ , and the position of the right-side peak is shifted toward the direction of decreasing Q . It implies that the presence of time delay enhances the role of additive noise in the noise-induced resonance and improves the response of the system when multiplicative noise intensity is sufficiently weak. Then, when the multiplicative noise intensity becomes large (e.g., $D = 0.1$ in Fig. 4b), there is a single peak in the curve of η_1 . On the contrary, the peak value is decreased and the optimal noise intensity of resonance remains almost unchanged with an increase in τ . In short, the noise-induced resonances are closely related to the cooperative effects of time delay and correlated noises.

4 Conclusions

In this work, the phenomena of noise-induced transition and resonance are investigated in a delayed triple-well potential subjected to correlated noises. The phenomena of reentrant transitions and double SR can occur when the two noises have the cross-correlation. With increasing cross-correlation strength, the SR effect is improved. Besides, the noise-induced resonance can be controlled, i.e., either enhanced or suppressed, for various values of the intensity of correlated noises by choosing the proper time delay.

Acknowledgment This work was supported by the National Natural Science Foundation of China under Grant No. 11772048.

References

1. Castro, F., Sanchez, A.D., Wio, H.S.: Reentrance phenomena in noise induced transitions. *Phys. Rev. Lett.* **75**, 1691–1694 (1995)
2. Xu, P.F., Jin, Y.F.: Mean first-passage time in a delayed tristable system driven by correlated multiplicative and additive white noises. *Chaos Solitons Fractals*. **112**, 75–82 (2018)
3. Doering, C.R., Gadoua, J.C.: Resonant activation over a fluctuating barrier. *Phys. Rev. Lett.* **69**, 2318 (1992)
4. Jin, Y.F., Ma, Z.M., Xiao, S.M.: Coherence and stochastic resonance in a periodic potential driven by multiplicative dichotomous and additive white noise. *Chaos Solitons Fractals*. **103**, 470–475 (2017)
5. Gammaitoni, L., Hänggi, P., Jung, P., Marchesoni, F.: Stochastic resonance. *Rev. Mod. Phys.* **70**, 224–283 (1998)
6. Grigoriu, M., Field Jr., R.V.: A method for analysis of linear dynamic systems driven by stationary non-Gaussian noise with applications to turbulence-induced random vibration. *App. Math. Model.* **38**, 336–354 (2014)
7. Nicolis, C.: Stochastic resonance in multistable systems: the role of intermediate states. *Phys. Rev. E* **82**, 011139 (2010)
8. Xu, P.F., Jin, Y.F.: Stochastic resonance in multi-stable coupled systems driven by two driving signals. *Phys. A* **492**, 1281–1289 (2018)
9. Jin, Y.F., Hu, H.Y.: Coherence and stochastic resonance in a delayed bistable system. *Phys. A* **382**, 423–429 (2007)
10. Vasilakos, K., Beuter, A.: Effect of noise on a delayed visual feedback system. *J. Theor. Biol.* **165**, 389–407 (1993)
11. Hu, H.Y., Dowell, E.H., Virgin, L.N.: Resonances of a harmonically forced duffing oscillator with time delay state feedback. *Nonlinear Dyn.* **15**, 311–327 (1998)
12. Frank, T.D.: Delay Fokker-Planck equations, perturbation theory, and data analysis for nonlinear stochastic systems with time delays. *Phys. Rev. E* **71**, 031106 (2005)
13. Jin, Y.F.: Noise-induced dynamics in a delayed bistable system with correlated noises. *Phys. A* **391**, 1928–1933 (2012)
14. Jin, Y.F.: Delay-independent stability of moments of a linear oscillator with delayed state feedback and parametric white noise. *Probab. Eng. Mech.* **41**, 115–120 (2015)
15. Wu, D., Zhu, S.Q.: Stochastic resonance in a bistable system with time-delayed feedback and non-Gaussian noise. *Phys. Lett. A* **363**, 202–212 (2007)
16. Ghosh, P.K., Bag, B.C., Ray, D.S.: Noise correlation-induced splitting of Kramers' escape rate from a metastable state. *J. Chem. Phys.* **127**, 044510 (2007)
17. ABerezovoj, V.P., Konchatnij, M.I., Nurmagambetov, A.J.: Tunneling dynamics in exactly solvable models with triple-well potentials. *J. Phys. A* **46**, 065302 (2013)
18. Panyam, M., Daqaq, M.F.: Characterizing the effective bandwidth of tri-stable energy harvesters. *J. Sound Vib.* **386**, 336–358 (2017)
19. Guillouzic, S., L'Heureux, I., Longtin, A.: Small delay approximation of stochastic delay differential equations. *Phys. Rev. E* **59**, 3970–3982 (1999)

Application of the Second Dimension Reduction Method in Nonlinear Rotor Dynamic System



Kuan Lu, Haopeng Zhang, Hao Zhou, Yulin Jin, Yongfeng Yang, and Chao Fu

Abstract The second dimension reduction method is proposed based on component mode synthesis (CMS) and proper orthogonal decomposition (POD) in this chapter. The dual rotor-bearing model is established by finite element (FE) method. The efficiency of the proposed second dimension reduction method is verified via comparing with the dynamical behaviors (frequency spectrum and axis orbit) of the first model dimension reduction (MDR) and second MDR based on mode expansion. The proposed second dimension reduction method can provide perfect connection between actual rotor system and qualitative analysis of the reduced system.

Keywords Second dimension reduction · Component mode synthesis method · POD method · Dynamical behaviors · Rotor system

1 Introduction

Dimension reduction of high-dimensional systems have become one central issue of concerns in nonlinear dynamics, attracting the attention of researchers in many actual engineering areas. A series of dimension reduction methods are summarized in Ref. [1]. The common dimension reduction methods include center manifold method, Lyapunov–Schmidt method, Galerkin method, CMS method, POD method, etc. [2]. The POD method is widely used for dimension reduction of high-dimensional rotor systems.

K. Lu (✉) · H. Zhang · H. Zhou · Y. Yang · C. Fu

Institute of Vibration Engineering, Northwestern Polytechnical University, Xi'an, P. R. China

MIIT Key Laboratory of Dynamics and Control of Complex Systems, Northwestern Polytechnical University, Xi'an, P. R. China
e-mail: lukuan@nwpu.edu.cn

Y. Jin

School of Aeronautics and Astronautics, Sichuan University, Chengdu, P. R. China

POD is an efficient method for data analysis aimed at obtaining low-order modes of the original system. The POD method could be applied to reduce the dimension of the rotor-bearing system, so that to study the qualitative properties of the reduced system in detail [3]. The transient POD (TPOD) method was proposed based on the inertial manifold method, and a 23-degrees-of-freedom (DOF) rotor system model is reduced to a 2-DOFs one [4]. The TPOD method was generalized to the rotor system supported by sliding bearing with looseness fault at one end and both ends [5]. The efficiency of the TPOD method was verified via comparing with the structure order reduction (SOR) method [6]. The rotor systems in the previous research are not actual; most cases are theoretical models. POD method is difficult to study the super-multiple degrees-of-freedom (DOF) actual rotor systems directly, the calculation amount is very huge and the DOF of the reduced system is also difficult to confirm. Therefore, the second dimension reduction method should be proposed, an appropriate method should be used for first dimension reduction, and the POD method is applied for second dimension reduction.

CMS method is an efficient dimension reduction method, the essence of the CMS method is a classical Galerkin method, which can be widely applied for model dimension reduction (MDR) of large complex structure system [7]. Bathe presented an approach to improve CMS solutions using subspace iterations to obtain frequency and mode shape predictions of controlled accuracy [8]. Krattiger and Hussein [9] presented a mode synthesis method for fast band-structure calculations that is generally applicable to problems of the elastic wave propagation in periodic media.

Disadvantages of the CMS and POD methods usually exist in the theoretical analysis of dynamics and actual dynamical system. Although the CMS method is suitable for processing the dimension reduction problems of large complex structures, e.g., the rotor systems, this method is mainly used for mode reduction of linear sub-structures. The high order and local modes of the system are neglected, and the error of MDR may be very large [10]. Meanwhile, the dimension of the reduced system obtained by the CMS method is still very high, the qualitative analysis is difficult, especially for the nonlinear rotor systems. Generally speaking, the CMS method can dispose actual rotor system models, and the nonlinear dynamics analysis of the reduced systems is still difficult; the POD method fits very well for the simple rotor system models, and the theory of the reduced systems is convenient, but the rotor system model is not actual. The PDE dynamics systems established by Hamilton principle instead of Lagrange approach can reflect the dynamical behaviors of the physical model better [11, 12]. The rotating shaft of the aero-engine is thick and short, the stiffness is large, and deformation is small. In this chapter, the Timoshenko beam element model is used, bending and shear deformation of the beam are considered. Hence, the model in this chapter is approximately equivalent to the dynamical model of PDE condition based on small deformation.

The motivation of this chapter is to propose the second dimension reduction method based on the CMS and POD method. In Sect. 2, a finite element model of

cylindrical shell-conical shell dual-rotor-bearing system is established. In Sect. 3, the basic theory and general process of the component mode synthesis are introduced. The second dimension reduction process based on the POD method is highlighted in Sect. 4. The efficiency of the proposed method is verified via comparing with the frequency–amplitude curve and displacement responses of the first dimension reduction and second dimension reduction method in Sect. 5.

2 Finite Element Model of Dual Rotor-Bearing System

The structure of the actual aero-engine rotor is very complex. As shown in Figs. 1 and 2, the complex geometry dual rotor-bearing system of an aero-engine turbine will be simplified as cylindrical shell-conical shell-wheel disc combined rotor structure so that to study the vibration problems of the rotor system more accurately. Consider that all levels of compressor of high pressure (HP) and low pressure (LP) rotor are geometrically neat with uniform material. The FE method [13] is used to discretize rotating shaft into several beam elements. Each supporting bearing

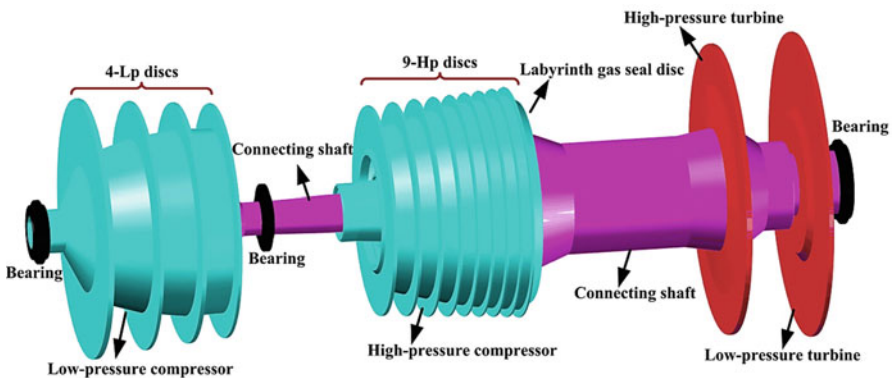


Fig. 1 A complex geometry dual rotor-bearing system of an aero-engine turbine

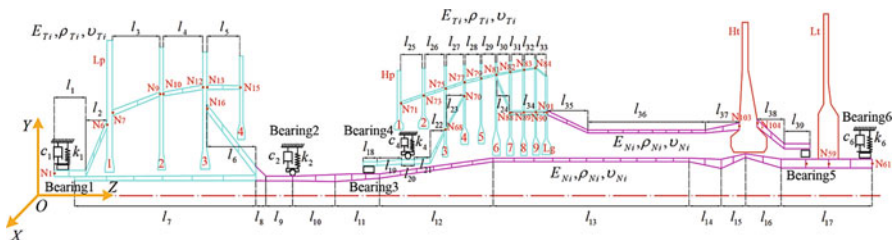


Fig. 2 Dynamics model of cylindrical-conical shaft element-disc-dual rotors with six supporting rolling element bearings

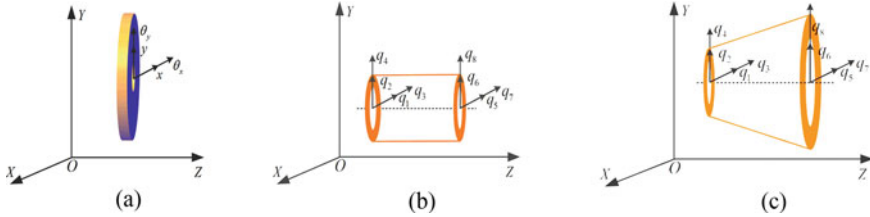


Fig. 3 Three types of beam finite elements. (a) Rigid disc element, (b) cylindrical shaft beam element, (c) conical shaft beam element

locates at the corresponding node position. The disc is considered to be rigid, centroid locates at the corresponding node, the elastic deformation of bearing in radial direction is considered, then a dynamical system model of cylindrical shell-conical shell dual rotor-bearing system can be established.

As shown in Fig. 3, the HP and LP rotors are divided into two kinds of units: conical shell and cylindrical shell when the FE method is used to establish the model. The LP rotor is divided into 39 units (41 nodes), two units of the nodes 3, 4 and 17, 18 are parallel, nodes 11 and 13 are parallel. Nodes 1, 23, 41 connect with Number 1, 2, 6 bearings. Nodes 25 and 39 connect with HP rotor via inter-shaft bearing, 1–4 level wheel discs of LP compressor and LP turbine disc locate at nodes 7, 9, 11, 13, 40, respectively. HP rotor is divided into 27 units (29 nodes), nodes 42 and 70 support at number 3 and 5 inter-shaft bearing, node 43 connects with number 4 bearing. Two units of the nodes 45, 46 and 49, 50 are parallel, each unit of nodes 52–56, 52, 57–60 is in parallel. 1–9 level wheel discs of HP compressor and HP turbine disc locate at nodes 47–55 and 67, respectively. Number 2 and 4 bearings are angular contact bearings, and others are rolling bearings.

Figure 3a shows the cone shaft unit, each unit contains two nodes, and each node contains four degrees of freedom (DOF). $\mathbf{q}_L = [q_1, q_2, q_3, q_4]^T$ represents the displacement and intersection angle of two directions of the left node, $\mathbf{q}_R = [q_5, q_6, q_7, q_8]^T$ represents those of the right node, r_{Li} , r_{Lo} are the inner and outer radius of unit left end face, r_{Ri} , r_{Ro} are those of unit right end face.

Shear deformation coefficient of variable section element φ_s is the function of unit length. For convenience, shear deformation coefficient of cone cell is considered to be constant, which can be expressed as

$$\varphi_s = \frac{12EI_m\chi}{GA_m l^2} \quad (1)$$

$$\text{where } I_m = \frac{\pi}{4} (r_{mo}^4 - r_{mi}^4), \quad A_m = \pi (r_{mo}^2 - r_{mi}^2), \quad \chi = \frac{7+6\mu}{6(1+\mu)} \left[1 + \frac{20+12\mu}{7+6\mu} \left(\frac{r_{mo}r_{mi}}{r_{mo}^2 + r_{mi}^2} \right)^2 \right],$$

$$r_{mo} = \sqrt{\frac{1}{2} (r_{Lo}^2 + r_{Ro}^2)}, \quad r_{mi} = \sqrt{\frac{1}{2} (r_{Li}^2 + r_{Ri}^2)}. \quad E, G, \text{ and } \nu \text{ are elastic modulus, shear modulus, and Poisson ratio, respectively.}$$

For the convenience of derivation, sectional area $A(\xi)$, cross-sectional moment of inertia $I(\xi)$, polar moment of inertia of unit length $I_p(\xi)$, and the moment of inertia in diameter $I_d(\xi)$ are represented by section position function $\xi = \frac{s}{l}$, see details in Eq. (2).

$$\begin{aligned} A(\xi) &= A_L(1 + \alpha_1\xi + \beta_1\xi^2), & I(\xi) &= I_L(1 + \alpha_2\xi + \beta_2\xi^2 + \gamma_2\xi^3 + \delta_2\xi^4), \\ I_p(\xi) &= \frac{\pi\rho}{2}(r_o^4 - r_i^4) = 2\rho I(\xi), & I_d(\xi) &= \frac{1}{2}I_p(\xi) = \rho I(\xi) \end{aligned} \quad (2)$$

where A_L , I_L are sectional area and cross sectional moment of inertia of left end, ρ is unit material density, l is unit length, other parameters are shown in Appendix.

The dynamical equation of cone cell versus fixed coordinate system can be obtained via Lagrange equation as follows:

$$(\mathbf{M}_T^e + \mathbf{M}_R^e)\ddot{\mathbf{q}}_e - \omega\mathbf{G}^e\dot{\mathbf{q}}_e + \mathbf{K}_B^e\mathbf{q}_e = \mathbf{F}_e \quad (3)$$

where $\mathbf{q}_e = [q_1, \dots, q_8]^T$ is unit generalized coordinate, \mathbf{M}_T^e and \mathbf{M}_R^e are unit mass and matrix and mass inertia matrix, \mathbf{G}^e is unit gyroscopic matrix, \mathbf{K}_B^e is unit stiffness matrix, \mathbf{F}_e is generalized external force vector, ω is angular frequency.

The unit mass matrix \mathbf{M}_T^e can be expressed as

$$\mathbf{M}_T^e = \frac{\rho A_L l}{1260(1 + \varphi_s)^2} \begin{bmatrix} M_1 & 0 & 0 & lM_2 & M_3 & 0 & 0 & -lM_4 \\ 0 & M_1 & -lM_2 & 0 & 0 & M_3 & lM_4 & 0 \\ 0 & -lM_2 & l^2M_5 & 0 & 0 & -lM_6 & -l^2M_7 & 0 \\ lM_2 & 0 & 0 & l^2M_5 & lM_6 & 0 & 0 & -l^2M_7 \\ M_3 & 0 & 0 & lM_6 & M_8 & 0 & 0 & -lM_9 \\ 0 & M_3 & -lM_6 & 0 & 0 & M_8 & lM_9 & 0 \\ 0 & lM_4 & -l^2M_7 & 0 & 0 & lM_9 & l^2M_{10} & 0 \\ -lM_4 & 0 & 0 & -l^2M_7 & -lM_9 & 0 & 0 & l^2M_{10} \end{bmatrix} \quad (4)$$

where the parameters are expressed in detail in Appendix.

The unit mass inertia matrix \mathbf{M}_R^e is shown as follows:

$$\mathbf{M}_R^e = \frac{\rho I_L}{210(1 + \varphi_s)^2} \left[\begin{array}{cccccccc} M_{11} & 0 & 0 & lM_{12} & -M_{11} & 0 & 0 & lM_{13} \\ 0 & M_{11} & -lM_{12} & 0 & 0 & -M_{11} & -lM_{13} & 0 \\ 0 & -lM_{12} & l^2M_{14} & 0 & 0 & lM_{12} & -l^2M_{15} & 0 \\ lM_{12} & 0 & 0 & l^2M_{14} & -lM_{12} & 0 & 0 & -l^2M_{15} \\ -M_{11} & 0 & 0 & -lM_{12} & M_{11} & 0 & 0 & -lM_{13} \\ 0 & -M_{11} & lM_{12} & 0 & 0 & M_{11} & lM_{13} & 0 \\ 0 & -lM_{13} & -l^2M_{15} & 0 & 0 & lM_{13} & l^2M_{16} & 0 \\ lM_{13} & 0 & 0 & -l^2M_{15} & -lM_{13} & 0 & 0 & l^2M_{16} \end{array} \right] \quad (5)$$

where the parameters in matrix \mathbf{M}_R^e are expressed in Appendix.

The unit gyroscopic matrix is

$$\mathbf{G}^e = \frac{\rho I_L}{105l(1 + \varphi_s)^2} \left[\begin{array}{cccccccc} 0 & G_1 & -lG_2 & 0 & 0 & -G_1 & -lG_3 & 0 \\ G_1 & 0 & 0 & -lG_2 & G_1 & 0 & 0 & -lG_3 \\ -lG_2 & 0 & 0 & l^2G_4 & -lG_2 & 0 & 0 & -l^2G_5 \\ 0 & -lG_2 & l^2G_4 & 0 & 0 & -lG_2 & l^2G_5 & 0 \\ 0 & G_1 & -lG_2 & 0 & 0 & G_1 & lG_3 & 0 \\ -G_1 & 0 & 0 & -lG_2 & G_1 & 0 & 0 & lG_3 \\ -lG_3 & 0 & 0 & l^2G_5 & lG_3 & 0 & 0 & l^2G_6 \\ 0 & -lG_3 & -l^2G_5 & 0 & 0 & lG_3 & l^2G_6 & 0 \end{array} \right] \quad (6)$$

where

$$G_1 = 126\alpha_2 + 72\beta_2 + 30\delta_2 + 45\gamma_2 + 252,$$

$$G_2 = -(42\alpha_2 + 21\beta_2 + 7.5\delta_2 + 12\gamma_2 + 105)\varphi_s + 21\alpha_2 + 15\beta_2 + 7.5\delta_2 + 10.5\gamma_2 + 21,$$

$$G_3 = -(63\alpha_2 + 42\beta_2 + 22.5\delta_2 + 30\gamma_2 + 105)\varphi_s - 6\beta_2 - 7.5\delta_2 - 7.5\gamma_2 + 21$$

$$G_4 = (17.5\alpha_2 + 7\beta_2 + 2\delta_2 + 3.5\gamma_2 + 70)\varphi_s^2 + (35 - 7\alpha_2 - 7\beta_2 - 3.5\delta_2 - 5\gamma_2)\varphi_s + 7\alpha_2 + 4\beta_2 + 2\delta_2 + 2.75\gamma_2 + 28$$

$$G_5 = -(17.5\alpha_2 + 10.5\beta_2 + 5\delta_2 + 7\gamma_2 + 35)\varphi_s^2 + (17.5\alpha_2 + 10.5\beta_2 + 5\delta_2 + 7\gamma_2 + 35)\varphi_s + 3.5\alpha_2 + 3\beta_2 + 2.5\delta_2 + 2.75\gamma_2 + 7$$

$$G_6 = (52.5\alpha_2 + 42\beta_2 + 30\delta_2 + 35\gamma_2 + 70)\varphi_s^2 + (42\alpha_2 + 42\beta_2 + 37.5\delta_2 + 40\gamma_2 + 35)\varphi_s + 21\alpha_2 + 18\beta_2 + 15\delta_2 + 16.25\gamma_2 + 28$$

The unit stiffness matrix \mathbf{K}_B^e is expressed as follows:

$$\mathbf{K}_B^e = \frac{EI_L}{105l^3(1+\varphi_s)^2} \begin{bmatrix} K_1 & 0 & 0 & lK_2 & -K_1 & 0 & 0 & lK_3 \\ 0 & K_1 & -lK_2 & 0 & 0 & -K_1 & -lK_3 & 0 \\ 0 & -lK_2 & l^2K_4 & 0 & 0 & lK_2 & l^2K_5 & 0 \\ lK_2 & 0 & 0 & l^2K_4 & -lK_2 & 0 & 0 & l^2K_5 \\ -K_1 & 0 & 0 & -lK_2 & K_1 & 0 & 0 & -lK_3 \\ 0 & -K_1 & lK_2 & 0 & 0 & K_1 & lK_3 & 0 \\ 0 & -lK_3 & l^2K_5 & 0 & 0 & lK_3 & l^2K_6 & 0 \\ lK_3 & 0 & 0 & l^2K_5 & -lK_3 & 0 & 0 & l^2K_6 \end{bmatrix} + \frac{GA_L\varphi_s^2}{12\chi l(1+\varphi_s)^2} \begin{bmatrix} K_7 & 0 & 0 & lK_8 & -K_7 & 0 & 0 & lK_8 \\ 0 & K_7 & -lK_8 & 0 & 0 & -K_7 & -lK_8 & 0 \\ 0 & -lK_8 & l^2K_9 & 0 & 0 & lK_8 & l^2K_9 & 0 \\ lK_8 & 0 & 0 & l^2K_9 & -lK_8 & 0 & 0 & l^2K_9 \\ -K_7 & 0 & 0 & -lK_8 & K_7 & 0 & 0 & -lK_8 \\ 0 & -K_7 & lK_8 & 0 & 0 & K_7 & lK_8 & 0 \\ 0 & -lK_8 & l^2K_9 & 0 & 0 & lK_8 & l^2K_9 & 0 \\ lK_8 & 0 & 0 & l^2K_9 & -lK_8 & 0 & 0 & l^2K_9 \end{bmatrix} \quad (7)$$

where the parameters in Eq. (7) are shown in Appendix.

The dynamical equation of cylindrical unit is established based on the FE method, which is expressed in Eq. (8):

$$(\mathbf{M}_{te_i} + \mathbf{M}_{re_i}) \ddot{\mathbf{q}}_{e_i} - \omega \mathbf{G}_{e_i} \dot{\mathbf{q}}_{e_i} + \mathbf{K}_{e_i} \mathbf{q}_{e_i} = \mathbf{F}_{e_i} \quad (8)$$

In Eq. (8), $\mathbf{q}_e = [q_1, \dots, q_8]^T$ are unit generalized coordinates, \mathbf{M}_{te_i} and \mathbf{M}_{re_i} represent unit mass matrix and mass inertia matrix, \mathbf{G}_{e_i} is unit gyroscopic matrix, \mathbf{K}_{e_i} is unit stiffness matrix, \mathbf{F}_{e_i} is generalized external force vector, ω is angular frequency. The DOF of the wheel disc is $\mathbf{q}_d = [x_d, y_d, \theta_{x_d}, \theta_{y_d}]^T$ relative to the fixed coordinate. m, J_d, J_p represent the mass of disc, equatorial moment of inertia, and polar moment of inertia, respectively. Similarly, the dynamical equation of wheel disc can be obtained by Lagrange equation,

$$(\mathbf{M}_{td} + \mathbf{M}_{rd}) \ddot{\mathbf{q}}_d - \omega \mathbf{G}_d \dot{\mathbf{q}}_d = \mathbf{F}_d \quad (9)$$

where \mathbf{F}_d is the generalized external force vector, and other parameters are shown as

$$\mathbf{M}_{td} = \begin{bmatrix} m & 0 & 0 & 0 \\ 0 & m & 0 & 0 \\ 0 & 0 & 0 & 0 \\ 0 & 0 & 0 & 0 \end{bmatrix}, \quad \mathbf{M}_{rd} = \begin{bmatrix} 0 & 0 & 0 & 0 \\ 0 & 0 & 0 & 0 \\ 0 & 0 & J_d & 0 \\ 0 & 0 & 0 & J_d \end{bmatrix}, \quad \mathbf{G}_d = \begin{bmatrix} 0 & 0 & 0 & 0 \\ 0 & 0 & 0 & 0 \\ 0 & 0 & 0 & -J_p \\ 0 & 0 & J_p & 0 \end{bmatrix}$$

The elastic deformation of number one, two, four, and six bearing and nonlinear factors are considered, assemble differential equation of motion of each shaft section and wheel disc, the dynamical equation of cylindrical shell-conical shell dual rotor-bearing system is shown as

$$\mathbf{M}\ddot{\mathbf{q}} + (\mathbf{C} - \omega\mathbf{G})\dot{\mathbf{q}} + \mathbf{K}\mathbf{q} + \mathbf{F}_b(\mathbf{q}, t) = \mathbf{F}_g + \mathbf{F}(t) \quad (10)$$

\mathbf{M} , \mathbf{K} , \mathbf{C} , \mathbf{G} are mass, stiffness, damping, and gyroscopic matrix, $\mathbf{C} = \alpha_0\mathbf{M} + \alpha_1\mathbf{K}$, α_0 , α_1 are constants, \mathbf{F}_g is gravity vector, $\mathbf{F}(t)$ is eccentricity excitation, $\mathbf{F}_b(\mathbf{q}, t)$ is Hertz contact force which can be expressed as follows:

$$\begin{bmatrix} F_{x_i} \\ F_{y_i} \end{bmatrix} = C_{b_i} \sum_{j=1}^{N_{b_i}} H(\delta_{ij}) \delta_{ij}^n \begin{bmatrix} \cos \theta_{ij} \\ \sin \theta_{ij} \end{bmatrix}, \quad \theta_{ij} = \frac{2\pi(j-1)}{N_{b_i}} + \Omega_i t,$$

$$\delta_{ij} = x_i \cos \theta_{ij} + y_i \sin \theta_{ij} - \delta_{i0} \quad (11)$$

θ_{ij} , δ_{ij} are instantaneous rotation and contact deformation of j rolling element of i bearing, n is Hertz contact nonlinearity, e.g., ball bearing case $n = 3/2$, $H(\delta_{ij})$ is Heaviside function, C_{b_i} , N_{b_i} , Ω_i , $2\delta_{i0}$ represent i bearing contact stiffness, number of rolling element, rotating speed of cage, initial radial internal clearance.

3 First Dimension Reduction for Dual Rotor-Bearing System

Because of the complicated structures of the dual rotor-bearing system and including multiple supporting rolling element bearings, the pre-computed high fidelity simulation signals of the physical system are costly for the direct MDR based on the POD method. Response signal of time length should be obtained in advance to construct POD reduced order mode (ROM) when the POD method is used for MDR. The CMS method is used for first dimension reduction of linear part of complex rotor system to avoid long time calculation.

The rotor-bearing model is divided into two sub-structures, one is LP rotor and the other is HP rotor system. Internal coordinate is \mathbf{q}_{il} and external coordinate is \mathbf{q}_{iB} , $i = L, H$. Dividing each structure into blocks, the dynamical equation of each structure can be written as

$$\mathbf{M}_i \ddot{\mathbf{q}}_i + \mathbf{C}_i \dot{\mathbf{q}}_i + \mathbf{K}_i \mathbf{q}_i = \mathbf{F}_i(\mathbf{q}_i, t) \quad (12)$$

In Eq. (12), the parameters are shown as

$$\mathbf{M}_i = \begin{bmatrix} \mathbf{M}_{iII} & \mathbf{M}_{iIB} \\ \mathbf{M}_{iBI} & \mathbf{M}_{iBB} \end{bmatrix}, \quad \mathbf{C}_i = \begin{bmatrix} \mathbf{C}_{iII} & \mathbf{C}_{iIB} \\ \mathbf{C}_{iBI} & \mathbf{C}_{iBB} \end{bmatrix}, \quad \mathbf{K}_i = \begin{bmatrix} \mathbf{K}_{iII} & \mathbf{K}_{iIB} \\ \mathbf{K}_{iBI} & \mathbf{K}_{iBB} \end{bmatrix},$$

$$\mathbf{q}_i = \begin{bmatrix} \mathbf{q}_{iI} \\ \mathbf{q}_{iB} \end{bmatrix}, \quad \mathbf{F}_i = \begin{bmatrix} \mathbf{F}_{iI} \\ \mathbf{F}_{iB} \end{bmatrix}$$

Calculate the primary mode $\Psi_{ik} \in R^{n_{iI} \times n_{ik}}$ and constrained release mode $\Psi_{iC} \in R^{n_{iI} \times n_{iB}}$. n_{il} , n_{iB} , n_{ik} represent number of internal node coordinate, boundary coordinate, constraint-preserved primary mode. Constrained release mode can be obtained by the equation as follows [14]:

$$\Psi_{iC} = -\mathbf{K}_{iII}^{-1} \mathbf{K}_{iIB} \quad (13)$$

Project the physical coordinate of each substructure to the subspaces spanned by truncation mode via Craig-Bampton conversion

$$\begin{bmatrix} \mathbf{q}_{iI} \\ \mathbf{q}_{iB} \end{bmatrix} = \begin{bmatrix} \Psi_{ik} & \Psi_{iC} \\ 0 & I_{iB} \end{bmatrix} \begin{bmatrix} \mathbf{u}_{ik} \\ \mathbf{u}_{iB} \end{bmatrix} = \mathbf{P}_i \begin{bmatrix} \mathbf{u}_{ik} \\ \mathbf{u}_{iB} \end{bmatrix} \quad (14)$$

Substituting Eq. (14) into Eq. (12), the dynamical equation of substructure can be obtained

$$\bar{\mathbf{M}}_i \ddot{\mathbf{u}}_i + \bar{\mathbf{C}}_i \dot{\mathbf{u}}_i + \bar{\mathbf{K}}_i \mathbf{u}_i = \bar{\mathbf{F}}_i \quad (15)$$

where $\bar{\mathbf{M}}_i = \mathbf{P}_i^T \mathbf{M}_i \mathbf{P}_i$, $\bar{\mathbf{C}}_i = \mathbf{P}_i^T \mathbf{C}_i \mathbf{P}_i$, $\bar{\mathbf{K}}_i = \mathbf{P}_i^T \mathbf{K}_i \mathbf{P}_i$, $\bar{\mathbf{F}}_i = \mathbf{P}_i^T \mathbf{F}_i$. Synthesizing MDRs of LP and HP rotor structures, the overall reduced model of dual rotor-bearing system can be got as follows:

$$\bar{\mathbf{M}} \ddot{\mathbf{u}} + \bar{\mathbf{C}} \dot{\mathbf{u}} + \bar{\mathbf{K}} \mathbf{u} = \bar{\mathbf{F}} \quad (16)$$

where $\bar{\mathbf{M}} = \{\bar{\mathbf{M}}_L, \bar{\mathbf{M}}_H\}$, $\bar{\mathbf{C}} = \{\bar{\mathbf{C}}_L, \bar{\mathbf{C}}_H\}$, $\bar{\mathbf{K}} = \{\bar{\mathbf{K}}_L, \bar{\mathbf{K}}_H\}$, $\bar{\mathbf{F}} = \{\bar{\mathbf{F}}_L, \bar{\mathbf{F}}_H\}$, $\mathbf{u} = \{\mathbf{u}_L, \mathbf{u}_H\}$.

In aero-engine, there are many supporting bearings that contain more boundary DOF, the MDR obtained by CMS method is also high-dimensional with dozens of DOF, so the POD method will be applied for second dimension reduction based on the first MDR obtained by CMS method.

4 Second Dimension Reduction for Dual Rotor-Bearing System

The ROMs of first dimension reduction method neglect the effects of high-order modes. The high-order modes truncated by CMS method are added when the POD method is applied for second dimension reduction to reduce the results of the first MDR. The CB transformation is used to obtain first MDR which contains high-order

mode response, then the POD method is applied for second dimension reduction. The basic idea of the proposed method is similar as the nonlinear Galerkin method, and the error of second dimension reduction can be reduced.

The numerical method is used to calculate the response signal $\hat{\mathbf{u}}(\mathbf{u}_0, \dot{\mathbf{u}}_0, \omega, t_s) = [\mathbf{u}_1, \dots, \mathbf{u}_m]_{N_s \times m}$ of a certain time length of Eq. (16) when we used the POD method for second dimension of the first MDR. For the sampling snapshot matrix, $\mathbf{u}_0, \dot{\mathbf{u}}_0, \omega, t_s$ represent initial position, initial velocity, rotational speed, sampling time length, m is the DOF number of first MDR. The eigenvector of autocorrelation matrix of Eq. (17) is calculated

$$\mathbf{S}_c = \frac{1}{N_s} \left[\hat{\mathbf{u}}(\mathbf{u}_0, \dot{\mathbf{u}}_0, \omega, t_s)^T \hat{\mathbf{u}}(\mathbf{u}_0, \dot{\mathbf{u}}_0, \omega, t_s) \right]_{m \times m} \quad (17)$$

The eigenvectors are ranked as the descending order of eigenvalues, and ROMs of POD $\{\varphi_i(\mathbf{u}_0, \dot{\mathbf{u}}_0, \omega, t_s)\}_{i=1 \dots m}$ can be obtained. The first MDR is projected to the subspace spanned by the first l ROMs

$$\mathbf{u}(t) = \sum_{i=1}^l v_i(t) \varphi_i(\mathbf{u}_0, \dot{\mathbf{u}}_0, \omega, t_s) = \Psi(\mathbf{u}_0, \dot{\mathbf{u}}_0, \omega, t_s) \mathbf{v}(t) \quad (18)$$

where $\Psi(\mathbf{u}_0, \dot{\mathbf{u}}_0, \omega, t_s) = [\varphi_1(\mathbf{u}_0, \dot{\mathbf{u}}_0, \omega, t_s), \dots, \varphi_l(\mathbf{u}_0, \dot{\mathbf{u}}_0, \omega, t_s)]_{m \times l}$. The dynamical equation of second MDR can be got via substituting Eq. (18) into Eq. (16)

$$\mathbf{M}_r \ddot{\mathbf{v}} + \mathbf{C}_r \dot{\mathbf{v}} + \mathbf{K}_r \mathbf{v} = \mathbf{F}_r(\mathbf{v}, \dot{\mathbf{v}}, t) \quad (19)$$

where $\mathbf{M}_r = \Psi^T \bar{\mathbf{M}} \Psi$, $\mathbf{C}_r = \Psi^T \bar{\mathbf{C}} \Psi$, $\mathbf{K}_r = \Psi^T \bar{\mathbf{K}} \Psi$, $\mathbf{F}_r = \Psi^T \bar{\mathbf{F}}$, the initial conditions can be confirmed by $\mathbf{v}_0 = \Psi^T \mathbf{u}_0, \dot{\mathbf{v}}_0 = \Psi^T \dot{\mathbf{u}}_0$.

Equation (19) is an approximation to first MDR, and vibration responses $\mathbf{u}(t)$ of first MDR obtained by different POD ROM transformation matrixes are different. CMS method truncates more high-order modes, and the CB transformation is used to get vibration response $\mathbf{q}_r(t)$ of physical coordinates of the original system. Vibration response $\mathbf{q}_r(t)$ exhibits larger error than $\mathbf{q}(t)$ of real physical coordinates of the original system through two non-one-to-one coordinate transformation. The numerical method is applied to calculate the response of the first MDR to solve this problem. We use mode expansion, the truncated high-order modes are added, the CB transformation is applied, and the response that contains high-order modes of first MDR can be obtained. The POD method is applied for second dimension reduction, and the detailed processes are shown as follows.

The numerical method is applied to calculate the vibration response of first ROM coordinate of Eq. (16), and the CB transformation is used

$$\mathbf{q}_r = \begin{bmatrix} \mathbf{q}_L \\ \mathbf{q}_H \end{bmatrix}_{N \times 1} = \begin{bmatrix} \mathbf{P}_L & \mathbf{0} \\ \mathbf{0} & \mathbf{P}_H \end{bmatrix}_{N \times m} \begin{bmatrix} \mathbf{u}_L \\ \mathbf{u}_H \end{bmatrix}_{m \times 1} \quad (20)$$

The number of the truncated constrained principal mode of HP and LP rotor is expanded respectively, n_H, n_L are the number of corresponding expanded mode, and $n = n_H + n_L$ is the total number. The coordinate transformation relation on the basis of mode expansion can be obtained via Eq. (20)

$$\mathbf{q}_r = \begin{bmatrix} \mathbf{q}_L \\ \mathbf{q}_H \end{bmatrix}_{N \times 1} = \begin{bmatrix} \mathbf{P}_L & \mathbf{0} \\ \mathbf{0} & \mathbf{P}_H \end{bmatrix}_{N \times (m+n)} \begin{bmatrix} \mathbf{u}_L \\ \mathbf{u}_H \end{bmatrix}_{(m+n) \times 1} \quad (21)$$

Transforming Eq. (21), we can get

$$\begin{bmatrix} \mathbf{u}_L \\ \mathbf{u}_H \end{bmatrix}_{(m+n) \times 1} = \left(\begin{bmatrix} \mathbf{P}_L & \mathbf{0} \\ \mathbf{0} & \mathbf{P}_H \end{bmatrix}_{(m+n) \times N}^T \begin{bmatrix} \mathbf{P}_L & \mathbf{0} \\ \mathbf{0} & \mathbf{P}_H \end{bmatrix}_{N \times (m+n)} \right)^{-1} \begin{bmatrix} \mathbf{P}_L & \mathbf{0} \\ \mathbf{0} & \mathbf{P}_H \end{bmatrix}_{(m+n) \times N}^T \begin{bmatrix} \mathbf{q}_L \\ \mathbf{q}_H \end{bmatrix}_{N \times 1} \quad (22)$$

The vibration response can be obtained via substituting Eq. (20) into Eq. (22)

$$\begin{bmatrix} \mathbf{u}_L \\ \mathbf{u}_H \end{bmatrix}_{(m+n) \times 1} = \left(\begin{bmatrix} \mathbf{P}_L & \mathbf{0} \\ \mathbf{0} & \mathbf{P}_H \end{bmatrix}_{(m+n) \times N}^T \begin{bmatrix} \mathbf{P}_L & \mathbf{0} \\ \mathbf{0} & \mathbf{P}_H \end{bmatrix}_{N \times (m+n)} \right)^{-1} \begin{bmatrix} \mathbf{P}_L & \mathbf{0} \\ \mathbf{0} & \mathbf{P}_H \end{bmatrix}_{(m+n) \times N}^T \begin{bmatrix} \mathbf{P}_L & \mathbf{0} \\ \mathbf{0} & \mathbf{P}_H \end{bmatrix}_{N \times m} \begin{bmatrix} \mathbf{u}_L \\ \mathbf{u}_H \end{bmatrix}_{m \times 1} \quad (23)$$

Snapshot response signals $\tilde{\mathbf{u}}(\mathbf{u}_0, \dot{\mathbf{u}}_0, \mathbf{u}_{m+n}, \omega, t_s) = [\tilde{\mathbf{u}}_1, \dots, \tilde{\mathbf{u}}_m]_{N_S \times m}$ of the corresponding mode coordinate of the first MDR in a certain time length are truncated, which are sampling snapshot matrices. The dynamical equation of second MDR can be obtained through Eqs. (17)–(19). The vibration response of physical coordinate of the original system can be got via calculating the response $\tilde{\mathbf{v}}(t)$ of second MDR and Eqs. (18) and (20).

$$\tilde{\mathbf{q}}_r(t)_{N \times 1} = \begin{bmatrix} \mathbf{P}_L & \mathbf{0} \\ \mathbf{0} & \mathbf{P}_H \end{bmatrix}_{N \times m} \Psi(\mathbf{u}_0, \dot{\mathbf{u}}_0, \mathbf{u}_{m+n}, \omega, t_s)_{m \times l} \tilde{\mathbf{v}}(t)_{l \times 1} \quad (24)$$

The vibration response of the physical coordinate of the original system obtained by direct second dimension reduction is expressed as

$$\mathbf{q}_r(t)_{N \times 1} = \begin{bmatrix} \mathbf{P}_L & \mathbf{0} \\ \mathbf{0} & \mathbf{P}_H \end{bmatrix}_{N \times m} \Psi(\mathbf{u}_0, \dot{\mathbf{u}}_0, \omega, t_s)_{m \times l} \mathbf{v}(t)_{l \times 1} \quad (25)$$

Equation (24) contains higher order mode information of the original system in comparison to Eq. (25); hence, it can better approximate the vibration response of the original system.

5 Results and Discussions

In this section, frequency spectrum, axis orbit, and frequency–amplitude curve of the first MDR, second MDR based on mode expansion and direct second MDR are discussed.

As shown in Fig. 4, in the case of LP rotation speed 520 rad/s, speed ratio 1.3, frequency spectrum and axis orbit of the first MDR, mode expansion second MDR, and direct second MDR of LP turbine are studied. The results show that the frequency components of the system response are very complex, the main

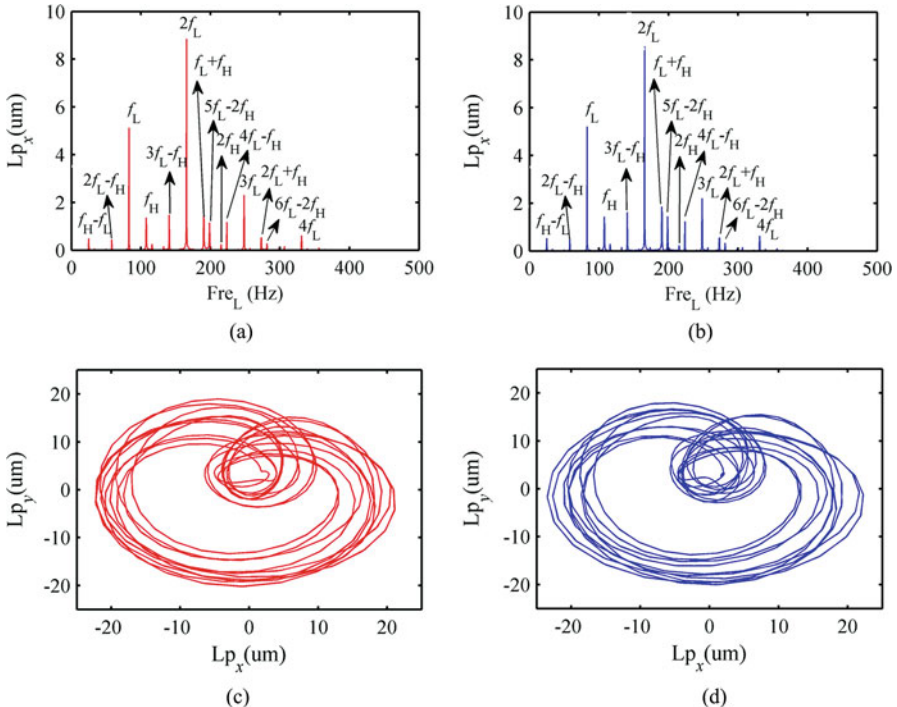


Fig. 4 Comparisons between the frequency spectrums and axis orbits of the LP turbine for the first ROM, the second ROM with modal expansion at the rotational speed of LP rotor 520 rad/s for $\lambda = 1.3$. (a) Frequency spectrum of the LP turbine for the first ROM, (b) Frequency spectrum of the LP turbine for the second ROM with modal expansion, (c) Axis orbit of the LP turbine for the first ROM, (d) Axis orbit of the LP turbine for the second ROM with modal expansion

frequencies are eccentric excitation of HP and LP frequencies $2f_L$, $2f_H$. The third, fourth frequency, other frequencies and many combination frequencies also appear in the frequency spectrum curves, e.g., $|f_L \pm f_H|$, $|2f_L \pm f_H|$, $3f_L - f_H$, $5f_L - 2f_H$, and the VC signal of bearing is weak. The frequencies and amplitude of mode expansion second dimension reduction agree well with those of first MDR. From the aspect of axis orbit, polycyclic 8 form occurs in the system at this speed, the axis orbit of second dimension reduction agrees well with the first MDR.

As shown in Fig. 5a, b, there are two main resonance peaks, which are motivated by the eccentric excitations of Hp and Lp rotors, respectively, in addition the two-superharmonic resonances and combination resonances are also excited which lead to characteristics of complicated nonlinear vibrations. Comparing Fig. 5c, d with Fig. 5a, b, the reader can observe that the frequency–amplitude curves of the second ROM with mode expansion are nearly identical with the first ROM, thus the dynamic properties of the two ROMs are almost the same.

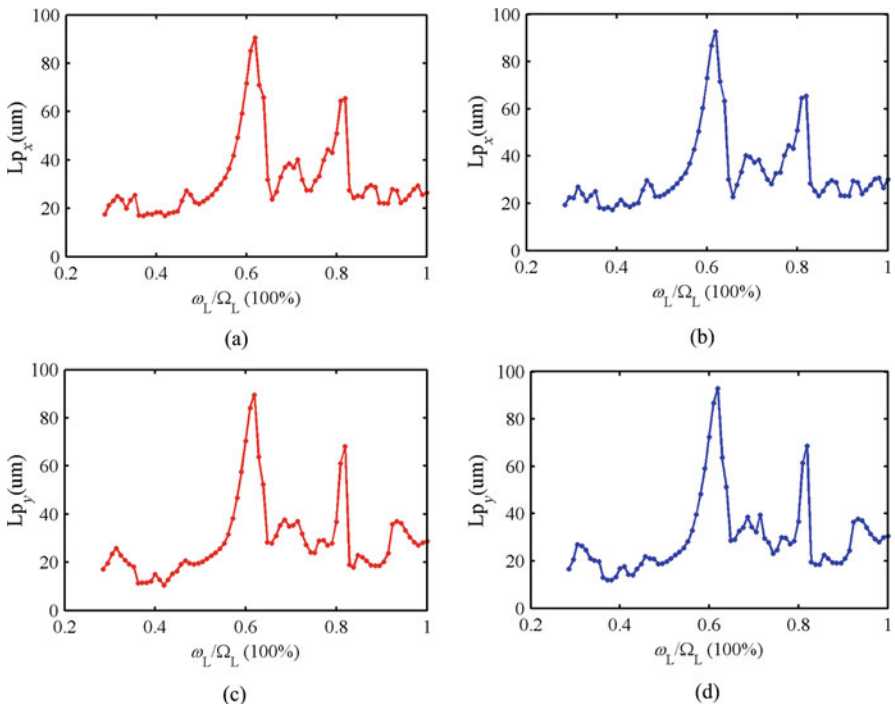
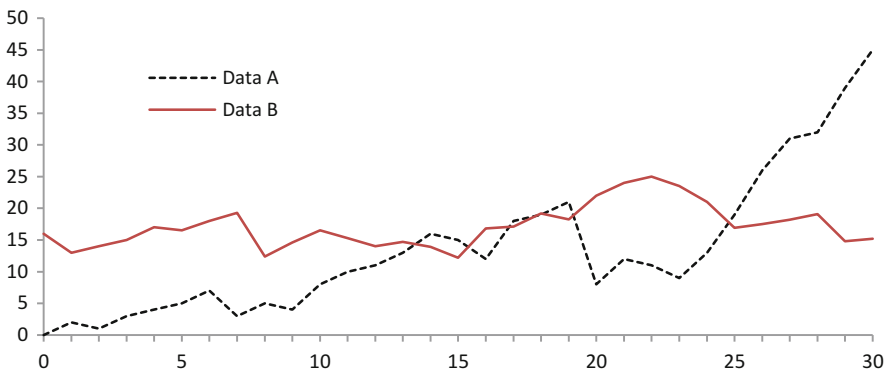


Fig. 5 Comparisons between the frequency–amplitude curves of Lp turbine for the first ROM, the second ROM with mode expansion for $\lambda = 1.3$ (ω_L , Ω_L are the rotational speed and rated speed of Lp rotor). (a) Frequency–amplitude curve of first ROM in the x -direction, (b) Frequency–amplitude curve of second ROM with mode expansion in the x -direction, (c) Frequency–amplitude curve of first ROM in the y -direction, (d) Frequency–amplitude curve of second ROM with mode expansion in the y -direction

As discussed above, mode expansion POD second dimension reduction method considers high-order mode information of the original system, second MDR can reflect the dynamical behaviors of the original system in high-precision after two times coordinate transformation. The proposed CMS-POD second dimension reduction method can be applied for high-precision MDR of large complex systems.

Remark The computational time of the proposed second dimension reduction method is ten times faster than the first dimension reduction method based on CMS. The second MDR needs at least 20 h and the first MDR needs only 1.5 h. The dynamical responses of both first and second MDR are calculated by Runge–Kutta method.

The mode expansion POD second dimension reduction method has been proposed based on the component mode synthesis method and proper orthogonal decomposition method in this chapter. The cylindrical shell-conical shell-wheel disc dual-rotor bearing system of aero-engine has been established by the FE method. The frequency spectrum and axis orbit curves of the first MDR and mode expansion second MDR have been studied. The efficiency of the proposed method has been verified via comparing the dynamical behaviors of the first MDR with the second MDR at different rotational speeds. The present authors will focus on two aspects in the future work: one is to generalize the second dimension reduction method to the rotor system model with common faults, e.g., looseness fault and rub-impact fault, the other is to combine the polynomial dimensional decomposition method [15, 16] with the proposed method to study the nonlinear dynamics system with uncertainties.



Acknowledgments I appreciate the valuable suggestions and comments of the reviewers and editor. Many thanks to technological support of Dr. Yulin Jin in School of Aeronautics and Astronautics of Sichuan University. We are grateful for the National Natural Science Foundation of China (Grant No. 11802235) and Basic Scientific Research Operating Expenses of Central Universities (Grant No. G2018KY0305). There is no conflict of interest between the authors.

Appendix

$$\begin{aligned}
\Delta r_o &= r_{Ro} - r_{Lo}, \quad \Delta r_i = r_{Ri} - r_{Li}, \quad \alpha_1 = \frac{2\pi}{A_L} (r_{Lo} \Delta r_o - r_{Li} \Delta r_i), \quad \beta_1 = \\
&\frac{\pi}{A_L} (\Delta r_o^2 - \Delta r_i^2), \quad \alpha_2 = \frac{\pi}{A_L} (r_{Lo}^3 \Delta r_o - r_{Li}^3 \Delta r_i), \quad \beta_2 = \frac{3\pi}{2I_L} (r_{Lo}^2 \Delta r_o^2 - r_{Li}^2 \Delta r_i^2), \\
\gamma_2 &= \frac{\pi}{2I_L} (r_{Lo} \Delta r_o^3 - r_{Li} \Delta r_i^3), \quad \delta_2 = \frac{\pi}{4I_L} (\Delta r_o^4 - \Delta r_i^4) \\
M_1 &= (105\alpha_1 + 42\beta_1 + 420) \varphi_s^2 + (210\alpha_1 + 78\beta_1 + 882) \varphi_s + 108\alpha_1 + 38\beta_1 + 468 \\
M_2 &= (42\alpha_1 + 21\beta_1 + 105) \varphi_s^2 / 2 + (81\alpha_1 + 36\beta_1 + 231) \varphi_s / 2 + (42\alpha_1 + 17\beta_1 + 132) / 2 \\
M_3 &= (105\alpha_1 + 63\beta_1 + 210) \varphi_s^2 + (189\alpha_1 + 111\beta_1 + 378) \varphi_s + 81\alpha_1 + 46\beta_1 + 162 \\
M_4 &= (42\alpha_1 + 21\beta_1 + 105) \varphi_s^2 / 2 + (81\alpha_1 + 42\beta_1 + 189) \varphi_s / 2 + (36\alpha_1 + 19\beta_1 + 78) / 2 \\
M_5 &= (21\alpha_1 + 12\beta_1 + 42) \varphi_s^2 / 4 + (36\alpha_1 + 18\beta_1 + 84) \varphi_s / 4 + (9\alpha_1 + 4\beta_1 + 24) / 2 \\
M_6 &= (63\alpha_1 + 42\beta_1 + 105) \varphi_s^2 / 2 + (108\alpha_1 + 69\beta_1 + 189) \varphi_s / 2 \\
&\quad + (42\alpha_1 + 25\beta_1 + 78) / 2 \\
M_7 &= (21\alpha_1 + 12\beta_1 + 42) \varphi_s^2 / 4 + (21\alpha_1 + 12\beta_1 + 42) \varphi_s / 2 + (9\alpha_1 + 5\beta_1 + 18) / 2 \\
M_8 &= (315\alpha_1 + 252\beta_1 + 420) \varphi_s^2 + (672\alpha_1 + 540\beta_1 + 882) \varphi_s + 360\alpha_1 \\
&\quad + 290\beta_1 + 468 \\
M_9 &= (63\alpha_1 + 42\beta_1 + 105) \varphi_s^2 / 2 + (150\alpha_1 + 105\beta_1 + 231) \varphi_s / 2 \\
&\quad + (90\alpha_1 + 65\beta_1 + 132) / 2 \\
M_{10} &= (21\alpha_1 + 12\beta_1 + 42) \varphi_s^2 / 4 + (24\alpha_1 + 15\beta_1 + 42) \varphi_s / 2 + (15\alpha_1 + 10\beta_1 + 24) / 2 \\
M_{11} &= 126\alpha_2 + 72\beta_2 + 30\delta_2 + 45\gamma_2 + 252 \\
M_{12} &= -(42\alpha_2 + 21\beta_2 + 7.5\delta_2 + 12\gamma_2 + 105) \varphi_s + 21\alpha_2 + 15\beta_2 + 7.5\delta_2 \\
&\quad + 10.5\gamma_2 + 21 \\
M_{13} &= -(63\alpha_2 + 42\beta_2 + 22.5\delta_2 + 30\gamma_2 + 105) \varphi_s - 6\beta_2 - 7.5\delta_2 - 7.5\gamma_2 + 21 \\
M_{14} &= (17.5\alpha_2 + 7\beta_2 + 2\delta_2 + 3.5\gamma_2 + 70) \varphi_s^2 + (35 - 7\alpha_2 - 7\beta_2 - 3.5\delta_2 - 5\gamma_2) \varphi_s \\
&\quad + 7\alpha_2 + 4\beta_2 + 2\delta_2 + 2.75\gamma_2 + 28 \\
M_{15} &= -(17.5\alpha_2 + 10.5\beta_2 + 5\delta_2 + 7\gamma_2 + 35) \varphi_s^2 \\
&\quad + (17.5\alpha_2 + 10.5\beta_2 + 5\delta_2 + 7\gamma_2 + 35) \varphi_s \\
&\quad + 3.5\alpha_2 + 3\beta_2 + 2.5\delta_2 + 2.75\gamma_2 + 7 \\
M_{16} &= (52.5\alpha_2 + 42\beta_2 + 30\delta_2 + 35\gamma_2 + 70) \varphi_s^2 \\
&\quad + (42\alpha_2 + 42\beta_2 + 37.5\delta_2 + 40\gamma_2 + 35) \varphi_s \\
&\quad + 21\alpha_2 + 18\beta_2 + 15\delta_2 + 16.25\gamma_2 + 28 \\
K_1 &= 630\alpha_2 + 504\beta_2 + 396\delta_2 + 441\gamma_2 + 1260 \\
K_2 &= -(105\alpha_2 + 105\beta_2 + 84\delta_2 + 94.5\gamma_2) \varphi_s + 210\alpha_2 + 147\beta_2 + 114\delta_2 \\
&\quad + 126\gamma_2 + 630 \\
K_3 &= (105\alpha_2 + 105\beta_2 + 84\delta_2 + 94.5\gamma_2) \varphi_s + 420\alpha_2 + 357\beta_2 + 282\delta_2 \\
&\quad + 315\gamma_2 + 630 \\
K_7 &= 6\alpha_1 + 4\beta_1 + 12, \quad K_8 = 3\alpha_1 + 2\beta_1 + 6, \quad K_9 = 1.5\alpha_1 + \beta_1 + 3 \\
K_4 &= (52.5\alpha_2 + 35\beta_2 + 21\delta_2 + 26.25\gamma_2 + 105) \varphi_s^2 + (-35\beta_2 - 42\delta_2 - 42\gamma_2 + 210) \varphi_s \\
&\quad + 105\alpha_2 + 56\beta_2 + 36\delta_2 + 42\gamma_2 + 420
\end{aligned}$$

$$\begin{aligned}
K_5 = & - (52.5\alpha_2 + 35\beta_2 + 21\delta_2 + 26.25\gamma_2 + 105) \varphi_s^2 \\
& - (105\alpha_2 + 70\beta_2 + 42\delta_2 + 52.5\gamma_2 + 210) \varphi_s \\
& + 105\alpha_2 + 91\beta_2 + 78\delta_2 + 84\gamma_2 + 210 \\
K_6 = & (52.5\alpha_2 + 35\beta_2 + 21\delta_2 + 26.25\gamma_2 + 105) \varphi_s^2 \\
& + (210\alpha_2 + 175\beta_2 + 126\delta_2 + 147\gamma_2 + 210) \varphi_s \\
& + 315\alpha_2 + 266\beta_2 + 204\delta_2 + 231\gamma_2 + 420
\end{aligned}$$

References

1. Rega, G., Troger, H.: Dimension reduction of dynamical systems: methods, models, applications. *Nonlinear Dyn.* **41**, 1–15 (2005)
2. Kerschen, G., Golinval, J.C., Vakakis, A.F., et al.: The method of proper orthogonal decomposition for dynamical characterization and order reduction of mechanical systems: an overview. *Nonlinear Dyn.* **41**, 147–169 (2005)
3. Lu, K., Chen, Y.S., Cao, Q.J., Hou, L.: Bifurcation analysis of reduced rotor model based on nonlinear transient POD method. *Int. J. Nonlinear Mech.* **89**, 83–92 (2017)
4. Lu, K., Yu, H., Chen, Y.S., Cao, Q.J., Hou, L.: A modified nonlinear POD method for order reduction based on transient time series. *Nonlinear Dyn.* **79**, 1195–1206 (2015)
5. Lu, K., Chen, Y.S., Jin, Y.L., Hou, L.: Application of the transient proper orthogonal decomposition method for order reduction of rotor systems with faults. *Nonlinear Dyn.* **86**, 1913–1926 (2016)
6. Lu, K., Lu, Z.Y., Chen, Y.S.: Comparative study of two order reduction methods for high-dimensional rotor systems. *Int. J. Nonlinear Mech.* **106**, 330–334 (2018)
7. Kim, S.M., Kim, J.G., Chae, S.W., et al.: Evaluating mode selection methods for component mode synthesis. *AIAA J.* **54**, 2852–2863 (2016)
8. Bathe, K., Dong, J.: Component mode analysis with subspace iterations for controlled accuracy of frequency and mode shape solutions. *Comput. Struct.* **139**, 28–32 (2014)
9. Dimitri, K., Mahmoud, I.H.: Bloch mode synthesis: ultrafast methodology for elastic band-structure calculations. *Phys. Rev. E* **90**, 063306 (2014)
10. Ulrich, H., Axel, K.: Error estimates for a two-dimensional special finite element method based on component mode synthesis. *Electron. Trans. Numer. Anal.* **41**, 109–132 (2014)
11. Krysko, A.V., Awrejcewicz, J., Saltykova, O.A., Vetsel, S.S., Krysko, V.A.: Nonlinear dynamics and contact interactions of the structures composed of beam-beam and beam-closed cylindrical shell members. *Chaos Solitons Fractals* **91**, 622–638 (2016)
12. Awrejcewicz, J., Krysko, A.V., Saltykova, O.A., Vetsel, S.S., Krysko, V.A.: Chaotic dynamics of two coaxially-nested cylindrical shells reinforced by two beams. *Commun. Nonlinear Sci. Numer. Simul.* **62**, 339–351 (2018)
13. Sun, Q., Ma, H.: Comparison of rubbing induced vibration responses using varying-thickness-twisted shell and solid-element blade models. *Mech. Syst. Signal Process.* **108**, 1–20 (2018)
14. Shammugam, A., Padmanabhan, C.: A fixed-free interface component mode synthesis method for rotordynamic analysis. *J. Sound Vibr.* **297**, 664–679 (2006)
15. Lu, K.: Statistical moment analysis of multi-degree of freedom dynamic system based on polynomial dimensional decomposition method. *Nonlinear Dyn.* **93**, 2003–2018 (2018)
16. Lu, K., Jin, Y.L., Chen, Y.S., Yang, Y.F., Hou, L., Zhang, Z.Y., Li, Z.G., Fu, C.: Review for order reduction based on proper orthogonal decomposition and outlooks of applications in mechanical systems. *Mech. Syst. Signal Process.* **123**, 264–297 (2019)

Vibration Analysis of Washing Machines in the Drum Plane



Cem Baykal, Ender Cigeroglu, and Yiğit Yazıcıoglu

Abstract In this study, a nonlinear mathematical model for drum-type washing machines is developed considering rotating unbalance type excitation. Nonlinear differential equations of motion are converted into a set of nonlinear algebraic equations by using harmonic balance method (HBM). The resulting nonlinear algebraic equations are solved by using Newton's method with arc-length continuation. Several case studies are performed in order to observe the effects of orientation angles of springs and dampers supporting the drum. In order to reduce the steady-state vibration amplitude of the drum and transmitted force through springs and dampers, suitable spring and damper orientation angles are identified. Moreover, in order to further reduce the vibration amplitude of the drum, dry friction dampers are introduced to the system. It is clearly observed that dry friction dampers are solving the walking problem of washing machines.

Keywords 2D washing machine model · Nonlinear vibrations · Dry friction damper · Harmonic balance method

1 Introduction

As the standards of living and customer expectations are going up, there has been a demand for reduced noise and minimized vibration of machines during operation. Since it is very critical to satisfy customers, the design criterion of any machine has a tendency toward the minimized vibration and noise. Washing machines are also being affected by this trend in both acoustical and visual terms. Therefore, there have been many studies to reduce/minimize vibration and noise of washing machines during the operation.

C. Baykal · E. Cigeroglu (✉) · Y. Yazıcıoglu
Middle East Technical University, Ankara, Turkey
e-mail: ender@metu.edu.tr

Türkay et al. [1, 2] modeled the washing machine with four dry friction shock absorbers containing linear spring. In the derivation of equations of motion, Newton's second law is used by neglecting Euler effects, and transient response of the system is considered by increasing the frequency of unbalance empirically. After solving the nonlinear differential equations of motion by Runge–Kutta integration, the forces on the dry friction dampers are minimized by selecting spring and dry friction damper constants.

Conrad and Soedel [3] worked on the oscillatory walking motion of the washing machine by using a 2D model. By considering the coulomb damping between the washing machine and ground, effects of frequency on the magnitudes of walking motion of horizontal axis washing machines are analyzed. Papadopoulos and Papadimitriou [4] created a different 2D model to observe the effects of frequency on the walking behavior of the horizontal axis washing machine. In the study, an active balancing system with one and two balancing masses is introduced.

Bae et al. [5] worked on a 3D vertical axis washing machine model with a hydraulic balancer. The fluid in the hydraulic balancer moves as the rotating unbalance excites the system, and the balancer acts as a passive balancing system. It provides an additional mass effect; however, the center of mass of the fluid also changes and makes the balancer more effective. Chen and Zhang [6, 7] worked on stability analysis of a vertical axis washing machine with and without hydraulic balancer by considering steady-state response via bifurcation diagrams. Tangential damping coefficients and unbalance mass are used as two parameters in bifurcation analyses. Later, the installation height of the hydraulic balancer is optimized with the aim of minimizing vibration amplitude in both transient and steady state response [8, 9].

Nygård and Berbyuk [10] created a detailed model of horizontal axis washing machines using commercial multi-body dynamic simulation programs. To minimize the magnitude of vibration, ball balancers, which are commonly used in counter-balancing, are used through a Pareto optimization [11]. Boyraz and Gündüz [12] derived a 2D dynamical model of a horizontal axis washing machine in the rotation plane. The transient solution of the system is obtained, and design parameters are optimized by utilizing the genetic algorithm.

Argentini et al. [13] worked on a linearized 3D dynamical model with both dry friction and tuned mass dampers for horizontal axis washing machines. Galavotti et al. [14] used a shaker and a PID controller to minimize the vibration amplitudes in the vertical axes washing machines. Campos and Nicoletti [15] introduced a dynamic absorber to prevent excessive amounts of vibrations, only for vertical axis washing machines. Buskiewicz and Pittner [16] introduced the disengaging dampers for washing machines, and vibration amplitudes are drastically reduced. Chrzan et al. [17] introduced magnetorheological fluid dampers to overcome the vibration problem.

Almost all of the studies are performed by solving the resulting nonlinear differential equations of motion by direct time integration and obtained transient response of the system. However, it is known that washing machines generate sound and vibration during their steady-state operation during spinning cycles,

i.e., >800 rpm. To analyze this problem, obtaining the steady-state solution and comparing the effect of spinning speed to the vibration amplitude is necessary. Moreover, using time integration to analyze steady-state response is expensive in terms of computational time.

In this work, a simple 2D dynamic model in the rotating plane is derived with three degrees of freedom by using two springs and two viscous dampers or two dry friction dampers. This configuration of springs and dampers are the most common models used in the literature. Resulting nonlinear differential equations of motion are converted to a set of nonlinear algebraic equations by using the harmonic balance method (HBM), which are solved by utilizing Newton's method. Since the vibration of the washing machine is directly related to the vibration of the cabinet, forces exerted to the cabinet through dampers and springs are to be minimized. Therefore, in this study, orientation angles of springs and dampers supporting the drum, spring stiffness, and damper constants are taken as parameters to be studied. It is observed that dry friction dampers have an enormous amount of reduction in the transmitted force to the cabinet and ground, especially at higher frequencies, compared to viscous dampers. Moreover, this is the first study in the literature that analyzes the frequency response functions of the washing machine drum.

2 Mathematical Modeling

2D dynamic model developed in this study includes the drum, springs, and dampers, as shown in Fig. 1a. Points 1–4 and f_1 – f_4 indicate the connection points of springs

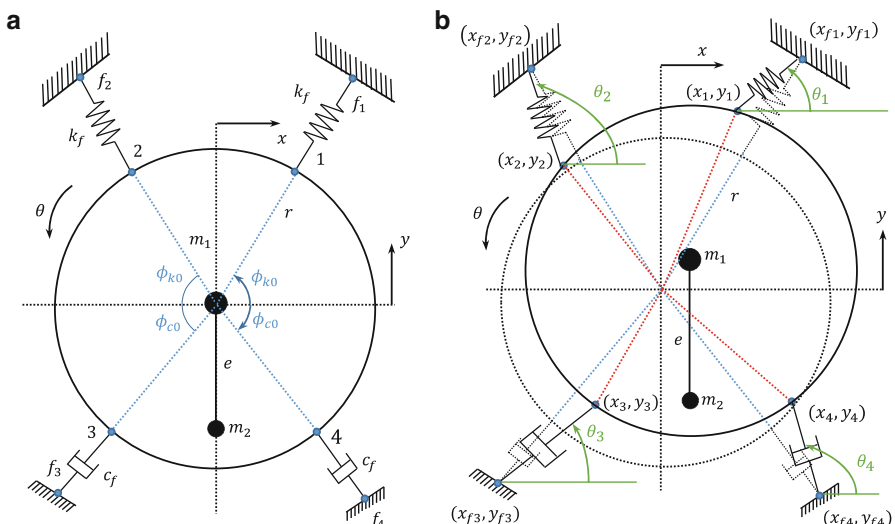


Fig. 1 (a) 2D model of the drum. (b) Exaggerated view of motion

Table 1 Nomenclature

m_1	Mass of the washing machine	k	Spring constant
m_2	Mass of the laundry	c	Viscous damping constant
ϕ_{c0}	Initial orientation angles of dampers	k_f	Free length of springs
ϕ_{k0}	Initial orientation angles of springs	c_f	Free length of dampers
e	Eccentricity of the mass center of laundry	r	Radius of the drum
θ_i	Instantaneous angles of point i	μN	Slip load of dry friction damper
x_i	Instantaneous horizontal position of point i	x_{fi}	x of fixed of resilient element at point i
y_i	Instantaneous vertical position of point i	y_{fi}	y of fixed of resilient element at point i

and dampers. For better understanding the motion and the forces applied to the drum, an exaggerated view of motion is shown in Fig. 1b. In the equation of motion (EOM), x , y , and θ are used as generalized coordinates, which are displacements with respect to the origin and the rotation of the drum, respectively. Nomenclature for other variables is given in Table 1. Related position variables are as follows:

$$x_1 = r \cos(\phi_{k0} + \theta) + x, \quad y_1 = r \sin(\phi_{k0} + \theta) + y \quad (1)$$

$$x_{f1} = (r + k_f) \cos(\phi_{k0}), \quad y_{f1} = (r + k_f) \sin(\phi_{k0}) \quad (2)$$

$$x_2 = r \cos(\pi - \phi_{k0} + \theta) + x, \quad y_2 = r \sin(\pi - \phi_{k0} + \theta) + y \quad (3)$$

$$x_{f2} = (r + k_f) \cos(\pi - \phi_{k0}), \quad y_{f2} = (r + k_f) \sin(\pi - \phi_{k0}) \quad (4)$$

$$x_3 = r \cos(\pi + \phi_{c0} + \theta) + x, \quad y_3 = r \sin(\pi + \phi_{c0} + \theta) + y \quad (5)$$

$$x_{f3} = (r + c_f) \cos(\pi + \phi_{c0}), \quad y_{f3} = (r + c_f) \sin(\pi + \phi_{c0}) \quad (6)$$

$$x_4 = r \cos(-\phi_{c0} + \theta) + x, \quad y_4 = r \sin(-\phi_{c0} + \theta) + y \quad (7)$$

$$x_{f4} = (r + c_f) \cos(-\phi_{c0}), \quad y_{f4} = (r + c_f) \sin(-\phi_{c0}) \quad (8)$$

Related angles are:

$$\theta_1 = \text{atan}_2(y_{f1} - y_1, x_{f1} - x_1), \quad \theta_2 = \text{atan}_2(y_{f2} - y_2, x_{f2} - x_2) \quad (9)$$

$$\theta_3 = \text{atan}_2(y_3 - y_{f3}, x_3 - x_{f3}), \quad \theta_4 = \text{atan}_2(y_4 - y_{f4}, x_4 - x_{f4}) \quad (10)$$

Forces on the springs can be given as:

$$F_{k_i} = k \left(\sqrt{(x_i - x_{fi})^2 + (y_i - y_{fi})^2} - k_f \right), \quad \text{where } i = 1, 2 \quad (11)$$

To write forces on the dampers, velocities of the connection points along the instantaneous orientation of dampers are necessary. Related velocity terms are given as:

$$\dot{x}_3 = -r \sin(\pi + \phi_{c0} + \theta) \dot{\theta} + \dot{x}, \quad \dot{y}_3 = r \cos(\pi + \phi_{c0} + \theta) \dot{\theta} + \dot{y} \quad (12)$$

$$\dot{x}_4 = -r \sin(-\phi_{c0} + \theta) \dot{\theta} + \dot{x}, \quad \dot{y}_4 = r \cos(-\phi_{c0} + \theta) \dot{\theta} + \dot{y} \quad (13)$$

Projections of the velocities along the dampers are as follows:

$$v_3 = \dot{x}_3 \cos(\theta_3) + \dot{y}_3 \sin(\theta_3), \quad v_4 = \dot{x}_4 \cos(\theta_4) + \dot{y}_4 \sin(\theta_4) \quad (14)$$

Forces on the viscous dampers can be written as:

$$F_{c3} = -cv_3, \quad F_{c4} = -cv_4 \quad (15)$$

To write the EOM in x , y , and θ directions, x and y components of these forces are obtained as follows:

$$F_{k_i x} = F_{k_i} \cos(\theta_i), \quad F_{k_i y} = F_{k_i} \sin(\theta_i), \quad \text{where } i = 1, 2 \quad (16)$$

$$F_{c_i x} = F_{c_i} \cos(\theta_i), \quad F_{c_i y} = F_{c_i} \sin(\theta_i), \quad \text{where } i = 3, 4 \quad (17)$$

Moments caused due to these forces can be expressed as:

$$M_1 = (x_1 - x) F_{k1y} - (y_1 - y) F_{k1x}, \quad M_2 = (x_2 - x) F_{k2y} - (y_2 - y) F_{k2x} \quad (18)$$

$$M_3 = (x_3 - x) F_{c3y} - (y_3 - y) F_{c3x}, \quad M_4 = (x_4 - x) F_{c4y} - (y_4 - y) F_{c4x} \quad (19)$$

EOM for all degrees of freedom can be written as:

$$\sum F_x = (m_1 + m_2) \ddot{x} = F_{k1x} + F_{k2x} + F_{c3x} + F_{c4x} + m_2 e \omega^2 \sin(\omega t) \quad (20)$$

$$\sum F_y = (m_1 + m_2) \ddot{y} = F_{k1y} + F_{k2y} + F_{c3y} + F_{c4y} + m_2 e \omega^2 \cos(\omega t) \quad (21)$$

$$\sum M = (I_1 + m_2 e^2) \ddot{\theta} = M_1 + M_2 + M_3 + M_4 \quad (22)$$

In the EOM, damper forces and spring forces are derived as forces acting on the drum; therefore, they are on the right hand side. To make a comparison, a linear system is also defined by just assuming small oscillations, i.e., neglecting θ and decoupling x and y coordinates. These nonlinear differential equations of motions are converted into a set of nonlinear algebraic equations by utilizing harmonic balance method (HBM). In HBM, periodic external forces, nonlinear internal forces and the response of the system are represented by Fourier series. These representations are substituted into the differential equations of motion, and coefficients of harmonics are balanced, which results in a set of nonlinear algebraic equations. More information on the method can be found in [18–20]. In the solution, all forces are represented by utilizing seven harmonics, and sample results obtained are given in Fig. 2. Consider single harmonic in the displacement representation and six nonlinear algebraic equations in terms of the unknown amplitudes of sine and cosine terms. Solution of this nonlinear algebraic equation set is obtained by Newton's method with arc-length continuation. Parameters used in this study are given in Table 2 unless otherwise specified.

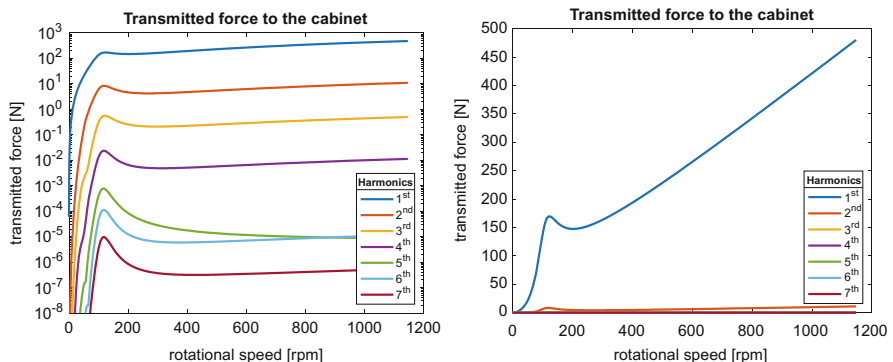
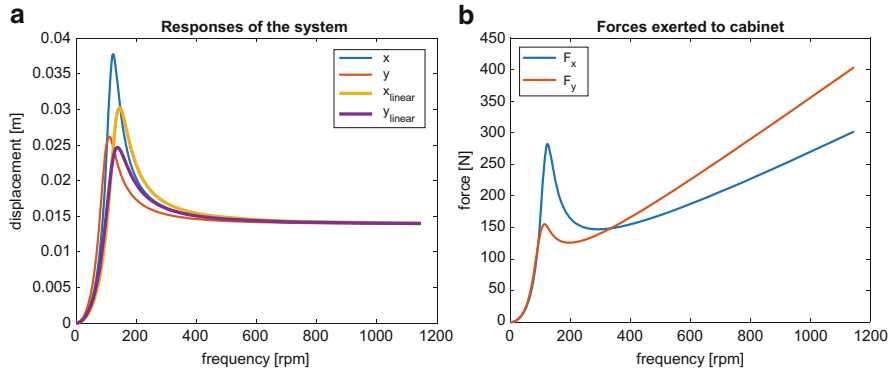


Fig. 2 Effect of number of harmonics

Table 2 Numerical values

m_1	40 kg	r	30 cm
m_2	6 kg	k	6000 N/m
ϕ_{k0}	45°	c	200 Ns/m
ϕ_{c0}	45°	μN	200 N
c_f, k_f	40 cm	γ	0.08

**Fig. 3** (a) Displacement of drum vs. spin speed. (b) Transmitted force vs. spin speed

3 Results and Discussion

If viscous dampers are used, at spinning frequencies (800–1000 rpm), washing machines tend to walk. Figures 2 and 3 show vertical forces and the displacement of the drum as a function frequency, respectively. It is clearly seen in Fig. 3b that vertical forces at high frequencies overcome the weight of the machine and friction force between washing machine and ground becomes not large enough to hold the washing machine stationary. As a result, since the horizontal forces on the cabinet are much higher than the friction force between the cabinet and the floor, it leads to walking motion.

To prevent excessive forces at high frequencies, dry friction dampers are introduced instead of viscous dampers. If a single harmonic motion as $x = X \sin(\psi)$ is considered, friction force can be expressed as:

$$f_{\text{dry}}(x) = \begin{cases} -\mu N + k(x + \delta) & \text{if } \frac{\pi}{2} \leq x \leq \psi_1 \\ -\mu N & \text{if } \psi_1 \leq x \leq \pi \end{cases} \quad (23)$$

where

$$\delta = \frac{2\mu N - kX}{k}; \quad \psi_1 = \pi - a \sin\left(-\frac{\delta}{X}\right) \quad (24)$$

HBM represents the EOM by sine and cosine components. This nonlinear friction force can be expressed in Fourier series utilizing a single harmonic for single harmonic motion as follows:

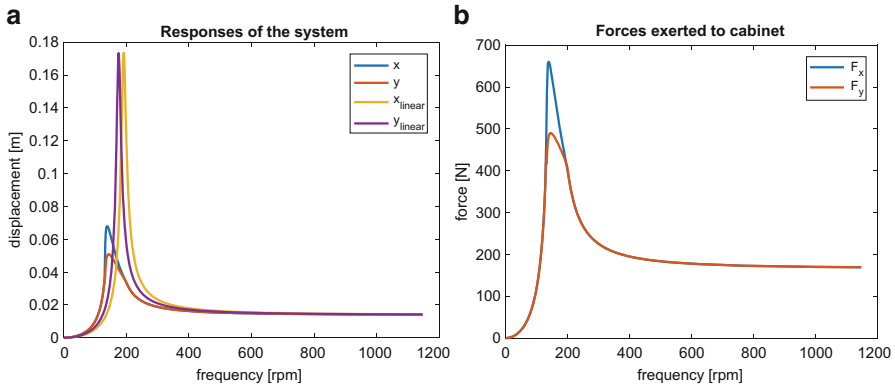


Fig. 4 (a) Displacement of drum vs. spin speed. (b) Transmitted force vs. spin speed

$$F_s = \frac{2}{\pi} \left(\int_{\pi/2}^{\psi_1} (-\mu N + k(x + \delta)) \sin(\psi) d\psi + \int_{\psi_1}^{3\pi/2} (-\mu N) \sin(\psi) d\psi \right) \quad (25)$$

$$F_c = \frac{2}{\pi} \left(\int_{\pi/2}^{\psi_1} (-\mu N + k(x + \delta)) \cos(\psi) d\psi + \int_{\psi_1}^{3\pi/2} (-\mu N) \cos(\psi) d\psi \right) \quad (26)$$

where F_s and F_c are Fourier coefficients of the sine and cosine components of the nonlinear friction force, respectively. In order to calculate these integrals, the relative displacement between the ends of dry friction dampers should be represented utilizing single harmonic. Relative displacement between the ends of dry friction dampers can be expressed similar to springs and dampers as follows:

$$d_i = \sqrt{(x_i - x_{f_i})^2 + (y_i - y_{f_i})^2} - c_f, \quad \text{where } i = 3, 4 \quad (27)$$

Orientation angles different than 45° are used, and the results obtained are given in Fig. 4. Results for both systems with viscous or dry friction dampers obey the expectations of the rotating unbalance excitation. FRF graph starts from zero and converges to me/M as the frequency goes to infinity. When the frequency is low, forces acting on the dry friction dampers are too small to move them; therefore, they are acting like springs. The system consists of a drum and four springs. Around the natural frequency of the drum, dry friction dampers start working and drastically decrease the amplitude of vibrations, as expected. For higher frequencies, dry friction dampers act like springs again. Studying Figs. 3b and 4b, it is clearly seen that for higher frequencies, the vertical and horizontal forces settle to a low value compared to viscous dampers, in which case they increase as frequency increases.

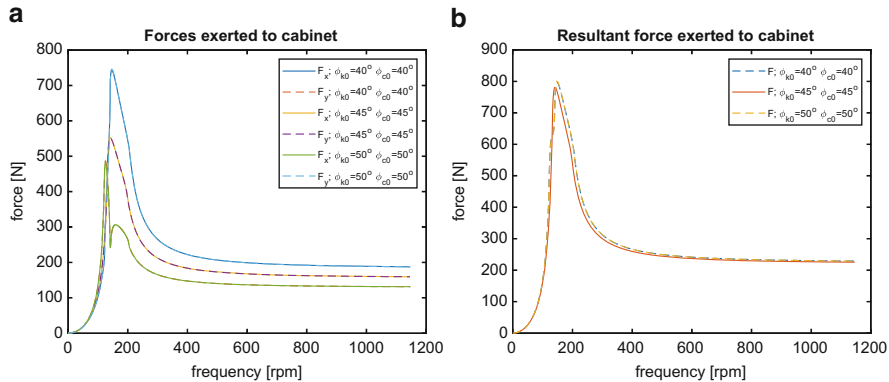


Fig. 5 (a) Effect of orientation angles on the transmitted force vs. spin speed. (b) Resultant force on the cabinet vs. rotation speed

Selecting a dry friction damper with a low slip load, μN , decreases the transmitted force to the cabinet at the spinning cycle; however, it increases the displacement of the drum and the transmitted force to the cabinet at the frequencies close to the natural frequency. This engineering trade-off is clearly seen by comparing Figs. 3b and 4b. At this point, observing the effects of k and μN values of the dry friction dampers are vital; however, they will be taken into consideration after analyzing the effects of orientation angles of springs and dampers.

It is expected to have a correlation between orientation angles and transmitted forces to the cabinet. As depicted in Fig. 5a, b, orientation angles have a direct effect on the transmitted force in x and y directions when the amplitude of the oscillations is high; however, they do not affect the spinning cycle process as observed from Fig. 4b. When ϕ_{k0} and ϕ_{c0} are selected as 45° , complete symmetry is produced along with both x and y directions, and total transmitted force in x and y direction becomes the same, as expected. Changing the orientation angles of springs and viscous dampers inversely lead to considerable differences in terms of transmitted force to the cabinet in x and y directions. However, the total transmitted force is almost the same in the whole frequency range, as seen from Fig. 5b.

Changing the orientation angles of the springs and viscous dampers in the same direction increases the total nonlinearity of the system. At limiting cases, it is equal to attaching components only in x or y directions, which is not feasible. In Fig. 6a, b, similar results with inversely changing orientation angles are given. In this case, there is a significant difference between transmitted forces in x and y directions. However, the resultant force exerted to the cabinet is almost the same for all frequency range. From Fig. 6a, b, it is clearly seen that even if the total transmitted forces are the same for three cases, their directions are not the same.

Choosing both of the implementation angles as 45° has many advantages. It provides the minimum resultant force exerted to the cabinet; moreover, it results in even distribution of the resultant force, which definitely prolongs the cabinet life.

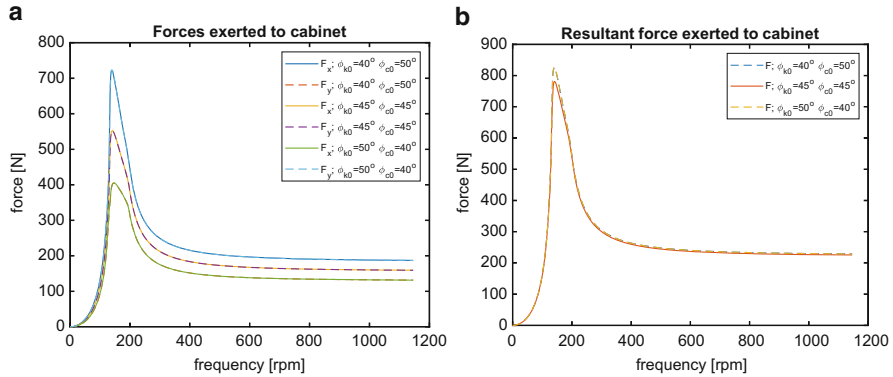


Fig. 6 (a) Effect of orientation angles on the transmitted force vs. spin speed. (b) Resultant force on the cabinet vs. rotation speed

It prevents nonlinearities in transmitted forces and in displacements as observed from Fig. 5a. For some special cases, manufacturers may want to have different magnitudes of forces in x and y direction; however, in this chapter minimizing total resultant force is considered, and 45° is selected as the best orientation for springs and dampers.

At this point, final parameters to be considered are the spring stand slip load of the dry friction dampers to minimize force acting on the cabinet. Dry friction damper starts to apply a constant force to the drum whenever the displacement gets larger. The value of the slip load becomes an important parameter for the low frequencies. However, in the spinning cycle, the total displacement of the drum is not enough to cause slip in the dry friction damper. Therefore, slip load loses its effect on the transmitted force to the cabinet, and contact stiffness k becomes the important parameter for high frequencies. Selecting both of them as small as possible leads to minimum transmitted force to the cabinet; but it will create large displacements, which is not feasible. The amplitude of the displacement becomes a physical constraint in this problem, and throughout an optimization process, it has to be taken into consideration.

In Fig. 7a, b, it is clearly seen that lower slip loads decrease the transmitted force to the cabinet around the resonance frequency and increase the total displacement of the drum. However, making the dry friction force very small causes the drum to vibrate in an asymmetrical way with different vibration amplitudes in x and y directions. In Fig. 8a, b, it is observed that lower spring constant values decrease the transmitted force to the cabinet in the spinning cycle. However, this leads to higher vibration amplitudes during the washing process, i.e., <400 rpm.

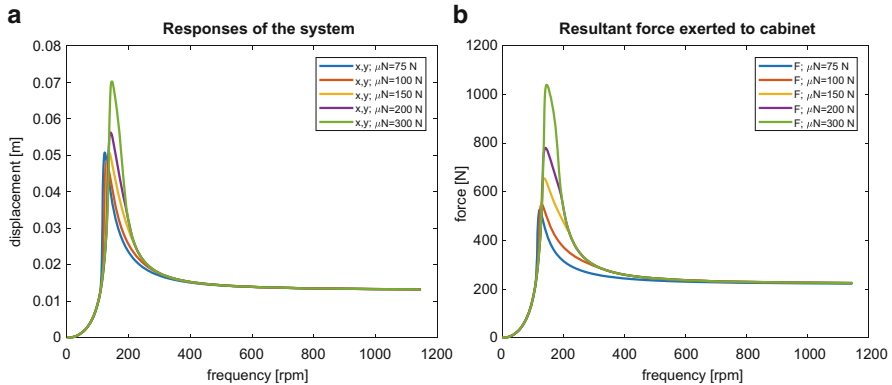


Fig. 7 (a) Effect of slip load on the displacement vs. spin speed. (b) Effect of slip load on the transmitted force vs. spin speed

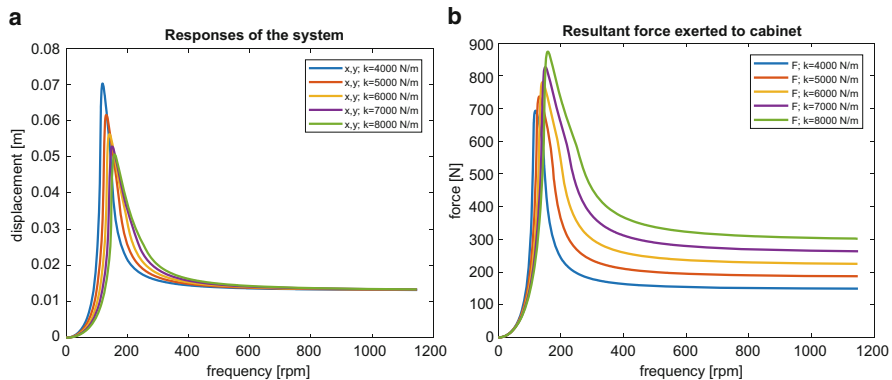


Fig. 8 (a) Effect of spring constant on the displacement vs. spin speed. (b) Effect of spring constant on the transmitted force vs. spin speed

4 Conclusion

A 2D nonlinear dynamical model of a washing machine drum is developed in this study. Viscous and dry friction dampers are considered separately in the model developed. Harmonic balance method is used to transfer the nonlinear differential equations of motion to frequency domain resulting into a set of nonlinear algebraic equations, and Newton's method with arc-length continuation is used to calculate the steady-state response. Several case studies are performed, and the effect of different parameters is studied. It is clearly seen that proper use of friction dampers can significantly limit the force transmitted to the cabinet and outperforms viscous dampers.

References

1. Türkay, O.S., Kiray, B., Tugcu, A.K., Sümer, T.: Formulation and implementation of parametric optimisation of a washing machine suspension system. *Mech. Syst. Signal Process.* **9**(4), 359–377 (1995)
2. Türkay, O.S., Sümer, I.T., Tuğcu, A.K., Kiray, B.: Modeling and experimental assessment of suspension dynamics of a horizontal-axis washing machine. *J. Vib. Acoust.* **120**(2), 534 (1998)
3. Conrad, D.C., Soedel, W.: On the problem of oscillatory walk of automatic washing machines. *J. Sound Vib.* **188**(3), 301–314 (1995)
4. Papadopoulos, E., Papadimitriou, I.: Modeling, design and control of a portable washing machine during the spinning cycle. 2001 IEEE/ASME International Conference on Advanced Intelligent Mechatronics. Proceedings (Cat. No.01TH8556), 2(July), pp. 899–904 (2001)
5. Bae, S., Lee, J.M., Kang, Y.J., Kang, J.S., Yun, J.R.: Dynamic analysis of an automatic washing machine with a hydraulic balancer. *J. Sound Vib.* **257**(1), 3–18 (2002)
6. Chen, H.W., Zhang, Q.J.: Stability analyses of a vertical axis automatic washing machine without balancer. *J. Sound Vib.* **329**(11), 2177–2192 (2010)
7. Chen, H.W., Zhang, Q.J.: Stability analyses of a vertical axis automatic washing machine with a hydraulic balancer. *Mech. Mach. Theory* **46**(7), 910–926 (2011)
8. Chen, H.W., Zhang, Q.J., Fan, S.Y.: Study on steady-state response of a vertical axis automatic washing machine with a hydraulic balancer using a new approach and a method for getting a smaller deflection angle. *J. Sound Vib.* **330**(9), 2017–2030 (2011)
9. Chen, H.W., Ji, W.X., Zhang, Q.J., Cao, Y., Fan, S.Y.: A method for vibration isolation of a vertical axis automatic washing machine with a hydraulic balancer. *J. Mech. Sci. Technol.* **26**(2), 335–343 (2012)
10. Nygård, T., Berbyuk, V.: Multibody modeling and vibration dynamics analysis of washing machines. *Multibody Syst. Dyn.* **27**(2), 197–238 (2012)
11. Nygård, T., Berbyuk, V.: Optimization of washing machine kinematics, dynamics, and stability during spinning using a multistep approach. *Optim. Eng.* **15**(2), 401–442 (2014)
12. Boyraz, P., Gündüz, M.: Dynamic modeling of a horizontal washing machine and optimization of vibration characteristics using Genetic Algorithms. *Mechatronics* **23**(6), 581–593 (2013)
13. Argentini, T., Belloli, M., Robustelli, F.C., Martegani, L., Fraternale, G.: Innovative Designs for the Suspension System of Horizontal-Axis Washing Machines: Secondary Suspensions and Tuned Mass Dampers. Volume 4B: Dynamics, Vibration and Control, 4 B, V04BT04A058 (2013)
14. Galavotti, T.V., Sanchez, J.P.: Hardware in the Loop As a Tool for the Development of Wash Machine Suspension, 6(Cobem), pp. 9301–9310 (2013)
15. Campos, R.O., Nicoletti, R.: Vibration reduction in vertical washing machine using a rotating dynamic absorber. *J. Braz. Soc. Mech. Sci. Eng.* **37**(1), 339–348 (2014)
16. Busiekiewicz, J., Pittner, G.: Reduction in vibration of a washing machine by means of a disengaging damper. *Mechatronics* **33**, 121–135 (2016)
17. Chrzan, M.J., & Carlson, J.D.: MR fluid sponge devices and their use in vibration control of washing machines, Proceedings of SPIE 4331, Smart Structures and Materials 2001: Damping and Isolation, <https://doi.org/10.1117/12.432719> (2001)
18. Von Groll, G., Ewins, D.: The harmonic balance method with arc-length continuation in rotor/stator contact problems. *J. Sound Vib.* **241**(2), 223–233 (2001)
19. Cigeroglu, E., An, N., Menq, C.H.: A microslip friction model with normal load variation induced by normal motion. *Nonlinear Dyn.* **50**(2), 609–626 (2007)
20. Erisen, Z.E., Cigeroglu, E.: Frequency domain optimization of dry friction dampers on buildings under harmonic excitation. *Conf. Proc. Soc. Exp. Mech. Ser.* **1**, 113–125 (2012)

Nonlinear Model for Wear Effects in Hydrodynamic Bearings Applied to Rotating Systems



Tiago Henrique Machado and Gustavo Chaves Storti

Abstract Wear of hydrodynamic bearings is one of the main causes of forced stops on machines and rotating systems. In this way, the purpose of this chapter is to investigate the time response effects of nonlinearities inserted by wear on hydrodynamic bearings in rotating systems. The rotor is modeled using traditional finite element method, and the Reynolds equation is solved by finite volume method, to evaluate the hydrodynamic bearing behavior. For the numerical time integrator, nonlinear Newmark scheme is used along with Newton—Raphson method to estimate the response at each time step. The orbit of the shaft inside the bearings revealed that for low speeds, even with the small size of orbits, the introduction of wear causes changes in center, size, and position of the orbits. At critical speed, the nonlinearities from the worn bearings became even more significant and tend to change dramatically the system response. In addition, the system response to different levels of rotating unbalanced mass proves the nonlinear profile due to the presence of wear on the hydrodynamic bearings.

Keywords Rotating system · Wear in hydrodynamic bearing · Nonlinear character

1 Introduction

Analysis of rotating systems involve many parameters and must include the rotor interaction with other components, such as bearings. Being responsible for machine support and force transmission between rotor and foundation, the role of these components are very important. Early fault detection is essential to avoid sudden failures during operation of rotating machines. Therefore, failures associated with

T. H. Machado (✉) · G. C. Storti

Department of Integrated Systems, School of Mechanical Engineering, University of Campinas, Campinas, Brazil
e-mail: tiagomh@fem.unicamp.br

hydrodynamic bearings are one of the most common causes of rotor shutdowns, and the wear of these bearing walls affects a large number of machineries.

Early fault detection in this type of component is essential to avoid sudden failures during operation of rotating machines in the industry. In addition, knowing the behavior of worn bearings is very important as well. Dufrane et al. [1] was one of the first to investigate the wear of bearings in steam turbines and established two models of wear geometry used for a more in-depth analysis. Since then one of the models (the assumption of an abrasive wear with an arc larger than the bearing diameter) proposed in Dufrane et al. [1] has been widely used to predict the behavior of worn bearings, since it was experimentally validated by Hashimoto et al. [2].

In the range of recent works, Papadopoulos et al. [3] presented a theoretical identification method for hydrodynamic bearing wear by means of rotor response measurements. Fillon and Bouyer [4] studied the performance of worn plain journal bearings considering the local thermal effects. Chun and Khonsari [5] estimated the wear depth due to material removal when the bearing experiences elastohydrodynamic lubrication. Sharma and Awasthi [6] made a theoretical study of worn bearing performance under specific length/diameter ratios.

Regarding the identification of wear parameters, several works have been published in recent years, with different approaches and results as can be seen, for instance, in Gertzos et al. [7] and Machado and Cavalca [8]. The wear effects on the characteristics of hydrodynamic bearings and its influence in rotating system response have been well studied. However, in the vast majority of works, the Reynolds equations for worn bearings are solved using linear models.

In this context, the purpose of this chapter is to use a nonlinear model for the wear in hydrodynamic bearings in order to analyze the time response of a rotor-bearing system, comparing the orbit of the shaft within the bearing in two critical conditions, namely high load at low rotating speed and high load at the critical speed. In addition, the system response is evaluated in varied conditions with different levels of rotating unbalance mass, in order to prove the nonlinear profile due to the presence of wear on the hydrodynamic bearings. The numerical model used in this work is best presented in Machado and Cavalca [9], since this model brings an evolution of the model initially proposed by Dufrane et al. [1].

2 Numerical Model

The numerical analysis assumptions considers a rigid support structure in order to isolate the effects originated by the bearings. Rotor is modeled using the finite element method employing Timoshenko's beam elements with four degrees of freedom per node, two translational and two rotational (lateral vibration). The resulting equation of motion is given by Eq. (1).

$$[M]\{\ddot{x}\} + ([C] + \Omega[G])\{\dot{x}\} + [K]\{x\} = \{F\} \quad (1)$$

where $[M]$, $[C]$, $[K]$, and $[G]$ are the global mass, damping, stiffness and gyroscopic matrices, respectively. Ω represents the rotating speed of the rotor, $\{x\}$ is the vector with the system's degrees of freedom, and $\{F\}$ contains the external forces, for this case, the unbalance force, and the hydrodynamic force of the bearings. The $[C]$ matrix, which represents the shaft equivalent structural damping, is modeled proportional to the mass and stiffness matrices, as shown in Eq. (2).

$$[C] = \alpha [M] + \beta [K] \quad (2)$$

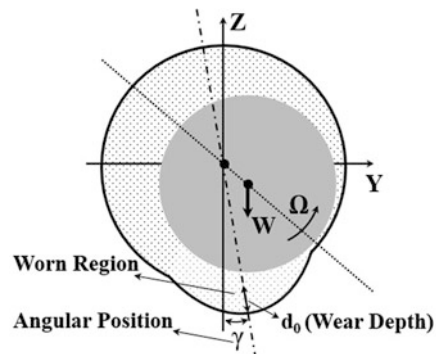
Reynolds equation is the basis of hydrodynamic lubrication theory, and its solution provides the pressure distribution in lubricating fluid. In this work, Reynolds equation (Eq. 3) is solved numerically by finite volume method, using a relaxation procedure to smooth the transition in the cavitation region (for cavitation, the Gumbel's model is used). The pressure field (p) is numerically integrated, using Euler's method, to obtain the supporting hydrodynamic forces. These forces are inserted into the force vector of the system's equation of motion for the computation of time domain response.

$$\frac{\partial}{\partial \theta} \left(h^3 \frac{\partial p}{\partial \theta} \right) + \frac{\partial}{\partial Z} \left(h^3 \frac{\partial p}{\partial Z} \right) = 6\mu \frac{\partial h}{\partial \theta} + 12\mu \frac{\partial h}{\partial t} \quad (3)$$

where μ is the absolute viscosity. The wear model used here was initially proposed by Dufrane et al. [1] and adapted by Machado and Cavalca [8] based on the hypothesis of abrasive wear. This model considers that the wear has a uniform thickness (h) in axial direction, can have a variable depth, and can be located in any region of the bearing bore (Fig. 1). This wear pattern introduces an additional oil film layer with thickness $\delta_h(\theta)$, and the lubricating film thickness in the presence of wear becomes:

$$h(\theta) = h_0(\theta) + \delta_h(\theta) \quad (4)$$

Fig. 1 Worn bearing model



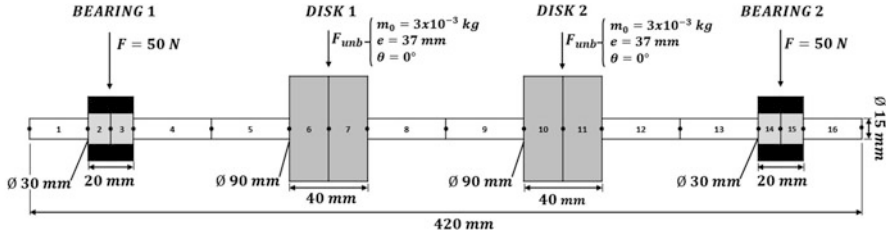


Fig. 2 Finite element model for the rotating system

For the numerical time integrator, nonlinear Newmark scheme, which combines prediction and correction variables, is used along with Newton–Raphson method in order to find the nodal position, velocity, and acceleration values for each time step [10].

As shown in Fig. 2 the model consists of 16 beam elements and 2 disk elements (nodes 7 and 11). Bearings are positioned at nodes 3 and 15. The steel shaft has an elastic modulus of 2.1×10^{11} N/m², 7800 kg/m³ density, poison coefficient 0.3, and a 0.796×10^{11} N/m² shear modulus. The coefficients of the proportional damping matrix are adjusted to $\alpha = 0$ and $\beta = 1.5 \times 10^{-5}$, as recommended by Liu and Novak [11]. For the system configuration showed in Fig. 2, the first critical speed occurs at approximately 72.3 Hz.

The purpose is to compare the shaft's orbit for the system with both undamaged bearings and worn bearings. Three different conditions are used: first, both bearings are undamaged and Reynolds equation is evaluated by the traditional linear approach; second, both bearings are undamaged and Reynolds equation is evaluated by a nonlinear approach; and third, both bearings are worn ($d_0 = 45\%$ of radial clearance and $\gamma = 10^\circ$) and Reynolds equation is evaluated by the proposed nonlinear approach. Tests are performed at two rotating speeds, 10 and 72.3 Hz, in order to evaluate the system behavior in low speed and at the critical speed. Two vertical forces are applied at the disk nodes to simulate high load condition. The excitation is given by unbalanced mass. Different levels of unbalance are tested in order to emphasize the high nonlinear character presented by the system when the bearings are worn. Since the system is symmetrical and following that usually just the bearing information is available in real machines, results are shown and compared just for Bearing 1.

3 Results and Discussion

Figure 3 shows that at low speeds (10 Hz), both the linear and nonlinear models for the undamaged bearings have a very similar response, being overlapped on the graph. By adding wear, it can be seen that the position of the orbit's center changes

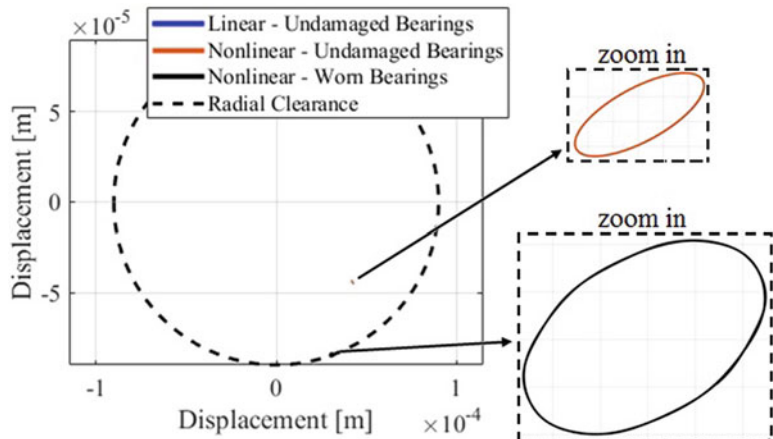
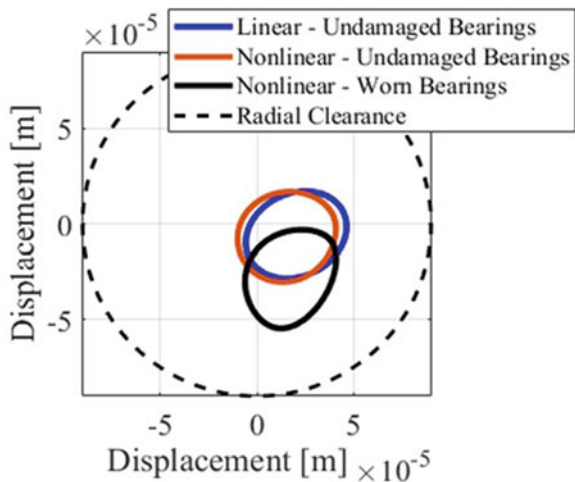


Fig. 3 Shaft's orbit inside Bearing 1 for rotating speed of 10 Hz

Fig. 4 Shaft's orbit inside Bearing 1 for rotating speed of 72.3 Hz



drastically, taking the shaft closer to the bearing wall. In addition, it is noted that the size of the orbit for the worn bearing case is larger and more nonlinear (distorted ellipse).

Figure 4 shows that at the critical speed (72.3 Hz), even for undamaged bearings, there is a certain degree of nonlinearity inherent for the hydrodynamic bearings, since the red and blue curves are no longer coincident. However, the differences between the orbits are not so striking. By including the wear, it is noted that both the shape of the orbit and the position of its center change drastically. This shows that, at the critical speed (region of high vibration amplitude), the presence of the wear on hydrodynamic bearings affects the behavior of the system response, greatly increasing the nonlinearities.

In order to highlight the rotating system nonlinear behavior at worn bearing condition, the system response was evaluated into three different levels of unbalance, as shown in Table 1.

As widely known, if the system has a linear behavior, its response will also preserve this property. Therefore, varying a certain amount of rotating unbalance mass will result in a response variation in the same ratio as the increase in the input excitation, since the system is linear, as mentioned before. In this way, the system responses were calculated for the three different cases presented in Table 1. For each case, the Bearing 1 orbit dimension was measured and compared for linear and nonlinear undamaged bearing models, in addition to the nonlinear worn bearing model. These results are shown in Table 2 for the rotating speed of 10 Hz and Table 3 for the rotating speed of 72.3 Hz (critical speed). As the orbits are not perfectly circular, it was necessary to establish an equivalent dimension as reference for the comparisons, taking into account the differences between the largest and smallest values of the vibration amplitudes in each direction, as shown in Eq. (5).

$$S = \sqrt{(y_{\max} - y_{\min})^2 + (z_{\max} - z_{\min})^2} \quad (5)$$

Analyzing Table 2, the linear behavior for undamaged bearings is clear: the proportion of unbalanced mass increased matches the gain in the orbit dimension. For case 1–2, the mass increases by a ratio of 1.5 and the same proportion is seen comparing the two orbits. The gain for case 2–3 respects this same property.

Also in Table 2, even in the case using the non-linear model for non-damaged bearings, the observed increase in the orbit dimension has a nearly linear behavior.

Table 1 Tested cases with different levels of rotating unbalance mass

Case	Unbalanced mass (g)
1	3.0
2	4.5
3	6.0

Table 2 Linear and nonlinear behavior of the unbalance response for rotating speed of 10 Hz

Case	Orbit dimension for undamaged linear model	Orbit dimension for undamaged nonlinear model	Orbit dimension for worn nonlinear model
1	9.13×10^{-7}	9.12×10^{-7}	3.26×10^{-7}
2	1.37×10^{-6}	1.37×10^{-6}	7.23×10^{-7}
3	1.83×10^{-6}	1.82×10^{-6}	9.64×10^{-7}

Table 3 Linear and nonlinear behavior of the unbalance response for rotating speed of 72.3 Hz

Case	Orbit dimension for undamaged linear model	Orbit dimension for undamaged nonlinear model	Orbit dimension for worn nonlinear model
1	1.41×10^{-4}	1.35×10^{-4}	6.98×10^{-5}
2	2.12×10^{-4}	1.86×10^{-4}	1.98×10^{-4}
3	2.82×10^{-4}	2.14×10^{-4}	2.36×10^{-4}

This is due to the small amplitudes of the orbit at low rotating speeds (in Machado et al. [12] there is a discussion about this fact). Regarding the system with worn bearings, it is noted in Table 2 that the response behavior is nonlinear, since the increase in vibration amplitude is not equivalent to the increase in excitation mass.

Finally, analyzing Table 3, where the rotating speed coincides with the first critical frequency, the linear response behavior appears only in the case in which the adopted model is also linear. The variation of the rotating unbalance mass does not match with the increase seen in the orbit dimension for other cases, even in the model with undamaged bearings. It is also noticed that for the case with worn bearings, the values observed for the orbit dimension is extremely nonlinear, and there is no way to directly relate the increase in the excitation magnitude with the increase in the vibration amplitude.

4 Conclusions

This work presents an analysis of the nonlinearities included in a rotating system due to the wear in the hydrodynamic bearings. The results show that the wear of the hydrodynamic bearings causes sensible changes in the dynamic behavior of rotating systems. These differences substantially increase the nonlinearity of vibrations, since it changes the magnitude and shape of the shaft's orbit.

Furthermore, it has been shown that by changing the magnitude of the excitation force present in the system, its response does not behave linearly when the bearings are affected by wear.

Therefore, once wear occurs on most machines after long periods of use, it can be concluded that it is very important to understand the nonlinear behavior of the system under these conditions.

Acknowledgments The authors would like to thank National Council for Scientific and Technological Development—CNPq, grant # 424899/2018-3, and grants # 2015/20363-6 and # 2017/07454-8 from the São Paulo Research Foundation (FAPESP) for the financial support to this research.

References

1. Dufrane, K.F., Kannel, J.W., McCloskey, T.H.: Wear of steam turbine journal bearings at low operating speeds. *J. Lubrication Technol.* **105**, 313–317 (1983)
2. Hashimoto, H., Wada, S., Nojima, K.: Performance characteristics of worn journal bearings in both laminar and turbulent regimes. Part I: steady-state characteristics. *ASLE Trans.* **29**, 565–571 (1986)
3. Papadopoulos, C.A., Nikolakopoulos, P.G., Gounaris, G.D.: Identification of clearances and stability analysis for a rotor-journal bearing system. *Mech. Mach. Theory* **43**, 411–426 (2008)
4. Fillon, M., Bouyer, J.: Thermohydrodynamic analysis of a worn plain journal bearing. *Tribol. Int.* **37**(2), 129–136 (2004)

5. Chun, S.M., Khonsari, M.M.: Wear simulation for the journal bearings operating under aligned shaft and steady load during start-up and coast-down conditions. *Tribol. Int.* **97**, 440–466 (2016)
6. Sharma, S., Awasthi, R.K.: Effect of aspect ratio on the performance of hydrodynamic journal bearing operating under wear. *Int. J. Theor. Appl. Mech.* **12**(3), 497–522 (2017)
7. Gertzos, K.P., Nikolakopoulos, P.G., Chasalevris, A.C., Papadopoulos, C.A.: Wear identification in rotor-bearing systems by measurements of dynamic bearing characteristics. *Comput. Struct.* **89**, 55–66 (2011)
8. Machado, T.H., Cavalca, K.L.: Investigation on an experimental approach to evaluate a wear model for hydrodynamic cylindrical bearings systems. *App. Math. Model.* **40**(21–22), 9546–9564 (2016)
9. Machado, T.H., Cavalca, K.L.: Modelling of hydrodynamic bearing wear in rotor-bearing systems. *Mech. Res. Commun.* **69**, 15–23 (2015)
10. Bathe, K.: Finite Element Procedures in Engineering Analysis. Prentice-Hall, Upper Saddle River (1982)
11. Liu, W., Novak, M.: Dynamic behaviour of turbine-generator-foundation. *Earthquake Eng Struct. Dyn.* **24**, 339–360 (1995)
12. Machado, T.H., Alves, D.S., Cavalca, K.L.: Discussion about nonlinear boundaries for hydrodynamic forces in journal bearing. *Nonlinear Dyn.* **92**, 2005–2022 (2018)

Author Index

A

- Abe, A., 248
Abed, E.H., 107
ABerezovoj, V.P., 524
Abramson, H.N., 187
Acampora, A., 400
Ackah, L., 320
Adamowski, J.C., 370
Adams, M.S.C., 10
Addessi, D., 237, 338
Aden, H., 76–78
Aguiar, R., 300
Ajovalasit, A., 358
Akbari, H., 320
Allemang, R.J., 332, 333
Al Shawa, O., 341
AL-Shudeifat, M.A., 485–490
Altintas, Y., 330, 465
Alves, D.S., 567
Amabili, M., 25, 217
Ambrosino, F., 340
Ames, W.F., 76
Andersen, P., 332
Anderson, J.D., 415
Andersson, S., 127–129
Andrade, M.A.B., 370
An, N., 554
Antali, M., 87–95
Antman, S.S., 238, 239
Antonelli, M., 347–354
Arena, A., 197, 290, 297, 429–436
Argentini, T., 550
Arkhipova, I.M., 14
Arnold, V.I., 19, 25, 410, 413
Arridge, S., 413

A

- Asadi, H., 247
Ashwear, N., 218
Asundi, 360–362
Atanasovska, I.D., 127–135
Attard, A.M., 237, 241
Audebert, S., 300
Au, F.T.K., 208
Augusti, G., 208
Avitabile, D., 237
Avzar, M., 504
Awasthi, R.K., 562
Awrejcewicz, J., 169–186, 514, 534
Axel, K., 534
Azevedo, J., 341

B

- Babilio, E., 267–274
Babitsky, V.I., 320
Bachrathy, D., 504, 510
Bae, S., 550
Bag, B.C., 524
Baily, E., 66
Balachadaran, B., 237
Balachadran, B., 472, 474, 477
Balachandran, B., 277, 514
Balling, O., 329–336
Balthasar, J.M., 472
Barbieri, N., 289–297
Barbieri, R., 289–297
Barthorpe, R., 27
Bartoli, G., 389–391, 394
Barton, D.A.W., 27, 464, 469, 514
Bathe, K., 534, 564
Batista, R.C., 180, 181

- Batou, A., 300
 Batra, R.C., 237
 Batzer, S.A., 504
 Bauchau, O.A., 3
 Bauer, H.F., 187, 188
 Bauomy, H.S., 218
 Baykal, C., 549–559
 Bayly, P.V., 514
 Bayo, E., 8
 Bayraktar, A., 338
 Bazzucchi, F., 237
 Becker-Weimann, S., 148
 Beck, J.L., 300
 Behmanesh, I., 300
 Belloli, M., 550
 Belyakov, A.O., 13–23
 Benedettini, F., 71
 Benettin, G., 480
 Ben Mekki, O., 198
 Berbyuk, V., 550
 Berg, M., 320, 324
 Bergman, L., 487
 Bergman, L.A., 277
 Beri, B., 463–469
 Bernardini, D., 227, 347–354
 Bernitsas, M.M., 380
 Bersani, A., 44
 Bersani, A.M., 43–52
 Bersani, E., 44
 Bertsekas, D.P., 4
 Betcke, T., 413
 Bettayeb, M., 55
 Beuter, A., 524
 Bhattacharjee, J., 137
 Bigoni, D., 362, 363
 Biolley, F., 380–382, 386
 Biot, M.A., 422
 Bisswanger, H., 44
 Biswas, S., 137
 Bitar, D., 218
 Blasius, B., 44
 Blekhman, I., 35, 36, 38
 Blevins, R.D., 380, 400
 Bloch, A.M., 3, 4, 97–99, 410
 Bogoliubov, N.N., 14, 279–281
 Borghans, J., 44, 47
 Borri, A., 43–52
 Bouaanani, N., 218
 Boubaker, O., 158
 Bouc, R., 316
 Bouhaddi, N., 218
 Bouyer, J., 562
 Boyraz, P., 550
 Bradford, M.A., 237
 Brandão, J.A., 128
 Brandt, E.H., 369
 Brasil, R.M.L.R.F., 472
 Brauer, J., 128, 129
 Brčić, S.V., 357–364
 Breccolotti, M., 338
 Brennan, M.J., 301
 Breunung, T., 26, 30–32
 Brewick, P.T., 348
 Bridge, J., 227–234
 Briggs, G.E., 44
 Brincker, R., 330–332
 Brissaud, D., 503
 Brogliato, B., 97
 Brown, D.L., 332
 Bruschi, M., 76
 Bucher, I., 369–376
 Budak, E., 504, 510
 Budd, C.J., 233
 Burns, T.J., 514
 Burton, T.D., 66, 69, 73
 Burton, W.S., 248
 Busdotkiewicz, J., 550
 Bussetta, P., 299
 Butcher, E., 137, 138, 141, 487
 Butikov, E.I., 14

C

- Calogero, F., 76, 77
 Calvert, G., 361, 362
 Cammarano, A., 27
 Campos, R.O., 550
 Cao, C.D., 370
 Cao, L., 444
 Cao, Q.J., 534
 Cao, Y., 550
 Capiez-Lernout, E., 300
 Capolungo, L., 237
 Capuani, F., 44
 Carboni, B., 347–354
 Cardona, A., 3
 Carillo, S., 75–82
 Carl, B., 76–78
 Carlson, J.D., 550
 Carpinteri, A., 237
 Carra, S., 217
 Cartraud, P., 290, 297
 Casau, P., 60, 61
 Castro, F., 524
 Castro, M.J.D., 128
 Caughey, T., 299
 Cavalagli, N., 337–344
 Cavalca, K.L., 562, 563, 567

- Cembrano, G., 55
Chae, E.J., 430, 433
Chae, S.W., 534
Chaigne, A., 25
Chai, W., 58
Champneys, A.R., 27
Chandra, Y., 237, 238
Chandra, Y., 237
Chang, C.-M., 309
Chang, C.-N., 289
Chang, W., 237
Chasalevris, A.C., 562
Chaudhry, Z., 499
Chaurasia, S.S., 147–155
Chelidze, D., 495, 496
Chen, B., 217
Chen, C.K., 503
Chen, H.W., 550
Chen, L., 217–224
Chen, L.Q., 218
Chen, S., 66, 73
Chen, W., 514
Chen, Y., 495, 496, 499
Chen, Y.S., 533, 534
Cheung, Y., 66, 69, 73
Cheung, Y.K., 267
Chia, C.Y., 248
Chipart, M.H., 404
Chrzan, M.J., 550
Chucheepsakul, S., 198, 203
Chun, S.M., 562
Ciano, M., 337–344
Cicek, I., 227
Cigeroglu, E., 549–559
Ciliberto, A., 44
Clemente, P., 208
Coleman, B.D., 419, 420
Collado, J., 137–145
Collet, M., 218
Collins, J.J., 480
Comak, A., 504, 510
Conrad, D.C., 550
Constantinou, M.C., 309
Cooper, R.M., 187
Coppotelli, G., 419
Corless, R.M., 390
Cornil, M.B., 237
Cornish-Bowden, A., 44
Cortese, G., 44
Coughran, C.S., 380
Courrech du Pont, S., 117
Cox, B.S., 237
Craighead, H.G., 277
Croll, J.G., 208, 210
Cuadrado, J., 8
Cunha, A. Jr., 299–306
Cuvalci, O., 227
Czaplewski, D.A., 277
- D**
- Dal Corso, F., 362, 363
D'Alessandro, A., 339, 340
Daley, S.F., 257
Dana, S.K., 148
Dang-Vu, B., 439, 440
Dang, X.-J., 309
Dankowicz, H., 30
Daqaq, M.F., 261, 524
Darling, J., 117
da Silva, S., 299–306
Das, K., 237
Dassanayake, A.V., 503
Dauxois, T., 277
Dávid, A., 137, 138, 141
Davies, M.A., 514
Davies, P., 290, 297
Davoudi, B., 433
de Boer, R., 44
De Canio, G., 338, 340
de Felice, G., 341
Degasperis, A., 76, 77
DeJong, M., 341
De Langre, E., 380–382, 386
Delchambre, A., 370
Dell'Acqua, G., 43, 44, 47
Del Prado, Z.J.G.N., 180, 181
Delp, S.L., 445
De Luca, C.J., 480
Demartino, C., 399–406
De Matteis, G., 423
Demetriadès, G.F., 309
De Moura, E., 494
De Paula, A., 227
de Sant'Anna Vitor Barbieri, G., 289–297
De Vivo, A., 419
Dharap, P., 267
di Bernardo, M., 87, 94
Dibold, M., 450
Dick, A., 277
Dimitri, K., 534
Ding, H., 218
Djamah, T., 55
Djurovic, Z., 494
Dmitrochenko, O., 450
Doering, C.R., 524
Dohnal, F., 137–145
Dolce, M., 338

Dolev, A., 369–376
 Dombovari, Z., 464, 469, 514
 Dong, J., 534
 Dong, J., 187
 Dong, L., 257
 Dopico, D., 8
 Dowell, E.H., 524
 Dronka, S., 325
 Dubina, D., 208
 Duchemin, J., 503
 Dudkowski, D., 158
 Dufrane, K.F., 562, 563
 Dufva, K., 450, 452, 459
 Du, H.-E., 65–73
 Duraisamy, K., 433
 Durieu C., 58
 Dutterer, B., 514

E

Eason, T.G., 237, 238
 Eason, T.G., 237
 Eastep, F.E., 430
 Edelman, E., 44
 Edelman, E.R., 44
 Egorov, O., 277
 Eilertsen, J., 45
 Ekwaro-Osire, S., 227
 Eldredge, J.D., 416
 El-Sayad, M.A., 187
 El-Sayed, A.T., 218
 Engelborghs, K., 467
 Erba, F., 419, 420
 Er, G.-K., 65–73
 Eriksson, A., 218
 Erisen, Z.E., 554
 Eroglu, U., 237–244
 Ertas, A., 227
 Eugeni, M., 419–426
 Ewins, D., 332, 554

F

Fabbrocino, G., 330
 Facchinetti, M.L., 380–382, 386
 Facchini, G., 117
 Fagotti, G., 337–344
 Faller, J.E., 169
 Fan, C.-C., 486
 Fang, H., 257–266
 Fan, S.Y., 550
 Fan, X.C., 237
 Farhat, C., 433

Farid, M., 187–194
 Farokhi, H., 217
 Feldman, M., 188, 191, 374–376
 Fenander, A., 320
 Feng, R., 514
 Feng, W., 361
 Feng, X., 320, 323
 Field, R.V. Jr., 524
 Fillon, M., 562
 Finchman, J.H.S., 430
 Fitzgerald, T., 237, 277
 Flach, S., 277
 Fleming, D., 486
 Flodin, A., 127, 128
 Floquet, G., 14
 Fokas, A.S., 76, 77
 Forster, E., 430
 Franciss, R., 380, 384–386
 Frankovsky, P., 362, 363
 Frank, T.D., 524
 Fransen, S., 419
 Franzini, G.R., 379–386
 Fraternale, G., 550
 Frigerio, L., 444
 Friswell, M., 488
 Friswell, M.I., 430
 Fu, C., 495, 496, 533–546
 Fuchssteiner, B., 76, 77
 Fujarra, A.L.C., 380, 384–386
 Fu, J.H., 107

G

Gadoua, J.C., 524
 Gagnon, L., 414
 Galavotti, T.V., 550
 Galgani, L., 480
 Galli, M., 444
 Gammaitoni, L., 524, 528
 Gao, B., 117
 Gao, J.R., 370
 Garvey, S., 488
 Gasch, R., 486
 Gaspar, Z., 208
 Gatta, C., 338
 Gattulli, V., 218–220, 338
 Gehan, O., 55, 56
 Geier, F., 148
 Geist, K., 480
 Gendelman, O., 277
 Gendelman, O.V., 169, 187–194
 Gennaretti, M., 439, 440
 Georgakis, C.T., 399–406
 George, P., 329

- Georgiades, F., 471–48
Geradin, M., 3
Gerasimenko, A., 503
Gere, J.M., 237
Gern, F.H., 430
Gerstmayr, J., 449, 450
Gertzos, K.P., 562
Geuzaine, C., 413
Geuzaine, P., 433
Ghayesh, M.H., 217
Ghoreishi, S.R., 290, 297
Ghosh, P.K., 524
Gioffrè, M., 337–344
Gioncu, V., 208
Giordano, F., 338
Giorgilli, A., 480
Gjelstrup, H., 400
Glam, B., 361
Glocker, C., 97
Goldbeter, A., 45
Goldenberg, A., 361, 362
Golinval, J.C., 299, 534
Gomez, J.T., 361, 362
Gonçalves, P.B., 179–181, 207–214
Gonçalves, R.T., 380
Goncharenko, V.M., 76
Gong, S., 319–328
Gong, X-S., 309
Gonzalez, F., 8
Gorbach, A.V., 277
Goretti, A., 338
Gor'kov, L.P., 370
Gosselin, C., 169
Gottwald, G., 233
Goudjil, A., 55, 56
Gounaris, G.D., 562
Gouskov, A., 503–510
Grassie, S.L., 320
Greco, F., 316
Greenwood, D.T., 3, 4, 97, 98
Grigoriu, M., 524
Groh, R.M.J., 237
Gross, T., 44
Gu, C., 320
Guckenheimer, J., 191, 472
Güémez, J., 107
Guillouzic, S., 525
Gündüz, M., 550
Guo, C., 487
Guo, Z., 217–224
Gusella, V., 337–344
Guskov, A.M., 504, 505
Guskov, M., 503
- H**
Hajj, M.R., 380
Haldane, J.B.S., 44
Haller, G., 26, 30
Hall, G., 139
Hancock, G.J., 208
Hänggi, P., 524, 528
Hanna, S.N., 187
Hao, H., 341
Haquang, N., 218, 221
Harata, Y., 187
Hariprasad, M.P., 362, 363
Harne, R.L., 258
Hashimoto, H., 562
Hayashi, C., 71
Hayasi, R., 362, 363
Hedrih (Stevanovic), K.R., 127–135, 357–364
Hegazy, U.H., 218
Heinrich, R., 148
Heitzig, J., 148
Henderson, J.P., 421
Henri, V., 44
Hens, C.R., 148
Henson, G., 486
Herzel, H., 148
Hicks, J.L., 445
Hikihara, T., 277
Hill, T., 27
Hill, T.L., 27
Hirokawa, K., 486
Hoff, C.N., 444
Hoffman, K., 191
Hökelekli, E., 338
Holmes, P., 472
Honeycutt, A., 514
Honlet, M., 361, 362
Hoover, W.G., 158, 165
Horvath, H.Zs., 117–126
Hou, L., 495, 496, 533, 534
Howard, J., 139
Howitt, F., 486, 488, 489
Huang, C., 218, 220, 221
Hubbard, B.E., 277
Hu, H.Y., 55, 524
Hu, J., 228, 444
Hunt, G.W., 208, 210
Hurwitz, A., 403
- I**
Ibrahim, R.A., 187
Ihlenfeldt, S., 330
Ikeda, T., 187

- Ilbeigi, S., 493–500
 Ilic, B., 277
 Imregun, M., 332
 Indeitsev, D., 35
 Inman, D.J., 429–436
 Insperger, T., 466, 514
 Ionita, A., 439, 440
 Irmao, M., 494
 Irshik, H., 450
 Irvine, H.M., 203, 218
 Ishida, Y., 486
 Iu, V.P., 65–73
- J**
 Jafari, S., 158
 Jairazbhoy, V.A., 237
 Jang, J.-S., 449–459
 Jauvtis, N., 380, 381
 Jex, H.R., 440
 Jezequel, L., 25
 Ji, J., 107–115
 Jing, X.J., 257
 Jin, W., 513–520
 Jin, Y., 495, 496, 523–530, 533–546
 Jin, Y.F., 524
 Jin, Y.L., 533, 534
 Ji, W.X., 550
 Johnson, D.R., 258
 Jones, D.I.G., 421
 Jones, M., 439, 440
 Jump, M., 439, 440
 Jung, P., 524, 528
 Ju, Y., 358, 361
- K**
 Kacem, N., 218
 Kaczmarczyk, S., 450
 Kahn, P.B., 25
 Kalmar-Nagy, T., 347–354, 464
 Kang, J.-H., 449–459
 Kang, J.S., 550
 Kang, Y.J., 550
 Kannel, J.W., 562, 563
 Kanso, E., 410, 412, 415
 Kapanin, R.K., 430
 Kapitaniak, T., 158
 Kappaganthu, K., 494
 Karadeniz, H., 338
 Kar, S., 44
 Katafygiotis, L.S., 300
 Katz, J., 431
- Kawaguti, K., 450
 Kecik, K., 514
 Keller, J.B., 98
 Kellermann, D.C., 237, 241
 Kelly, S.D., 415
 Kerschen, G., 277, 299, 533
 Khasawneh, F.A., 503
 Khesin, B.A., 410, 413
 Khesin, L., 362
 Khonsari, M.M., 562
 Kidambi, N., 258
 Kienzle, O., 465
 Kim, H.R., 450
 Kim, J.G., 534
 Kim, K.-W., 449–459
 Kim, S.M., 534
 Kimura, M., 277
 Kinaci, O.K., 380
 Kiray, B., 550
 Kiseleva, M.A., 158
 Kitano, H., 43
 Kitio Kuwimy, C.A., 494
 Knothe, K.L., 320
 Kobayashi, Y., 248
 Koiter, W.T., 208, 210
 Ko, J.M., 309, 316
 Konchatnij, M.I., 524
 Korkischko, I., 380, 384–386
 Korn, G.A., 281
 Korn, T.M., 281
 Koseska, A., 148
 Koshland, D.E., 45
 Koss, H., 405
 Koss, H.H., 400, 404
 Kouchakzadeh, M.A., 247
 Kovacic, I., 301
 Kovaleva, A., 277–285
 Kovecses, J., 8
 Kramer, A., 148
 Kremer, E., 35–41
 Krenk, S., 380, 382
 Kroese, D.P., 304
 Krysko, A.V., 534
 Krysko, V.A., 534
 Kudra, G., 88
 Kühn, O., 277
 Kupershmidt, B.A., 76, 79
 Kuriyama, T., 187
 Kurths, J., 148
 Kurushina, V., 379–386
 Kuznetsov, N., 158
 Kuznetsov, N.V., 158
 Kuznetsov, Y.A., 111

L

Lacarbonara, W., 198, 227, 237, 290, 297,
347–354, 429–436

Lagarde, A., 361

Lakes, R., 257

Lakie, M., 169

Lakka, S., 380

Lalji, F., 380, 381, 384–386

Lamarque, C.H., 25

Lambert, P., 370

Landl, R., 380, 382

Lanteigne, J., 289

Larose, G.L., 404

Larsen, A., 400

Lassoued, A., 158

Latalski, J., 472

Latinovic, I.V., 494

Latvis, M.P. Jr., 348

Lau, S., 66

Lauternborn, W., 480

Law, M., 330

Lebowitz, J.L., 44

Lederer, F., 277

Ledesma, R., 8

Lee, A.J., 430, 433

Lee, J.M., 550

Lee, J.-W., 449–459

Lee, S., 361

Lees, A., 488

Lee, Y.S., 277

Lefrancois, S., 169

Leine, R., 87

Leine, R.I., 97

Lemos, J.V., 341

Lenci, S., 208, 213

Leonard, N.E., 410

Leonov, G.A., 158

Leopold, C., 361

Lepidi, M., 218–220

Lesniak, J., 361, 362

Levi, D., 76

L'Heureux, I., 525

Liao, S.J., 66

Lichtwark, G.A., 441

Li, D., 257–266

Liebig, W.V., 361

Liebscher, S., 472

Liénard, A., 404

Lightfoot, E.N., 45, 46

Li, J., 290

Li, M., 257

Lim, C.W., 66, 218

Lindenlaub, J.C., 66

Lin, H., 217–224

Lin, Q., 513–520

Li, S., 218, 221

Litvak-Hinenzon, A., 277

Liu, C.C., 257

Liu, G., 247–255

Liu, H., 187

Liu, W., 564

Liu, X., 25–32, 107

Liu, Y.S., 55, 56, 58

Liu, Z.G., 55

Li, X., 187, 514

Li, Y., 61, 187

Li, Z., 267, 495, 496

Li, Z.G., 533

Llibre, J., 159

Lombaert, G., 300

Longtin, A., 525

Loram, I.D., 169

Lorong, P., 503

Losanno, D., 314

Lo Schiavo, M., 76–78

Luciano, R., 316

Lu, K., 495, 496, 533–546

Lu, L., 55, 439

Luo, M., 107

Luongo, A., 14, 218

Lu, Z.Y., 534

Luzyanina, T., 467

Lv, Y., 494

M

Macdonald, J.H.G., 400, 404

Machado, T.H., 561–567

MacKay, R., 139, 277

Madera Sierra, I.E., 314

Madill, D., 228

Magdaleno, R.E., 440

Ma, H., 414, 535

Mahmoud, I.H., 534

Mailybaev, A.A., 14

Maini, P., 47

Maisano, G., 444

Makris, N., 341, 421

Malecki, J., 439, 440

Manevitch, L.I., 177, 189, 280–282

Mannala, M.J., 289–297

Mann, B.P., 514

Mannini, C., 389–397

Manoach, E., 217

Mansour, A., 197–204

Mantegazza, M., 440

Manuello, A., 237

Mao, X.Y., 218

- Marchenko, V.A., 76
 Marchesoni, F., 524, 528
 Marcuzzi, P., 218
 Marmo, F., 309–316
 Marnetto, R., 338
 Marra, A.M., 389–391, 394
 Marsden, J., 160, 410
 Marsden, J.E., 410, 412
 Martarelli, F., 419
 Martegani, L., 550
 Marulanda, J., 314
 Marwan, N., 148
 Masana, R., 261
 Masarati, P., 414, 439–446
 Masri, S., 299
 Masri, S.F., 348
 Massai, T., 390, 391, 394
 Mastroddi, F., 419–426
 Materazzi, A.L., 338
 Matias, M.A., 107
 Matteoni, G., 399–406
 Mattos, H.S.C., 181, 182
 Mauro, A., 341
 May, V., 277
 Ma, Z.M., 524
 McCloskey, T.H., 562, 563
 McConnell, K.G., 289
 McFarland, D., 487
 McFarland, D.M., 277
 McRuer, D.T., 439
 Mehri, M., 247
 Meissner, E., 19
 Mekki, O.B., 197–204, 218
 Melbourne, I., 233
 Melli-Huber, J.B., 410, 412
 Melrose, R.B., 98–100
 Menck, P.J., 148
 Mendoza, C., 44
 Meneghini, J.R., 380, 384–386
 Meng, Q., 187
 Menq, C.H., 554
 Menten, M.L., 44
 Meoni, A., 339, 340
 Meral Halifeoğlu, F., 338
 Messagera, T., 290, 297
 Messias, M., 158–160, 163, 165
 Metrikine, A.V., 380
 Mettler, E., 237, 240
 Meyer, K., 139
 Michaelis, L., 44
 Mielke, A., 348
 Mikkola, A., 449
 Milanesi, A., 43–52
 Millsaps, K., 486
 Mishra, A., 433
 Misseroni, D., 362, 363
 Mitropolski, Y.A., 14, 279–281
 Mitrovic, R., 131
 Moaveni, B., 300
 Moghaddasie, B., 237
 Mohamad, T.H., 493–500
 Mohanty, M., 320
 Momcilovic, D.B., 127–135
 Mongelli, M., 340
 Montassar, S., 198, 218
 Mook, D.T., 218, 221, 372, 374
 Moosavian, A., 430, 433
 Morandini, M., 440
 Moroni, C., 338
 Mosallam, A., 338
 Mote C.D. Jr., 277
 Müller, A., 410, 411
 Munthe-Kaas, H., 412
 Murdock, J., 160, 161, 279, 280
 Murray, J., 44
 Muscarello, V., 439–446
 Musienko, A.I., 177
- N**
- Nagarajaiah, S., 267
 Nashif, A.D., 421
 Nataraj, C., 485–490, 493–500
 Natsiavas, S., 3–10, 97–105, 472
 Nayfeh, A.H., 25, 37, 46, 48, 74, 198, 248,
 372, 374, 380, 472, 474, 477
 Nazin, S.A., 58
 Neild, S.A., 26, 27, 32
 Nešović, M., 360
 Neugebauer, R., 330
 Newmark, N.M., 433
 Nguyen, V., 237
 Nicoletti, R., 550
 Nicolis, C., 524
 Nielsen, S.R.K., 380, 382
 Nigro, D., 338
 Nijmeijer, H., 87, 97
 Nikitas, N., 400
 Nikolakopoulos, P.G., 562
 Nilsson, S., 370
 Niu, L., 320
 Ni, Y.Q., 217, 309, 316
 Noël, J., 299
 Noh, M., 228
 Nojima, K., 562
 Noll, W., 419, 420

Noor, A.K., 248

Nordgren, R.P., 267

Nosé, S., 158

Novak, B., 44

Novak, M., 564

Nurmagambetov, A.J., 524

Nygård, T., 550

O

Oberst, S., 319–328

Odibat, Z.M., 66

Offin, D., 139

Ogink, R.H.M., 380

Ohayon, R., 300

Oh, J.Y., 450

Oh, K., 248

Oliveira, H., 227

Olusola, O.I., 148

O'Reilly, O.M., 117

Orlando, D., 207–214

Otto, A., 503

Owis, F., 380

Ozlu, E., 504

Ozturk, E., 504, 510

P

Pacejka, H.B., 121

Pacitti, A., 290, 297

Padmanabhan, C., 541

Pagalday, J.M., 290

Pagnini, L.C., 400

Pai, P.F., 248

Pal, P., 148

Palsson, B.O., 45–47

Palsson, H., 45

Panda, L.N., 218

Pandya, Y., 362, 363

Pandza, V., 409–416

Pan, F., 309

Pankonen, A.M., 430, 433

Pan, M.-C., 486

Panovko, G., 503–510

Panyam, M., 261, 524

Paolini, R., 439–446

Paolone, A., 198, 237

Papadimitriou, C., 300

Papadimitriou, I., 550

Papadopoulos, C.A., 562

Papadopoulos, E., 550

Paraskevopoulos, E., 3–10, 97–105

Parey, A., 362, 363

Paris, H., 503, 504

Parkinson, G.V., 390

Park, J.H., 55–62

Parks, H.V., 169

Parlitz, U., 480

Patel, Y., 329

Patil, P., 361

Paunović, S., 357–364

Pavel, M.D., 439, 440

Pavlovskaya, E., 379–386

Pedersen, M.G., 44

PedroCerqueira, P., 128

Peng, J., 218, 220, 221

Pennestrì, E., 441

Penny, J., 488

Pepi, C., 337–344

Pérez, N., 370

Perkins, E., 277

Peschel, U., 277

Peters, J.M., 248

Petracci, G., 358

Pfeiffer, F., 97

Phillips, J., 413

Piccardo, G., 400

Pigeon, E., 55, 56

Pignataro, M., 238, 239

Pilipchuk, V.N., 187

Pirrera, A., 237

Pittner, G., 550

Pi, Y.L., 237

Plaut, R.H., 117, 218, 221

Plotkin, A., 431

Pogorelov, D., 450

Pohit, G., 218

Poincaré, H., 25

Pokrovskii, A., 348

Polyak, B.T., 58

Ponzo, F.C., 338

Poplawski, J., 486

Porten, E., 76

Posch, H.A., 158, 165

Postnikov, A., 379–386

Potosakis, N., 3–10

Pouliquen, M., 55, 56

Prabhu, B., 486

Prasad, A., 158

Pratt, J.R., 514

Puig, V., 55

Q

Qiao, J., 58

Quaranta, G., 439–446

Qu, V.A., 237

R

- Radons, G., 503
 Ragazzi, A., 444
 Ragnisco, O., 76
 Rahman, Z., 66, 69
 Raimundo, J.M.P., 207–214
 Rainieri, C., 330
 Raithel, A., 208
 Rajagopal, A., 445
 Ramakrishnan, V., 358, 360
 Ramesh, K., 358, 360, 362, 363
 Ramírez Barrios, M., 137–145
 Ramírez, M., 144
 Ramji, M., 361
 Ramnarace, S., 227–234
 Rand, R.H., 268, 271–273
 Rauh, J., 325
 Ravichandran, G., 361
 Ray, D.S., 524
 Reed, G., 486
 Reed, M.P., 444
 Rega, G., 71, 197–204, 208, 213, 218, 219,
 270, 348, 533
 Reinhorn, A.M., 309
 Reinol, A.C., 158–160, 163, 165
 Reith, M.J., 504, 510
 Remacle, J.F., 413
 Renson, L., 299
 Ricciardelli, F., 400, 404, 405
 Ringgaard, K., 329–336
 Riso, C., 419, 423
 Ritto, T., 300
 Rizzi, N., 238, 239
 Robert, S., 515
 Robustelli, F.C., 550
 Rodrigues, L., 181
 Rogers, C., 76
 Rosa, P., 60
 Rosatelli, P., 429–436
 Rosati, L., 309–316
 Roselli, I., 340
 Rosenstein, M.T., 480
 Routh, E.J., 97, 98
 Rowley, C.W., 410, 412
 Rubinow, S., 44
 Rubinstein, R.Y., 304
 Ruby, L., 267
 Rupp, J.D., 444
 Rusinek, R., 514
 Ruta, G., 237–244

S

- Sabouri-Ghom, M., 44

Sacco, E., 338

- Sado, D., 169
 Saffmann, P.G., 415
 Sahoo, B., 218
 Saltari, F., 419–426
 Saltykova, O.A., 534
 Samadani, M., 494
 Samaey, G., 467
 Sampaio, R., 300
 Sanchez, A.D., 524
 Sanchez, J.P., 550
 Sanchez, N.E., 374
 Sanders, B., 430
 Sanders, J.A., 160, 161, 279, 280
 Santesson, S., 370
 Sathyamoorthy, M., 248
 Sato, M., 277
 Sattler, H.A.R., 180, 181
 Savi, M., 227
 Sawicki, J., 486
 Scafidi, M., 358
 Scheurle, J., 160
 Schiavo, M.L., 75–82
 Schiebold, C., 75–82
 Schilder, F., 30
 Schmitz, T., 514
 Schmitz, T.L., 514
 Schnell, S., 44, 45, 47
 Schulte, K., 361
 Schulze, T., 76
 Schweiger, M., 413
 Scussel, O., 299
 Seabra, J.H.O., 128
 Sedlaczek, K., 325
 Segel, L., 44
 Sekhar, A., 486
 Sekimoto, K., 117
 Selbig, J., 44
 Semperlotti, F., 258
 Serafini, J., 439, 440
 Serino, G., 313, 316
 Sersour, L., 55
 Sessa, S., 309–316
 Seth, A., 445
 Severini, L., 341
 Seydel, R., 480, 481
 Seyranian, A.A., 14
 Seyranian, A.P., 13–23
 Shabana, A.A., 329, 450, 459
 Shadwick, W.F., 76
 Shahzad, S., 362, 363
 Shanmugam, A., 541
 Sharma, A., 148, 361, 362
 Sharma, S., 562

- Shaw, J., 330
Shen, H.S., 217
Shen, J., 66, 73
Shepelev, D.S., 280–282
Shi, H., 324, 325, 464, 468, 469
Shi, J., 486
Shiki, S.B., 299
Shimada, K., 390
Shi, X., 444
Shoshani, O., 390
Shrimali, M.D., 148
Shukla, A., 361, 362
Shukla, R.K., 416
Sievers, A.J., 277
Silva, A., 494
Silva, F.M.A., 179–181
Silvestre, C., 60
Sincraian, G., 341
Sinha, S., 147–155
Sinha, S.C., 137, 138, 141
Sjöberg, M., 320, 323, 325
Smaili, H., 439, 440
Smigaj, W., 413
Smith, G.T., 503, 509
Sobolev, V., 348
Soedel, W., 550
Sogabe, K., 450
Soize, C., 300, 301
Soliman, M.S., 212
Song, G., 494
Sorrentino, L., 341
Souto, C., 494
Souza Junior, O.H., 290, 297
Spanoudaki, A., 277
Spizzuoco, M., 313, 314
Spottswood, S.M., 237, 238
Sprott, J.C., 158, 165
Srinil, N., 198, 203, 380
Stanciulescu, I., 237, 238
Stanciulescu, I., 237
Stappenbelt, B., 380, 381, 383–386
Starnes, J.H. Jr., 248
Starosta, R., 169–186
Starosvetsky, Y., 169, 188, 191
Starzhinskii, V., 138, 141, 144
Starzhinskii, V.M., 18
Stefanelli, R., 441
Steinbach, O., 413
Stepan, G., 87–95, 463–469, 504, 510, 514
Stépán, G., 514
Stepanic, P., 494
Steuer, R., 44
Storti, G.C., 561–567
Stoustrup, J., 60
Strano, S., 309, 314
Strelcyn, J.-M., 480
Stronge, W.J., 97, 98, 104, 105
Subic, A., 131
Sugiyama, H., 449
Suh, C.S., 503
Suherman, S., 117
Sümer, I.T., 550
Sümer, T., 550
Sun, H., 380
Sun, Q., 535
Sun, W., 66
Swift, J.B., 481
Swinney, H.L., 481
Sypniewska-Kami’nska, G., 169–186
Syu, J.-W., 486
Sze, K., 66, 73

T

- Tabatabaeipour, S.M., 60, 61
Taflanidis, A., 300
Taghirad, H.D., 330
Takacs, D., 117–126
Takehara, S., 450
Tallapragada, P., 415
Tamura, Y., 390
Tang, Z., 55–62
Taniguchi, T., 341
Taylor, F.W., 465
Terumich, Y., 450
Terze, Z., 409–416
Terzo, M., 309, 314
Tham, L.G., 267
Thomas, O., 25
Thompson, J.M.T., 208, 210, 212
Thompson, S., 117
Thomsen, J., 35, 36
Thomson, P., 314
Thota, M., 258
Tian, Q., 55
Tian, Q.L., 309
Tichkiewitch, S., 503
Tilley, D., 117
Timoshenko, S., 237
Tobias, S., 464, 468
Tomassetti, E., 43–52
Tomassetti, G., 43, 44
Tong, B., 414
Toti, J., 338
Touzé, C., 25, 26, 30–32
Trahair, N.S., 208
Trequattrini, F., 419
Treyssède, F., 218

Troger, H., 117, 270
 Tsao, W.-C., 486
 Tsao, Y.M., 503
 Tubino, F., 400
 Tufekci, E., 237
 Tuğcu, A.K., 550
 Tunc, L., 330
 Tung, D.D., 503–510
 Türkay, O.S., 550
 Tyson, J.J., 44
 Tzafriri, A., 44
 Tzafriri, A.R., 44, 47

U

Ubertini, F., 339, 340
 Uchida, T.K., 445
 Ulrich, H., 534
 Ungureanu, V., 208
 Usabiaga, H., 290

V

Vaiana, N., 309–316
 Vairo, G., 218
 Vaisberg, L., 35
 Vakakis, A.F., 277, 299, 534
 Valentini, P.P., 441
 Vandaele, V., 370
 Van der Zee, K.G., 433
 Vankerschaver, J., 410
 Varadi, P.C., 117
 Vasilakos, K., 524
 Vassoliou, M.F., 341
 Vastano, J.A., 481
 Vazquez, L., 277
 Vaz, W.A.S., 179, 181
 Vellucci, P., 43–52
 Ventura, C., 330
 Veprik, A.M., 320
 Verhulst, F., 138, 144, 160, 161, 279, 280
 Vesely, F.J., 158, 165
 Vestroni, F., 198, 227, 338
 Vetsel, S.S., 534
 Vidaković, M., 359
 Villani, L.G.G., 299–306
 Virgin, L.N., 237, 238, 299, 524
 Virgin, L.N., 237
 Vita, L., 441
 Vittal, P.R., 475, 476
 Vlajic, N., 237
 Volkov, E., 148
 Von Groll, G., 554
 Voronov, S.A., 504

Voros, J., 55
 Vyasarayani, C.P., 361

W

Wabner, M., 330
 Wada, S., 562
 Wagg, D.J., 25–32
 Walker, A.C., 208, 210
 Walter, E., 58
 Wang, A., 513–520
 Wang, D., 228
 Wang, G., 514
 Wang, H.-X., 309
 Wang, K.W., 258
 Wang, X., 319–328
 Wang, Y., 55–62, 320
 Wang, Y.H., 267
 Wang, Z., 55–62
 Wang, Z.H., 55
 Wang, Z.X., 217
 Warminska, A., 217
 Warminski, J., 217, 472, 514
 Wassermann, L., 302
 Watson, L.T., 117
 Weckesser, W., 191
 Wei, B., 370
 Wen, G., 110
 Weng, S., 217
 Wen, Y.K., 316
 Weremczuk, A., 514
 Wiebe, R., 237, 238
 Wiercigroch, M., 14, 379–386
 Wiggins, S., 472
 Williamson, C.H.K., 380, 381
 Wilson, A.M., 441
 Wilson, R.E., 464, 469, 514
 Wio, H.S., 524
 Wojewoda, J., 514
 Wolf, A., 481
 Wolf, J., 148
 Wong, C.W., 309, 316
 Worden, K., 299
 Wu, B., 66
 Wu, D., 524
 Wu, D.H., 61
 Wu, F.L., 55, 58
 Wu, P., 324, 325

X

Xiao, S.M., 524
 Xia, Y., 217
 Xin, Z., 27

Xiong, X., 320
Xu, C., 514
Xu, H., 107–115
Xu, P.F., 523–530
Xu, X., 14
Xu, Y.L., 217

Y

Yadav, M., 147–155
Yakobson, B., 267
Yakubovich, V., 138, 141, 144
Yakubovich, V.A., 18, 20
Yamada, G., 248
Yang, G., 237
Yang, J., 320, 323
Yang, Y., 495, 496, 533–546
Yang, Y.F., 533
Yan, J., 487
Yan, W.J., 300
Yan, Z.H., 208
Yazicioglu, Y., 549–559
Yilmaz, D., 439, 440
Yoo, W.-S., 449–459
Yuan, R., 494
Yu, D., 187
Yu, H., 534
Yun, J.R., 550
Yu, Y., 55, 414

Z

Zago, M., 444
Zaichik, L., 439, 440
Zanganeh, H., 380

Zanoni, A., 439–446

Zarmi, Y., 25
Zavodney, L.D., 374
Zeman, K., 117
Zemke, W.P., 289
Zhang, C., 187
Zhang, H., 533–546
Zhang, L., 332

Zhang, M., 290
Zhang, Q.J., 550
Zhang, W., 247–255
Zhang, Y., 320, 323
Zhang, Z., 495, 496
Zhang, Z.Y., 533
Zhan, S., 309, 316
Zhao, G., 290
Zhao, H.Q., 55
Zhao, Y., 55, 58, 217–224
Zheng, Z.S., 55
Zhong, S., 107
Zhou, H., 533–546
Zhou, S., 486
Zhou, W., 495, 496
Zhou, Y., 66, 341
Zhou, Y., 237
Zhu, H., 320, 323
Zhu, J., 237, 241
Zhu, S.Q., 524
Zlatar, D., 409–416
Zorzano, M.P., 277
Zounes, R.S., 268, 273
Zuchowski, B., 238
Zulli, D., 218
Zullo, F., 76
Zuo, Z., 27

Subject Index

A

Absolute nodal coordinate formulation (ANCF)
description, 449–450
formulation for a plate, 450
mass matrix, 450
non-dimensional equation (*see* Non-dimensional equation of motion)
Accelerometer sensors, 494
Acoustic levitation devices (ALDs), 370
Acoustic radiation forces, 370
Adimensionalization, 47
Aerodynamic damping, 391, 400, 402
Aerodynamic force coefficients, 405
Aeroelasticity, 421, 423, 425, 430, 431, 433, 434
Aeroelastic model, 401–402
Aeroviscoelastic model, 423–424
Aircraft attitude, 424
Aluminum conductor steel reinforced (ACSR)
mechanical behavior, 289–290
Amplitude modulation
analysis, 39
components, 40
example, 39–40
excitation, 36
problem formulation, 37
vibrational force, 37–39
Analogue models
mechanical, 117, 119–122
retro-reflective markers, 119
simulation, 124–125
Analytical dynamics, 4, 98
Analytical mechanics, 14, 65
Analytical solution, 372–374

Approximate analytical solution, 374
Artificial neural networks (ANN), 494, 495, 498
Associated smooth system
bifurcations, 92–93
equilibrium points, 92–93
in polar coordinates, 91–92
Asymmetric restoring force, 233, 258
Asymptotic analysis, 392–394
averaging, 14
phase-space plot, 396
resonant system, 279
Asymptotic expansions
competitive inhibition, 50
Goldbeter-Koshland switch, 51
phosphorylation, 51
tQSSA, 49
Asymptotic methods, 14, 137
Augmented Lagrangian formulation
equations of motion, 4–7
ground vehicle, 9–10
planar slider-crank mechanism, 7–9
Auxiliary enzyme reactions, 46–49
Averaging method, 15, 36
first order, 160–161
periodic orbit, 161–162

B

Backward whirl (BW), 488, 490
Basin stability
coupling, 148–150
discussion, 155
fractionally disconnected links, 150–155
Bayesian statistics, 300

- Bearing diagnostics, 494
 Berg's friction model, 320, 322
 Bernoulli-Euler beam, 504, 506
 Bifurcation analysis method, 514
Bifurcations
 associated and original system, 93–94
 control, 107, 108
 Coulomb, 87
 Filippov systems, 87
 fold of limit directions, 94
 numerical results, 103–106
SMA (see Shape memory alloy (SMA))
 tangency bifurcation, 94
 trajectories, 88
 zero-Hopf (*see* Zero-Hopf bifurcation)
- Bilateral motion constraints**
 configuration, 98
 and friction effects, 101–103
 standard modeling requirements, 8
- Biomechanics**, 440, 444, 446
- Biot damping model**, 422–423, 425, 426
- Bi-stable phase**, 526, 527
- Bluff body**, 389, 400
- Body-Freedom-Flutter (BFF) type aircraft**, 425, 426
- Borel theorem**, 420, 422
- Boundary element method (BEM)**, 412–414
- Bäcklund transformations**, 76–78
- C**
- Cable**
 multimodal theory (*see* Catenary)
 suspended (*see* Suspended cable)
- Cable model**, 404
- Calibration**, 311, 380–385
- Catenary**
 discretization, 198–200
 equations of motion, 198–200
 flexural torsional-extensible cables, 197
 kinematic condensation, 198
 multiple scale solution, 200–203
 numerical results, 203–204
- Chaos**
 bifurcations and transition, 273
 CF (cyclic fold bifurcation point), 516
 chaotic dynamics, spinning shaft (*see* Spinning shaft)
 EM, 472
 irregularity and information loss, 482
- Chatter**
 description, 463
 regeneration effect, 463
 in turning processes
- bifurcation analysis, 467–469
 chip removal, 464
 model formulation, 464–466
 motion of the tool, 464
 stability, 466–467
- Codimension-2 discontinuity**, 87, 88, 93, 95
- Component mode synthesis (CMS)**, 533–535, 540, 541, 546
- Computer algebra manipulation**, 78, 79
- Condensation**, 198, 200, 204, 219
- Condition-based maintenance (CBM)**, 493
- Continuous module**, 258, 265–266
- Correlated noises**, 524, 527, 529, 530
- Cracked rotor**
 analytical solution, 486
 Campbell diagrams, 486
 constant angular acceleration, 486
Jeffcott rotor Model, 486–488
 LTVs, 486
 numerical simulations, 488–490
- Craig-Bampton conversion**, 541
- Cutting law**, 505
- Cutting process**, 507
- Cylindrical panel**
 geometrical imperfection, 180
 numerical results, 181–185
 shells, 179
 theoretical formulation, 179–180
- Cylindrical unit**, 539
- D**
- Data uncertainties**, 300
- Degrees of freedom (DOF)**
 pendulum
 inverted, 19–20
 physical, 170
 stability conditions, 20–22
 velocity values, 124
- Degrees-of-freedom (DOF)**, 300, 534, 536
- Delay**, 507, 508, 510
- Differential-algebraic equations (DAEs)**, 3, 4, 10
- Domain dependency**, 494
- Double-turning process**
 calculation results, 509–510
 design scheme and dynamic models, 504–509
 machine-tool-workpiece, 503
 nonlinearity, 503
- Dry friction damper**, 558
- Dual rotor-bearing system**, 535–544
- Duffing equation**, 303

- Duffing–Mathieu equation
 bifurcation diagram, 272–274
 dimensionless equation of motion, 269
 Galerkin discretization, 270–271
 nonlinear dynamics, 267
 stability charts, 272–274
- Duffing oscillator, 306
- 2D washing machine model, 550–552, 559
- Dynamical behaviors, 534, 546
- Dynamic behaviour *vs.* excitation frequency, 327
- E**
- Early fault detection, 561, 562
- Eigenvectors, 542
- Elastic deformation, 540
- Elastic sub-model, 320
- Electromyography (EMG), 444–446
- Ellipsoidal space
 bounded colored noise, 56
 example, 60–62
 filtering algorithm, 57–60
 problem statement, 56–57
 system modeling, 55
- ε^2 -order, 27–30
 monodromy matrix, 21
 normal form method (*see* Normal form analysis)
- Equation of motion (EOM), 552–554
 augmented Lagrangian formulation, 4–7
 boundary layer, 102
 coupled subsystem, 123
 dimensionless form, 171
 and discretization, 198–200
 harmonic force, 278
 index-3 DAEs, 10
 linear stability, 119
 numerical simulations, 192
 resonant dynamics, 278–280
- Equilibrium manifolds (EMs), 472–474, 477, 483
- Ergonomy springs, 441
- Euler–Bernoulli beam, 259, 472
- Euler effects, 550
- Euler's method, 563
- Experimental data
 quasi-static conditions, 325
 semi-empirical wake oscillator, 380
- Experimental hysteresis
 analytical, 314
- Experimental modal analysis (EMA), 330
- Experimental modal data, 330
- Extended Filippov systems
 definition, 88–89
 limit directions, 88–89
 types, 90–91
- F**
- Fault detection, 499–500
- Feature extraction, 497–498
- Filtering method
 ellipsoid volume minimization, 57–60
 modeling algorithm, 56
- Finite element method (FEM), 363, 364, 420, 421, 430, 436
- Finite element (FE) model, 535–540
- Floquet multipliers, 14, 15, 18, 138
- Fluid-structure dynamical model, 410
- Fluid-structure interaction, 436
- Flutter, 425, 430–436
- Fokker–Planck equation, 525
- Fokker–Planck method, 524
- Fractional derivative model, 323
- Freedom motion simulation system, 331
- Frequency response curve (FRC)
 examples, 71–73
 HBM, 66
 modified perturbation methods, 66
 MSM (*see* Multiple-scales method (MSM))
 PSMS, 67
 and unstable region, 65
- Frictional contact
 bilateral constraints, 101–103
 codimension-2 discontinuities, 87
 linear viscous, 19
 and rolling resistance, 88
- G**
- Galerkin approach, 432
- Galerkin method, 534
- Galloping, 389
- Gaussian random homeomorphisms, 350–351
- GE/Bently Nevada 7200 series, 494
- Generalized aerodynamic forces (GAF), 424
- Geometrical imperfections, 180–183
- Gumbel's model, 563
- H**
- Hamiltonian systems
 coupled Mathieu equations, 142–144
 damping, 142–144
 Mathieu equations, 138
 periodic γ -Hamiltonian systems, 140–142

- Hamiltonian systems (*cont.*)
 structure, 76
 symplectic matrices (*see* Symplectic matrices)
- Hamilton's principle, 290
- Hammerstein system, 56
- Harmonic balance method (HBM), 551, 554
 and HAM, 65–66
 numerical methods, 66
 oscillator, 73
- Harmonic dynamic tests, 323
- Harmonics, 554
- Helicopter pilot biomechanics
 biodynamics, 440
 control inceptors, 439, 440
 EMG signals, 444–446
 models parameterization, 444
 ship landing task, 444, 445
 trunk model, 443
 upper limb multibody model, 440–443
- High-order shear deformation theory, 248, 250, 255
- Hilbert transform, 374–375
- Hilbert vibration decomposition (HVD), 375
- Hill-type muscular actuators, 411
- Homeomorphisms, 349–350
- Homotopy analysis method (HAM), 66
- Hurwitz matrix, 403
- Hydrodynamic bearings, 562
- Hysteresis dissipation, 263, 264
- Hysteresis loops
 experiment and simulation, 326
- Hysteretic behavior, *see* Wire rope isolators (WRI)
- I**
- Impulsive state feedback control, 108–109, 115
- Inertial frame of reference, 423
- Inner race (IR) defects, 493–495, 498–500
- Instability criterion, 138, 208, 210–212, 214
- Interactive buckling, 208, 210
- Invariant sphere, 158–160, 163, 164
- Invariant torus, 159, 162–165
- J**
- Jeffcott Rotor Model, 486–488
- K**
- Kelvin circulation theorem, 416, 431
- Kelvin–Voigt (KV) model, 320
- Kirchhoff–Love equation, 432
- Korteweg–de Vries (KdV), 76–78
- Kramers' formula, 528
- L**
- Lagrange equation, 537
- Lagrange multipliers, 412
- Landl and Krenk–Nielsen equations, 382
- Largest Lyapunov exponent (LLE), 519
- Lie groups, *see* Multibody system (MBS)
- Lienard–Chipart criterion, 404
- Limit direction
 bifurcations (*see* Bifurcations)
 discontinuity set, 89–90
 Filippov systems, 88
 finite time, 90
 fold, 94
 types, 90–91
- Lindstedt–Poincaré (LP) method, 66, 536, 540, 544, 545
- Linearized 3D dynamical model, 550
- Linearized system, 508
- Linearly parallel-elastic viscosity, 421
- Linearly stable periodic orbit, 159, 162, 163, 165
- Linearly viscous damping materials, 422
- Linear stability analysis
 pitch motion, 123
 yaw and roll motion, 123–124
- Linear time-varying systems (LTVs), 486
- Liquid sloshing
 hydraulic impacts, 187
 mechanical scheme, 188
 model description, 188–189
 numerical results, 192–194
 periodic responses, 189–190
 SIM, 188
 SMRs, 191–192
 weak quasi-periodic responses, 190–191
- Localization
 energy, 283–284
 non-dissipative chains, 280–283
 in oscillator arrays, 277
 resonant dynamics, 278–280
- Lorenz map, 468, 469
- Lyapunov exponents (LE)
 definition, 477
 variant (*see* Variant Lyapunov exponent)
- M**
- Machine learning, 493, 494
- Manifold with boundary, 98
- Markov process, 527

- Masonry structures, *see* Shaking table test
 Mass-damping parameter, 395
 Mass-spring-damper system
 approximate analytical solution, 172–173
 description, 170–171
 mathematical model, 171–172
 MSM, 170
 pendulum-like systems, 169
 resonance (*see* Resonance)
 Mathematical model, 381
 Matlab Optimization Toolbox, 383
 Matrix soliton solutions
 Bäcklund transformations, 76
 equations
 KdV-type, 76, 79–81
 mKdV, 79
 non-commutative potential, 77
 operator method, 78
 Maxwell model, 320, 323
 Mean squared errors (MSE), 325, 327
 Measured step response, 375
 Mechanical-mathematical modeling, 301–302
 Mechanical systems, 98–101
 Method of direct separation of motion, 35, 36, 38
 Method of multiple scales, 170, 172, 173, 176, 261
 Metropoli–Hastings Markov Chain Monte Carlo (MCMC), 304
 Michaelis–Menten (MM) kinetics, 44, 46
 Modal coupling, 179–181, 185, 201, 203, 204, 208, 214
 Modal interaction, 180–183, 185, 186, 208, 210
 Mode I fracture, 340
 Mode II fracture, 341
 Model dimension reduction (MDR), 534, 544–546
 Modified Korteweg-de Vries (mKdV), 76–82
 Monodromy matrix, 14, 15, 17–18, 20, 21, 138, 140–144
 Monte Carlo simulations (MCS), 526
 Morphing wing
 aeroelastic analysis, 430
 dynamic aeroelastic stability, 430
 flutter speed, 434
 Matlab-based VLM code, 433
 SMTE, 430, 431
 vertical aerodynamic pressure distribution, 434, 435
 Motion capture system, 340
 Mratinje dam models, 360
 Multibody
 biomechanical, 440
 models parameterization, 444
 torso model, 443
 trunk model, 443
 upper limb model, 440–443
 Multibody dynamics, 3, 8
 Multibody system (MBS)
 configuration space, 410
 Euclidean space, 411
 fluid-solid system, 415
 geometric modeling approach, 409
 viscosity effects, 415
 vortical effects, 415
 Multi-cutter process, 503
 Multimodal theory, 198, 204
 Multiple scales (MS)
 solution, 200
 in time domain, 176
 in traditional way, 261
 Multiple-scales method (MSM)
 parameter splitting, 67
 split system
 approximated response, 70–71
 FRC, 69–70
 parameters, 71
 unstable region, 70
 Multiplicative noise intensity, 530
 Multivariate analysis, 494
 Munthe–Kaas Lie group method, 412
- N**
- National Instruments NI USB 6363 data acquisition system, 495
 Near-wake oscillator, 390
 Neimark–Sacker bifurcation
 controls
 linear, 109–111
 nonlinear, 111–112
 numerical experiments, 112–115
 Newmark–beta method, 433, 436
 Newton–Raphson method, 564
 Newton's second law, 550
 Noise-induced transition and resonance
 multi-stable systems, 524
 nonlinear dynamical system, 524
 numerous physical systems, 523
 practical dynamical systems, 524
 small time delay approximation, 525
 triple-well potential systems, 524
 Nomenclature, 552
 Non-Abelian equations, 76
 Non-commutative equations, 76, 77
 Non-dimensional conservative force vector, 454

- Non-dimensional equation of motion
 commercial software, 454, 455
 conservative force vector, 454
 dimension of time, 450–451
 efficiency, 454, 455
 kinetic energy, 451–452
 mass matrix, 452
 non-dimensional position vector, 451
 non-dimensional variables, 450
 numerical solution, 454–459
 stiffness matrix, 453–454
 strain energy, 452
- Non-dimensional mass matrix, 452
- Non-inertial frame of reference, 423
- Nonlinear character, 564
- Nonlinear differential equations, 550
- Nonlinear dynamics
 analysis, 210–213
 composite cantilever plate, 248
 formulation, 250–254
*m*ultibody (*see* Multibody dynamics)
 subsonic aerodynamic force, 248–250
 trailer, 124
 vehicle design and aircraft, 247
- Nonlinear energy sink (NES), 227
- Nonlinear hysteretic device
 group A and B, 349–350
 group C, 350–351
 group D tests, 351–352
 homeomorphisms, 349
 rate-independent systems, 347–348
 test apparatus and experimental campaign, 348–349
- Nonlinear model, 56
- Nonlinear non-commutative equations, 26
- Nonlinear oscillator, 253
 coupled, 25
*F*requency *r*esponse *c*urve (FRC)
- Nonlinear parameters, 67
- Nonlinear vibrations
 characteristics, 218
*s*way buckling (*see* Sway buckling)
- Non-smooth dynamical model, 464
- Non-smooth mechanics, 97
- Non-smooth system, 97, 118
- Nonsymmetric restoring force, 350
- Normal form analysis
 dynamical systems, 25
 higher-order terms, 27
 manifold reduction theory, 111
 numerical results, 30–32
 oscillator system, 26
 polynomial differential systems, 159
 single-linear-mode approximation, 26
- Numerical simulation verification, 374
- Numerical values, 555
- O**
- One-dimensional (1D) beam model, 430
- Operational modal analysis (OMA)
 application, 331
 manipulator, 329
 pose dependency, 334–335
 recorded time signals, 332
 reproducibility, 332–333
 shaker reorientation and relocation, 333
- Orbit plots, 498
- Ordinary differential equations (ODEs), 4, 5, 13, 44, 76, 97, 98, 101, 123, 218, 221
- Orthogonal decomposition, *see* Proper orthogonal modes (POMs); Smooth orthogonal decomposition (SOD)
- Orthogonal turning process, 514
- Oscillation death (OD)
 cycle oscillators, 150
 IHSS, 148
 mean-field diffusive coupling, 150
 positive and negative, 150–154
- P**
- Parameter-splitting multiple-scales (PSMS)
 method, 67–73
See also Multiple-scales method (MSM)
- Parametric excitation, 267, 268, 371, 372, 374, 376
 dynamics, 267
 high frequency stabilization, 19–20
 stability conditions, 20–22
 unbounded oscillations, 268
- Parametric instability, 210–213
- Parametric pendulum
 damping, 23
 high frequency stabilization, 19–20
 impulse parametric excitation, 23
 stability conditions, 20–22
- Pareto optimization, 550
- Periodic γ -Hamiltonian systems, 140–142
- Periodic orbit, 159, 161–165
- Perturbation analysis
 analysis, 221
 second order, 202
 singular techniques (*see* Singular perturbation techniques)
 state variable, 14

- Phase modulation
and amplitude (*see* Amplitude modulation)
kinematic excitation, 39, 40
- Photoelasticity
development and application, 357
3D model, 361
dynamic and transient problems, 361
experimental testing and construction, dam,
358
invention and early development, 358–359
multistory building, 362
in nonlinear dynamics, 361–362
static photoelastic analysis, 359
stress concentration, composite matrix,
362–363
- Photoelastic testing, 360–363
3D model, 361
dynamic, 363
seismic impact, 363
- Planar slider-crank mechanism, 7–9
- Poincaré section, 519
- Post-buckling behavior, 208, 214, 238
- Principal component analysis (PCA), 496
- Principal parametric resonance (PPR), 370,
373, 376
- Probability density functions (PDFs)
mass and damping coefficient, 303
mechanical system stiffnesses, 304
nonparametric estimations, 303
- Proper orthogonal coordinates (POCs),
494–496
- Proper orthogonal decomposition (POD),
494–496, 534–535
- Proper orthogonal modes (POMs), 496
- Proper orthogonal values (POVs), 496
- Proposed hysteretic model (PHM)
generalized rate-independent force,
311–312
history variable, 312
parameters, 311, 316
parameter sensitivity analysis, 312–313
- Q**
- Quasi-static test, 323
- Quasi-steady 3-DoFs sectional aerodynamic
model
bridge cables, 400
wind engineering applications, 400
- Quasi-steady drag, 404
- R**
- Rate-dependence matrix, 352–353
- Rate-independent model, *see* Wire rope
isolators (WRI)
- Recursive models, 290
- Reduced-order model (ROM), 267, 443, 540,
542, 544, 545
- Relevant dynamics, 472
- Resonance
circular cylindrical panel (*see* Cylindrical
panel)
external, 173–174
internal, 175–176
localization (*see* Localization)
response curves, 30
- Restoring force surface (RFS)
application, 301
beam and a magnet, 300
experimental setup, 300
nonlinear behavior, 299
stochastic version, 300, 306
system nonlinear behavior, 301
- Reynolds equation, 563, 564
- Reynolds number, 380, 384
- Rigid structure, *see* Vortex-induced vibrations
(VIV)
- Rolling element bearings, 493–494
- Rotating fault simulator machine, 494, 495
- Rotating plane, 551
- Rotating system
amplitudes, 567
Bearing 1 orbit dimension, 566
bearings, 561
early fault detection, 561, 562
hydrodynamic bearings, 565
linear and nonlinear models, 564, 566
numerical model, 562–564
vibration amplitude, 567
- Rotor-bearing model, 540
- Rotorcraft, 439, 440
- Rotorcraft Pilot Couplings (RPCs), 440, 446
- Rotor response measurements, 562
- Rotor system, 534, 535, 540, 546
- Routh–Hurwitz criterion, 403
- Rubber shear springs (RSS)
amplitude-dependent behaviour, 325
elastic model, 321
experimental cyclic tests, 320, 323
experimental results, 320
friction model, 321–322
hysteresis loops, 324–325
quasi-static and harmonic dynamic tests,
323–324
and and Sjöberg's model, 325
viscous properties, 322

- Runge–Kutta algorithm, 394
 Runge–Kutta integration, 550
- S**
 Scruton number, 394
 Second dimension reduction method
 POD, 534
 rotor systems, 533
 Seismic action, 337, 343
 Sensible rate-dependent behavior, 354
 Shaking table test, 337–338
 dynamic response, 339
 experimental tests, 339
 tested masonry building model, 338–339
 Shallow arch
 applications, 237
 structural identification, 237–238
 uniformly loaded, 238–241
 vibration, 241–244
 Shape memory alloy (SMA)
 high-amplitude oscillations, 227
 mathematical model, 228–230
 NES, 227–228
 numerical simulation method, 230–234
 Shear deformation coefficient, 536
 Simplified rocking model, 341–343
 Simultaneous resonance, 177, 218, 221
 Single-axis ultrasonic levitator experimental system, 371
 Single-degree-of-freedom model, 514
 Single-mode approximation, 221, 267, 270
 Singular perturbation techniques
 enzymatic processes, 44
 Goldbeter–Koshland switch, 45
 MM kinetics, 44
 modules, 43
 numerical results, 49–51
 tQSSA, 44
 Singular value decomposition (SVD), 332
 Sjöberg’s model
 parameters, proposed model, 325
 Smooth Coulomb friction force, 320
 Smooth orthogonal decomposition (SOD), 494, 496–497
 Smooth orthogonal values (SOVs), 497
 Smooth projection modes (SPMs), 497
 Snap-buckling, 258, 264, 265
 Spanwise morphing trailing edge (SMTE), 430, 431, 433, 435
 Spectral amplification (SA), 528–529
 Spinning shaft
 analytical methods, 472–476
 chaotic dynamics, 483
 equations of motion, 472
 Euler–Bernoulli isotropic beam, 472
 nonlinear dynamics, 472
 numerical methods, 476–482
 Sprott A system, 158–160, 164, 165
 Spur gears
 analytical procedure, 129–130
 angular velocities, 130–131
 operation, 128
 Stability, 505, 507
 Stability boundaries
 averaging scheme, 15–17
 in 2-dimensional case, 18–19
 Lyapunov’s theorem, 13
 monodromy matrix, 14
 statement, problem, 14–15
 Standard hysteretic damping, 422
 Stationary probability density (SPD), 525, 526
 Steady states, 66, 70, 148, 151, 221, 222, 261, 262
 Steady-state solution stability, 374
 Stochastic model, 302, 304–306
 Stochastic resonance (SR), 529
 Stochastic system parameters, 302
 Straight beams, 268
 Strain energy, 452
 Stress relaxation function, 419
 Stress wave propagation, 362
 Strong nonlinearity, 107, 169
 Structural and aerodynamic parameters, 406
 Structure order reduction (SOR) method, 534
 Subsonic air flow, 248, 254
 Superelasticity, 228
 Supervised learning, 497–498
 Support vector machines (SVM), 494
 Suspended cable, 71, 218, 219, 222
 Sway buckling
 conceptual models, 208
 formulation, 208–210
 natural frequencies, 208–210
 static analysis, 208–210
 structural systems, 208
 Symmetry breaking, 155
 Symplectic matrices
 Floquet theory, 138
 γ -Hamiltonian matrices, 138–139
 μ -symplectic, 138–139
 perturbation techniques, 137–138
- T**
 Taylor expansion, 92, 161, 402, 464–467, 469
 Tensile rate-dependence matrix, 354
 Tension-torsion effect, 297

- Tern and phosphorus cables, 296
 Tested masonry building model, 338–339
 Testing machine (TM), 314
 Thermal environment
 discussions, 221–223
 mathematical modeling, 218–221
 numerical examples, 221–223
 perturbation analysis, 221
 pre-stressed situation, 218
 vibration characteristics, 217
 Thin plate, 431, 432, 451
 Time delay, 524–526, 529, 530
 Timoshenko's beam elements, 562
 Torque
 application position, 295
 vs. twist angle curves, 293–294
 Torque-less activation modes (TLAM), 442, 445
 Torsional analysis
 accelerometer, 291
 ACSR, 289–290
 adjusted curves, 293
 curve parameters, 295
 elastic cables, 290
 excitation system, 291
 experimental and adjusted curves, 293
 load application, 292
 test bench, 290
 torque applied, sample, 293
 transmission line cables, 289
 Trailer
 pitch motion, 123
 rectilinear motion, 117
 snaking, 118–122
 yaw and roll motion, 123–124
 Transient POD (TPOD) method, 534
 Transmission line cables, 290, 291
 Tri-stable phase, 526
 Turning
 chattering, 463
 chip removal, 464
 nonlinear delay system, 464
 regeneration effect, 463
 See also Chatter
 Turning process
 bifurcation analysis method, 514
 chatter, 513
 frictional and regenerative mechanisms, 514
 model, 514–515
 regenerative and frictional force
 bifurcation analysis, 515–517
 dynamic model, 515, 516
 Hopf bifurcation, 515, 516
 stable trivial motion, 518–519
 unstable trivial motion, 518–519
 vibration amplitude, 517, 519
 vibrational properties, 513–514
 Two-wheeled suitcase, 117, 125
- U**
 Unilateral constraint, 98
 Unknown noise term, 56, 62
 Unstable region, 65, 70–73, 144
- V**
 Validation, 383, 385, 386, 440
 Van der Pol and Rayleigh equations, 382
 Variant Lyapunov exponent, 481–483
 Vertical acceleration, 338, 341, 343, 344
 Vibrating flip-flow screens (VFFS), 320
 Vibration
 catenary (*see* Catenary)
 characteristics, 218, 223
 mechanics (*see* Vibrational mechanics)
 shallow arch (*see* Shallow arch)
 Vibrational mechanics
 amplitude and phase modulation, 37–40
 force, 36
 machines and technologies, 35
 slow motions, 36
 Vibration energy dissipation
 damping, 258
 dynamic excitation, 257
 FRC
 excitation, 262–264
 potential function, 264–265
 model development, 258–260
 oscillations
 interwell, 261–262
 intrawell, 260–261
 Vibro-impact system
 angular velocities, 130–131
 bifurcations, 107
 dynamics, 128
 impulsive state feedback control, 108–109
 input parameters, 131–132
 oscillations, 132–135
 sloshing, 188
 spur involute gears, 128, 130
 system state variables, 108
 tooth flanks, 128–129
 transmission ratio, 127
 Viscoelastic damping, 419, 421, 425–426
 Viscoelastic material
 Biot damping model, 422–423

- Viscoelastic material (*cont.*)
 damping behavior, 419, 420
 linearly viscous damping, 422
 standard hysteretic damping, 422
 viscoelastic discretized problem, 420
- Viscous sub-models, 321
- Vortex-induced vibrations (VIV)
 calibrated models, 386
 2DOF structures, 380
 experimental data, 384–385
 fluid density, 381
 fluid nonlinearities, 381, 384
 and galloping, 389
 modelling, 379
 nonlinear behavior, 390
 oscillating rigid structure, 381
 shedding frequency, 382
- Vortex Lattice (VL) method, 248, 249, 254
- Vortex lattice method (VLM), 248, 249,
 430–433
- W**
- Wake oscillator equations, 383
- Wake-oscillator model, 380, 390–392
- Washing machines
 acoustical and visual terms, 549
 amplitude, 558
 displacement *vs.* spin speed, 559
 2D model, 550
 drum *vs.* spin speed, 555, 556
 dry friction damper, 558
 engineering trade-off, 557
 Fourier coefficients, 555, 556
- function frequency, 555
 mathematical modeling, 551–555
 nonlinear friction force, 555
 orientation angles, 557, 558
 passive balancing system, 550
 transmitted forces, 557, 558
 transmitted force *vs.* spin speed, 555–557, 559
- Weak form of equations of motion, 4, 6
- Wear**
spur gears (*see* Spur gears)
vibro-impact (*see* Vibro-impact system)
- Wear parameters, 562
- Wire rope isolators (WRI)
 geometrical characteristics, 313–314
 rate-independent models, 309
 roll and shear directions, 310
 satisfactory agreement, 315
 shear direction, 314–315
 tested, 314
 and TM, 314
- Z**
- Zero-Hopf bifurcation
averaging theory (*see* Averaging theory)
 dynamical behavior, 158
 invariant spheres, 159–160
 nested invariant tori, 162–164
 polynomial differential system, 157–158
 quadratic polynomial differential systems, 158
- Zwick Roell testing machine, 348